Exploring the secrets of elementary particles

at the CERN LEP and LHC colliders

Doctoral dissertation

Dr. Gabriella Pásztor

Eötvös Loránd University
Institute of Physics

Hungarian Academy of Sciences
XI. Section of Physical Sciences

Budapest
October 2023

2023

Dr. Gabriella Pásztor

Contents

Foreword

The standard model (SM) of particle physics successfully describes the phenomena encountered in high-energy collisions of subatomic particles in the laboratory, even though it leaves many questions unanswered. This implies that it is a successful effective theory that hides a more fundamental description of Nature. The quest to measure precisely the phenomena predicted by the SM and find evidence for new physics beyond its validity is the leading motivation to construct ever more powerful particle colliders worldwide.

The Large Electron-Positron (LEP) collider operated at center-of-mass energies of $\sqrt{s} = 89 - 209$ GeV until 2000 at CERN, the largest particle physics laboratory in the world. The LEP experiments measured phenomena at the electroweak scale with high precision, in particular the properties of the weak gauge bosons. Its successor, the Large Hadron Collider (LHC) provides proton − proton collision data at $\sqrt{s} = 0.9 - 13.6$ TeV since 2009. It is the highest energy accelerator ever built, opening a window to the TeV energy regime. It was constructed to either discover the Higgs boson, the key evidence that our understanding of electroweak symmetry breaking and the generation of the masses of elementary particles is correct, or to find the consequences of an alternative solution realized in nature for the regularization of the electroweak vector boson scattering cross sections at high energies.

This work summarizes my results that contribute to today's understanding of particle physics. At the turn of the 21st century, the LEP data were used to study diboson (WW and ZZ) production and search for exotic phenomena predicted by extensions of the SM, such as those that assume the existence of supersymmetry or extra spatial dimensions. The negative direct and indirect search results were used to put constraints on these models and set the stage for the LHC physics program.

In the first years of the LHC, measurements of well-known processes were performed at the new energies, such as the high-rate inclusive b hadron production followed by a weak decay leading to leptons in the final state, or the electroweak Drell–Yan production of lepton pairs. These initial efforts pawed the way to the discovery of the Higgs boson in 2012. The study of the properties of this unique particle and the hunt for new phenomena by precisely measuring electroweak processes, in particular the pair production of electroweak gauge bosons, continue. These efforts are complemented by direct searches for new exotic phenomena.

The LHC studies presented here rely to a large extent on electrons and photons in the final state. The methodology development and the performance studies for the reconstruction of these physics objects, as well as for the fast real-time event selection by the trigger systems that allows to collect the necessary data samples are essential to reach the physics objectives. Due to the ever improving precision of the LHC measurements, new challenges also arise, such as the need for the precise determination of the luminosity, a common ingredient of most measurements.

This work is structured as follows. Chapter 1 sketches the theoretical framework of the SM and its extensions. Chapter 2 gives an overview of the legacy of the LEP collider, focusing on the results of the searches I participated in at the OPAL experiment for signs of new phenomena, such as an extended Higgs sector, supersymmetric partner particles and excited states due to the presence of extra spatial dimensions.

Chapter 3 highlights the complexity of high-energy physics research from the birth of an idea to the experimental results and discoveries, and the challenges along the road, including various sources of systematic effects that need to be countered. It also introduces the inner workings and the organization of large international collaborations, such as ATLAS and CMS at the LHC, and briefly reviews some of the technical and experimental developments I contributed to.

Chapter 4 discusses the physics aspects and the methods of precision luminosity measurements at hadron colliders, the CMS precision luminosity determination in Run 2, and the strategy and detector development efforts for the High-Luminosity Large Hadron Collider (HL-LHC).

Chapter 5 focuses on the SM Higgs boson, giving an account from my first auxiliary studies to the discovery and to the early property measurements by the ATLAS experiment. It discusses the experimental ingredients needed as well as the analysis methods. The discussion is closed with a summary of the present status of the research.

Chapter 6 looks at studies beyond the standard model at the LHC using the data of the ATLAS and CMS collaborations following two complementary approaches: measurements of electroweak gauge boson production interpreted in extended models including higher dimensional effective field theories, and direct searches for exotic phenomena, in particular the production of new heavy particles in models with supersymmetry and extra dimensions.

The work closes with a brief outlook on the future.

Chapter 1

The standard model and beyond

The standard model of particle physics (SM) [1–4] describing the elementary particles and their electroweak and strong interactions is a non-abelian $SU(3)_\mathrm{C} \times SU(2)_\mathrm{L} \times U(1)_\mathrm{Y}$ quantum field theory where the indices stand for the color (C) charge of the strong force, the left-handed (L) chiral doublets of fermions described by the weak isospin, and the weak hypercharge (Y). The theory is populated by three families of elementary fermions (lepton and quarks), among which the interactions are transmitted by gauge bosons (the photon, the W and Z bosons and the gluons) as shown in Figure 1.1.

The theory was developed by the late 1960s by many physicists. The non-abelian extension of gauge theories [1] necessary to describe the strong interaction of the quarks – mediated by the self-interacting gluons – was developed by Yang and Mills in 1954. The unification of the electromagnetic and weak forces and the inclusion of the Brout-Englert-Higgs (BEH) mechanism [5–7] are thanks to Glashow, Salam and Weinberg who received the Nobel prize in 1979, after the discovery of the weak neutral currents [8, 9] at the Proton Synchroton (PS) at CERN in 1973 by the Gargamelle bubble chamber experiment.

The W [10, 11] and Z [12, 13] bosons were experimentally observed in 1983 at the Super Proton–Antiproton Synchrotron (Sp$\bar{\mathrm{p}}$S) by the UA1 and UA2 experiments bring-

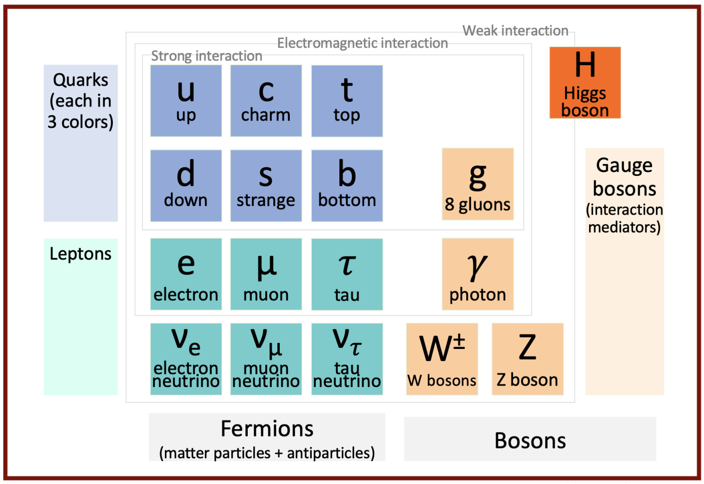

Produced by G. Pásztor, 2013

Figure 1.1: *The elementary particles of the standard model, including three families (or generations) of fermions forming the visible matter content of the universe, gauge bosons mediating the fundamental gauge interactions, and the Higgs boson.*

ing the first Nobel Prize to CERN, awarded to the UA1 spokesperson Carlo Rubbia and the accelerator physicist Simon van der Meer who developed the stochastic cooling technique [14]that allowed the preparation of intense particle beams. The SM predictions were tested at various particle colliders since then, in particular the properties of the Z [15] and W bosons [16–18] and the parameters of the SM [15–23] were measured with impressive precision at the Large Electron-Positron Collider (LEP), the Stanford Linear Collider (SLC), the Tevatron, the Large Hadron Collider (LHC), and various experiments targeting the flavor sector. The number of light neutrino species was measured to be 2.9840±0.0082 at LEP via the determination of the width of the Z boson [15].

The cornerstone of the SM is the Brout-Englert-Higgs (BEH) mechanism [5–7] that describes the spontaneous breaking of the electroweak $SU(2)_\mathrm{L} \times U(1)_\mathrm{Y}$ symmetry (EWSB) to the $U(1)_\mathrm{Q}$ group of the electromagnetic (EM) interaction. The BEH mechanism explains how the weak gauge bosons acquire their mass and thus makes the theory renormalizable [24]. It also predicts a physical scalar particle, the Higgs boson [5] whose mass depends on the parameters of the scalar potential that is instrumental in the symmetry breaking. The Higgs boson discovery [25, 26] with a mass[1] of $m_\mathrm{H} \approx 125$ GeV at the LHC in 2012 completed experimentally the predicted particle spectrum and brought the Nobel prize in 2013 to François Englert and Peter Higgs with a mention by the committee of the observation provided by the ATLAS and CMS Collaborations.

The Higgs contribution is also important to regularize the weak vector boson scattering amplitudes in the SM, thus the measurement of vector boson pair production processes at high energy colliders also provides a powerful test of the model. The LHC ”no-lose” theorem [27] was based on searching for the Higgs boson and studying electroweak diboson production. It stated that either a Higgs boson would be discovered with a mass below 1 TeV or the longitudinal components of the W and Z bosons would interact strongly and an enhanced diboson production was to be observed [28].

The masses of the elementary fermions are generated by Yukawa couplings to the Higgs field in the SM. They vary over about 11 orders of magnitude from neutrinos to heavy quarks, the masses increasing with the family index. The very light neutrinos ($m_{\nu_\mathrm{e}} < 0.8$ eV at the 90% CL [29]) are expected to be massless in the SM and thus call for its extension. The top quark is the only fermion that has a mass ($m_\mathrm{t} = 172.69 \pm 0.30$ GeV [30]) close in value to that of the Higgs boson and the energy scale of symmetry breaking (characterized by the vacuum expectation value of the Higgs field $v \approx 246$ GeV), thus it is speculated to have a special role in EWSB (see for example Refs. [31–33] for supergravity models where EW symmetry is broken radiatively by corrections from the top and the scalar top quarks). In any case, due to its large Yukawa coupling to the Higgs, it plays an important role in understanding the electroweak sector.

Even though the phenomena measured at colliders agree very well with the predictions, the SM cannot be the final word in particle physics as it leaves many open questions. It does not include gravity described by Einstein’s general relativity. It has no candidate for dark matter [34] that dominates over ordinary matter in the ΛCDM model of cosmology. It also has no mechanism that leads to cosmological inflation which is often hypothesized to solve some problems in standard cosmology [35]. While it provides a mechanism to generate a non-zero baryon asymmetry [36], it cannot explain its observed value [37]. Neutrino oscillations and the small but non-zero mass of neutrinos

---

[1] The common $\hbar = c = 1$ convention of natural units is used throughout this work. Accordingly not only energy, but also momentum and mass are quoted in units of eV. More generally, it means that units of length (l), time (t), and mass (m) are related to the unit of energy (E): $[E] = [m] = [l]^{-1} = [t]^{-1}$.

also lie outside of its realm. The three couplings of the gauge interactions do not meet in a single point at high energies, which suggests that so far undiscovered fields might also contribute to their running in the renormalization group evolution.

Moreover, the observed Higgs boson mass also raises its own problems, such as how it is protected against large quantum corrections from physics at higher energy scales, also known as the hierarchy or naturalness problem of the SM [38–40]. There is also the theoretical consideration related to the appearance of the Landau pole, called the triviality problem, even though for the observed Higgs mass, the pole can lie beyond the Planck scale. Nonetheless, the cut-off scale for the running self-coupling cannot be taken to infinity for an interacting scalar field or an abelian gauge theory.

All these considerations lead us to believe that the SM is an effective field theory (EFT) [41, 42] that hides a more fundamental description of nature. The hunt for direct manifestations of this ”beyond the standard model” (BSM) theory, often called the search for ”new physics” (NP), is the most exciting challenge in high energy physics (HEP) today. For detailed reviews of the state of the art in these areas, see Ref. [30].

1.1 The standard model and its parameters

The Lagrangian of the SM can be written considering four different contributions:

$$\mathcal{L}_{\mathrm{SM}} = \mathcal{L}_{\mathrm{YM}} + \mathcal{L}_{\mathrm{F}} + \mathcal{L}_{\mathrm{S}} + \mathcal{L}_{\mathrm{Yuk}} \tag{1.1}$$

Gauge invariance determines both the spin-1 particle content and their gauge interactions described by the Yang–Mills part ($\mathcal{L}_{\mathrm{YM}}$) of the Lagrangian. The spin-1/2 fermion particle content is given in Table 1.1. Left- and right-handed chiral projections of the fermions are defined by $P_{\mathrm{L/R}} = (1 \mp \gamma^5)/2$. The $U(1)_{\mathrm{Y}}$ quantum number, the weak hypercharge is calculated from the electric charge (Q, in units of the positron charge e) and the 3rd component of the $SU(2)_{\mathrm{L}}$ quantum number, the weak isospin (T_{L}) as $Y = 2(Q - T_{\mathrm{L},3})$, thus it gives twice the average electric charge of the particles in the weak isospin multiplet. As neutrinos appear to violate parity (P) maximally, no right-handed neutrino is introduced. Left-handed fermions are put into $SU(2)_{\mathrm{L}}$ doublets, while right-handed fermions are singlets. The quarks are charged under $SU(3)_{\mathrm{C}}$ and are in the fundamental triplet representation. The three values of the color charge also make the theory anomaly-free, ensuring that the sum of the electric charges within a family is zero. Each fermion has its antifermion pair with opposite quantum charges, the two linked by the operation of charge conjugation (C).

Fermion field	$SU(3)_{\mathrm{C}}$	$SU(2)_{\mathrm{L}}$	Y	Q [e]	$T_{\mathrm{L},3}$
$q_{a\mathrm{L}} \equiv \begin{pmatrix} u_{a\mathrm{L}} \\ d_{a\mathrm{L}} \end{pmatrix}$	**3**	**2**	+1/3	+2/3 −1/3	+1/2 −1/2
$\ell_{a\mathrm{L}} \equiv \begin{pmatrix} \nu_{a\mathrm{L}} \\ e_{a\mathrm{L}} \end{pmatrix}$	**1**	**2**	−1	0 −1	+1/2 −1/2
$u_{a\mathrm{R}}$	**3**	**1**	+4/3	+2/3	0
$d_{a\mathrm{R}}$	**3**	**1**	−2/3	−1/3	0
$e_{a\mathrm{R}}$	**1**	**1**	−2	−1	0

Table 1.1: *The chiral particle content of the SM, where a=1..3 is the family (or generation) index.* $SU(3)_{\mathrm{C}}$ *indices of quarks are implicit.*

Given these quantum number assignments, gauge invariance determines the fermion – gauge boson interactions in $\mathcal{L}_{\mathrm{F}}$. The last two parts of the Lagrangian describing the scalar sector and the Yukawa interactions of fermions, $\mathcal{L}_{\mathrm{S}}$ and $\mathcal{L}_{\mathrm{Yuk}}$, are instrumental to describe two crucial physical phenomena: the spontaneous breaking of the local $SU(2)_{\mathrm{L}} \times U(1)_{\mathrm{Y}}$ gauge symmetry down to $U(1)_{\mathrm{Q}}$ via the BEH mechanism, and the explicit breaking of the global flavor symmetry. They are responsible for the generation of the weak gauge boson and fermion masses by introducing a complex spin-0 $SU(2)_{\mathrm{L}}$ doublet, $SU(3)_{\mathrm{C}}$ singlet, $Y = 1$ field, the Higgs field: $\phi \equiv \begin{pmatrix} \varphi^{+} \\ \varphi^{0} \end{pmatrix}$. The mathematical form of the Lagrangian with the discussed field content is written as

$$\begin{aligned}
\mathcal{L}_{\mathrm{YM}} &= -\frac{1}{4} G^{\mu\nu\,A} G^{A}_{\mu\nu} - \frac{1}{4} W^{\mu\nu\,I} W^{I}_{\mu\nu} - \frac{1}{4} B^{\mu\nu} B_{\mu\nu}, &(1.2)\\
\mathcal{L}_{\mathrm{F}} &= i\bar{\Psi}_f \gamma^{\mu} D_{\mu} \Psi_f, &(1.3)\\
\mathcal{L}_{\mathrm{S}} &= (D_{\mu}\phi)^{\dagger}(D^{\mu}\phi) - V(\phi), &(1.4)\\
\mathcal{L}_{\mathrm{Yuk}} &= h^{e}_{ab} \bar{\ell}_{a\mathrm{L}} e_{b\mathrm{R}} \phi + h^{d}_{ab} \bar{q}_{a\mathrm{L}} d_{b\mathrm{R}} \phi + h^{u}_{ab} \bar{q}_{a\mathrm{L}} u_{b\mathrm{R}} \tilde{\phi} + h.c., &(1.5)
\end{aligned}$$

with

$$\begin{aligned}
G^{A}_{\mu\nu} &= \partial_{\mu} G^{A}_{\nu} - \partial_{\nu} G^{A}_{\mu} + g_s f^{ABC} G^{B}_{\mu} G^{C}_{\nu}, &(1.6)\\
W^{I}_{\mu\nu} &= \partial_{\mu} W^{I}_{\nu} - \partial_{\nu} W^{I}_{\mu} + g f^{IJK} W^{J}_{\mu} W^{K}_{\nu}, &(1.7)\\
B_{\mu\nu} &= \partial_{\mu} B_{\nu} - \partial_{\nu} B_{\mu}, &(1.8)\\
D_{\mu} &= \partial_{\mu} - i g_{\mathrm{s}} G^{A}_{\mu} \frac{\lambda_A}{2} - i g W^{I}_{\mu} \frac{\sigma_I}{2} - i g' B_{\mu} \frac{Y}{2}, &(1.9)\\
V(\phi) &= -\mu^{2} \phi^{\dagger}\phi + \lambda(\phi^{\dagger}\phi)^{2}, &(1.10)
\end{aligned}$$

where f^{ABC} and f^{IJK} are the fully antisymmetric $SU(3)$ and $SU(2)$ structure constants, γ^{μ} are the Dirac matrices, $\frac{\lambda_A}{2}$, $\frac{\sigma_I}{2}$ and $\frac{Y}{2}$ stand for the hermitian generators of the $SU(3)_{\mathrm{C}}$, $SU(2)_{\mathrm{L}}$ and $U(1)_{\mathrm{Y}}$ gauge groups (with λ_A being the Gell-Mann and σ_I the Pauli matrices), and g_{s}, g and g' are the corresponding coupling parameters. The parameters of the scalar potential $V(\phi)$, $\mu^{2} > 0$ and $\lambda > 0$, determine the mass and the self-coupling of the Higgs boson. h^{e}, h^{d} and h^{u} are arbitrary 3×3 complex matrices in generation space corresponding to up- and down-type quarks and charged leptons. Ψ_f runs over all fermion (matter) fields for the three generations: $\Psi_f \equiv (q_{a\mathrm{L}}, u_{a\mathrm{R}}, d_{a\mathrm{R}}, \ell_{a\mathrm{L}}, e_{a\mathrm{R}})_{a=1..3}$, which are described by spinors. The SU(3) color indices of quarks are left implicit for simplicity. The electroweak boson fields B_{μ} and $W^{I}_{\mu} (I = 1..3)$, as well as the gluon fields $G^{A}_{\mu} (A = 1..8)$ are vector fields with Lorentz indices μ. For the scalar Higgs field ϕ, we define $\tilde{\phi} = (i\sigma_2 \phi^{*})$.

The scalar potential has an infinite number of minima at

$$|\phi| = \frac{v}{\sqrt{2}} = \sqrt{\frac{\mu^{2}}{2\lambda}}. \tag{1.11}$$

The choice of the lowest energy (vacuum) state of the system breaks the $SU(2)_{\mathrm{L}} \times U(1)_{\mathrm{Y}}$ symmetry of the Lagrangian via the BEH mechanism. The EW fields mix to give the massless photon field (A), and the massive electrically neutral Z boson (Z) and charged W boson ($W^{\pm}$) fields with the Weinberg angle (θ_{W}) describing the rotation in the (W^{3}, B) plane in the neutral sector:

$$\begin{aligned}
A &= W^{3} \sin\theta_{\mathrm{W}} + B \cos\theta_{\mathrm{W}}, &(1.12)\\
Z &= W^{3} \cos\theta_{\mathrm{W}} - B \sin\theta_{\mathrm{W}}, &(1.13)\\
W^{\pm} &= (W^{1} \mp i W^{2})/\sqrt{2}. &(1.14)
\end{aligned}$$

The weak hypercharge is zero for these fields.

After the EWSB, the scalar Higgs field has a non-zero vacuum expectation value (VEV, v) and acquires a mass of

$$m_{\mathrm{H}} = \frac{\mu}{\sqrt{2}} = \sqrt{2\lambda}v. \tag{1.15}$$

The masses of the W and Z bosons can also be derived:

$$m_{\mathrm{W}} = \frac{vg}{2}, \tag{1.16}$$

$$m_{\mathrm{Z}} = \frac{v\sqrt{g'^2 + g^2}}{2}. \tag{1.17}$$

It is also useful to define the parameter

$$\rho \equiv m_{\mathrm{W}}^2/(m_{\mathrm{Z}}^2 \sin^2\theta_{\mathrm{W}}) \tag{1.18}$$

that is 1 at tree level in the SM. These relations are modified by higher order corrections. Experimental determination of ρ probes the mechanism of EWSB and could help to distinguish whether the minimal SM or an extended Higgs sector (see Section 2.2) is realized in nature [30].

The parameters of the flavor sector can be derived by diagonalizing the $h^{e,d,u}$ Yukawa matrices leading to "only" 13 parameters, instead of the $3{\cdot}3{\cdot}3{\cdot}2 = 54$ parameters in $\mathcal{L}_{\mathrm{Yuk}}$. The nine Yukawa couplings y_f of the fermions to the Higgs field can be exchanged to the fermion masses: $m_f = y_f v/\sqrt{2}$. The remaining four parameters arise in the CKM (Cabibbo–Kobayashi–Maskawa) matrix [43, 44] which describes flavor mixing in the quark sector. Its origin is related to the feature that h^d and h^u cannot be diagonalized simultaneously and thus a basis change is necessary for the charged current interactions which connect u- and d-type fermions. The CKM matrix, which also introduces charge conjugation times parity (CP) violation to the SM, brought the Nobel prize to Kobayashi and Maskawa in 2008.

For the case of massless neutrinos, the SM thus has 19 free parameters. There is some freedom in choosing these. It is customary to use the three lepton ($m_{\mathrm{e}}, m_\mu, m_\tau$) and the six quark ($m_{\mathrm{d}}, m_{\mathrm{u}}, m_{\mathrm{s}}, m_{\mathrm{c}}, m_{\mathrm{b}}, m_{\mathrm{t}}$) masses, the CKM mixing angles ($\theta_{12}, \theta_{23}, \theta_{13}$) and CP-violating phase (δ), the U(1), SU(2) and SU(3) gauge couplings (g', g, g_{s}), the Higgs mass (m_{H}), and the Higgs vacuum expectation value (v). The last one, the QCD vacuum phase (θ_{QCD}) is found experimentally to be ≈ 0. The CP-violating term of the QCD Lagrangian

$$\mathcal{L}_\theta = -\theta_{\mathrm{QCD}} \frac{g_{\mathrm{s}}^2}{32\pi^2} G^{\mu\nu\,A} \tilde{G}^A_{\mu\nu}, \tag{1.19}$$

$$\tilde{G}^A_{\mu\nu} = \frac{1}{2}\epsilon_{\mu\nu\alpha\beta} G^A_{\alpha\beta}, \tag{1.20}$$

with $\epsilon_{\mu\nu\alpha\beta}$ being the Levi-Civita symbol, is thus usually omitted from $\mathcal{L}_{\mathrm{SM}}$. The implied fine-tuning, often called the strong CP problem, has motivated the proposal of a hypothetical elementary particle and cold dark matter candidate, the axion by Peccei and Quinn in 1977 [45] but has not been observed experimentally.

The SU(3) coupling parameter is used to define the strong coupling strength α_{s}, and the electroweak U(1) and SU(2) coupling parameters can be substituted by the fine-structure constant α_{EM}, and the Weinberg angle θ_{W}:

$$\alpha_{\mathrm{s}} = \frac{g_{\mathrm{s}}^2}{4\pi}, \qquad \alpha_{\mathrm{EM}} = \frac{g^2 g'^2}{4\pi(g^2 + g'^2)}, \qquad \tan\theta_{\mathrm{W}} = \frac{g'}{g}. \tag{1.21}$$

The Higgs sector can be parametrized directly by the self-coupling λ and mass μ parameters of the scalar potential:

$$\lambda = \frac{m_{\mathrm{H}}^2}{2v^2}, \qquad \mu^2 = \frac{m_{\mathrm{H}}^2}{2}. \tag{1.22}$$

Accommodating non-zero masses in the neutrino sector requires seven additional parameters: three neutrino masses, three mixing angles and a CP-violating phase of the PMNS (Pontecorvo–Maki–Nakagawa–Sakata) neutrino mixing matrix [46, 47], and also new physics as in the absence of a right-handed neutrino the usual Yukawa term that describes fermion masses cannot be employed. Thus either a (right-handed) "sterile", i.e. not weakly interacting neutrino with $Y = 0$ need to exist, or the neutrino must be a Majorana particle by being its own anti-particle and thus having a different type of mass term. The explanation of the very small value of neutrino masses is also considered a gateway to new physics.

The self-consistency of the model can be tested by precisely measuring these parameters and verifying the predicted relations in the over-constrained system. Global SM fits to collider data thus provide a powerful tool to verify the validity of the SM. The global fits can also reliably predict unmeasured parameters of the theory as was the case for the masses of the top quark and the Higgs boson before their direct observation. The final results using the LEP and SLD data are shown in Figure 1.2 and give $m_{\mathrm{t}} = 178.1^{+10.9}_{-7.8}$ GeV and $m_{\mathrm{H}} = 148^{+237}_{-81}$ GeV [16]. They manifest an excellent agreement with the best direct measurements today: $m_{\mathrm{t}} = 172.52 \pm 0.33$ GeV [48] and $m_{\mathrm{H}} = 125.11 \pm 0.11$ GeV [49]. The latest results from the Gfitter collaboration [50] in Figure 1.3 also show consistency within the current uncertainties with a p-value of 0.23

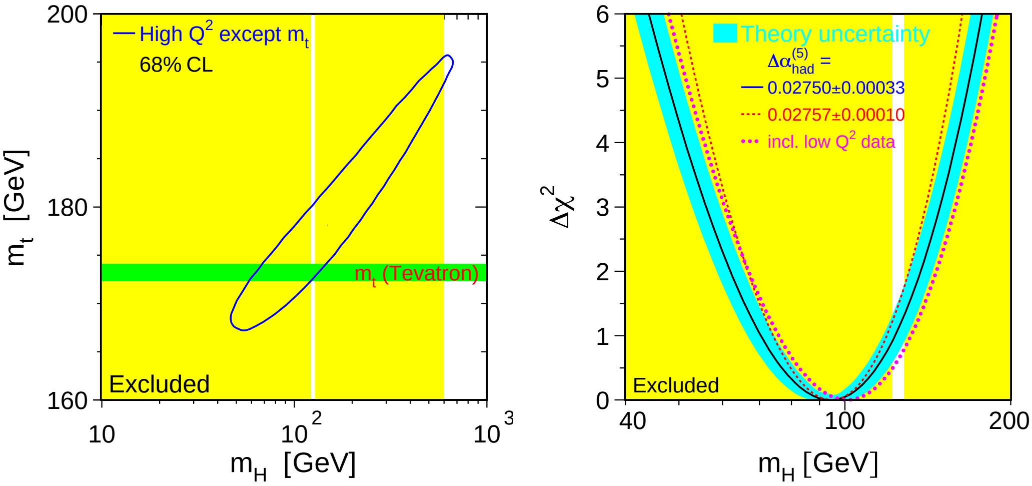

Figure 1.2: *(left) 68% confidence level (CL) contour in the (m_{t}, m_H) plane from the fit to LEP and SLC data, compared to the direct m_{t} measurement of Tevatron (shaded horizontal band of ±1σ width) and the 95% CL exclusion ranges on m_H from the direct searches (vertical bands) as of 2013 March. (right) Values of $\Delta\chi^2 = \chi^2 - \chi^2_{\mathrm{min}}$ as a function of the assumed m_H, including m_{t} measurement in the fit. The solid line with the blue band is the fit result using all high-Q^2 data with the theoretical uncertainty due to missing higher order corrections. The vertical bands show the 95% CL exclusion ranges on m_H. The dashed curve corresponds to an alternative evaluation of the hadronic contribution to $\alpha_{\mathrm{EM}}(m_Z)$, while the dotted curve includes the low-Q^2 data. [16]*

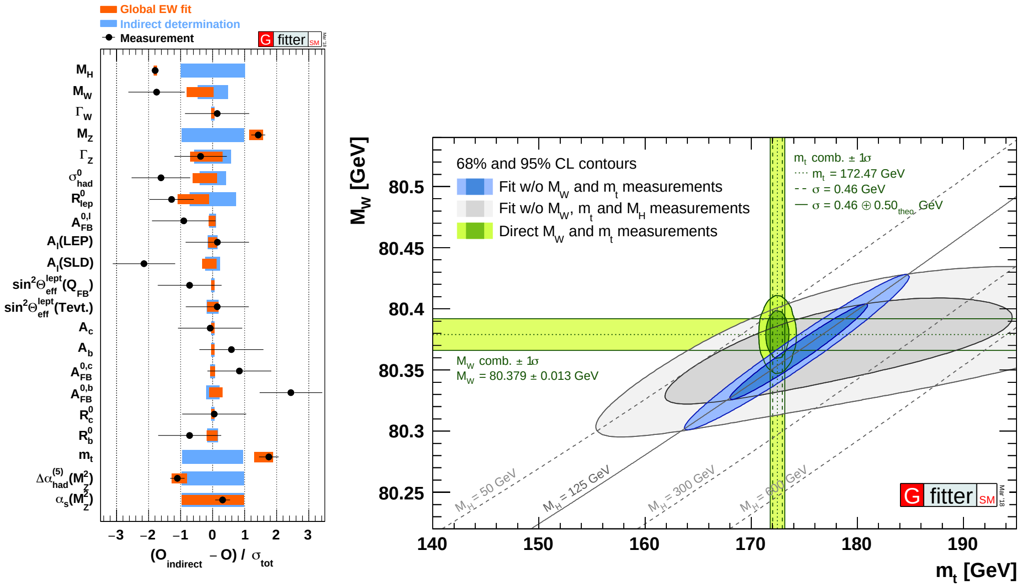

Figure 1.3: *(left) Gfitter global SM fit results (orange bars) and direct measurements (data points) compared to indirect determinations obtained without using the experimental measurement corresponding to the given variable. The plotted pull values are calculated as the deviations from the indirect determinations normalized by the total error (quadratic sum of errors on the indirect determination and the input measurement). The contributions of the in direct measurements to the total uncertainty are shown (blue bars). (right) Contours at the 68% and 95% CLs in the* (m_W, m_t) *plane. The blue and grey allowed regions are the fit results including and excluding the* m_H *measurement, respectively. The horizontal and vertical bands indicate the 1*σ *regions of the direct* m_W *and* m_t *measurements. [50]*

($\chi^2 = 18.6$ for 15 degrees of freedom). An improved W boson mass measurement would allow a more stringent test of the model and is therefore one of the precision physics goals of the LHC collaborations.

This came into the limelight recently when the CDF experiment published their final W mass determination of 80.4335 ± 0.0094 GeV [51] that claims a precision better than the current world average of 80.377 ± 0.012 GeV [30] and shows a significant tension with previous measurements and the global SM EW fit result of 80.356 ± 0.006 GeV [30]. The latest combination of the LEP, Tevatron and LHC W mass results in a value of 80.3946 ± 0.0115 GeV [52] and has a low probability of compatibility when including the CDF value: below 0.5% for all tested parton distribution function sets. The probability increases to 75–96% when the CDF result is excluded and the central value of 80.3692 ± 0.0133 GeV gets close to the world average and differs by 3.6σ from the CDF value. Further studies are needed to resolve this discrepancy.

1.2 Gauge couplings and new physics

In the SM at tree level only charged triple- and quartic gauge couplings (TGCs and QGCs) are allowed. In the electroweak sector these are: WWZ, WWγ, WWWW, WWZZ, WWZγ, and WW$\gamma\gamma$. However, higher-order (HO) corrections via fermion or boson loops can contribute to neutral vertices as well, as shown in Figure 1.4. Similarly, anomalous (i.e. beyond the SM) triple and quartic gauge couplings (aTGCs and aQGCs) could originate from new physics such as supersymmetry [53] through similar diagrams with new "exotic" particles in the loops.

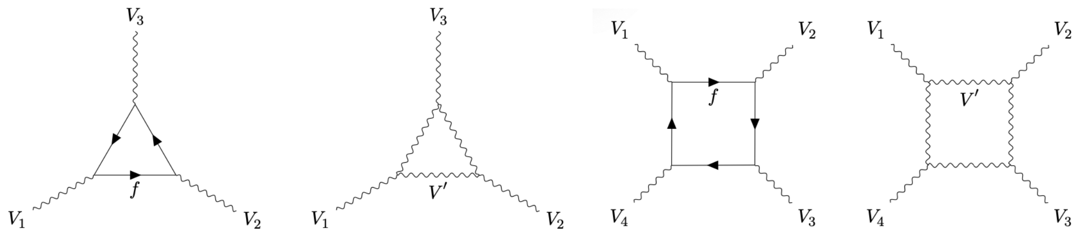

Figure 1.4: *Higher order diagrams contributing to (left) triple and (right) quartic gauge couplings via fermion or boson loops. In the SM, loops via light fermions give the largest contribution.*

To describe the effect from new physics two main approaches are used. Traditionally, in the interpretation of LEP electroweak measurements, the SM was extended with anomalous triple gauge boson couplings that do not necessarily preserve the SM gauge symmetries [54–57]. After the discovery of the Higgs boson and the precise measurements of electroweak processes in the last decade, it is no longer motivated to use such a permissive framework. The LHC experiments thus switched to a more natural, gauge invariant way [58, 59] to capture the effects of physics beyond the standard model using an effective field theory (EFT) approach [60–62] that also allows a consistent inclusion of higher order effects.

The SM is a renormalizable theory and thus its Lagrangian given in Eq. 1.1 contains only operators with four mass dimensions (dim-4), where fermion fields are dim-3/2, scalar and vector boson fields and covariant derivatives are dim-1. Acknowledging our ignorance of the details of the physics at high energy scales, one can extend the theory assuming that it respects certain symmetries, in particular the EW $SU(2)_\mathrm{L} \times U(1)_\mathrm{Y}$, and look at possible higher dimension (dim-N) operators suppressed at an energy E by $(E/\Lambda)^{N-4}$, with Λ being the energy scale of new physics. EFTs are thus non-renormalizable.

In the so-called standard model effective field theory (SMEFT) framework [63, 64], contributions from higher order operators are added to the SM Lagrangian:

$$\mathcal{L}_\mathrm{SMEFT} = \mathcal{L}_\mathrm{SM} + \sum_{n=1}^{\infty} \sum_{i} \frac{c_i^{(n)}}{\Lambda^n} \mathcal{O}_i^{(n+4)}, \tag{1.23}$$

where $c_i^{(n)}$ are the Wilson-coefficients associated to the dim-(n+4) operators of $\mathcal{O}_i^{(n+4)}$. The SM Lagrangian contains all operators consistent with its particle content up to dimension four. The powers of the energy scale Λ of new physics suppress the higher dimensional operators following the power counting rule shown in Eq. 1.23. The operators themselves are constructed based on the particle content at low energy. In the limit of $\Lambda \to \infty$ the SM is recovered.

The only dim-5 operator consistent with the field content and the local symmetries is the lepton number (L) violating ($\Delta L = 2$) Weinberg operator [65] that leads to a Majorana mass term for the SM neutrinos. The energy scale is expected to be high (the ”see-saw” scale [66, 67]), and thus not relevant for collider phenomenology. If baryon (B) and lepton numbers are conserved, only operators with even dimension can be considered, so new physics would appear in the form of dim-6 and dim-8 operators.

Concentrating on the EW boson interactions and assuming CP conservation, the

SMEFT Lagrangian up to dim-8 becomes [68]:

$$\begin{aligned}\mathcal{L}_{\mathrm{SMEFT}} &= \mathcal{L}_{\mathrm{SM}} + \sum_{i=WWW,W,B,\phi W,\phi B} \frac{c_i}{\Lambda^2}\mathcal{O}_i^{(6)} \\ &+ \sum_{i=0,1} \frac{f_{\mathrm{S},i}}{\Lambda^4}\mathcal{O}_{\mathrm{S},i}^{(8)} + \sum_{i=0,..,9} \frac{f_{\mathrm{T},i}}{\Lambda^4}\mathcal{O}_{\mathrm{T},i}^{(8)} + \sum_{i=0,..,7} \frac{f_{\mathrm{M},i}}{\Lambda^4}\mathcal{O}_{\mathrm{M},i}^{(8)} \qquad (1.24)\end{aligned}$$

From the 59 independent $\Delta L = \Delta B = 0$ dim-6 operators, only five contribute which are built from field-strength tensors and the Higgs field [68] (in the indices of c_i, B, W, ϕ refer to the electroweak U(1) and SU(2) gauge fields and the scalar Higgs field and implicate the construction of the operator $\mathcal{O}_i^{(6)}$). Two of these ($\mathcal{O}_{WWW}^{(6)}, \mathcal{O}_W^{(6)}$) also induce quartic charged gauge couplings. There are three types of dim-8 operators [69]: those built up of the covariant derivatives of the scalar Higgs field ($O_{\mathrm{S},i}^{(8)}$), of the field-strength tensors ($O_{\mathrm{T},i}^{(8)}$), and of the Higgs field covariant derivatives and the field-strength tensors mixed ($O_{\mathrm{M},i}^{(8)}$). The $O_{\mathrm{S},i}^{(8)}$ operators correspond to couplings of the longitudinal degrees of freedom, $O_{\mathrm{T},i}^{(8)}$ to those of the transverse degrees of freedom, while $O_{\mathrm{M},i}^{(8)}$ to a mixture of transverse and longitudinal degrees of freedom.

When several operators contribute to the amplitude, interference terms appear between the SM and EFT operators as well as between different EFT operators. It is typically expected that the largest non-SM contribution comes from the interference of SM and dim-6 operators as those terms will only be suppressed by Λ^{-2}. Products of dim-6 operators (and the squared contribution of an operator) and the interference term between SM and dim-8 operators, on the other hand, are multiplied by Λ^{-4}. Dim-6 and dim-8 interference would only come at Λ^{-6}, so are usually not considered. However, several factors could complicate this simple picture of power counting, for example, the dim-6 interference term could be suppressed by helicity selection rules [70], QCD NLO corrections may change the relative importance of each term [71, 72], or the dim-6 Wilson-coefficients can be suppressed by a symmetry in the ultraviolet-complete model [73].

Generic event simulation tools are available to test the various possibilities. To improve the portability of different models to these tools, the universal FeynRules output (UFO) format is in use, facilitating the implementation of new physics ideas to these tools. For example, the SMEFTsim [64, 74] package offers the possibility to test various flavor assumptions and parametrizations of the EW sector using these UFO models.

The charged EW triple gauge couplings, WWZ and WWγ, are sensitive to dim-6 operators, while neutral triple gauge couplings, ZZZ, ZZγ, and Z$\gamma\gamma$, appear first in dim-8. Vector boson scattering – the interaction of two EW vector bosons emitted by (anti)fermions from the two colliding particles – and Higgs boson production, on the other hand, are affected by both dim-6 and dim-8 operators.

As each operator contributes to various processes, global fits to vector boson (and Higgs boson) production data are needed to constrain the multi-parameter model. Frequently constraints are derived assuming only one or a small number of parameters being different from zero. In particular, to constrain dim-8 operator contributions, it is usually assumed that dim-6 Wilson-coefficients are known from elsewhere (and are zero). A first global EFT analysis was recently performed by the ATLAS experiment [75].

Alternative frameworks are also developed. A prominent example – used to interpret Higgs boson production measurements – is the more general Higgs Effective Field Theory (HEFT) [76–78] that does not assume that the SM-like Higgs boson is embedded in a complex doublet.

For the charged triple gauge couplings the so called LEP parametrization [56] is based on a Lagrangian approach adding anomalous couplings. From the 14 complex triple gauge couplings of the most general Lorentz-invariant Lagrangian, only six real parameters respect charge conjugation and parity symmetries:

$$\begin{aligned}\mathcal{L}_{\text{eff}}^{WWV} = -ig_{WWV} \quad & \Big[g_1^V V^\mu (W_{\mu\nu}^- W^{+\nu} - W_{\mu\nu}^+ W^{-\nu}) + \kappa_V W_\mu^+ W_\nu^- V^{\mu\nu} \\ & + \tfrac{\lambda_V}{m_W^2} V^{\mu\nu} W_\nu^{+\rho} W_{\rho\mu}^- \Big] \end{aligned} \tag{1.25}$$

where $V = Z, \gamma$, the couplings are $g_{WW\gamma} = e$, and $g_{WWZ} = e \cot\theta_{\text{W}}$, the field-strength tensors are $W_{\mu\nu} = \partial_\mu W_\nu - \partial_\nu W_\mu$, and $V_{\mu\nu} = \partial_\mu V_\nu - \partial_\nu V_\mu$.

Within the SM, $g_1^V = \kappa_V = 1$, and $\lambda_V = 0$. EW gauge invariance imposes relations between the parameters, leaving three independent couplings. These are typically chosen to be g_1^Z, κ_γ, and λ_γ, with the remaining ones satisfying:

$$g_1^\gamma = 1, \tag{1.26}$$

$$\lambda_{\text{Z}} = \lambda_\gamma, \tag{1.27}$$

$$\kappa_{\text{Z}} = g_1^{\text{Z}} - (\kappa_\gamma - 1)\tan^2\theta_{\text{W}}. \tag{1.28}$$

It is customary to introduce the anomalous part of the couplings: $\Delta\kappa_V = \kappa_V - 1$ and $\Delta g_1^V = g_1^V - 1$. When the LEP results are re-interpreted within dim-6 EFT, the EW parameters α_{EM} and $\sin^2\theta_{\text{W}}$ are taken at the scale of m_{Z}.

The LEP results for neutral triple gauge couplings were derived using a parametrization [53, 54] that conserves $U(1)_{\text{Q}}$ gauge invariance, with four parameters (f_i^V) to describe the CP-violating ($i = 4$) and CP-conserving ($i = 5$) couplings with two on-shell Z bosons ZZZ^* and $\text{ZZ}\gamma^*$ ($V = \text{Z}, \gamma$) and eight parameters (h_i^V) for CP-violating ($i = 1, 2$) and CP-conserving ($i = 3, 4$) couplings with an on-shell photon and an on-shell Z boson $\text{Z}\gamma\text{Z}^*$ and $\text{Z}\gamma\gamma^*$ ($V = \text{Z}, \gamma$).

Such a low-energy effective theory is only valid in the limit of $s \ll \Lambda^2$, which in some practical implementations (for example in Monte Carlo event generations) lead to the introduction of form factors of the type $1/(1 + \hat{s}/\Lambda^2)^n$ to preserve unitarity, with $\hat{s}$ being the final state diboson invariant mass squared. Results derived in the anomalous gauge coupling and EFT approaches can be compared using relations derived without form factors [79].

For quartic gauge couplings, the LEP collaborations adopted an EFT approach adding dim-6 operators to the SM Lagrangian which assumes that the EW symmetry is broken some other way than the BEH mechanism with a scalar doublet [80–85]. After the Higgs discovery, it became preferred [86] to go to the next higher dimensional representation, dim-8 operators as shown in Eq. 1.24, where the gauge symmetry is broken via the traditional Higgs scalar doublet [85, 87, 88]. Some early ATLAS results instead relied on the K-matrix formalism of Ref. [89].

1.3 Extensions of the standard model

While the EFT approach considers new physics in a model-independent way through its effects due to quantum corrections, the complementary method of working out predictions based on specific realizations of new physics allows to look for exotic phenomena in a targeted manner. To address the shortcomings of the SM, several extensions were proposed over the years. The most popular ones assuming supersymmetry [90] or extra spatial dimensions [91] are briefly introduced. These are not mutually exclusive, indeed both are predicted by string theory [92, 93].

1.3.1 Models with extra spatial dimensions

Models with extra spatial dimensions (EDs) have been introduced to solve the hierarchy problem of the SM through geometrical considerations. In this context, the hierarchy problem is phrased to highlight the large difference between the characteristic energy scales of the gravitational and weak interactions. These are characterized by the reduced Planck mass $M_{\mathrm{Planck}} = (8\pi G_{\mathrm{N}})^{-1/2} \approx 2.4 \cdot 10^{18}$ GeV, where G_{N} is the gravitational constant, and by the vacuum expectation value of the Higgs field $v = (\sqrt{2}G_{\mathrm{F}})^{-1/2} \approx 246$ GeV, where G_{F} is the Fermi coupling constant.

1.3.1.1 The Arkani-Hamed–Dimopoulos–Dvali model

The first proposal came from Arkani-Hamed, Dimopoulos and Dvali (ADD) to study a model with large extra dimensions [94, 95]. It assumes n compact EDs, with the D-dimensional Planck scale M_D in $D = 4 + n$ dimensions set close to the EW scale. SM particles propagate in a four-dimensional (4D) subspace called brane, while gravity in the full D-dimensional space. The 4-dimensional Planck scale satisfies $M^2_{\mathrm{Planck}} = V_n M_D^{n+2}$, where V_n is the volume of the EDs.

Measurements of the gravitational $1/r^2$ law by the Eöt-Wash Experiment limit the size of extra dimensions to 38.6 μm [96], presenting an about 2 orders of magnitude improvement compared to the results available [97, 98] around the time of the publication of the original ADD paper.

A general prediction of ED scenarios is the existence of massive Kaluza-Klein (KK) excitations of the graviton in the 4D effective theory. (Or more generally, of any particle that propagates in the extra dimensions.) In the ADD model, we expect these graviton states to appear with a mass-spacing of $1/R_i$, for each of the n extra dimensions, where R_i is the compactification radius of the ED ($i = 1, ..n$). Even though they couple with normal gravitational strength of order $1/M_{\mathrm{Planck}}$, their large multiplicity $E^n \Pi_i R_i$ below the relevant energy scale E can make their combined effect visible at high energy interactions.

The graviton KK excitations ($\mathrm{G_{KK}}$) couple to the energy-momentum tensor and contribute to most SM processes. The fermion- and boson-pair cross sections are modified

$$\sigma = \sigma_{\mathrm{SM}} + \alpha_{\mathrm{G}}\sigma_{\mathrm{int}} + \alpha^2_{\mathrm{G}}\sigma_{\mathrm{grav}} \tag{1.29}$$

with a typical parametrization of $\alpha_{\mathrm{G}} = \lambda/M^4_{\mathrm{S}}$ [99]. Here, λ depends on the details of the model and it is usually set either to $+1$ or -1 to allow for both positive and negative interference. M_{S} is the ultraviolet cut-off scale close to M_D. The functional form of the SM, the interference and the graviton-mediated cross section terms depend on the studied final state. Other parametrizations [100, 101] also exist, with the one in Ref. [101] also depending on the number of extra dimensions. Relations among these parametrizations are available [102].

1.3.1.2 The Randall–Sundrum model

The ADD idea prompted a fury of theoretical activity, and an other interesting geometry was suggested shortly. The Randall–Sundrum (RS) model [103, 104] assumes only one ED and generate the hierarchy by a specifically chosen “warped” geometry with a curvature k. Gravity is located close to a second brane at a distance r_0 from the SM brane and its propagation in the ED is exponentially damped. The small overlap between gravity and the SM particles and forces thus explains the weakness of gravity with respect to the electroweak interaction.

In the RS scenario, besides the KK gravitons [105], a new neutral scalar field, the radion ($\mathcal{R}$) appears. It corresponds to local fluctuations of the interbrane distance [106, 107]. The radion acquires mass as a consequence of the stabilization mechanism for the interbrane distance [108–110], which is expected to be below $\mathcal{O}$(TeV). The radion is likely the lightest exotic state in the RS model. Since the radion has the same quantum numbers as the Higgs boson, they mix, resulting in a radion-like and a Higgs-like state (see also Section 2.2.3).

Many other ED models have been proposed to solve the open questions of particle physics well beyond the hierarchy problem [111], with theorists and experimentalists working closely together (see e.g. Ref. [112] that I co-authored) to find verifiable predictions at present and future colliders, such as the LHC and the planned international linear collider [113].

1.3.2 Supersymmetric models

Supersymmetry [114] is an extension of the Poincaré-group that underlies special relativity. It extends the symmetry by allowing for commuting, as well as anticommuting generators for the symmetry algebra. Supersymmetry thus links fermionic and bosonic states and, as a result, a wealth of new particles, so called superpartners, arises [115, 116]. Each superpartner shares the quantum numbers of its SM equivalent, except for the spin, which differs by 1/2. It is illustrated in Table 1.2 which summarizes the particle content of the SM and its minimal supersymmetric extension, the MSSM (described below).

In the standard model fermion sector, charged leptons and neutrinos come in three flavors: $\ell = \mathrm{e}, \mu, \tau$, and $\nu = \nu_\mathrm{e}, \nu_\mu, \nu_\tau$. Quarks have color charges that can take three values r, g, b (left implicit in the table) and exist in six flavors: $q = \mathrm{u, d, c, s, t, b}$. A superpartner is assigned to each SM fermion chirality state, labeled as left (L) or right (R). Neutrinos are considered massless, thus neutrino mixing is not considered, and no right-handed neutrino (ν_R) – and thus right-handed scalar neutrino ($\widetilde{\nu}_\mathrm{R}$) – is introduced. The superpartners being scalar, the L / R index does not refer to their chirality.

SUSY fields with the same quantum numbers can mix, thus the interaction eigenstates can differ from the mass eigenstates, as indicated in Table 1.2. The mixing of left- and right-handed scalar fermions (L-, R-sfermions, $\tilde{f}_\mathrm{L}$, $\tilde{f}_\mathrm{R}$) is proportional to the

SM & Higgs fields	d.o.f.	SM & Higgs particles	d.o.f.	spin	SUSY fields	d.o.f.	SUSY particles	d.o.f.	spin
ℓ_L, ℓ_R	2	ℓ_L, ℓ_R	2	1/2	$\widetilde{\ell}_\mathrm{L}$, $\widetilde{\ell}_\mathrm{R}$	2	$\widetilde{\ell}_1$, $\widetilde{\ell}_2$	2	0
ν_L	1	ν_L	1	1/2	$\widetilde{\nu}_\mathrm{L}$	1	$\widetilde{\nu}_\mathrm{L}$	1	0
q_L, q_R	2	q_L, q_R	2	1/2	$\widetilde{q}_\mathrm{L}$, $\widetilde{q}_\mathrm{R}$	2	$\widetilde{q}_1$, $\widetilde{q}_2$	2	0
B, W_3	2·2	γ, Z	2+3	1	$\widetilde{B}$, $\widetilde{W}_3$	2·2	$\widetilde{\chi}^0_{1,2,3,4}$	4·2	1/2
W_1, W_2	2·2	$\mathrm{W}^\pm$	2·3	1	$\widetilde{W}_1, \widetilde{W}_2$	2·2	$\widetilde{\chi}^\pm_{1,2}$	2·2·2	1/2
H_u, H_d	2·4	$\mathrm{H}^0_{1,2,3}$, $\mathrm{H}^\pm$	5·1	0	$\widetilde{H}_u, \widetilde{H}_d$	2·4			1/2
g	2	g	2	1	$\widetilde{\mathrm{g}}$	2	$\widetilde{\mathrm{g}}$	2	1/2

Table 1.2: *The MSSM field and particle content with the numbers of degrees of freedom (d.o.f.) before and after symmetry breaking. See main text for detailed explanation. The hypothetical spin-2 tensor boson, the graviton (G) and its superpartner, the spin-3/2 gravitino ($\widetilde{G}$) are not considered in this table.*

corresponding fermion mass. It thus affects primarily the $\widetilde{\tau}$, $\widetilde{\mathrm{t}}$ and $\widetilde{\mathrm{b}}$ scalar fermion partners, and is negligible for the first two generations. It is due to the left-right mixing (and the contributions of the soft SUSY breaking A-parameters to the renormalization group equations as discussed below) that the lightest scalar fermions are expected to be those of the third generation, which motivates the search for scalar top quarks (see also Section 6.4.1).

In the electroweak boson sector, three degrees of freedom from the two complex Higgs doublets ($H_{u,d}$) give masses to the weak Z and $\mathrm{W}^{\pm}$ vector bosons (and provide their third longitudinally polarized component) via the BEH mechanism. If CP is conserved in the Higgs sector, the three neutral Higgs bosons ($\mathrm{H}^0_{1,2,3}$) are called h, H, A with the first two ($m_{\mathrm{h}} \leq m_{\mathrm{H}}$) being CP-even and the latter CP-odd. The superpartners of the EW gauge and Higgs bosons, the fermionic bino ($\widetilde{B}$), wino ($\widetilde{W}_{1,2,3}$) and higgsino ($\widetilde{H}_{u,d}$) states form six mass eigenstates: the electrically charged higgsino and wino states give two charginos ($\widetilde{\chi}^{\pm}_i$), and the neutral bino, wino and higgsino states give four neutralinos ($\widetilde{\chi}^0_j$), where the indices $i = 1, 2$ and $j = 1, ..4$ are ordered by increasing mass. The neutralinos are Majorana fermions.

There are eight gluons (g) with different color charges (not indicated). Their strongly interacting fermionic superpartners, the gluinos ($\widetilde{\mathrm{g}}$) are also Majorana fermions. They do not mix with the other states.

If supersymmetry (SUSY) is realized at high energies, it must be broken by some mechanism [117, 118] as no superpartner with a mass equal to the SM particle has been observed so far. Nonetheless, if the mass acquired due to SUSY breaking is sufficiently low, i.e., in the few TeV range, (some of) these new particles could be produced in high-energy particle interactions at collider experiments, in particular at the currently operational LHC [119, 120]. Searches for these are aplenty, targeting various versions of supersymmetric extensions.

The so-called "minimal" version of the supersymmetry-extended SM, called minimal supersymmetric standard model (MSSM) keeps the field (particle) content minimal. It contains two complex scalar Higgs doublets: the down-type quarks and the charged leptons couple to the first (H_d), while the up-type quarks to the second (H_u) doublet [121]. The corresponding VEVs are denoted by v_u and v_d, and it is customary to use the variables

$$v = \sqrt{v_u^2 + v_d^2}, \qquad \tan\beta = \frac{v_u}{v_d}. \tag{1.30}$$

MSSM belongs to the family of type-II two Higgs doublet models [122], as discussed in Section 2.2.

The superpotential is built using the chiral quark and lepton superfields (the $SU(2)$ doublet Q, L, and the conjugate singlet $\bar{u}, \bar{d}, \bar{e}$), as well as the two Higgs $SU(2)$ doublets. For each family, Q is formed by ($\widetilde{u}_{\mathrm{L}}\ \widetilde{d}_{\mathrm{L}}$) and ($u_{\mathrm{L}}\ d_{\mathrm{L}}$), while $\bar{u}$ is formed by $\widetilde{u}^*_{\mathrm{R}}$ and $u^\dagger_{\mathrm{R}}$ (and similarly for the superfields $L, \bar{d}, \bar{e}$), with quantum numbers as given in Table 1.1 for the participating SM fermions. Looking at the two superfields for the Higgs bosons and higgsinos: H_u is composed of ($H_u^+\ H_u^0$) and ($\widetilde{H}_u^+\ \widetilde{H}_u^0$), while H_d is composed of ($H_d^0\ H_d^-$) and ($\widetilde{H}_d^0\ \widetilde{H}_d^-$). The spin-0 fields are complex scalars, and the spin-1/2 fields are two-component Weyl fermions.

With this field content the most general gauge invariant and renormalizable superpotential has the form

$$\begin{aligned} W &= h^e L\bar{e}H_d + h^d Q\bar{d}H_d + h^u Q\bar{u}H_u - \mu H_d H_u \\ &+ \lambda LL\bar{e} + \lambda' LQ\bar{d} + \mu' LH_u \\ &+ \lambda'' \bar{u}\bar{d}\bar{d}, \end{aligned} \tag{1.31}$$

where the generation and the $SU(2)_{\rm L}$, $SU(3)_{\rm C}$ indices are left implicit. The couplings μ', (h^e, h^d, h^u) and $(\lambda, \lambda', \lambda'')$ are tensors with one, two and three generation indices, respectively. The first line contains only terms which respect total baryon and lepton number conservation, while the terms in the second line violate lepton number (L) conservation and the term in the third line violates baryon number (B) conservation. The three Yukawa matrices $h^{e,d,u}$ are arbitrary and complex, and the SUSY Higgs mass parameter μ takes a complex value. For simplicity, similarly to Eq. 1.5 color and isospin indices are left implicit above (as well as family indices this time). For clarity, as an example, the full details for the term $h^u Q \bar{u} H_u$ are as follow:

$$\bar{u}^{Aa} (h^u)_a^b Q_{\alpha Ab} (H_u)_\beta \epsilon^{\alpha\beta}, \tag{1.32}$$

where we form a sum over the family indices a, b, the $SU(3)_{\rm C}$ color index A, and the $SU(2)_{\rm L}$ weak isospin indices α, β with the help of the fully antisymmetric ϵ matrix, i.e. $\epsilon^{12} = -\epsilon^{21} = 1$ and $\epsilon^{11} = \epsilon^{22} = 0$ to form an $SU(2)$ singlet in a gauge invariant way.

The real matrix λ_{ijk} (λ''_{ijk}) is non-vanishing for generation indices $i < j$ ($j < k$), thus, including μ'_i, we have potentially $9 + 27 + 9 + 3 = 48$ couplings that violate L or B conservation. They may cause severe phenomenological problems, and their values are thus strongly bounded [123–128]. The most obvious constraints come from the non-observation of proton decay [129], since the simultaneous presence of terms with λ' and λ'' couplings would lead to fast proton decay mediated by the exchange of a squark.

Even though another discrete (or gauge) symmetry could also protect against such phenomena, most SUSY extensions assume the conservation of R-parity [90, 130], defined as

$$R_{\rm p} = (-1)^{2s+3B+L} = (-1)^{2s+3(B-L)}, \tag{1.33}$$

where s, B and L are the spin, the baryon and lepton numbers of the particle, respectively. $R_{\rm p}$ discriminates between SM particles and their superpartners, giving $R_{\rm p} = +1$ for the SM particles (quarks, leptons, gauge and Higgs bosons) and $R_{\rm p} = -1$ for their supersymmetric partners (scalar quarks or squarks, scalar leptons or sleptons, as well as charginos, neutralinos and gluinos). A number of experimental studies are also conducted under the assumption that only one R-parity violating coupling is different from zero (see also Section 2.3.2).

R-parity conservation has important consequences for the phenomenology at colliders. It implies that superpartners are always produced in pairs and decay through cascade processes to SM particles and to the lightest supersymmetric particle (LSP), which is stable. If the LSP is neutral and weakly interacting, as favored by cosmological considerations, it escapes detection, resulting in sizable missing energy.

On top of the 19 parameters of the SM, the $R_{\rm p}$-conserving MSSM has 105 new parameters (thus also called MSSM-124 [131]) primarily encompassing our ignorance of the SUSY breaking mechanism. They include the couplings in the superpotential; couplings for a restricted set of scalar interactions and Higgs mixing (proportional to the terms in the first line of Eq. 1.31) and scalar and gaugino superpartner masses that appear in the soft SUSY breaking terms of the Lagrangian:

$$\begin{aligned} -\mathcal{L}_{\rm soft}^{\rm MSSM} &= (T^e \tilde{L}\tilde{\bar{e}} H_d + T^d \tilde{Q}\tilde{\bar{d}} H_d + T^u \tilde{Q}\tilde{\bar{u}} H_u + h.c.) - (m_{12}^2 H_d H_u + h.c.) \\ &+ m_d^2 H_d^* H_d + m_u^2 H_u^* H_u \\ &+ M_{\tilde{L}}^2 \tilde{L}^\dagger \tilde{L} + M_{\tilde{e}}^2 \tilde{\bar{e}}^\dagger \tilde{\bar{e}} + M_{\tilde{Q}}^2 \tilde{Q}^\dagger \tilde{Q} + M_{\tilde{d}}^2 \tilde{\bar{d}}^\dagger \tilde{\bar{d}} + M_{\tilde{u}}^2 \tilde{\bar{u}}^\dagger \tilde{\bar{u}} \\ &+ \frac{1}{2}(M_1 \tilde{B}\tilde{B} + M_2 \tilde{W}\tilde{W} + M_3 \tilde{g}\tilde{g} + h.c.). \end{aligned} \tag{1.34}$$

Here fields with a tilde are the scalar components of the superfield. The gaugino mass parameters $M_{1,2,3}$ and the mixed Higgs mass squared m^2_{12} are in general complex, while $m^2_{d,u}$ are real. The matrices $T^{e,d,u}$ are 3×3 complex matrices in the generation space. The 3×3 complex squared-mass matrices $M^2_{\tilde{L},\tilde{e},\tilde{Q},\tilde{d},\tilde{u}}$ are hermitian. The soft SUSY breaking term thus introduces $3 \cdot 3 \cdot 3 \cdot 2 + 2 + 2 \cdot 1 + 5 \cdot (6 + 3) + 3 \cdot 2 = 109$ parameters, in addition to the $3 \cdot 3 \cdot 3 \cdot 2 + 2 = 56$ parameters of the superpotential.

It is customary to introduce the A-parameters (also referred to as soft SUSY breaking trilinear couplings) as $A^{e,d,u}_{ij} = T^{e,d,u}_{ij}/h^{e,d,u}_{ij}$ (with no summation over the generation indices i, j) and the Higgs bilinear coupling $B_0 = m^2_{12}/\mu$.

Similarly to the case of the SM Yukawa matrices, non-physical degrees of freedom can be removed by global rotations on the superfields, as well as imaginary d.o.f. in the scalar sector. More specifically, we can remove 15 real parameters and 28 phases in the flavor sector and two phases in the scalar sector. Thus, in addition to the SM parameters, there are five real parameters and three CP-violating phases in the gaugino–higgsino sector, 21 sfermion masses, 36 real mixing angles to define the sfermion mass eigenstates, and 40 CP-violating phases that can appear in sfermion interactions [30, 90, 131]. They are shown in Table 1.3.2 which also illustrates the reduction in the number of parameters after imposing certain constraints as described below.

The study of MSSM-124 is not practical, moreover in this most general form most of the parameter space features the violation of the individual lepton numbers $(L_\mathrm{e}, L_\mu, L_\tau)$,

Parameter	number	MSSM	pMSSM	CMSSM	SM
gauge couplings	3	g, g', g_s	x	x	x
QCD vacuum phase	1	θ_QCD	x	x	x
Higgs VEV	2	v, $\tan\beta$	x	x	v
Higgs mass	1	m_A (or $m_{\mathrm{H}^\pm}$)	x	x	m_H
SUSY Higgs mass	1	$\lvert\mu\rvert$	x		
gaugino mass	3	$\lvert M_{1,2}\rvert, M_3$	x	$m_{1/2}$	
SUSY Higgs mass phase	1	ϕ_μ	(x)	sign(μ)	
gaugino mass phase	2	$\phi_{1,2}$	(x)		
quark mass	6	$m_\mathrm{u,d,c,s,t,b}$	x	x	x
lepton mass	3	$m_{\mathrm{e},\mu,\tau}$	x	x	x
u-type squark mass	6	$m^{R,L}_{\tilde{\mathrm{u}},\tilde{\mathrm{c}},\tilde{\mathrm{t}}}$	$m_{\tilde{Q}_1,\tilde{u}_1,\tilde{Q}_3,\tilde{u}_3}$	m_0	
d-type squark mass	6	$m^{R,L}_{\tilde{\mathrm{d}},\tilde{\mathrm{s}},\tilde{\mathrm{b}}}$	$m_{\tilde{d}_1,\tilde{d}_3}$		
charged slepton mass	6	$m^{R,L}_{\tilde{\mathrm{e}},\tilde{\mu},\tilde{\tau}}$	$m_{\tilde{L}_1,\tilde{e}_1,\tilde{L}_3,\tilde{e}_3}$		
sneutrino mass	3	$m_{\tilde{\nu}_\mathrm{e},\tilde{\nu}_\mu,\tilde{\nu}_\tau}$			
CKM mixing angle	3	$\theta_{12,23,13}$	x	x	x
sfermion mixing angle	36	A_i	$A_{\mathrm{t,b},\tau}$ (A_μ)	A_0	
CKM CPV phase	1	δ	x	x	x
sfermion CPV phase	40	ϕ_i	$(\phi_{\mathrm{t,b},\tau})$		
Number of parameters	124		37 (44)	23.5	19

Table 1.3: *Parameters of MSSM-124, marking those that remain in pMSSM designed to allow for an increased variety of SUSY phenomena at experiments while satisfying existing constraints, the supergravity motivated CMSSM, and the SM. In the case of pMSSM, the variables in extended models beyond pMSSM-19 are in parenthesis. These aim either to describe the muon $g-2$ results [132], or introduce additional CP violation to the pMSSM.*

unsuppressed flavor changing neutral currents (FCNCs), and sources of CP violation that are excluded experimentally (e.g., by measurements of the electric dipole moments of the electron and neutron). It is thus customary to use more restricted frameworks that are phenomenologically viable by assuming a simple structure at a common high-energy scale and extrapolating the parameters to lower energies using the renormalization group equations.

Two scenarios are examined in this work which differ in the mechanism that connects the hidden sector where SUSY is broken to the visible sector where SM particles and their superpartners live. In models with gravity-mediated SUSY breaking (supergravity, SuGra), the gravitational interaction acts as the link between the sectors, while in models with gauge mediated SUSY breaking (GMSB) [133] the hidden sector couples to a messenger sector which in turn couples to the visible sector via SM gauge interactions. To circumvent constraints from observations, e.g. that of the Higgs mass, a generalized version of GMSB, called general gauge mediation (GGM) [134] was proposed.

Even within these frameworks with a highly restricted set of model parameters (typically about five), the experimental signatures can vary widely depending on the nature of the LSP, the next-to-LSP (NLSP) as well as further kinematically accessible particles, if any, and their couplings (and lifetimes).

In the constrained framework of MSSM (CMSSM), also called minimal supergravity (MSuGra), the soft SUSY breaking parameters take a simple form at the Planck scale (or the scale of grand unification) chosen as the renormalization scale [90]: the scalar squared masses and the scalar couplings are flavor diagonal and universal. Taking also the more general prediction of the unification of gaugino masses, the number of parameters in the soft SUSY breaking term can be reduced to four: the common scalar mass (m_0), the scalar trilinear coupling (A_0), the gaugino mass ($m_{1/2}$) and the bilinear coupling of Higgs fields (B_0). The SUSY Higgs mass parameter μ from the superpotential and B_0 can be exchanged for the ratio of the Higgs doublet VEVs $\tan\beta$ and the sign of μ.

In MSSM models, instead of the SM-like neutral CP-even Higgs mass (m_{H}), it is customary to choose the mass of the CP-odd Higgs boson (m_{A}) as h and H can mix (typically described by the angle α), or that of the charged Higgs ($m_{\mathrm{H}^{\pm}}$) as it is not affected even in the case when CP violation is allowed and thus A mixes with the other neutral states (see Section 2.2.1 for a variant of CMSSM with CP-violation in the Higgs sector).

The superpartner masses at lower energies are derived using the renormalization group (RG) equations as illustrated in Figure 1.5. Depending on the initial conditions and the assumptions of the model, varied phenomenology is possible at the currently accessible energies.

The number and choice of free parameters in MSSM models are typically adapted to capture the most important features under study, also leading to somewhat modified definitions of CMSSM. Using the RG evolution, instead of $m_{1/2}$, the SU(2) gaugino mass parameter at the EW scale (M_2) can be used. The general assumption of gaugino mass unification leads to $M_1 = 5/3 \cdot \tan^2\theta_{\mathrm{W}} \cdot M_2$ for the U(1) gaugino mass parameter. If SUSY is to remain a solution to the naturalness problem, the mass parameters should not exceed $\mathcal{O}(\mathrm{TeV})$.

Furthermore, to allow a less model-dependent analysis of the MSSM while enforcing the observational constraints, the phenomenological MSSM (pMSSM-19) [136] was developed using 19 parameters (three gaugino mass parameters $M_{1,2,3}$, the Higgs sector parameters of m_{A} and $\tan\beta$, the Higgsino mass parameter μ, five sfermion mass squared parameters for the degenerate first and second generations $m^2_{\tilde{Q}_1,\tilde{u}_1,\tilde{d}_1,\tilde{L}_1,\tilde{e}_1}$, five

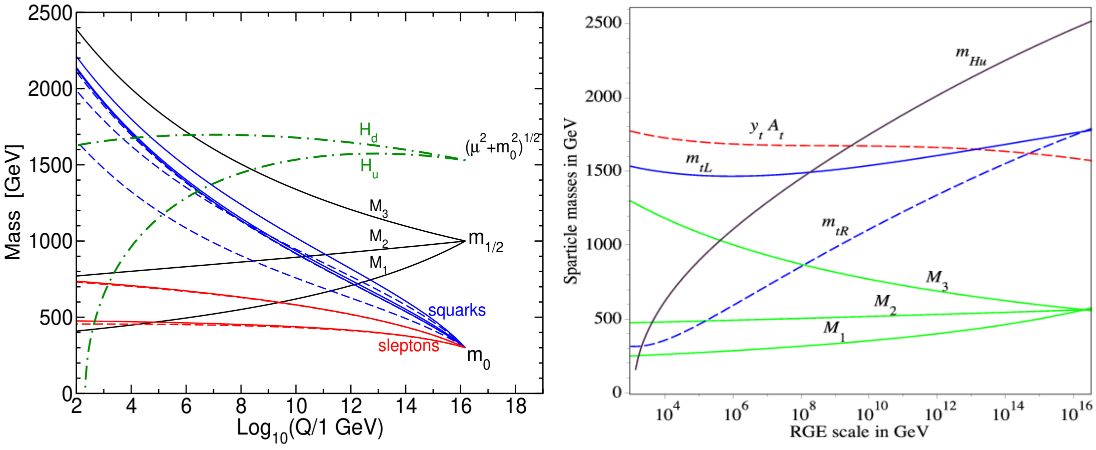

Figure 1.5: *Illustrative example of RG evolution of (left) scalar and gaugino mass parameters in supergravity inspired MSSM with the initial parameters taken at* $1.5 \cdot 10^{16}$ *GeV [90]. The parameter* $\mu^2 + m_0^2$*, which appears in the Higgs potential, runs negative because of the large top Yukawa coupling and triggers electroweak symmetry breaking. (right) An other example of the running of the parameters concentrating on the stop sector: the development of the mass parameters of the left and right-handed scalar top quark* ($m_{\mathrm{tL}}, m_{\mathrm{tR}}$) *and the product of the top Yukawa coupling* (y_{t}) *and the trilinear Higgs-stop-stop coupling* (A_{t})*. In this case, both the neutralino LSP and the scalar top quark NLSP [135] are kinematically accessible at the LHC and have a small mass difference. MSSM parameter notations are defined in the text.*

sfermion mass squared parameters for the third generation $m^2_{\tilde{Q}_3,\tilde{u}_3,\tilde{d}_3,\tilde{L}_3,\tilde{e}_3}$, and three soft-SUSY-breaking A-parameters describing the Higgs-sfermion-sfermion couplings for the third generation $A_{t,b,\tau}$ (while neglecting these for the first and second generations). Variants of pMSSM introduce non-zero $A_e = A_\mu$ [137] to describe the muon $g-2$ results or CP-violating phases for the EW gaugino ($\phi_{1,2}$) and Higgs (ϕ_μ) mass parameters, as well as for the third generation A-parameters ($\phi_{t,b,\tau}$) [138].

One of the main advantages of SUSY models is the presence of viable electrically neutral candidates of dark matter [139]. The Majorana neutralino [140] is the most popular choice. Sneutrino dark matter has been largely ruled out by direct searches in the MSSM, but they could be viable in non-minimal models after the inclusion of right-handed neutrino fields [141–143]. The gravitino serves as dark matter candidate in most models with gauge mediation of supersymmetry breaking [133, 144]. In certain models, the axion and its superpartner, the axino also contributes [145, 146]. Collider experiments are complementary to direct and indirect detection efforts in uncovering the nature of dark matter [147].

Searches for the production of supersymmetric partners and SUSY dark matter within various MSSM models are discussed in Sections 2.3 and 6.4.

Chapter 2

Setting the stage: constraints on new physics from the LEP era

The Large Electron - Positron collider (LEP) was the largest and most energetic lepton collider ever built. It provided in its first phase of operation (LEP1 era) from 1989 to 1995 electron – positron collision data around the Z resonance with center-of-mass energies between about 88 and 94 GeV to four large multi-purpose experiments, ALEPH, DELPHI, L3 and OPAL to precisely measure the mass ($m_{\mathrm{Z}} = 91.1875 \pm 0.0021$ GeV), the width ($\Gamma_{\mathrm{Z}} = 2.4952 \pm 0.0023$ GeV) and the couplings of the Z boson, to determine the number of light neutrino species ($n_\nu = 2.9840 \pm 0.0082$), as well as to measure various fundamental parameters of the SM, such as the effective electroweak mixing angle for leptons ($\sin^2\theta_{\mathrm{W}} = 0.23153 \pm 0.00016$) or the SM ρ parameter of Eq. 1.18 ($\rho = 1.0050 \pm 0.0010$) [15]. It also provided a reach to search for new physics[1] for pair-produced particles up to a mass of $m_{\mathrm{Z}}/2$.

In the second phase (LEP2 era) starting in late 1995, the energy was increased in several steps starting from 130 GeV. The energy reached 183 GeV in 1997, then 189 GeV in 1998, crossed the 200 GeV line in 1999 and topped ultimately at 209 GeV in the last year of operation in 2000. This data set allowed the study of WW and ZZ pair production for the first time and the precise measurement of the mass ($m_{\mathrm{W}} = 80.376 \pm 0.033$ GeV), the width ($\Gamma_{\mathrm{W}} = 2.195 \pm 0.083$ GeV), and the couplings including the trilinear gauge-boson self-couplings of the W boson [16]. LEP2 also significantly enlarged the kinematic range for new particle searches[2]. Amid a great excitement about a possible signal for the elusive Higgs boson with a mass of 114 GeV [156, 157], the LEP collider was shut down in November 2000 to allow the start of the construction of the LHC in the LEP tunnel.

Many extensions of the SM were scrutinized at LEP, of which the supergravity-inspired constrained MSSM was the most widely studied. As the lack of striking new physics signatures became apparent, new twists were added to CMSSM, such as CP-violation in the Higgs sector or mechanisms to suppress the dominant $\mathrm{b\bar{b}}$ decays (requiring the development of flavor-independent searches for Higgs bosons). Non-supersymmetric extensions of the Higgs sector, in particular various types of two Higgs

---

[1] In the MSc thesis I submitted to Eötvös University in 1995 titled ”Search for charged Higgs bosons with the OPAL detector at LEP”, I constrained the phase space for the pair production of these charged scalar particles using the full LEP1 data set [148, 149].

[2] In the PhD thesis I submitted to Eötvös University in 1999 titled ”Search for charged Higgs Bosons and supersymmetric particles”, I studied the pair production of heavy exotic particles using the early LEP2 data set collected at $\sqrt{s} = 130 - 184$ GeV, with also a preliminary analysis performed at 189 GeV to seek charged Higgs bosons [150–155].

doublet models (2HDMs) were also considered. Stepping outside the Higgs sector, final states predicted by models with gauge or anomaly mediation of supersymmetry breaking (GMSB or AMSB) were also sought, as well as diverse experimental signatures of alternative SM extensions with extra spatial dimensions or composite Higgs models with strong dynamics.

In this chapter, I primarily discuss (building on my earlier publications in Refs. [158–161]) those final results based on the data collected by the OPAL detector at LEP2 to which I contributed, where available also combined with those of the other three LEP experiments, ALEPH, DELPHI and L3 (labeled as ADLO). The data sample [162] with center of mass energies between 161 and 209 GeV corresponds to an integrated luminosity of around 700 pb^{-1} per experiment, of which 130 pb^{-1} was recorded at energies above 206 GeV [16, 163]

While LEP with its multi-purpose detectors provided a clean environment to explore possibilities beyond the SM both through direct searches and precise measurements of EW processes, none of these showed evidence for new phenomena. In most cases, cross section times branching ratio limits were computed at the 95% confidence level[3] (CL) with minimal model assumptions for each final state, providing the most general, almost model-independent results. These were then interpreted in the framework of specific theoretical models to constrain the accessible parameter space and the properties of the new particles, such as their masses.

2.1 SM cross section measurements

2.1.1 ZZ production

In the SM, the process $\mathrm{e}^+\mathrm{e}^- \to \mathrm{ZZ}$ at leading order occurs via the diagram shown on the left of Figure 2.1. While no tree level ZZZ and ZZγ couplings are expected and contributions from higher-order SM diagrams are too small to be measurable using the LEP data set, physics beyond the SM could lead to effective couplings contributing to the ZZ production cross section. BSM models with two Higgs doublets [164] or extra spatial dimensions [165] predict deviations of the ZZ cross section from the SM expectation.

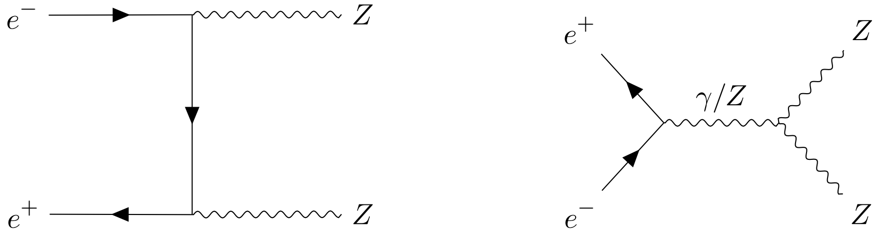

Figure 2.1: *(a) The dominant diagram to produce a Z boson pair at LEP2, and (b) s-channel production via anomalous ZZγ or ZZZ coupling.*

The LEP2 data at $\sqrt{s} = 183{-}209$ GeV were used to measure the total and differential ZZ production cross sections using all visible final states with at least a pair of oppositely charged leptons or a pair of hadronic jets [158, 166, 167]. The results for the inclusive cross section measurement, shown in Figure 2.2 (left), are in agreement with the SM

---

[3] All limits on rare or new physics processes and model parameters are quoted at the 95% confidence level throughout this work, unless otherwise specified.

predictions computed by the ZZTO code [168] with an accuracy of 2%. They – together with the measured angular distributions – allow to place constraints on new physics. I interpreted the data in various models with extra dimensions.

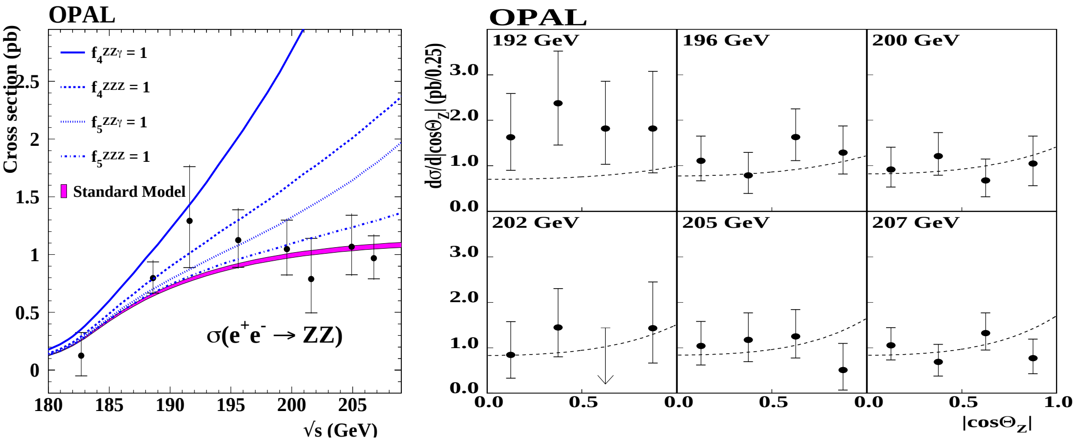

Figure 2.2: *(left) Production cross section of the* $e^+e^- \rightarrow ZZ$ *process as a function of the electron-positron center of mass energy as measured by the OPAL collaboration, compared to various theoretical calculations: the SM prediction of ZZTO with an uncertainty band of 2%, as well as various extensions with anomalous ZZZ and* $ZZ\gamma$ *couplings modeled by YFSZZ with coupling values shown in the legend. (right)* $e^+e^- \rightarrow ZZ$ *differential cross sections at various energies as a function of* $|\cos\theta_Z|$ *where* θ_Z *is the polar angle of the Z bosons. The measured values are compared to the YFSZZ prediction normalized to the ZZTO calculation. The error bars show the total uncertainties, dominated by the statistical component (as illustrated on the left figure by the horizontal marks). [167]*

2.1.1.1 Limits on anomalous couplings

Constraints were extracted on the ZZV (V = Z, γ) anomalous triple gauge couplings [54] using the observed angular differential cross sections. These were compared to the SM predictions of the YFSZZ Monte Carlo generator [169] normalized to the ZZTO calculation in Figure 2.2 (right). The effect of the ZZZ and ZZγ couplings were modeled by YFSZZ. The Z boson polar angle Θ_Z was calculated from a kinematic fit that assumed no initial state radiation, except for the channels with a neutrino pair where it was given by the direction of the reconstructed visible Z boson. The results are given in Figure 2.3 in the 2-dimensional plane as 95% CL contours, separately for the CP-odd (f_4^V) and the CP-even (f_5^V) assumptions. The derived lower limits on the couplings lie between -0.94 and -0.32, while the upper limits between 0.25 and 0.59, assuming only one aTGC is different from zero. Combination by the LEP collaborations brought typically a factor of two improvement, achieving the strongest constraint on the CP-odd ZZγ coupling: $-0.20 < f_4^\gamma < 0.18$ [16].

Measurements using the high-statistics LHC pp → ZZ data superseded these results, with the constraints strengthening by about 3 orders of magnitude as illustrated by Table 2.1, comparing the OPAL results to the latest – to date most stringent – measurements from CMS [170]. LHC results on diboson production and anomalous gauge couplings are discussed in Section 6.2.

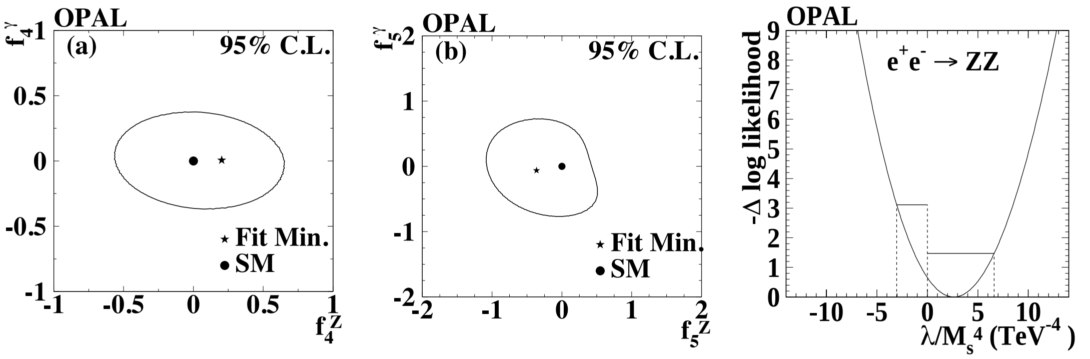

Figure 2.3: *95% CL contours in (left) the (f_4^Z, f_4^γ) and (middle) the (f_5^Z, f_5^γ) anomalous coupling planes from the LEP2 OPAL data. The stars show the minimum of the log-likelihood function, and the dot the SM prediction. (right) The negative log-likelihood as a function of λ/M_s^4 in the ADD model. [167]*

aTGC parameter	OPAL observed $\times 10^{-1}$	CMS observed $\times 10^{-4}$
f_4^Z	$-4.5; +5.8$	$-6.6; +6.0$
f_5^Z	$-9.4; +2.5$	$-5.5; +7.5$
f_4^γ	$-3.2; +3.3$	$-6.6; +6.0$
f_5^γ	$-7.1; +5.9$	$-6.6; +6.0$

Table 2.1: *95% confidence regions for anomalous neutral triple gauge couplings from the full OPAL LEP2 [167] and from the full CMS Run-2 [170] data sets.*

2.1.1.2 Limits on low scale gravity

Constraints on the ultraviolet (UV) cut-off scale (M_s) of the ADD model of large extra spatial dimensions with different assumptions for λ, the sign of the interference term between the SM and the ADD processes [99] as given in Eq. 1.29 or for the number of assumed extra dimensions using the convention of Ref. [101] were also derived. They are shown in Figure 2.3 (right) with the assumption that the Born-level amplitude is proportional to λ/M_s^4. The log-likelihood fit to the differential cross section as a function of the Z boson polar angle $|\cos\theta_Z|$ gives $\lambda/M_s^4 = 2.6 \pm 2.3$ TeV^{-4} for the coupling, consistent with zero. Limits on M_s were determined separately for the two classes of theories with $\lambda = +1$ and -1, giving lower limits of $M_s > 0.62$ and 0.76 TeV, respectively.

The constraints on the energy scale of the ADD model depend on the parametrization. Using Ref. [101], it is below 1 TeV for all assumptions on the number of extra dimensions ($n = 2 - 7$): 0.92 TeV for $n = 2$ and 0.59 TeV for $n = 7$. The case of $n = 1$ was already excluded by cosmological considerations. Superstring or M-theory predicts the existence of seven extra dimensions, so the number of large EDs is expected to be $n \leq 7$.

This analysis also illustrates how a deviation in the observed SM cross section can be interpreted not only in general EFT or anomalous coupling frameworks (described in Sec. 1.2) but also in specific BSM models. Indeed, pinpointing the origin of a new physics signal would require studies of the differential cross sections, as I showed in Ref. [171] using angular distributions for the case of a future linear electron-positron collider.

2.1.2 Fermion-pair production and low scale gravity

The most stringent constraints on the ADD model of large extra dimensions were derived from the study of fermion-pair production, with the best sensitivity coming from the measurements of Bhabha scattering. The analysis of the OPAL e^+e^- data that I co-authored gave $M_S > 1.00$ (1.15) TeV for $\lambda = +1(-1)$ [172].

When combined with results using $\mu^+\mu^-$, $\tau^+\tau^-$ [173], $\gamma\gamma$ [174], and ZZ [167] cross section measurements, the limits improved only marginally to $M_S > 1.03$ (1.17) TeV, showing a clear dominance of the e^+e^- final state to the experimental sensitivity due to the significant interference with the SM t-channel photon exchange. The combination of the results of the LEP experiments brought only a small gain: for the most sensitive e^+e^- channel the combined limit reached $M_S > 1.09$ (1.25) TeV [16], only a 6-7% increase.

The results of the LEP collaborations are now superseded by the LHC measurements that allow access to the multi-TeV energy range, with limits on the UV cut-off scale reaching 10 TeV [175].

2.2 Extended Higgs sector

The minimal extension of the SM Higgs sector, required for example by supersymmetric models, contains two Higgs field doublets leading to five Higgs bosons: three neutral and two charged ones. Due to the Higgs boson self-coupling, decays of Higgs bosons into other Higgs bosons become possible if kinematically allowed.

The 2HDMs [176] are well-motivated theoretically: at least two Higgs doublets are required by supersymmetric models [177], as well as by variations [178] of the Peccei–Quinn axion model [45]. Moreover, they also offer additional source of CP violation (either explicit or spontaneous) to generate the baryon asymmetry of the Universe with its observed size. Two types of these models were studied in detail at LEP which differ in the coupling structure to the fermions.

A feature of general 2HDMs is the existence of tree-level flavor-changing neutral currents (FCNC) which are avoided by imposing discrete symmetries. If all fermions with the same quantum numbers couple to the same Higgs multiplet, then FCNCs will be absent. This can be realized in two ways in the quark sector. In Type-I models (2HDM(I)), all quarks couple to the same Higgs doublet (chosen to be the second). In Type-II models (2HDM(II)), the right-handed (RH) up-type quarks couple to one Higgs doublet (chosen to be the second) and the down-type RH quarks couple to the other. It is traditionally assumed that in both models the RH leptons couple to the same Higgs field as the RH down-type quarks, though this is not necessary, and thus in total four tree-level FCNC-free models can be constructed with different phenomenology.

The introduction of supersymmetry adds new particles (thus possible new decay modes) but also constrains the parameter space of the Higgs sector. In the MSSM, which requires a 2HDM(II) structure, the Higgs potential is assumed to be invariant under CP transformation at tree level. It is possible, however, to break CP symmetry in the Higgs sector (either explicitly or) spontaneously by radiative corrections. Such a scenario could provide (some of) the missing contribution to the observed cosmic baryon asymmetry [179].

In this section I summarize the studies that I contributed to either as a main analyzer, an expert adviser, an internal reviewer, or the responsible physics coordinator. My role also included discussions with theoretical physicists to understand the best strategies to explore the extended models with our data.

2.2.1 Neutral Higgs bosons in the MSSM

Both CP-conserving (CPC) and CP-violating (CPV) scenarios were studied at LEP [160, 161]. In the CPC case, the three neutral Higgs bosons are CP eigenstates: h and H are CP even, A is CP odd. They are expected to be mostly produced in the Higgs-strahlung processes $\mathrm{e^+e^-} \to \mathrm{hZ}$ / HZ and the pair-production processes $\mathrm{e^+e^-} \to \mathrm{hA}$ / HA. In the CPV case, however, the three neutral Higgs bosons, H_i, are mixtures of CP-even and CP-odd Higgs fields and the $\mathrm{e^+e^-} \to \mathrm{H}_i\mathrm{Z}$ / $\mathrm{H}_i\mathrm{H}_j$ $(i, j = 1, 2, 3, i \neq j)$ processes may all occur.

The couplings of the light SM-like scalar to d- and u-type fermions and weak gauge bosons are modified with respect to the SM. In the CPC case [180], the couplings (normalized to the SM value where the equivalent coupling exists) are:

$$\begin{array}{rcl} g_{hdd} & \propto & -\dfrac{\sin\alpha}{\cos\beta}, \qquad g_{Hdd} \propto \dfrac{\cos\alpha}{\cos\beta}, \qquad g_{Add} \propto \tan\beta, \\ g_{huu} & \propto & \dfrac{\cos\alpha}{\sin\beta}, \qquad g_{Huu} \propto \dfrac{\sin\alpha}{\sin\beta}, \qquad g_{Auu} \propto \cot\beta, \\ g_{hVV} & \propto & \sin(\beta-\alpha), \qquad g_{HVV} \propto \cos(\beta-\alpha), \\ g_{hAZ} & \propto & \cos(\beta-\alpha), \qquad g_{HAZ} \propto \sin(\beta-\alpha), \\ g_{hH^\pm W^\mp} & \propto & \cos(\beta-\alpha), \qquad g_{HH^\pm W^\mp} \propto \sin(\beta-\alpha), \end{array} \tag{2.1}$$

with α being the mixing angle that relates the CP-even physical Higgs states h and H to the field doublets, and $\tan\beta$ the ratio of the VEVs. The couplings to a charged lepton pair behave like those to d-type quarks. The couplings of h and H are complementary: $g^2_{hxy} + g^2_{Hxy} = (g^{\mathrm{SM}}_{Hxx})^2$.

The decay properties of the Higgs bosons, while quantitatively different in the CPC and CPV scenarios, maintain a certain similarity: the largest branching ratios are typically those to $\mathrm{b\bar{b}}$ and $\tau^+\tau^-$, and cascade decays ($\mathrm{h} \to \mathrm{AA}$ or $\mathrm{H_2} \to \mathrm{H_1H_1}$) occur and can even be dominant when kinematically allowed.

A large number of search channels were targeted in the MSSM Higgs hunt: SM Higgs searches were reinterpreted; and a decay-mode independent hZ analysis was developed. Searches for hA associated production, including flavor-independent analyses were explored. Measurements of $\mathrm{e^+e^-} \to \mathrm{b\bar{b}h}$ and $\mathrm{b\bar{b}A}$ Yukawa production were designed. $\mathrm{h} \to \mathrm{AA}$ and $\mathrm{A} \to \mathrm{hZ}$ processes were considered in cascade decays leading to six-fermion final states. The search for the invisible decay of Higgs bosons to LSP pairs is also useful to explore specific areas of the MSSM parameter space. In general, searches designed to detect CPC Higgs production can be reinterpreted in the CPV scenario. However, in some parts of the CPV parameter space modified or newly developed searches were also necessary to cover new final-state topologies, such as $\mathrm{H_2Z} \to \mathrm{H_1H_1Z} \to \mathrm{b\bar{b}b\bar{b}Z}$ with $m_{\mathrm{H_2}} \approx 100 - 110$ GeV [181].

An important dedicated search, that closed an open window in the CMSSM phase space, was aimed at low-mass CP-odd Higgs bosons [182]. In 2HDM(II), the scalar coupling hAA is proportional to $\cos 2\beta \cdot \sin(\beta + \alpha)$. When kinematically allowed ($m_{\mathrm{A}} < m_{\mathrm{h}}/2$), the decay $\mathrm{h} \to \mathrm{AA}$ may thus dominate over the Higgs Yukawa couplings to fermion pairs, depending on the values of α and $\tan\beta$. To cover the region with $m_{\mathrm{h}} > 45$ GeV and $m_{\mathrm{A}} < 10$ GeV, where the traditional $\mathrm{A} \to \mathrm{b\bar{b}}$ searches had no sensitivity, a dedicated analysis was developed in the Higgs-strahlung process $\mathrm{e^+e^-} \to \mathrm{hZ} \to (\mathrm{AA})(\mathrm{e^+e^-}/\mu^+\mu^-/\nu\bar{\nu})$, allowing for the selection of events with very specific kinematics.

The results [182] were presented in a model-independent way as cross section upper limits for each of the six studied AA final states that can be formed from A →

$\tau^+\tau^-$, $c\bar{c}$, gg decays, as illustrated in Figure 2.4. They were also interpreted in the CMSSM "no-mixing" scenario [183] (see below) and excluded the full parameter region left open by the LEP1 searches for $45 < m_\mathrm{h} < 85$ GeV and $2 < m_\mathrm{A} < 9.5$ GeV. The results can also be re-interpreted within any model that predicts the existence of at least one scalar and one pseudoscalar Higgs-like boson.

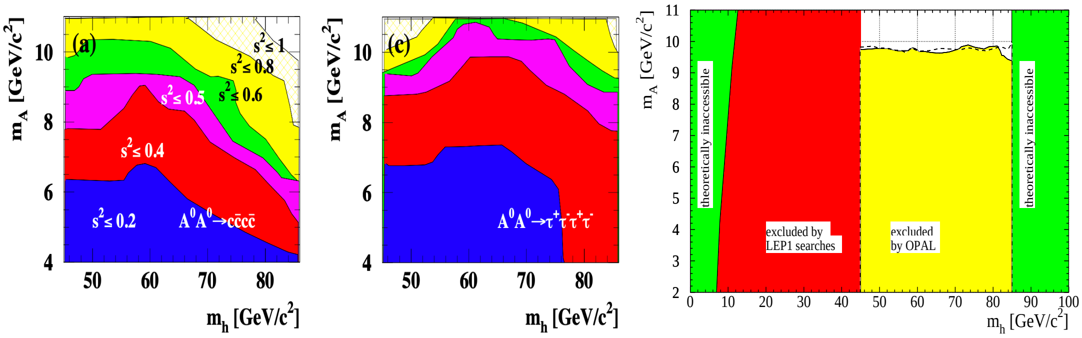

Figure 2.4: *Observed upper limits on the production cross section times branching ratio of the process* $e^+e^- \to hZ \to AAZ$ *scaled to the production cross section of the SM Higgs boson* $s^2 = B(h \to AA) \cdot \sigma_{hZ}/\sigma^{\mathrm{SM}}_{HZ}$ *on the* $(m_h,\, m_A)$ *plane from the dedicated low-mass CP-odd Higgs boson search in the OPAL LEP2 data for the (left)* $Zc\bar{c}c\bar{c}$ *and (middle)* $Z\tau^+\tau^-\tau^+\tau^-$ *final states. (right) Excluded regions in the CPC CMSSM no-mixing scenario. [182]*

In general, the quasi model-independent cross section bounds from the neutral Higgs searches were interpreted in the framework of a CMSSM variant extended to seven parameters (for the notations, see Section 1.3.2 and Table 1.3.2). At tree level two parameters are sufficient to describe the Higgs sector, they are chosen to be the ratio of the vacuum expectation values ($\tan\beta$) and a Higgs mass (m_A in CPC and $m_{\mathrm{H}^\pm}$ in CPV scenarios). Additional parameters appear after the radiative corrections: the soft SUSY breaking parameter in the sfermion sector at the EW scale ($m_\mathrm{SUSY} \equiv m_{\tilde{Q}_3} = m_{\tilde{t}} = m_{\tilde{b}}$), the SU(2) gaugino mass parameter (M_2), the common trilinear Higgs-squark coupling parameter ($A \equiv A_t = A_b$) for up-type and down-type quarks, the gluino mass ($m_{\tilde{\mathrm{g}}} \equiv M_3$) and the SUSY Higgs mass parameter (μ). The stop and sbottom mixing parameters are then defined as $X_t \equiv A_t - \mu\cot\beta$ and $X_b \equiv A_b - \mu\tan\beta$. CP-violation can then be introduced via the imaginary components (called phases and denoted by ϕ_i Table 1.3.2) of A and $m_{\tilde{\mathrm{g}}}$.

Instead of varying all the above parameters, only a certain number of representative benchmark sets were considered where the tree level parameters were scanned while all other parameters remained fixed [183, 184]. On top of the traditional three LEP benchmark scenarios (large-μ, no-mixing and m_h-max) several others were studied motivated by limits of the era from $\mathrm{b} \to \mathrm{s}\gamma$ and muon anomalous magnetic dipole moment measurements or by features of the searches expected at the LHC. A CPV scenario called CPX [179], and its several variants were also probed for the first time by the OPAL collaboration [181].

The **large-μ scenario**, designed to be kinematically always accessible and have the $\mathrm{h} \to \mathrm{b}\bar{\mathrm{b}}$ decay suppressed, was entirely excluded by the LEP combination [185] for any top mass satisfying $m_\mathrm{t} \le 174.3$ GeV, thanks to flavor-independent searches. The **no-mixing scenario** where the parameters are arranged to have no mixing between the left- and right-handed stop fields, was strongly constrained, with lower mass limits of 93.6 GeV for both the lightest CP-even and CP-odd Higgs bosons. In the **m_h-**

max scenario, which gives the maximal value of $m_{\rm h}$ for a given $\tan\beta$ and $m_{\rm A}$ choice, the lower limit on the Higgs boson masses were found to be $m_{\rm h} > 92.8$ GeV and $m_{\rm A} > 93.4$ GeV and the range $0.7 < \tan\beta < 2.0$ was excluded (Figure 2.5 top). The additional CPC benchmark scans of **"gluophobic"** (suppressing hgg coupling) and **"small-$\alpha_{\rm eff}$"** (suppressing hbb and h$\tau\tau$ couplings) **scenarios** did not present difficulties at LEP either: the derived lower limits on the Higgs boson masses are similar: 90.5 GeV and 87.6 GeV for h, and about 96.1 GeV and 98.6 GeV for A for the measured value of the top quark mass of 172.5 GeV, interpolated from the bounds given in Table 5 of Ref. [185].

It is striking how the introduction of CP violation changed the picture. While all CPC scenarios were very strongly constrained, as seen in the exclusion for the $m_{\rm h}$-max scenario in Figure 2.5, large regions remained open in the CPX scenario which was designed to maximize the CPV effects while fulfilling the experimental constraints from electron and neutron electric dipole moment (EDM) measurements. Notably, for a wide range of model parameters, CPX and its variants manifest a decoupling of $\rm H_1$ from Z bosons, as shown in Figure 2.6 in the range $4 < \tan\beta < 10$, as only the CP-even component couples to the Z. While $\rm H_2$ couples to the Z, its mass is close to or above the kinematic limit, being typically above 100 GeV. Moreover, the typical decays providing

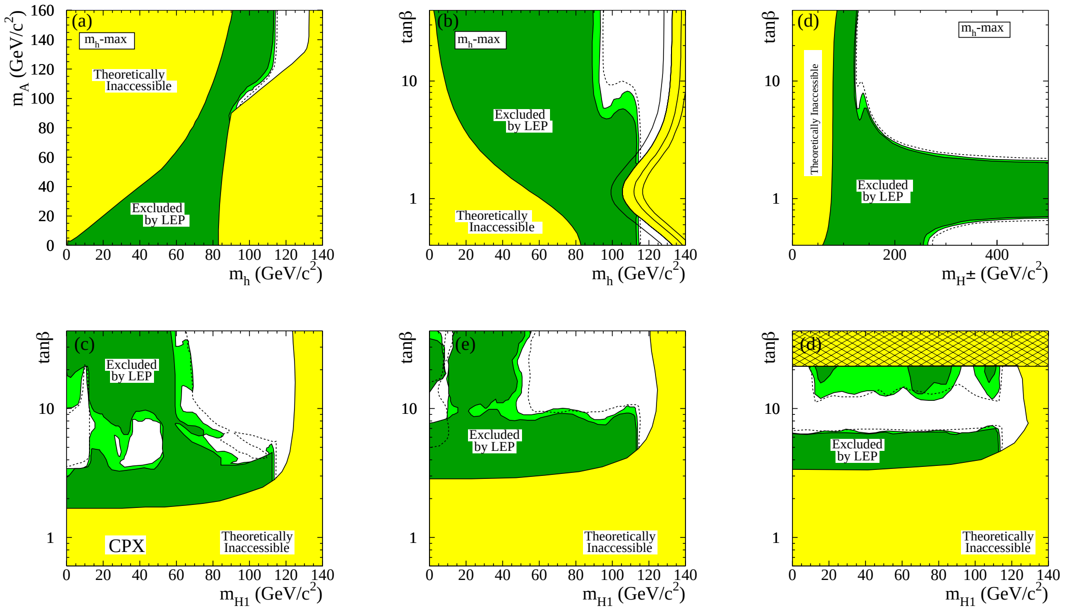

Figure 2.5: *Excluded regions by the LEP combination of neutral Higgs boson searches at the 95% CL (light-green) and the 99.7% CL (dark-green) in the case of (top) the CP-conserving MSSM m_h-max and (bottom) three CP-violating CPX benchmark scenarios for $m_{\rm t} = 174.3$ GeV. The theoretically inaccessible domains are also shown (yellow). The dashed lines indicate the boundaries of the regions which are expected to be excluded at 95% CL. Three projections of the parameters are shown for the m_h-max scenario at the top. In the $m_h - \tan\beta$ projection, the upper boundary of the parameter space is indicated for four values of the top quark mass; from left to right, $m_{\rm t}$ = 169.3, 174.3, 179.3 and 183.0 GeV. For the CPX scenario at the bottom, to illustrate the strong parameter dependence of the results, the $m_{H_1} - \tan\beta$ projection is shown (left) for the original CPX scenario, (middle) when the CP-violating phase is changed from 90° to 135°, and (right) when the Higgs mass parameter μ is increased from 2 to 4 TeV. The cross-hatched region on the right plot has large theoretical uncertainties. [185]*

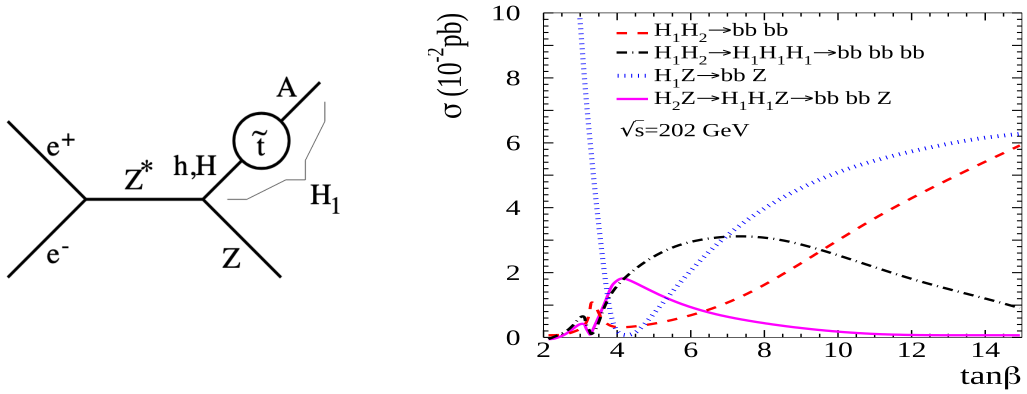

Figure 2.6: *(left) Illustration of the H_1 coupling to the Z via the CP-even component, leading to suppressed coupling [181]. (right) Cross sections as a function of* $\tan\beta$ *for some of the dominant Higgs boson production processes in the CP-violating CMSSM scenario CPX, using the FeynHiggs2.0 [186–189] calculation with an* e^+e^- *center-of-mass energy of* $\sqrt{s} = 202$ *GeV, assuming* $m_\mathrm{t} = 175$ *GeV and* $m_{H_1} = 35 - 45$ *GeV [185]*
.

the CPC discovery channels, such as $\mathrm{H_1 \to b\bar{b}}$, $\mathrm{H_2 \to b\bar{b}}$ and $\mathrm{H_2 \to H_1H_1 \to b\bar{b}b\bar{b}}$ may have lower branching ratios. The excluded areas for various versions of the CPX scenario are shown in the lower part of Figure 2.5. When compared to the equivalent (top middle) plot of the m_h-max scenario, it is apparent that the medium $\tan\beta$ and the higher m_{H_1} regions raised particular challenges.

In the light of the improved bound of the electron EDM by the ACME collaboration [190, 191] and the discovery of the SM-like Higgs boson with mass of 125 GeV at the LHC, CP-violation in the Higgs sector is severely constrained [192]. New MSSM scenarios have been proposed featuring additional heavy Higgs bosons that still allow for CPV [193, 194].

While in most of the LEP benchmark scenarios the SUSY breaking scale was chosen to be high, so that no exotic decay contributes to the width, the LEP1 and previous experimental data did not exclude the existence of a neutral weakly interacting LSP (such as the lightest neutralino) accessible at LEP2. Such models can be tested by looking for the invisible decay of neutral Higgs bosons such as $\mathrm{h} \to \tilde{\chi}^0_1\tilde{\chi}^0_1$. In the case of a pure photino-like LSP, for which the pair-production process is suppressed, and a compressed mass spectrum, i.e. a small mass difference between the LSP and the NLSP, nearly invisible decays via $\mathrm{h} \to \tilde{\chi}^0_2\tilde{\chi}^0_1 \to (\mathrm{Z}^{(*)}/\gamma)\tilde{\chi}^0_1\tilde{\chi}^0_1$ were studied instead. The OPAL experiment gave upper limits on the cross section times branching ratio of these processes, and lower mass limits in the range of 107.0 – 108.4 GeV on the Higgs boson under the extreme assumption of 100% (nearly) invisible decay [195], as shown in Figure 2.7.

2.2.2 Neutral Higgs bosons in general 2HDMs

Moving away from supersymmetric models, the OPAL collaboration played a leading role in the LEP era to study general 2HDM models, assuming CP-conservation in the Higgs sector and no additional non-SM particles other than the Higgs bosons [196].

In the neutral sector, searches for $\mathrm{e^+e^-} \to \mathrm{hZ}$ / hA production sensitive to the $\mathrm{h/A} \to \mathrm{b\bar{b}}, q\bar{q}, \mathrm{gg}, \tau^+\tau^-$, and $\mathrm{h} \to \mathrm{AA}$ decay modes of the Higgs bosons were interpreted in 2HDM(II), setting the masses of the other scalar particles (H^0 and $\mathrm{H}^\pm$) above

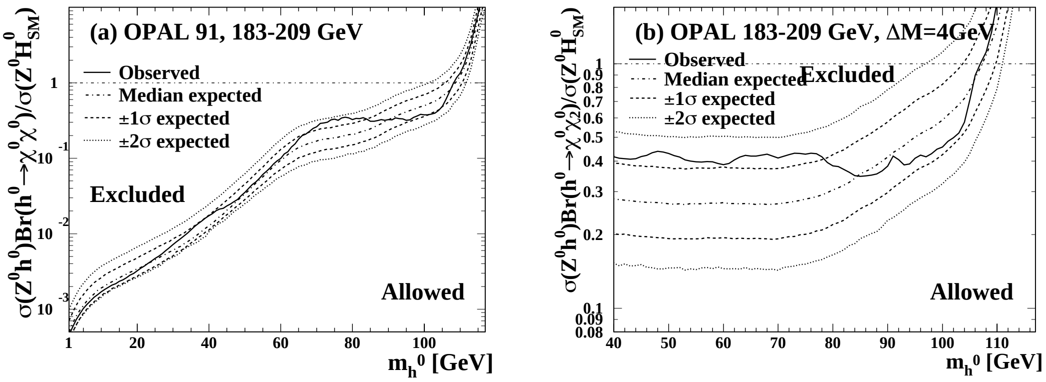

Figure 2.7: *Observed and expected upper limits on the production cross section times branching ratio for the (left) invisible and (right) nearly invisible decay of a neutral Higgs boson scaled to the production cross section of the SM Higgs boson, based on the analysis of the OPAL LEP2 data. For the nearly invisible decay, a mass difference between the lightest and second lightest neutralino of 4 GeV is assumed which determines the activity from soft particles co-produced with the invisible LSP. [195]*

the kinematically accessible region. Scanning the ranges from 210 GeV to 2 TeV for H^0 and from 1 to 2 TeV for $\mathrm{H}^{\pm}$ showed no sensitivity of the analysis to these parameters.

The cross section of the two dominant Higgs boson production processes $\mathrm{e}^+\mathrm{e}^- \to \mathrm{hZ}$ and hA depend on the values of $\beta - \alpha$:

$$\sigma_{\mathrm{hZ}} = \sin^2(\beta-\alpha)\sigma_{\mathrm{HZ}}^{\mathrm{SM}} \qquad \sigma_{\mathrm{hA}} = \cos^2(\beta-\alpha)\bar{\lambda}\sigma_{\mathrm{HZ}}^{\mathrm{SM}} \tag{2.2}$$

with $\bar{\lambda}$ accounting for the suppression of the P-wave cross section near the threshold and depending on the boson masses and the center-of-mass energy. The decay branching ratios are also affected by the values of β and α via the Higgs – fermion couplings (see Figure 2.1). This highlights the importance of flavor-independent searches for optimal sensitivity in 2HDM(II). These searches [197] can also be interpreted in a model-independent way, giving upper limits on the hA production times branching ratio to fully hadronic final states, as shown in Figure 2.8. The results were also presented in 2HDM(II) scanning the parameter space of (m_{h}, m_{A}, $\tan\beta$, α). The excluded regions were given combining all searches for neutral Higgs bosons in the general case of 2HDM(II) and for the MSSM-type parameter choices of $-\pi/2 \le \alpha \le 0$. The region of $1 \ge m_{\mathrm{h}} \ge 55$ GeV and $3 \ge m_{\mathrm{A}} \ge 63$ GeV was excluded for both cases. The largest sensitivity was observed for $\alpha = -\pi/4$, while the most limiting case was $\alpha = +\pi/4$.

2.2.3 Higgs - radion states

As discussed in Section 1.3.1, a scalar radion ($\mathcal{R}$) arises in the RS extension of the SM with extra dimensions, and mixes with the Higgs field. The radion couplings are similar to the Higgs couplings but suppressed by a factor of $v/(\sqrt{6}\Lambda_{\mathrm{W}})$, where v is the Higgs vacuum expectation value and $\Lambda_{\mathrm{W}} = M_{\mathrm{Planck}}e^{-kr_0}$ is the mass scale on the SM brane due to the exponential damping of the gravitational strength. The radion, however, also couples directly to gluon pairs, and the $\mathcal{R} \to \mathrm{gg}$ decay was expected to be dominant at LEP.

The OPAL Collaboration re-interpreted its SM, flavor and decay-mode independent Higgs boson searches in the RS model and derived limits on the $\mathcal{R}$ and h masses as a function of the mass scale on the SM brane Λ_{W} and the radion-Higgs mixing parameter

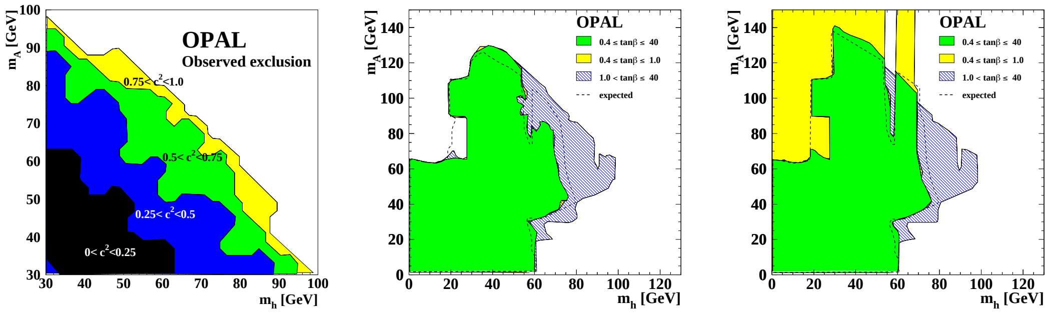

Figure 2.8: *(left) Upper limits on the cross section of* $e^+e^- \to hA$ *production times the branching ratio to fully hadronic decays based on flavor-independent searches in the OPAL LEP2 data, normalized to the maximal cross section predicted for* hA *at* $\cos^2(\beta-\alpha) = 1$. *(middle) Excluded regions in 2HDM(II) for various ranges of* $\tan\beta$ *on the* (m_h, m_A) *plane for all scanned values of* $\alpha = \pm\pi/2, \pm\pi/4, 0$. *(right) The excluded regions for non-positive* α *values as required by the MSSM. [197]*

ξ as shown in Figure 2.9 [161, 198]. As opposed to the Higgs-like state, searches for the radion-like state loose sensitivity for larger values of Λ_{W} due to the suppressed coupling, and for large negative values of ξ close to the theoretically inaccessible region. Therefore, no absolute limit on the radion mass was derived. The absolute lower limit on the mass of the Higgs-like state at large Λ_{W} approaches the limit derived for the SM hypothesis, as the mixing with the radion has a diminishing effect on the phenomenology.

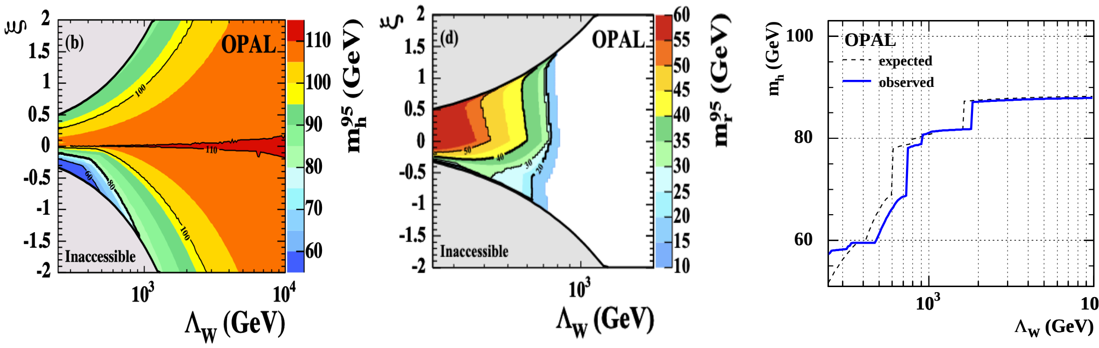

Figure 2.9: *Observed lower limits on the mass of (left) the Higgs-like and (middle) radion-like state in the RS model from the re-interpretation of the OPAL Higgs boson searches in the* $(\Lambda_{\mathrm{W}}, \xi)$ *plane. (right) Absolute lower limit on the mass of the Higgs-like state as a function of* Λ_{W}.

With the larger accessible collision energies and the discovery of a SM-like Higgs boson at the LHC, new possibilities have opened up for radion production and subsequent decay, moving the search sensitivity to the TeV mass region (e.g., see Refs. [199, 200]).

2.2.4 Charged Higgs bosons

Charged Higgs boson searches at an $\mathrm{e}^+\mathrm{e}^-$ collider are much less model-dependent than the ones at hadron colliders due to the simple production mechanism: $\mathrm{e}^+\mathrm{e}^- \to \mathrm{H}^+\mathrm{H}^-$. The searches were conducted in the framework of 2HDMs [201], as at tree-level in MSSM the mass of the charged Higgs boson is calculated as $m^2_{\mathrm{H}^\pm} = m^2_{\mathrm{A}} + m^2_{\mathrm{W}}$ [177, 202], thus its production was expected to be kinematically suppressed at LEP. The measured width of the Z boson [15] placed a stringent limit on the non-SM contribution $\Gamma_{\mathrm{NP}} < 2.9$ MeV and thus on the existence of new particles coupling to the Z. In the case of the charged Higgs bosons, this translates to a lower limit of $m_{\mathrm{H}^\pm} > 39.6$ GeV on the mass [203]. The direct search of OPAL at LEP1 (that I conducted as a part of my MSc research) increased this limit to 44.1 GeV [149] in Type-II 2HDM.

In 2HDM(I) all fermions couple to the charged Higgs with a strength proportional to $1/\tan\beta$, while in 2HDM(II) isospin $+1/2$ quarks couple with $1/\tan\beta$ and isospin $-1/2$ quarks with $\tan\beta$. This implies that in Type-II models (for not too small values of m_{A} and $\tan\beta$), charged Higgs bosons decay predominantly to the kinematically allowed heaviest fermions, which in the charged Higgs mass region of interest at LEP are expected to be $\mathrm{H}^+ \to \tau^+\nu_\tau, \mathrm{c\bar{s}}, \mathrm{c\bar{b}}$. In Type-I models, however, charged Higgs bosons can also decay into pairs of (possibly off-shell) gauge and Higgs bosons, and these modes can even become dominant at large $\tan\beta$ [204, 205]. Considering that light CP-even Higgs bosons were excluded independent of their decay mode at LEP by the OPAL Collaboration [206], the $\mathrm{H}^\pm \to \mathrm{W}^{\pm(*)}\mathrm{A}$ decay had thus to be considered. The search was conducted assuming $\mathrm{A} \to \mathrm{b\bar{b}}$ decay and thus addresses the region $m_{\mathrm{A}} > 12$ GeV.

The results for Type-1 and Type-2 models are summarized in Figure 2.10, both for the OPAL measurement [207] that I coordinated and brought to publication, and for the LEP combination [203] prepared by the LEP Higgs Working Group where I represented OPAL.

In 2HDM(II), the interpretation was carried out assuming $Br(\mathrm{H}^+ \to \tau^+\nu_\tau) + Br(\mathrm{H}^+ \to q\bar{q}') = 1$ where $q\bar{q}' = \mathrm{c\bar{s}} + \mathrm{c\bar{b}}$ in the OPAL and $q\bar{q}' = \mathrm{c\bar{s}}$ in the LEP analysis. The combination raised the lower limits on the charged Higgs mass typically by $3-4$ GeV. Masses below 80 GeV were excluded independent of the choice of the leptonic branching ratio (i.e. independent of the model parameters with the assumption that fermionic decays saturate the width). At $m_{\mathrm{H}^\pm} \approx m_{\mathrm{W}}$, the SM background from WW production became overwhelming in the hadronic channel, and limited the sensitivity. A small excluded island appeared just above the W mass for hadronic branching ratios close to 1.0 as the signal to background ratio improved off the W resonance.

In the case of 2HDM(I), regions of intermediate $\tan\beta$ with significant rate for both fermionic and $\mathrm{W}^{(*)}\mathrm{A}$ decays were the most challenging as can be seen from the valley (local minima) for the charged Higgs mass limit parallel to the $m_{\mathrm{H}^\pm} = m_{\mathrm{A}}$ diagonal. It separates the two regions where the fermionic or the $\mathrm{W}^{(*)}\mathrm{A}$ analyses dominate the sensitivity and appeared due to the switch between these. The four-fermion final states are sensitive close to the diagonal and those targeting $\mathrm{W}^{(*)}\mathrm{A}$ decays at lower values of m_{A}. Due to the presence of overlapping events only one set of these measurements could be used in the combination for a given parameter choice. The combination improves the limits by 2-7 GeV typically. In the region around $m_{\mathrm{H}^\pm} = 60$ GeV at low m_{A}, where an upward statistical fluctuation was present in the OPAL data and resulted in a significantly worse than expected result, the gain was more important and reached 16.5 GeV as the excess lost its statistical significance in the combination. The global mass limit thus improved to 72.5 GeV scanning a wide range of $\tan\beta = 0.1 - 100$ and $m_{\mathrm{A}} = 12 - 70$ GeV, the minimum being at $\tan\beta = 1.6$ and $m_{\mathrm{A}} = 12$ GeV. These results were made possible due to dedicated searches by the DELPHI and OPAL collaborations for $\mathrm{H}^+ \to \mathrm{W}^{(*)}\mathrm{A}$.

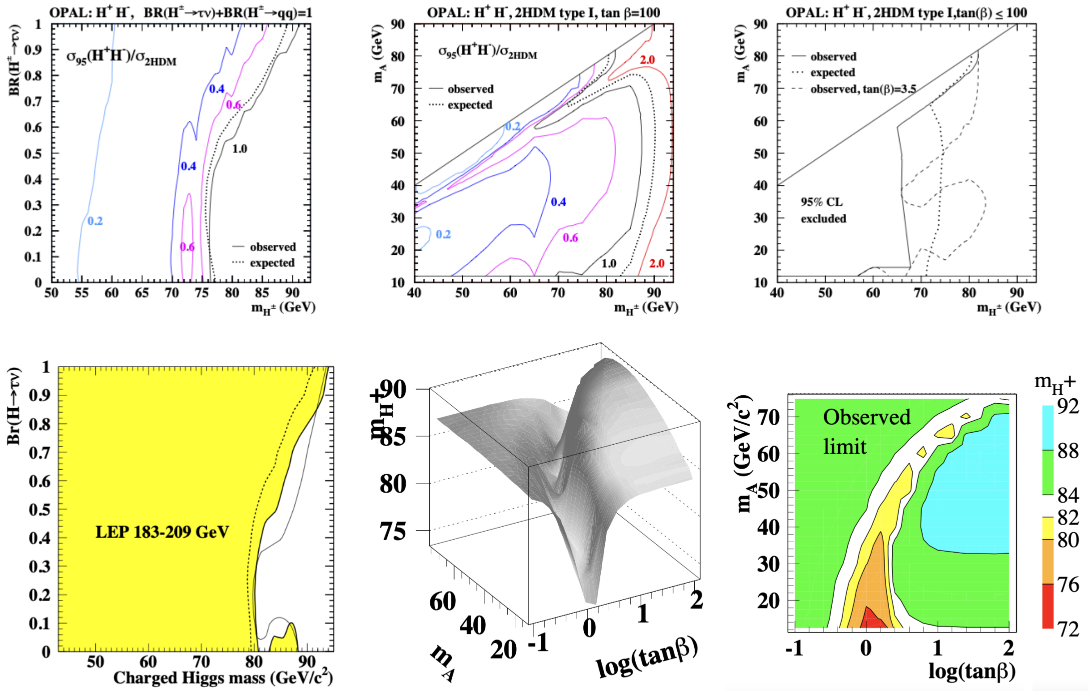

Figure 2.10: *(left top) Upper limits on the charged Higgs boson production cross section scaled to the 2HDM prediction on the* ($m_{H^\pm}$, $BR(H^+ \to \tau^+\nu_\tau)$) *plane based on the analysis of the OPAL LEP2 data [207], assuming that only fermionic decays contribute as expected in 2HDM(II). The area to the left of the solid black line is excluded, the dashed line indicates the expected exclusion in the absence of a signal. (left bottom) Excluded regions when combining the results of the four LEP collaborations [203]. (middle top) Excluded charged Higgs boson production cross section scaled to the 2HDM prediction on the* ($m_{H^\pm}, m_A$) *plane in 2HDM(I) model with* $\tan\beta = 100$ *from the OPAL analysis. (right top) Excluded region independent of the choice of* $\tan\beta$ *in the OPAL study. The unexcluded region reaching down to 56 GeV close to* $m_A = 12$ *GeV is due to a statistical upward fluctuation. (middle and right bottom) Lower mass limits on the charged Higgs mass as a function of* m_A *and* $\log(\tan\beta)$ *from the LEP combination. [203, 207]*

2.3 Supersymmetric partners

Naturalness arguments suggest that the energy scale of SUSY breaking is around the TeV scale and thus the supersymmetric partners of SUSY particles of SM fields acquire a mass that could be accessible at colliders.

All sparticles were expected to be pair-produced at LEP via s-channel γ or Z exchange, if kinematically allowed [208]. For third generation sfermions, the production cross section depends on the mixing between the left- and right-handed fields. The cross sections of first generation sfermion ($\tilde{\mathrm{e}}$, $\tilde{\nu}_{\mathrm{e}}$), and electroweak gaugino ($\tilde{\chi}_i^\pm$, $\tilde{\chi}_i^0$) pair-production get also t-channel contributions and depend strongly on the model parameters.

SUSY phenomenology is largely determined by the nature of the LSP and the NLSP. The LEP collaborations conducted an extensive program to explore supersymmetric phenomena in various models based on gravity, gauge and anomaly mediation of the SUSY breaking [159, 161].

2.3.1 R-parity conserving CMSSM

If R-parity is conserved and the LSP is electrically neutral and not strongly interacting, it is a dark matter candidate. In the supergravity inspired models described in this section, the LSP is usually considered to be the lightest neutralino or a sneutrino.

As single production in e^+e^- collisions would imply R-parity violation, the LEP studies concentrated on the pair-production processes, in particular on the following ones:

Chargino

- $\tilde{\chi}_1^+\tilde{\chi}_1^- \to (\tilde{\chi}_1^0 f\bar{f}')\,(\tilde{\chi}_1^0 \bar{f} f')$ via $\tilde{\chi}_1^\pm \to \tilde{\chi}_1^0 W^\pm$ or $\tilde{\chi}_1^+ \to \tilde{f}\bar{f}'$;
- $\tilde{\chi}_1^+\tilde{\chi}_1^- \to \tilde{\nu}\ell^+\bar{\tilde{\nu}}\ell^-$ when the LSP is a scalar neutrino;

Neutralino

- $\tilde{\chi}_1^0\tilde{\chi}_2^0 \to \tilde{\chi}_1^0\,(\tilde{\chi}_1^0 f\bar{f})$, and
- $\tilde{\chi}_2^0\tilde{\chi}_2^0 \to (\tilde{\chi}_1^0 f\bar{f})\,(\tilde{\chi}_1^0 f\bar{f})$ via $\tilde{\chi}_2^0 \to \tilde{\chi}_1^0$ Z/h/A, or $\tilde{\chi}_2^0 \to \tilde{f}\bar{f}$;

Scalar leptons

- $\tilde{\ell}^+\tilde{\ell}^- \to (\tilde{\chi}_1^0\ell^+)\,(\tilde{\chi}_1^0\ell^-)$;

Light scalar quarks and scalar bottom quark

- $\tilde{q}\bar{\tilde{q}} \to (\tilde{\chi}_1^0 q)\,(\tilde{\chi}_1^0\bar{q})$;

Scalar top quark

- $\tilde{t}_1\bar{\tilde{t}}_1 \to (\tilde{\chi}_1^0 q)\,(\tilde{\chi}_1^0\bar{q})$ via loop diagram with q=c,u;
- $\tilde{t}_1\bar{\tilde{t}}_1 \to (\tilde{\chi}_1^+ b)\,(\tilde{\chi}_1^-\bar{b}) \to (\tilde{\chi}_1^0 f\bar{f}'\, b)\,(\tilde{\chi}_1^0\bar{f} f'\,\bar{b})$ via $\tilde{\chi}_1^\pm \to \tilde{\chi}_1^0 W^\pm$ or $\tilde{\chi}_1^+ \to \tilde{f}\bar{f}'$;
- $\tilde{t}_1\bar{\tilde{t}}_1 \to (\tilde{\chi}_1^+ b)\,(\tilde{\chi}_1^-\bar{b}) \to (\tilde{\nu}\ell^+ b)\,(\bar{\tilde{\nu}}\ell^-\bar{b})$ when the LSP is a scalar neutrino.

The chargino production cross section is large, except if $\tilde{\nu}_e$ is light and the destructive interference between s- and t-channel processes becomes important. In this case, the search for neutralino production improves our sensitivity for SUSY. If sfermions are heavy ($m_0 > 500$ GeV), $\tilde{\chi}_1^\pm$ and $\tilde{\chi}_2^0$ decay dominantly via a W and a Z boson, respectively. For this case, the combined LEP (labeled as ADLO) result placed a limit of 103.6 GeV on the chargino mass [209].

The event properties depend significantly on the mass difference (ΔM) between the pair-produced supersymmetric particle and the LSP. For example, the 200 MeV $< \Delta M <$ 3 GeV range was treated separately in the chargino search using a dedicated analysis of events with initial state radiation to select more boosted topologies. In the range $\Delta M <$ 200 MeV, where the chargino lifetime becomes significant, events with tracks displaying kinks or impact parameter offsets and events with heavy stable charged particles were studied. In the CMSSM, for $|\mu| \ll M_2$, the lightest chargino and the second lightest neutralino are higgsino-like, and degenerate in mass with the neutralino LSP giving low values of ΔM; here a lower limit of 92.4 GeV was obtained on the chargino mass by the ADLO combination performed in the range $\Delta M <$ 10 GeV [210].

Scalar leptons are pair produced through s-channel exchange of a photon or a Z boson in e^+e^- collisions. The scalar electron cross section also gets a model-dependent contribution from t-channel neutralino exchange. The pair production cross section for

$\tilde{\ell}_\mathrm{R}$ is smaller than for $\tilde{\ell}_\mathrm{L}$ [211], therefore conservatively $\tilde{\ell}_\mathrm{L}$ was usually assumed to be out of the reach for the experiments, and results for $\tilde{\ell}_\mathrm{R}$ were given. For staus, left-right mixing can be sizable due to the larger Yukawa coupling of the τ, and can affect the cross section: the mass limits [212] shown in Figure 2.11 worsen by a few GeV when the Z boson is decoupled ($\theta_{\tilde{\tau}} = 52^\circ$).

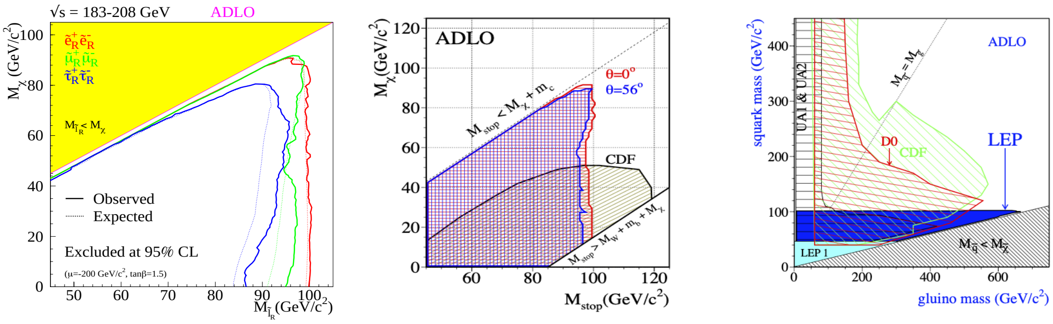

Figure 2.11: *(left) Expected and observed exclusion domains in the slepton – lightest neutralino mass plane taking into account the* $\tilde{\ell}_\mathrm{R} \to \ell\tilde{\chi}_1^0$ *branching ratio. (middle) Excluded domains in the stop – lightest neutralino mass plane for no mixing and for the mixing angle giving the smallest cross section. (right) Excluded domains in the squark – gluino mass plane assuming five mass-degenerate squark flavors.*

Several channels of scalar top decay were explored (Figure 2.12) at LEP. The flavor-changing $(\mathrm{c/u})\tilde{\chi}_1^0$ two-body decay is loop-induced, while the $\mathrm{b}f\bar{f}'\ \tilde{\chi}_1^0$ four-fermion mode proceeds through virtual chargino and W or sfermion cascade, thus they appear in the same perturbative order. If charginos and especially sleptons are light, the four-body mode can have a significantly enhanced contribution and can even dominate. If kinematically allowed, the $\tilde{\mathrm{t}}_1 \to \tilde{\nu}\ell^+\mathrm{b}$ decay mode is dominant over $\tilde{\chi}_1^0\mathrm{c}$. The combined LEP results [213] for the considered two- and three-body modes exclude stop and sbottom masses up to 94−100 GeV for values of the mass difference to the LSP $\Delta M > 10$ GeV, depending on the search channel and the mixing angle, and assuming 100% branching ratio to the decay under study. As an example, the result of the $\tilde{\mathrm{t}}_1 \to \mathrm{c}\tilde{\chi}_1^0$ search is shown in Figure 2.11 (middle). If charginos and sleptons are light and the four-body stop decay $\tilde{\mathrm{t}}_1 \to \tilde{\mathrm{t}}_1 \to \tilde{\nu}\ell^+\mathrm{b}$ is open, the limits on the stop mass become less stringent. For small ΔM, the stop has a significant lifetime and searches for long-lived charged particles constrain parameter space.

The supersymmetric partners of the light quarks were generally expected to be beyond the kinematic reach of LEP2, however their masses could receive large negative corrections from gluino loops. Moreover, to avoid large contributions from squarks to neutral meson mixing, they are frequently assumed to be mass-degenerate. The searches

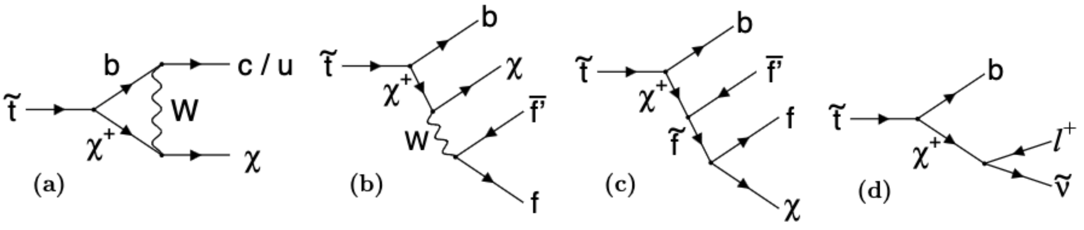

Figure 2.12: *Diagrams of the possible scalar top quark decays with neutralino or scalar neutrino LSP.*

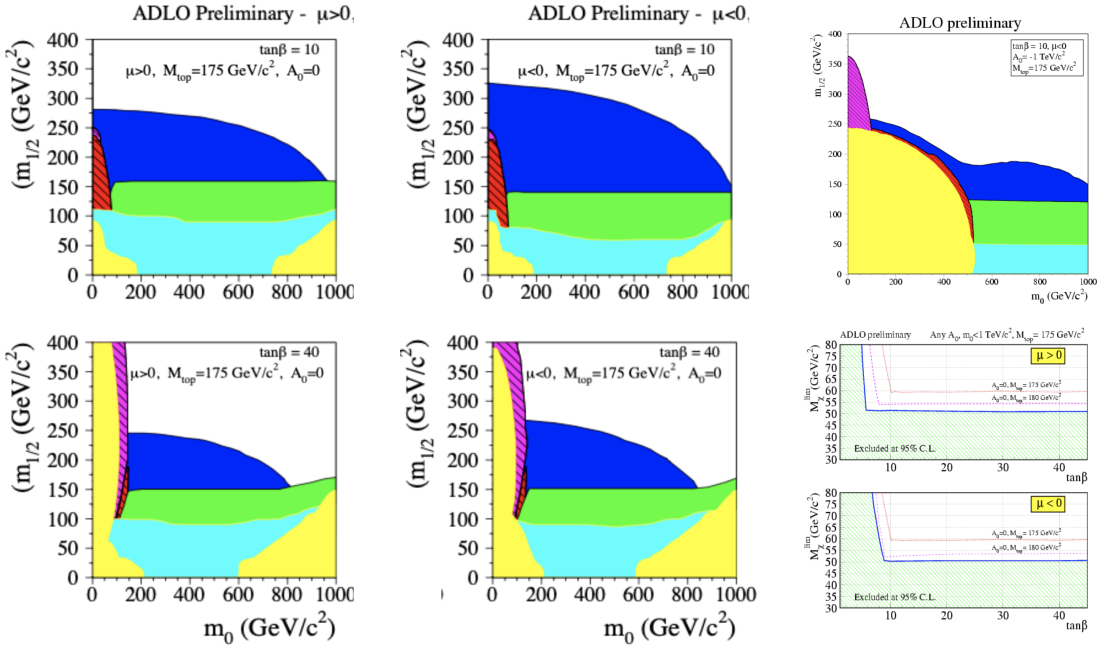

Figure 2.13: *Excluded regions in CMSSM in the* $(m_0, m_{1/2})$ *plane for various choices of* $\tan\beta, \text{sign}(\mu)$*, and* A_0*. The exclusions due to no CMSSM solution (yellow), constraints from LEP1 (light blue), from hZ searches (dark blue), from searches for chargino (green), "standard"* $\tilde{\ell}^{\pm} \to \tilde{\chi}_1^0 \ell^{\pm}$ *slepton (red), heavy stable stau (magenta) neutralino stau cascade decays* $\tilde{\chi}_2^0 \to \tilde{\tau}\tau \to \tilde{\chi}_1^0\tau\tau$ *(brown) are indicated. (bottom right) Absolute lower limits on the* $\tilde{\chi}_1^0$ *LSP mass in the scanned parameter space as a function of* $\tan\beta$ *for positive and negative values of the SUSY Higgs mass parameter* μ*.*

for acoplanar jets can also be translated into constraints shown in Figure 2.11 on the pair-production of mass-degenerate squarks (left-and right-handed $\tilde{\text{u}}, \tilde{\text{d}}, \tilde{\text{s}}, \tilde{\text{c}}, \tilde{\text{b}}$) $\tilde{q}\bar{\tilde{q}} \to q\tilde{\chi}_1^0\bar{q}\tilde{\chi}_1^0$ within the MSSM using lowest order relations between the soft SUSY-breaking gaugino mass term evolution from the grand unified theory (GUT) scale (relating the gluino and neutralino masses) [213].

Combining the results of chargino, neutralino, slepton and Higgs boson searches, limits on the $\tilde{\chi}_1^0$ LSP mass were obtained assuming gaugino and sfermion mass unification at the GUT scale. Using also the constraints from the measurement of the Z width, the obtained bounds on the CMSSM parameters are shown in Figure 2.13 in the $(m_0, m_{1/2})$ plane for various choices of CMSSM parameters to illustrate the strong parameter dependence of the results. The lower limit on the LSP mass was also presented as a function of $\tan\beta$: at low values, it depends strongly on the top mass via the Higgs mass constraint derived from the MSSM $\text{e}^+\text{e}^- \to \text{hZ}$ searches. The theoretical uncertainty is $\mathcal{O}(1\text{ GeV})$ due to the use of tree level gaugino masses and lowest order relations for gaugino unification. The absolute limit is 50.3 GeV (58.6 GeV) for $m_{\text{t}} = 175$ GeV, $m_0 < 1$ TeV and any value of A_0 ($A_0 = 0$), independent of sign(μ) [214]. The limit is almost insensitive of sign(μ): only about 0.5 GeV higher for positive values.

2.3.2 R-parity violating CMSSM and leptoquarks

As there are no theoretical arguments excluding R-parity violation (RPV), its existence needs to be tested experimentally. If R-parity is violated, superpartners can be singly produced and can decay directly to SM particles. The branching ratios of R-parity violating decay modes can be comparable or even larger than the R-parity conserving ones. Thus R-parity violation has a huge impact on experimental signatures and requires dedicated searches. As the LSP is no longer stable, the typical missing transverse momentum requirement cannot be applied.

To respect experimental constraints on the products of two R-parity violating couplings from low energy experiments, the single coupling dominance hypothesis is generally evoked. It is then usually assumed that the superpartners are pair-produced via R-parity conserving processes described in Section 2.3.1. For their decays, two different scenarios are probed [154, 155]. In the first scenario, called indirect decays, the decays of the superpartners via the lightest neutralino are considered (e.g., for sfermions $\tilde{\mathrm{f}} \rightarrow \mathrm{f}\tilde{\chi}_1^0$), where $\tilde{\chi}_1^0$ is treated as the LSP and assumed to decay via an R-parity violating Yukawa coupling ($\tilde{\chi}_1^0 \rightarrow \nu f \bar{f}^{(\prime)}$ / $\ell q \bar{q}'$). In the second scenario, direct decays of the superpartner to SM particles (e.g., $\tilde{\mathrm{e}}^- \rightarrow \mathrm{e}^- \bar{\nu}_\mu / \mu^- \bar{\nu}_\mu /...$; $\tilde{\nu}_\mu \rightarrow \mathrm{e}^- \mu^+ / \mu^- \mu^+$; $\tilde{\mathrm{b}} \rightarrow \mathrm{e}^-\mathrm{u}/\mu^-\mathrm{u}/...$; $\tilde{\mathrm{t}} \rightarrow \mathrm{b}\mathrm{e}^+/\mathrm{b}\mu^+/...$; $\tilde{\mathrm{t}} \rightarrow \bar{\mathrm{d}}\bar{\mathrm{b}}/\bar{\mathrm{s}}\bar{\mathrm{b}}/...$) are investigated, such that it is assumed to be the LSP and R-parity conserving modes do not contribute to the decay. In both scenarios, only one of the 45 Yukawa couplings is non-zero at a time. It is also assumed that the LSP decays promptly, implying a very short lifetime, and therefore a mass larger than 10 GeV for the lightest neutralino.

The topologies resulting from RPV decays of pair-produced sparticles are numerous and extremely varied: direct decays of sfermions lead to 4-fermion, direct decays of charginos and neutralinos to 6-fermion, indirect decays of sfermions to 8-fermion and finally indirect decays of charginos to 10-fermion final states with almost any combination of species and flavors of final state particles. I developed, performed and in the final years supervised the analysis at OPAL in the fully hadronic final states with or without missing momentum.

In general, the limits for λ' and λ'' couplings [215, 216] are less stringent due to the presence of more final state quark jets. This is illustrated by the OPAL results in Figure 2.14 (left) for first generation sleptons. The most stringent cross section limits were achieved for indirect scalar muon decays via λ couplings resulting in multi-lepton final states with missing transverse energy (0.01-0.04 pb), while the least constrained (1-2.5 pb) were scalar tau indirect decays via λ' couplings featuring two tau leptons and multiple jets. For low mass $\tilde{\chi}_1^0$, the $\tilde{\nu} \rightarrow \nu\tilde{\chi}_1^0$ branching ratio decreases. Furthermore, with the increase of the mass difference, the neutrino takes away more momentum, and thus the visible final state objects from the $\tilde{\chi}_1^0$ decay are expected to become softer and thus more difficult to detect, leading to unexcluded regions.

For the scalar top quarks, the theoretical cross section depends on the left-right mixing, and mass limits of 96-100 GeV and 77-88 GeV were derived for direct decays via λ' and λ'' couplings, respectively. In the latter case, the measurement was more challenging due to the large irreducible background from fully hadronic WW and ZZ decays leading to four jets as illustrated by the upper limit on the cross section in Figure 2.14 (bottom right).

The LEP combination [217], shown in Figure 2.15 for indirect decays of various scalar leptons via λ couplings, typically improved the results with respect to individual collaborations by 1-6 GeV: the farther the limit from the kinematically allowed maximum, the larger the improvement. The mass exclusions were similar to those in R-parity conserving models and were largely limited by the kinematic range of LEP. For the indirect decays of scalar neutrinos, the $\tilde{\nu} \rightarrow \nu\tilde{\chi}_1^0$ branching ratio limits the sensitivity at low values of the neutralino mass.

The apparent symmetry in terms of family and multiplet structure of the EW interactions motivate the introduction of a new type of exotic heavy particles, the lepto-

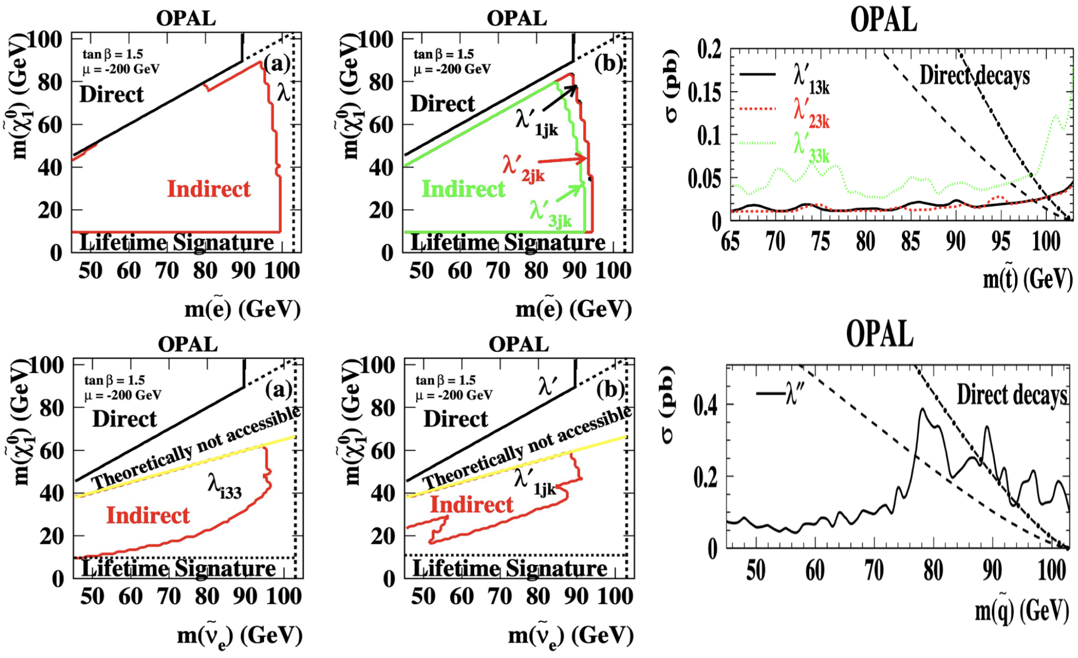

Figure 2.14: *Excluded regions in the scalar lepton – lightest neutralino mass plane from searches for scalar lepton decays via a λ (left) and λ' (middle) couplings in RPV CMSSM from (top) scalar electron and (bottom) scalar electron neutrino searches. (right) Pair-production cross section limits for scalar quarks decaying via λ' (top) and λ'' (bottom) couplings as a function of the hypothesized scalar quark mass, compared to the maximal and minimal theoretical prediction for L-R mixing angles of 0 (dash-dotted line) and 0.98 rad (dashed line). [215]*

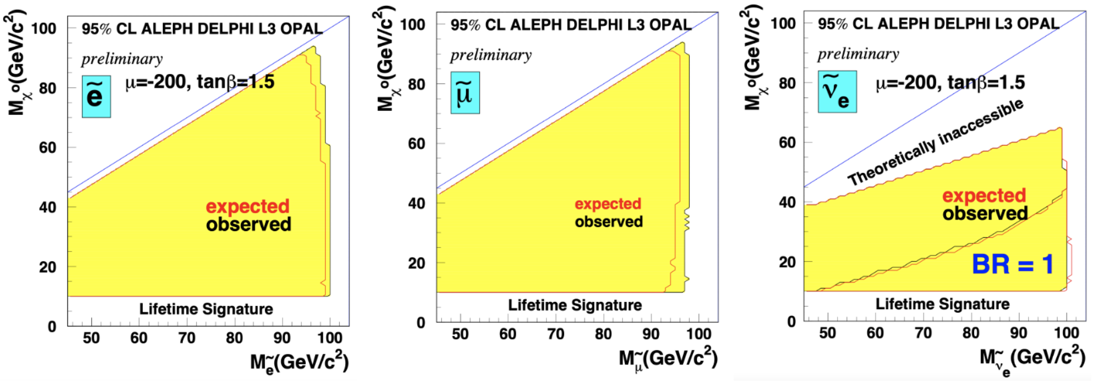

Figure 2.15: *Excluded regions in the scalar lepton – lightest neutralino mass plane from searches for indirect scalar lepton decays via a λ coupling in RPV CMSSM for (left) scalar electron, (middle) scalar muon and (right) scalar electron neutrino. In the latter case, the observed and expected exclusions are shown both for the CMSSM and for the case when the $\tilde{\nu} \to \nu\tilde{\chi}_1^0$ branching ratio is set to unity. [217].*

quarks (LQs). The experimental signatures of the hypothetical leptoquark (LQ) decays to $\nu q, \ell q$ are similar to those of direct RPV decays of scalar fermions via λ' couplings. I was thus invited to act as internal reviewer of several LQ measurements.

The search for the pair-production of scalar and vector LQs of all three generations, covering the region of small values of LQ couplings to fermions (from 10^{-6} to 10^{-2}) provided lower limits on the LQ masses of 93 – 102 GeV, close to the kinematic reach, except for scalar LQs with a charge of $-1/3$ (corresponding to $\tilde{d}_R$) due to a statistical upward fluctuation of the data [218]. The observed lower limits on the masses of the scalar quarks $\tilde{\bar{d}}_L$ and $\tilde{\bar{u}}_L$ are similar to those of the direct RPV SUSY analyses discussed above.

The kinematic reach at LEP can be extended by considering the single production of first generation LQs and squarks via λ'_{1jk} couplings in electron – photon collisions, with the photon being radiated off a beam electron. The photon then either fluctuates to a hadronic object whose quark interacts with the electron, or interacts point-like with the exotic charged particle, or absorbed by the electron that emits the exotic particle (Figure 2.16). Using the data collected at $\sqrt{s} = 189$ GeV, large regions in the coupling strength – mass plane were excluded. For couplings of electromagnetic strength ($\lambda = \sqrt{4\pi\alpha_{\rm EM}(m^2_{\tilde{q},LQ})}$), the excluded mass region extended to 121 – 188 GeV [219]. When adding the full LEP2 data set up to $\sqrt{s} = 209$ GeV [220], the mass reach (Figure 2.17) was extended by 17 GeV at high coupling values of about unity, and by significantly more at lower coupling values. Limits on the coupling strengths were derived as a function of the hypothetised mass. For EM strength coupling, the lower mass limits were raised to 182 – 202 GeV depending on the type of the LQ.

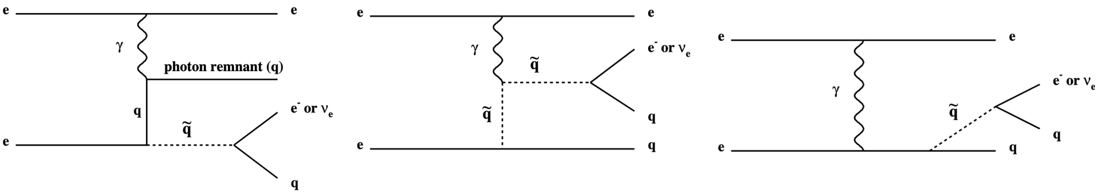

Figure 2.16: *Single squark production processes via λ'_{1jk} coupling in electron - photon interactions at LEP.*

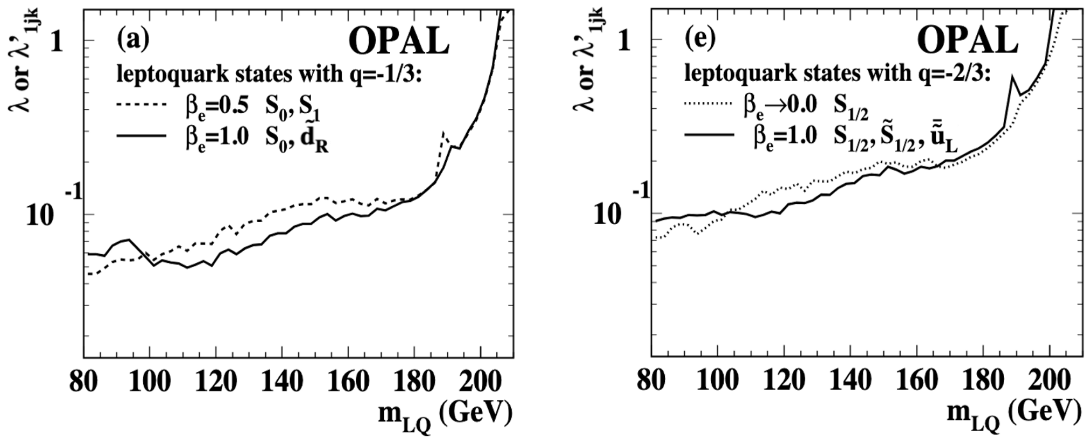

Figure 2.17: *Upper limits on the RPV λ'_{1jk} and leptoquark couplings as a function of the heavy charged particle mass for states with a charge of (left) $-1/3$ and (right) $-2/3$, derived from searches for single production of squarks and LQs in electron - photon interaction with the OPAL detector using the full LEP2 data set. [220]*

Many more searches for new phenomena were conducted at LEP [159, 161], with no evidence uncovered. These studies provided strong constraints on the models and served as the starting point for investigations at the LHC, some of which are summarized in Chapter 6.

The LHC discovery and subsequent measurements of the Higgs boson mass and couplings also place strong limits on the extended Higgs sectors as well as on supersymmetric models as discussed in Section 5.6.

Chapter 3

Experiments at the Large Hadron Collider

Progress in high-energy particle physics requires the construction of large experiments, many years of data taking and a complex data analysis. Experimental collaborations thus have a long lifetime from the birth of the original idea to the final results via the phases of *design*, *construction*, *commissioning* and *physics exploitation.* The example of the Large Hadron Collider (LHC) and the CMS (Compact Muon Solenoid) experiment demonstrates this excellently.

In 1984, the European Committee for Future Accelerators (ECFA) held a meeting in Lausanne, Switzerland to discuss a ”Large Hadron Collider in the LEP Tunnel”, and the *concept* of the LHC was born. The document ”CMS: letter of *intent* by the CMS Collaboration for a general purpose detector at LHC” [221] was submitted in 1992, followed by a more detailed ”Technical proposal” [222] in 1994 to prepare the path to the approval of the experiment – along with its competitor, ATLAS (A Toroidal LHC ApparatuS) – in 1997. The work got more frenzied and in the same year a series of *technical design* reports (TDRs) started to appear detailing the major subsystems of the detector: the magnet system [223], the electromagnetic [224] and hadron calorimeters [225] (ECAL and HCAL), the muon spectrometer [226] and a year later the inner tracking detectors (Tracker) [227]. As *design validation*, *prototyping*, and *testing* progressed, it became clear that a conceptual change at the heart of the detector was required, and an addendum [228] to the CMS Tracker TDR was published in 2000 February presenting the design of the largest fully silicon-based tracking system in the world. Detector design validation, *irradiation campaigns* and off-detector, so-called back-end (BE) electronics design intensified. Soon the first *pre-production* batches were launched, *system tests* performed, giving finally the go-ahead for the *production* of the components and the *assembly* of the larger and larger structures from which the gigantic detector system was built.

From 2000 to 2007, I contributed to the Silicon Strip Tracker [229] construction [230], including (i) design validation tests of the front-end application-specific integrated circuit (ASIC), called APV25, as it features a multi-channel analogue pipeline, fabricated with a 0.25 μm CMOS process; (ii) modeling the timing, trigger and control (TTC) system to understand the time synchronization of the detector; (iii) optimizing the output data format to minimize the required data acquisition (DAQ) bandwidth [231]; (iv) thermo-mechanical tests of the front-end (FE) module components; and finally (v) the assembly using an industrial robot and the subsequent testing of the front-end hybrid printed circuit board (PCB) housing all on-detector readout and control electronics that enables the collection, temporary ”pipeline” storage and – on the reception of a positive trigger decision – forwarding of the silicon sensor strip data [230] for further processing.

In 2008, 24 years after the planning started, the fully tested and operational ATLAS [232] and CMS [229] detector systems awaited the first beams in the LHC tunnel. The collaborations were eager to analyze the data to find the last missing ingredient of the standard model, test its predictions at the new TeV energy frontier and uncover new exotic phenomena shown to be in reach by a wealth of sensitivity studies, such as the ones summarized in Ref. [233] for the case of an extended Higgs sector.

The research summarized in the remainder of this document was carried out within the large international ATLAS and CMS collaborations that built the two largest, most complex general-purpose detector systems in the world to analyze the data provided by the LHC.

3.1 The LHC accelerator

The LHC, an $L_c = 26659$ m circumference synchrotron storage ring constructed 100 m underground in the LEP tunnel, accelerates and then collides bunches of protons or heavy ions (primarily Pb^{82+}). The ring consists of eight straight sections housing particle detectors or beam instrumentation devices and eight arcs with superconducting dipole magnets to bend the trajectory of the particles as illustrated by Figure 3.1.

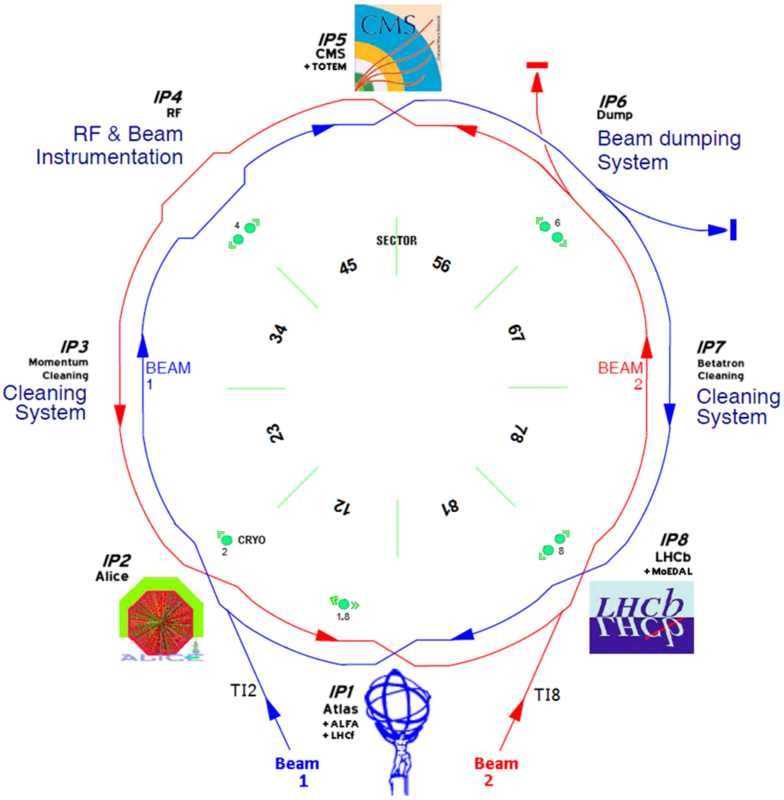

Figure 3.1: *The LHC storage ring with its beam instrumentation and detector systems.*

The LHC radiofrequency (RF) cavities, that generate the longitudinal oscillating electric field to accelerate the particle bunches, work at $f_{\mathrm{RF}} = 400.8$ MHz. This has to be synchronous with the orbit revolution frequency of the bunches $f_{\mathrm{rev}} = \beta c / L_c \approx c/L_c = 11245$ kHz. The harmonic number $h = f_{\mathrm{RF}}/f_{\mathrm{rev}} = 35640$ defines the number of the $1/f_{\mathrm{RF}} = 2.5$ ns (or $c/f_{\mathrm{RF}} = 0.75$ m) long RF buckets which can contain the circulating charges. Grouping ten consecutive RF buckets so that only the first one is potentially filled, the LHC orbit is divided into 25 ns long time windows (bunch crossing slots), defining the bunch crossing frequency of $f_{\mathrm{bc}} = 40.08$ MHz.

However, from the 3564 possible bunch locations (each identified by a sequential bunch crossing identification number, BCID, starting with 1), maximum 2808 are filled with the help of a chain of smaller accelerators that increase the beam energy in various steps as shown in Figure 3.2. The injector chain starts with a linear accelerator: LINAC2 accelerating protons in Run 1 and Run 2 to 50 MeV, or LINAC4 accelerating negatively charged Hydrogen ions H^- in Run 3 to 160 MeV that are then stripped from their electrons during the charge-exchange injection to the PS Booster that can produce twice as bright beams as the previous multi-turn injection. The beams proceed through the four superimposed rings of the Booster to gain an energy of 1.4 GeV. The Proton Synchrotron splits the high-intensity bunches 3×4-fold, and injects them to the Super Proton Synchrotron (SPS) at 25 GeV, which serves as the final pre-accelerator shooting 450 GeV protons to the LHC.

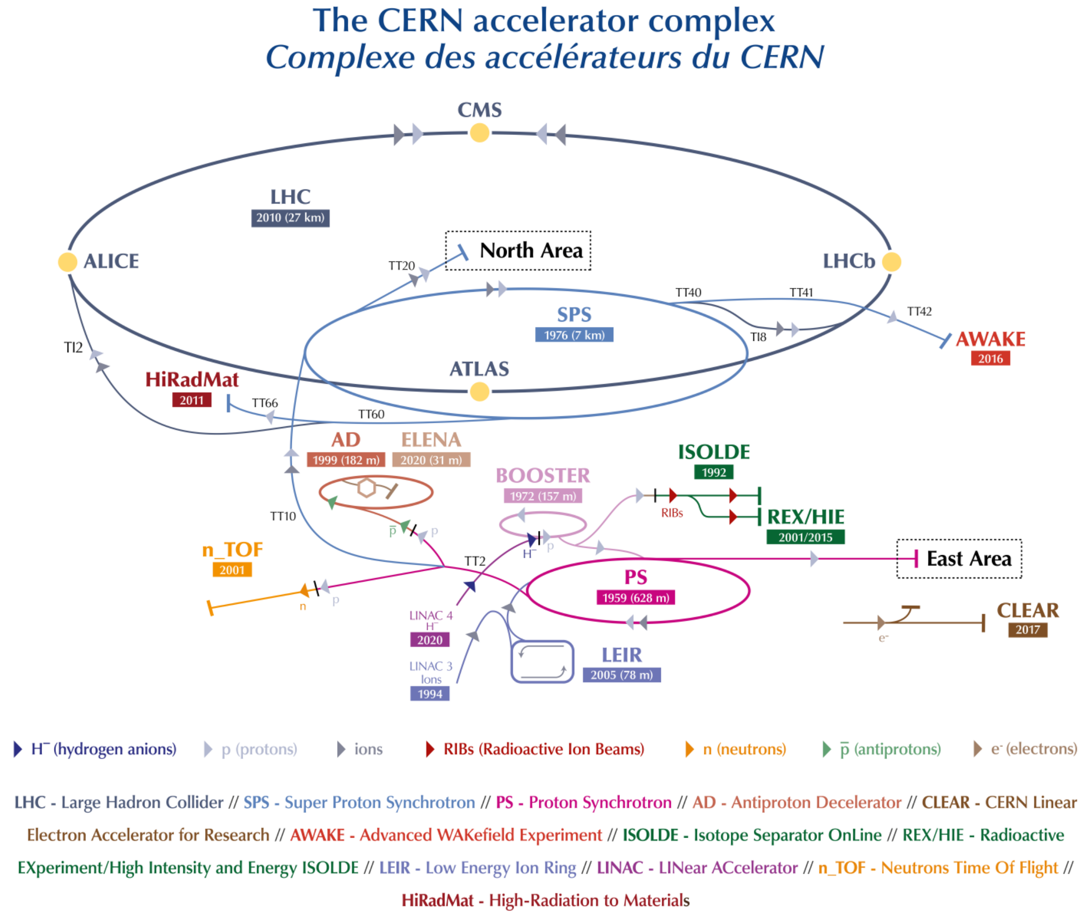

Figure 3.2: *The layout of the CERN accelerator system after 2020, allowing to follow the path of protons and heavy ions from the linear accelerators (LINAC 4 and LINAC 3) to the LHC.*

The number of bunches are limited by the choice of the beam production scheme in the injectors and by the rise times of injection and extraction kicker magnets in the various accelerators involved. Other effects – such as the maximal tolerable heat load on the beam screens of the superconducting magnets in the arcs due to electron clouds formed when the positive circulating charges liberate electrons from gas molecules trapped on the surface of the vacuum pipes, or safety considerations in the LHC injection system with very luminous beams – have also played a role in the definition of the filling pattern (called filling scheme) in a given data taking period [234]. These considerations limit the collision rate to a maximum of about 32 MHz.

A typical filling scheme is composed of long strings of up to 72 consecutive bunches (called a "train"), with the individual trains separated by gaps of varying lengths. Not all bunches collide at every interaction point (IP) due to the location and different requirements of the LHC experiments. The non-colliding bunch crossings, where the bunch location is filled for at most one of the beams, are used to study effects from beam-induced background. The longest, called abort gap is about 3 μs long and serves for the safe extraction of the LHC beams. The two LHC beams, circulating in the clockwise and counterclockwise directions as viewed from above, are designated as "beam 1" and "beam 2".

During typical physics runs, about $1.15{\cdot}10^{11}$ protons are squeezed to a bunch that has a transverse size of $\sigma_\mathrm{b} \approx 15$ μm (with slightly elliptical shape) and a length of $\sigma_z \approx 5$ cm. They are accelerated to a maximum of $E_\mathrm{beam} = 6.8$ TeV energy per proton (reached in 2022, corresponding to a velocity of $\beta_\mathrm{r} = 0.99999999$ and a relativistic Lorentz-factor of $\gamma_\mathrm{r} = 7247$), and brought into collisions at a maximum of four interaction points inside the large detector systems of ALICE [235], ATLAS [232], CMS [229], and LHCb [236] (Figure 3.1). While ATLAS and CMS are general purpose detectors, ALICE was designed to study the quark-gluon plasma created in heavy ion collisions, and LHCb to investigate the properties of heavy flavor hadrons to gain insight to small differences between matter and antimatter.

One of the most important parameters of a collider is the instantaneous luminosity ($\mathcal{L}_\mathrm{inst}$) [237] that determines the rate of a physics process "p" with cross section of σ_p:

$$R_\mathrm{p}(t) = \frac{\mathrm{d}N_\mathrm{p}(t)}{\mathrm{d}t} = \mathcal{L}_\mathrm{inst}(t) \cdot \sigma_\mathrm{p}, \tag{3.1}$$

and enters directly most measurements. See Chapter 4 on its precise determination that I led in CMS.

Instantaneous luminosity can be defined from the beam parameters [238] as given in Ref. [239]:

$$\mathcal{L}_\mathrm{inst} \equiv \sum_1^{n_\mathrm{b}} \mathcal{L}_\mathrm{b} = n_\mathrm{b} \cdot \frac{N_1 N_2 f_\mathrm{rev}}{2\pi \Sigma_x \Sigma_y} S; \qquad S = \left(1 + \frac{\theta_c^2 \sigma_z^2}{4\sigma_\mathrm{c}^2}\right)^{-1/2}. \tag{3.2}$$

Here the sum of single-bunch-crossing instantaneous luminosities ($\mathcal{L}_\mathrm{b}$, SBIL) goes over the number of colliding bunch pairs at the interaction point (n_b). Then it is assumed for simplicity that the numbers of particles per bunch in the two beams (N_1, N_2) are uniform over the bunches (about $(1.1 - 1.25) \cdot 10^{11}$ protons in Run 2). For head-on collisions, the effective convoluted beam size, also called the beam overlap width, is determined by the transverse bunch sizes of beam 1 and beam 2, i.e. for coordinate x:

$$\Sigma_x^2 = \sigma_{x,1}^2 + \sigma_{x,2}^2 = \beta_{x,1}^* \cdot \epsilon_{x,1} + \beta_{x,2}^* \cdot \epsilon_{x,2} \approx \beta^* \cdot (\epsilon_{x,1} + \epsilon_{x,2}) \tag{3.3}$$

The optics parameter β^*, typically assumed to be the same for both beams and both transverse directions, is the value of the $\beta(s)$ function at the interaction point (varying between $0.25 - 0.4$ m in Run 2). $\beta(s)$ determines the transverse beam size defined by the envelope of particle trajectories at a given position s along the orbit in the storage ring under the influence of all focusing fields. The root mean square (RMS) transverse emittance ($\epsilon_{x,i}$) is a measure of the average spread of particle coordinates within a bunch of beam i in the position-momentum phase space along the x coordinate – more precisely, in the (x, dx/ds) plane – with a dimension of length. It is conserved in the presence of only linear optical elements (bending dipoles and focusing quadrupoles). However, it is practical to use instead the transverse normalized emittance $\epsilon_\mathrm{n} = \beta_\mathrm{r}\gamma_\mathrm{r}\epsilon$ (typically $1.8 - 2.2$ μm in Run 2), as the normalization with the longitudinal velocity and the Lorentz-factor removes the dependence on the beam energy due to adiabatic damping, i.e. the decrease of emittance during acceleration. Finally, S is a geometrical reduction factor to the luminosity due to the crossing angle θ_c (typically $\theta_c/2 = 120 - 185$ μrad in Run 2). The transverse RMS beam size in the crossing (in CMS Run 2, horizontal) plane is σ_c.

The precision determination of the luminosity (see Chapter 4) requires a detailed understanding of the complex filling scheme and the sophisticated beam gymnastics of the LHC. The information required for this comes from various beam instrumentation devices installed along the accelerator ring monitoring the horizontal and vertical beam positions, the bunch intensities, and the transverse and longitudinal profiles. The precise knowledge of the optics parameters, such as β^*, the machine tunes Q_x, Q_y giving the characteristic frequency of the transverse betatron oscillation driven by the strength of the quadrupole magnets, and the chromaticity characterizing the spread in the machine tune due to the energy spread of the particles, are also essential. The quality of beam instrumentation determines (and can also limit) the performance of the accelerator.

3.1.1 The physics data set

The LHC started to deliver physics data at a center-of-mass energy of $\sqrt{s} = 2.36$ TeV in 2009, and after a commissioning year at 7 TeV in 2010 with low instantaneous luminosity, intensive data production began in 2011. The development of the collision energy and the time-integrated luminosity ($L_\mathrm{int} = \int \mathcal{L}_\mathrm{inst}(t)\mathrm{d}t$), together with plans for future operations are shown in Figure 3.3. It also shows the numbering of the LHC data taking periods (called Runs), as well as the long shutdowns, and extended year-end technical stops that allow the experimental and accelerator teams to execute more substantial, time-intensive maintenance and upgrade tasks for the detectors, the accelerator chain and the beam instrumentation. The LHC has an about 3-month long year-end technical stop each winter that allows for routine maintenance and smaller upgrade activities.

Details of the collected data sets in Run 1 and Run 2 are given in Figure 3.4 using the example of the CMS experiment. LHC is tuned to deliver within a few percent the same amount of data to ATLAS and CMS, and both experiments work with a high data taking efficiency of about $92 - 94\%$.

The high single-bunch-crossing instantaneous luminosity brings an experimental challenge, the high number of pp collisions per bunch crossing, also called pileup, with its average value indicated by $\langle\mu\rangle$. It scales with the total inelastic cross section (σ_tot):

$$\langle\mu\rangle = \sigma_\mathrm{tot} \cdot \langle\mathcal{L}_\mathrm{b}\rangle / f_\mathrm{rev}. \tag{3.4}$$

The pp event pileup complicates the precise reconstruction of individual pp interactions. An example is the identification (and thus position measurement) of the primary interaction vertices, the efficiency and purity of which depend on $\langle\mu\rangle$. The average number of collisions in Run 2 (Run 3) was $\langle\mu\rangle = 34$ (48) with the distribution reaching up to about 70 (85) in normal physics operations, as shown in Figure 3.5, with a few special runs reaching a peak even above 100. The 2017 distribution features a double peak structure due to a change in the filling scheme.

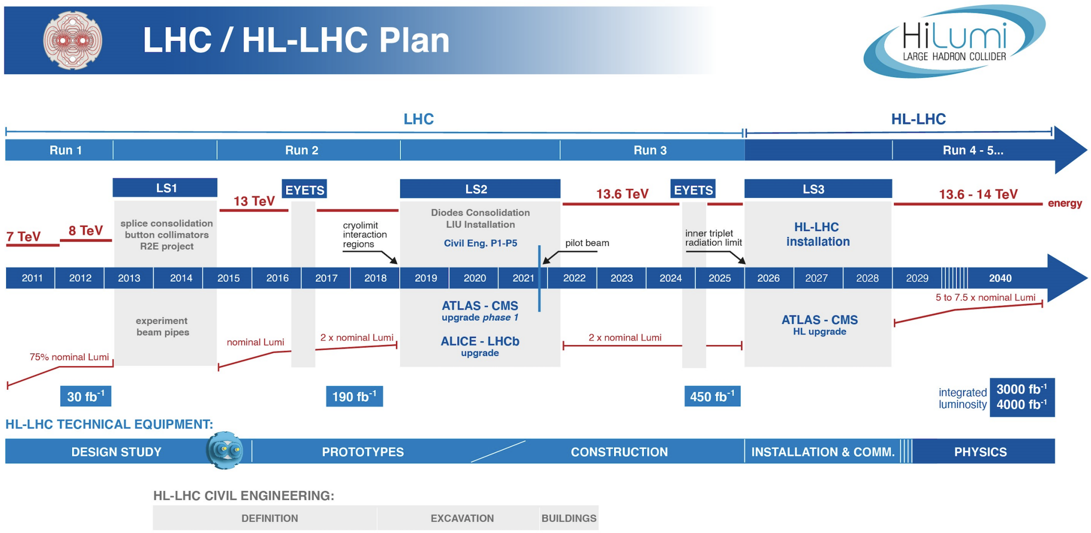

Figure 3.3: *The history and the future planning of the LHC project showing the development of the peak collision energy and the delivered luminosity as a function of time, including the High-Luminosity LHC (HL-LHC) era from 2029. While Run 1 started in 2009, the figure only starts at 2011 when luminosity production ramped up. LS stands for long shutdown, EYETS for extended year-end technical stop. During Run 1 the LHC operated with 50* ns *bunch spacing, since Run 2 with the design 25* ns.

3.1.1.1 The ATLAS data sample

The ATLAS data sample discussed in this work was mainly collected during LHC Run 1. These high-quality proton-proton (pp) collision data correspond to an integrated luminosity of $L_{\text{int}} = 4.57\ \text{fb}^{-1}$ at $\sqrt{s} = 7$ TeV in 2011 with an average number of collisions per beam crossing of $\langle\mu\rangle = 9.1$ [241, 242] (assuming a total inelastic pp cross section of 80 mb [243, 244]) and $L_{\text{int}} = 20.3\ \text{fb}^{-1}$ at $\sqrt{s} = 8$ TeV in 2012 with $\langle\mu\rangle = 20.7$ [242, 245]. The efficiency to record the delivered LHC data was more than 93%. Almost 95% of the recorded events also passed stringent quality criteria and were thus used for the physics analyses.

In 2015 in the first year of Run 2, data taking efficiency stayed high at 92% and the data quality efficiency reached 93% (87% if requiring the seamless operation of the Insertable B-Layer installed during LS1). Most of the data at the record $\sqrt{s} = 13$ TeV center-of-mass energy were taken with 25 ns bunch spacing (the remaining with 50 ns) and a mean number of interactions per beam crossing of $\langle\mu\rangle = 13.5$ with a total of L_{int} $= 3.9\ \text{fb}^{-1}$. The ATLAS detector proceeded to collect a large data sample in Run 2: the total pp data qualified for physics analysis amount to $L_{\text{int}} = 139\ \text{fb}^{-1}$ [246, 247].

3.1.1.2 The CMS data sample

Most of the results presented here are based on the high-quality CMS data collected in Run 2 between 2016–2018 at $\sqrt{s} = 13$ TeV corresponding to about 136 fb^{-1} integrated luminosity, where all subdetectors were in good working condition. More details about the data set are given in Figures 3.4 and 3.5.

In 2022 after the end of LS2, the LHC collision energy was raised to a record 13.6 TeV and the CMS collaboration recorded more than 70 fb^{-1} pp data until the end of July 2023.

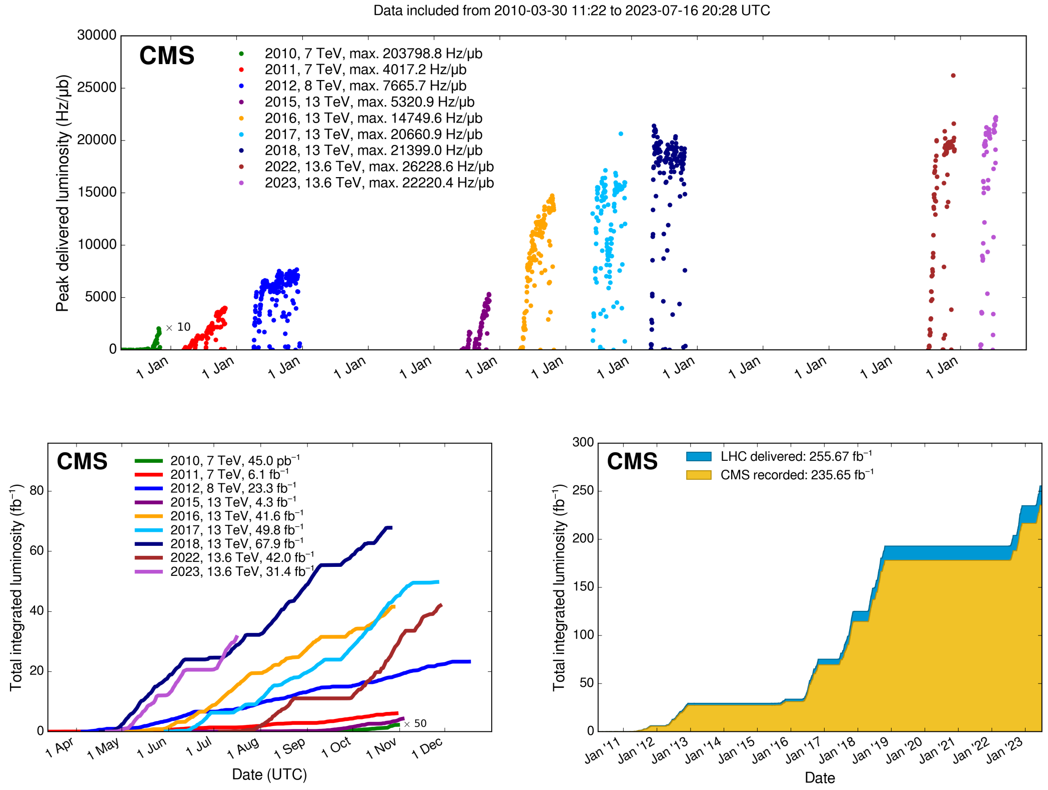

Figure 3.4: *(top) Peak luminosity versus day delivered to CMS during* pp *collisions with stable beams at nominal center-of-mass energy from 2010 to early July 2023. (bottom) Cumulative luminosity versus day (left) per year and (right) for the full period. On the right, the recorded luminosity is also shown, illustrating the high 92.2% average data taking efficiency.*

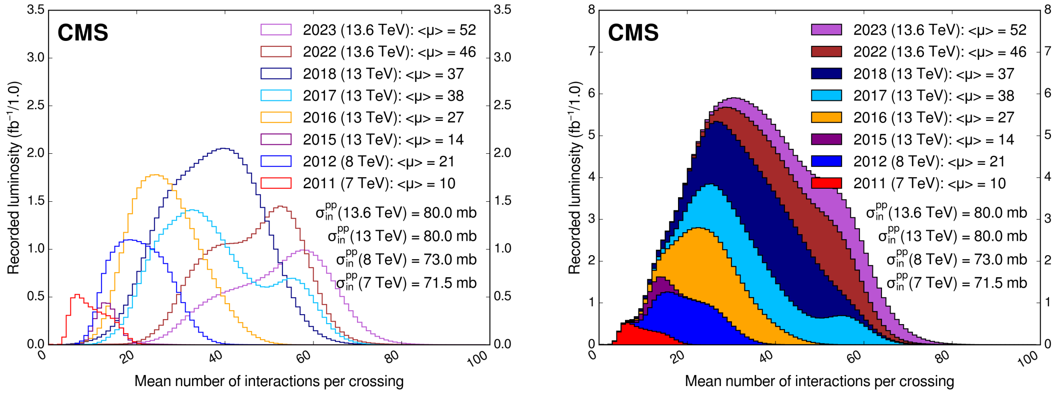

Figure 3.5: *Distribution of the average number of interactions per bunch crossing for* pp *collisions (left) from 2011 per year and (right) stacked, showing also the integrated distribution for the full LHC operation until the end of July 2023. The overall mean values are also given. Only data for which all CMS subdetectors were flagged to be good of good quality are included. The "LHC standard" values for the total inelastic (also called minimum-bias) cross sections, taken from the theoretical prediction of PYTHIA [240], are used to scale the measured single-bunch-crossing instantaneous luminosity according to Eq. 3.4.*

3.2 Detector systems

The physics aims and thus the basic philosophy of the two multi-purpose detector systems, ATLAS and CMS, are the same. Both are cylindrical, forward-backward symmetric, complex, multi-layered systems providing an almost full solid angle coverage around the interaction point.

They use right-handed coordinate systems with their origin at the nominal interaction point in the center of the detector and the z-axis along the beam line. The x-axis points from the interaction point to the center of the LHC ring (horizontally), and the y-axis points upward (vertically). Cylindrical coordinates (r, ϕ) are used in the transverse $(x,\, y)$ plane, ϕ being the azimuthal angle around the z-axis measured from the x-axis. The pseudorapidity is defined in terms of the polar angle θ as $\eta = -\ln[\tan(\theta/2)]$. The angular distance between two objects is defined as $\Delta R = \sqrt{\Delta\eta^2 + \Delta\phi^2}$, where $\Delta\eta$ and $\Delta\phi$ are the differences between the pseudorapidity and the azimuth angle of the two objects, respectively.

As the longitudinal component of the momentum along the beam line (projected to the z-axis) of the colliding partons are not known, many kinematic quantities of interest are defined as projections to the transverse plane. The transverse momentum is computed from the absolute value of the 3-momentum (p) as $p_\mathrm{T} = p \cdot \sin\theta$. The transverse energy is defined as $E_\mathrm{T} = \sqrt{m^2 + p_\mathrm{T}^2}$, following the $c = 1$ convention, which for particles with negligible mass $(m \approx 0)$ leads to $p_\mathrm{T} \approx E_\mathrm{T} \approx E \cdot \sin\theta$, where E is the energy of the particle.

The technological choices in the detector design are summarized in the next sections. Both experiments started with their Phase-0 detector and some of the systems (including, the pixel detectors and the hardware triggers) have been already upgraded just before or during Run 2 (Phase-1 upgrade). The HL-LHC conditions motivate the currently ongoing upgrade projects for the Phase-2 detectors.

While the two detectors were optimized to measure Higgs processes and provide very similar precision, they are rather different technologically and thus suffer from different instrumental biases to a large extent. This allows independent confirmation of physics measurements and a significant improvement when combining the results.

3.2.1 The ATLAS detector

At the heart of ATLAS [232], there is an inner tracking detector inside a superconducting solenoid providing a 2 T axial magnetic field. It is surrounded by a calorimeter system, and a muon spectrometer (MS) in a magnetic field of three large superconducting toroids (one surrounding the center of the experiment and two at the ends) with eight coils each. The results shown in this work correspond to the Run-1 and early Run-2 configurations of ATLAS. The latest Run-3 detector is described in Ref. [248].

The inner detector consists of a silicon pixel detector (Pixel) closest to the beam pipe, a silicon microstrip detector (SCT) consisting of four double-sided layers at intermediate radii covering the range $|\eta| < 2.5$, and a transition radiation tracker (TRT) built up from 73 and 160 layers of straw tube gaseous ionization detectors at outer radii in the barrel and endcap regions at $|\eta| < 1$ and $1 < |\eta| < 2$. The fourth, innermost pixel-detector layer, the insertable B-layer (IBL), was added during LS1 at a radius of 33 mm around a new beam pipe [249]. Track reconstruction is available within $|\eta| < 2.5$ and the achieved momentum resolution for charged particles is 2% at small $|\eta|$ for $p_\mathrm{T} \approx 25$ GeV and deteriorates to 10% at $|\eta| \approx 2$ for $p_\mathrm{T} \approx 120$ GeV [250].

The calorimeter system covers the region $|\eta| < 4.9$. In the central region, a lead –

Detector component	Experiment		
	ATLAS	CMS	OPAL
Data taking	Since 2009	Since 2009	1989−2000
Size	$\oslash 25\,\mathrm{m}\ \ 46\,\mathrm{m}\ (23000\,\mathrm{m}^3)$	$\oslash 14.6\,\mathrm{m} \times 21.6\,\mathrm{m}\ (3800\,\mathrm{m}^3)$	$12 \times 12 \times 12\,\mathrm{m}^3$
Weight	7000 t	14000 t	2800 t (magnet)
Beam pipe	0.8 mm Be $r_{\mathrm{in}} = 2.9\,\mathrm{cm}$ (Run 1), 2.35 cm (Run 2)	0.8 mm Be $r_{\mathrm{in}} = 3.0\,\mathrm{cm}$ (Run 1), 2.2 cm (Run 2)	0.1 mm Al + 1.3 mm carbon fiber $r_{\mathrm{in}} = 7.8\,\mathrm{cm}$ 1.1 mm Be $r_{\mathrm{in}} = 5.35$ cm from 1991
Tracker	Si pixel Run 1 $r = 5.1, 8.9, 12.3\,\mathrm{cm}$, $\lvert\eta\rvert < 2.5$ Run 2 + layer $r = 3.3\,\mathrm{cm}$, $\lvert\eta\rvert < 3$, 92M ch 4-layer Si strip up to $r = 0.51\,\mathrm{m}$, 6M ch Transition radiation straw tube tracker $\lvert\eta\rvert < 2$ (electron – hadron separation)	Si pixel Run 1 $r = 4.4, 7.3, 10.2\,\mathrm{cm}$, $\lvert\eta\rvert < 2.5$ Run 2 $r = 2.9, 6.8, 10.9, 16\,\mathrm{cm}$, $\lvert\eta\rvert < 2.5$, 124M ch 10-layer Si strip up to $r = 1.1\,\mathrm{m}$, 9M ch	2-layer Si strip single-sided from 1991, double from 1993 $r = 6.0, 7.5\,\mathrm{cm}$, $\lvert\eta\rvert < 1.47$, 65.5M ch from 1996 Precision drift chamber Jet chamber z-chambers
Time-of-flight counters	—	—	Scintillation counter $r = 2.36\,\mathrm{m}$, $\lvert\eta\rvert < 1.16$ from 1996 extended $\lvert\eta\rvert < 1.83$, $2.3 < \lvert\eta\rvert < 3.8$
Time resolution			3 ns
EM presampler	$\lvert\eta\rvert < 1.8$	$1.653 < \lvert\eta\rvert < 2.6$	$\lvert\eta\rvert < 1.83$
EM calorimeter	$25X_0$ Pb + LAr accordion sandwich $\lvert\eta\rvert < 3.2$ (photon pointing with 3 layers)	$25X_0$ PbWO$_4$ crystal	$20.5X_0$ lead glass crystal
Energy resolution	$10\%/\sqrt{E} \oplus 0.4\% \oplus 0.3/E$ (E in GeV)	$3\%/\sqrt{E} \oplus 0.5\% \oplus 0.2/E$ (E in GeV)	$5\%/\sqrt{E}$ (E in GeV)
Hadronic calorimeter	Steel + plastic scintillator tiles $\lvert\eta\rvert < 1.7$ Copper + LAr $1.5 < \lvert\eta\rvert < 3.2$	Brass + plastic scintillator $\lvert\eta\rvert < 3$	Iron + limited streamer tubes $\lvert\eta\rvert < 1.53$ Iron + MWPCs to $1.53 < \lvert\eta\rvert < 2.65$
Energy resolution	$52\%/\sqrt{E} \oplus 3\% \oplus 1.6/E$ (E in GeV)	$84.7\%/\sqrt{E} \oplus 7.4\%$ (E in GeV)	$63\%/\sqrt{E} \oplus 20\%$ (barrel) $(100-140)\%/\sqrt{E}$ (poletip) (E in GeV)
Forward calorimeter	EM & hadronic Cu/W + LAr $3.2 < \lvert\eta\rvert < 4.9$	Steel + quartz fibers $3 < \lvert\eta\rvert < 5.2$	Lead + scintillator
Muon system	Resistive plate chambers $\lvert\eta\rvert < 1.05$ Thin gap multi-wire proportional chambers $1.0\lvert\eta\rvert < 2.4$ Monitored drift tubes $\lvert\eta\rvert < 2.7$ Cathode strip chambers innermost layer $2.0 < \lvert\eta\rvert < 2.7$	Drift tubes $\lvert\eta\rvert < 1.2$ Cathode strip chambers $0.9 < \lvert\eta\rvert < 2.4$ Resistive plate chambers $\lvert\eta\rvert < 1.9$	Drift chambers, $\lvert\eta\rvert < 0.83$ Limited streamer tube chambers at $0.81 < \lvert\eta\rvert < 2.44$
Solenoid magnet	2 T, superconducting, outside inner detector	3.8 T, superconducting, outside hadron calorimeter	0.435 T, conventional warm, outside inner detector
Toroid magnet	<3.5 T, 3 systems with 8 superconducting coils each	—	—
Luminometer	Cherenkov counter	3-layer Pixel Luminosity Telescope	$22X_0$ W + 19-layer Si $3.5 < \lvert\eta\rvert < 4.4$, 39M ch from 1993
Beam condition monitor	pCVD diamond pads	pCVD diamond & Si pads	—
L1 Trigger Run 1 → Run 2	$75 \rightarrow 100\,\mathrm{kHz}$ in $2.5\,\mu\mathrm{s}$	$75 \rightarrow 100\,\mathrm{kHz}$ in $3.2 \rightarrow 4\,\mu\mathrm{s}$	5 Hz in 25 ms
L2 Trigger	Run 1 3.5 kHz in 40 ms	—	—
Event filter / HLT	$100 \rightarrow 1000\,\mathrm{Hz}$ in $1 \rightarrow 0.2\,\mathrm{s}$, 1.5 MB/event	$100 \rightarrow 1000\,\mathrm{Hz}$ in $\sim 0.2\,\mathrm{s}$, 1 MB/event	1 Hz, 100 kB/events

Table 3.1: *Comparison of the technologies used for the ATLAS, CMS and OPAL detector systems.*

liquid argon (LAr) sampling electromagnetic calorimeter covers $|\eta| < 3.2$. The amount of passive material before the electromagnetic calorimeter varies between 2.5 and 9.8 radiation length (X_0), motivating the installation of an additional thin LAr presampler layer at $|\eta| < 1.8$ to correct for energy loss in the upstream material by sampling the showers earlier at 1.8 to $5.8X_0$. The readout is arranged to have three longitudinal layers (without the presampler) and fine lateral segmentation with the smallest cell dimension measuring 4.7 mm corresponding to $\Delta\eta = 0.0031$ in the first "strip" layer and 36.8 mm corresponding to $\Delta\phi = 0.0245$ in the second, $18X_0$ deep "middle" layer. This allows the determination of photon direction.

The hadronic calorimeter uses two different detector technologies: steel absorber with scintillator tiles as active material at $|\eta| < 1.7$, and copper absorber with LAr at $1.5 < |\eta| < 3.2$. The forward region ($3.2 < |\eta| < 4.9$) is instrumented with a LAr calorimeter using tungsten and copper absorbers for electromagnetic and hadronic measurements. Electron and photon reconstruction [251–256] relies primarily on this finely segmented calorimeter system and on the inner tracking detectors, with the TRT providing also electron − hadron separation via the detection of transition radiation photons.

Electron energy resolution is measured using Z boson decays and is 0.05 - 0.2% depending on the pseudorapidity due to the different amounts of passive material traversed by the electrons before reaching the calorimeter [251].

The MS consists of a barrel ($|\eta| < 1.05$) and two end-cap sections ($1.05 < |\eta| < 2.7$). Three double layers of resistive plate chambers (RPC) for $|\eta| < 1.05$, and one triplet layer followed by two doublets of thin gap chambers (TGC) for $1.0 < |\eta| < 2.4$ provide triggering capability as well as (η, ϕ) position measurements. A precise momentum measurement for muons up to $|\eta| < 2.7$ is achieved using three layers of monitored drift tubes (MDT), with each chamber providing six to eight $|\eta|$ measurements along the muon trajectory. Instead of MDTs, for $|\eta| > 2$, the inner layer is instrumented with cathode strip chambers (CSC), consisting of four sensitive layers each. The muon momentum resolution varies between 1.7% ($p_{\mathrm{T}} = 10$ GeV and central pseudorapidity) and 4% ($p_{\mathrm{T}} = 100$ GeV and large pseudorapidity) [257].

3.2.2 The CMS detector

The central feature of the CMS apparatus [229] is a superconducting solenoid of 6 m internal diameter, providing a magnetic field of 3.8 T. Within the solenoid volume, there are silicon pixel and strip tracking detectors, a lead tungstate ($PbWO_4$) crystal electromagnetic calorimeter (ECAL), and a brass − scintillator hadron calorimeter (HCAL), each composed of a barrel and two endcap sections. Forward Cherenkov hadron calorimeters (HF), made of steel and quartz-fibers, extend the coverage to $|\eta| = 5$. Muons are measured in gas-ionization detectors embedded in the steel flux-return yoke outside the solenoid, using three different technologies: drift tubes (DT) for $|\eta| < 1.2$, cathode strip chambers for $0.9 < |\eta| < 2.4$, and resistive plate chambers for $|\eta| < 1.6$. The results presented here use mostly the Run-2 configuration of the detector. The evolution of the instrumentation for Run 3 is detailed in Ref. [258].

The silicon tracker measures charged particles within $|\eta| < 2.5$ and is composed of strip and pixel sensors. The original (Phase-0) pixel detector had three layers in the barrel and two disks in each endcap, while the Phase-1 detector, installed during the 2016–17 winter shutdown, have an extra barrel layer and an extra disk at both endcaps, containing in total 124 million pixels [259]. The closest barrel layer is 2.9 cm from the beam line. The strip detector has a four-layer inner and a six-layer outer barrel subsystem (the first two layers of both are double sided) and three inner and nine

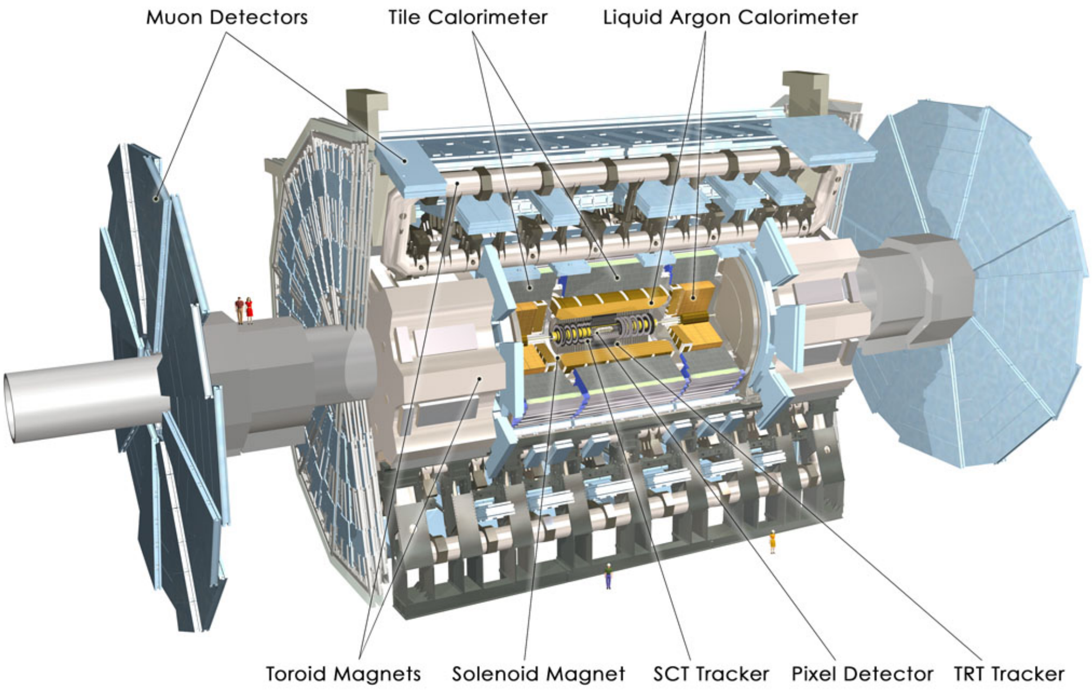

Figure 3.6: *The layout of the ATLAS detector.*

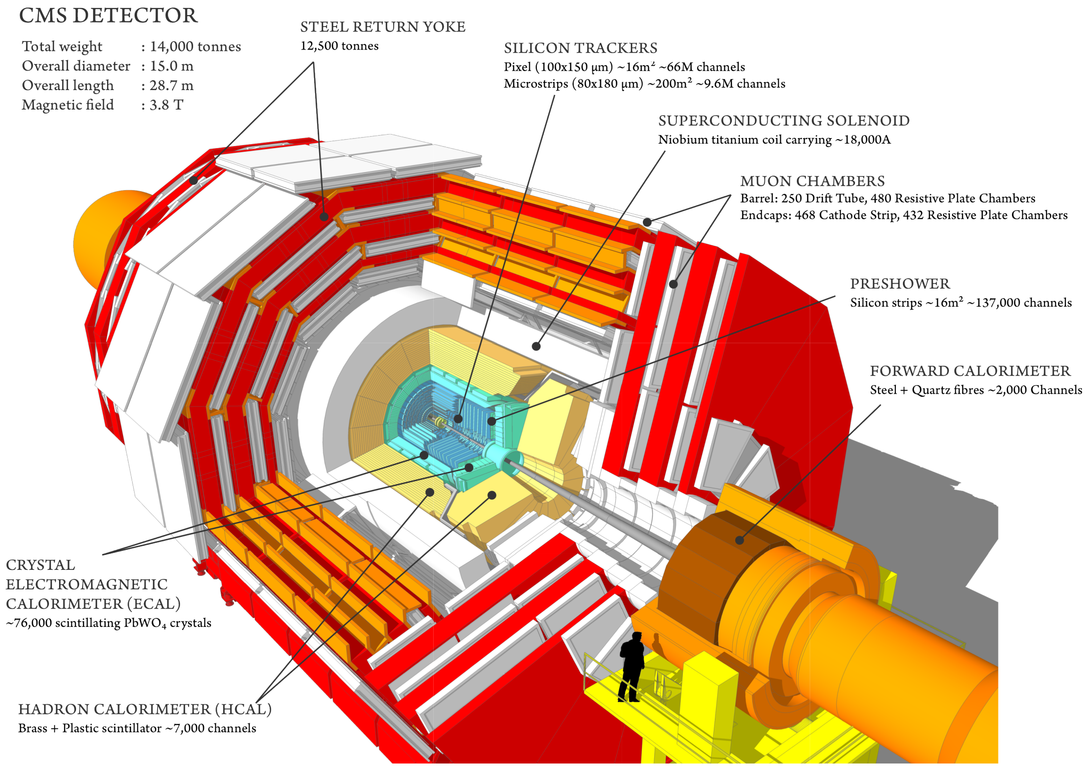

Figure 3.7: *The layout of the CMS detector.*

outer disks at each endcap (with the radius of double-sided modules matching their location in the barrel). This is the largest silicon detector ever constructed, measuring 2.4 m in diameter and 5.4 m in length, with 205 m^2 surface and 9.3 million channels. I contributed to the design validation of its readout and the construction of its more than 15 thousand detector modules.

For nonisolated particles in the range $1 < p_\mathrm{T} < 10$ GeV and $|\eta| < 1.4$, the track resolution is typically 1.5% in p_T, and 25–90 (45–150)μm in the transverse (longitudinal) impact parameter [260]. Vertex resolution depends on the number of tracks originating from the vertex as well as on the event pileup and can be as low as 10 μm.

The amount of material located in front of the ECAL — consisting of the tracker, the mechanical support and the cooling system — varies in radiation length between $0.39X_0$ and $1.94X_0$. The minimum is achieved at $|\eta| = 0$ and the maximum reached at $|\eta| = 1.4$

The ECAL [224] is divided into barrel (EB, $|\eta| < 1.48$) and endcap (EE, $1.48 < |\eta| < 3$) regions. The barrel contains 61200 $\mathrm{PbWO_4}$ tapered scintillator crystals of approximately 2.2 cm x 2.2 cm x 23 cm in size (matching the Molière radius value for the lateral dimensions). The produced light is read out by avalanche photodiodes (APDs). Each side of endcap contains 7324 crystals of somewhat larger size (3.0 cm x 3.0 cm x 22 cm) arranged in a pointing geometry and read out by vacuum phototriodes (VPTs). The loss of transparency due to radiation damage induced aging is continuously monitored using a dedicated laser calibration system. A preshower detector (ES), based on lead absorbers equipped with silicon strip sensors, is placed in front of the endcap crystals to enhance photon identification capabilities in the range $1.65 < |\eta| < 2.6$. In the barrel, an energy resolution of about 1% is achieved for unconverted (or late-converting) photons in the tens of GeV energy range, while for converted photons it is about 1.3% up to $|\eta| = 1$, changing to about 2.5% at $|\eta| = 1.4$. In the endcaps, the energy resolution is about 2.5% for unconverted (or late-converting) photons, and between $3 - 4\%$ for the others [261].

The HCAL is composed of a barrel (HB, $|\eta| < 1.3$) and an endcap (HE) system, covering the range $|\eta| < 3$. The scintillating light is read out by hybrid photo-detectors (HPDs), with the endcap upgraded to use silicon photomultipliers (SiPMs) in 2018. Outside the magnet, the hadron outer calorimeter (HO) composed of scintillator layers read out by SiPMs catches the tails of hadron showers, whereas the hadron forward calorimeter (HF) extends the acceptance in $2.9 < |\eta| < 5$. The HF readout was upgraded in 2017 to utilize new photomultipler tubes (PMTs) and new electronics. When combining information from the entire detector, the jet energy resolution amounts typically to 15–20% at 30 GeV, 10% at 100 GeV, and 5% at 1 TeV [262].

In CMS, the physics objects are reconstructed using the particle-flow algorithm [263] combining optimally the information from all subdetectors. In this method, the identification of the particle type (photon, electron, muon, charged or neutral hadron) plays an important role in the determination of the particle direction and energy. The case of electron and photon reconstruction is discussed in Section 3.5.1.1.

The dedicated instrumentation for precision luminosity measurements as well as the use of CMS subsystems for this purpose are described in Chapter 4.

3.3 From raw collision data to discovery

Precise measurements require well-understood instrumentation, state-of-the-art experimental and analysis techniques and a careful evaluation of all possible biases. It is thus interesting to review the various steps that lead us to a new particle physics result, such as the Higgs boson discovery [25, 26] in 2012.

Particle collisions in high-intensity colliders are too numerous to be all recorded for future analysis, thus a real-time (often called *online*) event selection is performed by the *trigger system*. The recorded data shall include all interesting physics events as well as auxiliary samples necessary for detector calibration. The first-level (level-1, L1) hardware trigger, based on a subset of the data, initiates the full *detector readout*. The high-level software trigger reconstructs the full event (i.e. the outgoing particles that were born in the interactions that happened during the crossing of the two particles bunches) and makes the final decision to permanently store it on magnetic tapes allowing its detailed (often called *offline*) analysis. Rejected events can not be recovered, therefore the trigger system design is a critical element of the experiment. I have contributed to the ATLAS [264] and CMS trigger efforts (Section 3.5.2), in particular to the development, operation and performance studies of electron and photon triggers [265–267], to the trigger strategy, and to the development of new algorithms for SM measurements. In particular, I lead the effort to upgrade the electron and photon triggers for Run 2 in ATLAS.

On a positive trigger decision, the data are read out from the on-detector (front-end) pipelines and processed by the off-detector (back-end) electronics boards before being sent for permanent storage. From the raw detector signals the physics objects (the particles passing through the detector) need to be reconstructed. This procedure, which can be considered as data reduction, happens in several steps. Local reconstruction acts on information available within a single subdetector module (for example, forms clusters of energy deposits measured in adjacent sensor cells). Global reconstruction within a full subdetector follows (for example, creates seeds of charged particle tracks from pixel clusters in adjacent layers). Finally the combination of subdetector information provides the final physics objects (for example, muon candidates from inner detector tracks and muon spectrometer track segments, also called stubs; or electron candidates from special inner detector electron tracks and ECAL energy deposit clusters). The position alignment of the various detector elements and the energy calibration of the electronic signals are essential for the precise reconstruction of the outgoing particles. The detailed properties of the reconstructed objects can be used to differentiate between particle types leaving similar signals in our detectors (for example, separating isolated photons coming from a Higgs boson decay from collimated photon pairs originating from a π^0 meson).

I have worked on the ATLAS electron and photon reconstruction and identification, starting with local reconstruction studies of calorimeter clusters, performance studies of dedicated electron tracking algorithm [268], and the optimization and performance studies of identification algorithms [252–256].

Detector designs (see Sections 3.2.1 and 3.2.2), reconstruction and analysis methods are optimized using *Monte Carlo simulations*. They play a central role in all steps of particle physics research (from the design of the experiments, to the development of research methods, sensitivity and optimization studies for specific measurements, interpretation of the data in theoretical models and more). Thus their quality is a major factor determining the success of the project: it is determined by the precision of the theoretical predictions (see Section 3.4), the accuracy of the detector description including its material composition and the features of its electronic read out, as well as the modeling of the interaction between the particles and the detector material implemented in the GEANT4 [269] simulation toolkit. However, even the best simulations manifest differences with respect to the actual world, and these differences need to be precisely determined. Biases (for example in the modeling of the energy scale and resolution of the instrumentation, or the reconstruction efficiency) are measured in situ and corrected for when comparing experimental data to simulation.

The quality of experimental data, including the operational state of the subdetectors that can affect the performance of object reconstruction, is constantly monitored and problematic data sets are excluded from the measurements. Such *data validation* online and offline plays a key role in ensuring accurate measurements. I was responsible for the CMS trigger-level data quality for electrons and photons and supervised the development of a new monitoring tool based on machine learning for the CMS Pixel Luminosity Telescope (see Section 4.2.2).

From the simple physics objects (electrons, muons, photons, charged and neutral hadrons), we build more complex ones, such as the narrow particle jets originating from the hadronic decay of a tau lepton, or the hadronic jets from the fragmentation of quarks and gluons. Global event quantities (such as missing transverse momentum, defined as the negative transverse momentum sum over all observed physics objects, important in dark matter and supersymmetric particle searches), as well as short-lived particles (such as hadron resonances like the J/ψ or Υ mesons, or the elementary electroweak Z and Higgs bosons) can also be reconstructed. These higher level objects can then be further used for event selection in specific measurements. To separate the sought-after signal from background processes, analyses rely increasingly on modern machine learning techniques, though systematic bias estimation presents a non-trivial challenge for these. This is important as event selection optimization needs to consider the expected signal and background rates together with their systematic uncertainties (see Section 3.5).

All measurements, including searches for rare phenomena providing upper limits of the cross section (σ_p) of a physics process rely on the simple formula

$$\sigma_\mathrm{p} = \frac{N_\mathrm{obs} - N_\mathrm{bgnd}}{L_\mathrm{int} \cdot \epsilon_\mathrm{total}}, \tag{3.5}$$

where N_obs is the observed number of events with the full event selection applied in the analysis, N_bgnd is the estimated number of events coming from ”background” processes (i.e. any other process except the sought-after signal), L_int is the integrated luminosity of the analyzed data sample, and ϵ_total is the total experimental efficiency to observe the signal events (including the detector acceptance, the efficiency of the trigger, the object reconstruction and identification algorithms and the global event selection). The accurate knowledge of N_bgnd, ϵ_total, and L_int requires detailed measurements of their own. Section 5.5 presents my contributions to simulation-based and data-driven background estimation techniques for the CMS Higgs boson search, and Section 3.5.1.1 to measurements of electron and photon trigger, reconstruction and identification efficiencies.

The precise determination of the luminosity directly affects the final precision, and can even be the dominant source of uncertainty. The CMS Beam Radiation Instrumentation and Luminosity Project (BRIL) that I lead since 2021 is responsible for 14 technical systems providing radiation monitoring in the experimental cavern, beam timing (giving input to the L1 trigger system), beam loss monitoring (enabling safety beam abort to protect the sensitive silicon-based tracking detectors), as well as beam-induced background and bunch-by-bunch luminosity measurements in real time. We achieved – with my leadership since 2018 – an outstanding accuracy of 1.2% [270] in the precision luminosity measurements for high-luminosity pp data taking in CMS [270–273] (see Chapter 4).

The interpretation of the measurements rely on sophisticated statistical methods. Searches for new phenomena, such as the ones presented in Chapters 2, 5 and 6, provide limits on or measurements of the signal strength (i.e. the cross section normalized to the theoretical prediction) using *hypothesis testing* [30, 274]. Precise fiducial and differential cross section measurements of SM processes allow the testing of higher-order theoretical predictions and sophisticated Monte Carlo generators, that in turn help to improve the sensitivity of new physics searches by improving their background predictions. Comparison of results between different experiments and to theoretical predictions necessitate the *unfolding of detector effects* [30, 275, 276], as illustrated in Sections 5.2 and 6.1. The theoretical uncertainties need to be carefully considered in the measurements both for the background and for the signal processes.

3.4 Theoretical uncertainties

The running of the strong coupling from large to low values with increasing momentum transfer (or decreasing distance) results in quark confinement at low and asymptotic freedom at high ($E \gg \Lambda_{\mathrm{QCD}}$) energies, with the QCD scale $\Lambda_{\mathrm{QCD}} \sim 200$ MeV. The perturbative calculations are only valid in the weakly coupled ($g_{\mathrm{s}} \ll 1$) region, where QCD predictions rely on the factorization theorem [277] stating that cross section computations can be factorized into two parts: process-dependent short-distance perturbative parton cross sections and universal long-distance functions that can be determined from global fits to experimental data describing the non-perturbative nature of hadron structure and parton hadronization [278].

Cross section predictions at hadron colliders thus rely on the description of the initial state by a set of **parton distribution functions** $f_i^h(x, Q^2)$ (PDFs), number densities as a function of the momentum fraction x of hadron h carried by parton i at a squared energy scale Q^2. Several groups provide such sets using different parametrizations (typically polynomials or multi-layer neural networks) and fitting a selected wide (and growing) set of experimental data relying on the Dokshitzer–Gribov–Lipatov–Altarelli–Parisi (DGLAP) equations [279–281] for the Q^2 scale evolution, as well as QCD calculable coefficient functions for PDF sets for higher order calculations. With a moderate number of parameters (∼10-30) a very wide set of measured data points from deep inelastic scattering (DIS) and collider experiments can be described, confirming the QCD description of strong interactions. Three main global fitters CTEQ, MSHT (previously MRS(T), MSTW, MMHT) and NNPDF, as well as a number of other groups like ABM(P), (J)GR(V), HERAPDF, ATLAS, CMS, and LHCb using a subset of data, extract the PDF sets. The central PDF sets are accompanied by eigenvector error sets that describe their uncertainties. Comparing the measurements to predictions using PDF sets from different groups allows to check the biases from the definition of the fitting framework and the theoretical assumptions made. The LHC collaborations follow the recommendations of the PDF4LHC working group on the use of the PDFs and on the determination of the uncertainties due to their limited knowledge. These recommendations have been updated from the original 2010 study [282, 283] for Run 2 [284] and most recently for Run 3 [285]. Modern PDF sets (e.g., MSHT 2.0 and NNPDF 4.0) reach percent level precision beyond which QED effects need also to be considered.

The cross section of high momentum transfer processes are computed at the parton level using perturbative expansions in the strong and EW couplings:

$$\hat{\sigma} = \sum_{i=0}^{\infty} \sum_{j=0}^{\infty} \alpha_{\mathrm{s}}^{i} \alpha_{\mathrm{EM}}^{j} \hat{\sigma}_{ij}. \tag{3.6}$$

Here $i = j = 0$ is the Born-level leading-order (LO) cross section, $i = 1, j = 0$ is next-to-leading order (NLO), $i = 2, j = 0$ is next-to-next leading order (NNLO), $i = 3, j = 0$ is next-to-next-to-next leading order (N^{3}LO) accuracy in QCD, etc. A precision challenge (not discussed further here) is the estimation of mixed EW and QCD higher-order contributions ($i \neq 0, j \neq 0$) [286].

The ultraviolet (UV) and infrared (IR) divergencies of the perturbative calculations are removed using the framework of dimensional regularization [287, 288]. UV divergencies arising due to high momentum partons in the loops are absorbed above an arbitrarily chosen "renormalization" scale (μ_R) into the physical (measurable) parameters of the model, the couplings and particle masses becoming a function of μ_R. The IR divergencies on the other hand arise from collinear emissions from the partons and can be considered as part of the PDFs: the collinear "factorization" scale (μ_F) defines above which transverse momenta the emission is included in the amplitude rather than in the PDFs. There are several renormalization schemes, of which the so-called modified minimal subtraction ($\overline{\mathrm{MS}}$) scheme is the most widely used. The values of the physical parameters, such as the quark masses or the strong coupling, as well as the amplitude of the processes of interest are computed at the chosen renormalization scale.

The **renormalization and factorization scales** are unphysical parameters and thus the theoretical cross section predictions should not depend on them. However, at any fixed order a dependence remains due to the neglected higher order terms and its effect need to be quantified. This is usually done by choosing the two scale parameters to be equal to the typical energy scale (momentum transfer) of the process and then varying their value by a factor of two up and down. The effect of **missing higher order terms** is estimated generally by these (largely arbitrary) scale variations. The development of methods to estimate the uncertainties with probabilistic foundations [289] is an active area of research.

When several energy scales (e.g. $Q_1 \gg Q_2$) appear in a renormalizable quantum field theory (QFT), perturbative terms of $\alpha_\mathrm{s}^n \log^m(Q_1^2/Q_2^2)$ arise enhancing higher-order corrections. The relation of m and n depends on the effect. For soft and collinear singularities the so-called Sudakov terms arise with $m \leq 2n$, other examples are "single logarithmic" terms with $m \leq n$ for example due the difference between the chosen value of the renormalization and factorization scales and an energy scale of the process. The resummation of these large logarithms is performed order-by-order, starting from leading logs (LL) up to the current state-of-the-art next-to-next-to-next-to-leading logs (N^{3}LL), using techniques suitable for the scale hierarchy of the given physics problem.

The inclusion of **quark masses** in theoretical predictions raises several issues. For heavier quarks the pole mass, corresponding to the position at which the propagator diverges, is often quoted and can be related to the renormalized mass. The pole mass is measured from kinematic distributions, while the renormalized mass can be obtained from cross section measurements. In pQCD calculations, it is common to work in an approximation where quark masses significantly smaller than the momentum transfer of the process are neglected. The effect of quark masses is especially important for processes including heavy quarks.

When bottom quarks appear in the hard process, two different approaches are used [290]. The four-flavor scheme (4FS) treats b quarks as massive objects which do not appear in the initial state and are created in pairs via gluon splitting or in a high-Q^2 electroweak process. If two characteristic scales are present (Q and m_b) logarithmic terms $\alpha_\mathrm{s}^n \log^m(Q^2/m_\mathrm{b}^2)$ arise. In the five-flavor scheme (5FS), b quarks are treated as light partons with their mass set to zero for the short-distance cross section. They arise from the initial state and the large collinear logarithms are resummed via the DGLAP evolution of the bottom PDF. These two schemes address different kinematic regions, and thus the matching of the two calculations provides the most accurate predictions. The Fixed Order + Next-to-Leading Log (FONLL) [291] scheme, featured in Section 5.2, allows (among others) such computations.

As colored particles cannot be observed free, being confined to color-neutral bound states, gluons and quarks produced in the hard process have to be transitioned to hadrons using **fragmentation functions** $D_i^h(x, \mu_{\mathrm{fr}}^2)$ extracted primarily from $\mathrm{e}^+\mathrm{e}^-$ collision (and also DIS) data. They are the final state equivalents of the initial state PFDs and give the probability density that an outgoing parton i produces a hadron h giving a fraction x of its momentum to the hadron. The scale μ_{fr} is known as the fragmentation factorization scale (and will be considered in the following as equal to μ_{F}, defined above). For short-lives particles, the **decay tables** defining the branching fractions to various final states also need to be considered.

Putting all together, we get the following prescription to compute the production of a heavy object (X) accompanied by two final state hadrons (f_1, f_2) with momenta p_1 and p_2, as an example, in the interaction of two colliding hadrons (h_1, h_2) summing over all possible parton level processes $ab \to cdX$ and integrating over the momentum fraction received by the initial and given by the final state partons as well as other kinematic variables defining the phase space (Φ):

$$\begin{aligned} &\sigma_{h_1h_2\to f_1f_2X} = \qquad (3.7) \\ &\sum_{a,b,c,d} \int_0^1 \mathrm{d}x_1 f_a^{h_1}(x_1, \mu_{\mathrm{F}}^2, \alpha_{\mathrm{s}}, \mathcal{P}_f) \int_0^1 \mathrm{d}x_2 f_b^{h_2}(x_2, \mu_{\mathrm{F}}^2, \alpha_{\mathrm{s}}, \mathcal{P}_f) \int_{p_1}^{z_1^{\max}} \frac{\mathrm{d}z_1}{z_1} \int_{p_2}^{z_2^{\max}} \frac{\mathrm{d}z_2}{z_2} \\ &\times \int \mathrm{d}\Phi\ \hat{\sigma}_{ab\to cdX}(x_1, x_2, z_1, z_2, \Phi, \mu_{\mathrm{R}}^2, \mu_{\mathrm{F}}, \alpha_{\mathrm{s}}(\mu_{\mathrm{R}}^2), \mathcal{P}_p)\ D_c^{f_1}(\frac{p_1}{z_1}, \mu_{\mathrm{F}}^2)\ D_d^{f_2}(\frac{p_2}{z_2}, \mu_{\mathrm{F}}^2) \end{aligned}$$

A number of model parameters appearing in the parton distribution functions $(\mathcal{P}_f)$ and the amplitude of the perturbative process $(\mathcal{P}_p)$ (e.g., quark masses, EW couplings, if relevant for the elementary cross section $\hat{\sigma}$) are left implicit, while the **strong coupling** (α_{s}) (also a parameter of the PDF sets) is written out explicitly. It has a significant uncertainty [30], with the world average being $\alpha_{\mathrm{s}}(m_{\mathrm{Z}}^2) = 0.1179 \pm 0.0009$.

Theoretical calculations need to be embedded into Monte Carlo (MC) **event generators** to produce simulated samples that are needed to design the measurements and to interpret the collected data. They also rely on the factorization of physics at different energy scales, allowing knowledge gained at lower energy measurements to be transferred to energies never probed before to predict the experimental signatures and attain a deeper understanding.

In HEP MC generators [292–294], in the case of composite beam particles like protons, the initial state is described by PDFs available via the LHAPDF package [295]. The initial state particles can emit radiation according to their charges, e.g. initial state quarks can radiate gluons (QCD ISR) or photons (QED ISR). The hard interaction is modeled by full perturbative computations including the interference of different diagrams belonging to the same initial and final states at the highest order that is practically possible. Tree-level (LO) as well as NLO cross sections for multi-leg $2 \to n$ partonic processes can be automatically calculated by several programs for physics processes of interest at the LHC within and beyond the SM. The main general purpose NLO generators are MadGraph 5 + aMCNLO (MG5_aMC) [296, 297], Sherpa [298], and POWHEG-BOX [299], the latter giving also access to NNLO predictions using the MiNNLO$_{\mathrm{PS}}$ method for selected processes. Particles produced in the hard interaction can then radiate several additional states using quasi-classical cascade models. To remove double counting, these parton showers (PS) – that are equivalent to LL resummation of soft and collinear parton emissions – are matched to the fixed-order QFT calculation using one of several theoretical prescriptions such that the matrix element (ME) describes the production of hard, well-separated particles while the PS accounts for the soft or collinear particles. The produced quarks and gluons are confined into color-neutral hadrons using phenomenological models implemented in PYTHIA 8 [240] (Lund string model [300]), Herwig++ [301, 302] (cluster fragmentation [303]) or Sherpa (modified cluster fragmentation [304]). QED radiation is handled by the YFS [305–307] or PHOTOS [308, 309] algorithms. Unstable particles (tau leptons, hadrons) are decayed according to their lifetimes taking into account spin correlations. Developments to achieve NLL accuracy for parton showers are pursued [310].

The remnants of the colliding hadrons (including all partons not participating in the hard process and their interactions) are referred as the **underlying event** (UE). It contains many different, typically soft processes and effects, such as initial and final state radiation (FSR), multi-parton interactions [311], color reconnection and cannot be modeled from first principles. The region orthogonal to the axis of the hard process is particularly sensitive to UE modeling. The LHC collaborations studying ”minimum bias” events derive a set of optimal parameters of the phenomenological model, called a **tune**, that provides the best description of the data [312, 313]. These tunes are specific to a given Monte Carlo generator and the utilized PDF. Different underlying event models are implemented in the three parton shower MC generators Herwig (using JIMMY [314] and then its improved version of Ref. [315]), PYTHIA and Sherpa.

Dedicated measurements are also performed to study the various components related to the underlying event and then used as inputs to the MC tune. For example, the first observation and measurement of the fiducial cross section of double parton scattering (DPS) in same-sign $\mathrm{W}^{\pm}\mathrm{W}^{\pm}$ production that we recently published [316]. These allow the extraction of the effective cross section (σ_{eff}) defined by the equation

$$\sigma_{AB}^{\mathrm{DPS}} = \frac{n}{2}\frac{\sigma_A \sigma_B}{\sigma_{\mathrm{eff}}}, \tag{3.8}$$

linking the cross sections of the single parton scattering processes A and B to that of the DPS process $A + B$, with the combinatorial factor $n = 1$ if $A = B$, and $n = 2$ otherwise. The value of σ_{eff} can be interpreted as being proportional to the average squared transverse distance between the interacting partons. It is useful to compare DPS processes in different production modes. Its value varies in the range $2 - 10$ mb in gluon-initiated and $10 - 25$ mb in quark-initiated DPS processes.

With increasing beam intensity, the modeling of the **event pileup** – by overlaying minimum bias events (from MC simulation or recorded data) on the event of interest containing the hard process – becomes essential.

The comparison of simulated event samples, using different MC generators, input parameters, PDF sets, LO or NLO calculations of the hard process, ME-PS matching prescriptions, fragmentation / hadronization, QED radiation and underlying event models, decay tables, etc. allows to estimate the relevant systematic uncertainties and are an essential part of all measurements.

The interactions of the stable (or sufficiently long-lived) particles with the detector layers are simulated using the physics models implemented in GEANT 4 [269] based on a detailed description of the detector material composition. To allow in-depth comparisons with the experimental data starting at the lowest levels (i.e. the electronic signals received channel-by-channel), the features of the read-out electronics are also modeled. The simulated data can then be put to the same format and processed using the same reconstruction software and analysis chain that are used for the collected detector data. The information about the generated (also called ”true”) quantities of the produced events and the particles they contain are saved in order to estimate any experimental bias related to the instrumentation, reconstruction techniques and analysis methods.

3.5 Analysis methods and experimental uncertainties

The highly complex environment of the LHC experiments requires sophisticated experimental methods. This section summarizes some of the most important aspects of data collection, processing and analysis, and gives a glimpse into the areas to which I significantly contributed.

3.5.1 Object reconstruction and identification

Combining the information from the different layers of multi-purpose collider experiments allows the reconstruction of the path of final state (stable or sufficiently long-lived) particles that reach at least the first layers of the detector, and the identification of their nature (see Figure 3.8). These *photons, electrons, muons*, as well as *charged*[1] *and neutral hadrons* can then be used to reconstruct composite physics objects: *tau leptons* decaying to narrow particle jets, hadronic *jets* produced from the fragmentation of colored quarks and gluons, as well as even higher level objects like interaction *vertices* at the origin of charged particle tracks, *b-tagged jets* from displaced secondary vertices, and – through their characteristic decays – short-lived hadrons (π^0, J/ψ, Υ, B mesons, etc.) and electroweak bosons (W, Z, H). Neutrinos (and hypothetical weakly interacting particles, like dark matter) do not leave signals in the detector layers, and their passing through the instrumentation can be deduced from the *missing transverse momentum* [263], which is defined as the vectorial sum of all undetectable particle transverse momenta, and computed as the negative vectorial sum of transverse momentum over all reconstructed particles (more precisely, calibrated physics objects including jets):

$$\vec{p}_{\mathrm{T}}^{\,\mathrm{miss}} = - \sum_{i=1}^{N_{\text{physics objects}}} \vec{p}_{\mathrm{T},i}. \tag{3.9}$$

The best reconstruction performance is achieved by the *particle-flow* method [263] that was championed at the LHC by the CMS collaboration. It builds from the locally reconstructed subdetector signals the physics objects using a *global event description* (GED), considering also overlapping objects. It follows the particle path through the detector and links nearby objects together if they are consistent with the hypothesis of a showering or decaying particle. For example, an opposite-charge electron pair originating from a vertex located at an inner detector tracking layer could be joined together as a photon that has converted into an $\mathrm{e}^+\mathrm{e}^-$ pair in the detector material. An electron emitting a photon while traversing an inner tracker detector layer would be linked to the radiated photon thus improving its energy measurement. In this method, the full detector information is used to identify the objects, determine their point of origin and their momentum as they travel through the detector. The objects and their kinematic properties are then used as inputs to the physics measurements.

The particle-flow approach significantly improves the momentum (energy) reconstruction of physics objects, thus the final measurement precision, for example, through

---

[1] The identification of charged hadrons using their specific energy loss ($\mathrm{d}E/\mathrm{d}x$) in the silicon tracking detector layers, and – in ATLAS – in the transition radiation tracker via the measurement of the time-over-threshold of the electric pulse, is available only at low momentum $\mathcal{O}(1$ GeV). As most unidentified charged tracks belong to pions at the LHC, in their reconstruction the pion hypothesis is used.

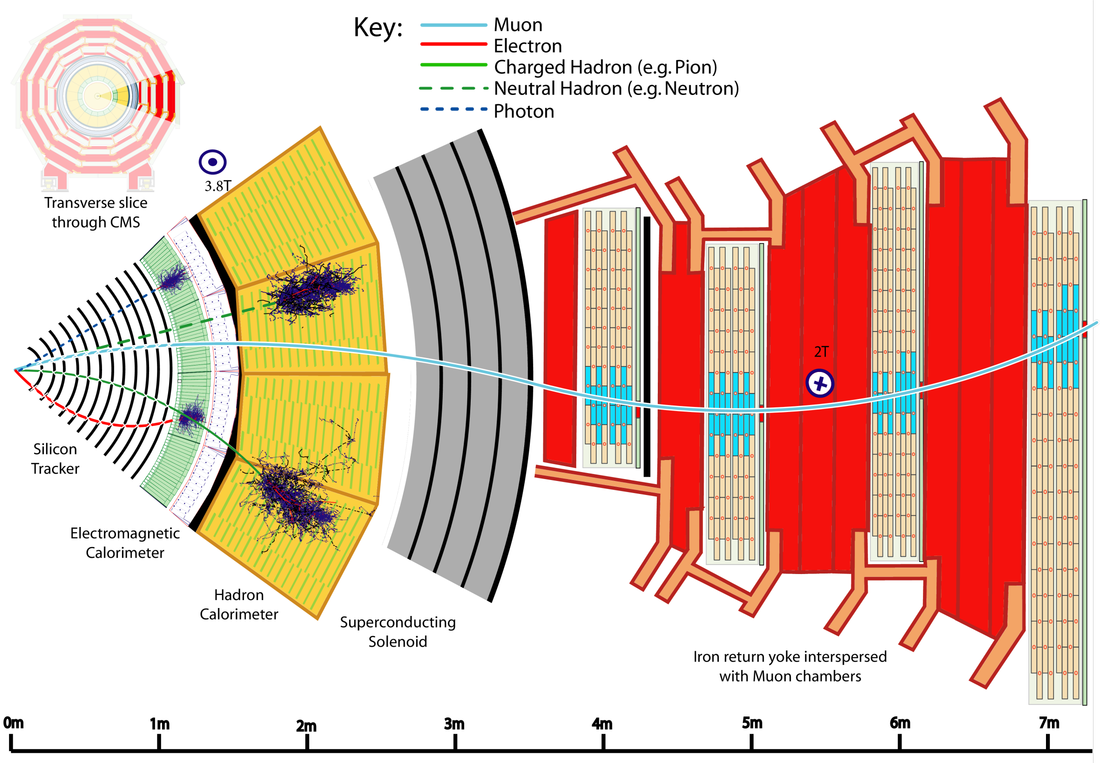

Figure 3.8: *A transverse slice of the CMS detector illustrating the interactions of different types of particles. The charge of the particle determines the direction and its momentum the radius of the bending in the magnetic field.* ***Muons*** *with a momentum between ∼100 MeV and ∼100 GeV loose only a small fraction of their energy in the detector material, leaving signals in each detector layer that are consistent with the passage of a minimum ionizing particle. Higher energy muons can also radiate photons. As they pass through the solenoid magnet and thus experience a change in the orientation of the magnetic field, their trajectory resembles that of an elongated "S" that reaches the outermost muon spectrometer layer. Low energy muons might curl back and not reach the outer layers.* ***Electrons*** *leave a small energy deposit in the inner tracking layers and are stopped, forming an electromagnetic shower in the crystal calorimeter. They can start showering already in the tracking layers by emitting a bremsstrahlung photon, resulting also in a decrease in the track bending radius.* ***Photons*** *can either pass through the tracking layers without leaving any signal or convert to a "collimated" electron - positron pair there. In regions with the largest amount of material, about 60% of photons convert before the last tracking layer in CMS. In both cases, as the photon or the* e^+e^- *pair reaches the EM calorimeter, each EM object starts a shower and is stopped. Very rarely can an EM shower caused by a high energy* e/γ *object reach the hadron calorimeter (longitudinal leakage) and deposit significant energy there.* ***Charged hadrons*** *leave some energy in the tracking layers and the EM calorimeter and then are stopped in the hadron calorimeter where they form a hadronic shower.* ***Neutral hadrons*** *typically leave signal only in the hadron calorimeter, though for any hadron, the first nuclear interaction can also happen earlier upstream of the calorimeter, modifying the experimental signature. Very high energy jets might produce a signal in the muon layers if they punch through the calorimeter. Hadrons decaying in flight in a jet can also result in secondary muons.*

its effect on the reconstructed mass of short-lived states (hadrons, EW bosons, exotic particles) as well as on the energy sums (like $p_{\mathrm{T}}^{\mathrm{miss}}$) that are frequently used in the event selection.

For standard physics objects, all performance studies are central tasks (which are performed by members of the collaboration to fulfill the authorship requirements). The eventual corrections are derived using *data-driven methods*, for example, the multiplication factor for the **momentum (energy) scale** and the eventual additional smearing of the **momentum (energy) resolution**. The prescriptions of how to apply these in physics analyses on the experimental data and / or the MC simulation, as well as the uncertainties to be considered (including, where relevant, the covariance matrices) are thus provided to the analysis teams. Their effects on the measurement, however, need to be evaluated individually as it depends on the studied final state and the analysis methods.

The **reconstruction** (ϵ_{reco}) and **identification** (ϵ_{ID}) **efficiencies** of "standard" physics objects are also derived centrally together with the relevant systematic uncertainties. There are typically several working points of the identification algorithms achieving different levels of purity. High (low) purity selections are called "Tight" ("Loose") and they have lower (higher) efficiencies. The choice of the *optimal working point* depends on the specific measurement. **Analysis-specific requirements** are often needed, such as those that ensure the *isolation* of the object of interest from other nearby particles. Their performance (ϵ_{iso}) need to be determined as part of the analysis.

The efficiencies are typically assumed to be independent and measured component by component (see Section 3.5.1.1.5) in sequence with the definition of the numerator of the previous term serving for the denominator of the next:

$$\epsilon_{\mathrm{object}} = \epsilon_{\mathrm{reco}} \cdot \epsilon_{\mathrm{ID|reco}} \cdot \epsilon_{\mathrm{iso|reco+ID}} \cdot \epsilon_{\mathrm{trigger|reco+ID+iso}}. \tag{3.10}$$

The last factor only appears if the object is also used in the real-time event selection. In that case, the trigger efficiency is measured with respect to the final analysis object selection, including the reconstruction, identification and other analysis-specific requirements (see Section 3.5.2.4). In the following a simplified notation without marking the denominator selection is used, i.e. $\epsilon_{\mathrm{ID|reco}}$ is replaced by ϵ_{ID}.

Mis-identification rates and their uncertainties need also to be quantified to understand the *background contributions* to the sample or the effect of *object veto* requirements on the event selection. A few notable examples are: lepton charge mis-identification, electrons or hadrons faking prompt photons, tau lepton decays or jets faking prompt electrons or muons, etc. As these can depend strongly on the selected event properties, they require dedicated, analysis-specific measurements. A few examples are shown in Sections 5.2 and 5.5.

While most of these performance measurements are realized *as a function of the object transverse momentum* and *pseudorapidity*, other quantities can also play an important role. *Nearby particles* can affect the measured properties of the object of interest introducing a dependence on isolation, distance to the closest jet, jet multiplicity, *pileup* or other quantities. *Azimuthal non-uniformities* can arise due to **detector features** or **operational issues**. These need to be studied carefully to avoid experimental biases.

3.5.1.1 Electrons and photons

As an example, this section gives a more detailed discussion of the reconstruction and identification of electron and photon objects, as I contributed to the optimization, calibration and systematic uncertainty determination studies in ATLAS and CMS both for the real-time environment of the trigger system (see Section 3.5.2) and for precision offline measurements. Similar techniques are used for other physics objects.

Electrons are built from clusters of calorimeter energy deposits and charged particle tracks reconstructed from hits in the inner tracking detector layers, see a picturial depiction in Figure 3.9 for the ATLAS example. Electrons with momentum above ∼10 MeV lose energy predominantly via photon radiation, called bremsstrahlung[2], as a consequence of their EM interaction with (typically) an atomic nucleus. This has several consequences for the reconstruction of electrons in HEP experiments.

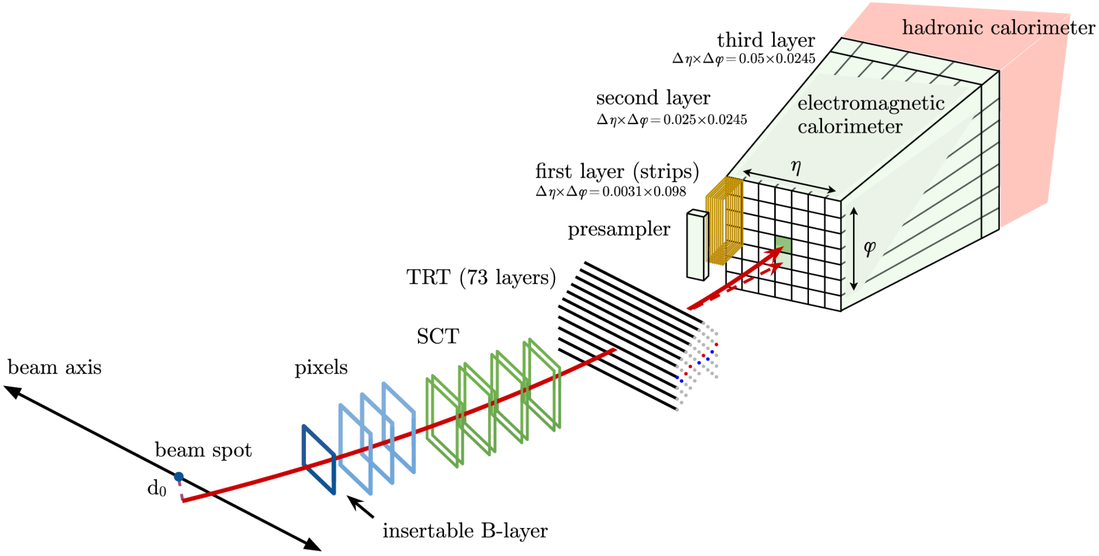

Figure 3.9: *Electron reconstruction and identification in ATLAS (barrel region): Hits in the pixel layer, especially the insertable B-layer help to discriminate prompt electron and conversion tracks. They, together with the hits in the SCT, allow precise vertex reconstruction and the determination of the transverse impact parameter d_0. The transition radiation tracker (TRT) provides additional points for precision tracking and the fraction of high-threshold hits (f_{HT}) and the average time-over-threshold of the electrical signal. The electrons lose f_{brem} fraction of their momentum in the tracker which is measured by the dedicated GSF electron track reconstruction. The early EM showers are sampled by a thin EM presampler layer, placed outside the thin solenoid magnet. The ECAL provides rich data about the shower profile. No or very little longitudinal leakage of the showers reach the hadron calorimeter.*

3.5.1.1.1 Track finding for generic charged particles (most of which are pions) is based on the iterative Kalman-filter (KF) algorithm [317] in the LHC experiments. It assumes a constant momentum and thus a path following a circular helix in the solenoidal magnetic field of the inner tracking detectors. Only small deviations – primarily due to multiple scattering in the tracking detector material – are allowed from this when the tracks are built from hits in subsequent detector layers. The method works well for muons and charged hadrons whose specific energy loss $\mathrm{d}E/\mathrm{d}x$ is dominated by ionization.

---

[2] The energy loss per unit path length via bremsstrahlung is proportional to E/m^2, where E is the energy and m is the mass of the charged particle. This explains why photon radiation plays an essential role for electrons but only becomes significant for muons at very high energies.

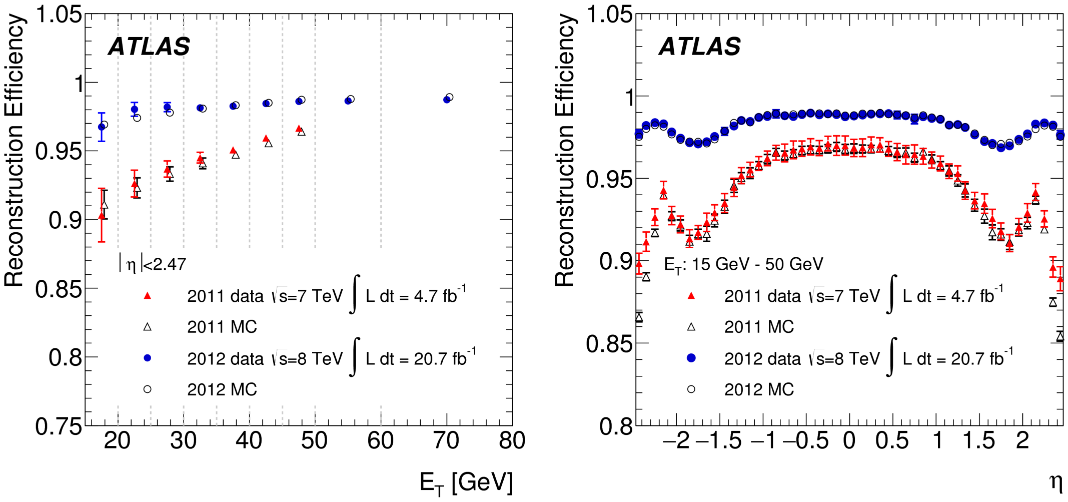

Figure 3.10: *Electron reconstruction efficiency in ATLAS as a function of the electron (left) transverse momentum and (right) pseudorapidity comparing the performance in 2011 when the standard Kalman-filter algorithm was applied for electron tracks and in 2012 after the introduction of GSF tracking. The efficiency to reconstruct the EM cluster in the calorimeter is assumed to be 100%, so the efficiency values corresponds to the track finding and track-cluster matching steps measured by the tag-and-probe method (see Section 3.5.1.1.5). The improvement is the most significant at low* p_{T} *where the change in track curvature is the most pronounced, and in the endcap region where the amount of material traversed by the electron is the largest.*

When electrons loose a notable fraction of their momentum through bremsstrahlung in a layer of the tracking detectors, the curvature of their track will increase, and the KF algorithm either fails with large reduced χ^2 of the fit or underestimates the initial momentum of the electrons. A dedicated track finding algorithm using a Gaussian Sum Filter (GSF) [318, 319] needs thus to be applied to measure accurately the track parameters.

The GSF algorithm estimates the radiative energy loss – described by the Bethe-Heitler distribution – by a weighted sum of Gaussian distributions. In this sense it resembles a set of parallel Kalman Filters, where the track parameters are evaluated at every tracker layer allowing for energy loss (typically up to 30%) to iteratively build the electron trajectory. Multiple candidate trajectories can be built (usually up to five for each tracker layer) for a given *track seed* (typically formed by hits in the pixel detector or a generic KF track) allowing at most one missing hit along the trajectory.

GSF electron tracking is computationally intensive – one of the reasons why it was introduced by the ATLAS experiment only in 2012 [268] – but brings a significant improvement for the reconstruction efficiency [254] as well as for the momentum scale and resolution, especially for low-p_{T} electrons, as we sowed (Figure 3.10). As the GSF track parameters are recalculated at each detector layer along the track, the measured relative momentum loss from the point of closest approach to the beam spot (”in”) to the exit of the tracking volume (”out”) can also be used as an unbiased estimator of energy loss in electron identification algorithms: $f_{\mathrm{brem}} = (p_{\mathrm{in}} - p_{\mathrm{out}})/p_{\mathrm{in}}$.

3.5.1.1.2 Calorimeter energy-deposit clustering is the basis of a precise energy measurement, and it is also the area where the largest difference is seen between the two experiments. Up to 2017, the ATLAS collaboration relied on simple, fixed-sized clusters using a sliding window algorithm, while CMS pioneered topological clusters linked together to form superclusters to collect the energy of the EM shower originating upstream of the calorimeter as the particle-flow philosophy requires.

In ATLAS Run 1 and early Run 2, electron and photon reconstruction started by identifying rectangular seed clusters of 3×5 cells (each cell measuring $\delta\eta \times \delta\phi = 0.025 \times 0.0245$ corresponding to the granularity of the middle ECAL layer) with $E_{\mathrm{T}} > 2.5$ GeV and $|\eta| < 2.47$ using a sliding window method, the algorithm and parameters of which I optimized before Run-1 data taking began. If a track extrapolated to the middle layer of the EM calorimeter was matched to the seed cluster within $|\Delta\eta| < 0.05$ and $|\Delta\phi| < 0.05$ (0.1) in the barrel (endcap) region, the object was classified as an electron. The electron cluster was then rebuilt with a fixed size of 3×7 (5×5) cells in the barrel (endcap) centered around the barycenter of the energy deposits in each layer. The larger size in ϕ in the barrel is due to the bending of the electron trajectory in the magnetic field. Photon clusters were rebuilt with a size of 3×5 cells. It is important that the position of the cluster can thus change from layer to layer depending on the energy distribution between the cells, providing "pointing" information from the calorimeter toward the origin of the EM object, improving significantly the diphoton mass resolution, and thus – among others – the sensitivity of the Higgs boson measurements in the $\mathrm{H} \rightarrow \gamma\gamma$ channel.

If several tracks were matched, priority was given to tracks with hits in the Si pixel and strip detectors, and then the track with the closest match in ΔR was selected. The electron direction was taken from the track reconstruction. If no track was matched to the seed cluster, it was retained as a photon. In 2017, the e/γ reconstruction algorithm in ATLAS was changed to use topological clusters of variable size and shape, moving closer to the philosophy followed by CMS.

Loosely matched tracks to the seed clusters (with or without hits in the silicon detector layers) also provide input to conversion vertex reconstruction. Two-track conversion vertices are formed if the vertex is consistent with a massless particle, and single-track vertices if there are no hits in the innermost sensitive layers of the tracker. To improve purity, conversion tracks should have a high probability to originate from electrons based on the signals in the TRT.

The CMS particle-flow algorithm [263], to which e/γ reconstruction [267] was fully integrated for Run 2, identifies ECAL energy deposits – grouped into superclusters to collect the contribution of showering particles – as electrons or photons based on the existence of an associated GSF track.

Cluster reconstruction groups together neighboring crystals with energy exceeding a predefined threshold (typically 80 MeV in the barrel, and 300 MeV in the endcaps, corresponding to about 2–3 times the electronic noise for the crystals), allowing energy deposits to be shared by overlapping clusters assuming Gaussian shower profiles. A cluster is identified as the *seed cluster* if it contains most of the energy in the specific region and its transverse energy is at least $E_{\mathrm{T}}^{\mathrm{seed}} \geq 1$ GeV. Clusters around a seed are then combined within a geometric area in the ($\Delta\eta$, $\Delta\phi$) plane of a slightly bent E_{T}-dependent shape resembling a "mustache" into a *supercluster* (SC) to include all energy lost by the primary object (i.e. bremsstrahlung photons and electrons from photon conversions). This so-called *mustache algorithm* brings a significant improvement to measure low energy deposits, and is motivated by the solenoidal structure of the magnetic field that spreads the radiated energy along ϕ.

The CPU-intensive GSF tracking step is only executed where electron objects are expected to be found: it is initiated either by a trajectory seed containing two or three hits in the pixel detector, (called *pixel seed*) or by a *generic track* with $p_{\mathrm{T}} > 2$ GeV reconstructed from hits in the tracker with the iterative KF algorithm. As iterating over all generic tracks to find matching ECAL clusters is CPU-intensive, it is only executed offline but not at the HLT.

The association of GSF tracks to superclusters is performed by a machine learning technique using a boosted decision tree (BDT) algorithm [600], or in the case of ECAL-driven electrons a simple geometrical match between the SC and the extrapolated track is also sufficient: $|\Delta\eta| < 0.02$ and $|\Delta\phi| < 0.15$.

A dedicated algorithm employing a BDT uses information on missing hits, the radius of the first hit, and the signed impact parameter of the track to identify conversion tracks without a pair. If such a track is associated to an ECAL cluster, it is flagged as single-track conversion.

Matching clusters from bremsstrahlung along electron tracks are sought using the track tangent at each detector layer. The algorithm flags if an ECAL cluster (without an associated track) belongs to a SC. The final list of linked ECAL clusters is called a *refined supercluster*.

Electron and photon objects are built from the refined superclusters based on loose selection requirements. All objects that pass the selection with an associated GSF track are labeled as *electron*, without a GSF track as *photon*. These form the *unbiased e/γ collection*, and are typically the starting point of physics analyses.

3.5.1.1.3 Electron and photon identification algorithms combine information from several variables either in a traditional cut-based selection or using a more performant but for systematic studies more complex multivariate discriminant.

EM *calorimeter shower shape* variables (including lateral width, lateral and – in ATLAS – longitudinal energy distribution, and longitudinal leakage to the hadron calorimeter) are essential to distinguish both electrons and photons from hadrons.

In addition, for electron (and converted photon) identification, *track quality* criteria (reduced χ^2 of track fit, number of hits, location of first hit, missing hits) as well as geometric $(\Delta\eta, \Delta\phi)$ and momentum $(1/p - 1/E$ or $E/p)$ *track - cluster matching* variables play an important role. The track-based identification variables based on *energy loss in the detector material* are very powerful: f_{brem} as measured by the GSF algorithm, and – in ATLAS – f_{HT} giving the fraction of hits with high-energy deposit in the TRT, in some cases combined with time-over-threshold information. The use of a selection of these variables will be demonstrated in Section 5.2, in particular in Figure 5.4. *Transverse and longitudinal impact parameters*, and their significance measured in units of their uncertainty, provide information on the origin of the electron (prompt or secondary).

Variables quantifying the *isolation* from other nearby particles can also be part of the standard identification algorithms, though frequently it is applied separately as analysis-specific requirement. Various isolation variables are defined by the experiments measuring the activity in a cone (typically with a half opening angle of $\Delta R = 0.2 - 0.5$) around the e/γ object. The cone size can depend on the e/γ p_{T}. The energy (or momentum) sum in the isolation cone is frequently normalized by p_{T} (*relative isolation*) to improve the performance at high momentum.

Calorimeter isolation is measured as the E_{T} deposited in the calorimeter in a cone around the object of interest excluding the contribution associated to the object itself. It is typically corrected for the expected lateral leakage for an electron parametrized as a function of p_{T}, and the contribution from pileup parametrized as a function of the number of reconstructed vertices.

Track isolation uses the scalar sum of track p_{T} within a cone over all good quality tracks originating from the same primary vertex, excluding the track belonging to the object itself.

The most sensitive variable uses particle flow (PF) objects associated to the same primary vertex as the object of interest. More precisely, in the latest CMS pileup per particle identification (PUPPI) method, the contribution of each object is weighted by the probability that it originates from the same vertex. Three isolation energy sums are available separately from charged hadrons, neutral hadrons and photons, and can be added to get the total *PF isolation*.

The optimization of the identification algorithms is typically performed in various bins of p_{T} and η using extensive simulation and, whenever possible, experimental data of key physics processes providing a number of working points to suit a wide range of analysis needs. For special measurements, such as the multi-lepton studies of $\mathrm{H} \to \mathrm{ZZ}^* \to \ell^+\ell^-\ell'^+\ell'^-$ including soft electrons (see also Section 3.5.1.1.5) or the extreme high-energy electrons expected from $\mathrm{Z}' \to \mathrm{e}^+\mathrm{e}^-$, dedicated optimizations are often performed. On top of the cut-based selections, ATLAS uses a simple likelihood method for real-time and offline electron identification [254, 264], while CMS has BDTs trained for photon and electron identification offline [267].

3.5.1.1.4 Energy calibration of e/γ objects is a complex multi-step process. It starts with a per-channel (cell, crystal) *electric calibration* that converts the digitized detector signal from ADC counts to energy units. The calibration factors are based on test-beam data, per-channel intercalibration, and time-dependent corrections for radiation-induced aging and other effects based on in-situ monitoring (e.g., the change in light yield of the CMS $\mathrm{PbWO_4}$ crystals is measured using the laser calibration system).

The next step is based on detailed *Monte Carlo simulations* where the reconstructed cluster energy is compared to the "true" energy that was generated and a *multivariate analysis* is performed to get the closest result. This can be performed in multiple steps following the sequence of the reconstruction algorithm (i.e. clusters, superclusters, refined superclusters, electrons or photons). Track and cluster measurements can also be combined to derive the best estimate of the 3-momentum.

Finally, *in-situ calibration* is performed using short-lived particles with well-known mass decaying into electrons (e.g., $\mathrm{Z} \to \mathrm{e}^+\mathrm{e}^-$, $\mathrm{J}/\psi \to \mathrm{e}^+\mathrm{e}^-$ and $\mathrm{W}^\pm \to \mathrm{e}^\pm\nu_\mathrm{e}$) and photons (e.g., $\mathrm{Z} \to \ell^+\ell^-\gamma$ and $\pi^0 \to \gamma\gamma$). By comparing the reconstructed invariant mass or the measured ratio of the calorimeter energy to the track momentum (E/p) in data and simulation, a data-driven scale factor can be determined as a function of the most relevant kinematic or identification variables to get the best performance. In this step, additional smearing can be derived for the simulation to match the resolution observed in data.

In Run 2, the electron energy scale in CMS is derived with about 0.1% (0.3%) precision in the barrel (endcap) for $p_{\mathrm{T}} = 10 - 50$ GeV, and estimated to be within 2-3% at higher energies [267]. The energy resolution measured in $\mathrm{Z} \to \mathrm{e}^+\mathrm{e}^-$ decays ranges from 2% to 5%, depending on the pseudorapidity and the bremsstrahlung energy loss in the detector material. Similar results were reported by the ATLAS collaboration [320].

3.5.1.1.5 Efficiency measurements of selection criteria on single physics objects (such as a lepton or a photon) are most frequently performed with the *tag-and-probe method* [252–254, 256, 267] which relies on the selection of a clean and unbiased sample of objects to test the efficiency of the selection requirements of interest.

The classic example at the LHC is the measurement of lepton selection efficiencies using a sample of Z boson leptonic decays $\mathrm{Z} \to \ell^+\ell^-$ collected using a single-lepton trigger, where one of the leptons, called the *tag*, is identified using a high-purity algorithm. To remove any trigger bias, the tag has to be matched to an online lepton that pass the single-lepton trigger criteria. A second lepton candidate with opposite electric charge (OS), called the *probe*, with requirements that correspond to the "denominator" of the efficiency to be measured is then paired with the tag and the invariant mass of the pair ($m_{\ell\ell}$) is calculated. If the probe is indeed a lepton from a Z decay, $m_{\ell\ell}$ should be close to m_{Z}. The $m_{\ell\ell}$ distribution can thus be used to extract the number of probe leptons that originate from $\mathrm{Z} \to \ell^+\ell^-$ decays in the sample (N_{probe}) using an analytic or (directly measured or simulated distribution based) template fit to subtract the probes that originate from processes other than $\mathrm{Z} \to \ell^+\ell^-$ ("background"). The fit procedure is repeated applying the selection corresponding to the "numerator" of the efficiency, and determining the number of probes from $\mathrm{Z} \to \ell^+\ell^-$ that pass the selection ($N_{\mathrm{probe}}^{\mathrm{pass}}$). The efficiency is given then by the ratio $\epsilon = N_{\mathrm{probe}}^{\mathrm{pass}}/N_{\mathrm{probe}}$. The measurement is typically performed in bins of the most important kinematic (p_{T}, η, ϕ) and "environmental" variables (distance to closest jet, pileup, etc) of the probe. The result is compared to the equivalent measurements performed on simulated $\mathrm{Z} \to \ell^+\ell^-$ samples, and a correction factor (often called a "scale factor") is calculated that can then be applied as an event weight to MC simulated events of any physics final state that includes a lepton with the given properties.

The tag-and-probe method using m_{Z} as a discriminant works very well for leptons with $p_{\mathrm{T}} \approx 20 - 50$ GeV, corresponding to the Jacobian peak [321]. At lower p_{T} (essential for Higgs boson studies in the $\mathrm{H} \to \mathrm{ZZ}^* \to \ell^+\ell^-\ell'^+\ell'^-$ final state described in Section 5.5), significant backgrounds appear, while at higher p_{T} (preferred by the decays of exotic heavy particles that might modify the mass spectrum of high-mass Drell-Yan production discussed in Section 6.1), the mass distribution is distorted and the fits become problematic. To overcome these challenges, I lead the development of two new methods.

To reach the highest possible p_{T} values for the efficiency measurement, the probe electron isolation (i.e. the normalized energy around the electron) was introduced as discriminating variable [322] to determine the background contribution in the probe sample. The dilepton invariant mass was required to be compatible with that of m_{Z} but not used in the fit. The p_{T}- and η-dependent isolation template shapes to describe the background distributions were determined from the data by inverting identification cuts. A fit to the high-isolation region was then performed. Based on this "sideband" fit, the background contribution was extrapolated to the low-isolation signal region and subtracted from the probe rate. The method is illustrated in Figure 3.11. The results were found to be consistent with those based on the fit to the invariant mass distribution [253] in the common measurement range of $p_{\mathrm{T}} = 20 - 50$ GeV, and extended the range up to $p_{\mathrm{T}} = 500$ GeV. The systematic uncertainty is below 1% for $p_{\mathrm{T}} > 35$ GeV, determined by varying the high-purity selection criteria on the tag, the isolation definition, the lower threshold for the isolation side band, and the probe identification cuts inverted to define the background template. The possible selection biases were also studied in detail in simulation. The measurement was an essential ingredient of the first high-mass Drell-Yan differential cross section determination by ATLAS in the $\sqrt{s} = 7$ TeV data sample (Section 6.1).

At low-p_{T}, the number of electrons from $\mathrm{Z} \to \mathrm{e}^+\mathrm{e}^-$ decays decreases. The purity of the probe sample can be somewhat improved for $p_{\mathrm{T}} \approx 10 - 15$ GeV by requiring that one of the final state electrons radiates a photon, and then using the $\mathrm{e}^+\mathrm{e}^-\gamma$ invariant mass as discriminating variable to determine the background contribution (Figure 3.12 top left). At even lower p_{T} values, the decays of hadronic resonances, such as J/ψ and

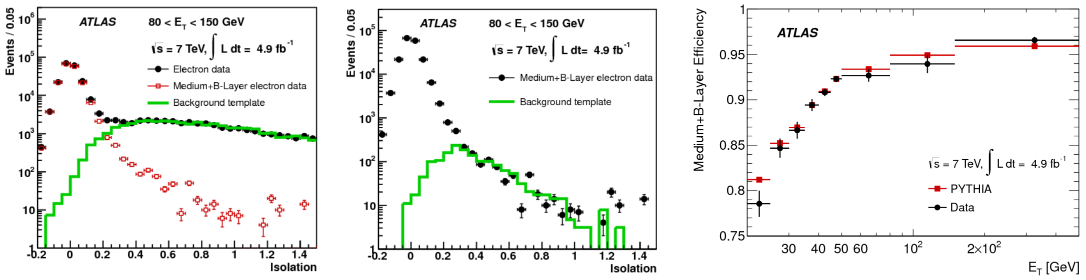

Figure 3.11: *(left) Distribution of the calorimeter isolation variable* $E_{\mathrm{T}}^{\mathrm{cone}}$*/(50 GeV) with a half opening angle of the cone of* ΔR *= 0.4 for reconstructed electron candidates with* $E_{\mathrm{T}} = 80 - 150$ *GeV, integrated over pseudorapidity in the ATLAS* $\sqrt{s} = 7$ *TeV data set (black dots). The background template (green histogram) was created requiring that the probe electron candidate fails the low-purity "loose" selection and that it has an electric charge with the same sign as the tag electron. For illustration, the distribution for electrons passing the identification requirements applied in the high-mass Drell-Yan analysis (medium-purity working point with an additional criteria to have a hit in the innermost tracking detector layer) are also shown (red markers). (middle) Distribution of the isolation variable for identified electrons (same as the red markers on the left). The background template is created as above except that no significant energy leakage was allowed to the hadron calorimeter. (right) The measured identification efficiency with respect to reconstructed electron candidates with good track quality as a function of the electron* E_{T} *for data and for MC simulation of the Drell-Yan process. The error bars indicate the total uncertainty.*

Υ can be harvested. The dielectron mass reconstruction resolution in ATLAS is not sufficient to cleanly separate the $\mathrm{b\bar{b}}$ bound states, Υ(1S), Υ(2S), Υ(3S) with masses of 9.46 GeV, 10.02 GeV and 10.36 GeV, thus attempts to use these resonances for efficiency measurements did not offer higher precision than those utilizing $\mathrm{Z} \to \mathrm{e^+e^-}$ decays. The $\mathrm{c\bar{c}}$ bound states, J/ψ and ψ(2S) with masses of 3.097 GeV and 3.686 GeV, however, allowed to extend electron identification measurements down to ~ 5 GeV.

There are a number of challenges when using low-mass $\mathrm{c\bar{c}}$ resonances [323] for efficiency measurements using the tag-and-probe method. Due to the small mass and thus large Lorentz boost of the mesons, the final state electrons are close to each other, as illustrated on Figure 3.13, potentially modifying the calorimeter shower shape and isolation distributions of each other and thus biasing the measurement. The close-by masses of the resonant states make the background determination using a fit to the invariant mass distribution more difficult. Furthermore, there is both prompt ($\mathrm{pp} \to \psi + X$) and non-prompt contribution to the production cross section, the latter via b hadron decays ($\mathrm{pp} \to B + X \to \psi + X' + X$). While a prompt meson is expected to be typically isolated from other objects (X) in the event, non-prompt ψ mesons are accompanied by other particles (X') produced in the b hadron decay, thus the final state electrons are expected to be less isolated. The measurement thus necessitates a careful estimation of the probe electron rate originating from prompt J/ψ and ψ(2S) decays as only they produce isolated electrons similar to those that arise from electroweak processes, for example Higgs boson decays. The extraction of the prompt component of the probe sample is performed in two steps [324]. First, the non-$\mathrm{c\bar{c}}$-resonance background contribution is subtracted based on the reconstructed invariant mass of the dielectron system, then the prompt fraction is determined based on the displacement of the dielectron production vertex, as illustrated in Figure 3.12 and described in its caption.

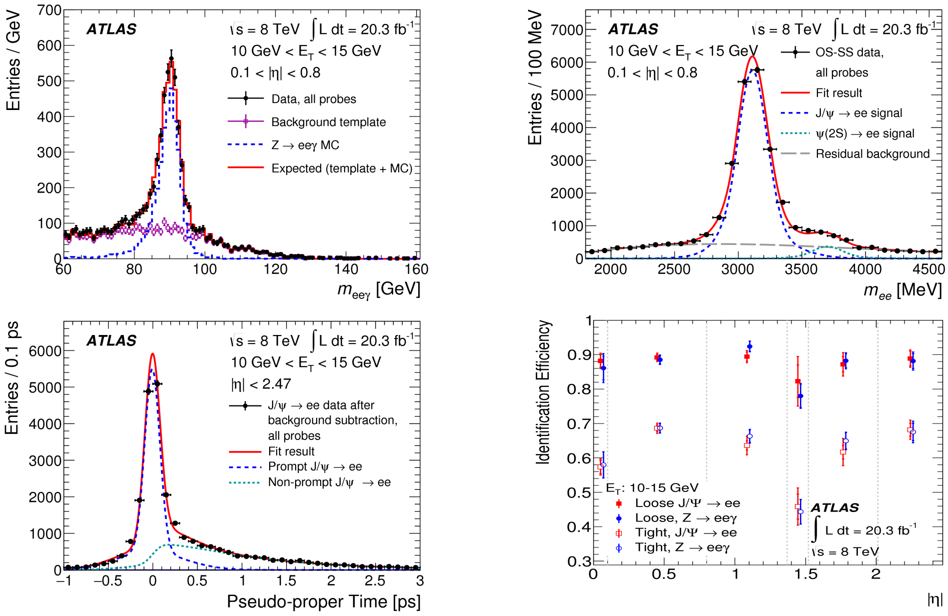

Figure 3.12: *(top left) Distribution of the reconstructed* $e^+e^-\gamma$ *mass for reconstruction-level probe selection in the* $Z \rightarrow e^+e^-\gamma$ *tag-and-probe analysis in the ATLAS* $\sqrt{s} =$ *8 TeV data set. The background template shape was created requiring that the probe electron candidate fails the low-purity "loose" selection on the shower width in the ECAL strip layer and on the fraction of high-threshold hits in the TRT. The* $Z \rightarrow e^+e^-$ *template comes from simulation. (top right) Distribution of the reconstructed opposite-charge (OS)* e^+e^- *mass in the* $J/\psi \rightarrow e^+e^-$ *tag-and-probe analysis for reconstruction-level probe selection. The combinatorial background is subtracted using the same-charge (SS)* $\mathrm{e}^{\pm}\mathrm{e}^{\pm}$ *distribution, the remaining background is modeled by a 2nd order Chebyshev polynomial, while the* J/ψ *and* $\psi(2S)$ *contributions are modeled each by the sum of a Crystal-Ball and a Gaussian function. (bottom left) Distribution of the pseudo-proper time in the* $J/\psi \rightarrow e^+e^-$ *tag-and-probe analysis for reconstruction level probe selection, after statistically subtracting the non-c*$\bar{\mathrm{c}}$*-resonance background contribution using the distributions of SS pairs as well as pairs in the dielectron mass distribution side bands. The prompt component is modeled by a sum of two Gaussian functions, and the non-prompt distribution by an exponential decay function convoluted with the sum of two Gaussian functions. (bottom right) Comparison of the measured identification efficiency using* $J/\psi \rightarrow e^+e^-$ *and* $Z \rightarrow e^+e^-\gamma$ *tag-and-probe techniques for a low-purity "loose" and a high-purity "tight" working point as a function of the electron pseudorapidity for* $p_{\mathrm{T}} = 10 - 15$ *GeV. The inner error bars indicate the statistical, the outer the total uncertainty.*

As b hadrons have a typical life time of $\tau \approx 10^{-12}$ s, they travel on average $L = \beta_{\mathrm{r}}\gamma_{\mathrm{r}}c\tau \approx p/m \cdot 300\ \mu$m (where p/m is the momentum over mass ratio of the b hadron) and thus decay in a "secondary" vertex displaced from the primary vertex where the b hadron was produced. Experimentally, the pseudo-proper time can be estimated from the transverse decay length (L_{xy}) which is given by the distance between the primary vertex and the J/$\psi \rightarrow \mathrm{e}^+\mathrm{e}^-$ decay vertex in the transverse plane:

$$\tau_{\mathrm{T}} = \frac{L_{xy} \cdot m_{\mathrm{J}/\psi}}{p_{\mathrm{T}}^{\mathrm{ee}}}, \tag{3.11}$$

where $m_{\mathrm{J}/\psi}$ is the mass of the J/ψ meson and $p_{\mathrm{T}}^{\mathrm{ee}}$ is the reconstructed transverse mo-

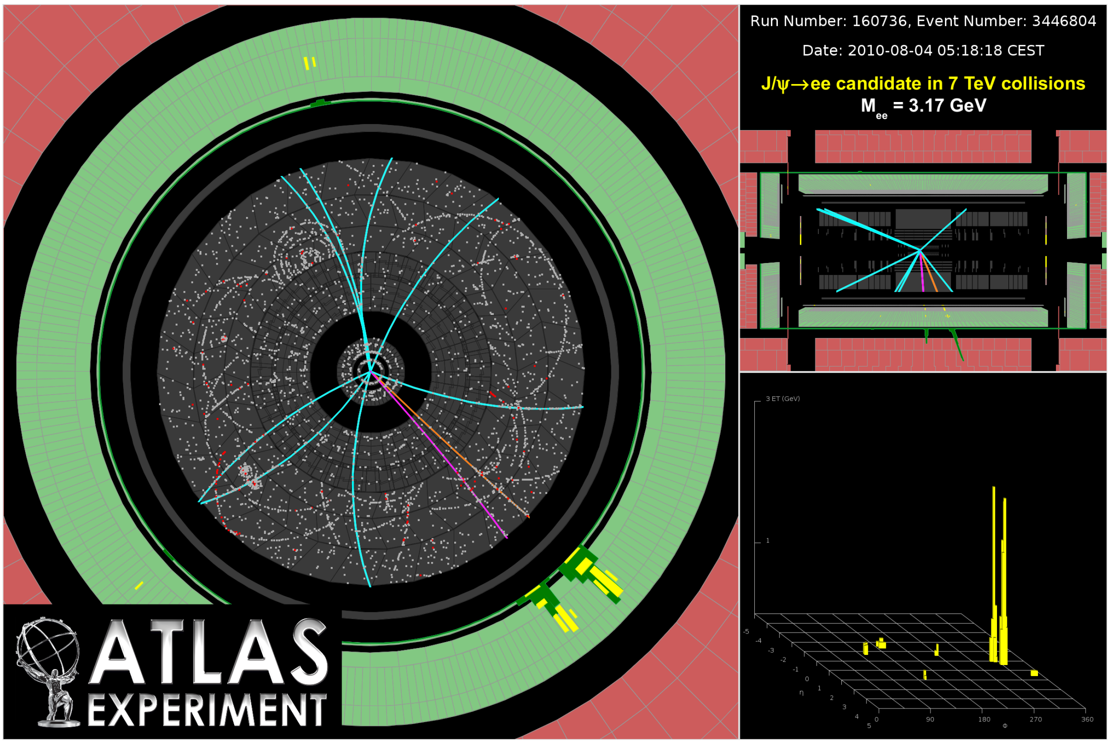

Figure 3.13: *Event display of a candidate for* $J/\psi \to e^+e^-$ *in the 2010 ATLAS data at* $\sqrt{s} = 7$ *TeV pp collisions. Events with two reconstructed opposite charge electrons passing high-purity tight identification criteria were selected. The invariant mass of the* J/ψ *candidate is 3.17 GeV, its* p_{T} *is 19.96 GeV. (left)* $r-\phi$*, and (top left)* $r-z$ *view of the event showing the signals in the tracking detectors and the energy deposits in the LAr calorimeter, and (bottom left) a lego plot indicating the amount of transverse energy measured in the calorimeters in* $\eta-\phi$*.*

mentum of the dielectron system. For prompt production $\tau_{\mathrm{T}} \approx 0$, while it is expected to be $\mathcal{O}(\mathrm{ps})$ for non-prompt J/ψ.

A comparison of the fully independent $\mathrm{J}/\psi \to \mathrm{e}^+\mathrm{e}^-$ and $\mathrm{Z} \to \mathrm{e}^+\mathrm{e}^-\gamma$ tag-and-probe measurements, where both are available, shows excellent agreement within the uncertainties (Figure 3.12 (bottom right)). The systematic uncertainties were determined by varying the tag-and-probe selection, the fitted shapes, the fit ranges, and the side band definitions. As an example, for the $\mathrm{J}/\psi \to \mathrm{e}^+\mathrm{e}^-$ method, 186 variations were considered. The $\mathrm{J}/\psi \to \mathrm{e}^+\mathrm{e}^-$ and $\mathrm{Z} \to \mathrm{e}^+\mathrm{e}^-(\gamma)$ measurements are combined at the level of data / simulation efficiency correction factors. Observed differences are taken into account in the final uncertainty. The combined results in the 2012 ATLAS data set are shown in Figure 3.14 for various identification working points from the lowest to the highest purity as a function of the electron E_{T} and η, as well as the number of reconstructed primary vertices, a measure of the pileup. As expected the efficiencies grow with E_{T}, lowest in the transition regions between the barrel and the endcaps, and fall with increasing pileup due to the higher detector occupancy that makes the electrons less isolated and thus modifies their shower shapes.

Our measurements allowed to decrease the lower p_{T} selection on the electrons to 7 GeV in the $\mathrm{H} \to \mathrm{ZZ}^* \to \ell^+\ell^-\ell'^+\ell'^-$ measurement (Sectionsec:Higgs4lepton) which increased the signal acceptance and thus improved the analysis performance.

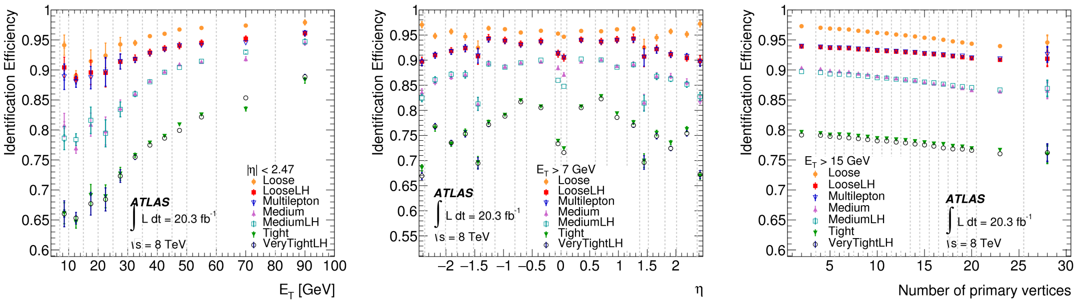

Figure 3.14: *Identification efficiencies for electrons from $Z \to e^+e^-$ decays from the combined tag-and-probe measurements in the ATLAS $\sqrt{s} = 8$ TeV data sample as a function of the electron (left) transverse momentum and (middle) pseudorapidity, as well as (right) the number of reconstructed vertices for various working points of cut-based and likelihood (LH) discriminator based multivariate identification algorithms. The Higgs boson studies in the $H \to ZZ^* \to \ell^+\ell^-\ell'^+\ell'^-$ final state in Section 5.5 use the high-efficiency "multilepton" selection that features the smallest dependence on pileup. The inner error bars indicate the statistical, the outer the total uncertainty.*

3.5.2 Trigger systems

The 40 MHz bunch crossing rate of the LHC, coupled with a data size of about 1 MB per event, necessitates the introduction of real-time data processing and selection to decide which events to record for future analysis. The ATLAS and CMS experiments have robust and efficient two-stage trigger systems to achieve high-quality physics results in an environment where the most interesting events are extremely rare. For example, Higgs boson production amounts to only 3 out of 10^{10} pp interactions. The trigger system allows to select such low-rate processes, as well as to collect control samples for detector calibration and background measurements.

The higher energy at Run 2 brought increased production cross sections by at least a factor of two for high momentum transfer processes. Together with the increasing instantaneous luminosity, they necessitated the upgrade of the ATLAS [264, 325] and CMS [326, 327] trigger systems to keep event rates under control while maintaining high efficiency for physics measurements, which requires to keep the trigger object transverse momentum thresholds low enough to access electroweak scale processes. The new systems feature finer granularity detector readout, enhanced object (e.g., for e, γ, μ, τ, jet, $p_{\mathrm{T}}^{\mathrm{miss}}$) reconstruction allowing a more accurate energy reconstruction in the presence of high pileup, and correlated multi-object (topological) triggers targeting specific physics final states. The trigger system designs of the experiments also became more similar, and their data acquisition systems upgraded to achieve higher readout and output rates.

3.5.2.1 Level-1 hardware trigger

The level-1 trigger has custom-designed electronics hardware and firmware that process the muon spectrometer, calorimeter and possibly other (e.g. in ATLAS, the Minimum Bias Trigger Scintillator (MBTS)) subdetector data with typically a coarser spatial segmentation and lower momentum resolution to decrease the event rate to about 100 kHz within a fixed latency of 2.5 and 4 μs in ATLAS and CMS, respectively.

The calorimeter and muon trigger processors receive the trigger primitives from the detectors. These are coarse-grain detector readout signals such as towers of local energy deposits in the calorimeters, or correlated hits in neighboring channels in a layer of the muon spectrometer, called stubs). The L1 trigger objects (e/γ objects, tau leptons, jets, energy sums and muon tracks) are built from these and then sent together with their kinematic properties (including the calibrated energy of calorimeter objects) and other information (such as isolation energy around the object, timing measurement and quality flag) to the central trigger processor, called Global Trigger (GT) in CMS.

The central processor executes every algorithm in the trigger menu (Section 3.5.2.3) in parallel for the final L1 trigger decision. It is also responsible for enforcing trigger rules to regulate the dead time, i.e. prevent the on-detector pipeline data storage from overflowing by restricting the minimum distance between L1 accepts and the number of L1 accepts for a given number of bunch crossings. After a positive L1 trigger decision, the events are read out from the front end, buffered and processed by the high-level trigger.

3.5.2.2 High-level trigger

The high-level trigger (HLT), a software-based system running on a computer farm fully reconstructs the events using high-resolution, full-granularity data of all subsystems in a few 100 ms and reduces the physics event rate to a few kHz (in Run 2 and Run 3) to fit into the data acquisition bandwidth limit of about 15 GB/s. The real-time software algorithms are very close to the state-of-the-art ones used in physics publications. Differences arise mainly for two reasons. Final detector calibrations are not available in the trigger and CPU-intensive algorithms need to be replaced by faster (and thus less precise) versions.

The geometrical, so-called Region-of-Interest (RoI) information from the L1 trigger can be used for regional reconstruction in the HLT algorithms to further suppress the rate before the full event building. This was a key design feature for the ATLAS Run-1 system [328] that had a two-stage HLT architecture with two separate computer farms and a fixed rate limit between them. These have been unified for Run 2 to allow resource sharing and a simplified hardware and software structure such that the reconstruction can either be executed within the RoIs or for the full detector, with the data retrieved on demand.

Events that are accepted by the HLT are stored locally at the experimental site and transferred to the CERN Tier-0 facility for offline reconstruction and then distributed for permanent storage among the various sites of the LHC Computing Grid.

3.5.2.3 Trigger menu

The *trigger menu* defines how the resources are shared between the various trigger families requiring the presence of physics *signatures*: electrons, photons, muons, tau leptons, jets, tagged b jets, missing transverse momentum ($p_{\mathrm{T}}^{\mathrm{miss}}$), scalar sum of all visible objects' transverse momenta (H_{T}) or high track multiplicity in the final state. It is the list of all *L1 trigger seeds* and *HLT trigger paths* together with their L1 and HLT *prescale* factors that determine in what fraction of the events the given trigger requirement is tested: a prescale of n signifies that the condition is tested for every n^{th} event, reducing the recorded event rate in an unbiased way.

The menu includes *primary physics triggers*, typically unprescaled and aimed to provide data for physics analysis; *supporting triggers* for trigger efficiency and performance monitoring; *alternative triggers* often implementing new algorithms to allow their full commissioning with their data heavily overlapping with those of a primary trigger; *backup triggers* with tighter requirements and thus lower expected rates in case the primary triggers cannot be kept unprescaled for the whole data taking period; and *calibration triggers* to ensure that all detector subsystems provide high-quality data. These are often operated at high rate but storing only the relevant information for the given subsystem and thus having very small event sizes. This is, for example, the case for the *pixel luminosity trigger* in CMS that only stores the number of clusters per pixel module per event, reducing the data bandwidth by a factor of $\sim 100 - 200$ depending on the data taking conditions.

There is an option to let a fraction of events to *pass-through* the HLT system and record (including all trigger information) irrespective of the decision made which is especially useful during the initial commissioning phases.

40 MHz *scouting* introduced in Run 2 allows to capture a part or all of the Level-1 trigger data streams using spare optical cables. This allows verification of the functionality of existing trigger algorithms, as well as development of new algorithms without disturbing data taking. The main advantage of scouting is the elimination of rate limitations by the HLT and DAQ systems, as well as biases associated with the L1 trigger combination algorithms. An interesting application is mentioned for luminosity determination in CMS in Section 4.4.

A similar philosophy is behind *data scouting* in which case the event is processed (fully or partially) by HLT, and the HLT reconstructed objects are saved in a minimal data format for physics analysis (for example, to search for low-p_{T} hadronically decaying resonances). In this case events can be written out at high rate due to the much smaller event size, however full offline reconstruction is no longer possible.

The menu can also contain triggers to collect data for *parking*, i.e. stored in raw format and only processed months later when computing resources are available (typical for b physics measurements that require large samples of low-p_{T} di-muon events) or in case when an intriguing hint is found (e.g., by data scouting).

The trigger menu composition and the applied trigger thresholds are optimized for several instantaneous luminosity ranges to maximize the physics output within the constraints of the experiment, such as the maximum L1 trigger rate and the average HLT physics output bandwidth. Flexibility is provided not only by the tightness of the selections (e.g., the p_{T} thresholds on the physics objects) and the prescale factors, but also by requirements on the bunch crossing identification number. The latter allows to sample specific bunch crossing groups: colliding, single outside of trains, first in trains, unpaired and empty. This is particularly useful for background studies, detector calibration and searches for exotic particles with a long lifetime.

The optimization of the trigger menu is a complex task that requires careful studies of the properties of all triggers, such as their efficiency, purity, (total and unique) rate, bandwidth, average and maximal CPU time, as well as an excellent understanding of the physics program of the experiment. It is performed using detailed simulations as well as previously collected data. Figure 3.15 illustrates the sharing of the trigger rate at L1 and HLT in a pp physics data taking fill in 2015 at ATLAS. For the HLT, the rate corresponding to triggers with partial event building (including data scouting and calibration triggers) are not included. These dominate the HLT rate but take only a small fraction of the bandwidth (the latter being the limiting factor for the menu design).

Trigger studies are often conducted using special data samples collected with minimal selection bias, i.e. with algorithms that are highly efficient for non-single-diffractive pp collision events. For example, in CMS such *minimum bias triggers* require — on top of the presence of a filled bunch crossing — a coincidence between trigger signals from the $+z$ and $-z$ sides of the hadron forward calorimeter (HF).

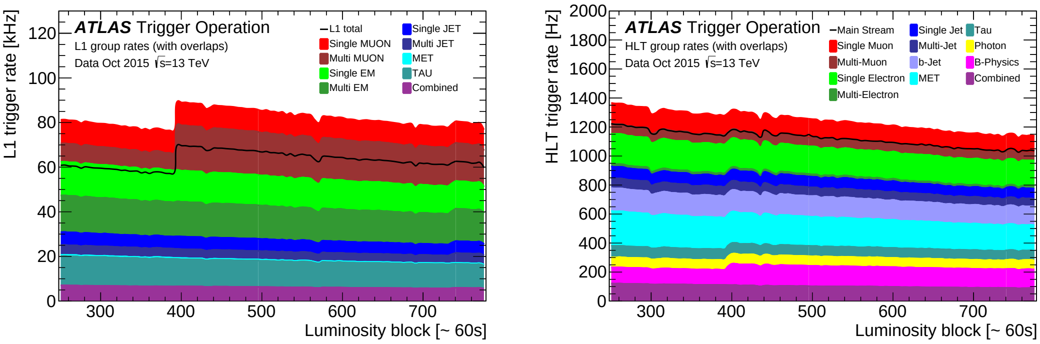

Figure 3.15: *(left) L1 and (right) HLT physics trigger rates grouped by trigger signature during a* pp *fill in October 2015 in ATLAS. Due to the overlaps, the sum of the individual groups (shown by the different colors stacked on top of each other) is larger than the total rate (solid black line). The "combined" group includes triggers with more than one physics signatures, e.g., an electron and a muon in the same event. The rate increase at luminosity block 400 is due to the removal of the L1 prescales for B-physics (low-*p_T *dimuon) triggers, while at block 740 due to a change for single jet triggers. The rate changes with the instantaneous luminosity as the beam intensities drop in time. The other irregularities at 430, 570 and 680 are due to beam orbit optimization scans to maintain head-on bunch collisions. [264]*

While most time is taken for "luminosity production" to collect large data sets for the mainstream LHC physics program, the machine also provides dedicated short data taking periods or even just single fills to collect specialized data, for example, very low intensity pp collisions for diffractive physics, or PU $\sim$ 1 samples for auxiliary electroweak studies to support the most challenging precision measurements (like W mass determination), or Van der Meer (VdM) transverse beam separation scans for accurate luminosity calibration (Chapter 4). These require dedicated trigger menus to optimize the physics output within the technical constraints.

For the VdM scans, the Level-1 trigger system selects events from a small number of bunch crossings (typically 5-25) from the LHC orbit at high rate with the so called *zero-bias* selection. It only requires a signal coincidence at the two sides of the Beam Pickup Timing eXperiment (BPTX) ensuring the crossing of filled bunches. For luminosity (and other) calibration(s), *random* triggers are also useful both in physics and special fills, as they sample all (filled, unpaired, empty) crossings in a completely unbiased way and allow the determination of the detector response and the background contributions, e.g., from late particles, electronics time walk, detector activation or noise.

I played a leading role in the upgrade and optimization of the electron and photon triggers for the ATLAS experiment during the long shutdown of the LHC in 2013–2015 (LS1), including the design of the trigger menu, and in the trigger commissioning with first collision data in 2015 [265]. Between 2016–2018, I coordinated the operation and optimization of the CMS electron and photon triggers, as well as the trigger studies for SM measurements. I was also responsible for designing the trigger menu for special low-PU data taking for precision SM measurements. Starting in 2018, I became responsible for the luminosity triggers, including the definition of the menu for special fills and the monitoring of data taking performance.

The similarities and differences of electron and photon reconstruction and identification between the two experiments are summarized in Section 3.5.1.1. The special considerations for the trigger algorithms are outlined below.

3.5.2.4 Electron and photon triggers

Electron and photon triggers play an essential role at the LHC. They are used to select events containing $\mathrm{W}^{\pm} \to \mathrm{e}^{\pm}\nu_{\mathrm{e}}$ and $\mathrm{Z} \to \mathrm{e}^{+}\mathrm{e}^{-}$ decays, processes that are important in their own right to test the standard model (see Sections 6.1 – 6.3) and to calibrate the experimental apparatus (see Sections 3.5.1.1.4 – 3.5.1.1.5) but can also be part of the decay of heavier objects and thus help us in our quest to find new phenomena. Indeed, these triggers enabled the ATLAS and CMS collaborations in 2012 to discover [25, 26] the Higgs boson via its decays to Z, W and photon pairs ($\mathrm{H} \to \mathrm{ZZ}^{*} \to \ell^{+}\ell^{-}\ell'^{+}\ell'^{-}$, $\mathrm{H} \to \mathrm{W}^{\pm}\mathrm{W}^{\mp *} \to \ell^{\pm}\nu_{\ell}\ell'^{\mp}\nu_{\ell'}$, and $\mathrm{H} \to \gamma\gamma$) as discussed in Chapter 5. They might also lead us to other new particles, such as new gauge bosons [329–331] (e.g., via $\mathrm{Z}' \to \mathrm{e}^{+}\mathrm{e}^{-}$, see Section 6.1.2), excited graviton states [332–335] (e.g., via $\mathrm{G}_{\mathrm{KK}} \to \gamma\gamma$), and supersymmetric particles [336, 337].

For electron and photon triggers, the menu optimization is thus driven by the requirement to efficiently and purely select events with weak bosons and to retain very high efficiency to record the production of rare exotic heavy particles. The HLT strategy in Run 2 aimed to keep online p_{T} thresholds at their Run-1 levels (e.g. 24 GeV for single electron triggers in ATLAS) as long as possible by tightening the L1 and HLT selections gradually (and thus trading efficiency for purity) as the instantaneous luminosity increased.

Considering the electron signatures, the most used *lowest threshold, tight, isolated single electron trigger* is thus complemented by a *higher threshold, loose single electron trigger*, as well as *lower, typically asymmetric-threshold, loose dielectron* and *trielectron triggers*. The $\mathrm{ZZ} \to \ell^{+}\ell^{-}\ell'^{+}\ell'^{-}$ studies (e.g. in Section 6.3.1) use a logical OR of single, di- and trilepton triggers achieving an almost 100% trigger efficiency. Numerous *auxiliary triggers* complete the menu. For example, in ATLAS to collect $\mathrm{J}/\psi \to \mathrm{e}^{+}\mathrm{e}^{-}$ events for tag-and-probe electron identification efficiency measurements, we developed an dielectron trigger with asymmetric tight + E_{T}-cut-only requirement and an invariant mass selection of $1 < m_{\mathrm{ee}} < 5$ GeV at the HLT. Similar strategy is followed for the photon trigger menu.

As an example, the rate and efficiency of the main e/γ triggers in ATLAS in the early Run-2 data are shown in Figure 3.16 to illustrate the various considerations needed to design a high-performance trigger menu. The trigger requirements of both collaborations were adjusted from year to year to cope with the increasing instantaneous luminosity: selections were tightened and – when inevitable – E_{T} thresholds were raised. The performance of the main CMS electron triggers in the second half of Run 2– after a reoptimization that increased the efficiency and the rejection power – are presented in Figure 3.17. The actual values of efficiencies cannot be directly compared between ATLAS and CMS as they are computed with respect to different offline selections.

Trigger efficiencies are always measured with respect to a given offline object selection that has to match the physics analysis choices. For multi-object triggers, the computation is performed per object and then combined at the analysis level.

Electron trigger efficiencies are typically measured using the tag-and-probe method introduced in Section 3.5.1.1.5. Photon trigger efficiencies are measured in a number of ways: (i) using $\mathrm{Z} \to \ell^{+}\ell^{-}\gamma$ tag-and-probe with the $\ell^{+}\ell^{-}$ pair acting as tag and a reconstructed photon as probe; (ii) with a bootstrapping method where the efficiency is measured with respect to an unbiased trigger whose efficiency (ϵ_{BS}) is measured independently: $\epsilon_{\mathrm{trigger}} = \epsilon_{\mathrm{trigger|BS}} \cdot \epsilon_{\mathrm{BS}}$; (iii) using an orthogonal trigger, for example, requiring the presence of a jet, a muon or $p_{\mathrm{T}}^{\mathrm{miss}}$ online object. It is essential to always ensure that the selected sample is bias free. To understand the observed inefficiencies

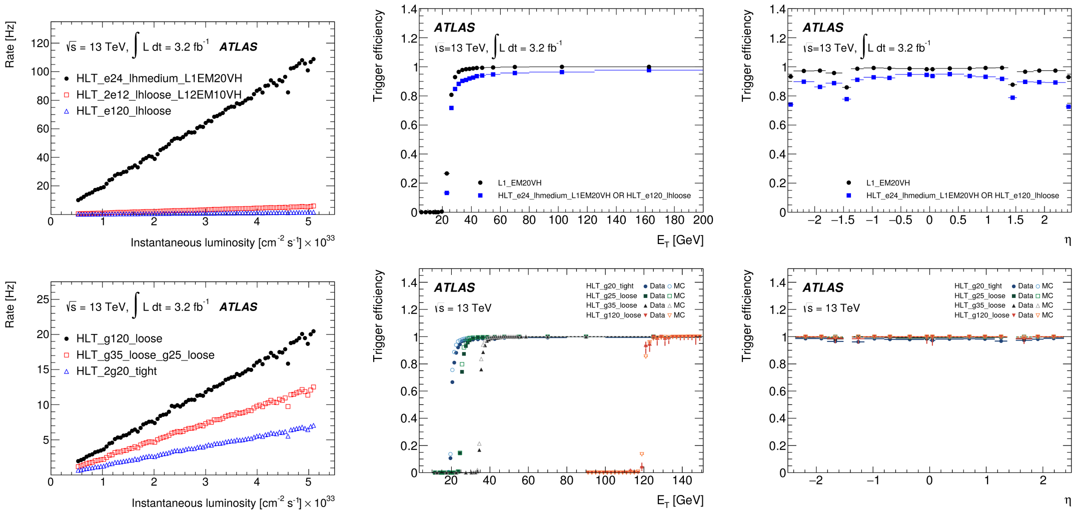

Figure 3.16: *(left) Trigger rates as a function of the instantaneous luminosity of the main (top) electron and (bottom) photon triggers in ATLAS in 2015. The e/γ trigger rate is dominated by the single electron trigger (HLT_e24_lhmedium_L1EM20VH) with an E_T threshold of $\sim$ 20 GeV at L1 and 24 GeV at HLT and a medium-purity multivariate likelihood selection. Raising the threshold or requiring more trigger objects have a dramatic effect on the rates. Trigger efficiencies as a function of the (middle) transverse energy and (right) pseudorapidity as a function of the offline (top) electron and (bottom) photon E_T. For electrons, the efficiency is calculated with respect to offline medium-purity likelihood selection using the tag-and-probe method, while for photons with respect to a high-purity offline selection using a bootstrapping method. (middle) The steepness of the rise of the efficiency (called "turn-on") around the applied trigger E_T threshold is determined by the energy resolution of the trigger calibration with respect to the precision offline calibration. (middle top) The L1 selection is fully efficient at high E_T. The logical OR of the lowest threshold medium and the high-threshold ($E_\mathrm{T} > 120$ GeV) loose single electron triggers serves to reach almost 100% efficiency for exotic physics signatures with high-E_T electrons. (middle bottom) Photon efficiencies per object are compared for data and simulation. (right top) The trigger efficiencies drop in the complex transition region between the barrel and the endcaps, as well as at the edge of the tracking and precision ECAL acceptance. (right bottom) Photon triggers are not used in these regions due to their impurity.*

of the trigger algorithms, it is essential to understand how they work.

As discussed previously, electron and photon reconstruction relies on the calorimeter system and on the inner tracking detectors based on silicon pixel and strip sensors, and – in ATLAS – a Transition Radiation Tracker (TRT) providing additional electron-hadron separation. As the tracking detectors produce a huge data volume, their information enters only at the HLT. Electron and photon triggers [264, 265, 267, 338] are based on the Region-of-Interest concept in which the HLT reconstruction is seeded by the L1 EM objects. A major difference appears here between the ATLAS and CMS algorithms: in ATLAS only one L1 trigger seed belongs to an HLT path, while in CMS several L1 trigger seeds can be joined by a logical OR condition to feed a single HLT path providing more flexibility and higher efficiency.

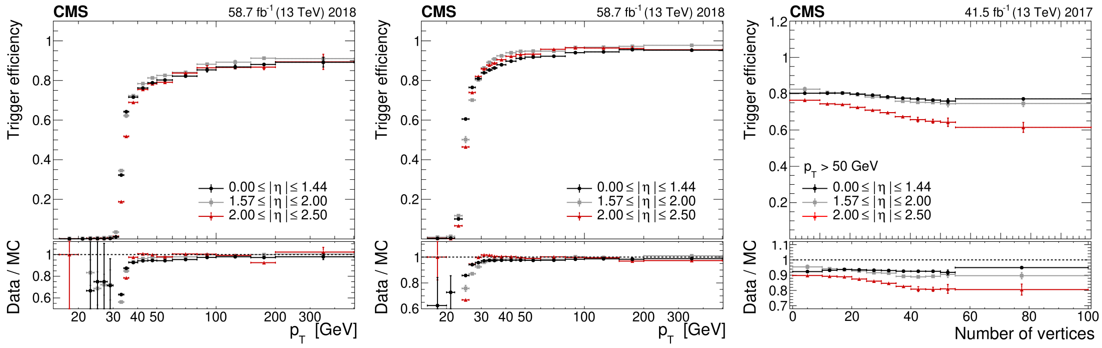

Figure 3.17: *Efficiency as a function of the offline electron transverse momentum in different regions of pseudorapidity of (left) the main single electron trigger HLT_Ele32_WPTight_Gsf with tight identification and isolation requirements and a 32 GeV p_{T} threshold, and (middle) the leading leg (Ele23) of the main double electron trigger HLT_Ele23_Ele12_CaloIdL_TrackIdL_IsoVL with loose identification and isolation requirements in the CMS experiment in 2018. The efficiency is measured w.r.t. offline reconstructed electrons with no identification cuts applied (in contrast to the ATLAS measurement in Figure 3.16). (right) Efficiency dependence on the number of reconstructed vertices, a proxy for the event pileup for t HLT_Ele32_WPTight_Gsf in the 2017 data. The observed drop is related to the failure of the pixel detector DC-DC adapters in the second half of 2017 when a large fraction of the high-pileup data were recorded. The bottom panels present the data-to-simulation ratios. They illustrate the different online and offline corrections for the ECAL response at low E_{T} in the turn-on region and the difficulty to simulate the dead regions due to the DC-DC failures in 2017.*

3.5.2.4.1 Level-1 EM objects are reconstructed by the L1 calorimeter processor (L1Calo). Due to the lack of tracking information, electrons and photons are indistinguishable at this stage.

For ATLAS Run 2, I have reoptimized the L1 selections to provide a more uniform and higher efficiency.

The building blocks of the ATLAS L1 calorimeter objects in Run 1 and Run 2 were the so called projective towers that contained calorimeter cells within a region of 0.1×0.1 size in the (η, ϕ) plane and were organized in a grid. L1Calo EM clusters were then formed by 2×2 towers, reconstructed by a sliding-window algorithm that searched for local energy maximum. It then provided the cluster energy collected in 2×2 trigger towers in the ECAL if the energy of one of the four possible pairs of neighboring 1×2 or 2×1 towers exceeded a predefined E_{T} threshold which was pseudorapidity dependent to take into account the energy loss in the detector material before the calorimeter.

To discriminate against hadron jets, the energy sum in the EM isolation ring formed by the surrounding 12 towers in the ECAL as well as the hadronic core energy behind the 2×2 EM cluster in the HCAL, as illustrated on the left of Figure 3.18 (left) were computed. For the main unprescaled EM triggers a veto on hadronic core energy above 1 GeV was typically required.

The energy of the trigger towers was calibrated at the EM scale, thus it underestimated the energy deposited by hadrons. In Run2, dynamic bunch-by-bunch pedestal correction became available to compensate for the increased out-of-time pileup.

CMS calorimeter trigger towers (TTs) are formed by 5×5 crystals in the ECAL barrel with the HCAL barrel cell directly behind them, thus the readout granularity at L1 is $\Delta\eta \times \Delta\phi = 0.087 \times 0.087$. In the endcaps, a more complicated grouping, due to the

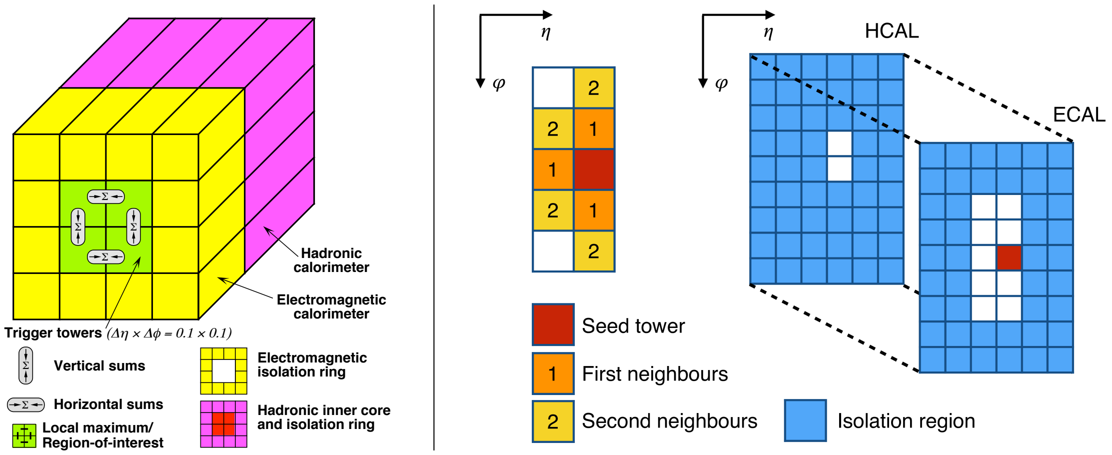

Figure 3.18: *(left) ATLAS and (right) CMS L1Calo cluster reconstruction for electron and photon triggers.*

ECAL endcap crystal layout and the progressively increasing size of the HCAL endcap cells, results in somewhat larger size of the TTs up to 0.174×0.174. Since Run 2, the e/γ reconstruction starts around a seed tower corresponding to a local energy maximum, including ECAL and HCAL deposits, with $E_{\mathrm{T}} > 2$ GeV, dynamically adding first and second neighboring towers with $E_{\mathrm{T}} > 1$ GeV. This dynamic clustering algorithm, illustrated in Figure 3.18 (right), had replaced the previous Run-1 sliding window technique (still in use by ATLAS though with an improved Super Cell granularity in Run 3 [248]). In the clustering, an extended region in the ϕ direction (up to five TTs) helps to recover energy lost by showering electrons and converted photons due to bremsstrahlung while moving in the magnetic field. Only a narrow region of at most 2 TTs is allowed in the η direction as EM showers are compact. The maximum size of clusters is limited to eight TTs in the initial clustering in order to minimize the impact of energy deposits from pileup. Then the cluster shape (e.g., EM showers are typically contain less than four TTs), the energy distribution between the seed and the neighboring towers, and the energy deposited in ECAL and downstream in the HCAL towers are used to identify electrons and photons, and differentiate them from tau leptons and hadron jets.

Isolation requirements can also be added to produce a collection of isolated L1 e/γ candidates. The isolation transverse energy is calculated using a 6×9 TT region around the seed tower, from which the e/γ candidate E_{T} is subtracted. The thresholds to pass the isolation criteria are stored in a look-up table (LUT) and depend on the e/γ candidate E_{T} and η, as well as a pileup estimator. The latter is calculated by counting the number of towers with $E_{\mathrm{T}} > 0.5$ GeV in the eight central η rings of the calorimeter corresponding to $|\eta| < 0.34$.

The position of the cluster is calculated using the distribution of the energy in the cluster by constructing an energy-weighted average position. The raw E_{T} of the candidate is the sum of the seed and the clustered towers. A scale factor is then applied to improve the calibration which is derived using $\mathrm{Z} \to \mathrm{e}^{+}\mathrm{e}^{-}$ collision events as a function of the seed tower η position, the cluster E_{T} and the cluster shape.

3.5.2.4.2 High-level trigger reconstruction defines *photons* as EM energy clusters with no requirement on a matching track and *electrons* as energy clusters matched to reconstructed charged particle tracks. A major difference between ATLAS and CMS is in the usage of GSF electron tracking at HLT. ATLAS only requires a generic KF track with $p_{\mathrm{T}} > 1$ GeV and having a minimum number of hits in the inner silicon tracking devices, while CMS runs GSF reconstruction in real time.

The ATLAS Run-2 HLT algorithm sequence [265, 266] is shown in Figure 3.19 for electron triggers. As calorimeter reconstruction is less resource intensive, it precedes the tracking step. Photon triggers operate in a similar fashion but are simpler as only calorimeter reconstruction and selection are applied. The initial fast reconstruction and selection step helps to reduce the event rate early. It can be skipped for the calorimeter, but fast track reconstruction using trigger-specific pattern recognition within the L1 RoI is always executed and seeds precision tracking that relies heavily on offline (non-electron-specific) algorithms.

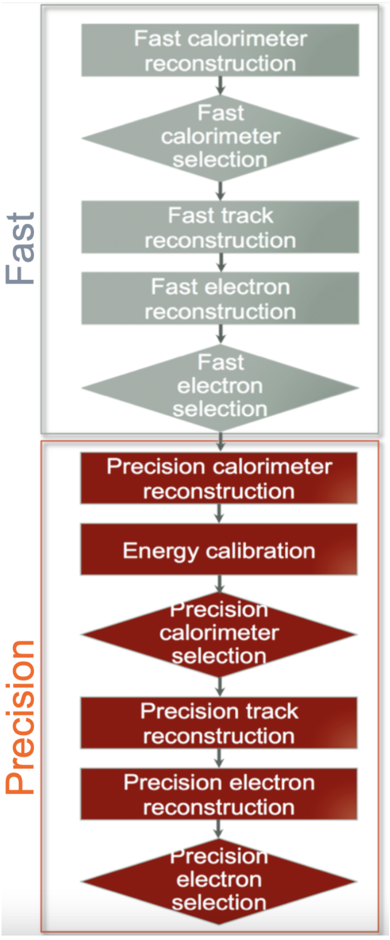

Figure 3.19: *ATLAS electron reconstruction algorithm sequence at the HLT.*

In Run 1 and Run 2, calorimeter cluster reconstruction was based on the sliding window algorithm providing a rectangular seed cluster where a local energy maximum had been found, if the sum of the energy in the member cells was above a threshold. The reconstruction followed the offline method with the difference that the window size for electrons and photons was the same online: 3×7 cells in the barrel and 5×5 cells in the endcap. (After 2017 for $E_{\mathrm{T}} > 15$ GeV EM objects, the ringer algorithm [266] was also used. In Run 3, following the offline changes, superclusters were introduced to HLT). The final online precision electron reconstruction uses offline-like algorithms (see Section 3.5.1.1) as much as possible. In particular, an improved electron and photon energy calibration and a new electron identification algorithm were introduced online for Run 2, both based on multivariate analysis techniques.

Photon identification in ATLAS relies on calorimeter shower-shape information and is based on rectangular cuts optimized in different pseudorapidity regions. Converted and unconverted photon candidates are separated offline and have different identification selections, while the looser cut of the two selections is applied on each variable online.

For electron identification to improve the purity of the triggered data sample, a new likelihood-based approach was adopted online which was successfully used offline already in Run 1 [254]. It uses input from calorimeter shower-shapes, tracking, track – cluster matching and a new electron probability derived from transition radiation information measured in the TRT. The largest difference between the online and the offline implementation originates from the lack of dedicated bremsstrahlung correction with the Gaussian Sum Filter method online.

The introduction of multivariate techniques online required careful commissioning. I designed the set of supporting and alternative triggers that allowed to compare the performance of the traditional cut-based selection with the new likelihood (LH) based one (using almost the same set of discriminating variables). As was previously seen in Run 1 for offline electron identification [254], the LH selection online also provides for the same efficiency about a factor two lower background rate with respect to the optimized cut-based selection, resulting in a purer online sample and thus a lower trigger rate [265].

Detailed studies primarily on Run-1 ATLAS data revealed the main sources of efficiency loss. The energy resolution at the L1 trigger contributed significantly close to the transverse energy threshold. Both fast and precision HLT algorithms introduced inefficiencies predominantly due to tracking related selections. At high transverse energies, track isolation losses became significant, which was recovered by introducing a non-isolated electron trigger with higher E_{T} threshold.

Similarly to ATLAS, in order to save computing resources and minimize the time necessary to run the HLT reconstruction (which has to be below 260 ms per event), all trigger selections have a modular structure in CMS. The faster, less complex algorithms are executed first, and their results are used immediately to filter the objects so that the more time-intensive reconstruction steps are run fewer times.

The main difference compared to the offline algorithms [267] appears in the track reconstruction which at the HLT is only attempted along trajectories extrapolated from reconstructed ECAL SCs (ECAL-driven).

An ECAL SC with a track matching its direction is labeled as an electron candidate. Identification of electrons and photons rely on similar quantities as offline (based on the transverse profile of the ECAL cluster energy, the HCAL energy behind the SC, and – for electrons – track quality, as well as matching variables between the SC and the associated track or pixel seed), together with a minimum threshold on $E_{\mathrm{T}}^{\mathrm{SC}}$, which at the HLT only uses ECAL information. Importantly, at the HLT the final calibrations of ECAL energy deposits (e.g., for transparency loss), as well as for electron and photon objects are not available, and a less accurate but simpler energy correction procedure is applied saving CPU resources.

Isolation requirements can also be added based on the energy deposited in the ECAL and HCAL, as well as on tracks reconstructed in the tracker detectors around the candidate. The more accurate PF isolation variables are not used online. Track reconstruction around electron candidates happen only at the very end of the trigger selection using an iterative algorithm similar to the offline one but customized for the HLT (e.g., having fewer iterations of the tracking procedure). For all selections, it is important to keep the requirements looser online so that potentially interesting events are not mistakenly rejected.

The available triggers, in many case, determine the final analysis selections as the efficiency measurements are generally more reliable far from the turn on and when the offline selections are more stringent than (or close to) the online ones, i.e. in regions with high trigger efficiency. The uncertainty on the trigger efficiency determination (a representative example from the CMS 2018 results are shown in Figure 3.17) directly enters all cross section measurements.

I have coordinated the CMS e/γ HLT activities during 2016-2018, including the reoptimization of the main electron trigger for 2017 and the review of all trigger efficiency measurements by the various analysis teams.

3.6 Putting all together

After the events are selected by the trigger system, and the objects are reconstructed offline using the methods described in Section 3.5.1, the measurement can proceed. The analysis methods are optimized using MC simulations of the signal and background processes, as well as data *control* and *validation regions* that are non-overlapping with the *signal region* where the main measurement is performed. These regions however are defined to be similar in many aspects to the signal region so that the background contributions can be studied and the procedures tested in them without biasing the final results. In Section 3.5.1.1.5 simple examples of control regions to derive the background shape and normalization are given. Figures 3.11 and 3.12 illustrate how inverted signal selection cuts are used to derive background shape templates, and the distribution sidebands to determine the normalization. More complex examples will be given in Chapter 5.

Simulations play a very important role in predicting the signal and background rates and distributions. They are affected by various theoretical uncertainties discussed in Section 3.4. Known shortcomings of the simulations, for example, due to missing higher order corrections, can sometimes be mitigated using experimental data and event reweighting techniques. Experimental biases can also appear, for example, due to the imperfect modeling of the detector material and electronics readout or the in-time and out-of-time event pileup. These can lead to differences in object reconstruction (for example for the momentum scale and resolution) and in selection efficiencies. These discrepancies between data and simulation are quantified and corrected.

Even after careful correction of known effects in the simulation, some aspects of the data cannot be properly modeled. This is especially true for the determination of background contributions, for example due to fakes and instrumental effects.This motivates the philosophy of using data-driven methods wherever possible.

Most analyses at the LHC are performed *"blind"*, meaning that the actual measurement can only be executed after the experimental strategy and methods are fixed, fully validated in simulation and in data validation regions, the systematic uncertainties computed, and the work approved by the relevant expert group. The measurements require many auxiliary studies that are documented in detail internally during this process. The most common sources of systematic uncertainty are listed below:

- Data and simulation sample statistics
- Trigger efficiency (Section 3.5.2.4)
- Object (γ, e, μ, τ, jet, b jet, $p_{\mathrm{T}}^{\mathrm{miss}}$) energy / momentum scale and resolution (Section 3.5.1.1.4)
- Object position and direction resolution (e.g., primary vertex resolution, photon pointing accuracy)
- Object reconstruction, identification and analysis specific (e.g. impact parameter or isolation) selection efficiencies (Section 3.5.1.1.5)
- Object identification fake rate, affecting background rates or object veto efficiency
- Theoretical model for signal and background processes, affected by missing higher order corrections (renormalization and factorization scales), the imperfect knowledge of SM parameters (masses, couplings, mixing angles...), parton distribution functions, fragmentation and hadronization models, unstable particle decay tables, underlying event description (MC tunes), etc. (Section 3.4)
- Detector modeling in simulation, including material description, electronic readout characteristics, detector activation, and also instrumentation problems. For example, in CMS Run 2 several issues arose that need special attention in the measurements: dynamic inefficiency of pixel modules in particular in the innermost layer due to buffer overflow; dead regions in the pixel detector due to the

failure of the DC-DC converters in 2017 (e.g., affecting electron trigger efficiencies in Figure 3.17); ECAL timing shift causing wrong bunch crossing association for high-pseudorapidity trigger primitives resulting in L1 trigger inefficiencies in 2016-2017; dead HCAL sectors in most of the 2018 data, etc.

Special attention is needed for hypothetical signals of exotic physics with many unknown parameters such as supersymmetric partner production, where only fast detector simulation is feasible to produce events for the whole parameter phase space due to limited computing resources leading to less accurate description of jet quantities, $p_{\mathrm{T}}^{\mathrm{miss}}$, etc.

- Pile up distribution in data to which simulated samples need to be reweighted, affected by total inelastic cross section uncertainty [339] and bunch-by-bunch instantaneous luminosity determination biases via Eq. 3.4 (see also Chapter 4). The modeling of minimum bias pp events, determined by the MC tune or taken directly from data, also affects the overall pileup modeling in simulation.

- Integrated luminosity to normalize event rates and derive cross sections using Eq. 3.5 (Chapter 4).

- Data-driven background predictions: many possible techniques exist with different sources of uncertainties such as limited data statistics, non-closure of the method – for example – due to neglected correlations between observables, signal contamination in the control region, imperfect templates or analytic fit models (for examples, see Sections 5.2 and 5.5); often, several methods with different sources of biases are employed and crosschecked against each other. Many of these biases are studied in Monte Carlo simulation. For example, method closure can be tested by simulating signal + background samples where the amount of background is known, and then verifying if we can determine the background contribution correctly when handling the simulated sample as data.

- Unfolding of detector effects [30, 275, 276] for differential cross section determination, affected by method closure, imperfect knowledge of detector response function and prior distributions (for an example, see Section 5.2).

- Statistical interpretation of search results: choices and approximations in hypothesis testing (typically performed by the common LHC tool ”combine” [274]).

In the next chapters, a few examples will be shown to illustrate the experimental techniques and the determination of the dominant uncertainties, but the discussion will concentrate to a large extent on the achieved physics results to limit the volume of the dissertation.

3.7 Organization within experimental collaborations

The complexity of the instrumentation as well as the data analysis explains the large size of HEP collaborations today, with several thousand signing authors. The collaborators are organized along the different hardware, software, reconstruction and analysis activities. The collaboration is lead by its spokesperson (the level-0 manager) and its deputies. Each subsystem (e.g., using CMS examples, Tracker, BRIL, ECAL, HCAL, Muon, L1 Trigger, DAQ, ...) and major coordination area (Trigger, Offline & Computing, Physics, ...) is lead by a project leader (level-1 manager). Within these projects a number of working groups are formed. For example, a detector project has a Detector Performance Group (DPG), an Upgrade Group etc. lead by conveners or coordinators (level-2 managers). Within the Physics Activity, Physics Object Groups (POGs) and Physics Analysis Groups (PAGs) are lead by conveners (level-2 managers). POGs are responsible for the online and offline reconstruction, calibration and identification of the corresponding physics objects (electron / photon, muon, tau lepton, b jet, jet / p_T^{miss}, luminosity), while PAGs cover the main analysis areas (standard model physics, Higgs physics, top quark physics, supersymmetric particle searches, ...) Depending on the size of the group, further subgroups are formed and their work is overseen by conveners and contacts (level-3 managers).

The current organigram of the CMS Collaboration is shown in Figure 3.20 and as an example that of the BRIL System in Figure 3.21.

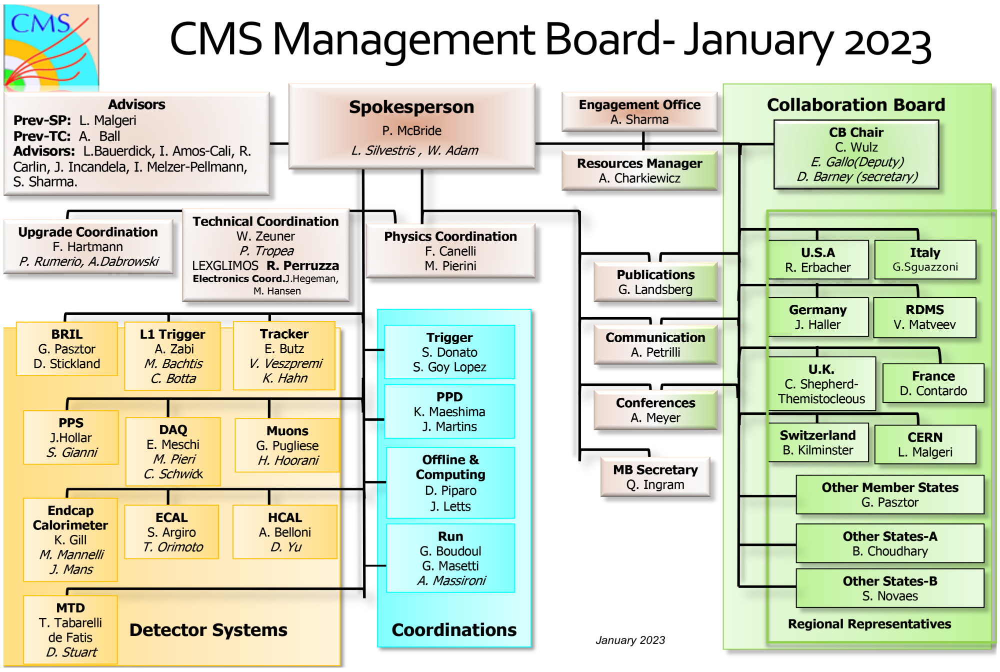

Figure 3.20: *The composition of the Management Board of the CMS Collaboration as of 2022 September. The collaboration is lead by the spokesperson, and the various detector systems and coordination areas by level-1 (L1) project managers. The collaborating institutes also elect regional representatives. The Hungarian teams are in the "Other Member States" group together with the institutes from twelve other European countries.*

Each planned publication belongs to one of these groups in which regular progress reports are presented by the main authors. Depending on the complexity, novelty, and competitive nature of the analysis, the number of main authors can widely vary from one to more than a hundred. Typically these teams have regular meetings, especially when multiple institutes are involved, so that ad-hoc discussions are less convenient. There, the collaborators discuss new results and ideas, current problems, and the next steps, with students, postdocs, supervisors, and experts working actively together. One or a few of the main authors play the role of the official analysis contact and the main editor, coordinating the completion of the analysis work and the publication process.

Before a result can be presented outside the collaboration and submitted to a peer-reviewed journal, a careful multi-stage (and thus lengthy) internal review is performed with its main steps being:

- a preapproval presentation organized by the responsible level-2 working group (e.g., in CMS a DPG, a POG, or a PAG),

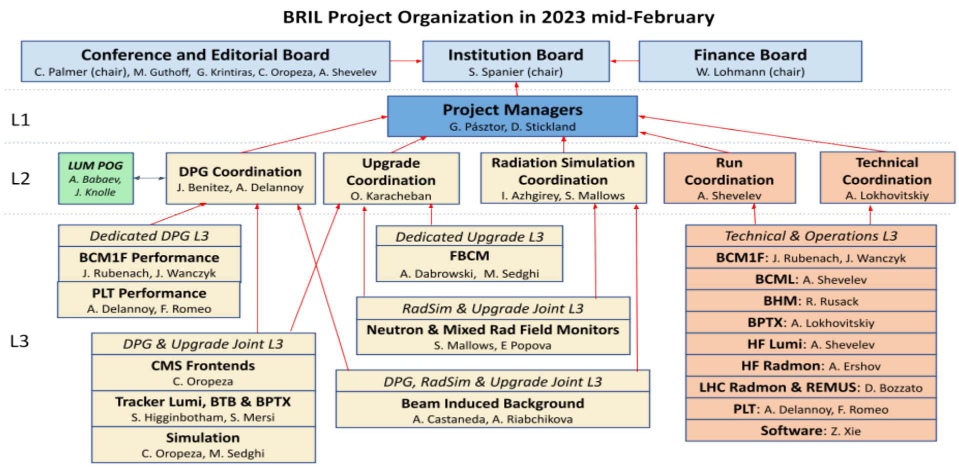

Figure 3.21: *Organization of the BRIL project as of 2022 October. The project is lead by two project managers (PMs) – or a manager and its deputy –, who make the executive decisions in consultation with the management team composed of level-2 (L2) managers, the chair of the BRIL Institution Board (composed of the leaders of the participating teams from various universities and research institutions) and the Resource Manager (chairing the BRIL Finance Board that is composed of representatives of each participating funding agency). The L2 managers coordinate the work among the various level-3 (L3) groups, which focus on operation, performance and upgrade of various technical systems as well as the deliverables of BRIL on radiation monitoring, beam timing, beam loss monitoring and safety abort, beam-induced background and luminosity measurements. The results of the BRIL project are published in peer-reviewed journals and disseminated in international conferences which is coordinated by the BRIL Conference and Editorial Board and the PMs.*

- a review by a dedicated analysis review committee (ARC) or editorial board (EB) depending on the experiment, formed via invitation of experts by the Publication Committee chair,
- an approval presentation organized centrally by Physics Coordination,
- a collaboration wide review (CWR) with 5-10 institutes responsible to provide careful feedback, in addition to interested individuals,
- a public reading organized by the Publication Committee,

with all events open to all collaborators. Conveners follow the analyses belonging to their (sub)group from the early stages and contacts advise and approve the work related to their field of expertise such as trigger usage, simulation, physics objects, statistical tools.

L1 and L2 managers are also responsible to ensure that the central tasks related to their field of activity are covered and completed on time and are therefore in charge of the assignment of ”Experimental Physics Responsibility” (EPR) points which allow individuals to stay authors of CMS. Currently each CMS author has to contribute 4 months of technical ”EPR” work per year which includes participation in data taking (e.g., shifts to operate the detector), detector maintenance, data quality monitoring, calibration, performance studies, software and hardware development, etc.

I have served in leadership roles in each collaboration I have participated in, reaching level-1 positions in OPAL as Physics Coordinator and in CMS as BRIL Project Manager.

Chapter 4

Luminosity measurement

With the LHC research program entering its precision physics phase, luminosity determination became a key area [340]. It requires a detailed understanding of various physical and instrumental effects that arise in the accelerator, the beam monitoring devices (beam instrumentation) and the luminosity detectors. Sophisticated experimental and analysis techniques are necessary to reduce the uncertainties.

Luminosity, via Eq. 3.5, enters all measurements where the cross section of a given process is targeted, including precision tests of the standard model and searches for new phenomena. It has become the single largest source of systematic uncertainty in the most precise measurements in the field of SM physics, such as the study of W [341] and Z boson [342], as well as top quark pair [343, 344] production. Even in the flagship Higgs boson production cross section measurements (Section 5.5.3), luminosity uncertainty is the dominant experimental contribution [345], which will become even more important at HL-LHC [346–348], as shown in Figure 4.1.

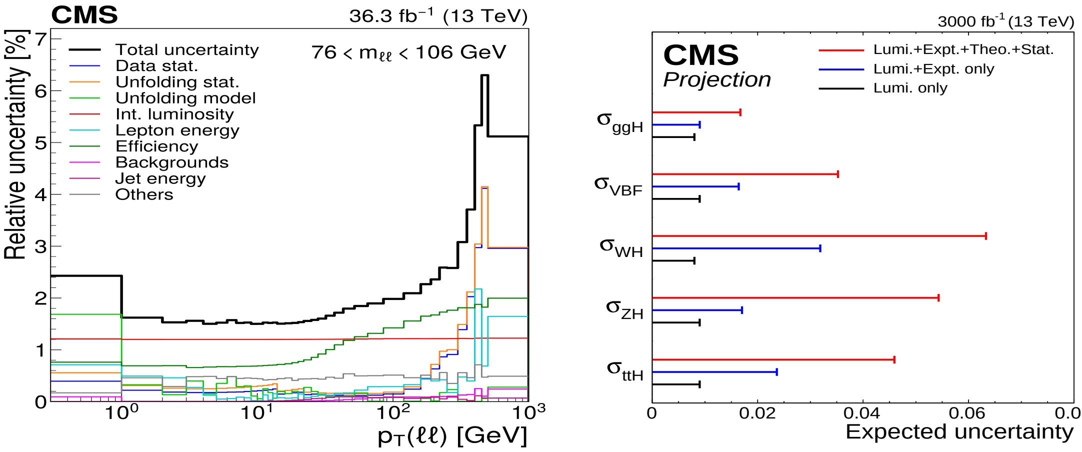

Figure 4.1: *(right) Relative systematic uncertainties in the differential Drell–Yan cross section measurement as a function of the dilepton transverse momentum* $p_{\mathrm{T}}(\ell\ell)$ *at 13 TeV energy [342]. The black line shows the total uncertainty, and the colored lines correspond to the various contributions. The luminosity uncertainty (red line) dominates below 40 GeV. (left) The expected uncertainties in the Higgs boson production cross sections per production mode (see Section 5.3) with 3000* fb^{-1} *of data expected at HL-LHC: contributions from the target 1% luminosity uncertainty (black bars), from the total experimental systematic uncertainty (blue), and the total uncertainty (red) including experimental statistical (0.8% for ggH) and theoretical sources [340].*

With reduced accuracy requirements, stable, high-availability luminosity information in real time is also crucial for the LHC operators to optimize the performance of the accelerator [349]. This is especially the case for luminosity leveling (i.e. keeping its value at a stable level below the maximum possible by means of adjusting the crossing angle, the β^* parameter or the transverse beam separation) which became essential as the peak instantaneous luminosity of the LHC increased [350, 351]. Real-time luminosity is also necessary to optimize the data taking (e.g., trigger) configuration of the experiment.

Luminosity measurements [352] rely on the precise determination of event rates (in a wide sense that can include, for example, energy sums) observed within the acceptance of a luminometer, a particle detector that – in ideal conditions – has a linear and stable response. Luminosity calibration is achieved via the determination of a detector- and method-specific constant, the visible cross section (σ_{vis}). It relates, using Eq. 3.1, the measured rate $R(t)$ in the luminometer to the instantaneous luminosity $\mathcal{L}_{\text{inst}}(t)$ through the relation

$$\sigma_{\text{vis}} = R(t)/\mathcal{L}_{\text{inst}}(t). \tag{4.1}$$

Contributions to the uncertainty on $\mathcal{L}_{\text{inst}}$ arise from the absolute calibration of σ_{vis} determined in special low luminosity conditions, as well as the response linearity and stability over time of the luminometer which affect the extrapolation of σ_{vis} to the high luminosity physics conditions.

There are two main counting methods to determine single bunch instantaneous luminosity (SBIL, or $\mathcal{L}_{\text{b}}$): rate counting and zero counting over a short time period. For rate counts (or energy sums), the calibration constant can be expressed as $\sigma_{\text{vis}} = \langle N_{\text{observable/interaction}} \rangle \cdot \sigma_{\text{tot}}$, where $\langle N_{\text{observable/interaction}} \rangle$ is the average number of the observables produced in the luminometer in inelastic interactions. Using the trivial relation for the average number of particle interactions per bunch crossing: $\langle \mu \rangle = \langle N_{\text{observable}} \rangle / \langle N_{\text{observable/interaction}} \rangle$ leads to the definition of SBIL using Eq. 3.4 which links $\langle \mu \rangle$ to $\mathcal{L}_{\text{b}}$ via the ratio of the total inelastic cross section σ_{tot} and the orbit revolution frequency f_{rev}:

$$\mathcal{L}_{\text{b}} = \langle \mu \rangle \cdot f_{\text{rev}}/\sigma_{\text{tot}} = \langle N_{\text{observable}} \rangle \cdot f_{\text{rev}}/\sigma_{\text{vis}}. \tag{4.2}$$

Zero counting on the other hand uses the average fraction of bunch crossings where no observable is detected in the luminometer. Assuming that the number of particle interactions k follows a Poisson distribution $P(k, \langle \mu \rangle)$ with a mean of $\langle \mu \rangle$, the average "zero fraction" can be expressed for an observable as

$$\langle f_0 \rangle = \sum_{k=0}^{\infty} P(k, \langle \mu \rangle) \cdot p^k = \sum_{k=0}^{\infty} \frac{\mathrm{e}^{-\langle \mu \rangle} \langle \mu \rangle^k}{k!} p^k = \mathrm{e}^{-\langle \mu \rangle (1-p)}, \tag{4.3}$$

where p is the probability of no observable seen in a single particle interaction, thus p^k gives the probability for k collisions. From here, $\langle \mu \rangle = -\ln\langle f_0 \rangle/(1-p)$. Using the definition of the visible cross section $\sigma_{\text{vis}} = (1-p) \cdot \sigma_{\text{tot}}$, the SBIL is

$$\mathcal{L}_{\text{b}} = -\ln\langle f_0 \rangle \cdot f_{\text{rev}}/\sigma_{\text{vis}}. \tag{4.4}$$

Zero counting has the advantage of being less sensitive to cases where two or more separate signals overlap in the detector and produce only one reconstructed observable. It becomes impractical (with large statistical uncertainty) at high rates where events with zero detected observable become rare, a phenomenon called zero starvation or saturation, therefore the optimal choice between zero and rate counting depends on the detector and the counted observable.

The rest of this section reviews the state of the art of luminosity calibration at LHC and in particular in CMS [270–273, 340, 353–356], including the first precision measurement with $\mathcal{O}(1\%)$ uncertainty at a high-intensity bunched-beam hadron collider experiment achieving 1.2% accuracy for the 2016 CMS pp data set [270], and the strategy for the future, the Phase-2 upgrade of CMS [340]. I had major contributions to the presented results, prepared in collaboration with the CMS Beam Radiation Instrumentation and Luminosity Project (BRIL) that I currently lead, and the CMS Luminosity Physics Object Group (Lumi POG) that I coordinated during 2018 – 2020. The study of beam-beam interactions [357] in Section 4.1.1 was conducted with colleagues in the LHC Luminosity Calibration and Monitoring Working Group (LLCMWG).

4.1 Absolute calibration with the Van der Meer method

The Van der Meer (VdM) [358] method was used successfully for the precise calibration of luminometers in various experiments, with the most precise results reported in Refs. [270, 359–361]. It requires a small number of dedicated calibration fills, typically one or two per running period (year).

During a VdM scan, the two beams are deflected by dipole magnets such that the beam-beam separation in the transverse plane changes in steps from -$6\sigma_\mathrm{b}$ to $+6\sigma_\mathrm{b}$ (where σ_b is the beam width) with the two beams moving symmetrically in opposite directions. At each separation step, data are taken for about 30 s. This is illustrated in Figure 4.2 which shows the positions of the two beams in the x and y directions during a special VdM data taking fill in 2018. Scans labeled as ”norm” are VdM scans (the others will be discussed in the following).

The measured rate is normalized by the bunch intensities, and – in the case of triggered data collection – by the number of triggered events and plotted against the beam separation as shown in Figure 4.3. The visible cross section is computed from the widths of the curves that give the convolved beam widths, also called beam overlap widths in the x and y directions (Σ_x and Σ_y), and the rate of the observable during head-on collisions (R_0):

$$\sigma_\mathrm{vis} = \frac{2\pi\Sigma_x\Sigma_y R_0}{N_1 N_2 f_\mathrm{rev}}. \tag{4.5}$$

The formula is derived from Eq. 3.2 which assumes that the bunch particle density function is factorizable in the x and y transverse directions:

$$\rho(x,y) = \rho_H(x)\cdot\rho_V(y). \tag{4.6}$$

The bunch intensities, i.e., the number of protons per bunch (N_1 and N_2) are measured combining the bunch-by-bunch measurement by the fast beam current transformers (FBCT) [362–364] with the more precise total intensity measured by the direct-current beam current transformers (DCCT or DCBCT) [365]. The relative distribution of charges in each beam is also measured by the longitudinal profile monitors: the beam quality monitor (BQM) [366] and the longitudinal beam synchrotron radiation telescope, also called longitudinal density monitor (BSRL or LDM) [367, 368]. The intensities have to be corrected for ghost charges (i.e. particles outside of the 25 ns time window of filled bunch crossings) and satellite charges (i.e. particles in a colliding bunch crossing window that are not in the 2.5 ns window of the RF bucket that contains the colliding charges).

Instead of being fitted from the vdM curve as in Figure 4.3, the detector noise affecting R_0 can also be measured directly either by using non-colliding bunches in

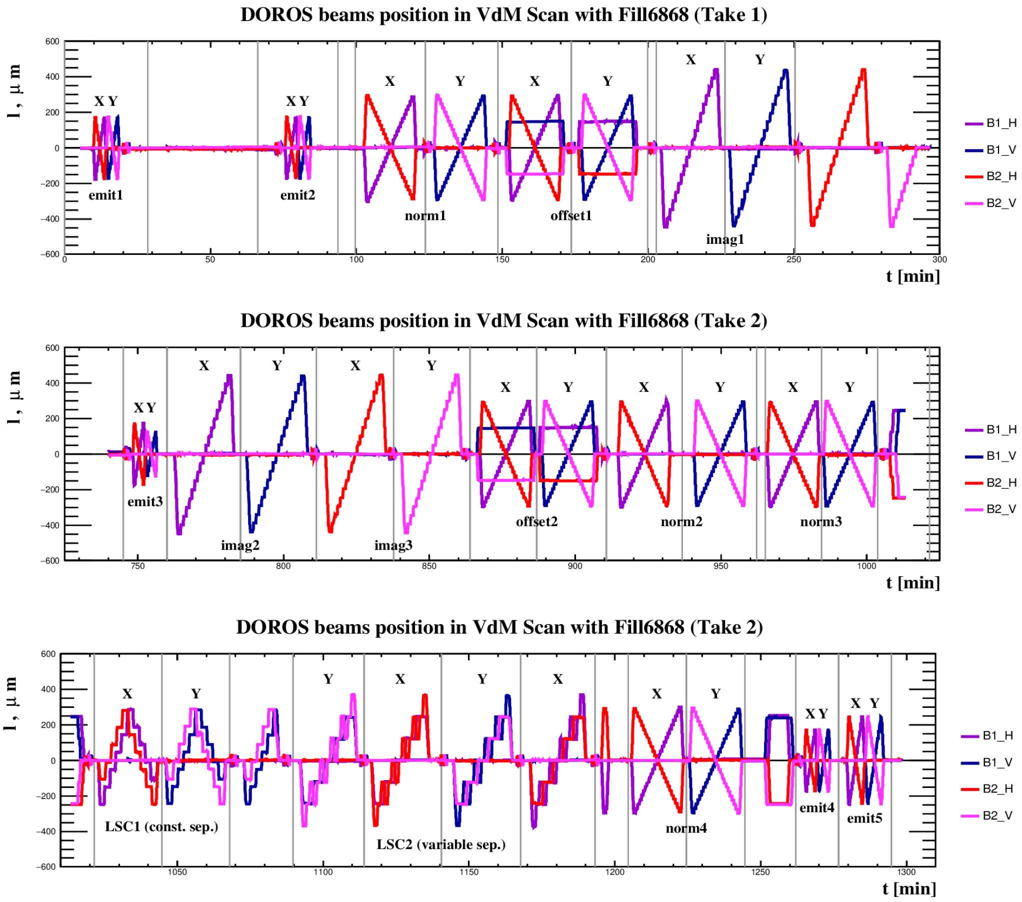

Figure 4.2: *The positions of the two beams in the horizontal (x) and vertical (y) directions during a typical sequence of various beam scans taken from the 2018* pp *VdM calibration fill measured by the DOROS beam position monitors. The various scans are labeled as follows: norm1... norm4 are standard VDM scans; imag1... imag3 are beam imagining scans while offset1 and offset2 are offset (off-axis) scans, both types are used to determine the $x-y$ non-factorization correction; LSC1 and LSC2 are the constant- and variable- separation length scale scans, respectively; emit1... emit5 are shorter versions of the VdM scans, called emittance scans that can also be performed in physics data taking for monitoring purposes. More details are given about each type of scan in the corresponding subsections. [272]*

the abort gap or in a special so called super-separation setting where the beams are separated by $6\sigma_\mathrm{b}$ in both the horizontal and vertical directions, effectively passing each other without interaction. In practice, all three methods are used and their results compared to estimate the related uncertainty.

In order to minimize systematic biases in σ_vis, VdM calibration is performed using special beam conditions. For pp calibration, the peak per-bunch pileup is adjusted to $\langle\mu\rangle \approx 0.6$ with an intensity per bunch about 30% lower than for nominal running. Only about 30 to 150 bunches per beam are injected with a separation of at least 500 ns. As the VdM optics[1] typically apply no crossing angle, the bunches must be well separated

---

[1] VdM measurements during heavy ion data taking (e.g. Pb-Pb, p-Pb or so-called reference lower energy p-p collisions) are not performed with specialized optics due to the long set up time. They still use special filling schemes with less bunches per beam.

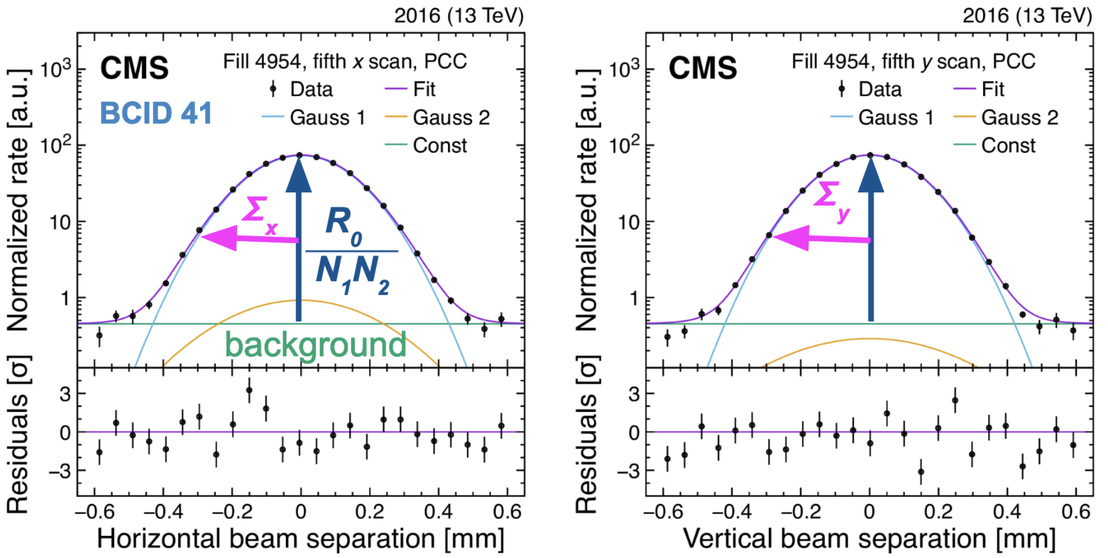

Figure 4.3: *Illustration of the VdM fit procedure. The rates measured by a luminometer (here the number of pixel clusters in the 2016* pp *VdM calibration fill) as a function of the transverse separation of the two beams in the horizontal (left) and vertical (right) directions are fitted by the sum of two Gaussian distributions plus a constant to account for noise in the detector. The width of the fitted distribution defines the beam overlap width* Σ_x *and the background subtracted peak rate gives the bunch intensity normalized* R_0 *in Eq. 4.5. The lower panel shows the difference between the measured data and the fitted function. Modified from Ref. [270].*

to prevent secondary interactions or parasitic collisions. This also significantly reduces any potential uncertainty from out-of-time contributions (Section 4.2.3).

The VdM measurement ideally also requires bunches with larger emittance (up to $\epsilon_\mathrm{n} \approx 3.5\ \mu$m) and optics with a larger $\beta^* = 19.17$ m, compared to nominal physics conditions, resulting in a beam width of $\sigma_\mathrm{b} \approx 90\ \mu$m at the interaction point. The wider beams allow for finer sampling of the beam shapes during the scan, and in particular allow the use of vertex position information (with a typical resolution in the transverse plane of 10 μm) to estimate subtle effects due to non-Gaussian particle distributions and transverse correlations, resulting in a more precise measurement of the beam overlap (Section 4.1.4). Together with the reduced beam intensity, the larger beam width also minimizes beam-beam effects (Section 4.1.1) and their related uncertainties.

In the following, I discuss the most important systematic effects, focusing on the studies I directly contributed to.

4.1.1 Beam-beam interactions

The colliding proton bunches interact via the generated electromagnetic field, leading to deflection (shift) of the nominal orbit as well as to distortion of the bunch shapes (called the dynamic-β or optical effect). The sizes of these depend on the beam separation and have opposite impacts on the luminosity. As they distort the VdM rate curve, they need to be corrected for. They lead to anticorrelated systematic biases that are combined to a single uncertainty.

4.1.1.1 Beam-beam deflection

The orbit shift [369] originates from a mutual repulsive angular kick between two bunches that collide with a non-zero transverse separation. It can be derived analytically from the Bassetti–Erskine formula [370] and increases the separation between the colliding bunches and thus decreases the instantaneous luminosity. Figure 4.4 (left) shows the beam-beam deflection for a representative pp VdM calibration analysis [270]. The correction for the luminosity was typically 1.5–1.8% for VdM calibrations at $\sqrt{s} = 13$ TeV.

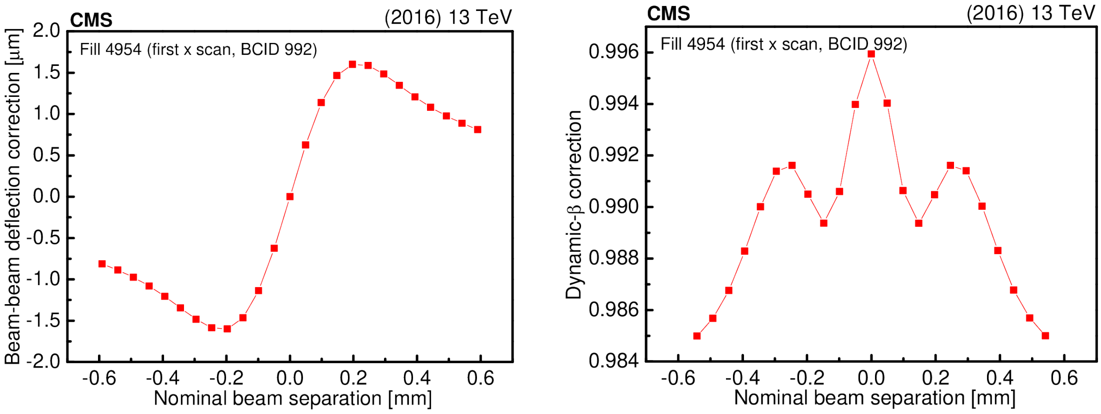

Figure 4.4: *(left) Calculated beam-beam deflection due to closed-orbit shift to correct the nominal separation, and (right) the multiplicative correction to be applied on the measured rate to account for the dynamic-β effect as a function of the nominal beam separation for a representative vdM calibration analysis at $\sqrt{s}$ = 13 TeV in 2015 by CMS. [270]*

At nominal physics conditions, during short VdM-like so-called "emittance" scans (Section 4.2.4), an increase in the beam-beam correction of up to 2.5% is estimated due to the smaller beam width and higher bunch intensity and, therefore, higher charge density. The bunch width also varies within a bunch train and the emittance of the bunches grows during the fill, so the size of the beam-beam corrections is time and bunch dependent.

Recently, the generalization of the analytic formula describing the coherent kick leading to the deflection was derived for elliptic bunches colliding with a crossing angle [371]. Although the effect on the correction is rather small, the new calculation increases the confidence in the assigned uncertainty.

4.1.1.2 Optical distortion of bunch shape

The impact of the optical effect is estimated using multi-particle simulations [357, 372] and generally leads to a squeezed bunch size (Figure 4.5) thus increases the luminosity. As shown in Figure 4.4 (left), the change of the bunch size in the scanning direction is more sensitive to the separation and can lead also to an increased size at large separation. The correction depends on the betatron tunes (Q_d) which describes the frequency of the transverse oscillations along the orbit in transverse direction $d = x, y$ and the beam-beam parameter ($\xi_{d,i}$) of the bunch in beam $i = 1, 2$. The latter is computed from the bunch transverse width ($\sigma_{d,i}$), the bunch intensity in number of particles (N_i), the Lorentz factor of the particles (γ_{ri}), and the value of the optics $\beta(s)$ function at the interaction point ($\beta^*_{d,i}$). As an example, the horizontal beam-beam parameter experienced by a ”witness” proton bunch in beam 2 is:

$$\xi_{x,2} = \frac{N_1 r_0 \beta^*_{x,2}}{2\pi\gamma_{\mathrm{r}2}\sigma_{x,1}(\sigma_{x,1}+\sigma_{y,1})}, \tag{4.7}$$

where $r_0 = e^2/(4\pi\epsilon_0 m_p c^2)$ is the classical proton radius.

Until recently, a linear approximation of the beam-beam force was used to estimate the optical distortion, as implemented in the code MAD-X [373, 374], which also uses a Gaussian approximation for the bunch densities. It was, however, realized that non-linear effects have a major influence [372] and two multi-particle simulations were developed to model these, as well as the resulting non-Gaussian distortions of the transverse particle distributions. The B*B code [372] was optimized for speed and thus uses the so-called weak-strong approximation, i.e. it models the transverse deformation of the density distribution of a ”witness” bunch caused by the electromagnetic field of an unperturbed ”source” bunch. The COMBI code [375] is more CPU-intensive but has a full implementation of beam-beam effects valid also in the strong-strong regime (i.e. when the strong non-linear EM fields of the two intense bunches perturb each other), as well as an option to switch on the simulation of longitudinal dynamics.

The results of the two codes with non-linear beam-beam force, B*B and COMBI were crosschecked [357] and found to be in excellent agreement in VdM conditions as illustrated in Figure 4.5. The linear approximation (MAD-X) fails to model the features of the optical distortion and overall predicts a too small negative correction to the visible cross section. The non-Gaussian distortion of the particle density plays an important role in this as illustrated by the COMBI simulation when comparing the results using the Gaussian approximation and the full overlap integral of the particle distributions.

For computational efficiency, B*B was adopted to extract a 3-dimensional parametrization of the beam-beam corrections as a function of the betatron tunes and the beam-beam parameter in the limit of round, initially Gaussian bunches of equal intensity colliding at a single interaction point with zero crossing angle. Differences with respect to this ideal configuration were studied by B*B and COMBI and either corrected for – as done below for the collisions at multiple interaction points (multi-IP) – or considered as systematic uncertainties.

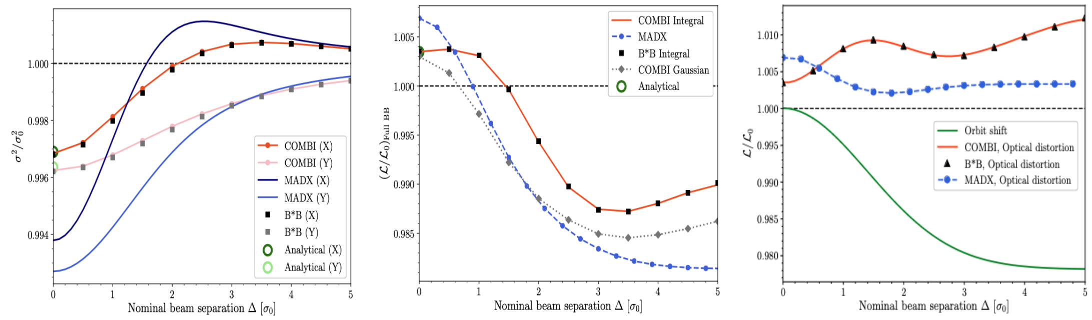

Figure 4.5: *Comparison of various calculations for the beam-beam effects as a function of beam separation in units of the transverse beam size during a simulated horizontal (x) scan. Analytic calculations are only available at zero beam separation. (left) Relative change of the RMS bunch width squared with respect to its unperturbed value (i.e. without beam-beam interactions) due to the optical effect. (middle) Relative change of the luminosity in the presence of the full beam-beam interactions. (right) Contributions to the relative change of the luminosity due to orbit shift and optical distortion. All computations were performed with a reference parameter set corresponding to the $\sqrt{s} =$ 7 TeV pp vdM scans in 2011. [357]*

4.1.1.3 Systematic effects for modeling beam-beam interactions

The LHC operates at nominal betatron tune values of $Q_x = 64.31$ in the horizontal plane and $Q_y = 59.32$ in the vertical plane. During the collisions these tunes are perturbed, depending on the strength of the interaction as well as the number of interaction points where the bunches collide. All bunches colliding at CMS also collide at ATLAS due to the symmetries of the accelerator, while some of the bunches can also collide at ALICE and LHCb depending on the filling scheme. It was shown using COMBI that by using the shifted tune due to the head-on collisions at other interaction points to calculate the correction based on the 3-dimensional parametrization, the multi-collision bias in the absolute luminosity can be accounted for [357]. The correction for the effect of multi-IP collisions brings an uncertainty of around 0.2% and the 3-dimensional parametrization itself is accurate to 0.1%.

The uncertainty for both the orbit shift and the optical distortion corrections gets a significant contribution from various other sources, including the limited knowledge of the optical configuration of the accelerator. These have to be propagated to the visible cross section determination. The precision of the measurement of β^*, which is currently estimated to be 15% [376], adds about 0.1%. The tune uncertainty of ±0.002 gives – according to our B*B studies – a leading contribution of 0.2%.

Sources related to the bunch properties were also considered: non-Gaussian transverse density distributions have the largest effect of up to $0.2 - 0.3\%$, bunch ellipticity gives 0.03%, a possible imbalance between the width of the colliding bunches contributes 0.01%, and the effect of non-zero crossing angle remains below 0.01% for the range of experimental conditions observed at pp VdM scans in Run 2.

All these result in a conservative uncertainty estimate of $0.4 - 0.5\%$ in the visible cross section depending on the number of colliding interaction points. For each specific VdM analysis, the uncertainties need to be considered taking into account the LHC optics, the filling scheme and the observed bunch properties. The overall accuracy reached 0.3% for Run-2 vdM calibration campaigns [361].

4.1.1.4 Total effect of beam-beam interactions on the luminosity

These detailed simulation studies showed that the total corrections to the luminosity calibration using the vdM method due to the EM interaction between the two beams range approximately between 0.2 to 1.2%, depending on the beam-beam parameter and the number of colliding interaction points [357]. It is similar in size to the total uncertainty of the most precise luminosity measurements to date of $\mathcal{O}(1\%)$ [270, 361].

The preliminary results for Run-1 and Run-2 pp luminosity calibrations of CMS were derived before the realization of the importance of non-linear contributions to the beam-beam force and therefore are biased, affecting also all cross section measurements that were performed based on them. These will have to be corrected. The expected decrease of the cross sections at $\sqrt{s} = 8$ and 13 TeV is at the percent level. For now, this is covered by the large total uncertainty of the preliminary luminosity calibrations [271, 272] of about 2.5%. The final Run-2 CMS luminosity measurements are close to completion.

4.1.2 Orbit movements

In the vdM formalism, it is implicitly assumed that the beam separation is perfectly known. Operationally, the nominal displacement of the beams at the interaction point is achieved based on a local distortion (bump) of the orbit using a pair of steering dipoles located on either side of the IP [377]. The size of the nominal separation is subject to potential uncertainty associated with the response of the steering dipoles themselves (e.g., magnet hysteresis) or imperfections of the magnetic lattice [378], i.e., the fields of the electromagnets along the ring.

Orbit drifts with respect to the nominal orbit during VdM scans lead to a bias in the obtained calibration via their effect on the beam separation. Two beam position monitor (BPM) systems are used at the LHC: the DOROS (diode orbit and oscillations system) BPMs located before the IP [379–381] on the first quadrupole magnet (Q1) of the triplet, and the arc BPMs [369] closest to CMS located in the LHC arcs L 33-9 and R 9-33. The arc BPM data are extrapolated to a beam position at the IP using a model of the LHC optics.

To account for a slow movement of the orbit, corrections to the nominal beam separation at each scan step are derived using a linear fit between the head-on positions directly before the scan and immediately after the scan (formerly also in the middle of the scan). The systematic uncertainty on this *linear orbit drift* correction is evaluated by comparing the results calculated using the DOROS and arc BPM measurements.

The approximation of linear orbit drift, however, does not perfectly describe the beam movements during the scans. Step-by-step corrections using the DOROS BPM measurements also at non-zero separation (after taking into account the expected beam-beam deflection) show potentially large residual drifts [270, 273, 361]. These seem to originate primarily from non-linear effects in the steering magnets, beam-beam cross talk, as well as beam jitters (sudden ”random” changes in the beam positions). An additional complication is the complex sensitivity of the DOROS BPM instrumentation to the beam-beam deflection, especially in the case when colliding and non-colliding bunches of different intensities are present in the accelerator. This stems from the intensity-dependent signal integration over an orbit in the DOROS electronics and from the different effect of the beam-beam force on the colliding and non-colliding bunches leading to different deflections. Comparisons with the arc BPMs are valuable but also challenging: due to their different locations, they are sensitive to sources of orbit drifts in different regions.

Recently, laboratory tests were performed to measure non-linear (hysteresis) effects in a magnet prototype, and a simulation study was also conducted to quantify how the observed non-linearity would manifest in the actual LHC setup [382, 383]. These results were compared to dedicated measurements performed by the ATLAS experiment in 2021 at $\sqrt{s} = 900$ GeV with settings optimized to show maximal effect and a good agreement was found [361]. This, together with our studies performed on the Run-2 LHC vdM data, confirmed that magnetic non-linearities and, more generally, non-linear movements during scans need to be considered for a precise orbit drift correction.

Orbit movements at present are among the leading sources of uncertainty [270, 361], which underlines the need for improved beam instrumentation. In particular, the requirements for BPMs are described in Ref. [384] for HL-LHC.

The orbit is also tracked using the movements of the luminous region based on the vertices reconstructed with the CMS tracker [260], though they are only sensitive to the average of the two beam positions. It is nonetheless the best tool to study instrumental effects for the BPMs, as discussed in the next section.

4.1.3 Length scale of transverse beam displacements

In VdM scans, the beams are steered over a much wider range of transverse displacement than in normal physics operation. While the LHC magnets are calibrated for the whole range of beam displacements, the precision can be improved using in-situ measurements.

Therefore, using dedicated beam scans, a length scale calibration is performed using reconstructed vertex [260] data from the CMS tracker to derive a correction to the nominal beam separation calculated from the magnet current settings.

During so-called constant-separation scans (labeled as LSC1 in Figure 4.2), the separation between the two beams is kept constant ($1.4\sigma_\mathrm{b}$) and they are moved together in five steps of σ_b in the x and y directions, providing a calibration for the average length scale of the two beams in the two transverse directions separately by tracking the movement of the luminous region via the average reconstructed vertex position as a function of the average nominal position of the two beams.

During variable-separation scans, one beam is moved in steps of σ_b and at each of its positions a 3-step VdM-like mini-scan within $\pm 1.25\sigma_\mathrm{b}$ is performed by the other beam to determine the head-on position. This is then compared to the average vertex position to compute the length scales of each beam separately.

The two methods are complementary: they are affected differently by the various sources of uncertainties. Moreover, the constant separation method – requiring less time and thus allowing the beams to be moved back and forth – can be used to check for direction dependence of the length scale which might arise from magnetic effects.

One of the dominant sources of uncertainty comes from potential orbit drifts during the scans which are monitored by the BPM systems as described in the previous section. We have developed two alternative methods to account for the orbit drift: either using a correction scan step by scan step [270, 272] or performing a two-step length scale determination. The latter factorizes the problem of measuring the nominal to tracker length scale. First the BPM scales are computed from a global fit of the full vdM period of 5-10 hours (not only the length scale scan) with respect to the nominal scale, thereby averaging out the effect of orbit drifts over many points. Then the data of the dedicated length scale scans are used to measure the BPM scales with respect to the tracker scales where the orbit drift effects largely cancel out as both instruments see the same movements. Thus the factorized method reduces the dominant uncertainty due to orbit drifts and is expected to improve the precision of the length scale by a factor of two (reaching below 0.2%) for the final Run-2 calibration.

4.1.4 Transverse factorization of the particle density function

In the VdM method, it is assumed that the bunch proton density functions are factorizable in the transverse directions (Eq. 4.6). When this assumption is not realized, it can lead to a bias in the measured calibration constant. A common approach is thus adopted at the LHC that includes a dedicated tailoring of the proton bunch injection chain to minimize the emergence of non-Gaussian bunch density distributions [385]. Nonetheless, percent level effects are still present that lead to one of the dominant sources of uncertainty in the VdM calibration. Three different methods are used at CMS to measure and correct for this effect. The traditional beam-imaging analysis [386, 387], and two alternative approaches developed recently by the ELTE team [388]: the luminous region [270] and the off-axis (or offset) scan analyses [272, 273].

In the **beam-imaging analysis** [386, 387], the beam shapes are measured using special scans (labeled as ”imag” in Figure 4.2), in which the bunch proton density of a stationary beam is inferred from the distribution of reconstructed vertices as the other beam scans across it in equidistant steps in the x and y directions separately. The data used for vertexing are collected using zero-bias triggers gated on a small number (five in Run 2 and up to 9 in Run 3) of the colliding bunch pairs. The collection of data for only a few bunch pairs is limiting but necessary to collect enough statistics per scan step of typically 60 s length for each studied bunch pair within the available trigger bandwidth. An other limitation of the method is that the vertex resolution needs to be much smaller than the beam width [354].

Different fit models are used (based on the sum of multiple two-dimensional Gaussian functions with x-y correlation) to obtain the two-dimensional bunch proton density functions of the two bunches by simultaneously fitting the measured vertex distributions of the four scans for the two beams and the two transverse directions. The correction and its uncertainty due to the factorization assumption are then calculated by making simulated VdM experiments assuming the best fit model for the beam shapes. In each experiment, the VdM results are compared to the “true” simulated beam overlap integral to study the bias. The dominant uncertainty (about 0.5%) comes from the possible intrinsic systematic bias of the beam-imaging method, estimated by a closure test in Monte Carlo simulation where the true and measured non-factorization corrections were compared.

The **luminous region analysis** is a fully analytic implementation (with models for the bunch proton density functions built from the sum of up to four three-dimensional Gaussian functions) of the method described in Ref. [389] with various improvements to increase the robustness of the fit. It does not require a dedicated special scan: it can be used in regular VdM scans as well as beam-imaging scans, giving the possibility to validate the two methods against each other. Like the beam-imaging method, the luminous region fit requires zero-bias vertex data. The vertex distribution is fitted with a three-dimensional Gaussian function yielding nine beamspot parameters [260] for each scan step where there is a sufficient number of vertices.

Subsequently, a global fit to the beamspot parameters and the normalized rates from one of the luminometers is performed to extract the 3-dimensional bunch shapes. Optionally data from the LHC longitudinal density monitor can also be used to constrain the bunch length. A scale factor for the vertex resolution is fitted from the data. Similarly to the beam-imaging method, the luminous region analysis conducts simulated VdM scans to measure any potential bias, and the main contribution to the uncertainty stems from the closure test (down to 0.3%).

This method monitors the evolution of the beam proton density functions and thus the non-factorization correction in time during the full VdM calibration data taking by independently analyzing all standard VdM and beam-imaging scans, with corrections for beam-beam effects and orbit drifts fully implemented. It thus improves the scan-to-scan consistency of the extracted σ_{vis}. Figure 4.6 shows the first experimental evidence for the time development of the non-factorization correction [270], with a first hint mentioned in Ref. [272].

Traditional VdM scan data can be paired with off-axis scans for the global fit which allows to check systematic biases in the fitted beam shapes due to the sampling of the bunch overlap distribution and also a direct comparison with the third method.

The **off-axis (or offset) scan analysis** uses special off-axis scans (labeled as ”offset” in Figure 4.2) to measure the non-factorizability of the overlap shape directly, sampling the tails of the bunch overlap distribution. In practice, it uses a special “offset scan”, a VdM scan with a fixed offset between the beam positions in the non-scanning direction [272]. Recently, diagonal scans with beam separations along the x and y axis satisfying $\Delta x = \Delta y$ or $\Delta x = -\Delta y$ were demonstrated to provide even more accurate information [273, 390] due to their higher statistical power, and other scan types with $\Delta x = \alpha \Delta y$ were also explored in the 2023 PbPb VdM data taking for future studies. The normalized rates from the luminometers measured during a normal VdM scan and a close-in-time off-axis scan are fit as a function of $(\Delta x, \Delta y)$ with a two-dimensional function that includes correlation and non-Gaussian features. The bias is calculated –

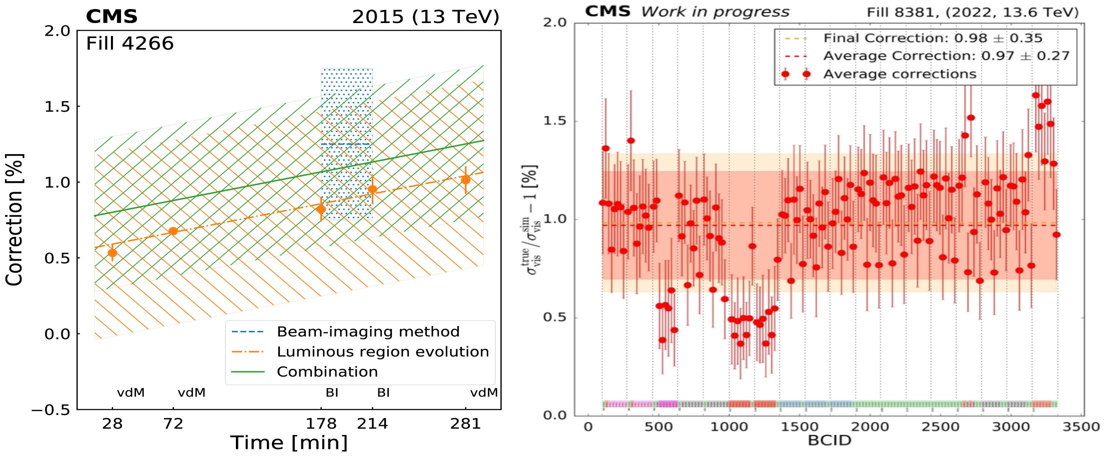

Figure 4.6: *(left) Non-factorization corrections as a function of time during the 2015 pp VdM calibration fill comparing and combining the beam-imaging and luminous region evolution methods. Each point corresponds to one x and y scan pair. The statistical uncertainty is shown by the error bars. The bands correspond to the total uncertainty dominated by the closure of the method which is correlated among all scan pairs. (right) Bunch crossing identification dependence of the factorization correction in the 2022 pp VdM calibration fill, derived using the off-axis scan method. The errors correspond to the total uncertainty except the dominant correlated uncertainty due to the limitation of the fit models. The color code close to the x axis indicate the collision pattern for the bunches in the colliding pair. [270]*

as for the other methods – from simulated vdM scans, using the best fit model in data as the true overlap shape for the simulation. Then the integral of the 2-dimensional fit function is compared to the result from the "factorized" VdM fits. More complex scans in two dimensions are also viable, as was shown by LHCb [391], but require more scan time and thus introduce further complications due to the evolution of the bunch properties, the possibility for unknown biases due to magnet hysteresis and orbit drifts.

As this simple complementary method does not need vertex information, it can use data from any luminometer for each colliding bunch pair to provide a useful cross-check. In PbPb VdM scans, where the transverse beam width is comparable to the vertex position resolution and thus the other methods experience large uncertainties, this analysis is especially well suited. The dominant uncertainty for the offset scan analysis originates from the lack of a priori knowledge of the bunch overlap shape. Various 2-dimensional functions are implemented: single and double Gaussian, the latter in various alternative parametrizations that restrict the number of free parameters, super-Gaussian, q-Gaussian, poly$N$-Gaussian where the constant normalization of the Gaussian is replaced by a symmetric $N = 2, 4$ polynomial. More complex functions with larger number of parameters, e.g. double super-Gaussian were tried but do not provide stable results due to the restricted number of measurement points. In the case of PbPb VdM scans, the statistical precision of the measured rates is poor (about 7-10% for 30 s head-on data) and thus the method closure also gives a significant uncertainty (of about 1%). For pp VdM scans with about 10 times smaller statistical uncertainty, the closure is excellent (better than 0.1%).

Even though the off-axis scan method has severe limitations, it is the only method that gives a handle to study the factorization correction for all bunches and thus study possible patterns that emerge due to the history of the bunches. For the first time, we observed a clear pattern in the 2022 pp VdM data depending on how many collisions per orbit the bunches in the pair experience and in which interaction points, as well as depending on their history of acceleration (which of the four PS Booster rings they traveled through) as shown in Figure 4.6 (right). This highlights the complementarity of the various methods and the need to use their combination to get a precise handle on factorization in the vdM analysis.

These developments, that I lead, reduced the previously dominant factorization uncertainty to the ∼0.5% level.

4.1.5 How to check for unknown biases?

After careful correction of all known effects, differences might still be observed in the σ_{vis} values of a luminometer extracted using data corresponding to different bunch crossing identifiers and VdM scan pairs in a calibration campaign. These differences are typically larger than expected from statistical fluctuations and are thus considered as measures of biases from unknown sources. When the observed differences are correlated between measurements made by different luminometers, they are likely coming from biases related to the properties of the beams. The uncorrelated parts on the other hand come from detector-specific effects. These are also tested by comparing the measured luminosity in the VdM calibration fill in time periods of stable head-on collisions (i.e. outside the specific scans) as measured by the various luminometers.

Typical uncertainties in the CMS Run-2 $\sqrt{s} = 13$ TeV pp luminosity calibrations are summarized in Table 4.1 [340].

Source of uncertainty	Correction [%]	Uncertainty [%]
Normalization		
Beam current calibration	+1 to +3	0.2
Ghosts and satellites	+0.2 to +0.4	0.1
Background (detector specific)	0 to +0.8	0.1
Beam-beam interactions	+0.4 to +0.6	0.3–0.5
Linear orbit drift	+0.2 to +1.0	0.1–0.2
Residual orbit drift	−0.6 to +0.4	0.3–0.8
Beam separation length scale	−1.3 to −0.4	0.1–0.3
Transverse non-factorization	+0.6 to +1.3	0.4–0.8
Bunch-to-bunch variation	N.A.	0.1
Scan-to-scan variation	N.A.	0.3–0.5
Cross-detector consistency	N.A.	0.5–0.6
Integration		
Out-of-time effects (detector specific)	−17 to 0	0.3–0.4
Cross-detector stability	N.A.	0.5–0.6
Linearity	N.A.	0.3–1.5

Table 4.1: *Summary of typical sizes of corrections and systematic uncertainties entering the CMS luminosity measurement for $\sqrt{s} = 13$ TeV pp collisions for Run-2 data [270–272] using the latest measurement techniques (some still under peer-review). When applicable, the percentage correction is shown. Adapted from Ref. [340] including new developments. The various sources of uncertainty appear in the order they are discussed in the text.*

4.2 Luminosity integration

VdM scans are performed in special conditions at low pileup $\langle\mu\rangle \approx 0.6$ optimized for minimal systematic bias due to beam related effects. An important source of uncertainty arises thus from the extrapolation of the calibration to physics conditions with a pileup of $\langle\mu\rangle \approx 20-50$ in Run 2 (and reaching up to $\langle\mu\rangle = 200$ in future Phase-2 data taking), due to non-linearities or long-term variations in luminometer response.

4.2.1 CMS luminosity instrumentation

Precision luminosity determination in real time and offline in the CMS experiment relies on the use of multiple precision luminometers that provide bunch-by-bunch measurements with 1.44 s time granularity. They are independently calibrated with the VdM method, and their efficiency and linearity are continuously monitored during physics data taking using short VdM-like "emittance" scans (Section 4.2.4). In addition, several stable and linear instruments are used, primarily for systematic studies, that may not have all these "ideal" properties.

Figure 4.7 presents the systems that contributed to luminometry in Run 2 and Run 3. The systems are listed from the center of CMS towards the outer layers (and their features that deviate from the ideal are explicitly noted):

Silicon pixel detector provides pixel clusters that are counted in events collected by a zero bias trigger using a dedicated data stream that contains only the pixel data to reduce the event size and thus the required bandwidth. Data recorded by random triggers are used to determine the out-of-time background corrections (Section 4.2.3). Due to statistics limitations of the trigger, continuous monitoring of the stability and linearity using emittance scans is not possible for pixel cluster counting (PCC). The measurement uses modules that show high stability during the full data taking period and is only available offline. Development work is ongoing to make it near real-time in Run 3: cluster counting was moved to the High Level Trigger (HLT) with ELTE contribution, and the data will be fed to BRILDAQ with some latency. It was the primary luminometer for the 2015 and 2016 pp data with $\langle\mu\rangle = 14$ and 27.

Pixel luminosity telescope (PLT), a dedicated luminometer just outside the pixel endcap that performs zero counting of three-fold coincidences of hits in telescopes built from three planes of silicon pixel modules (Section 4.2.2). Completely rebuilt for Run 3.

Beam conditions monitor (BCM1F), a dedicated luminometer that performs zero counting of hits on polycrystalline diamond (pCVD) and silicon pad sensors in Run 2, and upgraded to use actively cooled silicon pad sensors in Run 3. Since Run 3, a second independent back end provides real-time pulse height measurement. Its sub-bunch-crossing time resolution allows the measurement of beam-induced background.

Muon barrel (MB) drift tube (DT) back end sends the rate of untriggered muon track segments (stubs) – used also as input to the level-1 trigger – integrated over the full LHC orbit and for a time window of 23.3 s. Due to low statistics, no absolute calibration or continuous monitoring with VdM-like scans is possible. The data act as reference in systematic evaluations due to their stable and linear behavior.

Hadron forward calorimeter (HF), featuring a dedicated read out system for luminosity measurement, performs zero counting of calorimeter towers with an energy above a certain threshold (occupancy or HFOC method) and – from 2017 – computes the sum of transverse energy deposited in two outer rings of the quartz fiber calorimeter providing the most uniform occupancy (E_T-sum or HFET method). HF was the primary luminometer in 2017-2022 pp data taking.

Radiation monitoring system for the environment and safety (RAMSES) belongs to the radiation and environment monitoring unified supervision (REMUS) system. It reads out the data of air ionization chambers and provides a measurement of the ambient dose equivalent rate per 1.2 s and integrated over the full LHC orbit. It is used as a reference in systematic studies benefiting from its linear response with luminosity and stable operations. However, due to low statistics, it can not be independently calibrated.

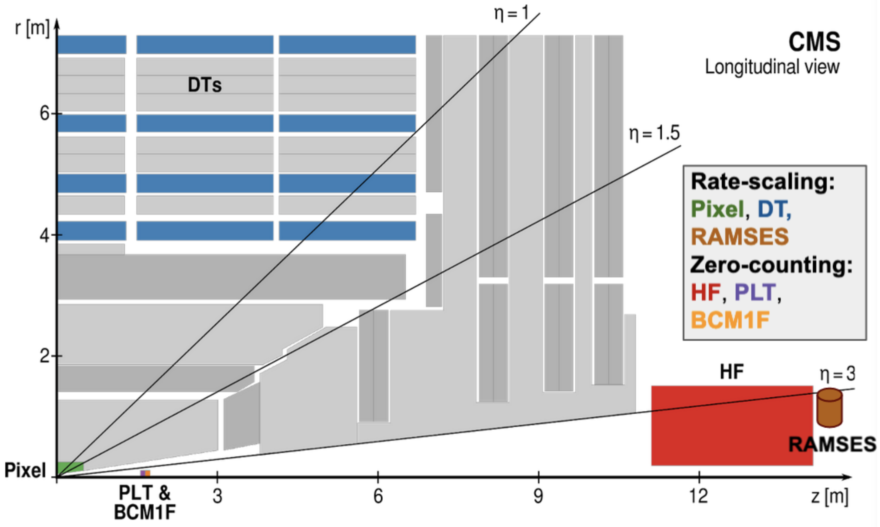

Figure 4.7: *Schematic cross section of one quarter of the CMS detector in the (r, z) plane with the main luminometers in Run 2 highlighted. The center of the detector, corresponding to the approximate position of the* pp *collision point, is located at the origin. Modified from Ref. [270].*

The use of different technologies and counting methods ensures that instrumentation-related systematics are independent to a very large extent. The systems have very high availability and in combination CMS reaches a practically 100% coverage for the periods when beams are present in the accelerator (with very few exceptions, like a general power cut affecting the cavern).

A dedicated data acquisition system (BRILDAQ) – used by all online BRIL luminosity detectors – provides independent run control, reads out and processes the luminosity histograms, as well as detector calibration and monitoring data. It allows real-time synchronization and sharing of the published data using a publisher-subscriber model with LHC and CMS clients. It provides common data storage in a relational database, and various monitoring and visualization interfaces. It is independent of central CMS data acquisition, so that it provides luminosity and beam-induced background (BIB) measurements whenever there is beam in the LHC, even when CMS is not running. This ensures that the dedicated, BRIL operated luminometers (PLT and BCM1F) can continue to take and provide data even when central services fail.

4.2.2 Data quality monitoring in real time

Data quality monitoring plays an important role in operating the BRIL detector systems [392, 393] reliably with high availability and excellent performance that is a prerequisite for response stability. A machine learning tool was developed at ELTE to provide feedback in real time for the operation of the Pixel Luminosity Telescope [394, 395],

At each end of CMS, PLT contains 24 silicon pixel sensors of 8×8 mm^2 arranged into 8 telescopes such that particles originating from the interaction point will pass through all three sensors of a telescope. The sensors are divided into 80 rows and 52 columns. Only the central region of the sensors is used to reduce the contribution from background. PLT measures the rate of triple coincidences among the three planes using a special "fast-or" readout at 40 MHz rate. The bunch-by-bunch luminosity is then determined by a statistical precision of about 1% in physics conditions at every 23.3 s.

For calibration and monitoring purposes, the full pixel data are also read out upon receipt of a zero-bias trigger at a rate of typically a few kHz (3.3 kHz in physics and up to 70 kHz in low-pileup special fills).

Not all operational issues affect the fast-or luminosity directly, however, they can cause difficulties using the pixel data in later analyses. One potential problem is a drift of the analog output levels from a readout chip leading to incorrect decoding of the data. Other problems (e.g., dead or hot channels) also affect the fast-or luminosity but might not be immediately visible. These features can, however, be easily visualized on an occupancy map of the sensor showing the number of hits over a given integration time window. In normal conditions, the maps show relatively uniform hit distribution, increasing slightly towards the edge closest to the beam. When errors occur, some areas will have decreased or increased occupancy.

The occupancy maps are preprocessed to compensate for the average trends either by fitting and subtracting a plane or by using a convolution filter. Then a set of variables describing the maps is defined, such as the average and standard deviation of the number of hits per pixel, the standard deviation within and among rows and columns, and the number of pixels with a significantly outlying number of hits. The variables are normalized to remove any dependence on the overall average occupancy. An unsupervised machine learning technique, the k-means clustering algorithm [396], is used to separate the occupancy maps into different sets, with one set (the largest) corresponding to good maps and the other sets containing data with different types of problems.

Figure 4.8 shows two occupancy maps and the 31 discriminating variables used in the classification: a period of good operation and a period with the decoding problem described above. When applied to the full Run-2 data set of 3 million maps using 5-minute integration windows, the k-means algorithm successfully identified good maps with a greater than 95% purity, and divided the bad maps into categories such as one or a few pixels with very low occupancy, row or column errors, and other types of issues. Fast feedback on such issues then allows a quick recovery and improves the overall data quality.

4.2.3 Out-of-time and noise contributions

To achieve high instantaneous luminosity during physics data taking, the LHC is operated with rather dense filling schemes built up from long bunch trains. For example, in 2018 about 72% of the possible locations have been filled with proton bunches. In such conditions, various "out-of-time" (OOT) effects will contribute to a higher observed rate

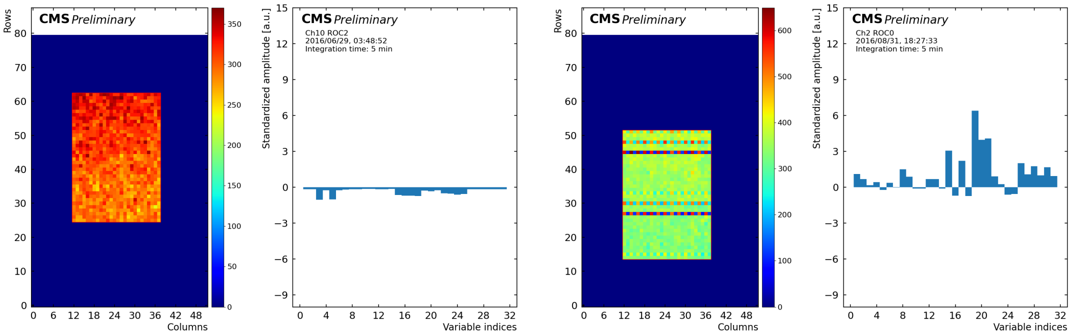

Figure 4.8: *Occupancy map for a single sensor and the corresponding values of the 31 variables used as input to the k-means clustering (left) during a period of good operating conditions and (right) when the pixel addresses corresponding to hits were incorrectly decoded, resulting in line errors.*

than expected from a linear extrapolation of the VdM measurements. Namely, when the characteristic time of a certain physical process in the detector is longer than the 25 ns between the adjacent bunch crossings, processes originating from previous crossings can contribute to the detector signal of the time window belonging to the current bunch crossing. The main contributors are:

Timewalk Detector signals go through various stages of signal processing resulting in a certain time structure of the pulses. A fraction of hits that arrive within a single bunch crossing are thus either not detected (if the signal is below threshold) or detected in the subsequent bunch crossing (if due to the combination of the time of arrival and the signal amplitude, the threshold is only crossed in the next clock cycle). For example, the Phase-2 CMS Tracker Endcap Pixel (TEPX) detector (Section 4.4) is expected to have significant timewalk [340].

Spillover A small signal spilling over from the previous bunch crossing contributes to the detection of a signal that otherwise would be below the threshold. Such a contribution is observed for the CMS HFOC method [272].

Late particles Low momentum particles from the primary interaction in a previous bunch crossing, e.g., so called loopers in the tracking detectors trapped by the magnetic field.

Albedo Particles reflected from the environment, primarily charged hadrons created in showers in nearby material.

Afterglow Activation of the detector material can contribute with **exponentially falling** rate. The time constant depends on the lifetime of short-lived activation products. It is observed in various CMS detectors with a characteristic time of a few $(10 - 100) \cdot 25$ ns.

Neutron background Neutrons generated in the accelerator components around and in the detector contribute for even longer, over ~1 ms, i.e., about 10 full orbits. The signal is due to photons emitted during the capture of slow neutrons which then generate electron-positron pairs with MeV energy and appear in the detector as **noise**.

These effects are detector specific, depending on the detector material and geometry, the readout electronics, the counting method, and the operating environment. The rate enhancement has been shown to be around 10% for the main CMS luminometers in Run 2, i.e. for the Phase-0 [270] and Phase-1 pixel detector using the pixel cluster counting algorithm, as well as for the hadron forward calorimeter using either the energy cluster counting or the energy sum method [272] .

OOT effects are only partially included in the CMS detector simulation based on GEANT4 [269]: proton-proton collisions from previous and following bunch crossings (out-of-time pileup), and the inefficiency due to electronic time walk are simulated, but out-of-time contributions that require a memory of previous events, e.g., extra hits due to time walk in the previous bunch crossing, late particles reflected from the environment (albedo), and signal from material activation (afterglow) and neutron background are not. These need dedicated simulation studies, either by special GEANT4 settings (e.g., using an increased simulation time window) or using different tools (e.g., FLUKA [397, 398] for neutron background), as well as laboratory measurements (e.g., to study the activation of the detector material).

Experimentally they need to be measured in situ, typically fitting an analytic model or a template to the data assuming the rate detected for non-colliding bunch pairs comes entirely from out-of-time processes. The corresponding uncertainty can be as high as 0.4%.

4.2.4 Linearity and stability monitoring

All luminometers suffer from some degree of non-linearity that must be measured and accounted for when extrapolating the luminometer visible cross section from the VdM calibration to the usual physics data-taking environment over a factor of 100 (400) in SBIL (or PU) at Run 2 (Phase 2).

Typical sources of non-linearity are intensity-dependent efficiency (such as the inefficiency observed in the CMS Phase-0 and Phase-1 pixel detectors due to the limited size of the readout buffer [260] leading to an observed rate less than expected for a linear SBIL dependence), as well as imperfect corrections for out-of-time effects that contribute to a higher observed rate than expected. Each of these can also be subject to time-dependent variations from detector or electronics aging, the effects of steadily increasing radiation dose (which can influence the stability of certain detectors), and changes in operating conditions.

Typical sources of instability in a luminometer measurement are short-term effects, such as overall rate-dependent efficiency factors (e.g., as observed [399] in the BCM1F [400, 401] pCVD diamond channels in Run 2), or inefficiencies related to dead time, as well as longer-term factors such as radiation damage dependent on the integrated fluence and annealing effects inherent to silicon detectors.

Linearity and stability issues are typically not independent of each other, and all systems suffer to some extent from such effects. The challenge is to identify detector technologies and analysis techniques that minimize the significance of these factors on the final integrated luminosity measurement.

There are two important pillars to improve integration biases: in-situ determination of the corrections for each luminometer independently, and the redundancy of independent luminosity measurements which allows to identify problematic results using a simple majority rule.

VdM-like scans with less steps and shorter data collection time per step, also called **emittance scans** [402, 403] (labeled as ”emit” in Figure 4.2) are routinely performed under standard physics conditions at the beginning and end of the fills. They are used to study the change in σ_{vis} relative to the value measured in the emittance scans of the

VdM fill or the physics fill that is closest to the VdM calibration campaign. To date, the corrections to enable the extraction of absolute visible cross sections from emittance scan data are not yet of sufficient precision. The scans can be used to compare the effective or relative visible cross sections that are taken in similar operating conditions of the luminometer and with the same filling scheme through the year.

Due to the wide range of single-bunch instantaneous luminosities in a typical physics fill, the bunch-by-bunch measurements can be used to determine the effective visible cross section, both as a function of SBIL to quantify non-linearity effects, and as a function of time to measure efficiency trends (stability). This method allows CMS to track the slow change of the performance of the luminometers (degradation mostly due to radiation damage and compensation of lost efficiency by operating conditions, e.g., higher bias voltage for Si sensors). The corrections, extracted entirely independently for each subsystem, then vastly improve the accuracy of each luminometer.

The latter statement is made based on the comparison of the luminosity results obtained by different detectors: they show much reduced relative non-linearity and time-dependent efficiency variation [404, 405] after the corrections derived from emittance scans. The expected systematically different behavior of the detectors is exploited to estimate residual biases. The combination of the available measurements by several luminometers could lead to higher precision in the future.

An other tool used to measure non-linearity is the so-called **μ scan**, executed only a few times per year. A VdM-like scan is run with high-luminosity beam conditions and longer integration time per scan step, though typically (but not necessarily) with a reduced number of colliding bunches. Due to the large range of separation and the nominal head-on conditions, it is possible to perform luminometer ratio measurements over a wide range of instantaneous luminosities that can crosscheck the non-linearity corrections determined in the emittance scans over the full luminosity range with large data samples and provide an independent measurement of residual non-linearities [404, 406].

Finally, due to its clean event signature and relatively high cross section, the $Z \to \mu^+\mu^-$ process is of particular interest for luminosity measurement [356, 407, 408] as it could allow the monitoring of long-term drift effects for high-rate luminometers and the comparison between different data-taking periods (and even the combination of different VdM calibrations) at the same center-of-mass energy. In the Z-counting method, the production rate of $Z \to \mu^+\mu^-$ is measured in a given time interval, corrected for the muon and dimuon efficiency determined in situ. The statistical precision limits the achievable time granularity: even the increased instantaneous luminosity of about 50 Hz/nb at Phase 2 will only allow monitoring the $Z \to \mu^+\mu^-$ production rate with a statistical precision of a bit better than 1% in time intervals of 8 min. The main challenge is the precise ”real-time” measurement of the efficiency (which is necessary to ensure independence from changing conditions, e.g., related to pileup). It is performed from the same events using the “tag-and-probe” technique [409] (Section 3.5.1.1.5) in a time-dependent way in relatively small intervals of about 20 pb^{-1}. The correlation between the two muons and the dependence on pileup have to be minimized by appropriate event selection using simulated data.

4.3 CMS luminosity measurement results in Run 2

The total luminosity uncertainty for high instantaneous luminosity data taking in CMS amounts to 1.6% in 2015, and 1.2% in 2016 [270]. For the years 2017 and 2018, only the preliminary calibration is available so far with an uncertainty of 2.3 [271] and 2.5% [272].

The 2016 result was the first high precision $\mathcal{O}(1\%)$ measurement in high instantaneous luminosity environment at bunched-beam hadron colliders. The final accuracy for 2017–2018 is expected to reach a similar precision and will benefit from several methodology improvements and new scan data mentioned above that became available after 2016: the regular use of emittance scans in physics fills, the availability of off-axis scan data for $x - y$ non-factorization studies, and the variable separation length scale scans.

For special low instantaneous luminosity periods ($\langle \mu \rangle \approx 2 - 3$), the preliminary calibrations are also available for the 2017 data: the total uncertainty is 1.9% at $\sqrt{s} = 5.02$ TeV [353] and 1.7% at $\sqrt{s} = 13$ TeV [271]. The lower uncertainty for the 13 TeV data, compared to the precision in the same year at high-$\langle \mu \rangle$, comes from the lower contribution of the linearity uncertainty which is assumed to be proportional to the average instantaneous luminosity.

For proton–lead ion collisions in 2016, the uncertainty increases to 3.2–3.7%, dominantly due to the difficulty to measure the $x - y$ non-factorization contribution from the vertex data as the vertex position resolution in the transverse plane was comparable to the beam size due to the lower $\beta^* = 0.6$ m optics parameter setting [354]. The introduction of diagonal scans for the 2018 Pb-Pb data by the ELTE team brought a large improvement for the calibration precision which reached 1.3% [273].

4.4 CMS luminosity measurement strategy for HL-LHC

The CMS BRIL detector systems [393], shown in Figure 4.7, deliver robust online bunch-by-bunch, as well as orbit-integrated, instantaneous luminosity measurements for CMS data taking and LHC beam optimizations with a time granularity of about 1 s. The robustness stems from the careful system design of each luminometer, and from the strategy of having multiple technologies and counting methods which provide redundancy and largely orthogonal systematics. Run 2 experience has proven that a minimum of three but ideally four or five independently calibrated and continuously linearity and stability monitored systems are necessary to achieve ultimate precision. With the even more challenging high-pileup environment at HL-LHC and a precision goal of 1%, multiple, high statistical power, stable and technologically diverse systems were proposed for Phase 2 [355].

To reach the 1% target, not only improved instrumentation but also more refined analysis techniques, especially for emittance scan data that provide precise efficiency corrections, are essential [340]. Without these, extrapolating the current Run-2 linearity systematics to HL-LHC gives a staggering 5% uncertainty. Linearity corrections will thus be dominant and have an increased importance in Phase 2 requiring an unprecedented accuracy. Detector design thus have to carefully minimize non-linear effects to deliver a robust system.

The planned subsystems for CMS luminosity measurement in Phase 2 are shown in Figure 4.9, including their locations in and around the CMS detector. Their capabilities are summarized in Table 4.2.

The functionality of the two dedicated BRIL detectors, the Beam Conditions Monitor (BCM1F) [400, 401] and the Pixel Luminosity Telescope (PLT) [410, 411], will need to be replaced for Phase 2 as their present location, directly behind the Phase-1 forward pixel detector (also to be replaced), will no longer be available [412]. The CMS hadron forward calorimeter (HF) as well as the RAMSES monitors will continue to provide luminosity measurements unchanged in Phase 2.

It is foreseen to expand the muon barrel functionality to provide bunch-by-bunch counts of trigger primitives in Phase 2 via a dedicated back end as well as 40 MHz

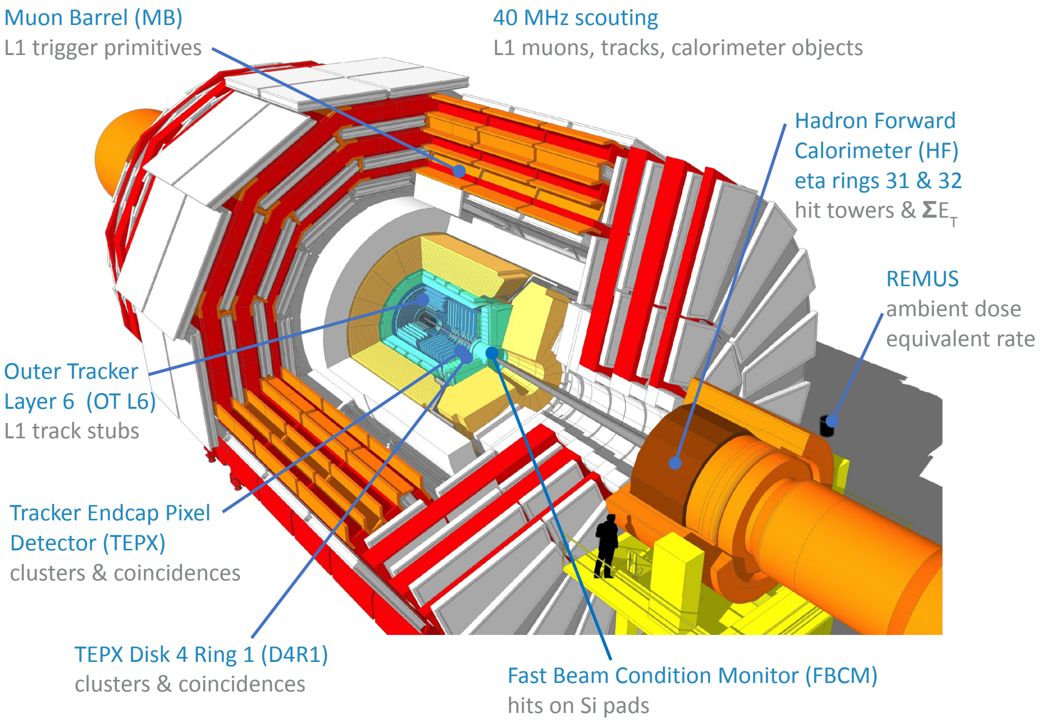

Figure 4.9: *Proposed subsystems for CMS Phase-2 luminosity measurement. [340].*

scouting [413]. The latter monitors Level-1 trigger data streams using spare optical cables. While primarily muon candidate counts from the barrel muon track finder (BMTF) have been studied as an example so far in detail, the 40 MHz scouting could also be used to access further Level-1 objects for luminometry from other systems, such as tracker charged particle tracks or calorimeter energy clusters. A demonstrator system was first implemented in 2018 for 40 MHz scouting. In Run 3, the new muon barrel back end is installed for a ϕ-slice and an advanced 40 MHz scouting demonstrator is operational, both providing a testing ground for Phase-2 luminosity insfrastructure.

With the upgrade of the CMS tracker detector for Phase 2, the forward extension of the inner tracker (the tracker endcap pixel detector, or TEPX) will serve as a high-precision online bunch-by-bunch luminometer using an additional dedicated trigger that samples all relevant bunch crossings in an unbiased way, with a total trigger rate of 75 kHz (equal to 10% of the 750 kHz allocated for physics). It will principally use pixel cluster counting, but will also benefit from the possibility of coincidence counting for overlapping neighboring TEPX modules for systematic studies. A subset of TEPX (disk 4 ring 1, D4R1) will be operated independently from the rest of the tracker to provide luminosity and beam-induced background measurements during all HL-LHC beam modes, including ramp, i.e., when the beam energy and the magnet currents increase. In addition, layer 6 of the CMS outer tracker (OT L6) will be exploited for bunch-by-bunch measurements, using two-hit coincidences (stubs) on two closely spaced silicon sensors at the full 40MHz bunch-crossing frequency. Coincidence counting methods benefit from Run-2 and Run-3 experience gained with the PLT.

Data taking experience has shown that a reliable bunch-by-bunch detector that can be operated independently from the rest of CMS, in particular its central data acquisition (DAQ) and timing and control distribution system (TCDS) is extremely valuable in providing online luminosity and fast feedback to the LHC and CMS during commissioning, as well as machine development periods with adverse beam conditions. As such a detector can feature asynchronous readout and sub-bunch-crossing timing capabilities, it is also essential to understand subtle systematic effects. Therefore, BRIL designed – with my co-leadership – for the Phase-2 upgrade [414] such a detector system, the fast beam conditions monitor (FBCM) using silicon-pad sensors which will be located inside the tracker cold volume and connected to its CO_2 cooling line. The FBCM will count hits on the Si-pads taking advantage of the zero counting technique. It will provide the functionality of the current BCM1F detector with an improved performance (higher statistics and better timing capabilities) and a focus on simple, modular design, ease of calibration and operations. It will complement the triggered measurements of D4R1, featuring orthogonal instrumental uncertainties [340, 415].

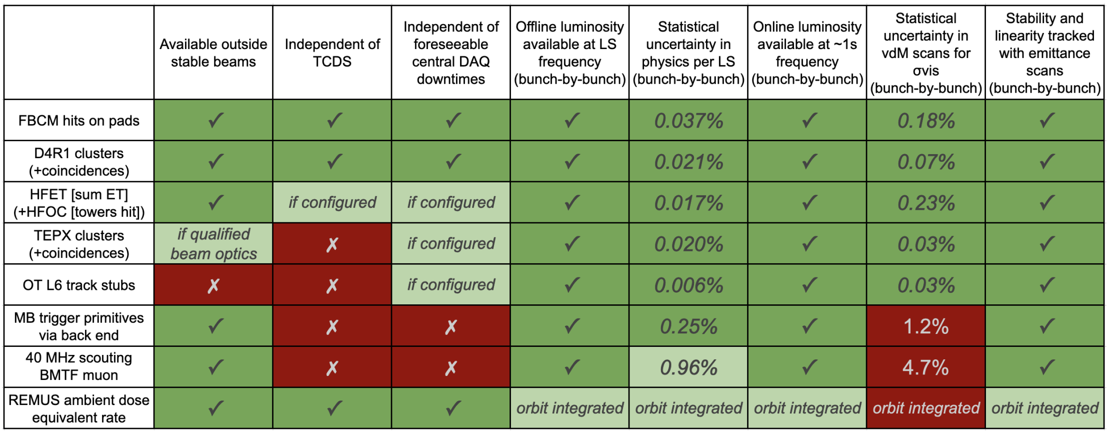

	Available outside stable beams	Independent of TCDS	Independent of foreseeable central DAQ downtimes	Offline luminosity available at LS frequency (bunch-by-bunch)	Statistical uncertainty in physics per LS (bunch-by-bunch)	Online luminosity available at ~1s frequency (bunch-by-bunch)	Statistical uncertainty in vdM scans for σvis (bunch-by-bunch)	Stability and linearity tracked with emittance scans (bunch-by-bunch)
FBCM hits on pads	✓	✓	✓	✓	*0.037%*	✓	*0.18%*	✓
D4R1 clusters (+coincidences)	✓	✓	✓	✓	*0.021%*	✓	*0.07%*	✓
HFET [sum ET] (+HFOC [towers hit])	✓	*if configured*	*if configured*	✓	*0.017%*	✓	*0.23%*	✓
TEPX clusters (+coincidences)	*if qualified beam optics*	✗	*if configured*	✓	*0.020%*	✓	*0.03%*	✓
OT L6 track stubs	✗	✗	*if configured*	✓	*0.006%*	✓	*0.03%*	✓
MB trigger primitives via back end	✓	✗	✗	✓	*0.25%*	✓	1.2%	✓
40 MHz scouting BMTF muon	✓	✗	✗	✓	*0.96%*	✓	4.7%	✓
REMUS ambient dose equivalent rate	✓	✓	✓	*orbit integrated*	*orbit integrated*	*orbit integrated*	*orbit integrated*	*orbit integrated*

Table 4.2: *Summary of the capabilities of the proposed CMS luminosity systems for HL-LHC. For explanation of the required capabilities and the proposed systems, see the main text. The color scale of the fields illustrates to what extent a luminometer fulfills the given requirement (dark green indicates full compliance, while dark red means that the criterion is not met). While each system provides data with about 1* s *time granularity, physics analyses offline use a different time granularity, the so called lumi section (LS) that is 23.3* s *(2^{18} LHC orbits) currently. [340].*

Table 4.2 summarizes the Phase-2 CMS system which fulfills the requirements [340] for robust, high precision luminometry: three almost ideal luminometers (FBCM, D4R1, HF) that are complemented with two high-statistics high-precision instruments (TEPX, OT L6) and three systems that have proven to be highly stable and linear in Run 2 (MB, 40 MHz scouting, REMUS) to help constrain the most important integration systematics.

For constructing and operating such a complex system of luminometers, the guiding principle of maximum commonality is essential. They will use the common BRILDAQ run control, data acquisition and monitoring system, the BRIL trigger board will provide the connection to the LHC machine interface and the TCDS system, and generate luminosity triggers for TEPX and D4R1, finally common firmware blocks will be installed at the back end of all participating detector systems to generate luminosity histograms. Many of the new ideas are tested and optimized in Run 3 to prepare the success of HL-LHC.

Chapter 5

Higgs boson discovery

The LHC was designed and built on the famous ”no-lose” theorem [27] which stated that either it will observe Higgs boson production or will see unmistakable signs of new physics, in particular in the rare WW scattering process (see Section 6.3.2). Fulfilling this promise and bringing to fruition decades of effort to observe the last missing ingredient of the SM at LEP [160] and other colliders, the discovery of the Higgs boson in 2012 completed the SM particle content and started a new era in particle physics.

However, many questions were and are still waiting to be answered. Is the observed particle really the SM Higgs boson? What is the form of the Higgs potential? What are its Yukawa couplings? The precise measurements of the Higgs boson mass and the differential distributions or cross sections for the various production and decay modes allow the extraction of the Higgs properties.

This chapter highlights some of the steps in the extraordinary journey leading to the Higgs boson discovery [25, 26] and the first measurements targeting this unique scalar particle, as well as a brief review of the current state of the art in this research field after 10 years and about 16 times more data analyzed [416–418].

5.1 Towards the discovery

After completing the construction, installation, initial verification and calibration of the detectors using test beams and comic rays, the most important task of the LHC collaborations – at the start of data taking in 2009 – was to commission the detectors with the early proton-proton collision data and to optimize the algorithms targeting the reconstruction of the various physics objects to achieve the best possible physics performance.

Final states with charged leptons and photons play a crucial role in Higgs boson studies, thus after joining the ATLAS Collaboration in 2008, I concentrated on electron and photon reconstruction studies [252–255, 268, 419] (Section 3.5.1.1), as well as one of the first auxiliary physics measurements for the Higgs boson discovery, the determination of the inclusive lepton production cross section at the LHC (Section 5.2). The latter also inspired the development of the most precise irreducible background estimation for the measurement of the $\mathrm{H} \to \mathrm{ZZ}^* \to \ell^+\ell^-\mathrm{e}^+\mathrm{e}^-$ process, where ℓ stands for electrons or muons (Section 5.5.2).

5.2 Inclusive lepton production from heavy-flavor hadron decays

Most of the interactions observed at the LHC are mediated by the strong force. In particular the production rate of hadronic events from the fragmentation of b quarks is more than seven orders of magnitude higher than that of the much coveted Higgs boson production (see Figure 5.1). This raises a number of challenges for Higgs physics studies. The highest probability Higgs decay, H → b$\bar{\mathrm{b}}$ has an enormous background from strong b$\bar{\mathrm{b}}$ production, and the "golden" H → $\mathrm{ZZ}^* \to \ell^+\ell^-\ell'^+\ell'^-$ final state gets a challenging background contribution where the low-p_T leptons originate from semi-leptonic b hadron decays (Figure 5.2). Therefore, the study of lepton production from heavy-flavor hadronic processes was one of the important prerequisites of Higgs studies at the LHC. This section presents – also as a demonstration of the experimental methods applied at the LHC in one of the first analyses – the main components of that analysis using the first ATLAS physics data.

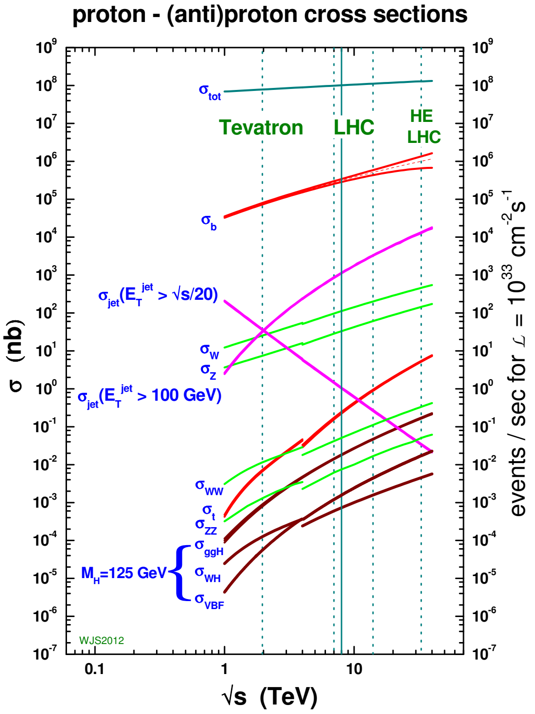

Figure 5.1: *Standard model cross sections as a function of hadron collider energy assuming m_H = 125 GeV for the Higgs boson mass, calculated either at NLO or NNLO pQCD, using MSTW2008 [420] (NLO or NNLO) parton distribution functions, with the exception of the total hadronic cross section which is based on a parametrization of the Particle Data Group [421]. The discontinuity in some of the cross sections at 4 TeV is due to the switch from proton-antiproton to proton-proton collisions at that energy. [422]*

Theoretical advances were prompted by b quark production measurements in p$\bar{\mathrm{p}}$ collisions at the Sp$\bar{\mathrm{p}}$S [423] and Tevatron [424–426] colliders that showed an excess of events over the SM expectations. Fixed order NLO pQCD calculations with NLL high-p_T resummation for the $\mathrm{e}^+\mathrm{e}^- \to \mathrm{b}\bar{\mathrm{b}}$ process at the LEP collider allowed a precise extraction of the b quark fragmentation function [427], which together with improved experimental techniques applied to the Tevatron data [428], resolved the discrepancy [429, 430]. How-

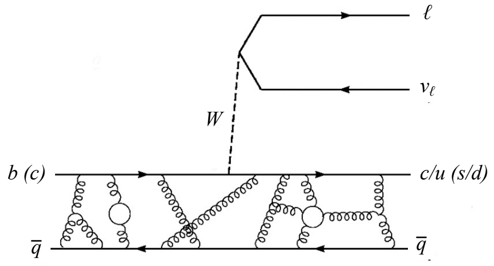

Figure 5.2: *Semi-leptonic decay of heavy-flavor mesons leading to a lepton, typically in the vicinity of one or more hadrons.*

ever, the higher $\sqrt{s}$ of the LHC also offered a probe to the effect of NLL resummation directly, as it becomes larger than the total theoretical uncertainty at high-p_T (at about 20 GeV in the lepton p_T, as will be demonstrated later in Figure 5.5).

The state-of-the-art Fixed Order Next-to-Leading Log (FONLL) [291, 431] framework provides heavy flavor (b and c) production cross sections in perturbative QCD at NLO+NLL accuracy using non-perturbative heavy-flavor fragmentation functions derived from $\mathrm{e}^+\mathrm{e}^-$ data within the same theoretical framework. For the decays of heavy hadrons to leptons, it employs decay tables and form factors derived from the data of b factories.

Monte Carlo simulations were produced to optimize the event selection, study the expected composition of the selected data, and interpret the results. All events were generated at $\sqrt{s} = 7$ TeV using the ATLAS MC09 tune [432] and simulating the detector response with a detailed GEANT4 [269] model. The largest statistics signal samples were made at LO by PYTHIA 6.421 [433] with the MRST LO* PDF set [434]. NLO predictions were produced by POWHEG-hvq v1.0 patch 4 [299, 435] with the CTEQ6.6 [436] PDF set, interfaced either to PYTHIA 6.421 or Herwig v6.510 [437], the latter using JIMMY v4.31 [314] for parton shower and underlying event simulation and PHOTOS v2.15 [308] for final state QED radiation modeling.

In 2010, the LHC started to deliver pp data at $\sqrt{s} = 7$ TeV at low instantaneous luminosities which allowed to rely exclusively on simple Level-1 electromagnetic (e/γ) objects with no requirement on isolation and no additional selection at the HLT to collect events with electrons in the final state. This provided ideal conditions to study electrons produced in hadronic decays which are typically not isolated, i.e. surrounded by other particles. Thus the data used for the measurement of inclusive electron and muon production were collected in April - August of 2010 corresponding to integrated luminosities of 1.28 ± 0.04 pb^{-1} and 1.42 ± 0.04 pb^{-1} [241, 438], respectively, after requirements on the tracker and the EM calorimeter or the muon spectrometer data quality. During this "ramp-up" period, the peak instantaneous luminosity increased from 10^{27} to 10^{31} cm^{-2}s^{-1} (and the peak number of average interactions per crossing from 4 to 15) leading to an increase from 3 GeV to 6 GeV, 11 GeV, and finally 15 GeV for the E_T threshold of the L1 e/γ triggers allowing to measure the differential cross section from 7 to 26 GeV in the electron p_T.

As muon reconstruction both online and offline is inherently cleaner, the L1 trigger requirement for muons started with no explicit p_T selection and increased only up to 10 GeV, providing a larger and purer data sample covering the 4 to 100 GeV range. However, the independent measurements of the cross section in the two final states in a common fiducial region provided an important experimental validation of the results.

The differential cross section (extending the simple formula given in Eq. 3.5) was defined as

$$\left(\frac{d\sigma}{dp_{\mathrm{T}}}\right)_i = \left(\frac{N_i - B_i}{w_{\mathrm{bin},i} \cdot L_{\mathrm{int}\,i}} - \sigma^{\mathrm{accepted}}_{\mathrm{W/Z/}\gamma^*}\right) \cdot \frac{C_{\mathrm{migration},i}}{\epsilon_{\mathrm{reco},i} \cdot \epsilon_{\mathrm{ID},i} \cdot \epsilon_{\mathrm{trigger},i}}, \tag{5.1}$$

where N_i is the number of electron or muon candidates with reconstructed p_{T} in bin i of width $w_{\mathrm{bin},i}$ and B_i is the number of expected background from light hadrons and photon conversions to an $\mathrm{e}^+\mathrm{e}^-$ pair. $\sigma^{\mathrm{accepted}}_{\mathrm{W/Z/}\gamma^*}$ is the accepted cross section after the event selection of prompt isolated leptons originating from W, Z and γ^* production estimated from PYTHIA 6.421 Monte Carlo simulation, with the W, Z contributions normalized to the NNLO prediction [439]. $L_{\mathrm{int}\,i}$ is the integrated luminosity of the data used for the analysis of the given bin. The second factor contains the corrections for experimental effects: $\epsilon_{\mathrm{reco},i}$, $\epsilon_{\mathrm{ID},i}$, and $\epsilon_{\mathrm{trigger},i}$ are the reconstruction, identification and trigger efficiencies for electrons or muons (introduced in Eq. 3.10). The correction factor $C_{\mathrm{migration},i}$ takes into account the migration of objects from a bin of true p_{T} to that of reconstructed p_{T} due to the experimental resolution of the lepton momentum, illustrated in Figure 5.3. It is defined as the ratio of the number of electron or muon candidates in bin i of true p_{T} over their number in bin i of reconstructed p_{T}. In the case of electrons, the second factor is specific to heavy-flavor electrons as the identification efficiency depends on the isolation properties.

Electrons were selected with simple E_{T}- and η-dependent cut-based criteria on a number of discriminating variables. To ensure high trigger efficiency, reconstructed electron candidates had to pass a minimum cluster E_{T} requirement between 7 and 18 GeV depending on the trigger condition (the offline threshold was set about 15-20% higher than the online to accommodate differences in the energy calibration). The trigger efficiency was measured using a bootstrapping method (Section 3.5.2.4) and was between 92-100% with a maximum uncertainty of 2%. Candidates in the transition regions between the barrel and endcap EM calorimeters ($1.37 < |\eta| < 1.52$), or outside the TRT coverage ($|\eta| > 2$), or passing through inactive B-layer modules were excluded. Accepted candidates were required to have at least ten TRT and four sili-

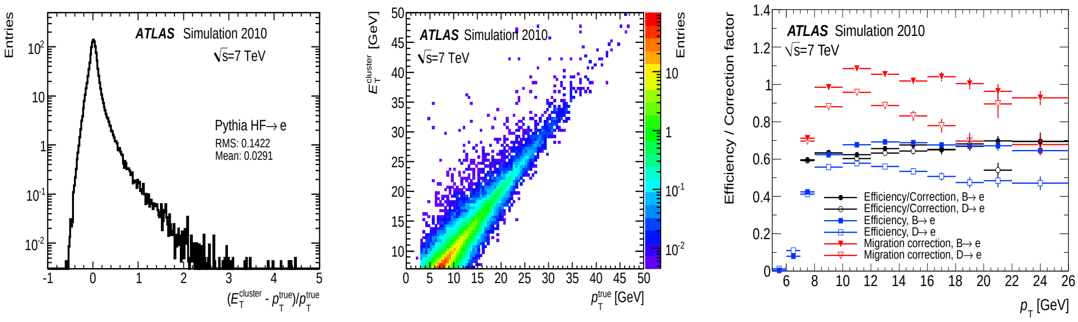

Figure 5.3: *(left) Fractional electron transverse energy residuals showing the relative* E_{T} *scale and resolution, and (middle) true vs. reconstructed transverse energy for electrons from heavy-flavor decays using the PYTHIA generator and the detailed simulation of the ATLAS 2010 detector configuration. For electrons appearing off the diagonal, bin migration occurs. (Right) Electron reconstruction and identification efficiency (*$\epsilon_{\mathrm{reco}} \cdot \epsilon_{\mathrm{ID}}$*), migration correction factor (*$C_{\mathrm{migration}}$*) and their ratio giving the overall offline correction factor as a function of the true electron transverse momentum for* $|\eta| < 2.0$ *excluding the* $1.37 < |\eta| |< 1.52$ *region, for electrons from heavy flavor decays. Errors are statistical only. [441]*

con hits, and a fraction of their energy deposited in the strip and middle layers of the ECAL, and satisfy track quality and track-cluster matching selections as described in Ref. [440]. The quantity $\epsilon_{\mathrm{corr},i} \equiv \epsilon_{\mathrm{reco},i} \cdot \epsilon_{\mathrm{ID},i}/C_{\mathrm{migration},i}$ that corrected for all offline reconstruction and selection effects was about 0.6-0.7, estimated from PYTHIA MC simulation (see Figure 5.3 (right)) with a relative statistical uncertainty of 0.4-3.5% and dominant systematic uncertainties coming from the modeling of the material distribution in GEANT 4 (5-10%), the efficiency measurement precision with the tag-and-probe method (7%), and the observed data – simulation differences in the efficiency (5%). The overall electron reconstruction and identification uncertainty was found to be between 12-14% depending on the true electron p_{T}.

The dominant contribution to the selected candidates came from misidentified hadronic fakes, about 20% from photon conversions to $\mathrm{e}^{+}\mathrm{e}^{-}$ pairs, and only about 10% from non-isolated electron signal from the decay of beauty and charm hadrons. The contribution of isolated electrons from W, Z and γ^{*} production was very small ($\ll 1\%$). The distribution of the selected candidates is shown in Figure 5.4 as a function of the candidate E_{T}, and three variables that provide discrimination against the background: the fraction of high threshold TRT hits (f_{TR}), the number of hits in the innermost silicon pixel layer (n_{BL}), and the ratio of the energy measured in the ECAL to the momentum measured in the tracker (E/p). As with simple selection cuts only a 50% purity could be achieved at best, these variables were used in a template-based binned maximum likelihood fit (also called the "tiles method" [442]). Three-dimensional templates of $2 \times 2 \times 3 = 12$ bins for the heavy flavor signal and for the photon conversion background were constructed from MC simulation, while the hadronic component was described by additional free parameters assuming that the three variables were independent. The fit was performed in bins of E_{T} and $|\eta|$. Possible biases were estimated from the finite statistics of the simulated samples (at most 2.5%), from differences between data and simulation for the discriminating variables (4%), from the assumption of uncorrelated template distributions for the hadronic component (7.3%), and from the uncertainty of the electron energy scale (3.5%). The overall statistical and systematic uncertainties on the signal extraction were 3% and 9%.

Two alternative measurements were also developed to verify the signal extraction. The first was a variant of the tiles method where the E/p variable was exchanged to the fraction of energy deposited in the ECAL strip layer. The second used the observed number of high threshold transition radiation detector hits and relied on the approximation that their distribution adheres to Poisson probability. Both gave compatible results within the quoted uncertainties.

I worked then on the statistical interpretation and uncertainty estimation. First, the measured distributions were corrected for the expected cross section from W, Z and γ^{*} production using PYTHIA MC simulation, with the high-mass W/Z contribution normalized to the NNLO total cross section [439], then unfolded for detector effects using the bin-by-bin method as shown by Eq. 5.1 that takes into account both the efficiencies and the bin migration due to imperfect E_{T} reconstruction. I also applied two alternative unfolding methods with different assumptions and statistical properties using the RooUnfold package [444]: the Singular Value Decomposition (SVD) [445] and the Bayesian [446] unfolding, both giving results within a few % of the bin-by-bin method. To account for possible biases due to the predicted p_{T} distribution of the heavy flavor signal, the unfolding was repeated using various signal predictions by PYTHIA, POWHEG + PYTHIA, POWHEG + Herwig, and a PYTHIA sample with a distorted GEANT4 detector material distribution as data, in all cases keeping the prior distribution and the response matrix built from the PYTHIA simulation in place.

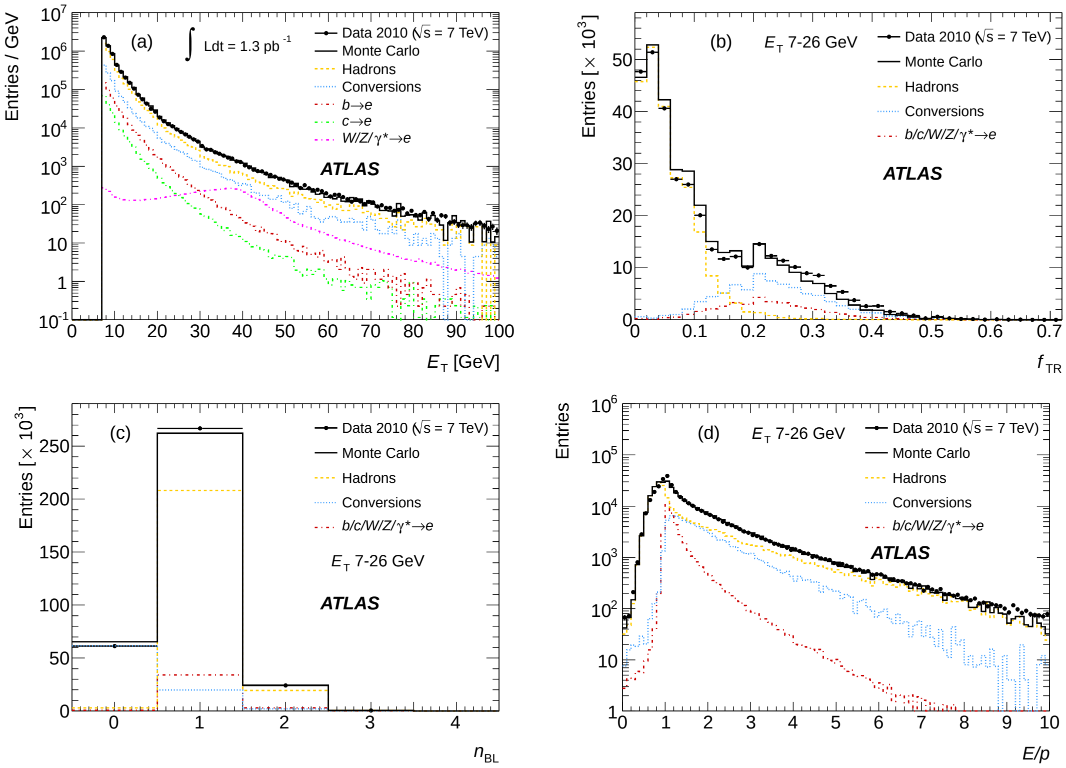

Figure 5.4: *Distributions of (left top) the electron cluster transverse energy (E_T) and the three discriminating variables used to extract the electron signal originating from heavy-flavor and $W/Z/\gamma^*$ decays in the ATLAS 2010 data set at $\sqrt{s} = 7$ TeV. (top right) The ratio (f_{TR}) between the number of high-threshold hits and all hits on the electron track in the TRT discriminates against the hadron fakes (yellow) that populate the region close to zero. (left bottom) The number of hits (n_{BL}) in the innermost B-layer of the pixel detector helps to identify background electrons from photon conversions to an e^+e^- pair (blue). (right bottom) The ratio (E/p) of the electron cluster energy and its track momentum has the sharpest distribution around one for the signal electrons (red). The contributions from different physics processes are indicated by different colors (given above) based on PYTHIA simulation. The W and Z/γ^* cross sections are normalized to NNLO predictions, and the remaining components to the observed events in data. The sum of the normalized distributions from simulation is compared to the ATLAS data (black dots with statistical uncertainties). [443]*

The largest deviations were seen for the distorted geometry sample, but they remained within the uncertainties assigned to the efficiency and resolution corrections $\epsilon_{\text{corr},i}$.

To estimate the final uncertainty, the correlations between the effects on the reconstruction and identification correction factors and the signal extraction from a given source were taken into account. The common sources were the electron energy scale, the modeling of the number of B-layer hits, and the fraction of high threshold hits in the TRT. The measured fiducial differential cross sections are shown in Figure 5.5, both in the common phase space measured by both the electron and muon channels showing an excellent agreement, and in the muon channel that reaches to high p_T even though with significant statistical uncertainties above about 40 GeV.

Several important conclusions were drawn. The FONLL (NLO+NLL) predictions agreed well with the data. The importance of the NLL high-p_T resummation at high lepton transverse momentum was seen for the first time at a hadron collider. Above

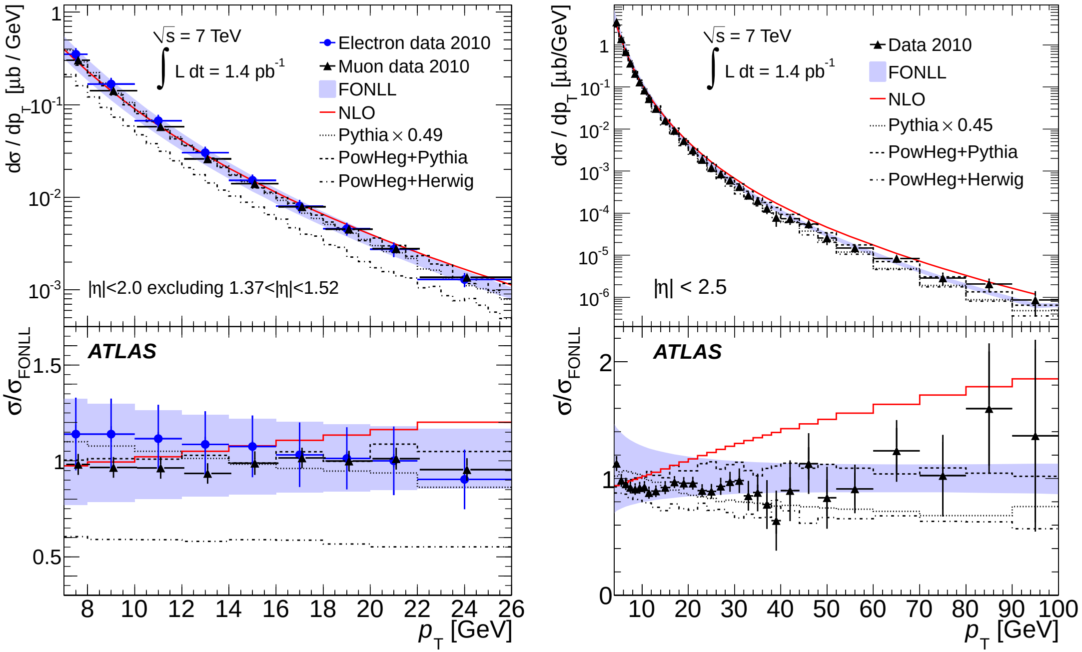

Figure 5.5: *(left) Electron and muon differential cross sections from heavy flavor processes as a function of the charged lepton transverse momentum for* $|\eta| < 2.0$ *excluding the* $1.37 < |\eta| < 1.52$ *region. (right) Muon differential cross section as a function of the muon transverse momentum for* $|\eta| < 2.0$*. The ratios of the measured cross section and the predicted cross sections by various MC generators to the FONLL calculation are given in the bottom panel. The PYTHIA (LO) cross sections are normalized to the data in order to compare the shape of the spectra. [443]*

$p_T = 20$ GeV the correction due to NLL resummation is larger than the full theoretical error that contains uncertainties in the renormalization and factorization scales (up to 35% at low p_T), in the heavy quark masses (up to 9% at low p_T), as well as in the parton distributions functions (below 8%, taken from the CTEQ6.6 PDF [447, 448] set which agreed within the uncertainties with the HERAPDF1.0 [449], MSTW2008 [420], and NNPDF2.1 [450] central predictions). Other contributions from the non-perturbative fragmentation function (less than 5%) [451] and from the value of the strong coupling α_s [448] (about 1%) were small and taken into account.

I also compared the results with MC simulation codes, in particular the NLO predictions of the POWHEG package, interfaced to the PYTHIA or Herwig codes for parton shower simulation (equivalent to a LL resummation). POWHEG + PYTHIA agrees well with the data and the FONLL predictions, while POWHEG + Herwig predicts a significantly lower cross section. Part of the difference comes from the different hadron decay models. This was evaluated by implementing a common decay simulation code EVTGEN [452] to both PYTHIA and Herwig. The use of EVTGEN raised the cross section by about 30-40% for Herwig, while only by about 10% for PYTHIA. The differences in the simulation of the underlying event using PYTHIA or JIMMY (up to about 5%) and the QED final state radiation using PYTHIA or PHOTOS (below about 1%) were also studied but have only small impact on the results. The PYTHIA LO simulation, which was used as baseline in the signal studies, predicted about a factor two lower cross section, but it described the dependence on p_T adequately, especially in the more restricted phase space used in the electron measurement.

Apart from the direct importance of these results for heavy flavor physics, this was also the first measurement in ATLAS that succeeded to go down in the electron E_T

to 7 GeV, which became crucially important in the search for the Higgs boson in the $\mathrm{H} \to \mathrm{ZZ}^* \to \ell^+\ell^-\ell'^+\ell'^-$ decay channel. The ideas developed in the measurement to separate the non-isolated electron signal have also been adapted for the Higgs boson search.

5.3 Higgs boson production at the LHC

Higgs bosons, once produced, decay in about 10^{-22} s to a variety of final states according to the SM. The performance requirements to precisely measure these signatures to determine the properties of this unique scalar particle drove the design of the multi-purpose LHC experiments. The need for precise computation of the relevant physics processes using higher order pQCD and EW calculations led to many theoretical developments.

Higgs boson production at the LHC can proceed through various diagrams as illustrated in Figure 5.6. These are among the hard scattering processes calculated at the highest accuracy at the LHC. The dominant gluon-gluon fusion (ggF or ggH) $\mathrm{gg} \to \mathrm{H}$ mode (providing 88.2% of the total cross section $\sigma_{\mathrm{H}}^{\mathrm{tot}}$ at $\sqrt{s} = 13$ TeV) is calculated at N^3LO in pQCD for inclusive and NNLO for differential quantities, both with NLO EW corrections. All decay modes – also shown in Figure 5.6 – are known to at least NNLO in pQCD with NLO EW corrections as well. Final states with extra jets are calculated at NLO in pQCD with matched parton shower simulation. To the total theoretical uncertainty of 3.9% many sources contribute: renormalization and factorization scales, proton PDFs (including theoretical uncertainty due to the missing N^3LO DGLAP kernels that control the scale dependence of the PDFs), strong coupling strength, quark mass effects, and electroweak contributions [453].

For the vector boson fusion (VBF) $qq \to \mathrm{H}qq$ (6.8% of $\sigma_{\mathrm{H}}^{\mathrm{tot}}$), the situation is similar

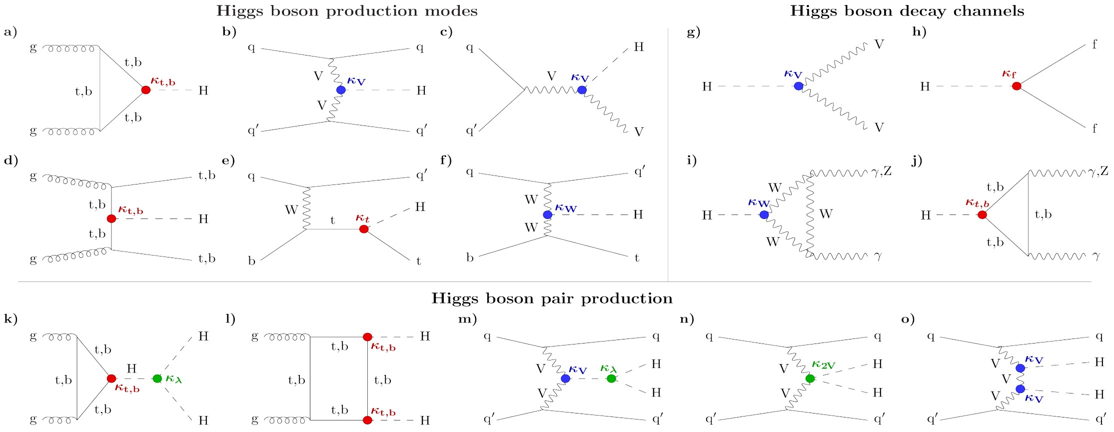

Figure 5.6: *Leading (a-f) single and (k-o) double Higgs boson production modes at the LHC, as well as (g-j) Higgs decay channels according to the SM. Higgs production through (a) gluon-gluon fusion (ggF) via a heavy quark loop, (b) weak vector boson fusion (VBF), (c) associated production with a weak vector boson (VH), also called Higgs-strahlung, (d) associated production with a top or bottom quark pair ($\mathrm{t\bar{t}}H$, $\mathrm{b\bar{b}}H$), and (e-f) associated production with a single top quark and a light quark (tqH). Higgs decay into (g) a heavy EW boson pair, (h) a fermion pair, and (i-j) a photon pair or $Z\gamma$. Di-Higgs production via (k-l) gluon fusion, and (m-o) vector boson fusion. The various Higgs boson interactions (vertices) are labeled by the corresponding κ_i coupling modifiers, i.e. the couplings normalized to the SM predictions. Particles and antiparticles are not differentiated for simplicity.*

but complicated by the fact that the production and decay processes are not factorizable [454]. Thus the inclusive cross section is calculated at N^3LO, while the differential at NNLO for $H \to b\bar{b}$ and $H \to W^+W^-$ channels. The N^3LO calculations for the Higgs-strahlung $q\bar{q}' \to VH$ process (4.1% of σ_H^{tot}) are close to completion, with VH + jets available at NNLO.

Many subtle effects need to be studied to improve the current precision, but there is a fantastic progress, such as the study of top-quark mass dependence at NNLO [455] and the mixed QCD-QED contributions at NLO [456] for $gg \to H$, or the inclusion of decays at LO for VBF [457] and bottom-quark mass effects for Higgs-strahlung followed by $H \to b\bar{b}$ [458]. Differential predictions at N^3LO seem also achievable in the near future [459]. Theoretical progress is most desirable in view of the HL-LHC program, especially when considering the experimental progress in measurement techniques. For the most precise differential cross section measurements performed for the $Z \to \ell^+\ell^-$ process, the experimental systematic uncertainty excluding luminosity is getting well below 1% [460], and — as discussed in Chapter 4 — luminosity precision has improved by about a factor of two recently, reaching 1.2% for the CMS pp data at $\sqrt{s}$ =13 TeV in 2016 [270]. It is therefore reassuring that the scientific community progresses steadily to fulfill the assumption of a factor two improvement in the theoretical uncertainty used in HL-LHC precision forecasts in Ref. [348] and in Figure 4.1.

A summary of the Higgs-boson production cross sections [453] is shown in Figure 5.7 (left) as a function of the pp center-of-mass energy for a Higgs-boson mass of m_H = 125 GeV. Depending on the process, the cross section grows from 7 TeV to 13 TeV by a factor of 2.4 ($q\bar{q}' \to WH$) to 6.1 ($qb \to tHq$) due to the change in the relative parton luminosities which is also dependent on the effective mass of the final state. At the start of the LHC Higgs boson hunt, the mass was constrained by the direct Higgs boson search data from LEP to be above 114 GeV [157], with the indirect limit from electroweak precision fits [16] and the direct search results from Tevatron suggesting an upper limit of 158 GeV [461]. Nonetheless, in the absence of an irrefutable direct upper limit on the Higgs mass, the LHC collaborations scanned a wide mass range in their analyses, where the predicted cross sections and decay branching ratios vary widely, as shown also in Figs. 5.7 (right) and 5.8.

At the observed m_H = 125 GeV mass, the Higgs boson total width is narrow, about 4 MeV, and all decay channels except $H \to t\bar{t}$ are kinematically open, giving ample opportunities to test the Higgs couplings to fermions and bosons. The dominant decay

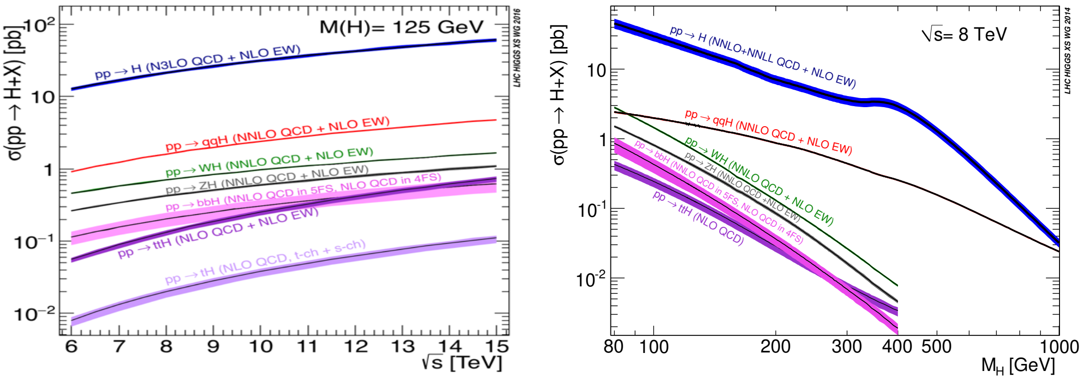

Figure 5.7: *Total SM Higgs boson production cross section (left) as a function of the center-of-mass energy assuming* m_H = *125 GeV for the Higgs boson mass [453] and (right) as a function of the Higgs mass for* $\sqrt{s} = 8$ *TeV [462]for the various production processes. The theoretical uncertainties are indicated by the colored bands.*

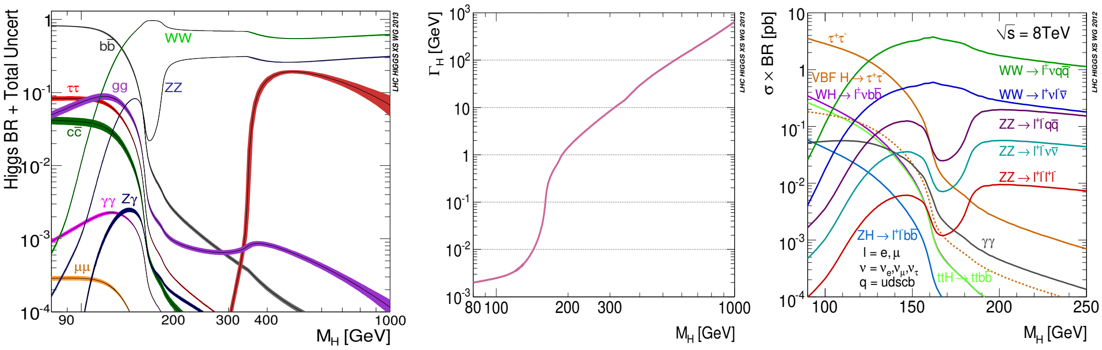

Figure 5.8: *(left) SM Higgs boson two-body decay branching ratios as a function of the Higgs boson mass with theoretical uncertainties indicated as the colored bands [462], and (middle) the resulting total width. (right) Final state specific cross section times branching ratio values for the various decay modes as a function of the Higgs boson mass [463] for the preferred search mass range at $\sqrt{s} = 8$ TeV.*

is $\mathrm{H} \rightarrow \mathrm{b\bar{b}}$ which is experimentally very challenging due to the overwhelming QCD-induced multi-jet background and can be primarily accessed when the Higgs is produced in association with other particles, e.g., in the VH final state [464, 465]. A further difficulty arises due to the jet energy calibration resulting in a wide reconstructed dijet-mass peak, with a resolution around $10 - 15\%$. The second largest branching ratio belongs to $\mathrm{H} \rightarrow \mathrm{W^+W^-}$, however only the leptonic final states offer decent signal-to-background ratio. Nonetheless, due to the presence of missing transverse momentum carried away by the neutrinos from the W decay, the mass resolution is rather poor even in this case [466]. Next is the $\mathrm{H} \rightarrow \mathrm{gg}$ decay which is unrecognizably hidden by QCD-induced processes. The $\mathrm{H} \rightarrow \tau^+\tau^-$ mode is made challenging by the τ decay producing at least one undetectable neutrino and either a single lepton or a narrow, low-multiplicity hadron jet. The best measurement channel in this case is via vector boson fusion that allows the tagging of the events by the presence of two back-to-back forward jets [467, 468]. The $\mathrm{H} \rightarrow \mathrm{c\bar{c}}$ process that would give access to a coupling of the Higgs to a second generation fermion is even more difficult than the dominant $\mathrm{H} \rightarrow \mathrm{b\bar{b}}$ due to its lower cross section and to the less efficient experimental tagging of charm. Significant recent progress [469, 470] gave birth to hope to access it at the HL-LHC.

$\mathrm{H} \rightarrow \mathrm{ZZ}$ offers one of the most sensitive measurements in the rare $\mathrm{H} \rightarrow \mathrm{ZZ}^* \rightarrow \ell^+\ell^-\ell'^+\ell'^-$ channel, which has the highest signal-to-background ratio of about four, excellent mass resolution ($1.6 - 2.2$ GeV [471]), and fully reconstructable event kinematics (Section 5.5). Other final states, $\ell^+\ell^-\nu\bar{\nu}$ and $\ell^+\ell^- q\bar{q}$, are primarily used to search for heavy additional scalar states. Finally, the $\mathrm{H} \rightarrow \gamma\gamma$ mode has provided the statistically strongest discovery channel with a large but well-understood background and excellent mass resolution ($1.3 - 1.9$ GeV [472]). These two final states drove the first observation [25, 26] and play a central role in Higgs property measurements ever since.

The very rare $\mathrm{H} \rightarrow \mathrm{Z}\gamma \rightarrow \ell^+\ell^-\gamma$, $\mathrm{H} \rightarrow \gamma^*\gamma \rightarrow \ell^+\ell^-\gamma$ and $\mathrm{H} \rightarrow \mu^+\mu^-$ decays offer important information, the former might shed light on CP violation in the Higgs sector [473] and the latter provides access to the Higgs coupling to second generation fermions.

The next sections discuss the discovery of the Higgs boson in 2012, then its first property measurements using $\mathrm{H} \rightarrow \mathrm{ZZ}^* \rightarrow \ell^+\ell^-\ell'^+\ell'^-$ events in Run 1 in the ATLAS experiment, and finally the current state of research in the Higgs sector at the LHC after Run 2.

5.4 Higgs boson discovery

The Higgs boson discovery – after nearly 50 years – was achieved by the ATLAS and CMS experiments based on about 10 fb^{-1} of data per experiment roughly equally distributed between pp collisions at $\sqrt{s} = 7$ and 8 TeV [25, 26].

For both experiments, the most significant signal came from $\text{H} \to \gamma\gamma$ process with two isolated, energetic photons in the final state. The display of a candidate event from ATLAS is shown in Figure 5.9. The reconstructed invariant mass of the photon pairs ($m_{\gamma\gamma}$) was calculated from the calibrated photon transverse energies measured in the calorimeter ($E_{\text{T}1}, E_{\text{T}2}$), the azimuthal angle between the photons based on the position of the photons in the calorimeter ($\Delta\phi$), and the pseudorapidity difference computed from the position of the identified primary vertex and the impact points of the photons in the calorimeter ($\Delta\eta$):

$$m_{\gamma\gamma} = \sqrt{2E_{\text{T}1}E_{\text{T}2}(\cosh\Delta\eta - \cos\Delta\phi)}. \tag{5.2}$$

The direction of flight of the photons was determined using the three-dimensional energy cluster information thanks to the longitudinal segmentation of the ECAL (photon pointing). It was then used as input to a global likelihood to identify the primary vertex, in addition to the parameters of the luminous region defined by the reconstructed interaction vertices (”beam spot”) and the $\sum p_{\text{T}}^2$ of the tracks associated to each reconstructed vertex. For converted photons with hits in the silicon tracking lay-

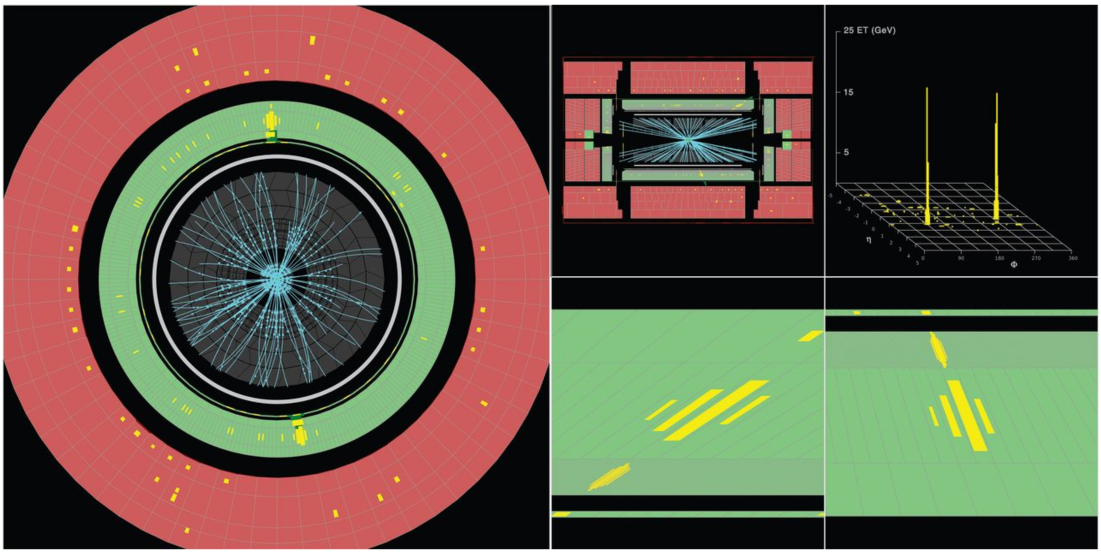

Figure 5.9: *Event display of a* $H \to \gamma\gamma$ *candidate with a reconstructed mass of 126.9 GeV in the 2012 ATLAS data at* $\sqrt{s} = 8$ *TeV. Energy deposits are shown in yellow in the ECAL (green) and hadronic calorimeter (red), with the size of the quadrilaterals representing the amount of deposited energy. Tracks from charged particles and the associated space points measured by the tracker are shown in light blue. (left) Transverse* $r - \phi$ *and (top middle) side* $r - z$ *views are shown, as well as (bottom middle and right) zooms to the fine-grained ECAL response of the two photons demonstrating the stopping of the photon showers in the dense material of the calorimeter and the ability to determine the photon flight direction (pointing). (top right) The amount of deposited transverse energy projected to the (*η*,* ϕ*) plane presents the map of activity in the calorimeter. [474]*

ers, the reconstructed conversion vertex information can further improve the primary vertex identification. Calorimeter photon pointing alone provided a z vertex resolution of about 15 mm, which for two reconstructed converted photons decreased to about 6 mm. After the likelihood selection of the primary vertex, the contribution to the mass resolution from the opening angle between the photons was negligible.

The $m_{\gamma\gamma}$ distribution manifested a clear, narrow peak at about 126.5 GeV over the large falling non-resonant diphoton background modeled by a polynomial (Figure 5.10). The event rate was somewhat larger than expected but consistent with the SM Higgs boson prediction within less than 2 s.d. The sensitivity of the measurement was improved by dividing the photon pair events into 10 categories, and then applying category-dependent event weights that reflected the expected signal-to-background ratio (S/B) for a predicted Higgs boson. In general, the algorithm gave larger weights to events with photons in the best understood regions of the detector and photons that did not start an electromagnetic shower before reaching the calorimeter. I contributed to these results through the ATLAS EM calorimeter energy cluster reconstruction optimization and the e/γ reconstruction and calibration efforts.

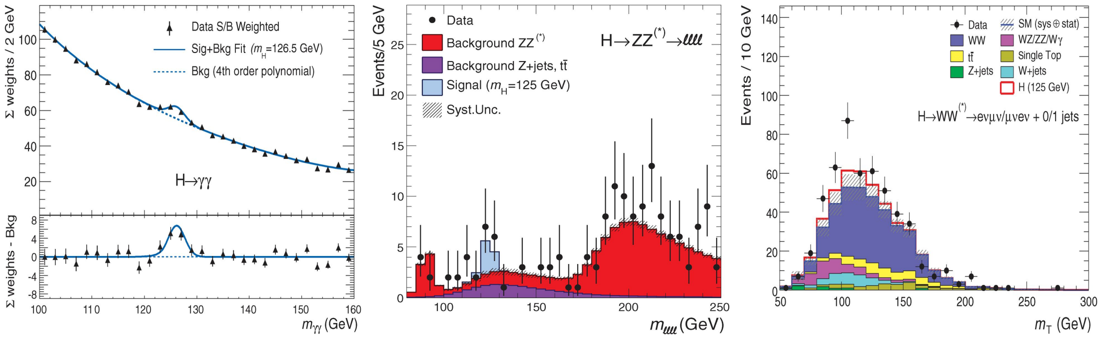

Figure 5.10: *(left) Observed distribution of the reconstructed diphoton mass* ($m_{\gamma\gamma}$) *using event weights based on expected the S/B in the* $H \rightarrow \gamma\gamma$ *search, with the residuals with respect to the background only 4th order Bernstein polynomial fit (dashed) shown in the bottom panel. (middle) Observed and expected distributions of the four-lepton mass* ($m_{4\ell}$) *in the* $H \rightarrow ZZ^* \rightarrow \ell^+\ell^-\ell'^+\ell'^-$ *search, comparing the data to a stacked histogram of the expected background and signal contributions. (right) Observed and expected transverse mass* (m_{T}) *distribution of the dilepton +* $p_{\mathrm{T}}^{\mathrm{miss}}$ *system in the* $H \rightarrow W^{\pm}W^{\mp *} \rightarrow e^{\pm}\nu_{\mathrm{e}}\mu^{\mp}\nu_{\mu}$ *analysis. The assumed Higgs boson mass is given in each subfigure as a label. The hatched bands indicate the total uncertainty on the background estimates. [474]*

The clean, but statistically very limited sample of $\mathrm{H} \rightarrow \mathrm{ZZ}^* \rightarrow \ell^+\ell^-\ell'^+\ell'^-$ events strengthened the consistency with the Higgs boson hypothesis by featuring an excess of events in the four-lepton invariant mass $m_{4\ell}$ in the same region around 125 GeV (Figure 5.10) with the expected rate. More details of the analysis methods applied in this measurement are given in the next section.

Finally, the search for the $\mathrm{H} \rightarrow \mathrm{W}^{\pm}\mathrm{W}^{\mp *} \rightarrow \ell^{\pm}\nu_{\ell}\ell'^{\mp}\nu_{\ell'}$ process also exhibited a signal. This channel required particular care due to the presence of neutrinos from the W decays that leave the detector unobserved giving rise to a significant missing transverse momentum. The analysis was restricted to the mixed-flavor final state, as about 85% of the sensitivity comes from it due to the large Drell-Yan background for same-flavor opposite-charge lepton pairs. An event candidate is shown in Figure 5.11 displaying an electron, a muon and large $p_{\mathrm{T}}^{\mathrm{miss}}$. The measurement showed a global excess of events over the SM prediction, even after the inclusion of the Higgs contribution. I

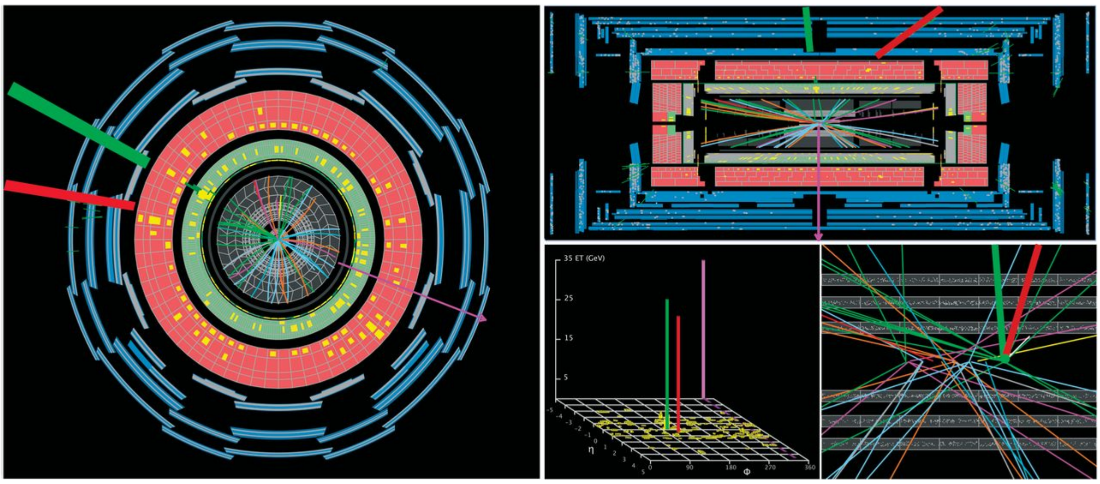

Figure 5.11: *Event display of a* $H \to W^{\pm}W^{\mp *} \to e^{\pm}\nu_{\mathrm{e}}\mu^{\mp}\nu_{\mu}$ *candidate in the 2012 ATLAS data at* $\sqrt{s} = 8$ *TeV. Electron (green) and muon (red) directions are highlighted. The momentum of the charged leptons is balanced by the* $p_{\mathrm{T}}^{\mathrm{miss}}$ *(purple arrow). (left) Transverse* $r - \phi$ *and (top right) side* $r - z$ *views are shown, as well as (bottom right) a zoom to the innermost pixel tracker layers showing the reconstructed vertices. Energy deposits are shown in yellow in the ECAL (green) and hadronic calorimeter (red), with the size of the quadrilaterals representing the amount of deposited energy. Tracks from charged particles and the associated space points measured by the tracker are shown with colored lines, and stubs in the muon chambers (blue) by thin green lines. (bottom middle) The amount of deposited transverse energy projected to the* (η, ϕ) *plane presents the map of activity in the detector. The* $\vec{p}_{\mathrm{T}}^{\mathrm{miss}}$ *pseudorapidity is not defined as the longitudinal momentum of the initial state is unknown, so it is arbitrarily placed to the farthest edge in* η*. [25]*

was part of the special expert task force that scrutinized the first ATLAS analysis using the 7 TeV data set. Later with the analysis of the full 2012 data, this turned out to be an upward statistical fluctuation. A somewhat mass sensitive discriminating variable, shown in Figure 5.10, is the transverse mass calculated from the kinematic variables of the dilepton system and the missing transverse momentum:

$$m_{\mathrm{T}} = \sqrt{(E_{\mathrm{T}}^{\ell\ell} + p_{\mathrm{T}}^{\mathrm{miss}})^2 + |\vec{p}_{\mathrm{T}}^{\,\ell\ell} + \vec{p}_{\mathrm{T}}^{\,\mathrm{miss}}|^2}, \tag{5.3}$$

with the dilepton transverse energy computed from its transverse momentum $\vec{p}_{\mathrm{T}}^{\,\ell\ell}$ and mass $m_{\ell\ell}$:

$$E_{\mathrm{T}}^{\ell\ell} = \sqrt{|\vec{p}_{\mathrm{T}}^{\,\ell\ell}|^2 + m_{\ell\ell}^2}. \tag{5.4}$$

The statistical analysis of the data [274, 475] employed a binned likelihood function constructed as the product of Poisson probability terms for the various channels at the two data samples with $\sqrt{s} = 7$ and 8 TeV, including the ten categories based primarily on the photon pair reconstruction quality in the $\mathrm{H} \to \gamma\gamma$, the four lepton flavor combinations (4μ, $2\mu 2\mathrm{e}$, $2\mathrm{e}2\mu$, and 4e) in the $\mathrm{H} \to \mathrm{ZZ}^* \to \ell^+\ell^-\ell'^+\ell'^-$, and the two lepton flavor combinations (μe and eμ, where the leptons are ordered by p_{T}) with zero, one or two jets in the $\mathrm{H} \to \mathrm{W}^{\pm}\mathrm{W}^{\mp *} \to \mathrm{e}^{\pm}\nu_{\mathrm{e}}\mu^{\mp}\nu_{\mu}$ measurements. At $\sqrt{s} = 7$ TeV, searches for the $\mathrm{H} \to \tau^+\tau^-$, $\mathrm{H} \to \mathrm{b}\bar{\mathrm{b}}$ and same-flavor $\mathrm{H} \to \mathrm{W}^{\pm}\mathrm{W}^{\mp *} \to \ell^{\pm}\nu_{\ell}\ell'^{\mp}\nu_{\ell'}$ were also considered.

The measured parameter was the *signal strength* (μ), a scale factor on the total number of events predicted by the SM for the Higgs boson signal, with $\mu = 0$ corresponding to the *background-only hypothesis* (the SM without the Higgs contribution) and $\mu = 1$ to the *signal + background* (the SM). It can be understood as the observed normalized cross section by the SM prediction. The likelihood function also included all parameters needed to model the systematic uncertainties and their correlations.

Statistical tests were performed as a function of the Higgs boson mass. *Exclusion limits* were computed using the *CL_s technique* [476]. A given Higgs mass hypothesis is excluded at the 95% CL if $CL_s = 0.05$ for $\mu = 1$. The *significance* of an excess is quantified by the *local* p_0 value which gives the probability that an excess with a size at least as large as the one observed in data appears in a background-only experiment. The *global* p_0 probability of the largest observed excess in the search was calculated correcting for the *"look-elsewhere" effect* [477] which depends on the mass range covered by the searches, the number and the individual mass resolution of the channels. The ratio of the global to local probabilities is the *trial factor*. These probabilities can also be translated to *significance measured in standard deviations* (s.d. or σ).

Figure 5.12 shows the 95% CL upper limit on the signal strength in the SM Higgs boson search as a function of the Higgs mass hypothesis: only a narrow region around 125 GeV was allowed for $\mu = 1$ in the region left open by the LEP results ($m_{\mathrm{H}} >$ 114 GeV) up to 559 GeV [25]. When calculating the local significance of the excess, the largest value of 5.9σ (local $p_0 = 1.7 \cdot 10^{-9}$) was observed for $m_{\mathrm{H}} = 126.5$ GeV. At this mass, the expected local significance was evaluated at 4.9σ. For the scanned mass range of $110-600$ GeV, the result corresponded to a global observed significance of 5.1σ (global $p_0 = 1.7 \cdot 10^{-7}$). The compatibility with the SM Higgs hypothesis was tested by measuring the observed signal strength for each decay mode. All dibosonic decays gave a consistent signal strength of $\mu \gtrsim 1$, with a combined value of $\mu = 1.4 \pm 0.3$. The mass of the new state was estimated to be 126.0 ± 0.4 (stat.) ± 0.4 (syst.), with the measurements of the $\mathrm{H} \to \gamma\gamma$ and $\mathrm{H} \to \mathrm{ZZ}^* \to \ell^+\ell^-\ell'^+\ell'^-$ modes giving compatible results at the 95% CL as shown by the confidence intervals in the (μ, m_{H}) plane.

Similar results were published at the same time by the CMS experiment [26]. The joint discovery successfully closed a five decade long quest to build a consistent theory that describes the phenomena observed in high-energy experiments probing the properties and interactions of elementary particles at the smallest achievable distances. However, every ending is a beginning. Thus, the detailed exploration of the new particle begun.

5.5 Property measurements in $\mathrm{H} \to \mathrm{ZZ}^* \to \ell^+\ell^-\ell'^+\ell'^-$

The study of the $\mathrm{H} \to \mathrm{ZZ}^* \to \ell^+\ell^-\ell'^+\ell'^-$ process is often called the "golden" channel of Higgs-boson studies as it provides a clean, high-S/B, fully reconstructable final state with excellent kinematic resolution and thus access to the precise measurement of the mass, the width, the spin, the parity and the HZZ couplings. The results in this section correspond to the first detailed studies published by ATLAS [471] after the discovery based on the full Run-1 data sample. The measurement was performed in four channels with different purity, efficiency, and mass resolution: $\mathrm{H} \to \mathrm{ZZ}^* \to \mu^+\mu^-\mu^+\mu^-$ (4μ), $\mu^+\mu^-\mathrm{e}^+\mathrm{e}^-$ ($2\mu 2\mathrm{e}$), $\mathrm{e}^+\mathrm{e}^-\mu^+\mu^-$ ($2\mathrm{e}2\mu$), and $\mathrm{e}^+\mathrm{e}^-\mathrm{e}^+\mathrm{e}^-$ (4e). Here, the lepton pair from the Z decay is typically harder (leading pair), and from the Z^* decay typically softer (subleading pair).

As the most probable value of the transverse momentum of the softest lepton was below 10 GeV at $\sqrt{s} = 7$-8 TeV, the efficient and precise reconstruction of electrons

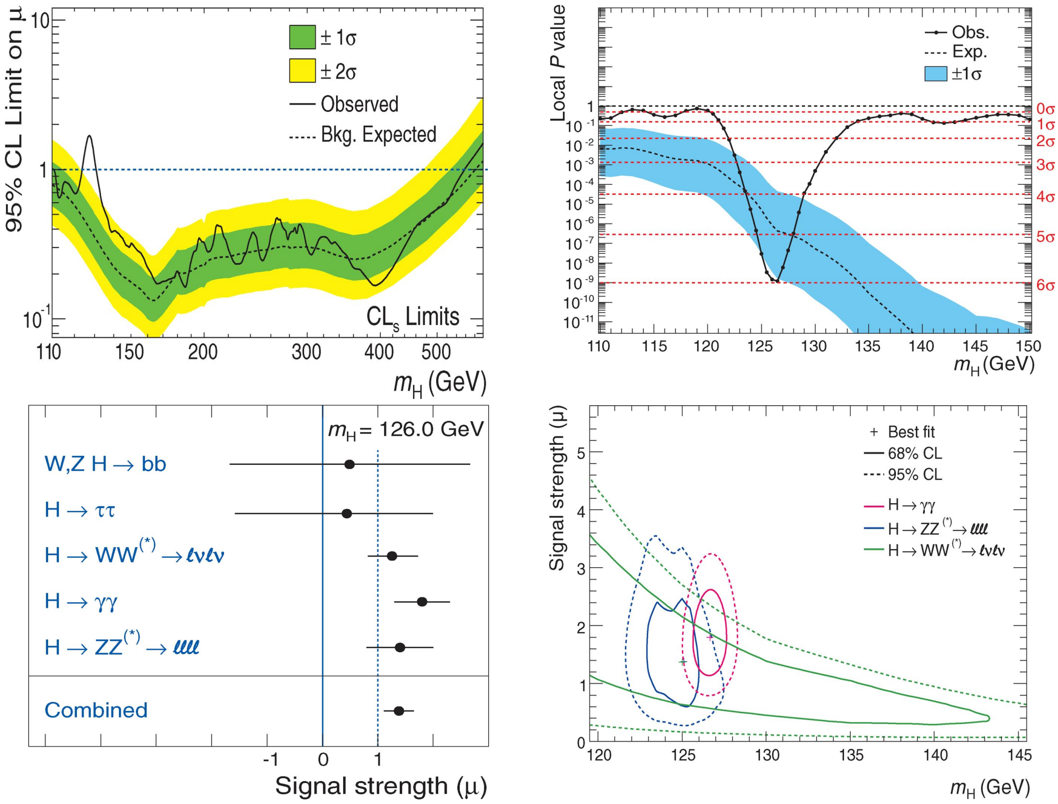

Figure 5.12: *Results of the SM Higgs boson search by the ATLAS experiment based on about 10* fb^{-1} *data collected at* $\sqrt{s} = 7 - 8$ *TeV. (top left) Observed 95% CL upper limit as a function of the SM Higgs boson mass hypothesis* (m_H) *on the signal strength* (μ)*, compared to the expected values in a background-only experiment with* 1σ *and* 2σ *uncertainty bands. (top right) Observed local* p_0 *values as a function of* m_H *quantifying the probability that the data are compatible with the background-only hypothesis, compared to the expected values in signal + background experiments. (bottom left) The Observed signal strength* (μ) *with total uncertainties for each decay mode and combined. (bottom right) Confidence intervals in the* (μ, m_H) *plane for the dibosonic modes illustrating the compatibility of the results. [25]*

and muons in a wide transverse momentum range, starting at the lowest values possible (achieved to be $p_{\mathrm{T}} = 7$ and 6 GeV, respectively) was a key challenge.

As discussed in Section 3.5.1.1.1, electron reconstruction covers the $|\eta| < 2.47$ region. At low transverse momentum, it is especially challenging due to the possibility of large energy loss via bremsstrahlung in the detector material, necessitating the introduction of a dedicated tracking algorithm using a Gaussian Sum Filter (GSF). GSF-enhanced electron reconstruction [268] was first used in the $\mathrm{H} \to \mathrm{ZZ}^* \to \ell^+\ell^-\ell'^+\ell'^-$ analysis [478] in ATLAS, raising the electron track finding efficiency by up to 7% at $p_{\mathrm{T}} < 20$ GeV, as well as improving the track parameter measurements. The latter lead to improved identification performance as well, using more precise track-cluster angular distance and E/p variables, and the estimated energy loss. Of particular interest was also the more accurate estimate of the transverse impact parameter (d_0) and its uncertainty-normalized significance ($d_0/\sigma(d_0)$), which helped to suppress the challenging background contribution from secondary electrons from heavy flavor decays, especially from $\mathrm{Z} \to \mathrm{b}\bar{\mathrm{b}}$ production. Moreover, the invariant mass reconstruction of the Z and Higgs boson candidates became less biased with a better central value and a decreased width of the distribution.

Muon reconstruction was extended to cover the $|\eta| < 2.7$ region for Higgs studies, by including not only *combined muons* with independent measurements in the inner tracking system and the outer muon spectrometer (MS), but also *segment-tagged muons* with partial MS tracks, *calorimeter-tagged muons* having an energy deposit consistent with a minimum ionizing particle (MIP) in the $|\eta| < 0.1$ region which had no MS coverage, and *standalone muons* in the forward region beyond the inner tracking acceptance at $2.5 < |\eta| < 2.7$. A procedure was developed as well to find photons originating from final state radiation off the muons [479] to enhance reconstructed Z boson and Higgs boson mass resolution.

The real-time event selection was based on single and dilepton triggers providing an efficiency of 97% for final states with muons, and almost 100% for 4e. Offline, two opposite-charge same-flavor lepton pairs were required with momentum thresholds of $p_{\mathrm{T}} > 20$, 15, 10, 7 (6) GeV from the hardest to the softest electron (muon) candidate. A cut-based electron identification algorithm (called multi-lepton) was specifically optimized for the analysis (see Figure 3.14). Additional criteria on the relative track and calorimeter isolation with a cone of $R = 0.2$, as well on the transverse impact parameter significance were applied to suppress non-prompt lepton contributions. A minimal angular distance was required $\Delta R > 0.1$ (0.2) between same (opposite) flavor leptons.

In the case of four-muon (4μ) and four-electron (4e) final states, the pairing of leptons into Z (Z^*) candidates need to be defined. The leading lepton pair (defined as the pair with invariant mass closest to m_{Z}) had to be consistent with on-shell Z boson production ($m_{\ell_1\ell_2} = 50 - 106$ GeV, allowing for radiative energy losses), while the requirement for the subleading pair was relaxed to include off-shell Z bosons ($m_{\ell_3\ell_4} = 12 - 115$ GeV for a four-lepton invariant mass $m_{4\ell} < 140$ GeV, with the lower cut increasing with $m_{4\ell}$). A veto against J/ψ production was also applied in the 4μ and 4e channels requiring all opposite-charge same-flavor lepton pairs to have a mass $m_{\ell\ell} > 5$ GeV. The overall acceptance for $m_{\mathrm{H}} = 125$ GeV, was about 40% for 4μ, 25% for 2μ2e, 20% for 4e final states, with a lepton mispairing rate below 10% for 4μ and 4e. A selected $\mathrm{H} \to \mathrm{ZZ}^* \to \mathrm{e}^+\mathrm{e}^-\mathrm{e}^+\mathrm{e}^-$ candidate is shown in Figure 5.13.

For the invariant mass reconstruction of the Higgs boson candidates, FSR photon recovery for the $\mathrm{Z} \to \mu^+\mu^-\gamma$ process was attempted both for collinear and non-collinear photons. A kinematic fit was applied constraining the leading (and for $m_{4\ell} > 190$ GeV, also the subleading) lepton pair mass to m_{Z} assuming a Breit-Wigner lineshape and Gaussian momentum resolution, bringing an improvement of 15% in the $m_{4\ell}$ resolution for Higgs signal events. In simulation the Gaussian mean showed a bias of -0.1 GeV (4μ), -0.2 GeV (2μ2e + 2e2μ) and -0.5 GeV (4e), the Gaussian width was measured to be 1.6 GeV, 1.8 GeV and 2.2 GeV, with a non-Gaussian tail fraction (outside 2σ) of 17%, 20% and 19% of the events. The reconstructed $m_{4\ell}$ mass distribution in the full Run-1 data is shown in Figure 5.14.

5.5.1 Event categorization

To measure the cross section of the various Higgs boson production processes, the selected events were categorized sequentially based on additional objects (jets or leptons) present in the event as illustrated in Figure 5.15.

Jets were reconstructed using the anti-k_t infrared- and collinear-safe sequential recombination jet clustering algorithm [480] with a cone size of $R = 0.4$ using three-dimensional clusters of energy deposited in the calorimeters and corrected for pileup. The jets had to have $p_{\mathrm{T}} > 25$ (30) GeV for $|\eta| < 2.5$ ($2.5 < |\eta| < 5$).

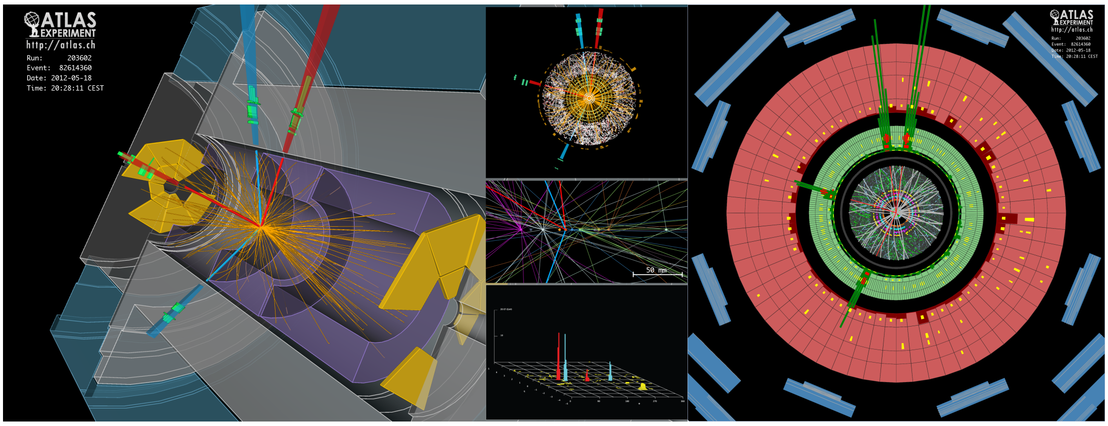

Figure 5.13: *Event display of a* $H \to ZZ^* \to e^+e^-e^+e^-$ *candidate event with a reconstructed mass of 124.5 (124.6) GeV without (with) Z mass constraint in the 2012 ATLAS data at* $\sqrt{s} = 8$ *TeV. The masses of the lepton pairs (colored to red and blue) are 70.6 GeV and 44.7 GeV. The three small displays in the middle show (top) the* $r - \phi$ *view of the event, (middle) a zoom into the vertex region, indicating that the 4 electrons originate from the same primary vertex, and (bottom) a lego plot in* $\eta - \phi$ *indicating the amount of transverse energy measured in the calorimeters. (right) A zoom to the inner region shows in* $r - \phi$ *view the signals in the tracking detectors and the energy deposits in the LAr calorimeter.*

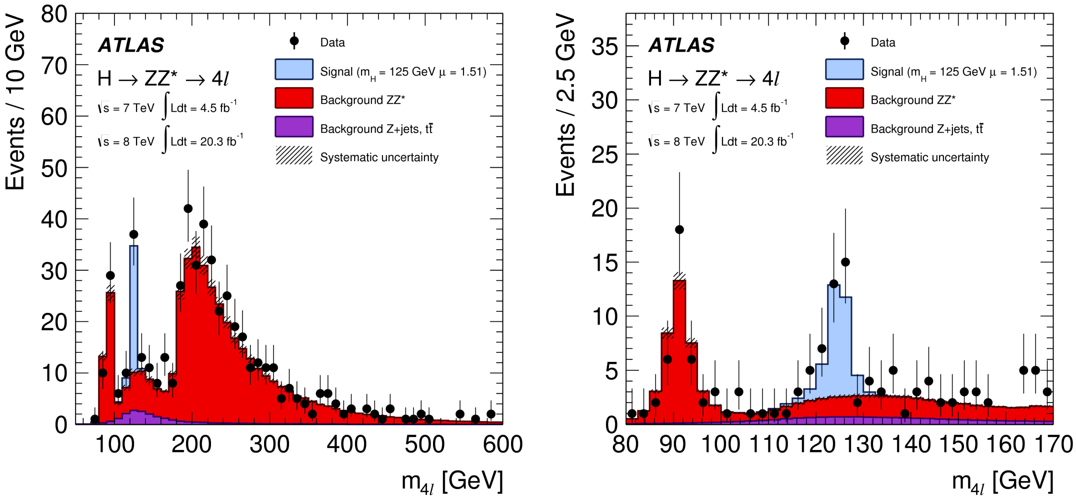

Figure 5.14: *Reconstructed four-lepton mass distribution (left) in the full mass range and (right) zoomed around the observed Higgs signal peak. The data are compared to the predicted background which is dominated by* $\mathrm{pp} \to (\mathrm{Z}^{(*)}/\gamma^*)(\mathrm{Z}^{(*)}/\gamma^*)$ *production (red). The* $Z \to \ell^+\ell^-(\gamma/Z^*) \to \ell^+\ell^-\ell'^+\ell'^-$ *peak at* $m_{4\ell} \approx m_Z$ *served as a control region to verify the analysis procedures. At* $m_{4\ell} > 2m_Z$*, the non-resonant production of two on-shell Z bosons open up. The reducible background containing non-prompt or misidentified leptons (purple) is estimated with data-driven methods and is the highest under the Higgs boson peak (blue). [471]*

The *VBF-enriched* sample was characterized by the presence of at least two jets with the leading jet pair (constructed from the two highest p_T objects) having a mass $m_{jj} > 130$ GeV.

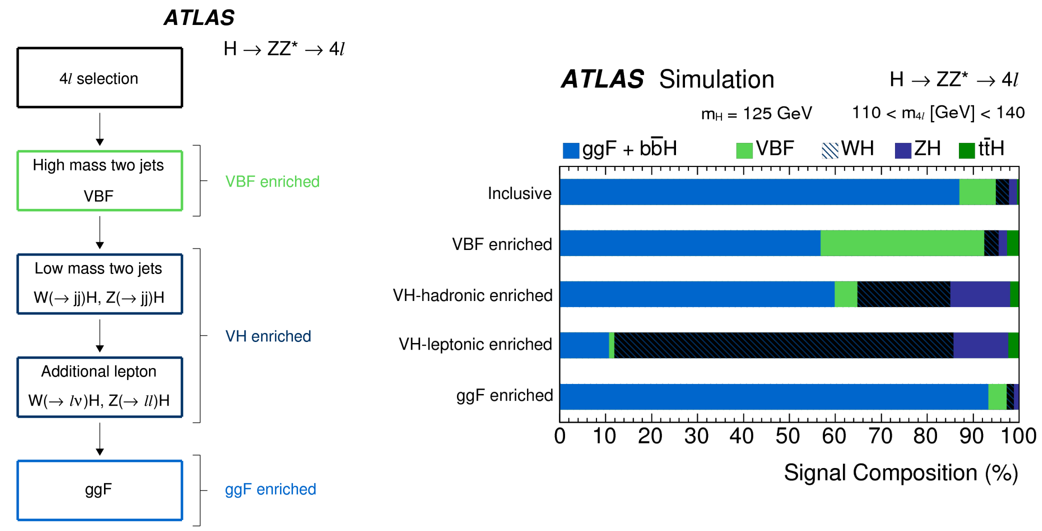

Figure 5.15: *(left) Sequential algorithm to categorize the selected four-lepton events to various samples enriched in vector boson fusion (VBF), hadronic and leptonic VH associated production, or gluon-gluon fusion (ggF) processes. (right) Expected signal composition of the various analysis categories after the full event selection. [471]*

Events with at least two jets but failing the high dijet mass criteria were considered as candidates for VH production followed a hadronic decay of the weak W or Z boson if $40 < m_{jj} < 130$ GeV. A boosted decision tree discriminant was then built using as input five variables to discriminate against ggF production with extra QCD radiation: the mass and pseudorapidity separation of the leading jet pair, the leading and subleading jet p_{T} and the leading jet pseudorapidity. The most sensitive variable was m_{jj} peaking at m_{W} for WH and m_{Z} for ZH production. An event was assigned to the *VH-hadronic enriched* sample if the BDT output $\mathcal{O}_{\mathrm{BDT}_{\mathrm{VH}}} > -0.4$.

The remaining events were examined for the presence of additional electron(s) or muon(s) with $p_{\mathrm{T}} > 8$ GeV to belong to the *VH-leptonic enriched* sample.

Events failing to be classified in any of the above categories formed the *ggF-enriched* sample. The composition of the various samples are also shown in Figure 5.15.

5.5.2 Background determination

An other key ingredient of the measurement is the evaluation of the background rate. Two types of contributions arise: an irreducible component of four-lepton production via the $\mathrm{pp} \to (\mathrm{Z}^{(*)}/\gamma^*)(\mathrm{Z}^{(*)}/\gamma^*)$ process (called for simplicity ZZ^*), and an reducible component containing non-prompt and misidentified leptons, dominantly from $\mathrm{pp} \to \mathrm{Z} + \mathrm{jet(s)}$ (including $\mathrm{pp} \to \mathrm{Zb\bar{b}}$) and $\mathrm{t\bar{t}}$ productions, and a small fraction of WZ with three prompt leptons.

The ZZ^* rate was studied in Monte Carlo simulated samples, see Figure 5.16 for the dominant diagrams. For quark - antiquark annihilation, POWHEG-BOX was used that provides NLO calculation taking into account Z/γ interference and singly-resonant contributions. For gluon fusion, the GG2ZZ [481] generator was used. The uncertainties due to the choice of QCD renormalization and factorization scale, as well as the limited knowledge of the PDFs and α_{s} were parametrized as a function of $m_{4\ell}$. At $m_{4\ell} = 125$ GeV, they amounted to 5% (25%) and 4% (8%), respectively, for the quark-antiquark (gluon fusion) processes.

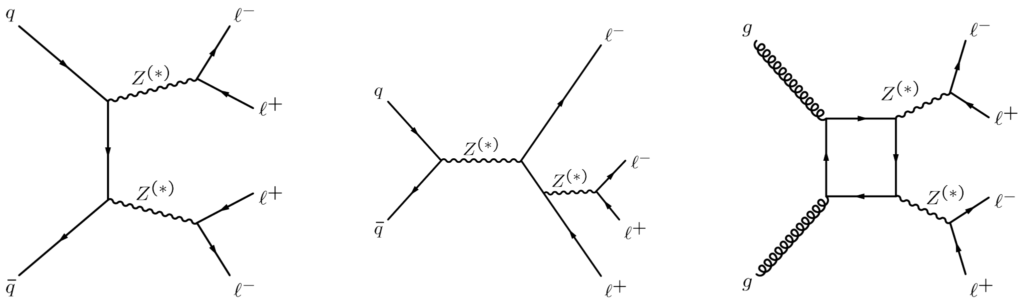

Figure 5.16: *Diagrams of the main irreducible background contributions to the* $H \to ZZ^* \to \ell^+\ell^-\ell'^+\ell'^-$ *measurements: (left) quark - antiquark annihilation, (middle) single-resonant production, and (right) gluon fusion.*

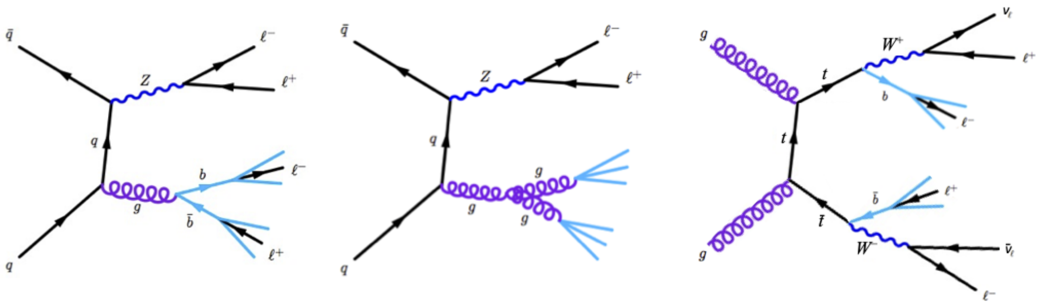

Figure 5.17: *Representative diagrams of the main reducible background contributions to the* $H \to ZZ^* \to \ell^+\ell^-\ell'^+\ell'^-$ *measurements: (left)* $Z + \mathrm{b\bar{b}}$, *(middle) Z + light jets, and (right)* $\mathrm{t\bar{t}}$ *production. Jets originating from b quark fragmentation frequently contain non-prompt leptons produced in the weak decay of a b-flavored hadron via a virtual W boson (Figure 5.2). Jets from gluon or light quark fragmentation can also contain secondary leptons (for example, muons from charged pion and kaon in-flight decays, or electrons from the conversion of photons originating from* π^0 *decays). Moreover, hadrons inside jets can also be misidentified as leptons, giving rise to a so called fake contribution.*

The reducible background contributions, for representative diagrams see Figure 5.17, were measured in data control regions where the analysis cuts were applied on the leading opposite-charge same-flavor lepton pair coming from the on-shell Z boson decay, and inverted and / or relaxed cuts on the subleading pair which was expected to have a higher contamination from non-prompt leptons and fakes. As the background composition depends on the flavor of the subleading pair, different methods were developed for the $\ell^+\ell^-\mu^+\mu^-$ and $\ell^+\ell^-\mathrm{e}^+\mathrm{e}^-$ channels. Most of the estimates relied to some degree on MC simulations which were performed with POWHEG-BOX for the $\mathrm{t\bar{t}}$, Sherpa for the WZ, and Alpgen [482] for the Z + jets background. For the $\mathrm{Z} \to \mathrm{b\bar{b}}$ component, the matrix-element calculation took into account the b quark mass, and special attention was paid to avoid double counting with events where the $\mathrm{b\bar{b}}$ pair was produced in the parton shower.

In the case of $\ell^+\ell^-\mu^+\mu^-$ final states, an unbinned maximum likelihood fit was performed on the mass distribution of the leading dilepton pairs simultaneously in four orthogonal control regions (CRs), with different compositions with respect to the main

$\mathrm{Z} \rightarrow \mathrm{b\bar{b}}$, Z + light-flavored jets, and $\mathrm{t\bar{t}}$ contributions. The CRs were defined to suppress events from Higgs and continuum ZZ^* production, and corrected for any remaining contribution from ZZ^* and WZ based on simulation. The fit results were expressed – with the help of MC-based transfer factors introduced as nuisance parameters of the fit – in a reference control region where all signal region selections were applied except the isolation and impact parameter cuts on the subleading lepton pair. The shapes of the $\mathrm{Z} \rightarrow \mathrm{b\bar{b}}$ and Z + light-flavored jets components were assumed to be a Breit-Wigner function convoluted with a Crystal Ball function, while the $\mathrm{t\bar{t}}$ distribution was modeled by a second order Chebyshev polynomial with shape parameters derived from simulation. The rates from the reference CR to the signal region (SR) were extrapolated using efficiencies derived from simulation (and validated in data CRs) for the isolation and impact parameter selections. The final estimates for the 8 TeV data were 4.0 ± 0.7 and 3.5 ± 0.6 events for the 4μ and $2e2\mu$ channels, respectively.

For the $\ell^+\ell^-\mathrm{e}^+\mathrm{e}^-$ final states [324], in addition to true prompt subleading electrons (e), three main sources of non-prompt or fake contributions were considered: non-prompt electrons from heavy flavor semi-leptonic decays (q) or from photon conversion to $\mathrm{e}^+\mathrm{e}^-$ pairs (γ), and light-flavored hadrons misidentified as electrons, also called fakes (f). Several methods were used and crosschecked with each other to estimate the background rate. They used to a large extent common definitions for reconstruction level objects. Good electron candidates (E) were required to deposit significant fraction of their energy in the first (strip) layer of the calorimeter, have a hit in the first B-layer of the pixel detector (if expected), and either have a significant fraction of high-threshold hits in the TRT for $|\eta| < 2$, or a shower shape compatible with the electron hypothesis for $|\eta| > 2$. The rest of reconstructed electrons (possibly with a very loose additional selection) were considered to have a high probability to come from background (F).

The original method at the start of Run 1, called "reco-truth unfolding" used a $Z + XX$ event selection applying all analysis selection cuts, except the identification, isolation and impact parameter cuts on the subleading lepton pair. With the definitions in the previous paragraph, $2 \times 2 = 4$ data control regions ($XX = EE, EF, FE, FF$) were formed. To extrapolate data rates observed in the CRs to the Higgs signal search region, transfer factors from the "E" and "F" selections to the electron identification in the signal region were computed. It was done using a $Z + X$ selection requiring an on-shell Z candidate (using the criteria applied on the leading lepton pair in the analysis) and an electron candidate using identical definition as for the subleading electrons in the $Z + XX$ region. The main complication arose due to the different composition of the selected object "X" in the $Z + XX$ and $Z + X$ regions which was overcome with the heavy use of MC simulations as each of the four data control regions had $4 \times 4 = 16$ background components ($ee, eq, e\gamma, ef, qe, qq, ...ff$).

5.5.2.1 The $3\ell + X$ method

To alleviate this, the baseline method for the first property measurements utilized a simpler CR called $3\ell + X$, where all analysis selection cuts were applied, except the identification, isolation and impact parameter cuts on the subleading lepton, which – to suppress the ZZ^* contribution – had to have the same charge as its pair. As only a single candidate had relaxed selection, the composition problem was simplified, but the reliance on simulation still remained, which was problematic as fake contributions are very difficult to accurately model.

To extract the composition of the $3\ell + X$ CR, a simultaneous fit was applied to the distributions of the number of B-layer hits and the fraction of high-threshold TRT hits of the subleading electron candidate as shown in Figure 5.18. These variables were first explored in the inclusive electron cross section measurement (Section 5.2).

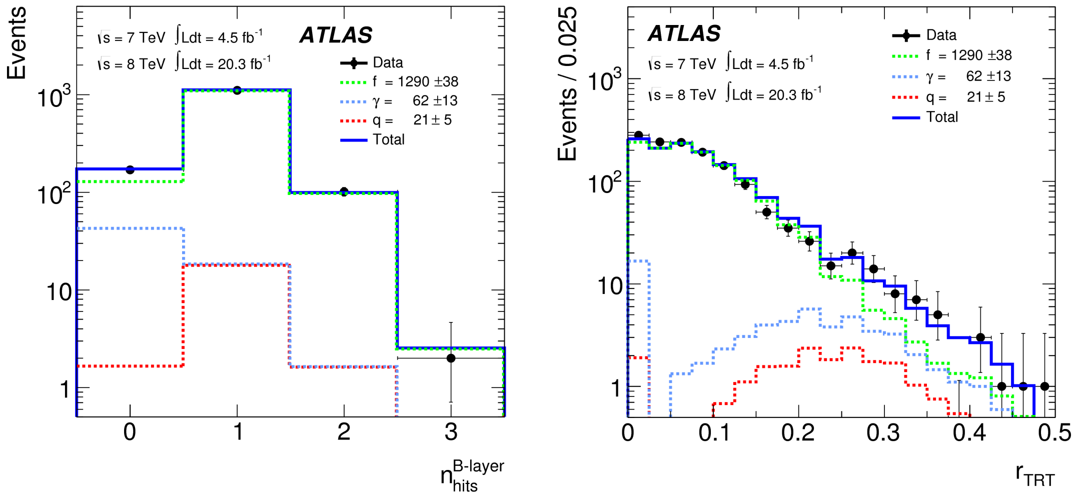

Figure 5.18: *Results of the simultaneous fit to (left) the number of hits in the innermost pixel B-layer and (right) the fraction of high-threshold hits in the TRT in the $3\ell + X$ CR to determine the contributions from non-prompt electrons from heavy flavor hadron decays (q), from photon conversions to e^+e^- pairs (γ) and from light-flavor hadrons (f) in the two $\ell^+\ell^-e^+e^-$ channels (fitted separately but summed in the figures). The total background (solid blue) matches well the data (black dots with statistical uncertainties). [471]*

The small ($< 2\%$) contribution from semi-leptonic heavy flavor decays was constrained based on MC simulation, corrected by data-driven scale factors of 1.2-1.5 (depending on the X electron candidate p_{T}) derived from data – simulation comparisons of the transverse impact parameter distribution in a b-enriched $Z + B$ region that was developed with my supervision. This $Z + B$ region was selected by using a multivariate b jet identification (see below) and had more than 80% purity, leading to an absolute uncertainty on the scale factor of 0.04-0.11.

The template shapes for the various background components (q, γ, f) were derived from simulation using a $Z + X$ selection requiring an on-shell Z candidate (using the criteria applied on the leading lepton pair in the analysis) and an electron candidate using identical definition as for the subleading electron in the $3\ell + X$ region. The derived rates were extrapolated to the signal region using efficiencies from simulation.

To take into account discrepancies between the data and the simulation, correction factors were applied based on specific $Z + X$ samples (CRs) enriched in the different contributions. They were as large as 1.6-2.5 for the fake f component, and close to 1 within 10% (5%) for electrons from conversions γ (heavy-flavor hadron decays q). An additional correction factor of 1.7 based on simulation was also applied for the heavy flavor component to account for the expected difference between same charge (as in the $3\ell + X$ CR) and opposite charge (as in the Higgs signal region) expectations.

The final estimates for the reducible background for the $\mathrm{H} \to \mathrm{ZZ}^* \to \ell^+\ell^-\mathrm{e}^+\mathrm{e}^-$ measurements at the 8 TeV data set were 2.9 ± 0.3 (stat.) ± 0.6 (syst.) and 2.9 ± 0.3 (stat.) ± 0.5 (syst.) for the $2\mu 2e$ and $4e$ channels, respectively.

5.5.2.2 The b-tagging assisted $Z + XX$ method

To minimize the use of background simulations, I led the development of a new transfer factor method with a b-enriched $Z + X$ control region to match the fraction of non-prompt electrons from heavy flavor hadron semi-leptonic decays expected in the $Z+XX$ CR. Here, the simulation was only used to tune the tightness of the b tagging selection which was then varied to account for possible data – simulation discrepancies. A variant of the method introduced a new reconstruction category B for electron candidates matched to a b-tagged jet.

To tag events with heavy flavor production a multivariate b jet identification algorithm was used, called MV1 [483, 484], which combined in an artificial neural network (ANN) the most discriminating variables from the previous taggers including impact parameter and secondary vertex information and a more refined method that aims to reconstruct the full b to c hadron decay chain. The latter exploited the topology of weak b and c hadron decays, searching for a common line connecting the primary vertex to beauty and charm vertices based on a Kalman filter. The selection criteria on the MV1 discriminator was determined by matching (increasing) the heavy flavor fraction of the $Z+X$ CR to that of the $Z+XX$. After having compatible composition of the samples, the transfer factors derived from the data $Z+X$ CRs could be applied directly on the rates observed in the $Z+XX$ CRs, with no reliance on simulation.

A closure test of the method performed on simulated events gave excellent agreement between prediction and true rate within the statistical uncertainties.

As the subleading leptons are expected to be soft, the agreement between the control region compositions improved when jets with $p_{\mathrm{T}} > 10$ GeV were considered for b tagging (instead of the typical ATLAS selection of jets with $p_{\mathrm{T}} > 20$ GeV). The variation of the lower jet p_{T} cut between these values gave the largest contribution (20-25%) to the uncertainty of the background estimate, followed by the variation of the MV1 cut (11%) and the choice of the $Z+XX$ control region definition (6-12%). The effect of introducing the new B category (3%) was small. Possible differences in the b tagging efficiency between data and simulation were well within the applied variation of the MV1 cut.

This was the only method to estimate the $\ell^+\ell^-\mathrm{e}^+\mathrm{e}^-$ reducible background event rate that had no (or minimal) dependence on the simulation modeling. The predictions on the reducible background rates, 3.2 ± 0.2 (stat.) ± 0.9 (syst.) and 2.9 ± 0.2 (stat.) ± 0.8 (syst.) for the $2\mu 2e$ and $4e$ channels, agreed well (within 0-10%) with the baseline estimates from the $3\ell+X$ method, after the heavy flavor contribution in the latter was corrected using the more than 80% pure $Z+B$ control region.

The reducible background shape was taken from the $3\ell+X$ control region weighted by the transfer factors. The shape uncertainty was defined by the differences to the shapes obtained using the alternative $Z+XX$ control regions.

The same method was applied in the differential cross section measurements for each variable of interest. For the jet-related variables, an extra uncertainty was applied on the ZZ^* and WZ contributions, comparing the simulation predictions to the data in the $m_{4\ell} > 190$ GeV region where they are dominant, and then propagating the observed shape differences to the uncertainty.

The reducible background calculation for the ggF, VBF, VH-hadronic and VH-leptonic enriched categories was based on the fraction of events expected from simulation with an additional uncertainty based on the validation of the fractions from $3\ell+X$ control region.

5.5.3 Higgs mass and $\mathrm{H} \to \mathrm{ZZ}^* \to \ell^+\ell^-\ell'^+\ell'^-$ inclusive signal strength

To extract the mass and the inclusive signal strengths, a BDT discriminant ($\mathcal{O}_{\mathrm{BDT}_{\mathrm{ZZ}^*}}$) was built to separate the inclusive Higgs boson signal from the irreducible ZZ^* background combining information from the four-lepton transverse momentum $p_{\mathrm{T}}^{4\ell}$ and pseudorapidity $\eta^{4\ell}$, and a matrix element (ME) discriminant defined as

$$D_{\mathrm{ZZ}^*} = \ln\left(\frac{|\mathcal{M}_{\mathrm{H}}|^2}{|\mathcal{M}_{\mathrm{ZZ}}|^2}\right), \tag{5.5}$$

where $\mathcal{M}_{\mathrm{H}}$ corresponds to the matrix element for the Higgs signal process with spin-parity $J^P = 0^+$ and $m_{\mathrm{H}} = m_{4\ell}$, while $\mathcal{M}_{\mathrm{ZZ}}$ is the matrix element for the ZZ^* background process, both computed at LO using MadGraph 5. The input variable and the discriminant distributions are shown in Figure 5.19.

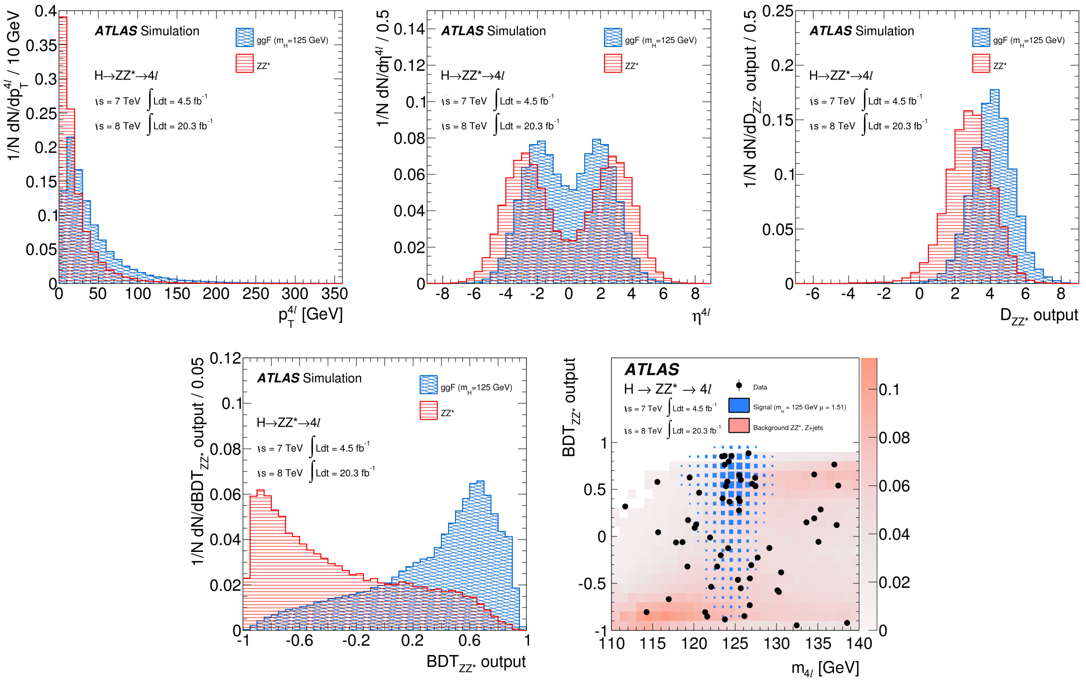

Figure 5.19: *(top) Input variables to compute the $\mathcal{O}_{\mathrm{BDT}_{ZZ^*}}$ discriminant: the four-lepton (left) transverse momentum and (middle) pseudorapidity, and (right) the D_{ZZ^*} matrix element discriminant for events satisfying the inclusive event selection requirements and having $115 < m_{4\ell} < 130$ GeV for the simulated ggF Higgs signal with $m_H = 125$ GeV and the irreducible ZZ^* background. (bottom left) Distribution of the $\mathcal{O}_{\mathrm{BDT}_{ZZ^*}}$ discriminant in simulation and (bottom right) the distribution of the selected events in data compared to the expected signal and background in the $(m_{4\ell}, \mathcal{O}_{\mathrm{BDT}_{ZZ^*}})$ plane. [471]*

The baseline method for the mass measurement used a two-dimensional (2D) fit to $m_{4\ell}$ and $\mathcal{O}_{\mathrm{BDT}_{\mathrm{ZZ}^*}}$ in the mass range $m_{4\ell} = 110 - 140$ GeV. The observed data distribution is shown in Figure 5.19. The detailed mathematical model was presented in Ref. [471]. The mass measurement results were cross checked with a simpler 1D fit to the $m_{4\ell}$ distribution, as well as with a method using per-event resolution which was also exploited to derive an upper limit of the Higgs boson total width (Section 5.5.6).

A likelihood function $\mathcal{L}(m_{\mathrm{H}}, \mu, \vec{\theta})$ was built using the smoothed 2D probability density functions of the Higgs signal $\mathcal{P}(m_{4\ell}, \mathcal{O}_{\mathrm{BDT}_{\mathrm{ZZ}^*}}|m_{\mathrm{H}})$ parametrized as a smooth function of the Higgs mass and of each (b) source of background $\mathcal{P}_b(m_{4\ell}, \mathcal{O}_{\mathrm{BDT}_{\mathrm{ZZ}^*}})$. The likelihood was a product of Poisson probabilities over the years (i) and the search channels (j) of observing N_{ij} events for the given signal and background expectations

$(\mu \cdot S_{ij}(m_{\mathrm{H}}, \vec{\theta}) + B_{ij}(\vec{\theta}))$ multiplied by the product of the values of the probability densities for all observed events formed using the signal and background 2D probability densities. The signal predictions were scaled by the global signal strength (μ) and the effect of correlated and uncorrelated systematic uncertainties were included via the introduction of a nuisance parameter for each ($\vec{\theta}$). The confidence intervals were based on profile likelihood ratios that depend on the parameter(s) of interest only. For details of the statistical method, see Refs. [475, 485].

The results are presented in Figure 5.20. Single channel discovery was achieved at 8.2σ at $m_{\mathrm{H}} = 125.36$ GeV, well above the expected 5.8σ due to an excess of events

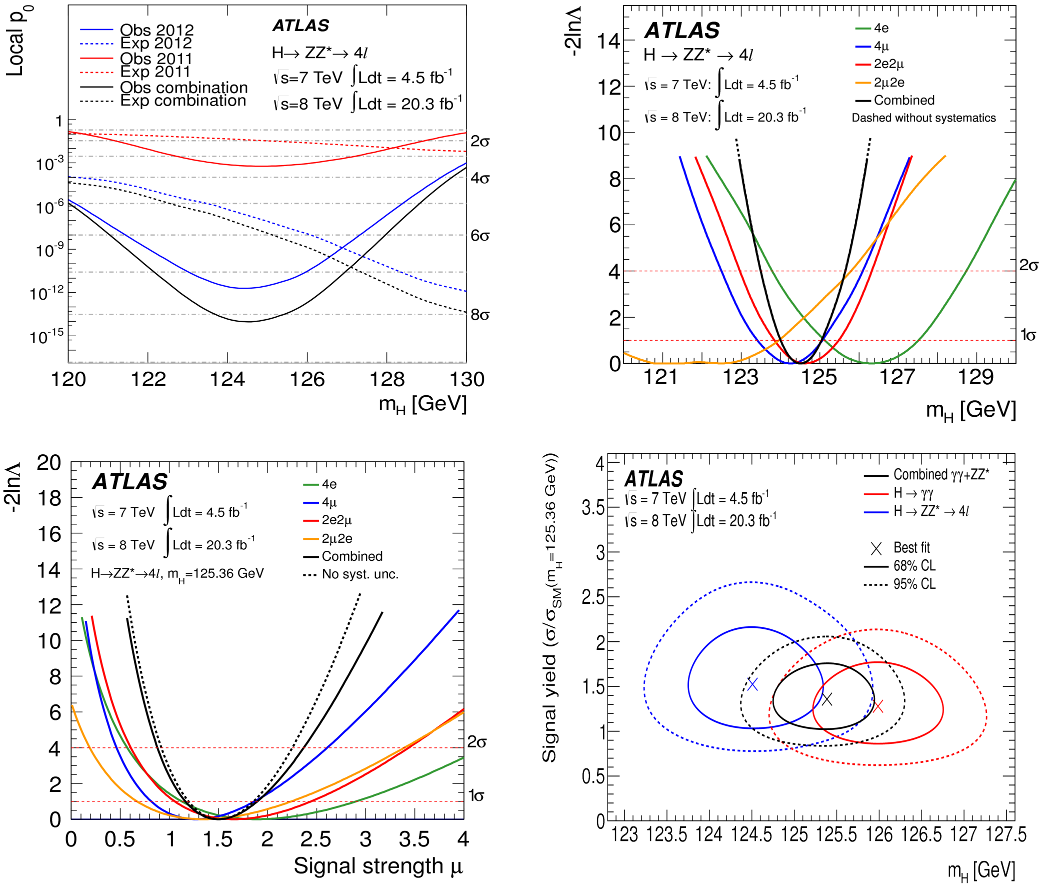

Figure 5.20: *Results of the first SM Higgs boson property measurements by the ATLAS experiment based on the full Run-1 data collected at* $\sqrt{s} = 7 - 8$ *TeV in the* $H \to ZZ^* \to \ell^+\ell^-\ell'^+\ell'^-$ *process [471]. (top left) Observed local* p_0 *values as a function of the Higgs mass* (m_H) *quantifying the probability that the data are compatible with the background-only hypothesis, compared to the expected values in signal + background experiments for the two years separately and combined. The profile likelihood as a function of (top right)* m_H *and (bottom left) the inclusive signal strength* (μ) *for the individual channels and their combination. (bottom right) Confidence intervals in the* (μ, m_H) *plane (blue), compared to the results from the* $H \to \gamma\gamma$ *analysis (red). The combined result is compatible with the SM prediction of* $\mu = 1$ *[486]. The statistical upper fluctuation in the* $H \to \gamma\gamma$ *measurement at the time of discovery (Figure 5.12) has mostly disappeared.*

above the SM expectation for Higgs boson production. The measured mass was

$$m_{\mathrm{H}} = 124.51 \pm 0.52 \text{ GeV}$$

and the signal strength at this value

$$\mu = 1.66^{+0.39}_{-0.34} \text{ (stat.) } ^{+0.21}_{-0.14} \text{ (syst.).} \tag{5.6}$$

All of the four final states observed $\mu > 1$, with the best sensitivity reached for the 4μ channel and the weakest for the $4e$ channel. The measurement was statistics limited.

The leading uncertainty on the measured Higgs mass came from the muon momentum scale (0.04% for 4μ, 0.02% for $2\mu2e$, 0.015% for $2e2\mu$), and the electron energy scale (0.04% for $2\mu2e$, 0.025% for $2e2\mu$, 0.04% for $4e$), the contribution from the imperfect knowledge of the background rates was negligible. Representative examples of the momentum and energy scale uncertainty are shown in Figure 5.21 as a function of p_{T}. When all final states were combined, the contributions to the mass measurement were 0.03% and 0.01%, respectively. The larger impact of the muon momentum scale is explained by the larger weight of the muon final states in the combined fit.

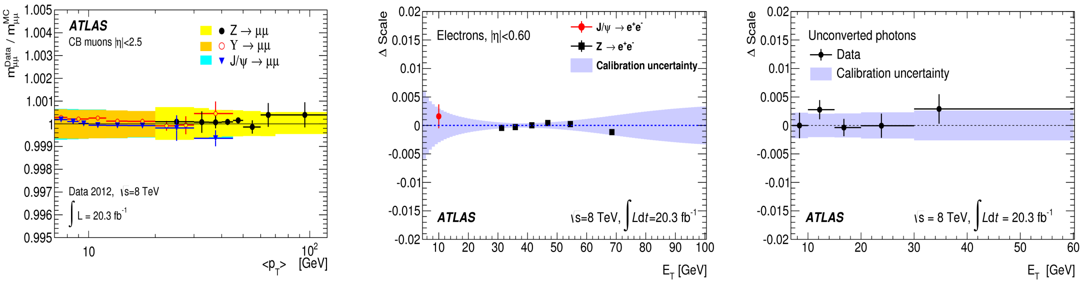

Figure 5.21: *Illustration of (left) the dimuon mass scale uncertainty as a function of the mean muon* p_{T} *of the pair; and the energy scale uncertainty for (middle) electrons in the* $|\eta| < 0.6$ *region and (right) unconverted photons as a function* E_{T}. *[486]*

The mass measurement was combined with the result from the H → $\gamma\gamma$ analysis, which has a larger statistical power and somewhat better mass resolution. Though the energy scale and resolution of photons does not exceed that of the charged leptons (Figure 5.21), only two objects contribute to the mass reconstruction. The 95% confidence intervals touch for the two channels (Figure 5.20) and the combined results are compatible with $\mu = 1$.

The uncertainty on the inclusive signal strength was dominated by the theoretical uncertainties due to the QCD scale (6%), the PDFs and α_{s} (6%), the H → ZZ branching ratio (4%), the Higgs boson p_{T} spectrum (< 1%), the ZZ* background rate (4% for $m_{4\ell} \approx 125$ GeV). The most important experimental systematic uncertainties were related to the efficiencies of lepton (electron and muon) reconstruction and identification (1.6% and 1.5%), the isolation and impact parameter selection (0.5% and 0.2%), and the trigger (< 0.2% and 1.2%). The reducible background determination also contributed (1.3% and 1.2% for subleading electrons and muons). The largest single experimental uncertainty came from the luminosity measurement (1.8% for 2011, 2.8% for 2012) demonstrating the need for precise luminometry at the LHC (Chapter 4).

5.5.4 Higgs couplings

Following the recommendations of the LHC Higgs Cross Section Working Group [462], coupling modifiers were derived assuming a narrow Higgs boson with a mass of $m_{\mathrm{H}} =$

125.36 GeV (the combined ATLAS value of the time). The computation relied on a LO tree-level-motivated framework using the SM tensor structure (i.e. imposing that the state is a CP-even scalar). In the zero-width approximation, the cross section from an initial state (i) to a final state (f) is factorized and thus written as

$$\sigma \cdot B(i \to \mathrm{H} \to f) = \sigma_i \cdot \Gamma_f / \Gamma_\mathrm{H}, \tag{5.7}$$

where σ_i is the production cross section through the initial state i, Γ_f is the partial decay width and Γ_H is the total Higgs width.

As the κ-framework [462] introduces a coupling modifier for each particle coupling to the Higgs (as also shown in Figure 5.6), the cross section of ggF production leading to the ZZ^* final state has the form:

$$\sigma \cdot B(\mathrm{gg} \to \mathrm{H} \to \mathrm{ZZ}^*) = \sigma_\mathrm{SM}(\mathrm{gg} \to \mathrm{H}) \cdot B_\mathrm{SM}(\mathrm{H} \to \mathrm{ZZ}^*) \cdot \kappa_\mathrm{g}^2 \cdot \kappa_\mathrm{Z}^2 / \kappa_\mathrm{H}^2, \tag{5.8}$$

where κ_g, κ_Z, κ_H are the scale factors for the Higgs couplings to g, Z and for the total Higgs width. The SM is recovered when all κ_i modifiers are equal to 1.

To measure the signal strengths for the different production modes, they were grouped based on the coupling that acts in a given process. The production modes ggF, $\mathrm{t\bar{t}H}$ and $\mathrm{b\bar{b}H}$ are affected by the coupling modifiers κ^t and κ^b, while VBF and VH by κ^W and κ^Z.

In the following, due to statistical limitations of the data, it is assumed that there are only two coupling modifiers, a common fermionic and a common bosonic value, thus

$$\kappa^\mathrm{F} = \kappa^\mathrm{b} = \kappa^\mathrm{t}, \qquad \kappa^\mathrm{V} = \kappa^\mathrm{W} = \kappa^\mathrm{Z}. \tag{5.9}$$

The coupling modifier ratio is then defined as

$$\lambda_\mathrm{FV} \equiv \kappa^\mathrm{F} / \kappa^\mathrm{V}. \tag{5.10}$$

Then a common signal strength can be assigned to each group: $\mu_{\mathrm{ggF+t\bar{t}H+b\bar{b}H}} \propto \kappa^\mathrm{F}$ and $\mu_\mathrm{VBF+VH} \propto \kappa^\mathrm{V}$, and the ratio becomes $\lambda_\mathrm{FV} = \mu_{\mathrm{ggF+t\bar{t}H+b\bar{b}H}} / \mu_\mathrm{VBF+VH}$. To extract these values, the categorized analysis was pursued with the four subsamples (Figure 5.15).

To improve the precision of the signal strength measurement, a multivariate discriminator was introduced to separate VBF and ggF production modes using the same input variables as for the discriminator $\mathcal{O}_{\mathrm{BDT}_\mathrm{VH}}$ benefiting from the observation that the leading jets tagging VBF production have larger jet p_T and $|\eta|$, as well as larger dijet mass and pseudorapidity separation than jets from QCD radiation. The BDT output $\mathcal{O}_{\mathrm{BDT}_\mathrm{VBF}}$ distributions are shown in Figure 5.22, as well as the VBF signal purity as a function of $\mathcal{O}_{\mathrm{BDT}_\mathrm{VBF}}$. Only one VBF signal candidate is observed in the $m_{4\ell} = 110$ - 140 GeV range with a high $\mathcal{O}_{\mathrm{BDT}_\mathrm{VBF}}$ value, corresponding to a high VBF purity around 60%.

For the signal strength extraction, two-dimensional probability density functions were utilized in the ggF and VBF enriched categories: $\mathcal{P}_\mathrm{ggF}(m_{4\ell}, \mathcal{O}_{\mathrm{BDT}_{\mathrm{ZZ}^*}} | m_\mathrm{H})$ and $\mathcal{P}_\mathrm{VBF}(m_{4\ell}, \mathcal{O}_{\mathrm{BDT}_\mathrm{VBF}} | m_\mathrm{H})$, while one-dimensional functions for the VH-hadronic and VH-leptonic enriched categories: $\mathcal{P}_\mathrm{VH-h}(m_{4\ell} | m_\mathrm{H})$ and $\mathcal{P}_\mathrm{VH-l}(m_{4\ell} | m_\mathrm{H})$. The introduction of a second dimension for the VBF and ggF categories reduced the expected uncertainty by 25% and 6%, respectively, on $\mu_\mathrm{VBF+VH}$. While adding the VH enriched regions with the 1D functions brought about 10% improvement.

The theoretical systematic uncertainty on the expected yields in the different categories arose mainly due to the jet requirements [462, 487]. It was the largest for ggF production reaching 20.4% for the VBF- and VH-hadronic enriched categories, 12% for

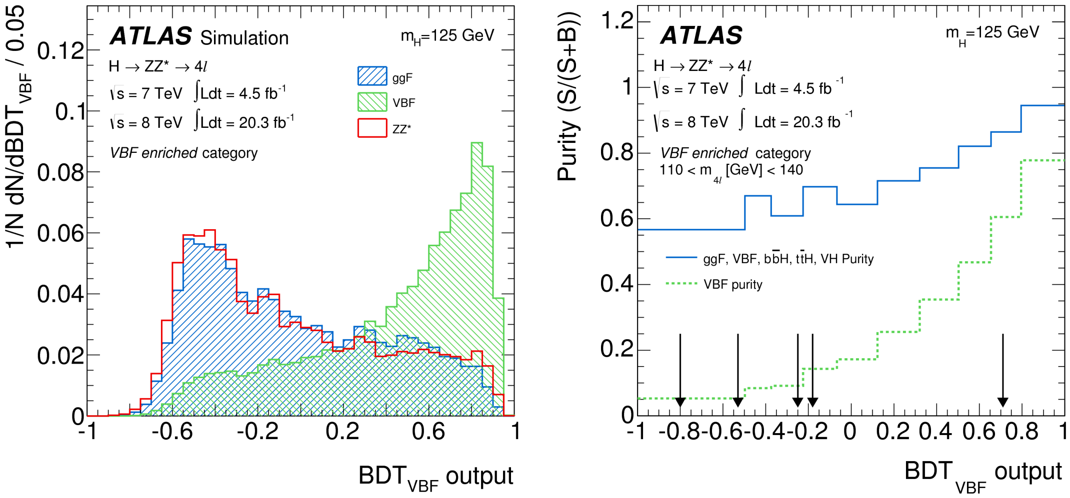

Figure 5.22: *(left) Expected distribution of the BDT output ($\mathcal{O}_{\mathrm{BDT}_{\mathrm{VBF}}}$) to discriminate VBF and ggF Higgs production for the irreducible ZZ* background, for ggF and VBF Higgs production. (right) The purity of the sample for VBF and inclusive Higgs production as a function of $\mathcal{O}_{\mathrm{BDT}_{\mathrm{VBF}}}$. The discriminant values for selected events in data are marked by black arrows. [471]*

the VH-leptonic and ggF-enriched categories. It was subdominant for Higgs production via quark-induced processes (4-8%) and for the irreducible ZZ* background (2-8%). The modeling of the underlying event contributed for the VBF- and VH-hadronic enriched categories (1.4-7.5% for ggF and VBF production modes). The main experimental uncertainty was due to the jet energy scale: it amounted to about 10% for the VBF-enriched, 8% for the VH-hadronic, and 1.5% for the VH-leptonic and ggF-enriched category. There was an anti-correlation in the rates among the categories as the energy scale change causes events to migrate from one subsample to the other. Jet energy resolution had only a small effect (0-1.8%). For the VH-enriched category, the additional lepton selection criteria introduced further uncertainty (5% for VH and 1% for ggF and VBF production modes). The total uncertainty varied between 5.5-8.8% for VH, 6.4-10.7% for VBF and 12.2-23.7% for ggF, 4.1-12.9% for background ZZ* simulation.

The results are shown in Figure 5.23 and are statistically limited. There was a downward fluctuation in the data for the VH enriched category (no event observed, with

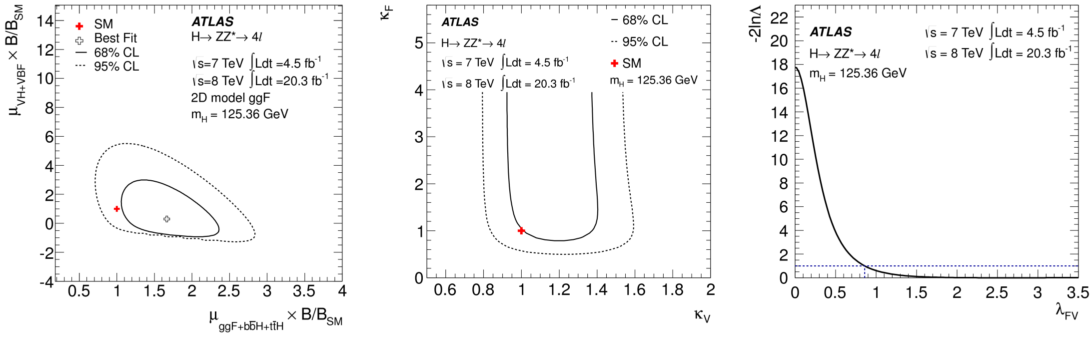

Figure 5.23: *Confidence intervals in (left) the ($\mu_{\mathrm{VBF+VH}} \times B/B_{\mathrm{SM}}$, $\mu_{\mathrm{ggF}+\mathrm{t\bar{t}}H+\mathrm{b\bar{b}}H} \times B/B_{\mathrm{SM}}$) and (middle) the ($\kappa^{\mathrm{F}}$, κ^{V}) planes. (right) The profile likelihood as a function of the ratio of the fermionic and bosonic coupling modifier λ_{FV}. [471]*

about 1.2 expected), while an upward fluctuation for ggF. The observed signal strengths multiplied by a branching ratio scale factor for the four-lepton channel (B/B_{SM}) were

$$\mu_{\mathrm{ggF+t\bar{t}H+b\bar{b}H}} \times B/B_{\mathrm{SM}} = 1.7^{+0.5}_{-0.4},$$

$$\mu_{\mathrm{VBF+VH}} \times B/B_{\mathrm{SM}} = 0.3^{+1.6}_{-0.9},$$

both statistically limited. As the measured $\mu_{\mathrm{VBF+VH}}$ value was consistent with zero, κ^{F} remained unbounded from above. The measurement was consistent with the SM.

When the two values were constrained to be the same, the overall signal strength became

$$\mu \times B/B_{\mathrm{SM}} = 1.44^{+0.34}_{-0.31}(\mathrm{stat.})^{+0.21}_{-0.11}(\mathrm{syst.}),$$

slightly improving the precision compared to the measurement using the inclusive selection (Eq. 5.6). To remove the dependence on the decay mode, the signal strength ratio was also derived:

$$\mu_{\mathrm{VBF+VH}}/\mu_{\mathrm{ggF+t\bar{t}H+b\bar{b}H}} = 0.2^{+1.2}_{-0.5}.$$

The observed value of λ_{FV} was 4σ away from zero.

5.5.5 Total, fiducial and differential cross sections

The extracted signal strength (μ) can be used to compute the observed cross section × branching ratio:

$$(\sigma_{\mathrm{tot}} \cdot B)_{\mathrm{obs}} = \frac{\mu \cdot N^{\mathrm{sig}}_{\mathrm{fid,exp}}}{\epsilon_{\mathrm{tot}} \cdot \int \mathcal{L}} = \frac{1}{\mathcal{A}_{\mathrm{fid}}} \cdot \frac{\mu \cdot N^{\mathrm{sig}}_{\mathrm{fid,exp}}}{\epsilon_{\mathrm{fid}} \cdot \int \mathcal{L}} = \frac{(\sigma_{\mathrm{fid}} \cdot B)_{\mathrm{obs}}}{\mathcal{A}_{\mathrm{fid}}} \tag{5.11}$$

Measuring the total cross section (σ_{tot}) requires an acceptance correction ($\mathcal{A}_{\mathrm{fid}}$) from the measured to the total phase space based on a theoretical model, and thus introduces a potentially large extrapolation uncertainty to the measurement. This motivates the study of the fiducial cross section (σ_{fid}) which corresponds to the experimentally explored phase space.

ATLAS has measured the total cross section of Higgs production via the $\mathrm{H} \to \mathrm{ZZ}^* \to \ell^+\ell^-\ell'^+\ell'^-$ and $\mathrm{H} \to \gamma\gamma$ channels at $\sqrt{s} = 7$, 8 and 13 TeV as shown in Figure 5.24. The values at 7 and 8 TeV have large statistical uncertainties and are somewhat higher than the updated theoretical predictions [453]. They are compatible with the SM within $\sim 1.5\sigma$. The 13 TeV measurements are more precise and show an excellent agreement.

The cross section for a fiducial phase space, which closely follows the experimental selections described for the inclusive analysis above and also requires $m_{4\ell} = 118-129$ GeV (optimized for the lowest expected uncertainty on the cross section) was measured [488]:

$$\sigma_{\mathrm{fid}} = 2.11^{+0.53}_{-0.47}(\mathrm{stat.}) \pm 0.08(\mathrm{syst.})\ \mathrm{fb},$$

and compared to the theoretical prediction [462] for a Higgs boson mass of 125.4 GeV:

$$\sigma^{\mathrm{theory}}_{\mathrm{fid}} = 1.3 \pm 0.13\ \mathrm{fb}.$$

The differential fiducial cross section of $\mathrm{H} \to \mathrm{ZZ}^* \to \ell^+\ell^-\ell'^+\ell'^-$ was also extracted using a bin-by-bin unfolding (similar to the one described in Section 5.2). A selection of the results – dominated by the statistical uncertainty – is presented in Figure 5.25. The largest sources of systematic uncertainty are the estimate of the reducible background, the theoretical prediction for the irreducible ZZ^* background, the jet energy scale and

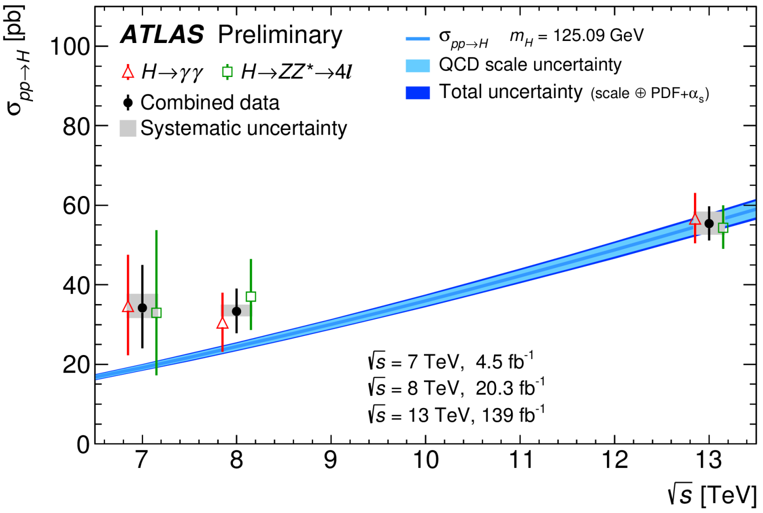

Figure 5.24: *Observed total Higgs boson production cross sections as a function of the pp center of mass energy* ($\sqrt{s}$)*, extracted from the* $H \to \gamma\gamma$ *and* $H \to ZZ^* \to \ell^+\ell^-\ell'^+\ell'^-$ *measurements, with systematic and total uncertainties. The theoretical uncertainty corresponds to the scale uncertainty – estimating the effects of missing higher order corrections – summed in quadrature with the PDF and* α_s *uncertainties. It is partially correlated across values of* $\sqrt{s}$*.*

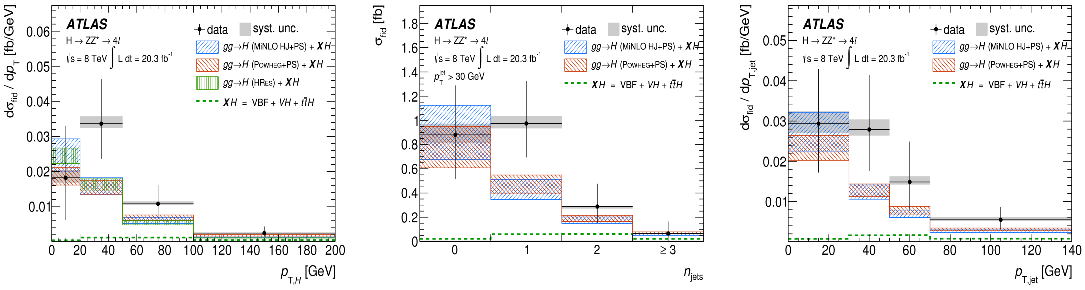

Figure 5.25: *Differential cross sections of* $H \to ZZ^* \to \ell^+\ell^-\ell'^+\ell'^-$ *production as a function of (left) the Higgs* p_T*, (middle) the jet multiplicity, and (right) the leading jet* p_T*. The ATLAS measurements are compared to theoretical predictions. The VBF, VH,* $\mathrm{t\bar{t}}H$ *predictions (dashed histogram) were added to the ggF theoretical predictions, the latter having a relative total contribution of 87.3% at* $\sqrt{s} = 8$ *TeV. All predictions were normalized to the most precise inclusive cross section prediction of the time [462]. The data points are shown with systematic and total uncertainties, the theoretical calculations with total uncertainty. [488]*

resolution (including the flavor composition), and the relative fraction of the different production modes. Other uncertainties include the luminosity, the lepton trigger, reconstruction and identification efficiencies, and the Higgs boson mass.

The Higgs p_T distribution is sensitive to the Higgs production mechanisms, the spin and CP quantum numbers and is used to test pQCD. The Higgs rapidity can be used to probe the proton PDFs. The subleading dilepton mass and the Higgs decay angle are sensitive to the Lagrangian structure of Higgs interaction (spin, CP, higher dimensional operators). The jet multiplicity and p_T distributions provide information on quark and gluon radiation, as well as the relative fraction of the production modes.

The compatibility of the data with various calculations of ggF production was tested: POWHEG (NLO), POWHEG interfaced to MINLO (Multiscale Improved NLO, providing NLO prediction for jet variables for H + 1 jet final states) and HRES2 (NNLO+NNLL, with b quark mass effects up to NLO+NLL, but no showering and QED final state radiation). The p values varied between 0.16 and 0.6, showing no significant discrepancy and no preference among the HO predictions [488].

5.5.6 Higgs total width

In the SM, the Higgs boson total width (Γ_H) is around 4 MeV, more than two orders below the experimental mass resolution of $\sim 1-2$ GeV, thus the direct measurement of the Higgs boson lineshape is not feasible. The total width was probed by searching for the invisible decays of the Higgs boson [489], as well as in global fits to the Higgs production data to extract the couplings [490].

The most precise determination comes from the study of the pp → (H) → ZZ process (with or without Higgs production) at the high-mass off-peak region of $\sqrt{\hat{s}} > 2m_\mathrm{Z}$, where interference effects play an important role. The dominant LO diagrams to consider are ggF Higgs production followed by a decay to a pair of Z bosons (gg → H → ZZ), gluon-induced continuum gg → ZZ process via a fermion box, and quark-induced $q\bar{q} \to$ ZZ (Figure 5.16). For the gg → H → ZZ signal, the on-shell (μ) and off-shell (μ_off) signal strengths at an energy of $\hat{s}$ can be written as

$$\mu \equiv \frac{\sigma_\mathrm{H}^\mathrm{obs}}{\sigma_\mathrm{H}^\mathrm{SM}} = \frac{\kappa_\mathrm{g}^2 \cdot \kappa_\mathrm{Z}^2}{\Gamma_\mathrm{H}/\Gamma_\mathrm{H}^\mathrm{SM}}, \qquad \mu_\mathrm{off}(\hat{s}) \equiv \frac{\sigma_\mathrm{H,off}^\mathrm{obs}(\hat{s})}{\sigma_\mathrm{H,off}^\mathrm{SM}(\hat{s})} = \kappa_\mathrm{g,off}^2(\hat{s}) \cdot \kappa_\mathrm{Z,off}^2(\hat{s}), \tag{5.12}$$

using the κ coupling modifier framework introduced in Section 5.5.4. Here σ_H is the cross section of the gg → H → ZZ process with an on-shell Higgs boson, and $\sigma_\mathrm{H,off}$ belongs to off-shell gg → $\mathrm{H}^\star$ → ZZ. Assuming identical coupling modifiers on and off shell, the total width can be measured. The running $\kappa_\mathrm{g}(\hat{s})$ is sensitive to new physics entering the loop, and could be probed in the high m_ZZ region. The available statistics of Run 1, however, only allowed to place an upper limit on Γ_H, under the less stringent assumption that the on-shell couplings are not larger than the off-shell:

$$\Gamma_\mathrm{H}/\Gamma_\mathrm{H}^\mathrm{SM} \leq \mu_\mathrm{off}/\mu. \tag{5.13}$$

The extraction was performed under the condition that the off-shell signal kinematics are not affected considerably by the new physics and that the background shape is not modified. As no higher order calculations were available for the gg → ZZ background, the measurement was performed as a function of the unknown K-factor, introducing $R_{\mathrm{H}^\star}^\mathrm{B}$ as the ratio of the unknown K-factor for gg → ZZ to the known gg → $\mathrm{H}^\star$ → ZZ signal K-factor [491] for the NNLO / LO cross section ratio including NLO EW corrections. As the signal scale factor (~ 2) only mildly depends on the energy ($< 10\%$) in the mass range considered ($m_{4\ell} = 220-1000$ GeV), $R_{\mathrm{H}^\star}^\mathrm{B}$ was considered constant and varied in the range $0.5-2$. To minimize the theoretical uncertainties, the measurement was inclusive in jet multiplicity and optimized to minimize dependence on the boost of the ZZ system.

A matrix element based discriminator (Figure 5.26) was exploited [492] to extract the upper limit on the off-shell signal strength. It varied between $5.1-9.8$ depending on the background K-factor and the assumption for the VBF Higgs production off-shell signal strength. Using the on-shell signal strength discussed in Section 5.5.3, the total Higgs width was determined in a profile likelihood fit. The 95% CL limit on the normalized width $\Gamma_\mathrm{H}/\Gamma_\mathrm{H}^\mathrm{SM}$ was derived, combining the $\mathrm{H} \to \mathrm{ZZ}^* \to \ell^+\ell^-\ell'^+\ell'^-$ measurements with the less sensitive $\mathrm{H} \to \mathrm{ZZ}^* \to \ell^+\ell^-\nu\bar{\nu}$ and $\mathrm{H} \to \mathrm{W}^\pm\mathrm{W}^{\mp *} \to \ell^\pm\nu_\ell\ell'^\mp\nu_{\ell'}$ results. The sensitivity did not reach down to the SM width: the upper limits ranged from 4.5 to 7.5 growing with the value of $R^{\mathrm{B}}_{\mathrm{H}^\star}$. Theoretical sources dominate the systematic uncertainty. For $R^{\mathrm{B}}_{\mathrm{H}^\star} = 1$, $\Gamma_{\mathrm{H}} < 22.7$ MeV (with an expected value of 33.0 MeV).

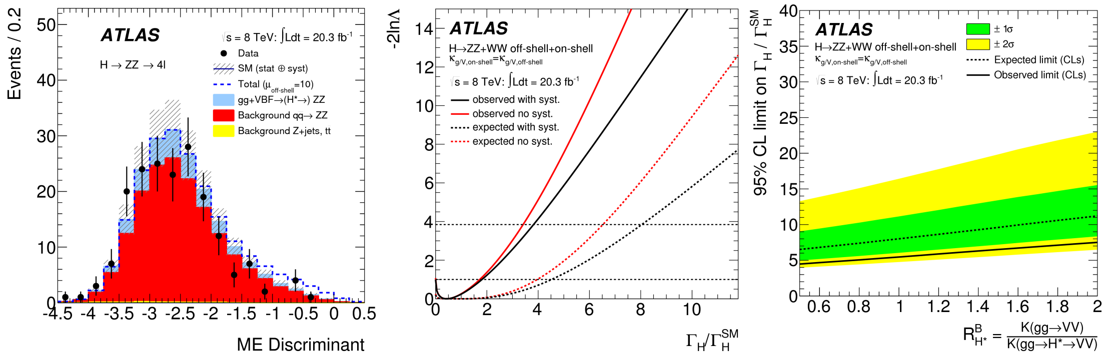

Figure 5.26: *(left) Matrix element ratio discriminant in the off-shell Higgs boson measurement defined as* $\log_{10}(\mathcal{M}_{\mathrm{gg}\to H\to ZZ}/(\mathcal{M}_{\mathrm{gg}\to(H)\to ZZ}+0.1\cdot\mathcal{M}_{q\bar{q}\to ZZ}))$. *(middle) The profile likelihood as a function of the normalized total Higgs width. (right) Observed and expected 95% CL upper limits on the Higgs total width normalized by the SM value as a function of the unknown normalized K-factor for the gluon-induced background.*

5.5.7 Spin and parity

No elementary scalar particle has been observed before the Higgs boson discovery, so proving the spin-0 nature of the new particle was of significant importance. As the new state was observed in the di-photon final state, the spin-1 hypothesis was immediately disfavored by the Landau–Yang theorem [493, 494], putting the spin-0 (scalar) and spin-2 (tensor) nature to the main subject of the investigations [495, 496]. For pure states in a charge conjugation (C) invariant theory, $C = +1$ also follows from the di-photon decay.

The SM Higgs boson has spin (J), parity (P) and charge conjugation quantum numbers: $J^{CP} = 0^{++}$, while extensions of the SM, like supersymmetry, can contain CP-odd (pseudoscalar) states, or states that are mixtures of CP-even and CP-odd components. Gravitational theories inspire the existence of a graviton-like tensor boson with $J^P = 2^+$.

The theoretical framework for Higgs spin-parity characterization [462, 497] is based on an effective theory approach that is valid until an energy scale Λ (set to 1 TeV) and includes various models compared pair-wise.

In the case of a spin-0 particle, the interaction via a pair of Z bosons is described by

$$\mathcal{L}_0^{\mathrm{Z}} = \left\{\frac{1}{2}\cos\alpha\cdot\kappa_{\mathrm{SM}}g_{\mathrm{HZZ}}Z_\mu Z^\mu - \frac{1}{4}\frac{1}{\Lambda}\left[\cos\alpha\cdot\kappa_{\mathrm{HZZ}}Z_{\mu\nu}Z^{\mu\nu} + \sin\alpha\cdot\kappa_{\mathrm{AZZ}}Z_{\mu\nu}\tilde{Z}^{\mu\nu}\right]\right\}X_0, \tag{5.14}$$

where Z^μ is the vector boson field, $Z^{\mu\nu}$ the reduced field tensor, and $\tilde{Z}^{\mu\nu}$ its dual tensor as defined in Section 1.1. Λ is the EFT scale, κ_{SM}, κ_{HZZ} and κ_{AZZ} are the real coupling values corresponding to the SM, BSM CP-even and BSM CP-odd state's (X_0) interaction with ZZ pairs. The mixing angle α allows the production of CP-mixed states and results in CP violation if $\alpha \neq 0, \pi$. The SM g_{HZZ} coupling is proportional to m_{Z}^2.

The tested spin-0 models include: (i) the SM Higgs boson (0^+) with $\kappa_{\rm SM} = 1, \alpha = 0$; (ii) a BSM scalar boson with higher dimensional operators present (0^+_h) with $\kappa_{\rm HZZ} = 1, \alpha = 0$; and (iii) a BSM pseudoscalar boson (0^-) with $\kappa_{\rm AZZ} = 1, \alpha = \pi/2$, with non-listed coupling parameters in Eq. 5.14 chosen to be zero. In the general BSM spin-0 case, the new state is a mixture of the SM spin-0 and a BSM spin-0 CP-even or CP-odd state (and thus imply CP violation in the Higgs sector). Various graviton-inspired (2^+) states with universal (graviton-like) or non-universal couplings to quarks and gluons were also studied scanning over various choices for $\kappa^{\rm q}$ and $\kappa^{\rm g}$. The hypothesis tests of these fixed J^P states assumes that the decay involves only a single CP eigenstate, the state is narrow with respect to the experimental resolution (as was shown in Section 5.5.6). They assume only a single new kinematically accessible state, and ignore interference between the BSM signal and the SM backgrounds.

Only the kinematic properties of the final states were used, the expected change due to BSM contributions of the relative production rates via ggF, VBF and VH processes were not included to keep the analysis as general as possible. The $\rm H \to ZZ^* \to \ell^+\ell^-\ell'^+\ell'^-$ decay can be fully reconstructed providing maximal information.

Two approaches were used: a BDT discriminant built from the most sensitive kinematic variables (the invariant masses of the two dilepton pairs and various decay angles), and a more sensitive matrix element based method. Both used the BDT introduced earlier to separate the Higgs signal from the ZZ* background ($\mathcal{O}_{\rm BDT_{ZZ^*}}$). Figure 5.27 compares the distributions of the ME discriminant [462, 498] for the SM Higgs and the pseudoscalar hypotheses. It was calculated using the probabilities $\mathcal{P}(J^P)$ of observing an event with the given kinematics under the J^P hypothesis, corrected using simulation for detector acceptance and analysis selection, as well as mispairing for the 4μ and $4e$ channels: $\mathcal{D} = \mathcal{P}(J^P)/(\mathcal{P}(J^P) + \mathcal{P}(0^+))$. The results were then obtained by a 2D likelihood fit in the ($\mathcal{O}_{\rm BDT_{ZZ^*}}$, $\mathcal{D}$) plane. The method is often called J^P-MELA, spin-parity

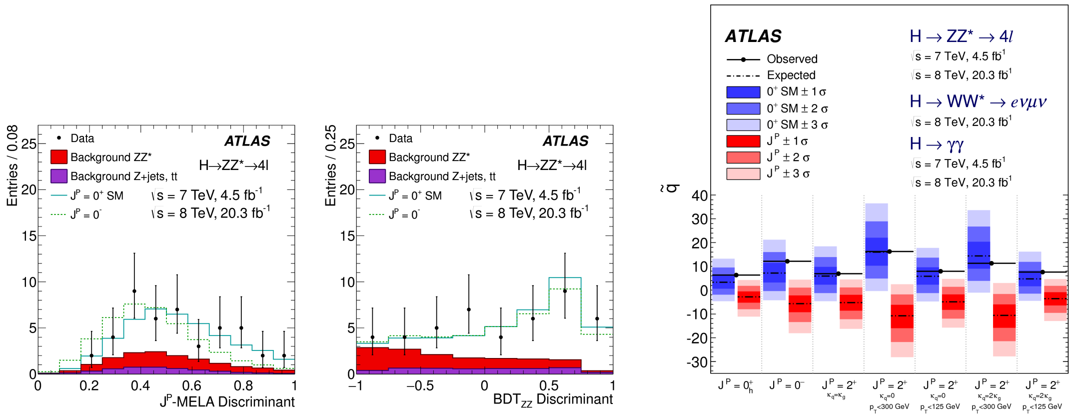

Figure 5.27: *Distributions of (left) the* $H \to ZZ^* \to \ell^+\ell^-\ell'^+\ell'^-$ *matrix element discriminant and (middle) the BDT discriminant* $\mathcal{O}_{\rm BDT_{ZZ^*}}$ *to separate the* ZZ^* *background in the* J^P*-MELA spin-parity analysis of ATLAS in Run 1. The data are compared to the expectation from simulation using the SM* 0^+ *and a BSM pseudoscalar hypothesis. (right) Distributions of the test statistic q, calculated from the ratio of the profiled maximum-likelihood estimators under the two compared hypotheses, for the SM Higgs boson sample (blue) and for the sample with the tested alternative* J^P *hypothesis (red) in the combined analysis of diboson events. The observations in data (black line) prefer the SM for every pair-wise measurement. [496]*

matrix element likelihood analysis [496].

A combination was performed with similar measurements of the $\mathrm{H} \to \mathrm{W}^{\pm}\mathrm{W}^{\mp *} \to \mathrm{e}^{\pm}\nu_{\mathrm{e}}\mu^{\mp}\nu_{\mu}$ and $\mathrm{H} \to \gamma\gamma$ processes. All pair-wise measurements favored a 0^{+} SM-like state at more than 99.9% CL (Figure 5.27) using the modified definition of $CL_s(J^P) = p(J^P)/(1 - p(0^{+}))$ with $p(J^P)$ denoting the p-value of the J^P hypothesis. The study also tested the tensor structure of the interactions, and constraints were derived on the non-SM couplings.

The LHC Run-1 data thus allowed to check the compatibility of the new particle with the SM Higgs hypothesis. The mass, a free parameter of the model had to be determined from the data. Both experiments, and both discovery channels gave a consistent value around 125 GeV. The observed rates for the measured mass agreed well with the expectations. All extracted properties, the couplings, the width, J^P showed good consistency with the SM.

5.6 Where we are after LHC Run 2?

Since the discovery and the first property measurements based on the $\sqrt{s} = 7 - 8$ TeV data of about 25 fb^{-1} integrated luminosity per experiment, the LHC ATLAS and CMS experiments each recorded and analyzed more than five times larger, high-quality pp data sets corresponding to almost 140 fb^{-1} at $\sqrt{s} = 13$ TeV. The increased luminosity and higher center-of-mass energy (raising the production cross section by a factor of two to four with respect to 8 TeV) multiplied the available statistics by about a factor 10–20 depending on the final state. Coupled with more refined experimental methods and improved theoretical predictions, these data allow for a leap in measurement precision. This section briefly summarizes the status of Higgs studies after LHC Run 2.

The mass of the boson is measured to an amazing 0.1% precision (Figure 5.28) using the $\mathrm{H} \to \mathrm{ZZ}^{*} \to \ell^{+}\ell^{-}\ell'^{+}\ell'^{-}$ and $\mathrm{H} \to \gamma\gamma$ modes [499–504], with the most precise value $m_H = 125.11 \pm 0.11$ GeV coming from the recent ATLAS combination of $\sqrt{s} = 7 - 13$ TeV data [49].

While the direct measurement of the width is limited by detector resolution to $\Gamma_{\mathrm{H}} < 1.1$ GeV [500], the measurement of the off-shell Higgs production rates with a reconstructed mass above $2m_{\mathrm{Z}}$ yields a strong constraint on the width [506, 507]. A new CMS measurement [505] combining the results of the $\mathrm{H} \to \mathrm{ZZ}^{*} \to \ell^{+}\ell^{-}\ell'^{+}\ell'^{-}$ and $\mathrm{H} \to \mathrm{ZZ}^{*} \to \ell^{+}\ell^{-}\nu\bar{\nu}$ analyses have reached evidence at the 3.6σ level for off-shell production with a signal strength in the range [0.0061, 2.0] at the 95% CL and yielded the first measurement of the width $\Gamma_{\mathrm{H}} = 3.2^{+2.4}_{-1.7}$ MeV, in full agreement with the SM prediction of 4.1 MeV. The lifetime has also been constrained by the Higgs boson flight distance in the CMS detector: $\tau_{\mathrm{H}} < 1.9 \cdot 10^{-13}$ s (corresponding to $\Gamma_{\mathrm{H}} = \hbar/\tau_{\mathrm{H}} > 3.5 \cdot 10^{-9}$ MeV) [508].

All main Higgs production and decay modes have been observed. The most challenging and thus the last being established was $\mathrm{t\bar{t}H}$ production in 2018 [509, 510]. As top quark pair production in association with an electroweak vector boson is the main background for $\mathrm{t\bar{t}H}$ studies with Higgs boson decays to a photon pair or a leptonic final state, the study of these processes in the early LHC data was essential and prepared the way for the discovery. $\mathrm{t\bar{t}}\gamma$ production was first observed by the ATLAS collaboration in the $\sqrt{s} = 7$ TeV data sample [511], while $\mathrm{t\bar{t}Z}$ and $\mathrm{t\bar{t}W}$ in the combined Run-1 data set [512, 513].

The observed signal strengths are compatible with unity within uncertainties [416, 417] (Figure 5.29). The global signal strength is measured with 6% precision, though

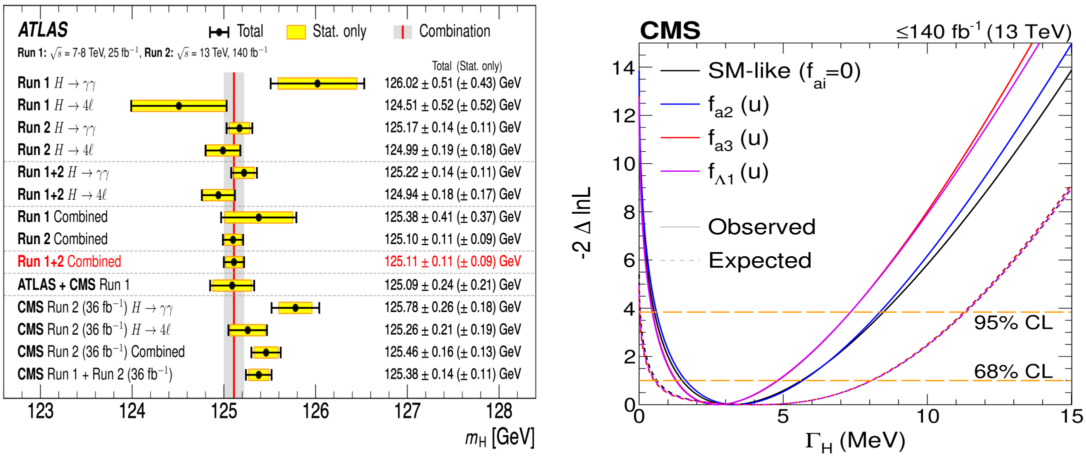

Figure 5.28: *(left) Summary of the measured Higgs boson mass* m_H *in the* $H \to \gamma\gamma$ *and* $H \to ZZ^* \to \ell^+\ell^-\ell'^+\ell'^-$ *channels by the ATLAS and CMS collaborations, and for their various combinations [49] (right) Constraints from the CMS experiment on the Higgs width* Γ_H *with and without allowing anomalous HVV couplings [505]. The anomalous coupling parameters* $f_i(i = a2, a3, \Lambda1)$ *are defined in Ref. [506]. The horizontal lines indicate the 68% and 95% CL regions. The lower (upper) boundary of the allowed region is stable within 0.2 (1.2) MeV for the different anomalous coupling assumptions.*

individual production modes can still have large uncertainties (about 20% for Higgs-strahlung and $\mathrm{t\bar{t}H}$).

Higgs decays to all EW bosons ($\mathrm{W^+W^-}$, ZZ, $\gamma\gamma$, and very recently $\mathrm{Z}\gamma$ [514]) and third generation fermions ($\mathrm{b\bar{b}}$, $\tau^+\tau^-$) are established. Evidence for decay to second generation fermions ($\mu^+\mu^-$) has also emerged [515, 516] with a signal strength of 1.19 ± 0.43 in the CMS analysis, but measurements targeting the $\mathrm{H} \to \mathrm{c\bar{c}}$ decay are not yet sensitive. Recent ATLAS and CMS projections for HL-LHC with an integrated luminosity of 3000 fb^{-1} at $\sqrt{s} = 14$ TeV predict that a signal strength measurement of

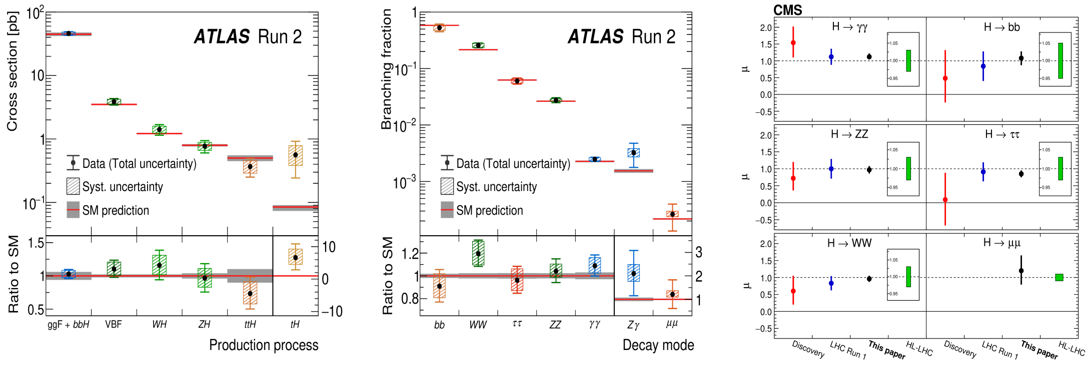

Figure 5.29: *(left) Cross sections for ggF, VBF, WH, ZH and* $\mathrm{t\bar{t}}H$ *production modes assuming SM values for the decay branching fractions, and (middle) for the various decay modes assuming SM values for the production cross sections as measured by ATLAS [417]. The lower panels show ratios of the measured and predicted values. (right) The evolution of the measured values for the signal strength in the different channels of the CMS study [416] from the time of discovery, to final Run-1 and today's best Run-2 measurements, as well as the expected sensitivity in HL-LHC.*

about 1.0 ± 3.0 is achievable for VH followed by H → c$\bar{c}$ by analyzing simultaneously bottom and charm Yukawa couplings in Higgs-strahlung events [469, 517].

The coupling strength to the SM particles follow the expected scaling with the particle mass (see Figure 5.30). The measured coupling modifiers with respect to the SM are in good agreement with unity within uncertainties, amounting to 6–11% for weak bosons and third generation fermions in the most precise measurements to date [416, 417].

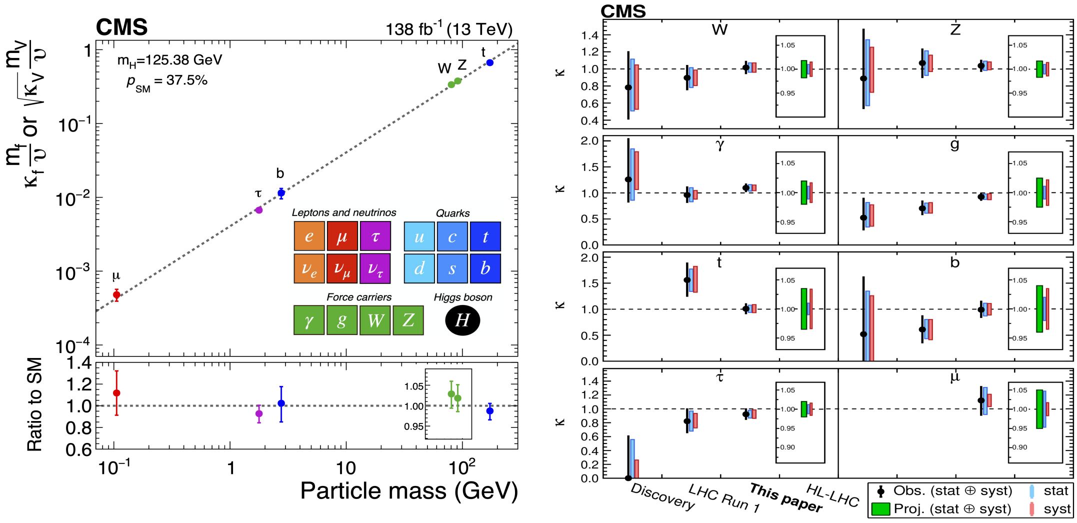

Figure 5.30: *(left) The reduced coupling modifiers extracted by CMS for fermions and weak bosons from the resolved κ-framework [462] compared to their corresponding prediction in the SM. The lower panel shows ratios of the measured and predicted values. (right) The evolution of the coupling modifier values in different CMS data sets: at the time of the discovery, using the full Run-1 data, the best measurement available by 2022, and the expected 1 s.d. uncertainty at the HL-LHC. [416]*

While the original signal strength and multiplicative coupling modifier framework is practical to show direct (dis)agreement with the SM, it has built-in model dependence and significant systematic uncertainties. To better separate the measurement and interpretation steps, the simplified template cross sections (STXS) framework was developed [453, 518]. It allows to reduce dependencies on theoretical uncertainties and the underlying physics model and provides more granular information for global combination of the measurements including all (available) decay channels. It targets the region of Higgs-boson rapidity $|y_{\mathrm{H}}| < 2.5$ which has a good coverage by the experimental acceptance and is fully inclusive in Higgs decays. It measures cross sections in mutually exclusive regions of phase space separated into production modes. Non-Higgs backgrounds are subtracted, and acceptance corrections are applied to use simplified (idealized) bin definitions abstracted from the actual measurement categories. A graphical representation is visible in Figure 5.31. The bins are defined in Higgs p_{T}, number of additional jets, dijet or weak vector boson mass by finding a balance between maximizing experimental sensitivity, minimizing theory dependence, and isolating beyond the SM effects. Recent global STXS fits by ATLAS find a high-level of agreement with the SM (94%) as illustrated in Figure 5.32.

These inputs can be used to interpret the data also in SM effective field theoriesand in full UV-complete BSM models giving complementary constraints to direct measurements [519, 520]. The data show a high-level of agreement with the SM and no sign of

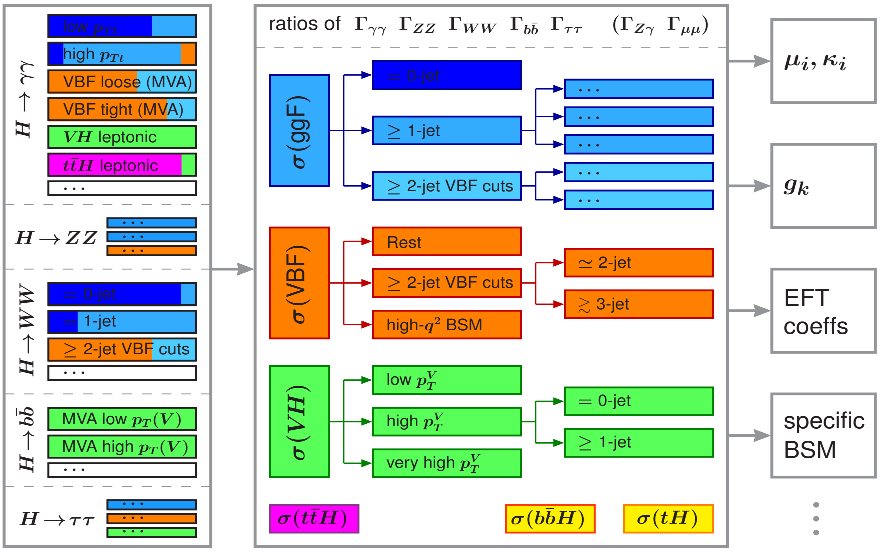

Figure 5.31: *Illustration of the STXS framework showing the experimental inputs on the left, how they contribute to the various bins of the simplified template cross sections in the middle, and the possible interpretations using the standardized inputs on the right [518].*

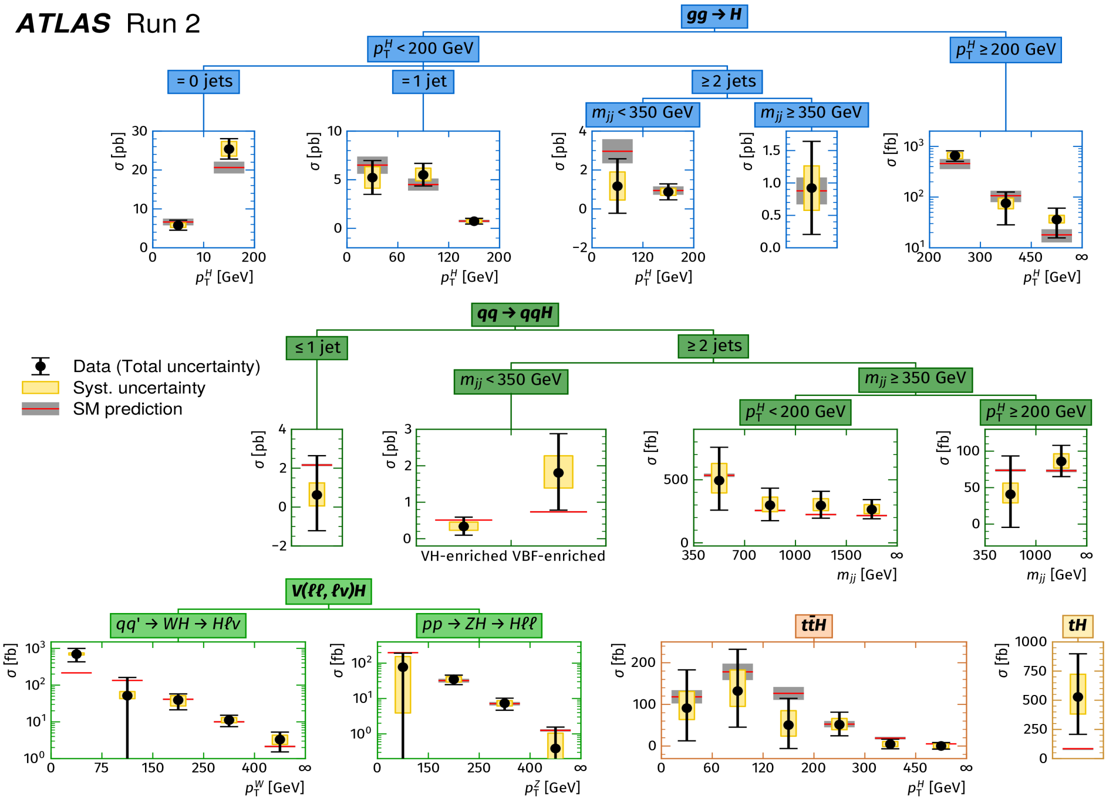

Figure 5.32: *Best-fit values for the cross sections in different kinematic regions of the STXS framework in the Run-2 ATLAS data. The 'VH-enriched' and 'VBF-enriched' regions are defined by requirements on the dijet mass: a selection within (outside) the range $m_{jj} = 60 - 120$ GeV is enhanced in signal events from Higgs-strahlung (VBF) production. A p-value of 94% indicates full compatibility with the SM. [417]*

new physics is evident so far. A picture highly consistent with the SM emerged from the LHC Run-1 and Run-2 data.

HL-LHC, foreseen to start delivering data at $\sqrt{s} = 14$ TeV towards the end of the decade and to increase the statistics tenfold compared to LHC Run 1- Run 3, will lead to the precision era of Higgs physics as illustrated on Figures 5.29 and 5.30. The precision of coupling modifier measurements will be limited by systematic uncertainties (except for the rarest decays like $\mathrm{H} \to \mu^+\mu^-$), even after the expected improvement for theoretical predictions and analysis methods. Indeed, since the start of LHC, we witness an explosion in sophistication at every level of data taking, event reconstruction and physics analysis. Even processes that were once thought to be outside the reach for LHC are now foreseen to be observed, as commented above for $\mathrm{H} \to \mathrm{c\bar{c}}$.

Of particular interest, to determine the shape of the Higgs potential, is the measurement of di-Higgs production (Figure 5.6) that gives access to the Higgs self-interaction parameter λ (Eq. 1.6). The measurement using the full Run-2 data is not yet sensitive to the SM signal strength but already provides a weak constraint on the associated coupling modifier $\kappa_\lambda = 1.7^{+2.8}_{-1.7}$ [416] as seen in Figure 5.33. In combination of the most sensitive channels ($\mathrm{b\bar{b}}$ $\mathrm{b\bar{b}}$, $\mathrm{b\bar{b}}$ $\tau^+\tau^-$ and $\mathrm{b\bar{b}}$ $\gamma\gamma$) at HL-LHC with 3000 fb^{-1} this rare process will be established at about 4 s.d. significance.

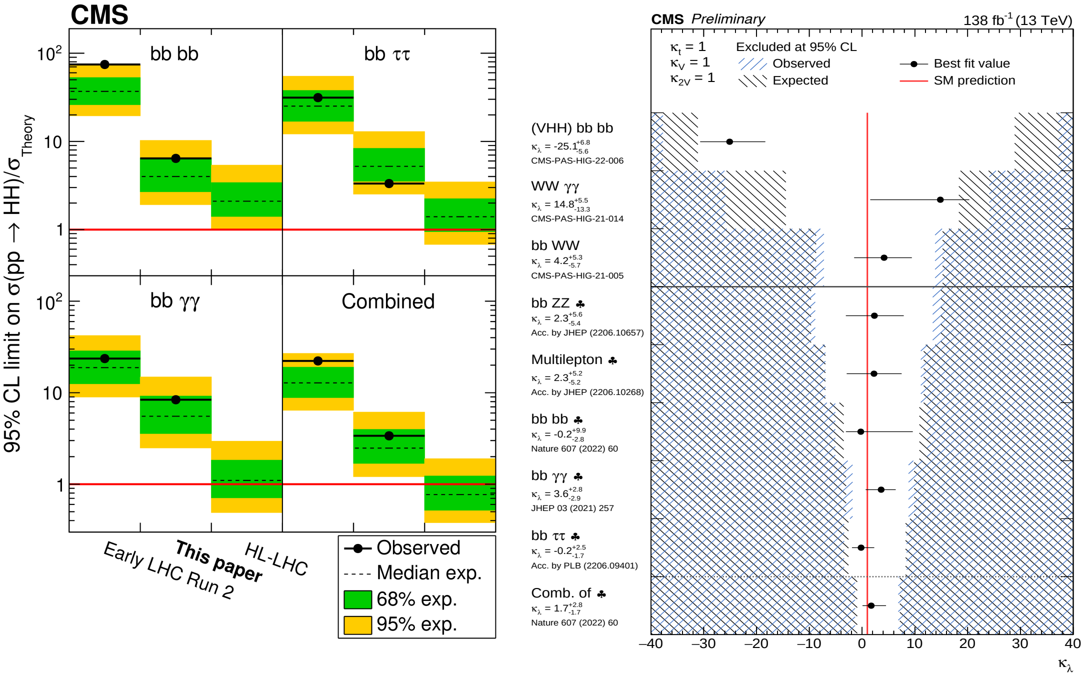

Figure 5.33: *(left) Expected and observed limits on di-Higgs production in different CMS data sets: early LHC Run 2 data (35.9* fb^{-1}*), full Run 2 data (138* fb^{-1}*), and projections for the HL-LHC (3000* fb^{-1}*) [416]. (right) Observed and expected 95% confidence intervals on the Higgs self-coupling modifier* κ_λ *superimposed by the best fit value with its 1*σ *interval [521].*

These measurements might offer a Higgs window to physics beyond the SM. They are complemented by searches for rare exotic decays, many of which had been performed since the start of LHC. A very early example is Ref. [522] targeting Higgs boson decays to hidden sector particles leading to spectacular clusters of collimated electrons, known as electron-jets in WH production. With new data being recorded and new ideas being born continuously, a large number of exotic signatures are sought today.

Chapter 6

Looking beyond the standard model at the LHC

Beyond the Higgs boson search and property measurements, the main physics goal of the LHC is the study of the highest energy phenomena to test the validity of the standard model and to search for exotic processes beyond the SM.

This chapter reviews measurements of the Drell–Yan process [523–526], especially at high invariant masses [527] and the search for new dilepton resonances [528]. It also discusses the first measurement of inclusive Wγ and Zγ diboson production, and its interpretation in various new physics models [529], concentrating on Run-1 ATLAS data. It then proceeds to the results of the exploitation of the higher energy and larger statistics Run-2 CMS data set at $\sqrt{s}$ =13 TeV, describing the studies of vector boson pair production in association with jets [530], in particular targeting EW production and vector boson scattering [531–535], and searches for high-mass exotic bosons [536] and supersymmetric partner particles [537, 538].

6.1 Drell–Yan lepton pair production

The s-channel Drell-Yan (DY) production of lepton pairs via a virtual photon or Z boson exchange, shown in Figure 6.1, is one of the simplest processes to study at a hadron collider. It offers a clean signature (Figure 6.2) and large statistics. After precise detector calibration, the experimental uncertainty (excluding that of the luminosity) can be as low as 1%. Naturally, the inclusive Z cross section measurement is among the first results to be completed at a new center of mass energy. Theoretical calculations at N^{3}LO using the n3loxs tool [539] are compared in Figure 6.3 to the observed values in CMS as a function of $\sqrt{s}$.

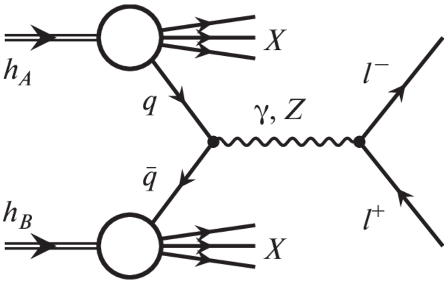

Figure 6.1: *Drell-Yan production of an opposite-charge lepton pair in hadron collisions.*

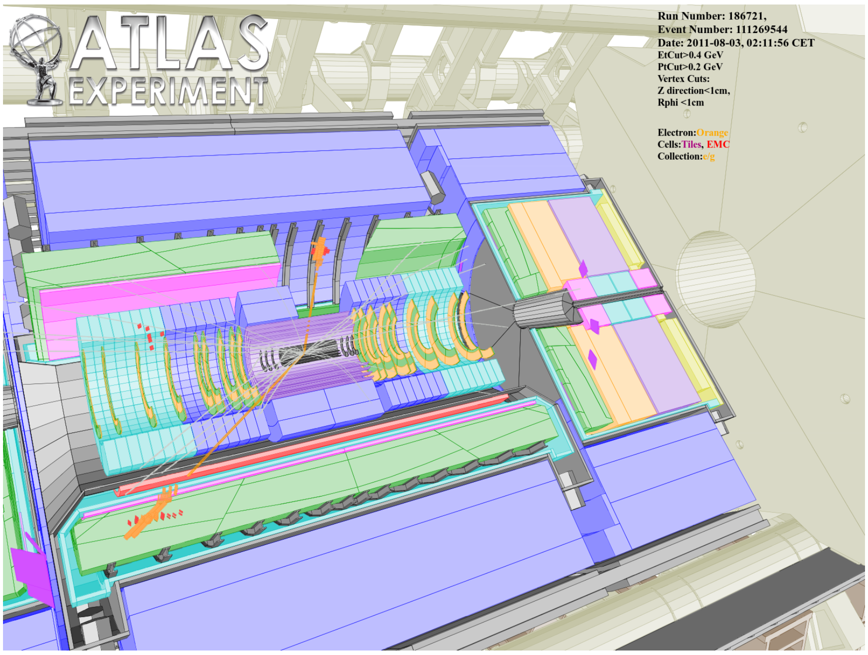

Figure 6.2: *An electron-positron pair in the* $\sqrt{s} = 7$ *TeV data of the ATLAS experiment, with a dielectron mass of 1.2 TeV. The electron tracks are highlighted by orange and point to clusters of energy deposited in the LAr electromagnetic calorimeter.*

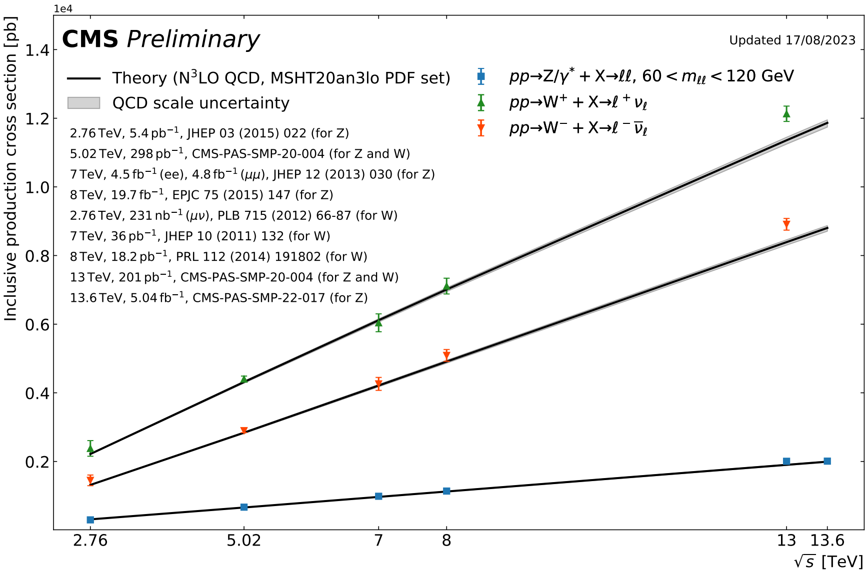

Figure 6.3: *W and Z boson inclusive cross section measurements by CMS compared with* N^{3}LO *predictions. [540]*

The DY process provides a stringent test of higher order electroweak and QCD predictions, it is sensitive to resummation techniques and it constrains the parton distribution functions. For example, QCD effects (higher order contributions, parton shower modeling) can be probed by the measurement as a function of the Z boson p_{T} of the dimensionless angular coefficients ($A_{0-7}(p_{\mathrm{T}})$) appearing in the DY differential cross section $\mathrm{d}^2\sigma/\mathrm{d}\cos\theta\mathrm{d}\phi$ expressed by a sum of harmonic polynomials $P_i(\cos\theta, \phi)$ with the lepton polar θ and azimuth ϕ angles in the Z boson rest frame [541].

The precise measurements of lepton pairs from Z decays is also essential for electroweak measurements, such as the determination of the weak mixing angle and the W mass. For the latter, the precise measurement of the Z boson p_{T} distribution constrains that of the W boson, a crucial component of the measurement [542, 543].

6.1.1 Differential cross section measurement

The background contributions are low as shown in Figure 6.4 as a function of the reconstructed dilepton mass in the electron and muon channels. The relative contribution from non-DY processes increases however at high mass. For the electron channel, the dominant background comes from events with at least one jet misidentified as a prompt electron (primarily multi-jet, jet+photon, and W+jet processes). These ”fake” backgrounds are measured from data. First the probability that a jet is misidentified as an electron is determined in jet-enriched samples in bins of the electron candidate E_{T} and pseudorapidity, then these ”fake rates” are applied to the data observed in control regions with electrons passing loose but failing the analysis identification cuts. Diboson and $\mathrm{t\bar{t}}$ processes with true leptons also contribute, and are estimated using Monte Carlo simulations. The efficiency to identify electrons from DY production is measured with a dedicated tag-and-probe technique described in Section 3.5.1.1.5.

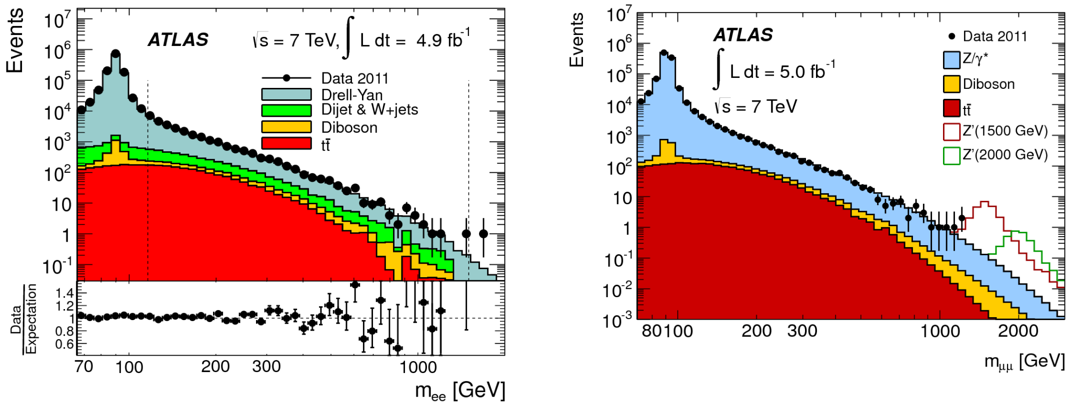

Figure 6.4: *Dilepton mass spectrum as a function of the dilepton mass in the ATLAS measurement at* $\sqrt{s} = 7$ *TeV for the (left) electron [527] and (right) muon [528] channel. The observed data are compared to the SM prediction. On the left, the lower panel shows the ratio of the data to the expectation demonstrating an excellent agreement. On the right, contributions from hypothetical* Z' *boson production at high mass are added to the SM prediction.*

The differential cross section as a function of the dielectron invariant mass in the range $m_{\mathrm{ee}} = 116 - 1600$ GeV was measured in pp collisions at $\sqrt{s} = 7$ TeV with the ATLAS detector [527] in a fiducial region requiring electrons with $p_{\mathrm{T}} > 25$ GeV and $|\eta| < 2.5$ that is close to (slightly larger than) the experimental acceptance. To remove (”unfold”) the effect of experimental resolution a bin-by-bin correction was applied, similar to the one described in Section 5.2. At the particle level, the electron four-momentum was also determined by adding the four-momenta of the photons that are within $\Delta R = 0.1$ of the electron to correct for final state radiation that is included in the reconstructed electron momentum (”dressed electron”). The measurements shown in Figure 6.5 were performed with ”dressed” electrons to test various Monte Carlo generators and with Born-level electrons to compare to the analytic calculations performed at NNLO in pQCD and NLO in EW corrections by FEWZ 3.1 [544, 545].

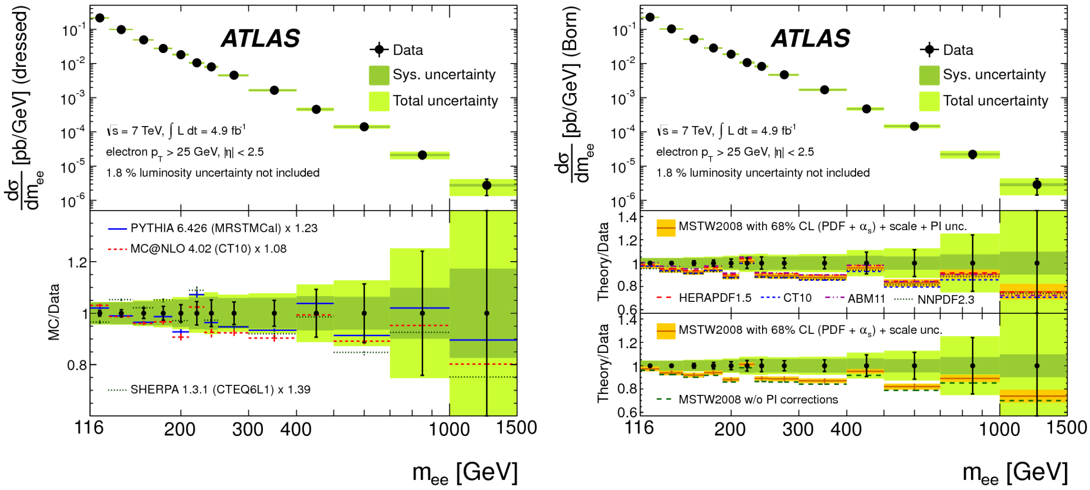

Figure 6.5: *Measured fiducial differential cross section with systematic and total uncertainties (green bands), excluding luminosity, compared to predictions of (left) PYTHIA, MCNLO and Sherpa MC generators scaled to the observed number of events in the data as indicated, and (right) FEWZ 3.1 NNLO QCD with NLO EW corrections using the G_μ EW parameter scheme for five PDF sets, including a small additional correction for real emission of single W and Z from a final state electron. Photon-induced production is added on the upper theory / data ratio plot, while its effect is illustrated in the lower ratio plot. The theoretical uncertainty (orange band) includes contributions due to PDF, α_s, renormalization and factorization scales, as well as the photon-induced correction. [527]*

The small extrapolation of about 10% from the experimental acceptance to the fiducial region was estimated using Monte Carlo simulation and introduces an uncertainty of up to 0.5% derived from the comparison of simulated samples using LO PYTHIA 6.426with the modified MRSTMCal [434, 546] PDF set and NLO MCNLO 4.02 [547] with CT10 [548] PDF set, both reweighted to the systematic PDF eigenvectors, as well as to alternative NLO PDF sets (CT10, HERAPDF1.5 [449]).

The experimental uncertainty (4.2–9.8%) came dominantly from the electron energy scale (2.1–3.3%), the reconstruction and identification efficiency (1.6–1.7 and 2.3–2.5%) at low mass, and from the fake background estimate (1.3–8.2%) at high mass. The luminosity uncertainty (1.8%) affects the normalization. The measurement was statistics (1.1–50%) dominated at high mass. The ranges given here cover the full studied mass range and serve also to illustrate that all uncertainties increase with m_ee.

The studied MC generators, PYTHIA 6.426 (LO), MCNLO 4.02 (NLO) and Sherpa 1.3.1 [298] (LO with up to three additional partons, and CTEQ6.6 [436] PDF set) describe well the shape of the distribution though generally predict lower rates by a factor of 1.23, 1.08 and 1.39, respectively.

The FEWZ 3.1 predictions were corrected upward to account for LO photon-induced $\gamma\gamma \to \mathrm{e}^+\mathrm{e}^-$ corrections using the LO MRST2004qed [549] PDF set, and for real W and Z emission off an electron in single-boson production using Madgraph 5 [550]. The correction is illustrated on the right lowest panel of Figure 6.5. The observed rates were still systematically higher than expected for all studied PDF sets (HERAPDF1.5, CT10, ABM11 [551], NNPDF2.3 [552], MSTW2008 [553]), but were in agreement within uncertainties with χ^2 values of 13.5–18.9 for 13 data points. These data can be used to constrain the proton PDF sets in the global fits, especially for antiquarks at large

Bjorken x. The higher energy LHC data with its large statistics also allow to measure double-differential cross sections and improve the sensitivity to the PDFs [342, 554, 555].

6.1.2 Z' interpretation

The high dilepton mass region is sensitive to the production of heavy, short-lived bosonic states coupling to a lepton pair. Many models with new forces, extra spatial dimensions, or composite structure predict such a new state.

A common benchmark model of new heavy vector bosons is the sequential standard model (SSM) [556] that assumes a Z' with coupling strength to SM fermions equal to that of the Z boson. Other models embed the SM gauge group to a larger symmetry group motivated by gauge unification [556, 557] or the restoration of left-right symmetry [558, 559] that is violated by the weak interaction. The minimal Z' model [560] uses two effective coupling constants and the Z' mass to cover various proposals including left-right symmetric and $B-L$ (baryon number − lepton number) conserving [561] models.

Models with extra spatial dimensions also propose exotic resonances. The Randall–Sundrum model, introduced in Section 1.3.1, contains excited states of the graviton that couple to lepton pairs with a strength dependent on the curvature and the reduced Planck mass, k/M_{Planck}. Models with 1/TeV scale extra dimensions where the gauge bosons feel the extra dimensions include KK excitations of the photon and the Z boson that would decay to lepton pairs [562–565].

These and many other models were constrained by performing a template based hypothesis test on the reconstructed dilepton mass distributions. For the narrow Z' hypothesis shown in Figure 6.4 (right), the observed upper limit on the production cross section times branching ratio ($\sigma \cdot B$) was computed based on the $\sqrt{s} = 7$ TeV ATLAS data [528]. It is shown in Figure 6.6 and agreed well with the expectation from the background-only hypothesis. In the absence of a significant excess, comparing this limit to the theoretical predictions for the SSM and an E_6 unification motivated model [556, 557], lower mass limits were derived on new heavy spin-1 states, typically of about 2 TeV.

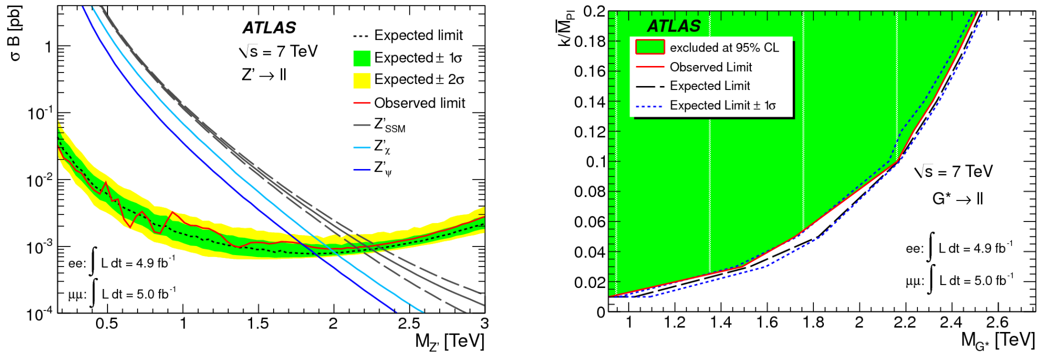

Figure 6.6: *(left) Observed (red) and expected (dashed black with* 1σ *and* 2σ *experimental uncertainty bands) 95% CL limits on* $\sigma \cdot B$ *and the values predicted for* Z' *production in SSM (with the dashed lines illustrating the theoretical uncertainty) and two E6 unification motivated models with the lowest and the highest possible* $\sigma \cdot B$*. (right) Excluded regions (green) in the* k/M_{Planck} *versus graviton mass plane in the Randall-Sundrum model. The results were derived using the combination of the ATLAS dielectron and dimuon search channels at* $\sqrt{s}$ *=7 TeV. [528]*

An alternative interpretation in the the Randall-Sundrum model is also presented as a function of the coupling of the spin-2 excited graviton state to leptons. These were the most stringent limits at the time of publication ranging between 0.92 - 2.51 TeV for $k/M_{\text{Planck}} = 0.01 - 0.2$. The search also placed limits for the first time on other extensions of the SM, including more manifestations of new vector bosons, techni-mesons in dynamical models of EWSB (technicolor) [38, 39, 566–568], EW gauge boson KK excitations in 1/TeV scale extra dimensions, and a Torsion resonance in quantum gravity [569–571].

All limits on dilepton resonances had been significantly extended with the analysis of the full Run-1 and Run-2 data sets [572, 573] which did not yet unearth a deviation from the SM.

6.2 Electroweak diboson production

An essential part of the LHC research program is the study of EW diboson production, a sensitive probe of the non-abelian gauge structure of the SM, the mechanism of EWSB as well as possible New Physics. Precise measurements of diboson final states either inclusive or accompanied by a pair of hadronic jets at large polar angles have been performed at various center of mass energies between 5 to 13 TeV with ever-improving precision. Primarily the leptonic decays of the massive vector bosons are considered leading to electron(s) and / or muon(s) in the final state[1] to fight the large multi-jet cross section at the LHC. Such events can be efficiently selected in real time using lepton triggers (see Section 3.5.2). The results have been compared to state-of-the-art higher-order perturbative calculations, and constraints have been derived on anomalous triple and quartic gauge couplings that could arise in extended (such as supersymmetric or general two-Higgs-doublet) models with new heavy states.

6.2.1 Inclusive Wγ and Zγ measurements

The measurement of the associated production of a weak massive boson and a photon, Wγ and Zγ, at the LHC tests at the highest available energies the couplings of these bosons, governed by the $SU(2)_{\text{L}} \times U(1)_{\text{Y}}$ gauge group. In particular, the high diboson invariant mass region allows to constrain possible new contributions to triple gauge boson couplings and allows a search for heavy narrow resonances such as techni-mesons predicted by "Higgs impostor" technicolor models of dynamical symmetry breaking [38, 39, 574]. I contributed as expert internal reviewer to the long effort to provide the first comprehensive study of Wγ and Zγ production in pp collisions at $\sqrt{s} = 7$ TeV with the ATLAS detector [529]. Similar results were achieved by the CMS Collaboration [575]. Several studies were performed at higher energies with larger data sets. Of these, the double-differential cross section measurements at $\sqrt{s}$ =13 TeV with the full Run-2 data set are of particular interest [576, 577].

6.2.1.1 Cross section measurement

To allow efficient triggering and suppression of background, only leptonic decays of the W and Z bosons are considered: pp $\rightarrow \ell^+\ell^-\gamma$, $\ell\nu\gamma$ and $\nu\bar{\nu}\gamma$, with ℓ standing for an

---

[1] In this chapter, measurements cover only charged leptons of the first two families in the final states, as tau leptons are challenging to reconstruct and cleanly identify as they have a proper lifetime of about $3 \cdot 10^{-13}$ s and thus decay within about 100 μm of the primary vertex to softer particles: either an electron, a muon or a narrow, low multiplicity hadronic jet, always accompanied by at least one neutrino.

electron or muon. In the SM, such final states can arise in a variety of ways, including charged WWγ TGC, but also QED initial state radiation (ISR) from a quark, and final state radiation from a charged lepton produced in the weak boson decay, as well as from fragmentation of a final state jet accompanying the production of the weak boson (Figure 6.7). Tree-level neutral TGC is not present in the SM.

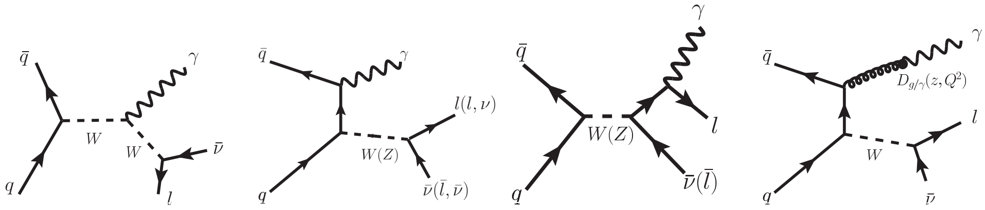

Figure 6.7: *Representative diagrams of* pp $\rightarrow$ $W\gamma$, $Z\gamma$ *processes in the SM producing leptons in the final state. From left to right: charged TGC, QED ISR from a quark, QED FSR from a charged lepton, jet fragmentation.*

The signal was defined by fiducial cuts on the transverse momentum and pseudorapidity of the final state objects (leptons, photons, and – in the inclusive case – jets), the $\ell^+\ell^-$ invariant mass and the $\nu\bar{\nu}$ transverse momentum, as well as the isolation and the angular separation (ΔR) of the charged lepton(s) and the photon. The latter requirements on the photon were aimed to mirror the experimental selections to reduce the contribution from fragmentation and FSR. At the particle level, the lepton four-momentum was corrected for final state photon radiation within $\Delta R = 0.1$ (”dressed”). For final states with at least one charged lepton, the largest contribution to the background came from W/Z + jets (often called non-prompt photon background). In final states with at least one neutrino, events with an unreconstructed (”lost”) lepton from W/Z decays, and γ + jets (also) contributed. For Wγ, the latter is called the non-prompt or fake lepton background as the reconstructed lepton arises from the jet. Other smaller contributions are also indicated in Figure 6.8 that compares the observed data to the SM expectation for distributions that are particularly sensitive to contributions from new physics at high energy scales, such as the reconstructed mass of the final state for $\ell^+\ell^-\gamma$ and $\ell\nu\gamma$, and the missing transverse momentum in the case of the $\nu\bar{\nu}\gamma$ selection.

The measurement uncertainty was dominated by experimental systematic sources (7-8%), with leading contributions from photon identification (6%), jet energy scale

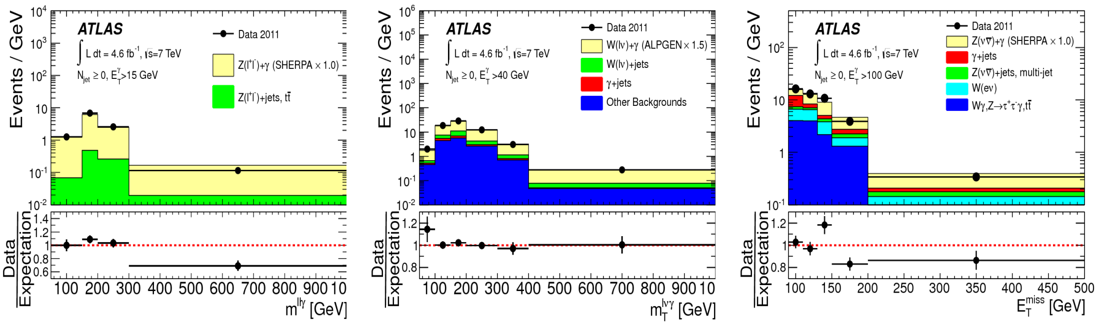

Figure 6.8: *Distribution of events selected in the* $\sqrt{s}$ = *7 TeV ATLAS data compared to stacked SM expectations of various background processes and the* $V\gamma$ *signal: (left) invariant mass of the* $\ell^+\ell^-\gamma$ *system, (middle) transverse mass of the* $\ell\nu\gamma$ *system and (right) missing transverse momentum in the* $\nu\bar{\nu}\gamma$ *selection. [529]*

and resolution for the exclusive cross section vetoing events with a jet above $p_T = 30$ GeV, energy scale and resolution of photons and electrons, and lepton (especially electron) identification efficiency. For Wγ, muon trigger efficiency and missing transverse momentum calibration also contributed above the % level.

The observed fiducial cross sections were compared to higher order predictions: they were found higher than the NLO SM calculation with the MCFM parton-level generator [578, 579] both in the inclusive case (allowing the presence of jets) and in the exclusive measurements. For Wγ, the differences reached about 2 s.d. After the publication of the results, new theoretical calculations at NNLO became available, which are in agreement with the data, as shown in Figure 6.9. The figure also summarizes recent results from the ATLAS Collaboration at higher energies for various diboson processes manifesting a general agreement between NNLO theory and experiment.

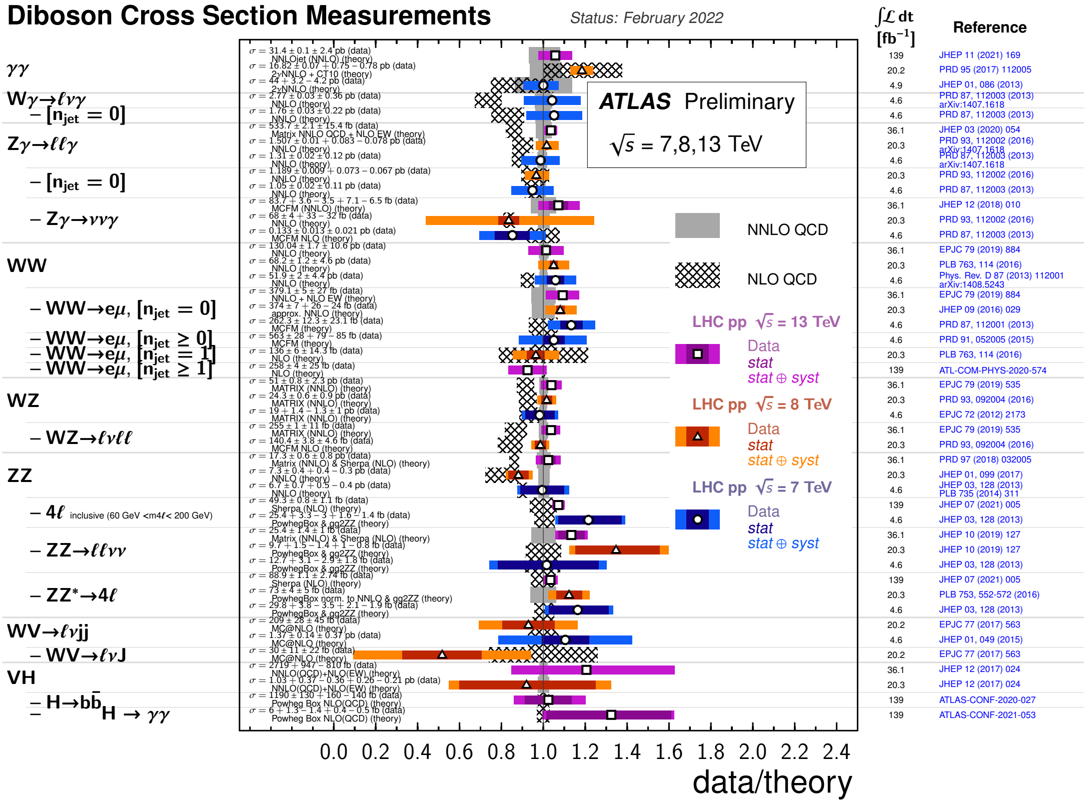

Figure 6.9: *Diboson cross sections measured by the ATLAS Collaboration at LHC at various pp collision energies, compared to NLO and NNLO theoretical predictions.* [580]

The differential cross sections as a function of the photon p_T, the jet multiplicity and the diboson invariant mass were extracted, by correcting the measured distributions to the underlying particle-level distributions using a Bayesian iterative unfolding technique [446] to remove the effects of experimental acceptance and resolution. The excess in data with respect to MCFM were more pronounced at higher photon p_T, where jet multiplicity increases, as MCFM provided prediction for Zγ up to only two extra jets, and for Wγ up to a single extra jet. The measurements were also compared to LO MC generators (Sherpa 1.4.0 and Alpgen 2.14 [482]) including multiple quark/gluon emissions in the matrix element calculations. These provided a better description of the photon p_T distribution as shown in Fig 6.10.

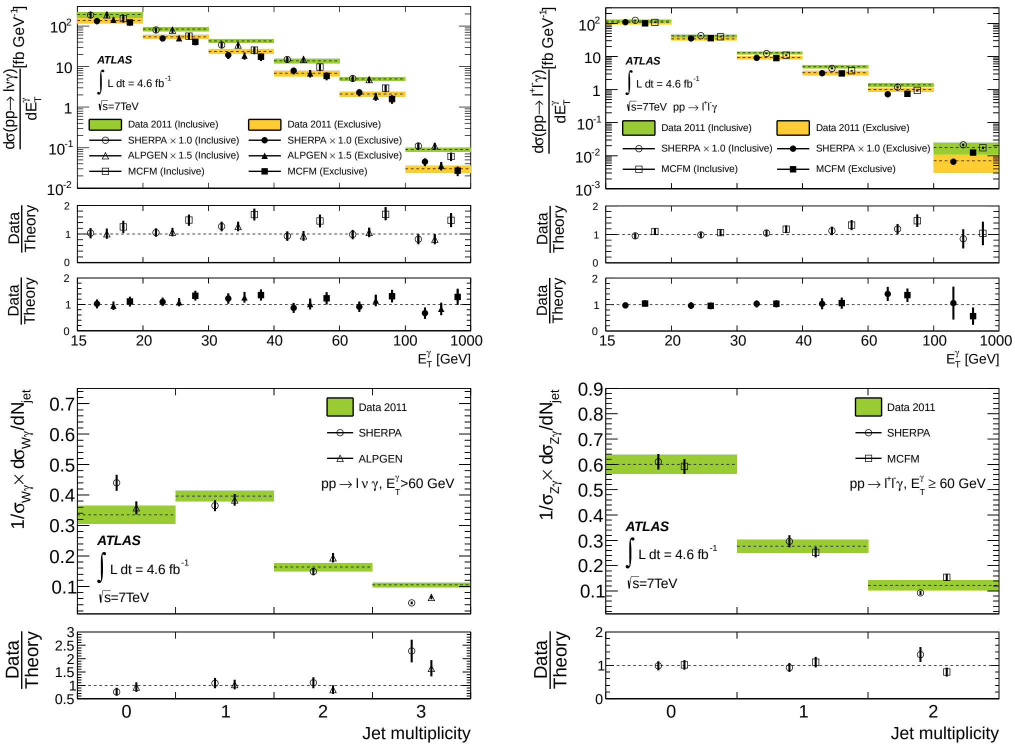

Figure 6.10: *Differential fiducial cross sections as a function of (top) the photon* p_{T} *and (bottom) the jet multiplicity at* $\sqrt{s} = 7$ *TeV, compared to various LO and NLO theoretical predictions for the (left) W*γ *and (right) Z*γ *processes. [529]*

6.2.1.2 Determination of triple gauge couplings

Triple gauge couplings assuming C and P conservation (introduced in Section 1.2) were measured using the reconstructed photon p_{T} distribution in the exclusive 0-jet selection: namely the measured exclusive fiducial cross section above 100 GeV (shown in the last bins of Figure 6.10 (top)). Form factors are introduced to avoid unitarity violation at high energy using $1/(1 + \hat{s}/\Lambda^2)^n$ scaling for the anomalous couplings, where $\hat{s}$ is the diboson invariant mass squared, Λ is the new physics scale, and $n = 2$ for the charged WWγ aTGCs of λ_γ and $\Delta\kappa_\gamma$, $n = 3$ for the neutral aTGCs of h_3^V, and $n = 4$ for h_4^V with V=γ for the Z$\gamma\gamma^\star$ and V=Z for the ZγZ* couplings. Predictions for non-zero aTGCs are obtained from the MCFM generator.

The results are visualized in Figure 6.11 for the charged couplings, and are less stringent than the combined values of the four LEP experiments. These have since been superseded by the LHC measurements at $\sqrt{s}$ = 8-13 TeV (also shown). The latest results based on the full Run-2 data of CMS [576, 581] were interpreted in dim-6 EFT, following the shift in the community towards a framework that can consistently include higher-order corrections, and are thus not presented in the figure. When the EFT results were converted to the LEP parametrization [59] a limit of $-0.0035 < \lambda_\gamma < 0.0035$ [581] was derived, which is about a factor of 2 better than the most stringent result in Figure 6.11.

The results for the neutral couplings are shown in Figure 6.12 (top) and were the most stringent at the time of their publication. Recent LHC results up to 13 TeV have improved the limits by several orders of magnitude and are shown in the bottom of the figure. All measurements so far are consistent with the SM and do not indicate the presence of new physics.

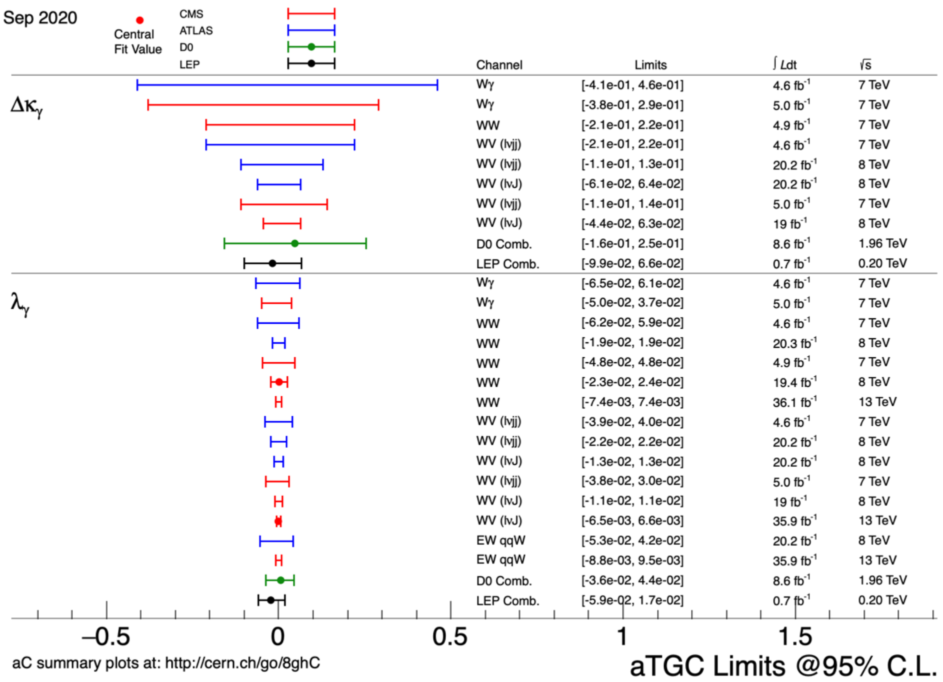

Figure 6.11: *Constraints on charged anomalous triple gauge couplings from various measurements at collider experiments [582]. The latest results are interpreted in dim-6 EFT and are thus not included in the plot.*

6.2.1.3 Search for a narrow resonance

The diboson invariant mass distributions in the $\ell^+\ell^-\gamma$ and $\ell\nu\gamma$ final states were also searched for the presence of a narrow resonance, using a spin-1 techni-meson model (simulated using the technicolor strawman [567] model in PYTHIA) as benchmark to guide the analysis and – as no significant excess was observed over the SM expectation – the limit setting. The model was chosen as at the time of the analysis the then-recent discovery of a Higgs-like particle had not excluded the full phase-space of low-scale technicolor models [583–585], and it allowed the existence of other new particles with a mass accessible at the LHC. The highest invariant mass candidate was observed in the $\mu\nu\gamma$ final state with a mass exceeding 900 GeV. No significant excess was seen in the studied mass range of 200 – 1000 GeV. Fiducial cross section upper limits for narrow spin-1 charged and neutral resonances decaying to a lepton pair ($\ell^+\ell^-$ or $\ell\nu$) and a photon are shown in Figure 6.13 up to 650 and 800 GeV and go down to 1 and 3 fb at large masses, respectively.

6.2.2 Inclusive measurements of heavy gauge boson pairs

Detailed studies were also conducted in final states with two heavy weak vector bosons WW, WZ, ZZ decaying leptonically: they show good agreement with SM predictions at all energies. In Figure 6.14 the observed production cross sections in p$\bar{\text{p}}$ and pp collisions are compared to perturbative calculations up to NNLO in QCD and NLO in EW interactions by MATRIX [586] as a function of the center of mass energy. The largest deviation is seen in the WZ cross section at 5.02 TeV with a deviation below 2 s.d. This statistically limited measurement [587] was conducted using data collected in 2017 with a special trigger menu I designed to optimally use the low instantaneous luminosity conditions and the short data taking time.

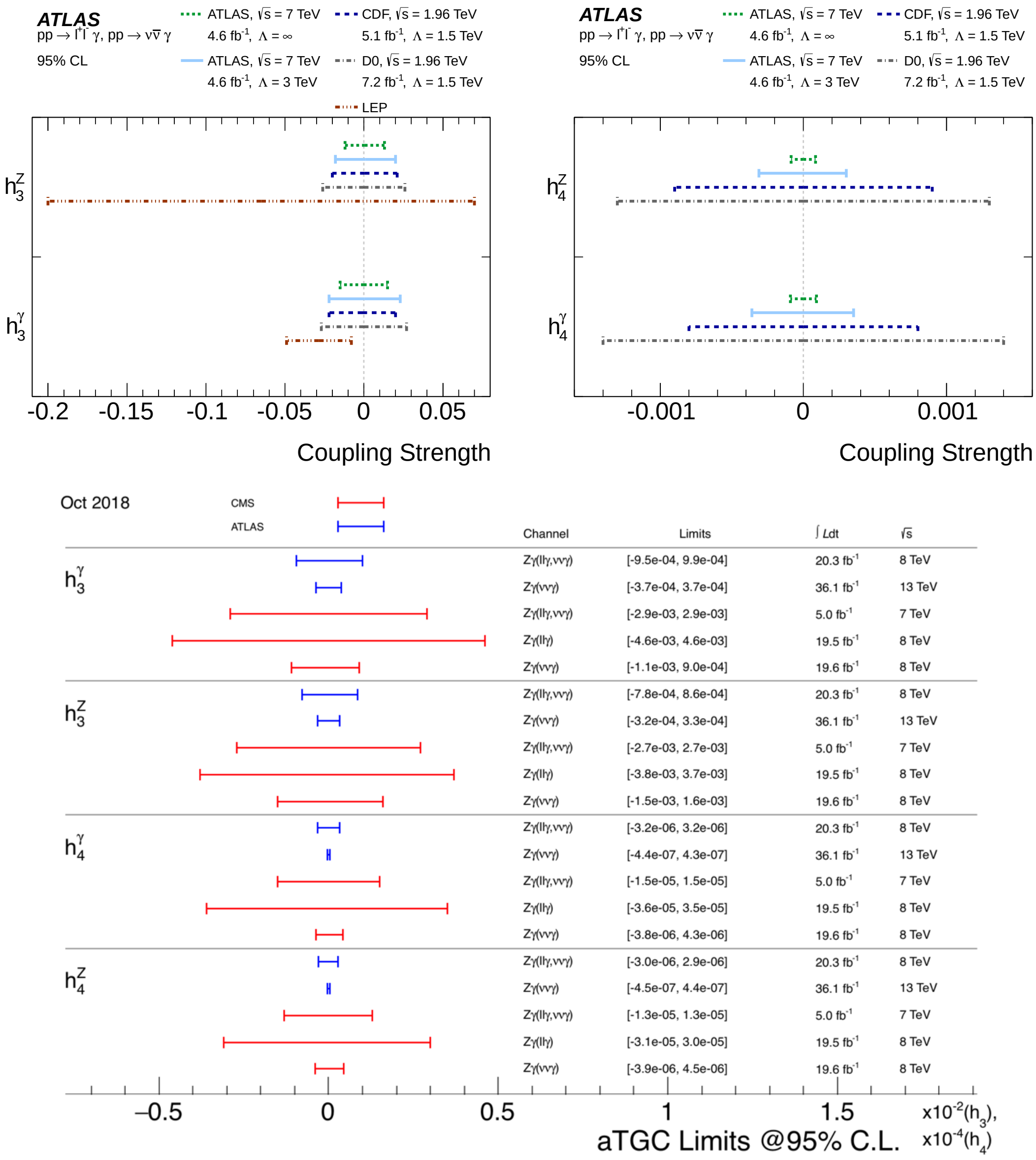

Figure 6.12: *Constraints on neutral anomalous triple gauge couplings (top) derived from the Zγ analysis at $\sqrt{s} = 7$ TeV by the ATLAS experiment compared to the most stringent limits of the time [529], and (bottom) more recent results from the LHC experiments [582].*

The differential cross section measurements and the extraction of triple gauge couplings did not bring to light any significant effect that could be considered as a sign of beyond the standard model (BSM) phenomena so far. Indeed, early discrepancies between observations and theory have motivated improved theoretical calculations. As an example, the most discrepant value in Run-1 LHC measurements was that of the WW cross section with a 2.1 s.d. excess seen in data with respect to the MCFM calculation at NLO in QCD including off-shell bosons and decays. Investigations then pointed to underestimated uncertainties related to missing higher order contributions as well as to the jet veto (necessary to suppress the large top quark pair background) [523]. Detailed measurements of the differential cross sections help to uncover these effects by provid-

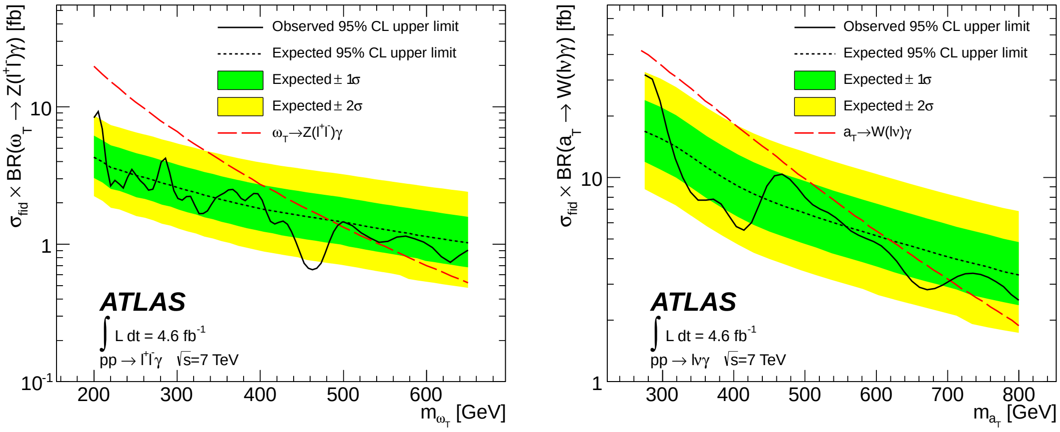

Figure 6.13: *Fiducial cross section upper limits for narrow spin-1 (left) neutral and (right) charged resonances decaying to a lepton pair ($\ell^+\ell^-$ or $\ell\nu$) and a photon. Theoretical prediction for a benchmark low-scale technicolor model [566, 568] is given assuming that the sum of the masses of the techi-ρ and the techi-π is m_W. [529]*

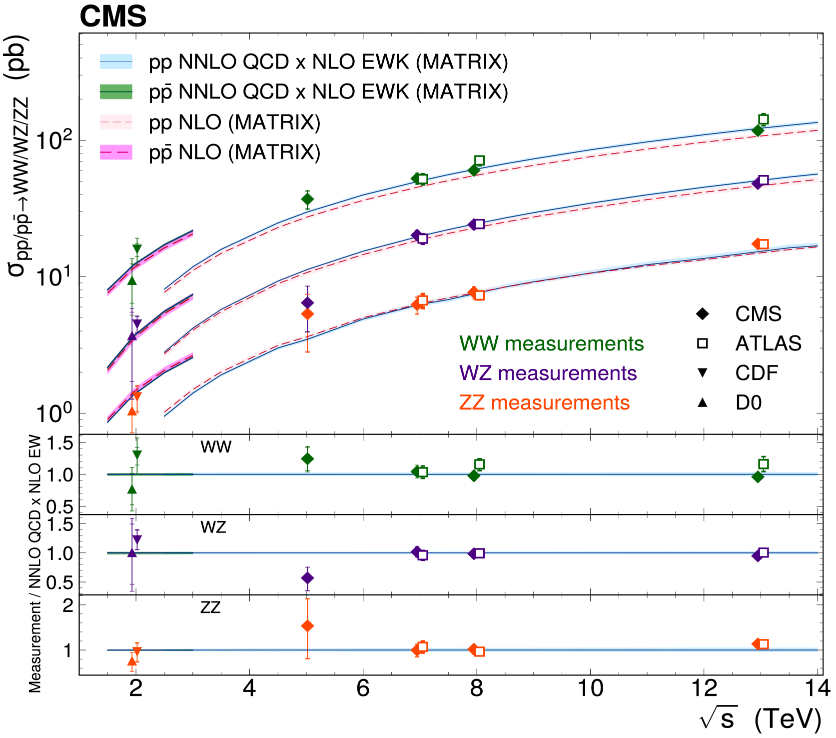

Figure 6.14: *Observed WW, WZ and ZZ production cross sections by the Tevatron and the LHC experiments compared to SM predictions calculated by MATRIX as a function of the center of mass energy. The quark-induced NNLO QCD and NLO EW contributions are combined multiplicatively (NNLO QCD × NLO EW). For WW and ZZ, the gluon-induced processes are added up to NLO in QCD, and the photon-induced contributions to NLO in EW theory, following the procedure described in Ref. [588]. The vertical error bars represent the uncertainty in the measured cross sections, with the inner most line representing the statistical component. [587]*

ing information on event kinematics, production modes, and the presence of additional radiation.

The extraction of the Wilson coefficients for dim-6 operators inducing charged TGCs is particularly important, as these would also influence Higgs boson interactions and the rare vector boson scattering processes, and are typically assumed to be zero in the analysis of the latter in dim-8 EFT. Recent results based on the Run-2 LHC data put stringent limits on the coefficients of the operators $\mathcal{O}^{(6)}_{WWW}$ and $\mathcal{O}^{(6)}_{W}$ that also induce quartic charged gauge couplings: c_{WWW}/Λ^2 is restricted to [–0.062, 0.052] [576] and c_W/Λ^2 to [–2.5, 0.3] [170] in units of TeV^{-2}.

6.2.3 Search for exotic diboson production with a large area jet

Exotic heavy bosons (such as spin-0 radions, spin-1 Z′ or W′ bosons, or spin-2 Randall-Sundrum gravitons introduced previously) can also be sought in diboson final states.

The production of high-mass ZZ or ZW pairs was studied [536] in final states consisting of a large area jet, missing transverse momentum, and – optionally – a pair of forward-backward hadronic jets targeting a Z boson decaying to a pair of neutrinos, and the other boson to a boosted quark pair with large momentum. For the production mechanism, gluon-gluon fusion (ggF), s-channel quark-induced Drell–Yan production (DY) and vector-boson fusion (VBF) processes were considered (Figure 6.15). For vector and tensor particles, the decay angle to the SM EW vector bosons depends very strongly on the production process. The hadronically decaying boson is identified as a wide jet reconstructed by the anti-k_t algorithm with $R = 0.8$ radius parameter and a substructure compatible with two merged narrow jets originating from the hadronic decay of an EW vector boson.

An excess of events is searched for in the transverse mass distribution calculated for the highest p_T fat jet and the p_T^{miss}, separating the data into two samples based on the presence of forward jets (VBF-tagged) or their absence (ggF/DY). No discrepancy with respect to the SM was found as shown in Figure 6.16. The results – on which I worked as the member of the analysis review committee – were interpreted in terms of radion, W′ boson, and graviton models, under the assumption of different production hypotheses. Limits on the production cross section times branching ratio ($\sigma \cdot B$) range between 0.2 and 9 fb for radions, 0.5 and 20 fb for W′ resonances, and 0.3 and 10 fb for gravitons in the mass range 1–4.5 TeV, with more stringent limits at high mass where very little SM background remains. These results can be turned into lower limits on the boson masses that depend on the exact choice of model parameters, and typically are between 1.2 and 4.0 TeV.

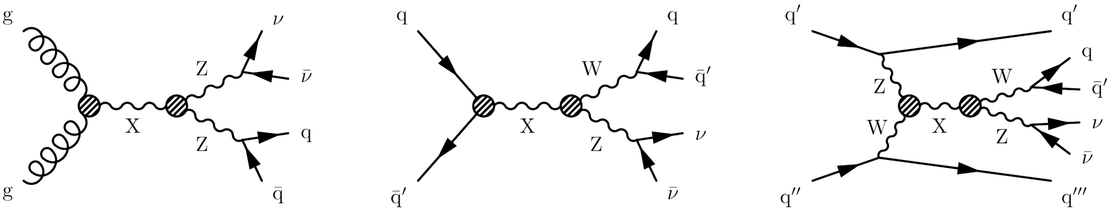

Figure 6.15: *Representative diagrams of heavy resonance production followed by the decay to two EW vector bosons. From left to right: gluon-gluon fusion, s-channel quark-induced (Drell-Yan) production and vector boson fusion.*

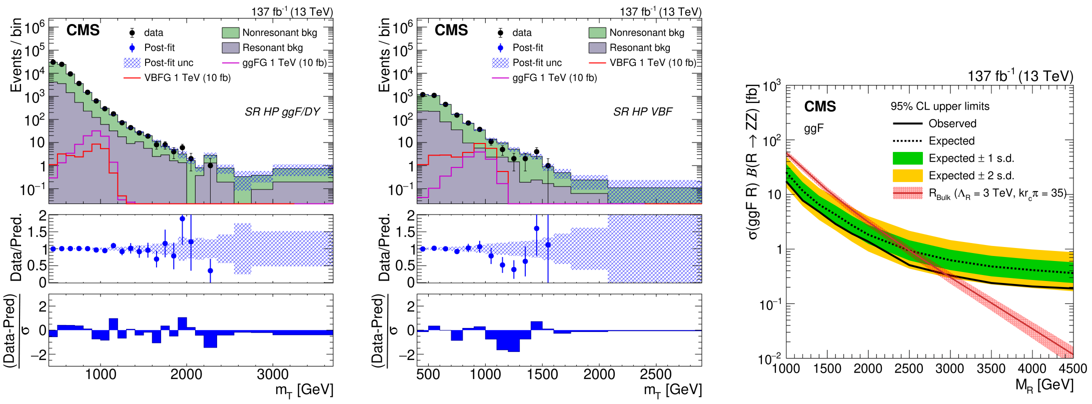

Figure 6.16: *Distribution of the observed and predicted event yields versus the transverse mass for the high-purity (left) ggF/DY and (middle) VBF signal regions in the heavy exotic boson search in the Run-2 CMS data. A hypothetical graviton signal with a mass of 1 TeV is overlayed assuming VBF or ggF production. The middle panel shows the ratio of data and predictions, with the hashed area representing the total uncertainty on the prediction. The bottom panel shows the pull of the observed event yields wrt. the predictions, normalized by the quadratic sum of the data statistical uncertainty and the total uncertainty on the prediction. (right) Observed (solid black) and expected (dashed with 1σ and 2σ bands) upper limits on $\sigma \cdot B$ and the predicted signal cross sections (red with uncertainties due to PDF and scale choices) for ggF-produced radions as a function of the hypothesized radion mass. [536]*

6.3 Electroweak diboson production accompanied by jets

Moving from inclusive diboson measurements to those that require a forward-backward jet pair, a new type of processes becomes accessible: vector boson scattering which includes diboson production via a quartic gauge coupling.

While neutral gauge boson vertices are first induced by dim-8 terms of the SMEFT, charged quartic couplings get contributions both from dim-6 and dim-8 terms, the former being also restricted by WW, WZ and Wγ measurements, as discussed in the previous section. It is thus important to recall that the interpretation of any discrepancy from the SM would require a complex analysis and results assuming the dominance of a single contribution only serve as benchmarks.

The work presented in this section was performed in a series of analyses to which I contributed as supervisor and internal expert reviewer, as well as through my activities leading the trigger effort in the electron-photon and standard model physics groups.

6.3.1 Studies of ZZ + jets production

The pp $\to$ ZZ $\to \ell^+\ell^-\ell'^+\ell'^-$ process provides the cleanest, fully reconstructable diboson final state at LHC and thus has an important role in studying the SM gauge structure and EWSB as evidenced by the discovery of the SM Higgs boson described in Section 5.5.

The production of ZZ pairs in association with a forward-backward jet pair (often called ZZjj production) includes the rare vector boson scattering process. The study of EW ZZjj production, however, necessitates a detailed understanding of the QCD corrections to the associated production of diboson pairs and jets.

ZZjj production is sensitive to the largest number of EFT higher-dimensional operators introduced in Section 1.2.

6.3.1.1 Cross section measurement

The measurement of the differential cross sections for pp → ZZ + jets production provides essential information to test the state-of-the art theoretical predictions. It was conducted using pp collision data at $\sqrt{s} = 8$ and 13 TeV corresponding to 19.7 and 35.9 fb^{-1} integrated luminosity collected in 2012 and 2016 by CMS, considering Z decays to opposite-sign electron and muon pairs [530]. The data sample was collected using single, di- and trilepton triggers requiring the real-time reconstruction of electrons and / or muons [267, 409] in the event, with an overall efficiency of more than 98%.

The cross section as a function of the number of jets, the transverse momentum (p_T) and pseudorapidity of the p_T-leading and subleading jets, as well as the invariant mass of the two p_T-leading jets and their separation in pseudorapidity was studied. The systematic uncertainty, dominated by the jet energy scale and resolution with sizable contributions also from the background yield and the signal MC model, was of the same size, or smaller, than the statistical uncertainty.

The fiducial region for the measurement was defined in terms of the p_T and pseudorapidity of the leptons and the invariant mass of the lepton pairs. The total background contribution after requiring four isolated leptons with kinematics compatible with the ZZ production hypothesis was 3-4% of the expected signal rate, primarily from WWZ, $\mathrm{t\bar{t}Z}$ giving genuine four-lepton events, as well as Z+jets and $\mathrm{t\bar{t}}$ events with non-prompt or misidentified leptons.

The response matrix describing the relation between the generated and the reconstructed quantities were prepared with alternative signal models for the dominant $q\bar{q} \to \ell^+\ell^-\ell'^+\ell'^-$ process that contains contributions from ZZ, $\mathrm{Z}\gamma^\star$, $\gamma^\star\gamma^\star$ and Z production. The first sample was produced by MadGraph 5 1.3.3 [296, 589] at LO in pQCD with 0-2 jets in the matrix element at 8 TeV and by MadGraph 5_aMCNLO 2.3.3 [296, 590] (abbreviated as MG5_aMC in the figures) at NLO in pQCD with 0-1 jets at 13 TeV. The other sample used POWHEG 2.0 [299, 435, 591, 592] at NLO in pQCD with 0-1 jets at both energies, and scaled by a factor of 1.1 at 13 TeV to reproduce the total cross section calculated at NNLO [593]. The loop-induced gg → ZZ was simulated by MCFM 6.7 or 7.0 at LO (Figure 6.17) and scaled to the NLO cross section by a factor of 1.7 [594]. Electroweak production of $q\bar{q} \to \mathrm{ZZ}q\bar{q}$ was generated at LO by PHANTOM [595] and includes triboson processes and quartic vertices (Figure 6.18). The robustness of the Bayesian unfolding of the detector effects was checked with the method.

The differential cross section as a function of the jet multiplicity is shown in Figure 6.19. The data indicate that due to a softer p_T spectrum of the hadronic particles recoiling against the ZZ system, less jets pass the $p_\mathrm{T} > 30$ GeV lower cut in data, and thus more events fall to the zero-jet bin. This observation is also supported by

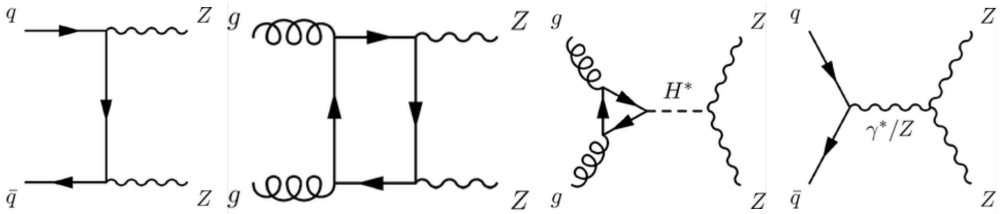

Figure 6.17: *Representative diagrams of* pp → ZZ *production. From left to right: LO* t*-channel* $q\bar{q} \to ZZ$*, loop-induced* gg → ZZ *via a quark box and via gluon-fusion Higgs production,* s*-channel quark-induced process with anomalous nTGC.*

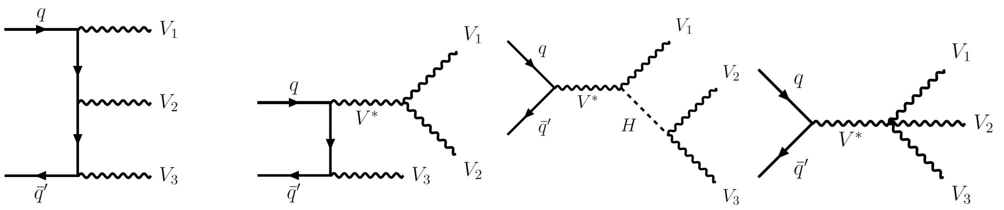

Figure 6.18: *Representative diagrams of EW triboson production in pp collisions:* $q\bar{q} \to VVV$*. From left to right: three boson emissions from the quark line, two boson emissions followed by a TGC interaction, Higgs-strahlung followed by a HVV interaction, and s-channel vector boson production followed by a QGC interaction. Only charged TGCs and QGCs are present in the SM.*

the softer observed p_{T} spectrum of the ZZ system [596, 597] and could originate from missing higher-order corrections or the parton shower model.

The cross section as a function of various single and dijet quantities are also shown in Figure 6.20 at $\sqrt{s} = 13$ TeV. The jet p_{T} distributions and the dijet invariant mass tend to agree with the simulation. The pseudorapidity distributions of the leading and subleading jets tend to be steeper in the data, as well as the pseudorapidity difference between the two jets.

In general, good agreement is found between the measurements and the pQCD predictions of NLO matrix-element calculations interfaced to the PYTHIA parton shower simulation. Cross sections for ZZ production in association with jets have been measured with a precision of $10-72\%$ at 8 TeV and $8-38\%$ at 13 TeV for jet multiplicities ranging from 0 to ≥ 3.

As this measurement is statistically limited, the inclusion of the full 13 TeV data

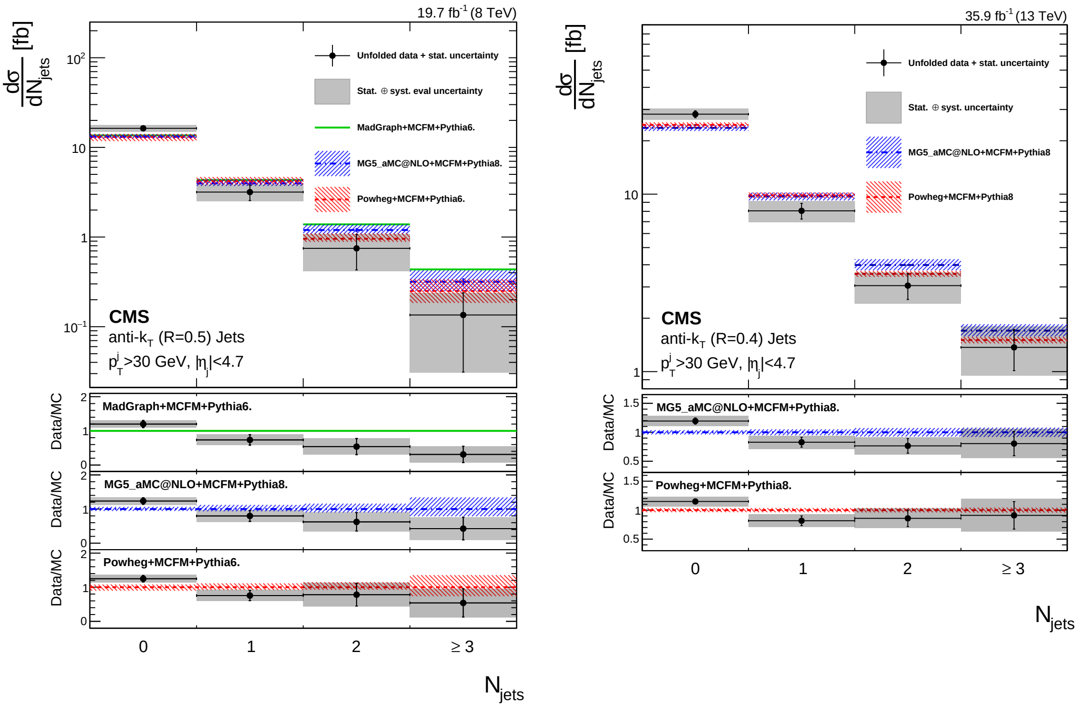

Figure 6.19: *Differential cross sections of* $\mathrm{pp} \to ZZ \to \ell^+\ell^-\ell'^+\ell'^-$ *as a function of the number of jets with* $p_{\mathrm{T}} > 30$ *GeV and* $|\eta| < 4.7$ *at (left) 8 TeV and (right) 13 TeV collision energy, compared to different theoretical predictions. [530]*

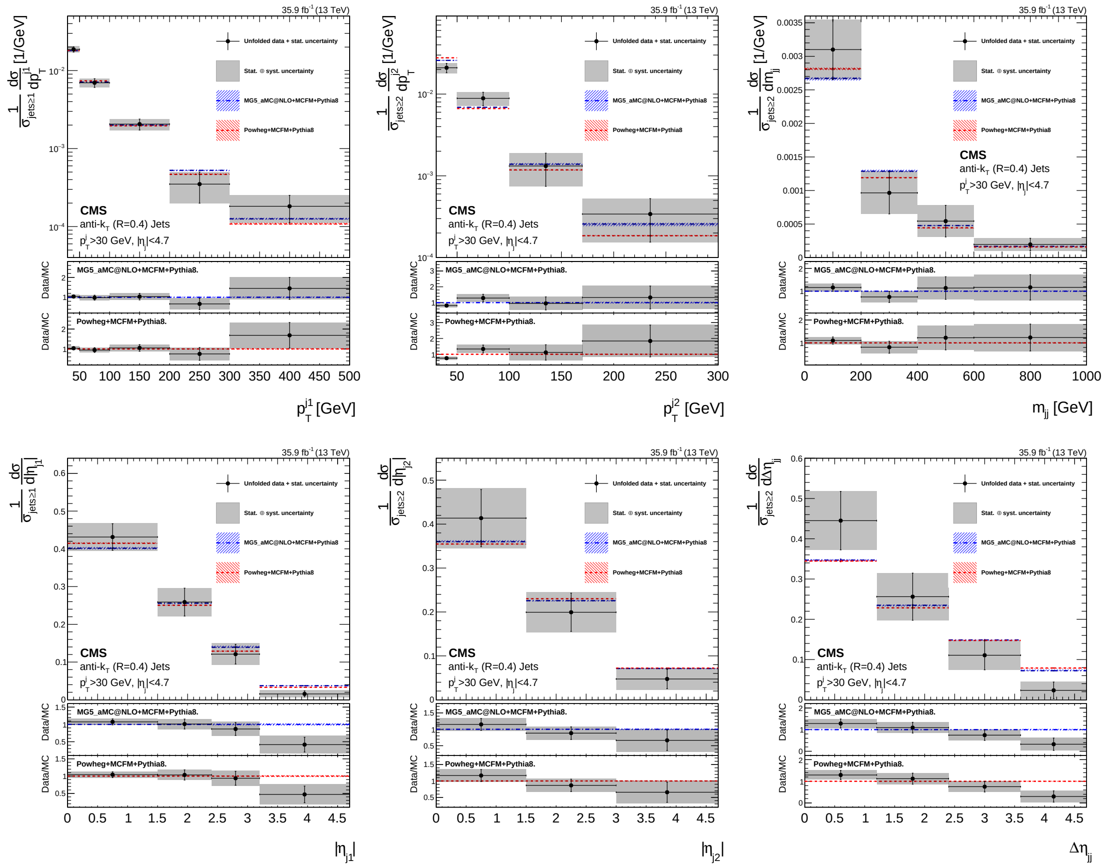

Figure 6.20: *Differential cross sections of* pp $\to ZZ \to \ell^+\ell^-\ell'^+\ell'^-$ *as a function of the (top left) leading and (top middle) subleading jet* p_{T}*, (top right) the dijet invariant mass, the (bottom left) leading and (bottom middle) subleading jet pseudorapidity, and (bottom right) the pseudorapidity difference between the leading and subleading jets at 13 TeV, compared to different theoretical predictions. The jets were required to have* $p_{\mathrm{T}} > 30$ *GeV and* $|\eta| < 4.7$*. [530]*

set improves the precision and strengthens the test of the SM perturbative predictions. Preliminary results on the normalized differential cross sections from CMS have recently appeared [598] testing more refined theoretical predictions. These include more jets in the matrix element for NLO samples, and a recent sample dubbed nNNLO+PS [599] using the POWHEG framework. The latter prediction includes NNLO computations for $q\bar{q} \to$ ZZ process combined with parton shower using the MiNNLO$_{\mathrm{PS}}$ method and NLO for loop-induced gluon fusion processes matched to PS, and takes into account spin correlations, interferences and off-shell effects. These samples are expected to better describe the high jet multiplicity region. nNNLO+PS describes the jet multiplicities better than the NLO predictions up to one additional jet. However, important differences remain that necessitate further improvements to the calculations to provide an accurate description of the full phase space.

6.3.1.2 Observation of vector boson scattering

The scattering of massive EW vector bosons is intimately connected to the mechanism of EWSB. The W and Z bosons acquire their mass and a third degree of freedom in the form of a longitudinally polarized component during electroweak symmetry breaking through their coupling to the Higgs field (as opposed to the photon that remains massless with only two transverse polarization states). If the values of the triple and quartic gauge couplings and the couplings between the Higgs and the gauge bosons are different from their SM predictions, the cross sections of the longitudinal vector boson scattering processes will increase with energy and violate unitarity at high energies. This implies that in such a case, the SM would prove incomplete, and new contributions to the scattering amplitude from additional non-SM fields would become necessary.

The vector boson scattering (VBS) cross section cannot be extracted directly from the data. Strongly VBS-enriched event samples from pp $\to$ ZZ$q\bar{q} \to \ell^+\ell^-\ell'^+\ell'^- q\bar{q}$ can however be selected by requiring the production of a forward-backward jet pair in association with the ZZ pair (ZZjj). In VBS events, no hadronic activity from the hard scattering is expected in the rapidity region defined by the four-momenta of the two jets. The total and the electroweak ZZjj production cross sections (representative diagrams shown in Figure 6.21) are then measured and compared to the pQCD predictions. The EW component is given by all $2 \to 6$ tree-level diagrams for $q\bar{q} \to \ell^+\ell^-\ell'^+\ell'^- q\bar{q}$ at α_{EM}^6 order, including their interference terms. The QCD induced background contains processes at $\alpha_{\mathrm{EM}}^4\alpha_s^2$ order. The terms from the interference between the EW and the QCD-induced diagrams have a small contribution to the event rate in the strongly VBS-enriched region (3.5% of the EW signal). This is taken into account when extracting the EW signal with a square-root scaling of the signal strength, approximated by a linear expansion.

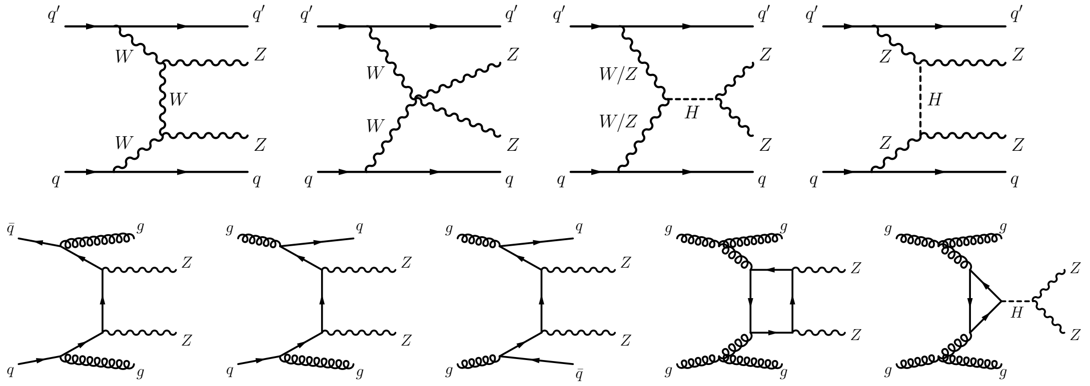

Figure 6.21: *Representative diagrams for* pp $\to$ *ZZjj production via (top) EW and (bottom) QCD-induced processes. From left to right: (top) EW production via two TGCs, via a QGC, via s-channel Higgs exchange, via t-channel Higgs exchange. (bottom) QCD-induced leading order production from* $q\bar{q}$*, qg and gg interactions, and loop-induced process from gg with a quark box emitting the Z bosons and via Higgs production.*

The extracted EW signal was interpreted in a dim-8 effective field theory containing a collection of linearly independent operators to derive constraints on the Wilson coefficients corresponding to these operators, normalized according to the power counting rule by the cut-off scale, i.e. Λ^{-4} (see Section 1.2).

The CMS measurements were produced first using a partial data set, corresponding to 35.9 fb^{-1} integrated luminosity collected in 2016 at 13 TeV [531]. Then the full Run-2 data set corresponding to 137 fb^{-1} at 13 TeV collected in 2016 - 2018 were analyzed – with the help of improved MC simulations – to increase the sensitivity and achieve the observation of the EW ZZjj production process [532].

The fiducial region was defined in terms of ”dressed” lepton and jet kinematic variables at particle level (p_{T} and η), the dilepton and four-lepton invariant masses, and the jet-lepton angular separation (ΔR). It closely reflects the reconstruction level event selection criteria. In addition, for the inclusive measurement $m_{jj} > 100$ GeV was prescribed for the dijet invariant mass, while for the VBS-enriched measurements a pseudorapidity separation of $|\Delta\eta_{jj}| > 2.4$, and either a loose $m_{jj} > 400$ GeV or a tight $m_{jj} > 1$ TeV mass selection were required.

The non-ZZ background is below 10% and mostly originates from genuine four-lepton final states from $\mathrm{t\bar{t}Z}$ and ZVV (with V = Z, W) processes (estimated from simulation), as well as from reducible sources, especially from Z+jets with leptons primarily from semi-leptonic b hadron decays or jets misidentified as leptons (below 2-3%, estimated from a control region using lepton fake rates measured in the data).

The extraction of the tiny EW signal was rather challenging as illustrated by the dijet invariant mass and the dijet pseudorapidity separation in Figure 6.22. While in the analysis of the partial data sample the baseline to discriminate the EW signal from the QCD-induced background was a boosted decision tree using seven kinematic variables of the dijet, dilepton, four-lepton systems and the event balance, in the final full Run-2 measurement a matrix element method [498] was applied. The signal to background ratio increased from 3 to 4 in the highest, and from 1 to 2 in the second highest bin of the event-by-event discriminator.

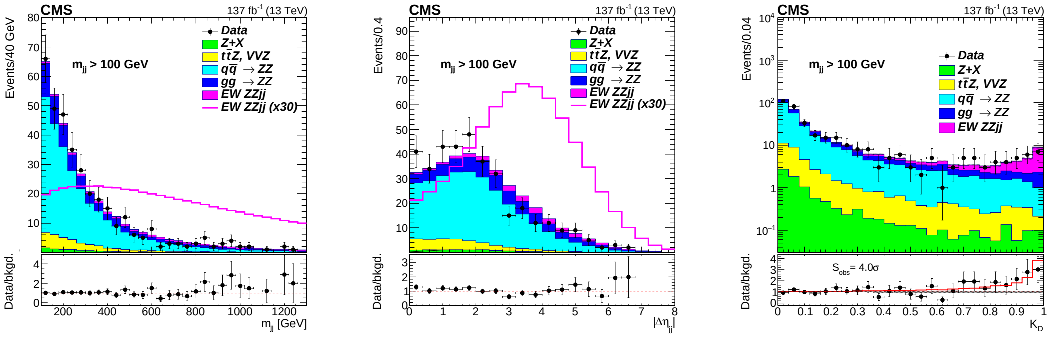

Figure 6.22: *Distributions of (left) the dijet invariant mass m_{jj}, (middle) the pseudorapidity separation $|\Delta\eta_{jj}|$, and (right) the matrix element discriminator K_D in the inclusive selection of the CMS ZZjj analysis in the full Run-2 data set. The data are compared to the stacked expectations from the background and the signal processes. To illustrate the shape of the m_{jj} and $|\Delta\eta_{jj}|$ distributions, the signal scaled up by a factor of 30 is also shown. For the matrix element discriminator distribution, the weights extracted from the fit to determine the EW contribution are applied. [532]*

The matrix element likelihood approach (MELA) – introduced in Section 5.5 – combines the maximal amount of theoretical information at LO with reconstruction level information to provide the probability that the event matches the hypothesis, using as input the 4-momenta of the final state reconstructed particles. The probability is calculated taking into account the parton density functions, the LO matrix element (ME) of the process and a transfer function to account for showering and hadronization effects, as well as the experimental resolution of the instrumentation. The ME is calculated by MCFM for EW ZZjj and for QCD-induced $q\bar{q} \to$ ZZjj processes. The discriminant is formed from the probabilities that a given event is from the EW signal or from the QCD-induced background: $K_D = \mathcal{P}_{\mathrm{EW}}/(\mathcal{P}_{\mathrm{EW}} + \mathcal{P}_{\mathrm{QCD}})$. The kinematic distributions of both leptons and jets are considered.

Expected distributions of the signal and irreducible background were taken from simulation while the reducible background from data control region. When determining the signal strength, the shape and normalization of the distributions were allowed to vary within their uncertainties in the fit to the discriminant distribution. The measured

EW signal strength in the ZZjj inclusive region is

$$\mu_{\mathrm{EW}}(\mathrm{ZZjj}) = 1.22^{+0.47}_{-0.40},$$

while the EW+QCD signal strength is

$$\mu_{\mathrm{EW+QCD}}(\mathrm{ZZjj}) = 0.99^{+0.13}_{-0.12}.$$

The significance of the observed EW signal is 4.0 s.d. with an expected value of 3.5 s.d. The ATLAS experiment has recently made a 5 s.d. observation of the EW ZZjj process [601].

The fiducial cross sections are measured for the inclusive selection with an expected EW contribution of 5%, as well as for the loose and tight VBS-enriched selections with and expected EW contribution of 15 and 47%. A good agreement is observed in the data when compared to LO, NLO EW and NLO QCD calculations. For example, the cross section in the tight VBS-enriched region was found to be

$$\sigma_{\mathrm{EW,fid}}(\mathrm{ZZj}j) = 0.09^{+0.04}_{-0.03}\ (\mathrm{stat})\ \pm 0.02\ (\mathrm{syst})\ \ \mathrm{fb},$$

showing an excellent agreement with the NLO QCD prediction of 0.108 ± 0.007 fb within the experimental uncertainties dominated by statistics. EW ZZjj production is among the rarest processes at the LHC that has been measured so far, as illustrated on Figure 6.24 that collects di- and triboson, as well as VBF single gauge boson cross section results.

6.3.1.3 Determination of quartic gauge couplings

The four-lepton invariant mass distribution, shown in Fig 6.23 can be used to probe new physics searching for evidence of contributions from dim-8 operators. EW ZZjj production is particularly sensitive to the charged $\mathcal{O}_{T,0-2}$ and the neutral current $\mathcal{O}_{T,8-9}$ operators, corresponding to couplings of the transverse degrees of freedom in the SM EFT extension. Stringent constraints were placed on the corresponding aQGCs, as summarized in Table 6.1. These were derived without imposing a unitarity bound, which is then estimated as the $m_{4\ell}$ scattering energy at which the aQGC strength is equal to the observed limit. They lie between 1.8 to 2.6 TeV, depending on the operator. No event was observed in data at such high masses (see also Section 6.3.4 for more discussion on the EFT validity). The limits on $f_{T,8-9}/\Lambda^4$ are the most stringent to date.

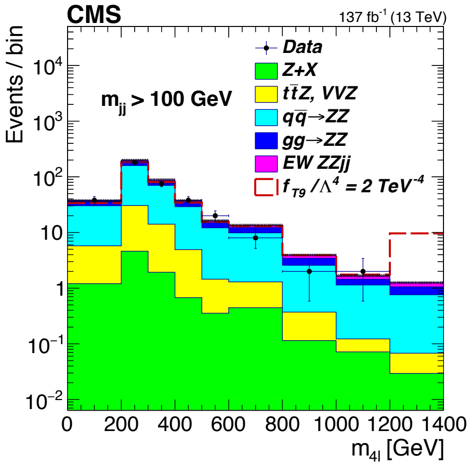

Figure 6.23: *The four-lepton invariant mass distribution for events passing the inclusive selection in the CMS ZZjj analysis at 13 TeV using the full Run-2 data set. The measured data are compared to the stacked expectation of various background processes and the signal, using the weights extracted from the fit to determine the EW contribution. [532]*

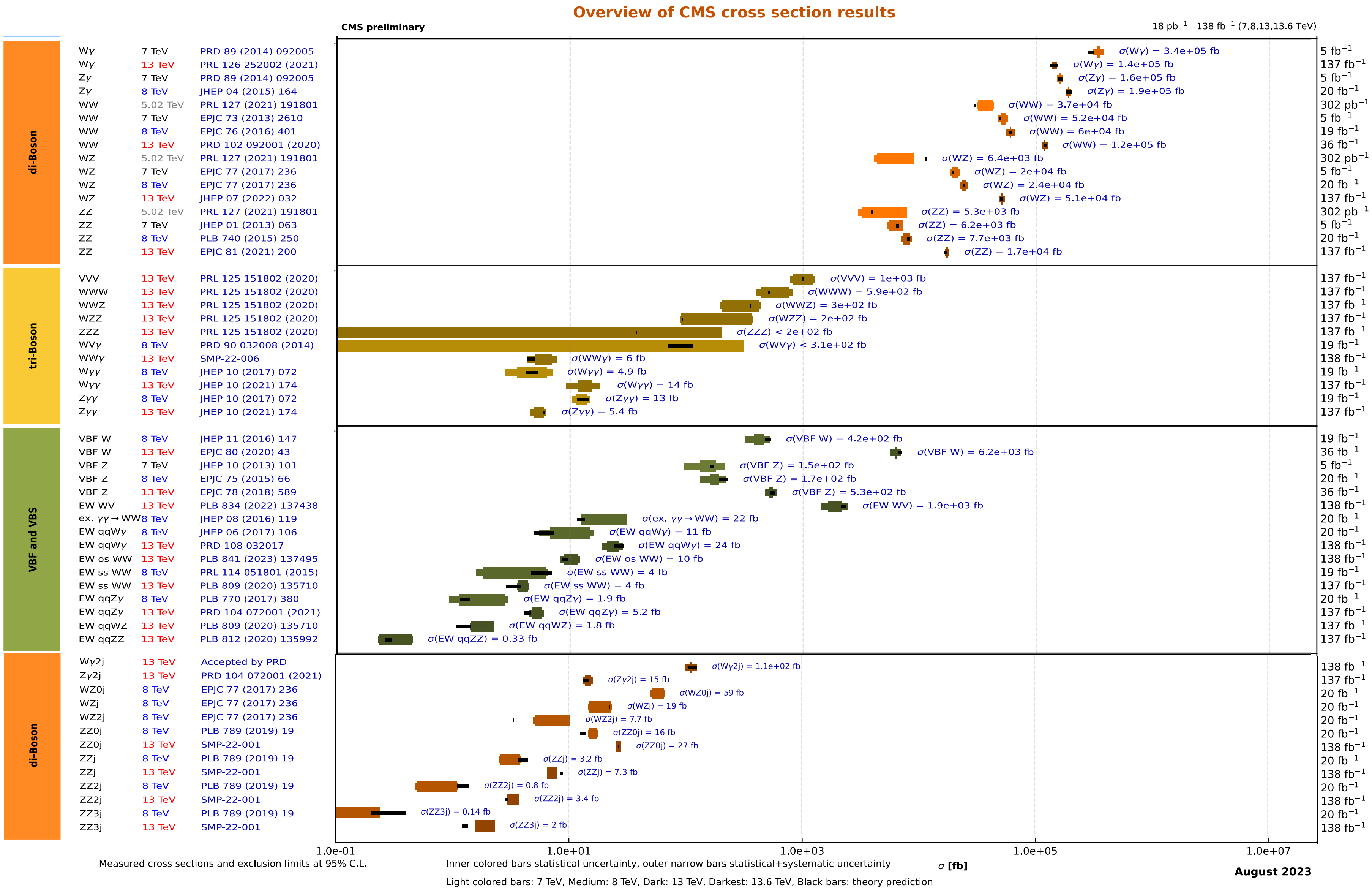

Figure 6.24: *Summary of di- and triboson cross sections measured by CMS and compared to state-of-the art theoretical calculations. Based on Ref. [602].*

6.3.2 WWjj measurements

The first experimental observation of massive EW vector boson pair production in association with a forward-backward jet pair was made for the same-charge $\mathrm{W}^{\pm}\mathrm{W}^{\pm}$jj process [603, 604] using the 13 TeV LHC data collected in 2016. The requirement of a same-charge lepton pair reduces the contribution from QCD-induced production of WW pairs. The main background comes from non-prompt leptons and WZ production, with a signal-to-noise ratio of about 0.5 for a dijet invariant mass of $m_{jj} > 500$ GeV, and above 1.0 for $m_{jj} > 900$ GeV. The relatively high purity of the event selection makes the $\ell^{\pm}\nu\ell^{\pm}\nu$jj final state an ideal topology for VBS studies.

This was also the first channel where the possibility to study polarized VBS had been demonstrated [605]. The CMS collaboration using the full Run-2 data set applied a BDT to exploit kinematic differences between the polarized scattering processes. The cross section for final states where at least one of the W bosons is longitudinally polarized was measured in a fiducial region to be $1.40^{+0.60}_{-0.57}$ fb, in good agreement with the prediction of 1.71±0.19 fb at LO calculated by MADGRAPH5_aMC@NLO 2.7.2 with additional $\mathrm{O}(\alpha^7_{\mathrm{EM}})$ corrections. The observed significance of the process reaches only 2.3 s.d. (3.1 s.d. expected). Due to statistics limitations, the SM EW $\mathrm{W^{\pm}}_\mathrm{L}\mathrm{W^{\pm}}_\mathrm{L}$ and $\mathrm{W^{\pm}}_\mathrm{L}\mathrm{W^{\pm}}_\mathrm{T}$ cross sections could not yet be separately extracted.

6.3.2.1 $\mathrm{W}^{+}\mathrm{W}^{-}$jj cross section measurement

While $\mathrm{W}^{\pm}\mathrm{W}^{\pm}$jj can get contribution from new physics, such as doubly charged Higgs production, the experimentally more challenging $\mathrm{W}^{+}\mathrm{W}^{-}$jj final state is more sensitive to exotic phenomena that could affect the couplings of the W bosons to the Higgs boson. Anticipating also a future combined EFT analysis, the opposite-charge EW WWjj production cross section measurement [533] was performed targeting the processes shown in Figure 6.25 (top).

To suppress the challenging irreducible contribution of top quark pairs and of the QCD-induced production of W boson pairs (Figure 6.25 (bottom)) a deep neural network (DNN) was utilized using nine kinematic variables formed from the four-momenta of the final state leptons and jets. As in all VBS measurements, the most sensitive variables are related to the dijet system: the mass (m_{jj}) and the separation in pseudorapidity ($|\Delta\eta_{jj}|$) of the two jets, the jet transverse momenta, the two Zeppenfeld variables[2] (Z_{ℓ_i}) looking at the lepton - jet balance, the p_T and the azimuthal separation of the lepton system, and the transverse mass[3] calculated using the leading lepton kinematic variables and those of the missing transverse momentum ($m_\mathrm{T}^{\ell_1}$). The DNN output was used in the $\mathrm{e}^{\pm}\mu^{\mp}$jj final state as discriminating variable, while the signal region was divided to bins in m_{jj} and $|\Delta\eta_{jj}|$ in the same flavor $\mathrm{e}^{+}\mathrm{e}^{-}$jj and $\mu^{+}\mu^{-}$jj channels. The phase space was divided into two regions by the variable $Z_{\ell\ell} = |Z_{\ell_1} + Z_{\ell_2}|/2$, with $Z_{\ell\ell} < 1$ being richer in EW $\mathrm{W}^{+}\mathrm{W}^{-}$jj signal. The signal regions are shown in Figure 6.26 for $Z_{\ell\ell} < 1$. The highest purity EW WWjj signal was achieved for the highest DNN output values (above 50%) and for the largest m_{jj} bin (around 30%).

The cross section in a fiducial region motivated by the experimental acceptance was measured to be 10.2 ± 2.0 fb consistent with the SM prediction of 9.1 ± 0.6 fb. The total uncertainty of 20% is almost equally divided between the statistical (15%)

---

[2] The Zeppenfeld variable is defined from the pseudorapidity values of the lepton and the two jets: $Z_\ell = \eta_\ell - (\eta_{\mathrm{j}_1} + \eta_{\mathrm{j}_2})/2$.

[3] The transverse mass is defined from the kinematic variables of the lepton and the missing transverse momentum: $m_\mathrm{T}^{\ell} = \sqrt{2p_\mathrm{T}^{\ell}p_\mathrm{T}^{\mathrm{miss}}[1 - \cos\Delta\Phi(\vec{p}_\mathrm{T}^{\ell}, \vec{p}_\mathrm{T}^{\mathrm{miss}})]}$.

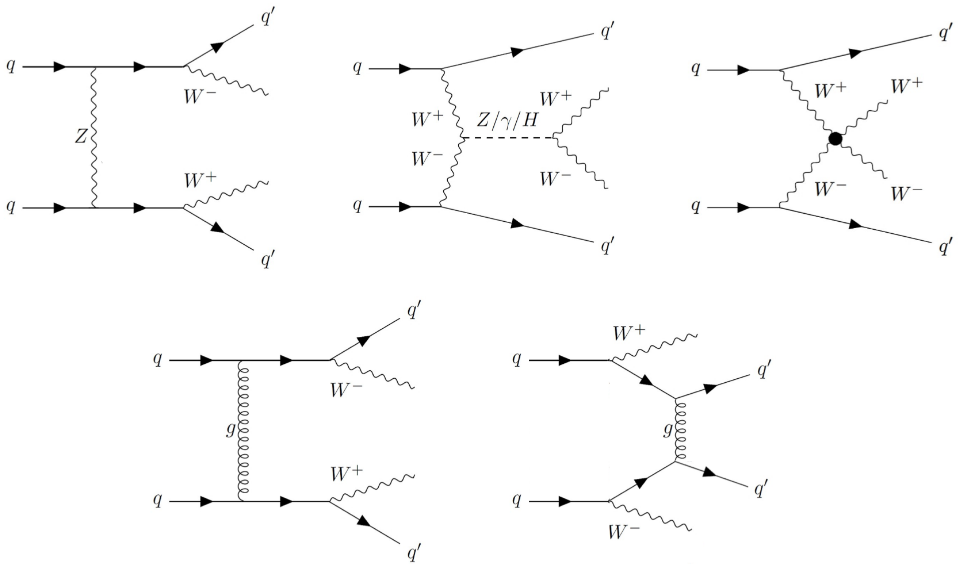

Figure 6.25: *Representative diagrams of quark-induced* W^+W^-jj *production. (top) Electroweak processes: t-channel Z exchange followed by double final state W radiation,* W^+W^- *s-channel interaction via a Z boson, a photon or a Higgs boson, and* W^+W^- *scattering via a quartic interaction vertex. (bottom) QCD production with t-channel gluon exchange between the initial state quark pair and the final state quark pair.*

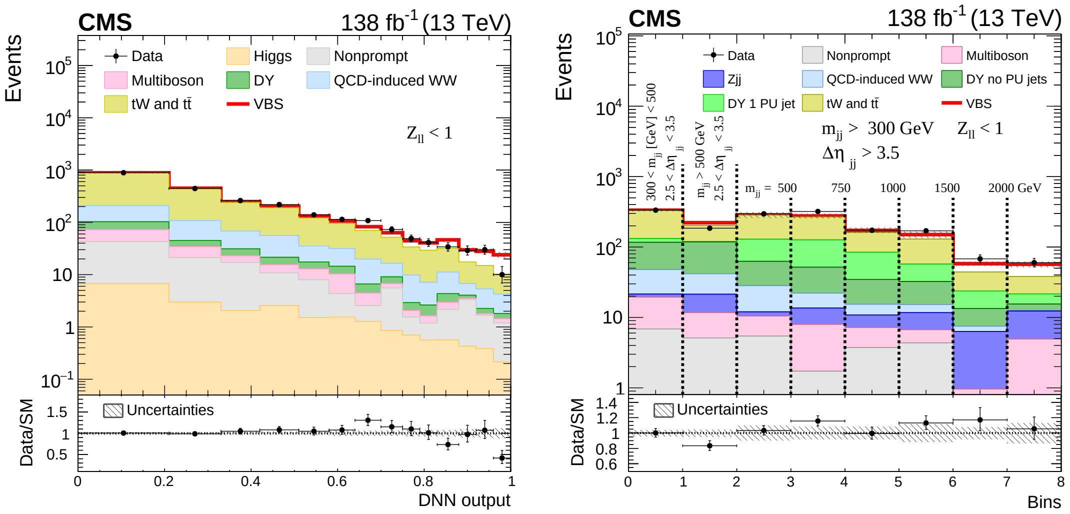

Figure 6.26: *The discriminating variables for the extraction of the EW* W^+W^-jj *contribution in the more signal rich* $Z_{\ell\ell} < 1$ *region. (left) The distribution of the DNN output in the* $e^{\pm}\mu^{\mp}$jj *final state. (right) The number of events in different* m_{jj} *and* $|\Delta\eta_{jj}|$ *bins as labeled in the figure for the same-flavor* e^+e^-jj *and* $\mu^+\mu^-$jj *final states. [533]*

and systematic (13%) components. To the latter the main contributions come from the normalization of the background rates, and the shape uncertainties when varying the renormalization and factorization scales in the signal and background simulations. Other notable sources are related to the reconstruction of the physics objects.

An observation of the EW production of opposite-sign WW bosons in association with two jets was reached for the first time, with a significance of 5.6 s.d. while 5.2 s.d. was expected. Studies of the the gauge couplings are under way in the SMEFT framework.

6.3.3 Wγjj measurements

The first observation of the EW production of W boson – photon pairs accompanied by two jets in proton-proton collisions was made by the CMS collaboration analyzing the data collected in 2016 at $\sqrt{s} = 13$ TeV studying the leptonic decays of the W boson producing an electron or muon and missing transverse momentum due to the outgoing neutrino [534]. Representative diagrams of the contributions to the EW signal and the QCD-induced background are shown in Figure 6.27. Requiring the two jets to have a high dijet mass and a large separation in pseudorapidity, the observed (expected) significance was 4.9 (4.6) standard deviations. In combination with the results achieved at $\sqrt{s} = 8$ TeV, the significance surpassed the value needed for an observation reaching 5.3 s.d (with 4.8 s.d. expected).

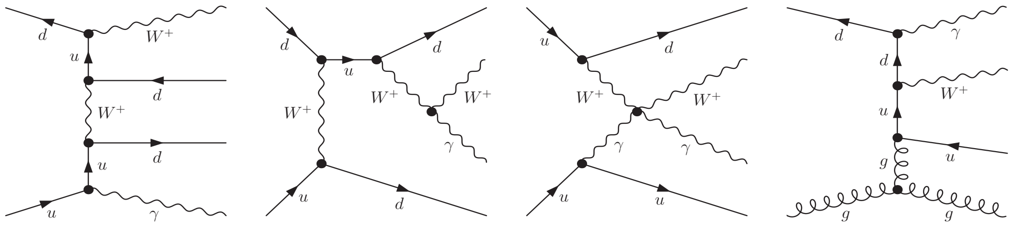

Figure 6.27: *Representative Feynman diagrams for $W\gamma$jj production in pp collisions. From left to right: EW production without a gauge coupling, via a TGC, via a QGC, and finally a QCD-induced background process.*

Extending the analysis to the full Run-2 data [535] confirmed the discovery, reaching a significance of 6.0 s.d. (6.8 s.d. expected) for the 13 TeV data alone, with an EW signal strength of $0.88^{+0.19}_{-0.18}$ compatible with the SM. It also allowed to perform differential studies as a function of various kinematic variables for the EW and the EW+QCD production.

The EW signal region was defined by requiring a large dijet mass above 500 GeV, a large separation in pseudorapidity of the two jets, a significant Wγ mass of at least 100 GeV, and momentum balance in pseudorapidity and azimuthal angle between the Wγ and the jj system as expected in the absence of further QCD radiation. Such a selection achieved a 10% EW signal purity and allowed the definition of control region at intermediate dijet masses between 200 and 500 GeV, where the background predictions can be validated with a signal contamination of less than 1%. The systematic uncertainties were evaluated in bins of the kinematic variables separately for each process: the largest contributions came from the jet energy scale and resolution, the statistical limitations of the data and simulated samples, and the determination of the non-prompt lepton and photon background.

The cross section measurement in a fiducial region covering 3.4% of the total phase space is dominated by systematic uncertainty, but it still has a sizable statistical component for the EW-induced Wγjj production:

$$\sigma^{\text{fid}}_{\text{EW}} = 23.5 \pm 2.8\ (\text{stat})\ {}^{+1.9}_{-1.7}\ (\text{theo})\ {}^{+3.5}_{-3.4}\ (\text{syst})\ = 23.5^{+4.9}_{-4.7}\ \text{fb},$$

whereas the total EW+QCD cross section measurement is largely dominated by systematic uncertainties: 113 ± 13 fb, and it is just 2% below the SM calculation. Differential cross sections were measured with the distributions unfolded to the particle level both for the EW and the EW+QCD processes. The results are in general in good agreement with the Standard Model expectations as the examples of the photon p_T and the dijet mass distributions for EW production show in Figure 6.28.

Similarly to the ZZjj and WWjj measurements, constraints were placed on anomalous quartic gauge couplings (aQGCs) in dim-8 EFT using the invariant mass distribution of the Wγ system for the high photon transverse momentum ($p_\mathrm{T} > 100$ GeV) and dijet mass ($m_{jj} > 800$ GeV) region, as shown in Figure 6.28. The derived 95% confidence intervals are summarized in Table 6.1. Among these are the most stringent limits to date on the aQGCs parameters $f_{M,2-5}/\Lambda^4$ and $f_{T,6-7}/\Lambda^4$.

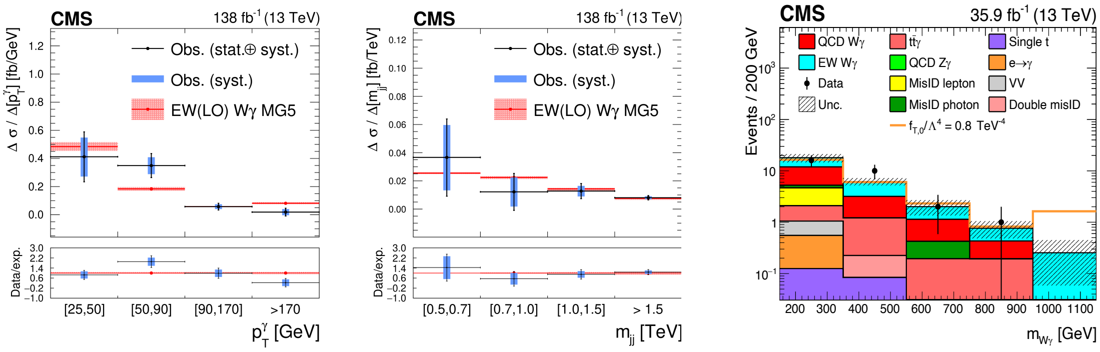

Figure 6.28: *Observed differential cross section of EW Wγjj production as a function of (left) the photon transverse momentum and (middle) the dijet mass extracted from the full Run-2 data of the CMS experiment at $\sqrt{s}$ =13 TeV and compared to LO theoretical predictions of Madgraph5. (right) The observed invariant mass distribution of the W boson - photon system in the 2016 data compared to the SM prediction as a stacked histogram of the different contributions and to a hypothetical new physics signal realized via the $\mathcal{O}_{T,0}$ operator setting $f_{T,0}/\Lambda^4 = 0.8$ TeV^{-4}.*

6.3.4 Summary and directions

The measured signal strengths, the observed cross sections normalized by the SM prediction, are shown in Figure 6.29 for EW production of single and diboson states accompanied by a jet pair: these feature an excellent consistency between experiment and theory. The experimental uncertainty, in most cases dominated by data statistics, is still sizable for diboson production and will be improved significantly when LHC Run-3 and Phase-2 data become available for analysis. The results of the ATLAS collaboration [580] show a similar level of agreement.

A summary of the CMS Run-2 measurements of possible aQGCs are given in Table 6.1 for EW diboson production in association with two jets and for triboson production. In all cases, only the leptonic decays of the massive bosons to the first or second generation are considered. The table illustrates how the various studies complement each other, with the different final states having different sensitivity.

For the operators which contribute to WWjj, more precisely W$^\pm$W$^\pm$jj production (namely, $O_{S,0-1}, O_{M,0-1}, O_{M,6-7}, O_{T,0-2}$)), the same-charge WWjj analysis gives the most precise measurement of the Wilson coefficient (except for $O_{T,0}$ where the four-lepton ZZjj measurement slightly outperforms it). ZZjj is the only final state that is

aQGC coefficient	95% CL intervals for the different coefficients in dim-8 EFT (TeV^{-4})									Unitarity limit (TeV)
	WWjj [609]	WZjj [609]	WVjj [609]	WVjj [609] clipped	ZZjj [532]	Wγjj [535]	Zγjj [612]	W$\gamma\gamma$ [613]	Z$\gamma\gamma$ [613]	
$f_{S,0}/\Lambda^4$	−6.0; +6.4	−19; +19	−5.7; +6.1	−34; +35	N.D.					1.6
$f_{S,1}/\Lambda^4$	−18; +19	−30; +30	−16; +17	−86; +99	N.D.					1.3
$f_{M,0}/\Lambda^4$	−3.0; +3.2	−5.8; +5.8	−2.7; +2.9	−11; +12	N.D.	−5.6; +5.5	−15.8; +16.0	N.D.	N.D.	1.8
$f_{M,1}/\Lambda^4$	−4.7; +4.7	−8.2; +8.3	−4.1; +4.2	−15; +14	N.D.	−7.8; +8.1	−35.0; +34.7	N.D.	N.D.	2.3
$f_{M,2}/\Lambda^4$		N.D.			N.D.	−1.9; +1.9	−6.55; +6.49	−39.9; +39.5	N.D.	2.0
$f_{M,3}/\Lambda^4$		N.D.			N.D.	−2.7; +2.7	−13.0; +13.0	−63.8; +65.0	N.D.	2.7
$f_{M,4}/\Lambda^4$		N.D.			N.D.	−3.7; +3.6	−13.0; +12.7	N.D.	N.D.	2.3
$f_{M,5}/\Lambda^4$		N.D.			N.D.	−3.9; +3.9	−22.2; +21.3	N.D.	N.D.	2.7
$f_{M,6}/\Lambda^4$	−6.0; +6.5	−12; +12	−5.4; +5.8	−22; +25	N.D.	−11; +11	−32; +32	N.D.	N.D.	1.8
$f_{M,7}/\Lambda^4$	−6.7; +7.0	−10; +10	−5.7; +6.0	−16; +18	N.D.	−14; +14	−56.6; +55.9	N.D.	N.D.	2.5
$f_{T,0}/\Lambda^4$	−0.28, 0.31	−0.62, 0.65	−0.25, 0.28	−1.1; +1.6	−0.24; +0.22	−0.47; +0.51	−0.64; +0.57	−1.30; +1.30	−5.70; +5.46	2.4
$f_{T,1}/\Lambda^4$	−0.12, 0.15	−0.37, 0.41	−0.12, 0.14	−0.69; +0.97	−0.31; +0.31	−0.31; +0.34	−0.81; +0.90	−1.70; +1.66	−5.70; +5.46	2.3
$f_{T,2}/\Lambda^4$	−0.38, 0.50	−1.0, 1.3	−0.35, 0.48	−1.6; +3.1	−0.63; +0.59	−0.85; +1.0	−1.68; +1.54	−3.64; +3.64	−11.4; +10.9	1.9
$f_{T,5}/\Lambda^4$		N.D.			N.D.	−0.31; +0.33	−0.58; +0.64	−0.52; +0.60	−2.92; +2.92	2.6
$f_{T,6}/\Lambda^4$		N.D.			N.D.	−0.25; +0.27	−1.30; +1.33	−0.60; +0.68	−3.80; +3.88	2.9
$f_{T,7}/\Lambda^4$		N.D.			N.D.	−0.67; +0.73	−2.15; +2.43	−1.16; +1.16	−7.88; +7.72	3.1
$f_{T,8}/\Lambda^4$					−0.43; +0.43		−0.47; +0.47		−1.06; +1.10	1.8
$f_{T,9}/\Lambda^4$					−0.92; +0.92		−0.91; +0.91		−1.82; +1.82	1.8

Compiled by G. Pásztor, June 2023

Table 6.1: *95% CL intervals in TeV^{-4} for the aQGC coefficients in dim-8 EFT derived from the full Run-2 data of the CMS experiment studying various multi-boson final states as given in the header. Only one coefficient at a time is allowed to be different from zero. Only leptonic decays of the heavy gauge bosons are considered leading to electron(s) and / or muon(s) in the final state.* WVjj *labels the combined result from* WWjj *and* WZjj. *The best constraints are highlighted in blue. The unitarity limit in the last column corresponds to this best result. To illustrate the problem due to the unitarity limit lying in the kinematically accessible region, the conservative interpretation of the data with the new physics contribution "clipped" at the limit is also given for the combined* WVjj *results. As the operators are not independent, the intervals are always a factor of 2 larger for* $f_{M,6}/\Lambda^4$ *than for* $f_{M,0}/\Lambda^4$ *[614]. The gray numbers are calculated with this scaling. "N.D." signifies that the analysis is sensitive to the given coefficient but the constraint has not (yet) been derived from the data.*

affected by all couplings, however CMS has only derived limits for the subset of the $O_{T,i}$ operators for which it is expected to be the best performing. Of these, three $(O_{T,0}, O_{T,8-9})$ give the most accurate results to date. The ATLAS Collaboration has extracted preliminary limits on further coefficients in Ref. [606] though the results are generally less stringent. Wγjj is also sensitive to a wide range of couplings, and sets the limit for seven of them $(O_{M,2-5}, O_{T,5-7})$. While Zγjj, W$\gamma\gamma$, Z$\gamma\gamma$ hold no record, in an eventual combined analysis they will also play an important role to decipher new physics.

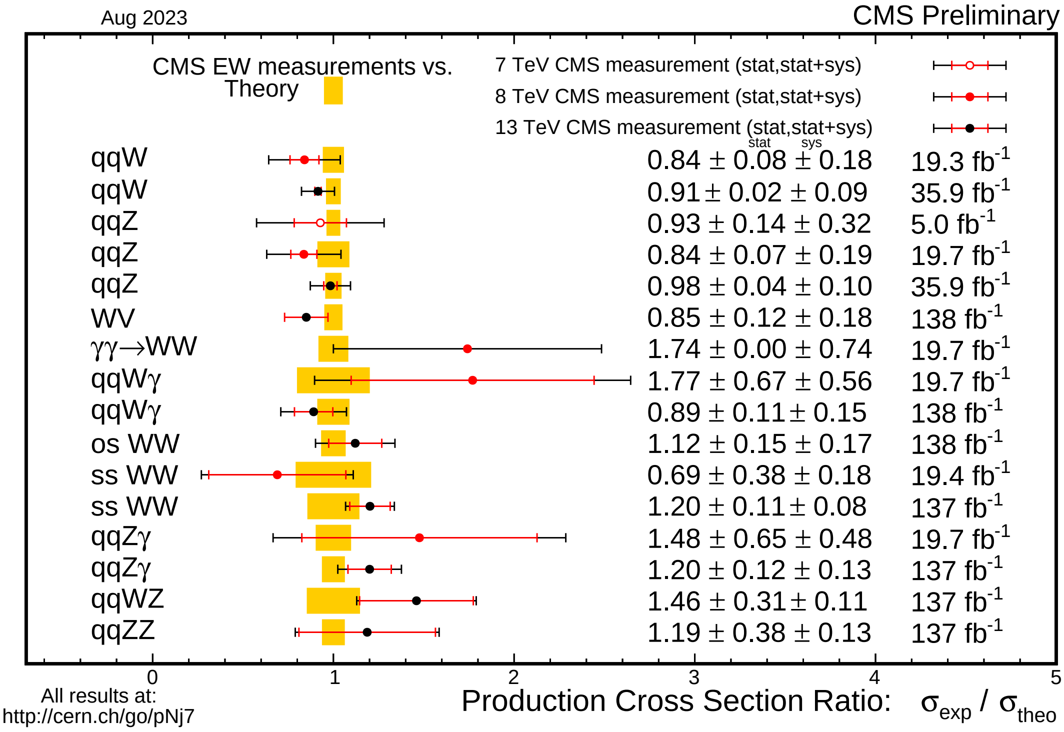

Figure 6.29: *Summary of measured signal strengths (observed to predicted cross section ratios) for vector boson fusion and scattering processes by the CMS collaboration at* $\sqrt{s}$ *=7–13 TeV, using state-of-the art theoretical calculations for the normalization. [602]*

One also needs to consider the physics validity of the EFT expansion. By construction, it is restricted to diboson center of mass energies (diboson masses) up to a cut-off scale Λ, whose maximum value is given by the requirement of unitarity. In Table 6.1, all obtained 95% CL intervals involve unitarity violation, i.e. the diboson invariant mass from the processes due to the anomalous couplings are higher in a significant fraction of events than the unitarity limit for Λ. More physical limits can be obtained by applying somewhat arbitrary theoretical templates that ensure unitarity, such as form factors described in Section 1.2. One can, on the other hand, calculate the most conservative limits on new physics for a given operator by the so-called "clipping" method, where the EFT expansion is applied up to the unitarity limit, thus no anomalous contribution from new physics above that scale is considered. The resulting templates will be unnatural, with a discontinuity at the unitarity limit. Nonetheless, the constraints derived on the coefficients with these templates represent the limiting case and can be considered as the widest intervals consistent with the data. For the combined WVjj measurement these clipped results are also given: they widen the interval by a factor of 4 to 6.

While I discussed above only the final states I worked on, primarily with leptons, the collaborations have started to cover almost all possible final states, including also decays to tau leptons and hadrons. Results from the analysis of semi-leptonic final states have started to appear [607], and work on the fully hadronic channel is close to completion. The latter is especially interesting as it promises to constrain further the EFT parameters.

As already noted for the Wγjj analysis, other recent highlights are the first VVjj differential cross section measurements. They were performed in the two- [608], three- [609] and four-lepton [610] topologies as a function of the dijet mass, the mass or transverse mass of the VV system, and angular variables. They are expected to constrain the modeling of these rare processes and test (within the limits of the statistical precision) the higher order effects, the unitarization of the cross section by the Higgs boson exchange, the gauge boson polarization states, and more.

An other important future direction is the move towards a global EFT analysis of diboson production which is necessary – as discussed in Section 1.2 – to get a proper handling of interference effects and a more general interpretation of the data. There are also proposals to consider anomalous coupling contributions to the background processes, as well.

The LHC data, so far, did not show any evidence for new physics manifested as anomalous gauge couplings. However, with the factor two and then further factor ten increase of the data statistics in Run 3 and Phase 2 of LHC, coupled with continuous improvements in experimental techniques and theoretical precision, our reach will significantly increase in the next 10 years.

As most of the measurements have significant statistical limitations and several leading experimental uncertainties can be considered uncorrelated between the LHC experiments, the combination of the results of the ATLAS and CMS collaborations can bring significant improvements. This is one of the goals of the LHC Electroweak Working Group, as well as of common experiment - theory efforts [611] in the framework of COST (European Cooperation in Science and Technology) actions funded by the European Union, VBScan and now COMETA, where I was and am the Hungarian member of the Management Committee. My group has contributed from the CMS side to the first detailed, systematic comparisons between the experiments to prepare for an eventual combination.

6.4 Search for supersymmetric particles

Supersymmetry at a high energy scale is one of the most popular assumptions when extending the SM, due to its amazing flexibility to put in place many issues arising in the SM. The predicted supersymmetric partner particles stabilize the Higgs boson mass in a natural way, without the need for large fine-tuning. Under moderate theoretical assumptions (e.g., R-parity conservation [130]), it also predicts that the lightest supersymmetric particle (LSP) has all the properties of a dark matter candidate and thus allows the reconciliation of particle physics with the universe at its largest scales. The observed Higgs mass and couplings are consistent with model predictions. SUSY can also stabilize the electroweak vacuum that appears to be in a metastable state in the SM for the observed Higgs mass of 125 GeV [615].

Direct searches for SUSY partner particles are therefore at full steam at the LHC. However, there are no signs of supersymmetry to date: the recent searches for "spectacular" signals have not found any significant deviation from the SM [616, 617]. Moreover, the measured Higgs boson mass is found close to the approximate upper bound of 135 GeV imposed by the MSSM [188]. For softly broken SUSY, the logarithmic corrections to the Higgs mass thus constrain the SUSY partners mostly to the multi-TeV regime.

This raises a number of questions on the future directions for BSM searches. Is low-energy SUSY – offering the cancellation of fermionic and bosonic loop corrections – still feasible [117, 118]? Can the dark matter relic density be produced by the SUSY candidate? While turning our attention to other solutions, like composite models or accepting fine-tuning, has been proposed by many in the scientific community, the LHC data provide rich hunting ground with hidden corners. So to close our excursion to the unknown territories of elementary particles, this section gives a glimpse to two exciting directions that are being explored.

6.4.1 Search for scalar top quarks

Due to its large mass, the top quark gives the largest loop contribution to the Higgs mass and thus the dominant source of fine tuning is expected to be canceled by its scalar partner, the scalar top quark (stop, denoted by $\widetilde{t}$) in SUSY models. Large left–right top squark mixing naturally results in a relatively light $\widetilde{t}_1$ (an illustrative example was given in Figure 1.5), because the off-diagonal terms in the mass matrix are proportional to the large top Yukawa coupling [90]. Taking into account loop calculations, however, a light stop quark is not considered to be a necessary condition for naturalness.

Nonetheless, studies of the scalar partner of the top quark have an important role in the physics program of LHC and have been pursued by both ATLAS and CMS [616, 618, 619]. Figure 6.30 shows a compilation of CMS results.

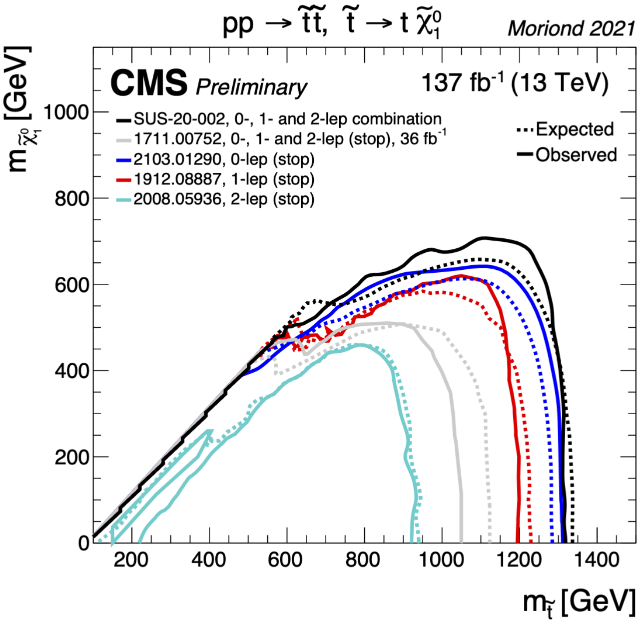

Figure 6.30: *Excluded areas in the stop quark mass ($m_{\widetilde{t}_1}$) - neutralino LSP mass ($m_{\widetilde{\chi}_1^0}$) plane in simplified models of top squark pair production with stop decays to an on- or off-shell top quark and the LSP, leading to final states with two bottom quarks, two (possibly virtual) W bosons, and two LSPs.*

The dedicated search based on the full Run-2 data for the fully hadronic decay of scalar top quark pairs is so far the most sensitive analysis (labeled as ”0-lep” on the figure). It did not reveal a sign of new physics, but it extended the reach toward higher masses and softer decay products [537]. The analysis is sensitive to both direct stop pair

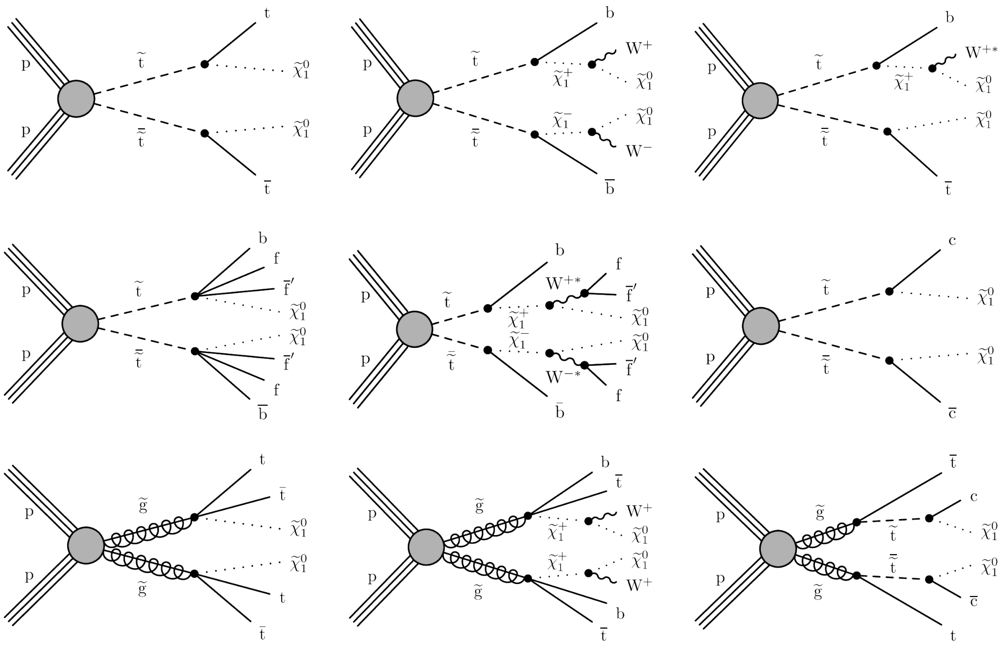

Figure 6.31: *Representative diagrams of direct scalar top pair production processes in pp collisions. For left to right: (top) for a mass difference to the LSP of $\Delta m = m_{\tilde{t}_1} - m_{\tilde{\chi}_1^0} > m_{t}$, decay to an on-shell top and an LSP [T2tt]; for $\Delta m > m_{\tilde{\chi}_1^\pm}$, m_W decay via a light chargino [T2bW]; a mixture of the two previous decays [T2tb]; (middle) in compressed spectra scenario for $\Delta m < m_W$, decay via a four-body process [T2ttC]; via a light chargino [T2bWC]; via a two-body process in the presence of flavor mixing [T2cc]. (bottom) Gluino pair production processes, followed by a decay to a top pair and an LSP [T1tttt]; a cascade via a chargino [T1ttbb]; a cascade via a stop that decays through a two-body process [T5ttcc]. The standard names of the considered simplified models are given in square brackets.*

production and its production in cascade decays of gluinos produced in pairs illustrated in Figure 6.31.

It is especially interesting to target models that predict compressed mass spectra which are attractive (still open) options for natural SUSY [620]. For nearly maximally mixed top squarks, the Higgs mass bound can be saturated with top squark masses as low as $m_S = \sqrt{m_{\tilde{t}_1} m_{\tilde{t}_2}} = 500$ GeV [621, 622]. Furthermore, top squark co-annihilation [623–625] leads to a prediction of the correct dark matter relic abundance for mass differences between the top squark and the LSP of $\Delta m = m_{\tilde{t}_1} - m_{\tilde{\chi}_1^0} = 15 - 30$ GeV [135]. In this compressed regime, the top squark decay products are soft and difficult to detect. When Δm is below the mass of the W boson, the decay can proceed either via $\tilde{t}_1 \to t^{*}\tilde{\chi}_1^0$ or, if the chargino is light, via $\tilde{t}_1 \to b\tilde{\chi}_1^{\pm(*)}$, both leading to $bf\bar{f}\tilde{\chi}_1^0$ competing with a model-dependent contribution from $\tilde{t}_1 \to c\tilde{\chi}_1^0$ (see middle row in Figure 6.31).

The analysis has benefited from novel deep neural network based tagging algorithms for top quarks and W bosons both at low and high p_{T}. The identification of soft b jets based on secondary vertex tagging allowed to cover regions where the masses of the scalar top and the LSP are close. The selected events were binned according to the number of jets, number of b-tagged jets, number of soft b jets, number of tagged boosted and resolved reconstructed top quarks, number of tagged W bosons, the highest jet p_{T}, the highest b jet p_{T}, the scalar sum of all jet p_{T} values, $p_{\mathrm{T}}^{\mathrm{miss}}$, as well as the minimum transverse mass calculated by any b jet and the missing transverse momentum ($m_{\mathrm{T}}^{\mathrm{b}}$), with a total of 183 signal regions considered. All but six search bins have agreement within 2σ, and no disagreement outside 3σ was observed, in excellent agreement with the expected 95% and 99.7% probability for measurements to fall within these ranges.

Limits on gluino and scalar top quark production cross sections were obtained for the various production and decay modes in simplified models, with a selection shown in Figure 6.32. Lower limits were derived on the SUSY particle masses: as high as 1310 GeV on the scalar top mass for direct production models, and 2260 GeV on the gluino mass for gluino-mediated production models. Thanks to the special attention to the low Δm region, where the stop and the LSP masses are close, in particular the use of soft b jets, the region $m_{\tilde{t}_1} \lesssim m_{\tilde{\chi}_1^{\pm}}$ was also explored. The lower mass limit can, however, be as low as 520 GeV in these models.

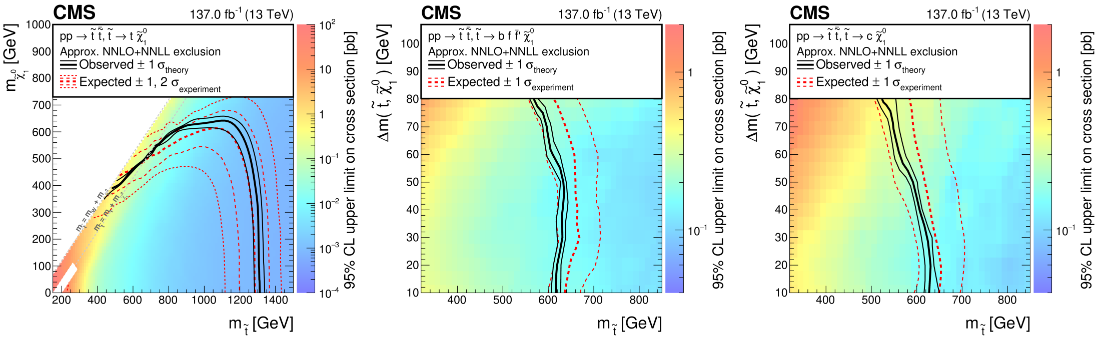

Figure 6.32: *The 95% CL upper limit on the production cross section in three simplified models of stop pair production: (left) for T2tt direct decays to a top quark and an LSP in the* $[m_{\tilde{t}_1}, m_{\tilde{\chi}_1^0}]$ *mass plane, (middle) for T2ttC direct four-body decays and (right) for T2cc direct two-body decays in the* $[m_{\tilde{t}_1}, \Delta m]$ *mass plane. The solid black curves represent the observed exclusion contour with respect to approximate NNLO+NNLL signal cross sections and the change in this contour due to theoretical uncertainties. The dashed red curves indicate the expected exclusion contour under the background-only hypothesis with 68 and 95% confidence regions due to experimental uncertainties. [537]*

However, in the low Δm region, the top squarks can also have macroscopic lifetimes and thus the decay vertex can be displaced from the primary collision vertex. The above results do not consider this challenging experimental feature for soft particles, and is under investigation in various analyses with soft leptons.

6.4.2 Compressed mass spectra in the gaugino sector

Electroweak gauginos are also expected to be accessible at the LHC and the current constraints on their masses are typically lower than those on colored particles [616, 617]. The region with a small mass difference between the pair-produced second lightest EW gaugino and the neutralino LSP (Δm) is experimentally challenging due to the soft final state particles, as can be seen in a recent combination of CMS Run-2 results in Figure 6.33.

A dedicated analysis was performed in the vector boson fusion (VBF) topology (Figure 6.34) with early 13 TeV data to target this compressed mass scenario [538]. Two well-separated jets that appear in opposite hemispheres with a large invariant dijet mass were used to tag the VBF process. It has two advantages. The requirement of the jet pair reduces the SM background contribution and also provides a recoil effect that boosts the $p_{\mathrm{T}}^{\mathrm{miss}}$ and the lepton p_{T} making their reconstruction more efficient. While

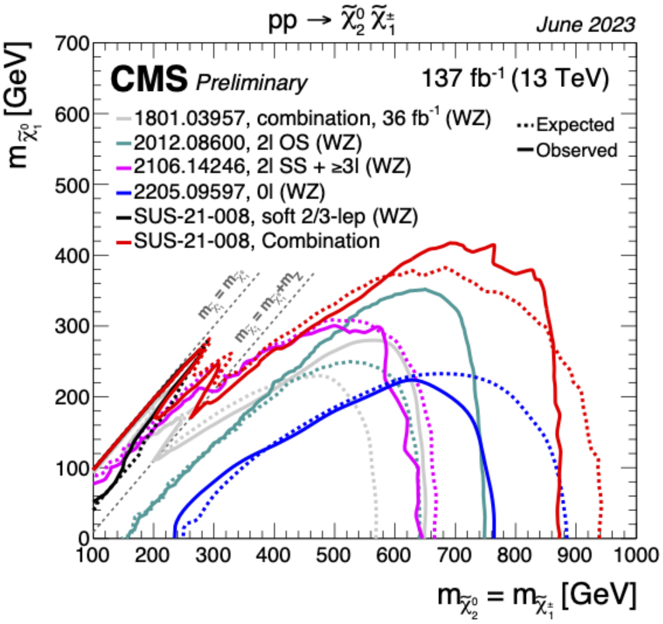

Figure 6.33: *Excluded areas in the second lightest versus lightest EW gaugino mass plane in simplified models for the production of a pair of the lightest chargino and the second-lightest neutralino, with their decay to the LSP and a W or Z boson, respectively. The two directly produced gauginos are assumed to have the same mass.*

the diagrams show the production of two charged leptons, they are still very soft and frequently not reconstructed in the detector. Thus, 0-lepton and 1-lepton (e, μ, τ) final states were analyzed in the 2016 data set. It was the first SUSY VBF analysis targeting the EW sector, and the first requiring a single soft lepton in the VBF final state.

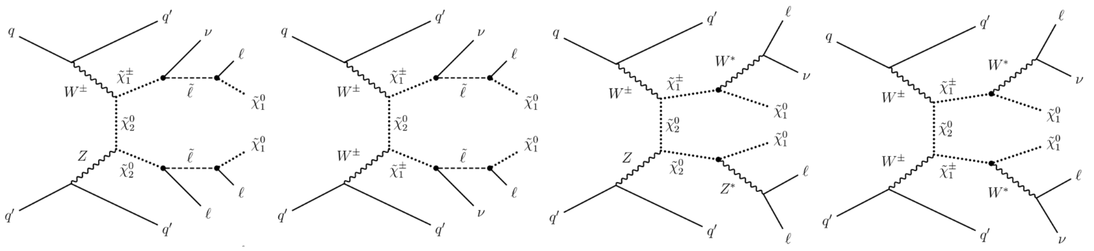

Figure 6.34: *Representative diagrams of chargino-neutralino and chargino-chargino pair production through vector boson fusion, followed by their decays to leptons and the neutralino LSP via (left) a light slepton or (right) a virtual W or Z.*

As the distributions of the observed dijet mass and the transverse mass of the lepton – missing momentum system did not reveal evidence for new physics (Figure 6.35), the search for non-colored gaugino pair (chargino – chargino or mass-degenerate chargino – second lightest neutralino) production succeeded to set the world's most stringent limits at the date of publication for charginos and neutralinos decaying to leptons in compressed mass spectrum scenarios for a mass difference between 1-3 GeV and 25-50 GeV. The observed lower limit on the second lightest EW gaugino, assuming it decays with 100% probability to a lepton pair and the LSP, ranges between 112 GeV for $\Delta m = 1$ GeV, and 175 GeV or 225 GeV for $\Delta m = 30$ GeV depending on the assumed intermediate particle in the simplified model (either a virtual SM EW vector boson or a light scalar lepton).

These results demonstrated that the VBF topology is a powerful tool for analyses

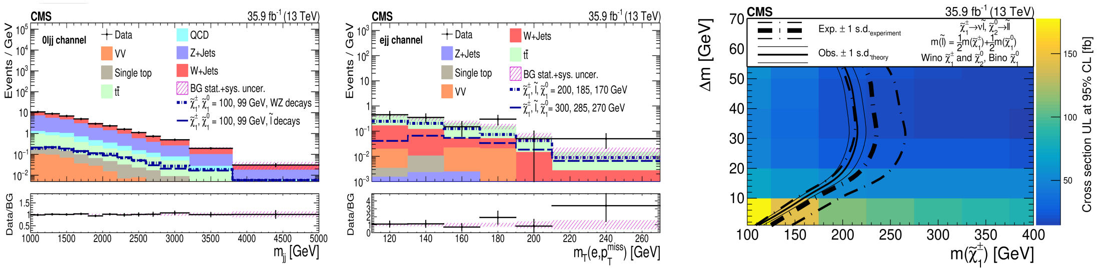

Figure 6.35: *Observed and predicted (left) dijet mass distribution in the 0-lepton channel and (middle) transverse mass distribution in the single electron channel, with representative signal contributions overlaid. The lower panel shows the data to background prediction ratio. The hashed region around 1 presents the total uncertainty on the prediction. (right) Observed and expected 95% CL upper limit on the signal cross section as a function of the second lightest EW gaugino mass and the mass difference to the LSP, assuming a light slepton model with the slepton mass defined as the average of the EW gaugino masses. The observed and expected excluded regions are indicated with the 1σ theory and experimental uncertainty bands. [538]*

targeting a compressed spectra.

6.4.3 To (re)search or not to (re)search SUSY?

No supersymmetric particle, no exotic phenomena, no significant discrepancy was seen at the LHC so far, though a few interesting excesses are being followed. Even though nature seems very SM-like at the high-energy LHC proton-proton collisions, the observations of the universe at large scales provide ample evidence that we need to look even harder, collect more data, develop better detectors and improved analysis techniques as a more fundamental description of elementary particles is needed, and its first direct proof might hide just around the corner for us to discover. Those who seek shall find. As the experimental and theoretical communities worked tirelessly together for decades to observe the Higgs boson and finally succeeded at the LHC, we shall continue the hunt for the direct manifestation of new physics created in a laboratory with more data, novel ideas and ever-improving tools.

Chapter 7

Looking ahead

Particle physics has made immense progress in the past 24 years. The succession of high-energy colliders LEP, Tevatron and LHC provided precision data to verify the predictions of the SM. The legacy LEP results showed a picture consistent with the SM and excluded a rather large range of extended models where new states couple to the Z boson. As an expert in alternative theories, especially of extended Higgs models and the then-arising solutions with extra dimensions, as well as the physics coordinator of OPAL from early 2004 to the end of the experiment's life, I had a significant contribution to these results.

The LHC has fulfilled its main promise: with a lot of meticulous preparatory work, we discovered the Higgs boson in 2012 and measured its properties within a few years using the Run-1 data set. The challenge usually hides in the details. I showed some of these in this work related to electron and photon reconstruction, the real-time selection of the data, as well as the evaluation of biases from poorly known backgrounds and systematic effects related to either the theoretical predictions or our limited understanding of the experimental effects. To exploit our data to the fullest, we strive to develop the best performing methods and use sophisticated analysis techniques. Machine learning is now used everywhere from data quality monitoring to object reconstruction, event selection, and more.

Due to the complexity and high resource needs, doing experimental higher energy physics today is a truly collaborative effort, with all of its rewards and drawbacks. Succeeding in a global environment requires cooperation, planning, hard work, resources and innovation. As the LHC has not yet brought a discovery of new physics, there is a long way to explore. We need to use the complementary *precision measurements* where new physics might be glanced at in a model-agnostic way – for example, in the high energy tails, as I discussed for electroweak diboson processes –, and *dedicated, optimized searches for exotic phenomena* predicted by a wealth of alternative models. LHC Run-3 data, and especially that of the HL-LHC can then bring us new knowledge and hopefully a discovery.

We will, however, only succeed if the instrumentation keeps up with the demands of the physics program in the harsh, high-intensity collider environment. This is why *designing and constructing the upgraded detectors* of CMS for HL-LHC are essential and are at the forefront of my activities. As a chain is just as strong as its weakest element, a measurement can only be as precise as the least known uncertainty. For the most precisely measured physics processes, this still originates from *luminosity determination* on the experimental side. Therefore, I judge it as a key area of development.

There is cause for optimism. As already the final LEP combination on SM Higgs boson searches concluded [157] ”The searches for the [Standard Model Higgs boson] carried out by the [four LEP] experiments extended the sensitive range well beyond that anticipated at the beginning of the [LEP] program.This is due to the higher [energy] achieved and to more sophisticated detectors and analysis techniques.” I believe this statement (replacing a few words appropriately) will also apply to the HL-LHC. Ingenuity will boost the performance we expect today and LHC will have a shot at reaching beyond what we expect today. Of course, there will be a limit that nature might or might not look at favorably: this motivates the need for the community to look beyond the HL-LHC and already now plan further ahead.

The Future Circular Collider [626] at CERN would be the most versatile option that is being discussed today: starting as a precision electron-positron electroweak (Z, ZH, WW) and top factory and in a second stage being converted to a high-energy ($\sim$ 100 TeV) hadron collider to push further the energy frontier and open up the field for new discoveries.

Acknowledgements

I was fortunate to work with many talented colleagues who have contributed to the research described here, from whom I have learned about various aspects of physics, research, collaboration and more. They also made scientific research as a career and life choice not only intellectually challenging but also highly rewarding. I can not attempt to list everyone who has touched positively my professional life in the past almost 24 years, so I would like to start by expressing my thanks and appreciation to all the collaborators I worked with in the ATLAS, CMS and OPAL experiments as well as in the efforts to shape the present and plan the future of particle physics and to my colleagues at all the research institutions I worked at, but in particular at RMKI (now Wigner RCP), CERN, the University of Geneva, and ELTE.

Every scientist needs a series of mentors, senior supporters to succeed. György Vesztergombi made the first overtures to engage me with the Hungarian experimental high-energy physics community and introduced me to Péter Igó-Kemenes, who became my MSc advisor. Péter stood by me and had an enormous impact on my early years and my success in the OPAL Collaboration, my first professional home. Dezső Horváth, my PhD advisor, was always available to provide his support, and I am grateful that I could always count on him to this day. My return to Hungary, after being for 15 years at CERN, and reintegration to the community was also encouraged by Péter Lévai and Zoltán Trócsányi.

I am also grateful to Gábor Veres with whom we came up with the idea of how ELTE could join CMS, which led to the successful Lendület grant application and ultimately to the formation of the group. I highly appreciate the support of Zsolt Frei, the head of the Department of Atomic Physics, who works tirelessly and very successfully to provide resources for the astro-, particle- and nuclear physics teams at the Physics Institute to lead cutting-edge scientific research.

I am grateful to my past employers, Gail Hanson (University of California, Riverside), Alan Clark (University of Geneva), and Manuela Vincter (Carleton University) for giving me independence to conduct research and develop my own interests.

David Plane, OPAL spokesperson, and Pippa Wells, my co-coordinator taught me a lot about science management (and human support) when I became OPAL Physics Coordinator (while expecting our first child).

Alessandro Marchioro exposed me first to R&D on instrumentation in particle physics and to modern electronics as my supervisor while being a CERN Fellow. Allan Honma taught me how to work in a clean lab, motivated me to build from A to Z my first fully independent measurement setup, and introduced me to the ”industrial” side of particle physics.

Moving from LEP physics to LHC was challenging due to the significantly increased complexity of the data analysis. I learned a lot from David Froidevaux about how to do physics at a hadron collider, as well as about detectors and event reconstruction.

I am thankful to the succession of CMS management teams who embraced our new group to CMS, offered their assistance and support, and put their trust in me by offering professional challenges and opportunities.

In the CMS BRIL project I also met lots of fantastic colleagues. I am grateful to Anna Dabrowski and David Stickland with whom I worked very closely together on leading this fantastic project to the future. I learned a lot from them, and I appreciate the constructive and supportive atmosphere that welcomed me to the project.

I would like to thank my postdocs at ELTE who strengthened our group, brought interesting topics, and provided enormous technical help to the students in their research in the complex CMS environment: Ruchi Chudasama, Koushik Mandal and Ankita Mehta.

I am grateful for having worked with so many students during the years, it is one of the perks of research that I truly love. Two of them deserve a special note. I directed the PhD research of Eleonora Benhar on the SM Higgs boson search and property measurements in ATLAS, which was the biggest, most competitive project I ever participated in, and the most stressful time of my professional life. It was through our combined effort that we persevered and developed two new methods that contributed to one of the most notable recent results in particle physics. Peter Major became my right hand at ELTE in our quest to improve luminosity precision in CMS and I am very proud of all the innovative work we did together, his leadership role as well as his well earned CMS prize.

Parts of this manuscript were read by Dezső Horváth and Zoltán Trócsányi whose advice I always very highly value; Ankita Mehta who became an expert on the research we started together; and my brother, Attila Pásztor who gave excellent suggestions on how to improve the clarity. My husband, Ákos Csilling read it all carefully and provided the so much needed second eye to make the material consistent.

I would like to close by expressing my thanks and love to the most important people in my life who are also my greatest supporters: my parents Gabriella and Zsolt, my brother Attila, my mother-in-law Márta, my partner in life and best friend Ákos, and our children Beáta, Dániel and Katalin. Without them, I could never have had both a fantastic family and a successful career in science, and reach the happy moment to write the last words of this work. I am grateful and I am very proud of them.

Abbreviations

2HDM two Higgs doublet model

4D four-dimensional

ADD extra dimensional model proposed by Nima Arkani-Hamed, Savas Dimopoulos, and Gia Dvali

ADLO LEP (ALEPH–DELPHI–L3–OPAL) combined

ALEPH Apparatus for LEP PHysics

ALICE A Large Ion Collider Experiment at LHC

aQGC anomalous quartic gauge coupling

aTGC anomalous triple gauge coupling

ATLAS A Toroidal LHC ApparatuS

B barion number

BCID bunch crossing identification number

BDT boosted decision tree, a machine learning technique

BEH Brout-Englert-Higgs, refers to the mechanism to spontaneous break the electroweak symmetry proposed by three groups independently, Robert Brout and François Englert; Peter Higgs; Gerald Guralnik, Carl Richard Hagen and Tom Kibble

BPM beam position monitor

BRIL Beam Radiation, Instrumentation and Luminosity Project

BSM beyond the standard model

C stands for color in subscripts, also denotes charge parity quantum number

CERN European Council for Nuclear Research (in French Conseil Européen pour la Recherche Nucléaire), the largest particle physics laboratory in the world located at the French-Swiss border near Geneva

CKM Cabibbo–Kobayashi–Maskawa, in reference to the quark mixing matrix introduced for three generations of quarks by Makoto Kobayashi and Toshihide Maskawa, adding one generation to the matrix previously introduced by Nicola Cabibbo

CL confidence level

CMOS complementary metal-oxide-semiconductor, a type of metal–oxide–semiconductor field-effect transistor (MOSFET) fabrication process

CMS Compact Muon Solenoid at LHC

CMSSM constrained minimal supersymmetric extension of the standard model

CP charge parity × parity quantum number

CPC CP conserving

CPU central processing unit

CPV CP violating

CPX CP violating MSSM benchmark scenario proposed for Higgs studies at LEP

d.o.f. degrees of freedom

DAQ data acquisition

DC direct current

DELPHI Detector with Lepton, Photon and Hadron Identification at LEP

dim dimension, e.g. dim-4 (dimension-4) operator

DNN deep neural network, a machine learning technique

DOROS diode orbit and oscillation system, a beam position monitor at LHC

DPS double parton scattering

DT drift tube

DY Drell–Yan process (quark–antiquark annihilation via a virtual photon or Z boson exchange leading to the creation of a lepton pair)

ECAL electromagnetic calorimeter

ED extra dimension or extra dimensional

EDM electric dipole moment

EFT effective field theory

EF event filter, the second stage of high level trigger in ATLAS during Run 1

EM electromagnetic

$\boldsymbol{E}_{\mathbf{T}}$ transverse energy, defined as $E_{\mathrm{T}} = \sqrt{m^2 + p_{\mathrm{T}}^2}$

EW electroweak

EWSB electroweak symmetry breaking

F stands for fermionic in subscripts

FB forward–backward (typically in subscripts)

FBCM fast beam condition monitor, a luminometer under construction for HL-LHC CMS

FSR final state radiation

GMSB gauge mediated supersymmetry breaking

GSF Gaussian sum filter (used for electron track fitting)

GUT grand unified theory

HCAL hadronic calorimeter

HEP high-energy physics

HF hadron forward calorimeter

HFOC hadron forward calorimeter occupancy luminosity counting method

HL-LHC high-luminosity Large Hadron Collider

HLT high-level trigger

HO higher-order

IP interaction point

ISR initial state radiation

KF Kalman filter (used for track fitting)

KK model proposed by Theodor Kaluza and Oskar Klein with massive excitations in the 4-dimensional theory of the fields that propagate in the extra spatial dimensions

L lepton number; also stands for left in subscripts

L1, L2, L3 level-1, level-2, level-3, used for the classification of management positions, and also for the stages of the trigger system (L1 = hardware, L2 = software)

L3 LEP detector proposed in the 3rd submitted letter of intent, L3 also can refer to the three lepton species studied at LEP

LAr liquid Argon

LEP Large Electron-Positron Collider

LH likelihood

LHC Large Hadron Collider

LHCb Large Hadron Collider beauty experiment

LL leading log

LO leading order

LS long shutdown

LSP lightest supersymmetric particle

MB muon barrel

MC simulation using the Monte Carlo method

MDT monitored drift tubes

ME matrix element

MS muon spectrometer

MSSM minimal supersymmetric extension of the standard model

MWPC multi-wire proportional chamber

NLL next-to-leading log

NLO next-to-leading order

NLSP next-to-lightest supersymmetric particle

NNLL next-to-next-to-leading log

NNLO next-to-next-to-leading order

$\mathbf{N^3LL}$ next-to-next-to-next-to-leading logarithm

$\mathbf{N^3LO}$ next-to-next-to-next-to-leading order

NP new physics beyond the standard model

OPAL Omni-Purpose Apparatus for LEP

PAG physics analysis group, a level-2 group within CMS physics coordination that is responsible for the measurements in a particular area (e.g., Higgs physics, SUSY searches, ...)

pCVD plasma chemical vapor deposition (process to grow diamond sensors)

PDF parton distribution function

PF particle flow

pMSSM phenomenological minimal supersymmetric standard model, if followed by an integer, it gives the number of extra (non-standard-model) parameters

POG physics object group, a level-2 group within CMS physics coordination that is responsible for the calibration, performance studies and usage of the given physics object (e.g., electron, photon, muon, ...)

pQCD perturbative quantum chromodynamics

PS Proton Synchrotron at CERN

$\boldsymbol{p_\mathrm{T}}$ transverse momentum

PU pileup (multiple particle collisions during a bunch crossing in a collider experiment)

Q stands for electric charge in subscripts

QCD quantum chromodynamics

QED quantum electrodynamics

QFT quantum field theory

QGC quartic gauge coupling

RF radiofrequency

RG renormalization group

RMS root mean square

RoI region of interest (for the high-level trigger)

RPV R-parity violation

RS extra dimensional model proposed by Lisa Randall and Raman Sundrum

s spin

S stands for scalar in subscripts

SBIL single bunch instantaneous luminosity

SC supercluster

SCT semiconductor tracker

SLAC Stanford Linear Accelerator Center

SLC Stanford Linear Collider

SLD SLAC Large Detector

SM the standard model of particle physics

SMEFT an effective field theory extension of the standard model

SSM sequential standard model

STXS simplified template cross sections, a framework to interpret Higgs boson measurements

SUSY supersymmetry or supersymmetric

SVD singular value decomposition (unfolding method)

TEPX tracker endcap pixel detector, a forward tracking detector under construction for HL-LHC CMS

Tevatron proton – antiproton accelerator at Fermi National Accelerator Laboratory in Batavia, US

TGC triple gauge coupling

TRT transition radiation tracker

TT trigger tower

UA1 Underground Area 1, a CERN experiment

UA2 Underground Area 2, a CERN experiment

VBF vector boson fusion

VBS vector boson scattering

VdM named from Simon van der Meer, a transverse beam separation scan method to measure the beam overlap width

VEV vacuum expectation value of the Higgs field

WG working group

Y stands for weak hypercharge in subscripts

YM stands for Yang-Mills in subscripts

Yuk stands for Yukawa in subscripts

Bibliography

[1] C. Yang and R. Mills, "Conservation of Isotopic Spin and Isotopic Gauge Invariance," *Physical Review*, vol. 96, pp. 191–195, 1954. DOI: `10.1103/PhysRev.96.191`.

[2] S. Glashow, "Partial-symmetries of weak interactions," *Nuclear Physics*, vol. 22, pp. 579–588, 1961. DOI: `10.1016/0029-5582(61)90469-2`.

[3] S. Weinberg, "A Model of Leptons," *Physical Review Letters*, vol. 19, pp. 1264–1266, 1967. DOI: `10.1103/PhysRevLett.19.1264`.

[4] A. Salam, "Weak and Electromagnetic Interactions," in *Elementary Particle Physics: Relativistic Groups and Analyticity, Proc. of Eighth Nobel Symposium, Stockholm, Sweden, 1968*, N. Svartholm, Ed., Almquvist and Wiksell, Stockholm, 1968, pp. 367–377.

[5] P. Higgs, "Broken symmetries and the masses of gauge bosons," *Physical Review Letters*, vol. 13, pp. 508–509, 1964. DOI: `10.1103/PhysRevLett.13.508`.

[6] F. Englert and R. Brout, "Broken symmetry and the mass of gauge vector mesons," *Physical Review Letters*, vol. 13, pp. 321–323, 1964. DOI: `10.1103/PhysRevLett.13.321`.

[7] G. Guralnik, C. Hagen, and T. Kibble, "Global conservation laws and massless particles," *Physical Review Letters*, vol. 13, pp. 585–587, 1964. DOI: `10.1103/PhysRevLett.13.585`.

[8] F. Hasert *et al.*, "Search for Elastic ν_μ Electron Scattering," *Physics Letters*, vol. B46, pp. 121–124, 1973. DOI: `10.1016/0370-2693(73)90494-2`.

[9] F. Hasert *et al.*, "Observation of neutrino-like interactions without muon or electron in the gargamelle neutrino experiment," *Physics Letters*, vol. B46, pp. 138–140, 1973. DOI: `10.1016/0370-2693(73)90499-1`.

[10] G. Amison et al., "Experimental Observation of Isolated Large Transverse Energy Electrons with Associated Missing Energy at $\sqrt{s} = 540$ GeV," *Physics Letters*, vol. B122, pp. 103–116, 1983. DOI: `10.1016/0370-2693(83)91177-2`.

[11] M. Banner et al., "Observation of Single Isolated Electrons of High Transverse Momentum in Events with Missing Transverse Energy at the CERN anti-p p Collider," *Physics Letters*, vol. B122, pp. 476–485, 1983. DOI: `10.1016/0370-2693(83)91605-2`.

[12] G. Amison et al., "Experimental Observation of Lepton Pairs of Invariant Mass Around 95 GeV/c^2 at the CERN SPS Collider," *Physics Letters*, vol. B126, pp. 398–410, 1983. DOI: `10.1016/0370-2693(83)90188-0`.

[13] P. Bagnaia et al., "Evidence for $Z^0 \to e^+e^-$ at the CERN anti-p p Collider," *Physics Letters*, vol. B129, pp. 130–140, 1983. DOI: `10.1016/0370-2693(83)90744-X`.

[14] D. Mohl, G. Petrucci, L. Thorndahl, and S. Van Der Meer, "Physics and Technique of Stochastic Cooling," *Phys. Rept.*, vol. 58, pp. 73–119, 1980. DOI: `10.1016/0370-1573(80)90140-4`.

[15] S. Schael *et al.* [incl. G. Pásztor], "Precision Electroweak Measurements on the Z Resonance," *Physics Reports*, vol. 427, pp. 257–454, 2006, arXiv:hep-ex/0509008. DOI: `10.1016/j.physrep.2005.12.006`.

[16] S. Schael *et al.* [incl. G. Pásztor], "Electroweak Measurements in Electron-Positron Collisions at W-Boson-Pair Energies at LEP," *Physics Reports*, vol. 532, pp. 119–244, 2013, arXiv:1302.3415 [hep-ex]. DOI: `10.1016/j.physrep.2013.07.004`.

[17] Tevatron Electroweak Working Group (for the CDF and D0 Collaborations), "2012 Update of the Combination of CDF and D0 Results for the Mass of the W Boson," Fermilab, FERMILAB-TM-2532-E, 2012. arXiv: `1204.0042 [hep-ex]`.

[18] M. Aaboud *et al.*, "Measurement of the W-boson mass in pp collisions at $\sqrt{s} = 7$ TeV with the ATLAS detector," *Eur. Phys. J. C*, vol. 78, no. 2, p. 110, 2018, [Erratum: Eur.Phys.J.C 78, 898 (2018)]. DOI: `10.1140/epjc/s10052-017-5475-4`. arXiv: `1701.07240 [hep-ex]`.

[19] CDF and D0 Collaborations, T. Aaltonen et al., "Tevatron Run II combination of the effective leptonic electroweak mixing angle," *Physics Reviews*, vol. D97, 112007 (20 pages), 2018, arXiv:1801.06283 [hep-ex]. DOI: `10.1103/PhysRevD.97.112007`.

[20] Tevatron Electroweak Working Group for the CDF and D0 Collaborations, "Combination of CDF and D0 results on the mass of the top quark using up 9.7fb^{-1} at the Tevatron," FERMILAB-CONF-16-298-E, Aug. 2016. arXiv: `1608.01881 [hep-ex]`.

[21] ATLAS Collaboration, "Measurement of the effective leptonic weak mixing angle using electron and muon pairs from Z-boson decay in the ATLAS experiment at $\sqrt{s} = 8$ TeV," CERN, ATLAS-CONF-2018-037, 2018. `http://cdsweb.cern.ch/record/2630340`.

[22] A. M. Sirunyan *et al.*, "Measurement of the weak mixing angle using the forward-backward asymmetry of Drell-Yan events in pp collisions at 8 TeV," *Eur. Phys. J. C*, vol. 78, no. 9, p. 701, 2018. DOI: `10.1140/epjc/s10052-018-6148-7`. arXiv: `1806.00863 [hep-ex]`.

[23] LHC Top Working Group, "Top Quark Mass, LHCTopWG Summary Plots," Sep. 2023, See also references therein. `https://twiki.cern.ch/twiki/bin/view/LHCPhysics/TopMassHistory`.

[24] G. 't Hooft, "Renormalizable Lagrangians for massive Yang-Mills fields," *Nuclear Physics*, vol. B35, pp. 167–188, 1971. DOI: `10.1016/0550-3213(71)90139-8`.

[25] G. Aad *et al.* [incl. G. Pásztor], "Observation of a new particle in the search for the Standard Model Higgs boson with the ATLAS detector at the LHC," *Phys. Lett. B*, vol. 716, pp. 1–29, 2012. DOI: `10.1016/j.physletb.2012.08.020`. arXiv: `1207.7214 [hep-ex]`.

[26] S. Chatrchyan *et al.*, "Observation of a New Boson at a Mass of 125 GeV with the CMS Experiment at the LHC," *Phys. Lett. B*, vol. 716, pp. 30–61, 2012. DOI: `10.1016/j.physletb.2012.08.021`. arXiv: `1207.7235 [hep-ex]`.

[27] G. Altarelli, “Proton proton physics at the LHC: An Overview,” in *ECFA Large Hadron Collider (LHC) Workshop: Physics and Instrumentation*, Dec. 1990, pp. 153–187.

[28] M. Chanowitz and M. Gaillard, “The TeV physics of strongly interacting W’s and Z’s,” *Nuclear Physics*, vol. B261, pp. 379–431, 1985. DOI: `10.1016/0550-3213(85)90580-2`.

[29] M. Aker *et al.*, “Direct neutrino-mass measurement with sub-electronvolt sensitivity,” *Nature Phys.*, vol. 18, no. 2, pp. 160–166, 2022. DOI: `10.1038/s41567-021-01463-1`. arXiv: `2105.08533 [hep-ex]`.

[30] R. Workman *et al.*, “Review of Particle Physics,” *Prog. Theor. Exp. Phys.*, vol. 2022, no. 8, p. 083C01, 2022, Latest update available at `http://pdg.lbl.gov`. DOI: `10.1093/ptep/ptac097`.

[31] L. Ibanez, “Grand unification with local supersymmetry,” *Nuclear Physics*, vol. B218, pp. 514–544, 1983. DOI: `10.1016/0550-3213(83)90378-4`.

[32] J. Ellis, D. Nanopolous, and K. Tamvakis, “Grand unification in simple supergravity,” *Physics Letters*, vol. B121, pp. 123–129, 1983. DOI: `10.1016/0370-2693(83)90900-0`.

[33] L. Alvare-Gaume, J. Polchinski, and M.Wise, “Minimal low-energy supergravity,” *Nuclear Physics*, vol. B221, pp. 495–523, 1983. DOI: `10.1016/0550-3213(83)90591-6`.

[34] N. Aghanim *et al.*, “Planck 2018 results. VI. Cosmological parameters,” *Astron. Astrophys.*, vol. 641, A6, 2020, [Erratum: Astron.Astrophys. 652, C4 (2021)]. DOI: `10.1051/0004-6361/201833910`. arXiv: `1807.06209 [astro-ph.CO]`.

[35] A. H. Guth, “The Inflationary Universe: A Possible Solution to the Horizon and Flatness Problems,” *Phys. Rev. D*, vol. 23, L.-Z. Fang and R. Ruffini, Eds., pp. 347–356, 1981. DOI: `10.1103/PhysRevD.23.347`.

[36] A. Sakharov, “Violation of CP Invariance, c Asymmetry, and Baryon Asymmetry of the Universe,” *Pisma Zh. Eksp. Teor. Fiz.*, vol. 5, pp. 32–35, 1967.

[37] A. Riotto, “Theories of Baryogenesis,” in *Proc. of Summer School in 119901 Physics and Cosmology, Trieste, Italy, 1998*, A. S. A. Masiero G. Senjanovic, Ed., ser. ICTP Ser. Theor. Phys. arXiv:hep-ph/9807454, vol. 15, World Scientific, Singapore, 1999, pp. 326–436.

[38] S. Weinberg, “Implications of Dynamical Symmetry Breaking,” *Phys. Rev.*, vol. D13, pp. 974–996, 1976, [Addendum: Phys. Rev.D19,1277(1979)]. DOI: `10.1103/PhysRevD.19.1277,10.1103/PhysRevD.13.974`.

[39] L. Susskind, “Dynamics of Spontaneous Symmetry Breaking in the Weinberg-Salam Theory,” *Phys. Rev.*, vol. D20, pp. 2619–2625, 1979. DOI: `10.1103/PhysRevD.20.2619`.

[40] G. ’t Hooft, C. Itzykson, A. Jaffe, H. Lehmann, P. K. Mitter, I. M. Singer, and R. Stora, “Recent Developments in Gauge Theories. Proceedings, Nato Advanced Study Institute, Cargese, France, August 26 - September 8, 1979,” *NATO Sci. Ser. B*, vol. 59, pp.1–438, 1980. DOI: `10.1007/978-1-4684-7571-5`.

[41] S. Weinberg, “Phenomenological Lagrangians,” *Physica A*, vol. 96, no. 1-2, S. Deser, Ed., pp. 327–340, 1979. DOI: `10.1016/0378-4371(79)90223-1`.

[42] S. Weinberg, “Effective Gauge Theories,” *Phys. Lett. B*, vol. 91, pp. 51–55, 1980. DOI: `10.1016/0370-2693(80)90660-7`.

[43] N. Cabibbo, “Unitary Symmetry and Leptonic Decays,” *Phys. Rev. Lett.*, vol. 10, pp. 531–533, 1963. DOI: `10.1103/PhysRevLett.10.531`.

[44] M. Kobayashi and T. Maskawa, “CP Violation in the Renormalizable Theory of Weak Interaction,” *Prog. Theor. Phys.*, vol. 49, pp. 652–657, 1973. DOI: `10.1143/PTP.49.652`.

[45] R. D. Peccei and H. R. Quinn, “CP Conservation in the Presence of Instantons,” *Phys. Rev. Lett.*, vol. 38, pp. 1440–1443, 1977. DOI: `10.1103/PhysRevLett.38.1440`.

[46] Z. Maki, M. Nakagawa, and S. Sakata, “Remarks on the unified model of elementary particles,” *Prog. Theor. Phys.*, vol. 28, pp. 870–880, 1962. DOI: `10.1143/PTP.28.870`.

[47] B. Pontecorvo, “Neutrino Experiments and the Problem of Conservation of Leptonic Charge,” *Zh. Eksp. Teor. Fiz.*, vol. 53, pp. 1717–1725, 1967.

[48] ATLAS and CMS Collaborations, “Combination of measurements of the top quark mass from data collected by the ATLAS and CMS experiments at $\sqrt{s} = 7$ and 8 TeV,” ATLAS-CONF-2023-066,CMS-PAS-TOP-22-001, Oct. 2023. `https://cds.cern.ch/record/2873520`.

[49] G. Aad *et al.*, “Combined measurement of the Higgs boson mass from the $H \to \gamma\gamma$ and $H \to ZZ^* \to 4\ell$ decay channels with the ATLAS detector using $\sqrt{s} = 7$, 8 and 13 TeV *pp* collision data,” CERN-EP-2023-156, Aug. 2023. arXiv: `2308.04775 [hep-ex]`.

[50] The Gfitter Group, J. Haller, A. Hoecker, R. Kogler, K. Mönig, T. Peiffer and J. Stelzer, “Update of the global electroweak fit and constraints on two-Higgs-doublet models,” *European Physical Journal*, vol. C78, p. 675, 2018, arXiv:1803.01853 [hep-ph]. DOI: `10.1140/epjc/s10052-018-6131-3`.

[51] T. Aaltonen *et al.*, “High-precision measurement of the W boson mass with the CDF II detector,” *Science*, vol. 376, no. 6589, pp. 170–176, 2022. DOI: `10.1126/science.abk1781`.

[52] S. Amoroso *et al.*, “Compatibility and combination of world W-boson mass measurements,” Aug. 2023. arXiv: `2308.09417 [hep-ex]`.

[53] G. J. Gounaris, J. Layssac, and F. M. Renard, “New and standard physics contributions to anomalous Z and gamma selfcouplings,” *Phys. Rev. D*, vol. 62, p. 073 013, 2000. DOI: `10.1103/PhysRevD.62.073013`. arXiv: `hep-ph/0003143`.

[54] K. Hagiwara, R. D. Peccei, D. Zeppenfeld, and K. Hikasa, “Probing the Weak Boson Sector in $\mathrm{e}^+ \mathrm{e}^- \to \mathrm{W}^+ \mathrm{W}^-$,” *Nucl. Phys. B*, vol. 282, pp. 253–307, 1987. DOI: `10.1016/0550-3213(87)90685-7`.

[55] U. Baur and E. L. Berger, “Probing the weak boson sector in $Z\gamma$ production at hadron colliders,” *Phys. Rev. D*, vol. 47, pp. 4889–4904, 1993. DOI: `10.1103/PhysRevD.47.4889`.

[56] G.J. Gounaris *et al.*, “Triple gauge boson couplings,” hep-ph/9601233, 1996. DOI: `10.5170/CERN-1996-001-V-1.525`. `http://cds.cern.ch/record/293937`.

[57] G. Altarelli, T. Sjostrand, and F. Zwirner, Eds., *Physics at LEP2: Vol. 1*, CERN Yellow Reports: Conference Proceedings, Feb. 1996. DOI: `10.5170/CERN-1996-001-V-1`. `http://cds.cern.ch/record/300671`.

[58] K. Hagiwara, S. Ishihara, R. Szalapski, and D. Zeppenfeld, "Low-energy effects of new interactions in the electroweak boson sector," *Phys. Rev. D*, vol. 48, pp. 2182–2203, 1993. DOI: `10.1103/PhysRevD.48.2182`.

[59] C. Degrande, N. Greiner, W. Kilian, O. Mattelaer, H. Mebane, T. Stelzer, S. Willenbrock, and C. Zhang, "Effective Field Theory: A Modern Approach to Anomalous Couplings," *Annals Phys.*, vol. 335, pp. 21–32, 2013. DOI: `10.1016/j.aop.2013.04.016`. arXiv: `1205.4231 [hep-ph]`.

[60] W. Buchmuller and D. Wyler, "Effective Lagrangian Analysis of New Interactions and Flavor Conservation," *Nucl. Phys. B*, vol. 268, pp. 621–653, 1986. DOI: `10.1016/0550-3213(86)90262-2`.

[61] B. Grzadkowski, M. Iskrzynski, M. Misiak, and J. Rosiek, "Dimension-Six Terms in the Standard Model Lagrangian," *JHEP*, vol. 10, p. 085, 2010. DOI: `10.1007/JHEP10(2010)085`. arXiv: `1008.4884 [hep-ph]`.

[62] I. Brivio and M. Trott, "The Standard Model as an Effective Field Theory," *Phys. Rept.*, vol. 793, pp. 1–98, 2019. DOI: `10.1016/j.physrep.2018.11.002`. arXiv: `1706.08945 [hep-ph]`.

[63] J. Aebischer *et al.*, "WCxf: an exchange format for Wilson coefficients beyond the Standard Model," *Comput. Phys. Commun.*, vol. 232, pp. 71–83, 2018. DOI: `10.1016/j.cpc.2018.05.022`. arXiv: `1712.05298 [hep-ph]`.

[64] I. Brivio, Y. Jiang, and M. Trott, "The SMEFTsim package, theory and tools," *JHEP*, vol. 12, p. 070, 2017. DOI: `10.1007/JHEP12(2017)070`. arXiv: `1709.06492 [hep-ph]`.

[65] S. Weinberg, "Baryon- and lepton-nonconserving processes," *Phys. Rev. Lett.*, vol. 43, pp. 1566–1570, 21 Nov. 1979. DOI: `10.1103/PhysRevLett.43.1566`.

[66] P. Minkowski, "$\mu \to e\gamma$ at a Rate of One Out of 10^9 Muon Decays?" *Phys. Lett. B*, vol. 67, pp. 421–428, 1977. DOI: `10.1016/0370-2693(77)90435-X`.

[67] P. Fileviez Perez, "New Paradigm for Baryon and Lepton Number Violation," *Phys. Rept.*, vol. 597, pp. 1–30, 2015. DOI: `10.1016/j.physrep.2015.09.001`. arXiv: `1501.01886 [hep-ph]`.

[68] C. Degrande *et al.*, "Monte Carlo tools for studies of non-standard electroweak gauge boson interactions in multi-boson processes: A Snowmass White Paper," in *Snowmass 2013: Snowmass on the Mississippi*, Sep. 2013. arXiv: `1309.7890 [hep-ph]`.

[69] O. J. P. Éboli and M. C. Gonzalez-Garcia, "Classifying the bosonic quartic couplings," *Phys. Rev. D*, vol. 93, no. 9, p. 093 013, 2016. DOI: `10.1103/PhysRevD.93.093013`. arXiv: `1604.03555 [hep-ph]`.

[70] A. Azatov, R. Contino, C. S. Machado, and F. Riva, "Helicity selection rules and noninterference for BSM amplitudes," *Phys. Rev. D*, vol. 95, no. 6, p. 065 014, 2017. DOI: `10.1103/PhysRevD.95.065014`. arXiv: `1607.05236 [hep-ph]`.

[71] J. Baglio, S. Dawson, and S. Homiller, "QCD corrections in Standard Model EFT fits to WZ and WW production," *Phys. Rev. D*, vol. 100, no. 11, p. 113 010, 2019. DOI: `10.1103/PhysRevD.100.113010`. arXiv: `1909.11576 [hep-ph]`.

[72] C. Degrande, G. Durieux, F. Maltoni, K. Mimasu, E. Vryonidou, and C. Zhang, "Automated one-loop computations in the standard model effective field theory," *Phys. Rev. D*, vol. 103, no. 9, p. 096 024, 2021. DOI: `10.1103/PhysRevD.103.096024`. arXiv: `2008.11743 [hep-ph]`.

[73] J. Lang, S. Liebler, H. Schäfer-Siebert, and D. Zeppenfeld, "Effective field theory versus UV-complete model: vector boson scattering as a case study," *Eur. Phys. J. C*, vol. 81, no. 7, p. 659, 2021. DOI: `10.1140/epjc/s10052-021-09428-7`. arXiv: `2103.16517 [hep-ph]`.

[74] I. Brivio, "SMEFTsim 3.0 — a practical guide," *JHEP*, vol. 04, p. 073, 2021. DOI: `10.1007/JHEP04(2021)073`. arXiv: `2012.11343 [hep-ph]`.

[75] ATLAS Collaboration, "Combined effective field theory interpretation of Higgs boson and weak boson production and decay with ATLAS data and electroweak precision observables," ATL-PHYS-PUB-2022-037, Jul. 2022. `https://cds.cern.ch/record/2816369`.

[76] R. Contino, M. Ghezzi, C. Grojean, M. Muhlleitner, and M. Spira, "Effective Lagrangian for a light Higgs-like scalar," *JHEP*, vol. 07, p. 035, 2013. DOI: `10.1007/JHEP07(2013)035`. arXiv: `1303.3876 [hep-ph]`.

[77] A. Alloul, B. Fuks, and V. Sanz, "Phenomenology of the Higgs Effective Lagrangian via FEYNRULES," *JHEP*, vol. 04, p. 110, 2014. DOI: `10.1007/JHEP04(2014)110`. arXiv: `1310.5150 [hep-ph]`.

[78] O. J. P. Eboli, M. C. Gonzalez-Garcia, and M. Martines, "Electroweak Higgs effective field theory after LHC run 2," *Phys. Rev. D*, vol. 105, no. 5, p. 053 003, 2022. DOI: `10.1103/PhysRevD.105.053003`. arXiv: `2112.11468 [hep-ph]`.

[79] A. Falkowski and A. Falkowski, "Higgs Basis: Proposal for an EFT basis choice for LHC HXSWG," Mar. 2015. `http://cds.cern.ch/record/2001958`.

[80] G. Belanger and F. Boudjema, "Probing quartic couplings of weak bosons through three vectors production at a 500-GeV NLC," *Phys. Lett. B*, vol. 288, pp. 201–209, 1992. DOI: `10.1016/0370-2693(92)91978-I`.

[81] W. J. Stirling and A. Werthenbach, "Anomalous quartic couplings in $\mathrm{W}^+\mathrm{W}^-\gamma$, $\mathrm{Z}^0\mathrm{Z}^0\gamma$ and $\mathrm{Z}^0\gamma\gamma$ production at present and future $\mathrm{e}^+\mathrm{e}^-$ colliders," *Eur. Phys. J. C*, vol. 14, pp. 103–110, 2000. DOI: `10.1007/s100520050737`. arXiv: `hep-ph/9903315`.

[82] W. J. Stirling and A. Werthenbach, "Anomalous quartic couplings in neutrino anti-neutrino gamma gamma production via W W fusion at LEP-2," *Phys. Lett. B*, vol. 466, pp. 369–374, 1999. DOI: `10.1016/S0370-2693(99)01165-X`. arXiv: `hep-ph/9907235`.

[83] A. Denner, S. Dittmaier, M. Roth, and D. Wackeroth, "Probing anomalous quartic gauge boson couplings via $\mathrm{e}^+\mathrm{e}^- \to$ four fermions $+ \gamma$," *Eur. Phys. J. C*, vol. 20, pp. 201–215, 2001. DOI: `10.1007/s100520100678`. arXiv: `hep-ph/0104057`.

[84] G. Montagna, M. Moretti, O. Nicrosini, M. Osmo, and F. Piccinini, "Quartic anomalous couplings at LEP," *Phys. Lett. B*, vol. 515, pp. 197–205, 2001. DOI: `10.1016/S0370-2693(01)00834-6`. arXiv: `hep-ph/0105120`.

[85] G. Belanger, F. Boudjema, Y. Kurihara, D. Perret-Gallix, and A. Semenov, "Bosonic quartic couplings at LEP-2," *Eur. Phys. J. C*, vol. 13, pp. 283–293, 2000. DOI: `10.1007/s100520000305`. arXiv: `hep-ph/9908254`.

[86] M. Baak *et al.*, "Working Group Report: Precision Study of Electroweak Interactions," in *Community Summer Study 2013: Snowmass on the Mississippi*, Oct. 2013. arXiv: `1310.6708 [hep-ph]`.

[87] O. J. P. Eboli, M. C. Gonzalez-Garcia, and S. M. Lietti, “Bosonic quartic couplings at CERN LHC,” *Phys. Rev. D*, vol. 69, p. 095 005, 2004. DOI: `10.1103/PhysRevD.69.095005`. arXiv: `hep-ph/0310141`.

[88] O. J. P. Eboli, M. C. Gonzalez-Garcia, and J. K. Mizukoshi, “p p $\to$ j j $e^{\pm}\mu^{\pm}\nu\nu$ and j j $e^{\pm}\mu^{\mp}\nu\nu$ at $O(\alpha_{em}^{6})$ and $O(\alpha_{em}^{4}\alpha_{s}^{2})$ for the study of the quartic electroweak gauge boson vertex at CERN LHC,” *Phys. Rev. D*, vol. 74, p. 073 005, 2006. DOI: `10.1103/PhysRevD.74.073005`. arXiv: `hep-ph/0606118`.

[89] A. Alboteanu, W. Kilian, and J. Reuter, “Resonances and Unitarity in Weak Boson Scattering at the LHC,” *JHEP*, vol. 11, p. 010, 2008. DOI: `10.1088/1126-6708/2008/11/010`. arXiv: `0806.4145 [hep-ph]`.

[90] S. P. Martin, “A Supersymmetry primer,” *Adv. Ser. Direct. High Energy Phys.*, vol. 18, G. L. Kane, Ed., pp. 1–98, 1998. DOI: `10.1142/9789812839657_0001`. arXiv: `hep-ph/9709356`.

[91] H.-C. Cheng, “Introduction to Extra Dimensions,” in *Theoretical Advanced Study Institute in Elementary Particle Physics: Physics of the Large and the Small*, 2011, pp. 125–162. DOI: `10.1142/9789814327183_0003`. arXiv: `1003.1162 [hep-ph]`.

[92] M. B. Green, J. H. Schwarz, and E. Witten, *Superstring Theory.* Cambridge University Press, 1987.

[93] J. Polchinski, *String Theory.* Cambridge University Press, 1998.

[94] N. Arkani-Hamed, S. Dimopoulos, and G. R. Dvali, “The Hierarchy problem and new dimensions at a millimeter,” *Phys. Lett. B*, vol. 429, pp. 263–272, 1998. DOI: `10.1016/S0370-2693(98)00466-3`. arXiv: `hep-ph/9803315`.

[95] N. Arkani-Hamed, S. Dimopoulos, and G. R. Dvali, “Phenomenology, astrophysics and cosmology of theories with submillimeter dimensions and TeV scale quantum gravity,” *Phys. Rev. D*, vol. 59, p. 086 004, 1999. DOI: `10.1103/PhysRevD.59.086004`. arXiv: `hep-ph/9807344`.

[96] J. G. Lee, E. G. Adelberger, T. S. Cook, S. M. Fleischer, and B. R. Heckel, “New Test of the Gravitational $1/r^2$ Law at Separations down to 52 μm,” *Phys. Rev. Lett.*, vol. 124, no. 10, p. 101 101, 2020. DOI: `10.1103/PhysRevLett.124.101101`. arXiv: `2002.11761 [hep-ex]`.

[97] J. C. Long, H. W. Chan, and J. C. Price, “Experimental status of gravitational strength forces in the subcentimeter regime,” *Nucl. Phys. B*, vol. 539, pp. 23–34, 1999. DOI: `10.1016/S0550-3213(98)00711-1`. arXiv: `hep-ph/9805217`.

[98] V. Mitrofanov and O. Ponomareva, “Experimental test of gravitation at small distances,” *Sov. Phys. JETP*, vol. 67, no. 10, p. 1963, 1988.

[99] J. L. Hewett, “Indirect collider signals for extra dimensions,” *Phys. Rev. Lett.*, vol. 82, pp. 4765–4768, 1999. DOI: `10.1103/PhysRevLett.82.4765`. arXiv: `hep-ph/9811356`.

[100] G. F. Giudice, R. Rattazzi, and J. D. Wells, “Quantum gravity and extra dimensions at high-energy colliders,” *Nucl. Phys. B*, vol. 544, pp. 3–38, 1999. DOI: `10.1016/S0550-3213(99)00044-9`. arXiv: `hep-ph/9811291`.

[101] T. Han, J. D. Lykken, and R.-J. Zhang, “On Kaluza-Klein states from large extra dimensions,” *Phys. Rev. D*, vol. 59, p. 105 006, 1999, Correction: arXiv:hep-ph/9811350 v4. DOI: `10.1103/PhysRevD.59.105006`. arXiv: `hep-ph/9811350`.

[102] K.-m. Cheung and G. L. Landsberg, "Drell-Yan and diphoton production at hadron colliders and low scale gravity model," *Phys. Rev. D*, vol. 62, p. 076 003, 2000. DOI: `10.1103/PhysRevD.62.076003`. arXiv: `hep-ph/9909218`.

[103] L. Randall and R. Sundrum, "A Large mass hierarchy from a small extra dimension," *Phys. Rev. Lett.*, vol. 83, pp. 3370–3373, 1999. DOI: `10.1103/PhysRevLett.83.3370`. arXiv: `hep-ph/9905221`.

[104] L. Randall and R. Sundrum, "An Alternative to compactification," *Phys. Rev. Lett.*, vol. 83, pp. 4690–4693, 1999. DOI: `10.1103/PhysRevLett.83.4690`. arXiv: `hep-th/9906064`.

[105] H. Davoudiasl, J. L. Hewett, and T. G. Rizzo, "Experimental probes of localized gravity: On and off the wall," *Phys. Rev. D*, vol. 63, p. 075 004, 2001. DOI: `10.1103/PhysRevD.63.075004`. arXiv: `hep-ph/0006041`.

[106] G. F. Giudice, R. Rattazzi, and J. D. Wells, "Graviscalars from higher dimensional metrics and curvature Higgs mixing," *Nucl. Phys. B*, vol. 595, pp. 250–276, 2001. DOI: `10.1016/S0550-3213(00)00686-6`. arXiv: `hep-ph/0002178`.

[107] C. Csaki, M. L. Graesser, and G. D. Kribs, "Radion dynamics and electroweak physics," *Phys. Rev. D*, vol. 63, p. 065 002, 2001. DOI: `10.1103/PhysRevD.63.065002`. arXiv: `hep-th/0008151`.

[108] C. Csaki, M. Graesser, L. Randall, and J. Terning, "Cosmology of brane models with radion stabilization," *Phys. Rev. D*, vol. 62, p. 045 015, 2000. DOI: `10.1103/PhysRevD.62.045015`. arXiv: `hep-ph/9911406`.

[109] W. D. Goldberger and M. B. Wise, "Phenomenology of a stabilized modulus," *Phys. Lett. B*, vol. 475, pp. 275–279, 2000. DOI: `10.1016/S0370-2693(00)00099-X`. arXiv: `hep-ph/9911457`.

[110] W. D. Goldberger and M. B. Wise, "Modulus stabilization with bulk fields," *Phys. Rev. Lett.*, vol. 83, pp. 4922–4925, 1999. DOI: `10.1103/PhysRevLett.83.4922`. arXiv: `hep-ph/9907447`.

[111] T. G. Rizzo, "Pedagogical introduction to extra dimensions," *eConf*, vol. C040802, J. Hewett, J. Jaros, T. Kamae, and C. Prescott, Eds., p. L013, 2004. arXiv: `hep-ph/0409309`.

[112] G. Pásztor and T. G. Rizzo, "Report of the Snowmass subgroup on extra dimensions," *eConf*, vol. C010630, N. Graf, Ed., P333, 2001. arXiv: `hep-ph/0112054`.

[113] G. Aarons *et al.* [incl. G. Pásztor], "International Linear Collider Reference Design Report Volume 2: Physics at the ILC," SLAC-R-975,FERMILAB-DESIGN-2007-04,FERMILAB-PUB-07-795-E, Sep. 2007. arXiv: `0709.1893 [hep-ph]`.

[114] J. Wess and B. Zumino, "Supergauge transformations in four dimensions," *Nucl. Phys*, vol. B 70, p. 39, 1974.

[115] H. P. Nilles, "Supersymmetry, Supergravity and Particle Physics," *Phys. Reports*, vol. 110, p. 1, 1984.

[116] R. Barbieri, S. Ferrara, and C. A. Savoy, "Gauge Models with Spontaneously Broken Local Supersymmetry," *Phys. Lett.*, vol. B119, p. 343, 1982. DOI: `10.1016/0370-2693(82)90685-2`.

[117] E. Witten, "Dynamical Breaking of Supersymmetry," *Nucl. Phys.*, vol. B 188, p. 513, 1981.

[118] S. Dimopoulos and H. Georgi, "Softly Broken Supersymmetry and SU(5)," *Nucl. Phys.*, vol. B 193, p. 150, 1981.

[119] H. E. Haber and G. L. Kane, "The Search for Supersymmetry: Probing Physics Beyond the Standard Model," *Phys. Reports*, vol. 117, p. 75, 1987.

[120] S. Dawson, E. Eichten, and C. Quigg, "Search for Supersymmetric Particles in Hadron - Hadron Collisions," *Phys. Rev.*, vol. D31, p. 1581, 1985. DOI: `10.1103/PhysRevD.31.1581`.

[121] J.Gunion, H. E. Haber, G. L. Kane, and S. Dawson, *The Higgs Hunters Guide.* Addison-Wesley, 1990.

[122] G.C. Branco, P.M. Ferreira, L. Lavoura, M.N. Rebelo, M. Sher, and J.P. Silva, "Theory and phenomenology of two-higgs-doublet models," *Physics Reports*, vol. 516, no. 1, pp. 1–102, 2012, ISSN: 0370-1573. DOI: `https://doi.org/10.1016/j.physrep.2012.02.002`.

[123] H. K. Dreiner, "An Introduction to explicit R-parity violation," *Adv. Ser. Direct. High Energy Phys.*, vol. 21, G. L. Kane, Ed., pp. 565–583, 2010. DOI: `10.1142/9789814307505_0017`. arXiv: `hep-ph/9707435`.

[124] B. C. Allanach, A. Dedes, and H. K. Dreiner, "Bounds on R-parity violating couplings at the weak scale and at the GUT scale," *Phys. Rev. D*, vol. 60, p. 075 014, 1999. DOI: `10.1103/PhysRevD.60.075014`. arXiv: `hep-ph/9906209`.

[125] M. Chemtob, "Phenomenological constraints on broken R parity symmetry in supersymmetry models," *Prog. Part. Nucl. Phys.*, vol. 54, pp. 71–191, 2005. DOI: `10.1016/j.ppnp.2004.06.001`. arXiv: `hep-ph/0406029`.

[126] R. Barbier *et al.*, "R-parity violating supersymmetry," *Phys. Rept.*, vol. 420, pp. 1–202, 2005. DOI: `10.1016/j.physrep.2005.08.006`. arXiv: `hep-ph/0406039`.

[127] H. K. Dreiner, M. Kramer, and B. O'Leary, "Bounds on R-parity violating supersymmetric couplings from leptonic and semi-leptonic meson decays," *Phys. Rev. D*, vol. 75, p. 114 016, 2007. DOI: `10.1103/PhysRevD.75.114016`. arXiv: `hep-ph/0612278`.

[128] F. Domingo, H. K. Dreiner, J. S. Kim, M. E. Krauss, M. Lozano, and Z. S. Wang, "Updating Bounds on R-Parity Violating Supersymmetry from Meson Oscillation Data," *JHEP*, vol. 02, p. 066, 2019. DOI: `10.1007/JHEP02(2019)066`. arXiv: `1810.08228 [hep-ph]`.

[129] M. Anderson *et al.*, "Search for invisible modes of nucleon decay in water with the SNO+ detector," *Phys. Rev. D*, vol. 99, no. 3, p. 032 008, 2019. DOI: `10.1103/PhysRevD.99.032008`. arXiv: `1812.05552 [hep-ex]`.

[130] G. R. Farrar and P. Fayet, "Phenomenology of the Production, Decay, and Detection of New Hadronic States Associated with Supersymmetry," *Phys. Lett. B*, vol. 76, pp. 575–579, 1978. DOI: `10.1016/0370-2693(78)90858-4`.

[131] H. E. Haber, "The Status of the minimal supersymmetric standard model and beyond," *Nucl. Phys. B Proc. Suppl.*, vol. 62, M. Cvetic and P. Langacker, Eds., pp. 469–484, 1998. DOI: `10.1016/S0920-5632(97)00688-9`. arXiv: `hep-ph/9709450`.

[132] D. P. Aguillard *et al.*, "Measurement of the Positive Muon Anomalous Magnetic Moment to 0.20 ppm," *Phys. Rev. Lett.*, vol. 131, no. 16, p. 161 802, 2023. DOI: `10.1103/PhysRevLett.131.161802`. arXiv: `2308.06230 [hep-ex]`.

[133] G. F. Giudice and R. Rattazzi, "Theories with gauge mediated supersymmetry breaking," *Phys. Rept.*, vol. 322, pp. 419–499, 1999. DOI: `10.1016/S0370-1573(99)00042-3`. arXiv: `hep-ph/9801271`.

[134] P. Meade, N. Seiberg, and D. Shih, "General Gauge Mediation," *Prog. Theor. Phys. Suppl.*, vol. 177, T. Takayanagi and S. Yahikozawa, Eds., pp. 143–158, 2009. DOI: `10.1143/PTPS.177.143`. arXiv: `0801.3278 [hep-ph]`.

[135] A. Delgado, G. F. Giudice, G. Isidori, M. Pierini, and A. Strumia, "The light stop window," *Eur. Phys. J.*, vol. C73, no. 3, p. 2370, 2013. DOI: `10.1140/epjc/s10052-013-2370-5`. arXiv: `1212.6847 [hep-ph]`.

[136] C. F. Berger, J. S. Gainer, J. L. Hewett, and T. G. Rizzo, "Supersymmetry Without Prejudice," *JHEP*, vol. 02, p. 023, 2009. DOI: `10.1088/1126-6708/2009/02/023`. arXiv: `0812.0980 [hep-ph]`.

[137] S. S. AbdusSalam, B. C. Allanach, F. Quevedo, F. Feroz, and M. Hobson, "Fitting the Phenomenological MSSM," *Phys. Rev. D*, vol. 81, p. 095 012, 2010. DOI: `10.1103/PhysRevD.81.095012`. arXiv: `0904.2548 [hep-ph]`.

[138] J. Berger, M. W. Cahill-Rowley, D. Ghosh, J. L. Hewett, A. Ismail, and T. G. Rizzo, "CP-violating phenomenological MSSM," *Phys. Rev. D*, vol. 93, no. 3, p. 035 017, 2016. DOI: `10.1103/PhysRevD.93.035017`. arXiv: `1510.08840 [hep-ph]`.

[139] F. D. Steffen, "Dark Matter Candidates - Axions, Neutralinos, Gravitinos, and Axinos," *Eur. Phys. J. C*, vol. 59, pp. 557–588, 2009. DOI: `10.1140/epjc/s10052-008-0830-0`. arXiv: `0811.3347 [hep-ph]`.

[140] G. Jungman, M. Kamionkowski, and K. Griest, "Supersymmetric dark matter," *Phys. Rept.*, vol. 267, pp. 195–373, 1996. DOI: `10.1016/0370-1573(95)00058-5`. arXiv: `hep-ph/9506380`.

[141] C. Arina and N. Fornengo, "Sneutrino cold dark matter, a new analysis: Relic abundance and detection rates," *JHEP*, vol. 11, p. 029, 2007. DOI: `10.1088/1126-6708/2007/11/029`. arXiv: `0709.4477 [hep-ph]`.

[142] T. Faber, Y. Liu, W. Porod, and J. Jones-Pérez, "Revisiting neutrino and sneutrino dark matter in natural SUSY scenarios," *Phys. Rev. D*, vol. 101, no. 5, p. 055 029, 2020. DOI: `10.1103/PhysRevD.101.055029`. arXiv: `1909.11686 [hep-ph]`.

[143] D. E. Lopez-Fogliani, A. D. Perez, and R. R. de Austri, "Dark matter candidates in the NMSSM with RH neutrino superfields," *JCAP*, vol. 04, p. 067, 2021. DOI: `10.1088/1475-7516/2021/04/067`. arXiv: `2102.08986 [hep-ph]`.

[144] G. Pásztor, "Search for gauginos and gauge mediated SUSY breaking scenarios at LEP," *PoS*, vol. HEP2005, G. Barreira, Ed., p. 346, 2006. DOI: `10.22323/1.021.0346`. arXiv: `hep-ex/0512054`.

[145] H. Baer, A. Lessa, S. Rajagopalan, and W. Sreethawong, "Mixed axion/neutralino cold dark matter in supersymmetric models," *JCAP*, vol. 06, p. 031, 2011. DOI: `10.1088/1475-7516/2011/06/031`. arXiv: `1103.5413 [hep-ph]`.

[146] K. J. Bae, H. Baer, and E. J. Chun, "Mainly axion cold dark matter from natural supersymmetry," *Phys. Rev. D*, vol. 89, no. 3, p. 031 701, 2014. DOI: `10.1103/PhysRevD.89.031701`. arXiv: `1309.0519 [hep-ph]`.

[147] A. Boveia *et al.*, "Snowmass 2021 Dark Matter Complementarity Report," Nov. 2022. arXiv: `2211.07027 [hep-ex]`.

[148] G. Pásztor, "Search for charged Higgs bosons with the OPAL detector at LEP," MSc. thesis, Eötvös University, Budapest, May 1995. `http://cds.cern.ch/record/578013`.

[149] G. Alexander *et al.* [incl. G. Pásztor], "Search for charged Higgs bosons using the OPAL detector at LEP," *Phys. Lett. B*, vol. 370, pp. 174–184, 1996. DOI: `10.1016/0370-2693(96)00029-9`.

[150] G. Pásztor, "Search for charged Higgs Bosons and supersymmetric particles," PhD. dissertation, Eötvös University, Budapest, Apr. 1999. `http://cds.cern.ch/record/493154`.

[151] K. Ackerstaff *et al.* [incl. G. Pásztor], "Search for charged Higgs bosons in e^+e^- collisions at $\sqrt{s}$ = 130 GeV - 172 GeV," *Phys. Lett. B*, vol. 426, pp. 180–192, 1998. DOI: `10.1016/S0370-2693(98)00360-8`. arXiv: `hep-ex/9802004`.

[152] K. Ackerstaff *et al.* [incl. G. Pásztor], "Search for an excess in the production of four jet events from $\mathrm{e}^+\mathrm{e}^-$ collisions at $\sqrt{s}$ = 130 GeV - 184 GeV," *Phys. Lett. B*, vol. 429, pp. 399–413, 1998. DOI: `10.1016/S0370-2693(98)00470-5`. arXiv: `hep-ex/9802015`.

[153] G. Abbiendi *et al.* [incl. G. Pásztor], "Search for Higgs bosons in e^+e^- collisions at 183 GeV," *Eur. Phys. J. C*, vol. 7, pp. 407–435, 1999. DOI: `10.1007/s100529901102`. arXiv: `hep-ex/9811025`.

[154] G. Abbiendi *et al.* [incl. G. Pásztor], "Searches for R-parity violating decays of gauginos at 183 GeV at LEP," *Eur. Phys. J. C*, vol. 11, pp. 619–642, 1999. DOI: `10.1007/s100520050660`. arXiv: `hep-ex/9901037`.

[155] G. Abbiendi *et al.* [incl. G. Pásztor], "Search for R-parity violating decays of scalar fermions at LEP," *Eur. Phys. J. C*, vol. 12, pp. 1–24, 2000. DOI: `10.1007/s100529900226`. arXiv: `hep-ex/9904015`.

[156] R. Barate *et al.*, "Observation of an excess in the search for the standard model Higgs boson at ALEPH," *Phys. Lett. B*, vol. 495, pp. 1–17, 2000. DOI: `10.1016/S0370-2693(00)01269-7`. arXiv: `hep-ex/0011045`.

[157] R. Barate *et al.*, "Search for the standard model Higgs boson at LEP," *Phys. Lett. B*, vol. 565, pp. 61–75, 2003. DOI: `10.1016/S0370-2693(03)00614-2`. arXiv: `hep-ex/0306033`.

[158] G. Pásztor, "Study of ZZ production at LEP at $\sqrt{s} = 183 - 209$-GeV," *Int. J. Mod. Phys. A*, vol. 16S1A, K. K. Gan and R. Kass, Eds., pp. 311–314, 2001. DOI: `10.1142/S0217751X01006784`. arXiv: `hep-ex/0012008`.

[159] G. Pásztor, "Search for supersymmetry, extra dimensions and exotic phenomena at LEP," *Frascati Phys. Ser.*, vol. 27, M. Greco, Ed., pp. 665–680, 2002. arXiv: `hep-ex/0210015`.

[160] G. Pásztor, "Search for SM and MSSM Higgs bosons at LEP," in *11th International Conference on Supersymmetry and the Unification of Fundamental Interactions (SUSY2003)*, Mar. 2004. arXiv: `hep-ex/0403049`.

[161] G. Pásztor, "The LEP testimony: Exotic searches and studies," in *41st Rencontres de Moriond on Electroweak Interactions and Unified Theories*, May 2006, pp. 247–261. arXiv: `hep-ex/0605095`.

[162] R. Assmann, M. Lamont, and S. Myers, "A brief history of the LEP collider," *Nucl. Phys. B Proc. Suppl.*, vol. 109, F. L. Navarria, M. Paganoni, and P. G. Pelfer, Eds., pp. 17–31, 2002. DOI: `10.1016/S0920-5632(02)90005-8`.

[163] G. Abbiendi *et al.*, "Determination of α_s using OPAL hadronic event shapes at $\sqrt{s}$ = 91 - 209 GeV and resummed NNLO calculations," *Eur. Phys. J. C*, vol. 71, p. 1733, 2011. DOI: `10.1140/epjc/s10052-011-1733-z`. arXiv: `1101.1470 [hep-ex]`.

[164] D. Chang, W.-Y. Keung, and P. B. Pal, "CP violation in the cubic coupling of neutral gauge bosons," *Phys. Rev. D*, vol. 51, pp. 1326–1331, 1995. DOI: `10.1103/PhysRevD.51.1326`. arXiv: `hep-ph/9407294`.

[165] K. Agashe and N. G. Deshpande, "Limits on low scale gravity from $e^+e^- \to W^+W^-$, ZZ and $\gamma\gamma$," *Phys. Lett. B*, vol. 456, pp. 60–67, 1999. DOI: `10.1016/S0370-2693(99)00432-3`. arXiv: `hep-ph/9902263`.

[166] G. Abbiendi *et al.*, "Z boson pair production in e+ e- collisions at $\sqrt{s} = 183$ GeV and 189 GeV," *Phys. Lett. B*, vol. 476, pp. 256–272, 2000. DOI: `10.1016/S0370-2693(00)00197-0`. arXiv: `hep-ex/0003016`.

[167] G. Abbiendi *et al.* [incl. G. Pásztor], "Study of Z pair production and anomalous couplings in e^+e^- collisions at $\sqrt{s}$ between 190 GeV and 209 GeV," *Eur. Phys. J.*, vol. C32, pp. 303–322, 2003. DOI: `10.1140/epjc/s2003-01467-x`. arXiv: `hep-ex/0310013`.

[168] M. W. Gruenewald, G. Passarino, E. Accomando, A. Ballestrero, P. Bambade, D. Bardin, W. Beenakker, F. Berends, E. Boos, A. Chapovsky, A. Denner, S. Dittmaier, M. Dubinin, J. B. Hansen, V. Ilyin, S. Jadach, Y. Kurihara, M. Kuroda, E. Maina, G. Montagna, M. Moretti, O. Nicrosini, A. Olshevsky, M. Osmo, A. Pallavicini, C. G. Papadopoulos, H. T. Phillips, F. Piccinini, R. Pittau, W. Placzek, T. Riemann, M. Roth, A. S. Schmidt-Kaerst, Y. Shimizu, M. Skrzypek, R. Tanaka, M. Verzocchi, D. Wackeroth, B. F. L. Ward, and Z. Was, "Four-fermion production in electron-positron collisions," CERN-2000-009-A, Sep. 2000. arXiv: `hep-ph/0005309 [hep-ph]`.

[169] S. Jadach, W. Placzek, and B. F. L. Ward, "Gauge invariant YFS exponentiation of (un)stable Z pair production at and beyond LEP-2 energies," *Phys. Rev. D*, vol. 56, pp. 6939–6941, 1997. DOI: `10.1103/PhysRevD.56.6939`. arXiv: `hep-ph/9705430`.

[170] A. Tumasyan *et al.*, "Measurement of the inclusive and differential WZ production cross sections, polarization angles, and triple gauge couplings in pp collisions at $\sqrt{s} = 13$ TeV," *JHEP*, vol. 07, p. 032, 2022. DOI: `10.1007/JHEP07(2022)032`. arXiv: `2110.11231 [hep-ex]`.

[171] G. Pásztor and M. Perelstein, "Exploring new physics through contact interactions in lepton pair production at a linear collider," *eConf*, vol. C010630, N. Graf, Ed., P315, 2001. arXiv: `hep-ph/0111471`.

[172] OPAL Collaboration [incl. G. Pásztor], "Limits on Low Scale Quantum Gravity in Extra Spatial Dimensions from Measurements of $e^+e^- \to e^+e^-$ at LEP2," CERN, CERN-OPAL-PN-471,OPAL-PN-471, Feb. 2001. `https://cds.cern.ch/record/837790`.

[173] G. Abbiendi *et al.*, "Tests of the standard model and constraints on new physics from measurements of fermion pair production at 189-GeV to 209-GeV at LEP," *Eur. Phys. J. C*, vol. 33, pp. 173–212, 2004. DOI: `10.1140/epjc/s2004-01595-9`. arXiv: `hep-ex/0309053`.

[174] G. Abbiendi *et al.*, "Multiphoton production in e^+e^- collisions at $\sqrt{s} = 181$ GeV to 209 GeV," *Eur. Phys. J. C*, vol. 26, pp. 331–344, 2003. DOI: `10.1140/epjc/s2002-01074-5`. arXiv: `hep-ex/0210016`.

[175] A. M. Sirunyan *et al.*, “Search for new physics in dijet angular distributions using proton–proton collisions at $\sqrt{s} = 13$ TeV and constraints on dark matter and other models,” *Eur. Phys. J. C*, vol. 78, no. 9, p. 789, 2018, [Erratum: Eur.Phys.J.C 82, 379 (2022)]. DOI: `10.1140/epjc/s10052-018-6242-x`. arXiv: `1803.08030 [hep-ex]`.

[176] G. C. Branco, P. M. Ferreira, L. Lavoura, M. N. Rebelo, M. Sher, and J. P. Silva, “Theory and phenomenology of two-Higgs-doublet models,” *Phys. Rept.*, vol. 516, pp. 1–102, 2012. DOI: `10.1016/j.physrep.2012.02.002`. arXiv: `1106.0034 [hep-ph]`.

[177] H. E. Haber and G. L. Kane, “The Search for Supersymmetry: Probing Physics Beyond the Standard Model,” *Phys. Rept.*, vol. 117, pp. 75–263, 1985. DOI: `10.1016/0370-1573(85)90051-1`.

[178] J. E. Kim, “Light Pseudoscalars, Particle Physics and Cosmology,” *Phys. Rept.*, vol. 150, pp. 1–177, 1987. DOI: `10.1016/0370-1573(87)90017-2`.

[179] M. Carena, J. R. Ellis, A. Pilaftsis, and C. E. M. Wagner, “CP violating MSSM Higgs bosons in the light of LEP-2,” *Phys. Lett. B*, vol. 495, pp. 155–163, 2000. DOI: `10.1016/S0370-2693(00)01215-6`. arXiv: `hep-ph/0009212`.

[180] A. Djouadi, “The Higgs particles in the MSSM,” in *2001 Gif summer school on particle physics, Annecy, France, 10-14 Sep 2001*, 1996. `https://inis.iaea.org/search/search.aspx?orig_q=RN:36033125`.

[181] G. Abbiendi *et al.*, “Search for neutral Higgs boson in CP-conserving and CP-violating MSSM scenarios,” *Eur. Phys. J. C*, vol. 37, pp. 49–78, 2004. DOI: `10.1140/epjc/s2004-01962-6`. arXiv: `hep-ex/0406057`.

[182] G. Abbiendi *et al.* [incl. G. Pásztor], “Search for a low mass CP-odd Higgs boson in e^+e^- collisions with the OPAL detector at LEP2,” *Eur. Phys. J. C*, vol. 27, pp. 483–495, 2003. DOI: `10.1140/epjc/s2003-01139-y`. arXiv: `hep-ex/0209068`.

[183] M. Carena *et al.*, “Higgs physics at LEP-2,” in *CERN Workshop on LEP2 Physics (followed by 2nd meeting, 15-16 Jun 1995 and 3rd meeting 2-3 Nov 1995)*, Feb. 1996. arXiv: `hep-ph/9602250`.

[184] M. Carena, S. Heinemeyer, C. E. M. Wagner, and G. Weiglein, “Suggestions for improved benchmark scenarios for Higgs boson searches at LEP-2,” in *Workshop on New Theoretical Developments for Higgs Physics at LEP-2*, Dec. 2004. arXiv: `hep-ph/9912223`.

[185] S. Schael *et al.* [incl. G. Pásztor], “Search for neutral MSSM Higgs bosons at LEP,” *Eur. Phys. J. C*, vol. 47, pp. 547–587, 2006. DOI: `10.1140/epjc/s2006-02569-7`. arXiv: `hep-ex/0602042`.

[186] S. Heinemeyer, W. Hollik, and G. Weiglein, “FeynHiggs: A Program for the calculation of the masses of the neutral CP even Higgs bosons in the MSSM,” *Comput. Phys. Commun.*, vol. 124, pp. 76–89, 2000, The code is accessible via http://www.feynhiggs.de. DOI: `10.1016/S0010-4655(99)00364-1`. arXiv: `hep-ph/9812320`.

[187] S. Heinemeyer, W. Hollik, and G. Weiglein, “The Masses of the neutral CP - even Higgs bosons in the MSSM: Accurate analysis at the two loop level,” *Eur. Phys. J. C*, vol. 9, pp. 343–366, 1999. DOI: `10.1007/s100529900006`. arXiv: `hep-ph/9812472`.

[188] G. Degrassi, S. Heinemeyer, W. Hollik, P. Slavich, and G. Weiglein, "Towards high precision predictions for the MSSM Higgs sector," *Eur. Phys. J. C*, vol. 28, pp. 133–143, 2003. DOI: `10.1140/epjc/s2003-01152-2`. arXiv: `hep-ph/0212020`.

[189] M. Frank, T. Hahn, S. Heinemeyer, W. Hollik, H. Rzehak, and G. Weiglein, "The Higgs Boson Masses and Mixings of the Complex MSSM in the Feynman-Diagrammatic Approach," *JHEP*, vol. 02, p. 047, 2007. DOI: `10.1088/1126-6708/2007/02/047`. arXiv: `hep-ph/0611326`.

[190] J. Baron *et al.*, "Order of Magnitude Smaller Limit on the Electric Dipole Moment of the Electron," *Science*, vol. 343, p. 269, 2014. DOI: `10.1126/science.1248213`. arXiv: `1310.7534 [physics.atom-ph]`.

[191] V. Andreev *et al.*, "Improved limit on the electric dipole moment of the electron," *Nature*, vol. 562, no. 7727, p. 355, 2018. DOI: `10.1038/s41586-018-0599-8`.

[192] Y. Nakai and M. Reece, "Electric Dipole Moments in Natural Supersymmetry," *JHEP*, vol. 08, p. 031, 2017. DOI: `10.1007/JHEP08(2017)031`. arXiv: `1612.08090 [hep-ph]`.

[193] M. Carena, J. Ellis, J. S. Lee, A. Pilaftsis, and C. E. M. Wagner, "CP Violation in Heavy MSSM Higgs Scenarios," *JHEP*, vol. 02, p. 123, 2016. DOI: `10.1007/JHEP02(2016)123`. arXiv: `1512.00437 [hep-ph]`.

[194] E. Bagnaschi *et al.*, "MSSM Higgs Boson Searches at the LHC: Benchmark Scenarios for Run 2 and Beyond," *Eur. Phys. J. C*, vol. 79, no. 7, p. 617, 2019. DOI: `10.1140/epjc/s10052-019-7114-8`. arXiv: `1808.07542 [hep-ph]`.

[195] G. Abbiendi *et al.* [incl. G. Pásztor], "Search for invisibly decaying Higgs bosons in $e^+e- \to Z^0h^0$ production at $\sqrt{s} = 183 - 209$ GeV," *Phys. Lett. B*, vol. 682, pp. 381–390, 2010. DOI: `10.1016/j.physletb.2009.09.010`. arXiv: `0707.0373 [hep-ex]`.

[196] G. Abbiendi *et al.* [incl. G. Pásztor], "Two Higgs doublet model and model independent interpretation of neutral Higgs boson searches," *Eur. Phys. J. C*, vol. 18, pp. 425–445, 2001. DOI: `10.1007/s100520000544`. arXiv: `hep-ex/0007040`.

[197] G. Abbiendi *et al.* [incl. G. Pásztor], "Flavor independent $\mathrm{h}^0\mathrm{A}^0$ search and two Higgs doublet model interpretation of neutral Higgs boson searches at LEP," *Eur. Phys. J. C*, vol. 40, pp. 317–332, 2005. DOI: `10.1140/epjc/s2005-02122-4`. arXiv: `hep-ex/0408097`.

[198] G. Abbiendi *et al.* [incl. G. Pásztor], "Search for radions at LEP2," *Phys. Lett. B*, vol. 609, pp. 20–34, 2005, [Erratum: Phys.Lett.B 637, 382 (2006)]. DOI: `10.1016/j.physletb.2006.04.045`. arXiv: `hep-ex/0410035`.

[199] A. Tumasyan *et al.*, "Search for heavy resonances decaying to WW, WZ, or WH boson pairs in the lepton plus merged jet final state in proton-proton collisions at $\sqrt{s} = 13$ TeV," *Phys. Rev. D*, vol. 105, no. 3, p. 032 008, 2022. DOI: `10.1103/PhysRevD.105.032008`. arXiv: `2109.06055 [hep-ex]`.

[200] A. Tumasyan *et al.*, "Search for heavy resonances decaying to a pair of Lorentz-boosted Higgs bosons in final states with leptons and a bottom quark pair at $\sqrt{s}$= 13 TeV," *JHEP*, vol. 05, p. 005, 2022. DOI: `10.1007/JHEP05(2022)005`. arXiv: `2112.03161 [hep-ex]`.

[201] T. D. Lee, "A Theory of Spontaneous T Violation," *Phys. Rev. D*, vol. 8, G. Feinberg, Ed., pp. 1226–1239, 1973. DOI: `10.1103/PhysRevD.8.1226`.

[202] A. Djouadi, “The Anatomy of electro-weak symmetry breaking. II. The Higgs bosons in the minimal supersymmetric model,” *Phys. Rept.*, vol. 459, pp. 1–241, 2008. DOI: `10.1016/j.physrep.2007.10.005`. arXiv: `hep-ph/0503173`.

[203] G. Abbiendi *et al.* [incl. G. Pásztor], “Search for Charged Higgs bosons: Combined Results Using LEP Data,” *Eur. Phys. J. C*, vol. 73, p. 2463, 2013. DOI: `10.1140/epjc/s10052-013-2463-1`. arXiv: `1301.6065 [hep-ex]`.

[204] A. G. Akeroyd, “Three body decays of Higgs bosons at LEP-2 and application to a hidden fermiophobic Higgs,” *Nucl. Phys. B*, vol. 544, pp. 557–575, 1999. DOI: `10.1016/S0550-3213(98)00845-1`. arXiv: `hep-ph/9806337`.

[205] A. G. Akeroyd, A. Arhrib, and E.-M. Naimi, “Yukawa coupling corrections to the decay $H^+ \to W^+$ A0,” *Eur. Phys. J. C*, vol. 12, pp. 451–460, 2000, [Erratum: Eur.Phys.J.C 14, 371 (2000)]. DOI: `10.1007/s100529900266`. arXiv: `hep-ph/9811431`.

[206] G. Abbiendi *et al.*, “Decay mode independent searches for new scalar bosons with the OPAL detector at LEP,” *Eur. Phys. J. C*, vol. 27, pp. 311–329, 2003. DOI: `10.1140/epjc/s2002-01115-1`. arXiv: `hep-ex/0206022`.

[207] G. Abbiendi *et al.* [incl. G. Pásztor], “Search for Charged Higgs Bosons in e^+e^- Collisions at $\sqrt{s} = 189-209$ GeV,” *Eur. Phys. J. C*, vol. 72, p. 2076, 2012, CERN-PH-EP-2008-016. DOI: `10.1140/epjc/s10052-012-2076-0`. arXiv: `0812.0267 [hep-ex]`.

[208] G. F. Giudice *et al.*, “Searches for new physics,” in *CERN Workshop on LEP2 Physics (followed by 2nd meeting, 15-16 Jun 1995 and 3rd meeting 2-3 Nov 1995)*, Feb. 1996. arXiv: `hep-ph/9602207`.

[209] Joint SUSY Working Group, LEPSUSYWG, The ALEPH, DELPHI, L3 and OPAL Collaborations, “Combined LEP Chargino Results up to 208 GeV for large m_0,” LEPSUSYWG/01-03.1, Feb. 2001, See also references therein. `https://lepsusy.web.cern.ch/lepsusy/www/inos_moriond01/charginos_pub.html`.

[210] Joint SUSY Working Group, LEPSUSYWG, The ALEPH, DELPHI, L3 and OPAL Collaborations, “Combined LEP Chargino Results up to 208 GeV for low Δm,” LEPSUSYWG/02-04.1, Jun. 2002, See also references therein. `https://lepsusy.web.cern.ch/lepsusy/www/inoslowdmsummer02/charginolowdm_pub.html`.

[211] H. Baer, A. Bartl, D. Karatas, W. Majerotto, and X. Tata, “Searching for Supersymmetry at e^+e^- Supercolliders,” *Int. J. Mod. Phys. A*, vol. 4, p. 4111, 1989. DOI: `10.1142/S0217751X89001709`.

[212] Joint SUSY Working Group, LEPSUSYWG, The ALEPH, DELPHI, L3 and OPAL Collaborations, “Combined LEP Selectron, Smuon, Stau Results at 183-208 GeV,” LEPSUSYWG/04-01.1, Jun. 2004, See also references therein. `https://lepsusy.web.cern.ch/lepsusy/www/sleptons_summer04/slep_final.html`.

[213] Joint SUSY Working Group, LEPSUSYWG, The ALEPH, DELPHI, L3 and OPAL Collaborations, “Combined LEP stop and sbottom Results 183-208 GeV,” LEPSUSYWG/04-02.1, Jun. 2004, See also references therein. `https://lepsusy.web.cern.ch/lepsusy/www/squarks_summer04/stop_combi_208_final.html`.

[214] Joint SUSY Working Group, LEPSUSYWG, The ALEPH, DELPHI, L3 and OPAL Collaborations, "Interpretation of the results in Minimal SUGRA," LEPSUSYWG/02-06.2, Nov. 2002, See also references therein. `https://lepsusy.web.cern.ch/lepsusy/www/lspmsugra_summer02/02-06.2/mSUGRA_208.html`.

[215] G. Abbiendi *et al.* [incl. G. Pásztor], "Search for R parity violating decays of scalar fermions at LEP," *Eur. Phys. J. C*, vol. 33, pp. 149–172, 2004. DOI: `10.1140/epjc/s2004-01596-8`. arXiv: `hep-ex/0310054`.

[216] G. Pásztor, "Search for R-parity violating decays of supersymmetric particles at LEP," *Int. J. Mod. Phys. A*, vol. 16S1B, K. K. Gan and R. Kass, Eds., pp. 781–785, 2001. DOI: `10.1142/S0217751X01008084`. arXiv: `hep-ex/0012007`.

[217] Joint SUSY Working Group, LEPSUSYWG, The ALEPH, DELPHI, L3 and OPAL Collaborations, "Combined LEP R-parity Violation Results up to 208 GeV for LLE couplings," LEPSUSYWG/02-10.1, Jun. 2002, See also references therein. `https://lepsusy.web.cern.ch/lepsusy/www/rpvllesummer02/lle_pub.html`.

[218] G. Abbiendi *et al.* [incl. G. Pásztor], "Search for pair produced leptoquarks in e^+e^- interactions at $\sqrt{s} = 189 - 209$ GeV," *Eur. Phys. J. C*, vol. 31, pp. 281–305, 2003. DOI: `10.1140/epjc/s2003-01325-y`. arXiv: `hep-ex/0305053`.

[219] G. Abbiendi *et al.* [incl. G. Pásztor], "Search for single leptoquark and squark production in electron photon scattering at $\sqrt{s_{ee}} = 189$ GeV at LEP," *Eur. Phys. J. C*, vol. 23, pp. 1–11, 2002. DOI: `10.1007/s100520100859`. arXiv: `hep-ex/0106031`.

[220] G. Abbiendi *et al.*, "Search for leptoquarks in electron photon scattering at s$(ee)^{(1/2)}$ up to 209-GeV at LEP," *Phys. Lett. B*, vol. 526, pp. 233–246, 2002. DOI: `10.1016/S0370-2693(01)01485-X`. arXiv: `hep-ex/0112024`.

[221] M. Della Negra *et al.*, "CMS: The Compact Muon Solenoid: Letter of intent for a general purpose detector at the LHC," CERN-LHCC-92-03,CERN-LHCC-I-1, Oct. 1992. `https://cds.cern.ch/record/290808`.

[222] G. Bayatian *et al.*, "CMS, the Compact Muon Solenoid: Technical proposal," CERN-LHCC-94-38,CERN-LHCC-P-1, Dec. 1994. `https://cds.cern.ch/record/290969`.

[223] G. Acquistapace *et al.*, "CMS, the magnet project: Technical design report," CERN-LHCC-97-10, May 1997. `https://cds.cern.ch/record/331056`.

[224] G. Bayatian *et al.*, "The CMS electromagnetic calorimeter project: Technical Design Report," CERN-LHCC-97-033,CMS-TDR-4, 1997. `https://cds.cern.ch/record/349375`.

[225] G. Bayatian *et al.*, "The CMS hadron calorimeter project: Technical Design Report," CERN-LHCC-97-031,CMS-TDR-2, 1997. `https://cds.cern.ch/record/357153`.

[226] G. Bayatian *et al.*, "The CMS muon project: Technical Design Report," CERN-LHCC-97-032,CMS-TDR-3, 1997. `https://cds.cern.ch/record/343814`.

[227] G. Bayatian *et al.*, "The CMS tracker system project: Technical Design Report," CERN-LHCC-98-006,CMS-TDR-5,CERN-LHCC-98-006,CMS-TDR-5, 1997. `https://cds.cern.ch/record/368412`.

[228] CMS Collaboration, “The CMS tracker: addendum to the Technical Design Report,” CERN-LHCC-2000-016,CMS-TDR-5-add-1,CERN-LHCC-2000-016,CMS-TDR-5-add-1, 2000. `https://cds.cern.ch/record/490194`.

[229] S. Chatrchyan *et al.* [incl. G. Pásztor], “The CMS experiment at the CERN LHC,” *JINST*, vol. 3, S08004, 2008. DOI: `10.1088/1748-0221/3/08/S08004`.

[230] G. Pásztor, “The CMS silicon strip tracker,” *AIP Conf. Proc.*, vol. 842, no. 1, P. D. Barnes, M. D. Cooper, R. A. Eisenstein, H. van Hecke, and G. J. Stephenson, Eds., pp. 1067–1069, 2006. DOI: `10.1063/1.2220455`. arXiv: `physics/0602117`.

[231] K.W. Bell, J.A. Coughlan, C. Foudas, K. Gill, N. Marinelli, G. Pásztor, and I.R. Tomalin, “User Requirements Document for the Final FED of the CMS Silicon Strip Tracker,” CERN, CMS-NOTE-2001-043, Sep. 2001. `https://cds.cern.ch/record/687365`.

[232] G. Aad *et al.*, “The ATLAS experiment at the CERN large hadron collider,” *Journal of Instrumentation*, vol. 3, no. 08, S08003–S08003, Aug. 2008. DOI: `10.1088/1748-0221/3/08/s08003`.

[233] G. Pásztor, “Discovery potential for Higgs bosons beyond the SM,” *J. Phys. Conf. Ser.*, vol. 110, R. Barlow, Ed., p. 072 032, 2008. DOI: `10.1088/1742-6596/110/7/072032`. arXiv: `0802.1000 [hep-ex]`.

[234] B. Salvachua, “Overview of proton-proton physics during Run 2,” in *Proceedings of the 9th Evian Workshop on LHC beam operation*, 2019, p. 7. `http://cds.cern.ch/record/2750272`.

[235] K. Aamodt *et al.*, “The ALICE experiment at the CERN LHC,” *JINST*, vol. 3, S08002, 2008. DOI: `10.1088/1748-0221/3/08/S08002`.

[236] A. A. Alves Jr. *et al.*, “The LHCb Detector at the LHC,” *JINST*, vol. 3, S08005, 2008. DOI: `10.1088/1748-0221/3/08/S08005`.

[237] W. Herr and B. Muratori, “Concept of luminosity,” in *CERN Accelerator School: Intermediate Course on Accelerator Physics, Zeuthen, Germany, 15-26 Sep 2003*, D. Brandt, Ed., 2006, pp. 361–378. DOI: `10.5170/CERN-2006-002`.

[238] O. S. Brüning, P. Collier, P. Lebrun, S. Myers, R. Ostojic, J. Poole, and P. Proudlock, “LHC design report vol. 1: The LHC main ring,” CERN-2004-003-V-1, 2004. DOI: `10.5170/CERN-2004-003-V-1`.

[239] M. Hostettler, “LHC luminosity performance,” CERN-THESIS-2018-051, PhD. dissertation, University of Bern, 2018. `https://cds.cern.ch/record/2319396`.

[240] T. Sjostrand, S. Mrenna, and P. Z. Skands, “A Brief Introduction to PYTHIA 8.1,” *Comput. Phys. Commun.*, vol. 178, pp. 852–867, 2008. DOI: `10.1016/j.cpc.2008.01.036`. arXiv: `0710.3820 [hep-ph]`.

[241] G. Aad *et al.*, “Improved luminosity determination in pp collisions at $\sqrt{s} = 7$ TeV using the ATLAS detector at the LHC,” *Eur. Phys. J. C*, vol. 73, no. 8, p. 2518, 2013. DOI: `10.1140/epjc/s10052-013-2518-3`. arXiv: `1302.4393 [hep-ex]`.

[242] ATLAS Collaboration, “Luminosity Public Results,” downloaded in Dec. 2021. `https://twiki.cern.ch/twiki/bin/view/AtlasPublic/LuminosityPublicResults`.

[243] P. Skands, S. Carrazza, and J. Rojo, "Tuning PYTHIA 8.1: The Monash 2013 tune," *Eur. Phys. J. C*, vol. 74, p. 3024, 2014. DOI: `10.1140/epjc/s10052-014-3024-y`. arXiv: `1404.5630 [hep-ph]`.

[244] T. Sjöstrand, S. Ask, J. R. Christiansen, R. Corke, N. Desai, P. Ilten, S. Mrenna, S. Prestel, C. O. Rasmussen, and P. Z. Skands, "An introduction to PYTHIA 8.2," *Comput. Phys. Commun.*, vol. 191, p. 159, 2015. DOI: `10.1016/j.cpc.2015.01.024`. arXiv: `1410.3012 [hep-ph]`.

[245] M. Aaboud *et al.*, "Luminosity determination in pp collisions at $\sqrt{s} = 8$ TeV using the ATLAS detector at the LHC," *Eur. Phys. J. C*, vol. 76, no. 12, p. 653, 2016. DOI: `10.1140/epjc/s10052-016-4466-1`. arXiv: `1608.03953 [hep-ex]`.

[246] ATLAS Collaboration, "Luminosity determination in *pp* collisions at $\sqrt{s} = 13$ TeV using the ATLAS detector at the LHC," CERN, ATLAS-CONF-2019-021, Jun. 2019. `http://cds.cern.ch/record/2677054`.

[247] ATLAS Collaboration, "Luminosity Public Results for Run2," downloaded in Dec. 2022. `https://twiki.cern.ch/twiki/bin/view/AtlasPublic/LuminosityPublicResultsRun2`.

[248] G. Aad *et al.*, "The ATLAS Experiment at the CERN Large Hadron Collider: A Description of the Detector Configuration for Run 3," CERN-EP-2022-259, May 2023. arXiv: `2305.16623 [physics.ins-det]`.

[249] B. Abbott *et al.*, "Production and Integration of the ATLAS Insertable B-Layer," *JINST*, vol. 13, no. 05, T05008, 2018. DOI: `10.1088/1748-0221/13/05/T05008`. arXiv: `1803.00844 [physics.ins-det]`.

[250] ATLAS Collaboration, "Alignment of the ATLAS Inner Detector and its Performance in 2012," ATLAS-CONF-2014-047, 2014. `http://cds.cern.ch/record/1741021`.

[251] G. Aad *et al.*, "Electron and photon energy calibration with the ATLAS detector using LHC Run 1 data," *Eur. Phys. J. C*, vol. 74, no. 10, p. 3071, 2014. DOI: `10.1140/epjc/s10052-014-3071-4`. arXiv: `1407.5063 [hep-ex]`.

[252] G. Aad *et al.* [incl. G. Pásztor], "Electron performance measurements with the ATLAS detector using the 2010 LHC proton-proton collision data," *Eur. Phys. J. C*, vol. 72, p. 1909, 2012. DOI: `10.1140/epjc/s10052-012-1909-1`. arXiv: `1110.3174 [hep-ex]`.

[253] G. Aad *et al.* [incl. G. Pásztor], "Electron reconstruction and identification efficiency measurements with the ATLAS detector using the 2011 LHC proton-proton collision data," *Eur. Phys. J. C*, vol. 74, no. 7, p. 2941, 2014. DOI: `10.1140/epjc/s10052-014-2941-0`. arXiv: `1404.2240 [hep-ex]`.

[254] M. Aaboud *et al.* [incl. G. Pásztor], "Electron efficiency measurements with the ATLAS detector using 2012 LHC proton-proton collision data," *Eur. Phys. J. C*, vol. 77, no. 3, p. 195, 2017. DOI: `10.1140/epjc/s10052-017-4756-2`. arXiv: `1612.01456 [hep-ex]`.

[255] M. Aaboud *et al.* [incl. G. Pásztor], "Measurement of the photon identification efficiencies with the ATLAS detector using LHC Run-1 data," *Eur. Phys. J. C*, vol. 76, no. 12, p. 666, 2016. DOI: `10.1140/epjc/s10052-016-4507-9`. arXiv: `1606.01813 [hep-ex]`.

[256] G. Aad *et al.*, "Electron and photon performance measurements with the ATLAS detector using the 2015–2017 LHC proton-proton collision data," *JINST*, vol. 14, no. 12, P12006, 2019. DOI: `10.1088/1748-0221/14/12/P12006`. arXiv: `1908.00005 [hep-ex]`.

[257] G. Aad *et al.*, "Measurement of the muon reconstruction performance of the ATLAS detector using 2011 and 2012 LHC proton–proton collision data," *Eur. Phys. J. C*, vol. 74, no. 11, p. 3130, 2014. DOI: `10.1140/epjc/s10052-014-3130-x`. arXiv: `1407.3935 [hep-ex]`.

[258] A. Hayrapetyan *et al.* [incl. G. Pásztor], "Development of the CMS detector for the CERN LHC Run 3," CERN, CERN-EP-2023-136,CMS-PRF-21-001-003, 2023, Submitted to JINST. arXiv: `2309.05466 [physics.ins-det]`. `https://cds.cern.ch/record/2870088`.

[259] S. Chatrchyan *et al.*, "CMS Technical Design Report for the Pixel Detector Upgrade," CERN, CERN-LHCC-2012-016,CMS-TDR-011, Sep. 2012. DOI: `10.2172/1151650`. `https://cds.cern.ch/record/1481838`.

[260] S. Chatrchyan *et al.*, "Description and performance of track and primary-vertex reconstruction with the CMS tracker," *JINST*, vol. 9, P10009, 2014. DOI: `10.1088/1748-0221/9/10/P10009`. arXiv: `1405.6569 [physics.ins-det]`.

[261] V. Khachatryan *et al.*, "Performance of Photon Reconstruction and Identification with the CMS Detector in Proton-Proton Collisions at $\sqrt{s} = 8$ TeV," *JINST*, vol. 10, P08010, 2015. DOI: `10.1088/1748-0221/10/08/P08010`. arXiv: `1502.02702 [physics.ins-det]`.

[262] V. Khachatryan *et al.*, "Jet energy scale and resolution in the CMS experiment in pp collisions at 8 TeV," *JINST*, vol. 12, P02014, 2017. DOI: `10.1088/1748-0221/12/02/P02014`. arXiv: `1607.03663 [hep-ex]`.

[263] A. M. Sirunyan *et al.*, "Particle-flow reconstruction and global event description with the CMS detector," *JINST*, vol. 12, P10003, 2017. DOI: `10.1088/1748-0221/12/10/P10003`. arXiv: `1706.04965 [physics.ins-det]`.

[264] M. Aaboud *et al.* [incl. G. Pásztor], "Performance of the ATLAS Trigger System in 2015," *Eur. Phys. J. C*, vol. 77, no. 5, p. 317, 2017. DOI: `10.1140/epjc/s10052-017-4852-3`. arXiv: `1611.09661 [hep-ex]`.

[265] G. Pásztor, "The Upgrade of the ATLAS Electron and Photon Triggers towards LHC Run 2 and their Performance," in *Meeting of the APS Division of Particles and Fields (DPF2015)*, Nov. 2015. arXiv: `1511.00334 [hep-ex]`.

[266] G. Aad *et al.*, "Performance of electron and photon triggers in ATLAS during LHC Run 2," *Eur. Phys. J. C*, vol. 80, no. 1, p. 47, 2020. DOI: `10.1140/epjc/s10052-019-7500-2`. arXiv: `1909.00761 [hep-ex]`.

[267] A. M. Sirunyan *et al.* [incl. G. Pásztor], "Electron and photon reconstruction and identification with the CMS experiment at the CERN LHC," *JINST*, vol. 16, P05014, 2021. DOI: `10.1088/1748-0221/16/05/P05014`. arXiv: `2012.06888 [hep-ex]`.

[268] ATLAS Collaboration [incl. G. Pásztor], "Improved electron reconstruction in ATLAS using the Gaussian Sum Filter-based model for bremsstrahlung," CERN, ATLAS-CONF-2012-047, May 2012. `http://cds.cern.ch/record/1449796`.

[269] S. Agostinelli *et al.*, "GEANT4 — a simulation toolkit," *Nucl. Instrum. Meth. A*, vol. 506, p. 250, 2003. DOI: `10.1016/S0168-9002(03)01368-8`.

[270] A. M. Sirunyan *et al.* [incl. G. Pásztor], "Precision luminosity measurement in proton-proton collisions at $\sqrt{s} = 13$ TeV in 2015 and 2016 at CMS," *Eur. Phys. J. C*, vol. 81, p. 800, 2021. DOI: `10.1140/epjc/s10052-021-09538-2`. arXiv: `2104.01927 [hep-ex]`.

[271] CMS Collaboration [incl. G. Pásztor], "CMS luminosity measurement for the 2017 data-taking period at $\sqrt{s} = 13$ TeV," CERN, CMS-PAS-LUM-17-004, 2018. `https://cds.cern.ch/record/2621960`.

[272] CMS Collaboration [incl. G. Pásztor], "CMS luminosity measurement for the 2018 data-taking period at $\sqrt{s} = 13$ TeV," CERN, CMS-PAS-LUM-18-002, 2019. `https://cds.cern.ch/record/2676164`.

[273] CMS Collaboration [incl. G. Pásztor], "CMS luminosity measurement using nucleus-nucleus collisions at $\sqrt{s_{\mathrm{NN}}} = 5.02$ TeV in 2018," CERN, CMS-PAS-LUM-18-001, 2022.

[274] ATLAS, CMS, LHC Higgs Combination Group, "Procedure for the LHC Higgs boson search combination in Summer 2011," CMS-NOTE-2011-005,ATL-PHYS-PUB-2011-011, Aug. 2011. `https://cds.cern.ch/record/1379837`.

[275] L. Brenner, R. Balasubramanian, C. Burgard, W. Verkerke, G. Cowan, P. Verschuuren, and V. Croft, "Comparison of unfolding methods using RooFitUnfold," *Int. J. Mod. Phys. A*, vol. 35, no. 24, p. 2 050 145, 2020. DOI: `10.1142/S0217751X20501456`. arXiv: `1910.14654 [physics.data-an]`.

[276] S. Schmitt, "Data Unfolding Methods in High Energy Physics," *EPJ Web Conf.*, vol. 137, Y. Foka, N. Brambilla, and V. Kovalenko, Eds., p. 11 008, 2017. DOI: `10.1051/epjconf/201713711008`. arXiv: `1611.01927 [physics.data-an]`.

[277] J. C. Collins, D. E. Soper, and G. F. Sterman, "Factorization of Hard Processes in QCD," *Adv. Ser. Direct. High Energy Phys.*, vol. 5, pp. 1–91, 1989. DOI: `10.1142/9789814503266_0001`. arXiv: `hep-ph/0409313`.

[278] D. Horváth, and Z. Trócsányi, *Introduction to Particle Physics.* Cambridge Scholars Publishing, 2019.

[279] G. Altarelli and G. Parisi, "Asymptotic Freedom in Parton Language," *Nucl. Phys. B*, vol. 126, pp. 298–318, 1977. DOI: `10.1016/0550-3213(77)90384-4`.

[280] Y. L. Dokshitzer, "Calculation of the Structure Functions for Deep Inelastic Scattering and e^+e^- Annihilation by Perturbation Theory in Quantum Chromodynamics.," *Sov. Phys. JETP*, vol. 46, pp. 641–653, 1977.

[281] V. N. Gribov and L. N. Lipatov, "Deep inelastic e p scattering in perturbation theory," *Sov. J. Nucl. Phys.*, vol. 15, pp. 438–450, 1972.

[282] M. Botje *et al.*, "The PDF4LHC Working Group Interim Recommendations," Jan. 2011. arXiv: `1101.0538 [hep-ph]`.

[283] S. Alekhin *et al.*, "The PDF4LHC Working Group Interim Report," Jan. 2011. arXiv: `1101.0536 [hep-ph]`.

[284] J. Butterworth *et al.*, "PDF4LHC recommendations for LHC Run II," *J. Phys. G*, vol. 43, p. 023 001, 2016. DOI: `10.1088/0954-3899/43/2/023001`. arXiv: `1510.03865 [hep-ph]`.

[285] R. D. Ball *et al.*, "The PDF4LHC21 combination of global PDF fits for the LHC Run III," *J. Phys. G*, vol. 49, no. 8, p. 080 501, 2022. DOI: `10.1088/1361-6471/ac7216`. arXiv: `2203.05506 [hep-ph]`.

[286] A. Huss, J. Huston, S. Jones, and M. Pellen, "Les Houches 2021—physics at TeV colliders: report on the standard model precision wishlist," *J. Phys. G*, vol. 50, no. 4, p. 043 001, 2023. DOI: `10.1088/1361-6471/acbaec`. arXiv: `2207.02122 [hep-ph]`.

[287] C. G. Bollini and J. J. Giambiagi, "Dimensional Renormalization: The Number of Dimensions as a Regularizing Parameter," *Nuovo Cim. B*, vol. 12, pp. 20–26, 1972. DOI: `10.1007/BF02895558`.

[288] G. 't Hooft and M. J. G. Veltman, "Regularization and Renormalization of Gauge Fields," *Nucl. Phys. B*, vol. 44, pp. 189–213, 1972. DOI: `10.1016/0550-3213(72)90279-9`.

[289] M. Cacciari and N. Houdeau, "Meaningful characterisation of perturbative theoretical uncertainties," *JHEP*, vol. 09, p. 039, 2011. DOI: `10.1007/JHEP09(2011)039`. arXiv: `1105.5152 [hep-ph]`.

[290] F. Maltoni, G. Ridolfi, and M. Ubiali, "b-initiated processes at the LHC: a reappraisal," *JHEP*, vol. 07, p. 022, 2012, [Erratum: JHEP 04, 095 (2013)]. DOI: `10.1007/JHEP04(2013)095`. arXiv: `1203.6393 [hep-ph]`.

[291] M. Cacciari, M. Greco, and P. Nason, "The P(T) spectrum in heavy flavor hadroproduction," *JHEP*, vol. 05, p. 007, 1998. DOI: `10.1088/1126-6708/1998/05/007`. arXiv: `hep-ph/9803400`.

[292] A. Buckley *et al.*, "General-purpose event generators for LHC physics," *Phys. Rept.*, vol. 504, pp. 145–233, 2011. DOI: `10.1016/j.physrep.2011.03.005`. arXiv: `1101.2599 [hep-ph]`.

[293] S. Alioli *et al.*, "Monte Carlo event generators for high energy particle physics event simulation," MCnet-19-02, Feb. 2019. arXiv: `1902.01674 [hep-ph]`.

[294] J. M. Campbell *et al.*, "Event Generators for High-Energy Physics Experiments," in *Snowmass 2021*, Mar. 2022. arXiv: `2203.11110 [hep-ph]`.

[295] A. Buckley, J. Ferrando, S. Lloyd, K. Nordström, B. Page, M. Rüfenacht, M. Schönherr, and G. Watt, "LHAPDF6: parton density access in the LHC precision era," *Eur. Phys. J. C*, vol. 75, p. 132, 2015. DOI: `10.1140/epjc/s10052-015-3318-8`. arXiv: `1412.7420 [hep-ph]`.

[296] J. Alwall *et al.*, "The automated computation of tree-level and next-to-leading order differential cross sections, and their matching to parton shower simulations," *JHEP*, vol. 07, p. 079, 2014. DOI: `10.1007/JHEP07(2014)079`. arXiv: `1405.0301 [hep-ph]`.

[297] R. Frederix, S. Frixione, V. Hirschi, D. Pagani, H. .-S. Shao, and M. Zaro, "The automation of next-to-leading order electroweak calculations," *JHEP*, vol. 07, p. 185, 2018, [Erratum: JHEP 11, 085 (2021)]. DOI: `10.1007/JHEP11(2021)085`. arXiv: `1804.10017 [hep-ph]`.

[298] T. Gleisberg, S. Hoeche, F. Krauss, M. Schonherr, S. Schumann, F. Siegert, and J. Winter, "Event generation with SHERPA 1.1," *JHEP*, vol. 02, p. 007, 2009. DOI: `10.1088/1126-6708/2009/02/007`. arXiv: `0811.4622 [hep-ph]`.

[299] S. Alioli, P. Nason, C. Oleari, and E. Re, "A general framework for implementing NLO calculations in shower Monte Carlo programs: the POWHEG BOX," *JHEP*, vol. 06, p. 043, 2010. DOI: `10.1007/JHEP06(2010)043`. arXiv: `1002.2581 [hep-ph]`.

[300] B. Andersson, G. Gustafson, G. Ingelman, and T. Sjostrand, "Parton Fragmentation and String Dynamics," *Phys. Rept.*, vol. 97, pp. 31–145, 1983. DOI: `10.1016/0370-1573(83)90080-7`.

[301] M. Bahr *et al.*, "Herwig++ Physics and Manual," *Eur. Phys. J. C*, vol. 58, pp. 639–707, 2008. DOI: `10.1140/epjc/s10052-008-0798-9`. arXiv: `0803.0883 [hep-ph]`.

[302] J. Bellm *et al.*, "Herwig 7.0/Herwig++ 3.0 release note," *Eur. Phys. J. C*, vol. 76, no. 4, p. 196, 2016. DOI: `10.1140/epjc/s10052-016-4018-8`. arXiv: `1512.01178 [hep-ph]`.

[303] S. Gieseke, P. Stephens, and B. Webber, "New formalism for QCD parton showers," *JHEP*, vol. 12, p. 045, 2003. DOI: `10.1088/1126-6708/2003/12/045`. arXiv: `hep-ph/0310083`.

[304] J.-C. Winter, F. Krauss, and G. Soff, "A Modified cluster hadronization model," *Eur. Phys. J. C*, vol. 36, pp. 381–395, 2004. DOI: `10.1140/epjc/s2004-01960-8`. arXiv: `hep-ph/0311085`.

[305] D. R. Yennie, S. C. Frautschi, and H. Suura, "The infrared divergence phenomena and high-energy processes," *Annals Phys.*, vol. 13, pp. 379–452, 1961. DOI: `10.1016/0003-4916(61)90151-8`.

[306] K. Hamilton and P. Richardson, "Simulation of QED radiation in particle decays using the YFS formalism," *JHEP*, vol. 07, p. 010, 2006. DOI: `10.1088/1126-6708/2006/07/010`. arXiv: `hep-ph/0603034`.

[307] M. Schonherr and F. Krauss, "Soft Photon Radiation in Particle Decays in SHERPA," *JHEP*, vol. 12, p. 018, 2008. DOI: `10.1088/1126-6708/2008/12/018`. arXiv: `0810.5071 [hep-ph]`.

[308] P. Golonka and Z. Was, "PHOTOS Monte Carlo: A Precision tool for QED corrections in Z and W decays," *Eur. Phys. J. C*, vol. 45, pp. 97–107, 2006. DOI: `10.1140/epjc/s2005-02396-4`. arXiv: `hep-ph/0506026`.

[309] N. Davidson, T. Przedzinski, and Z. Was, "PHOTOS interface in C++: Technical and Physics Documentation," *Comput. Phys. Commun.*, vol. 199, pp. 86–101, 2016. DOI: `10.1016/j.cpc.2015.09.013`. arXiv: `1011.0937 [hep-ph]`.

[310] M. Dasgupta, F. A. Dreyer, K. Hamilton, P. F. Monni, G. P. Salam, and G. Soyez, "Parton showers beyond leading logarithmic accuracy," *Phys. Rev. Lett.*, vol. 125, no. 5, p. 052 002, 2020. DOI: `10.1103/PhysRevLett.125.052002`. arXiv: `2002.11114 [hep-ph]`.

[311] T. Sjostrand and M. van Zijl, "A Multiple Interaction Model for the Event Structure in Hadron Collisions," *Phys. Rev. D*, vol. 36, p. 2019, 1987. DOI: `10.1103/PhysRevD.36.2019`.

[312] A. Buckley, H. Hoeth, H. Lacker, H. Schulz, and J. E. von Seggern, "Systematic event generator tuning for the LHC," *Eur. Phys. J. C*, vol. 65, pp. 331–357, 2010. DOI: `10.1140/epjc/s10052-009-1196-7`. arXiv: `0907.2973 [hep-ph]`.

[313] A. Buckley and H. Schulz, "Tuning of MC generator MPI models," *Adv. Ser. Direct. High Energy Phys.*, vol. 29, P. Bartalini and J. R. Gaunt, Eds., pp. 281–301, 2018. DOI: `10.1142/9789813227767_0013`. arXiv: `1806.11182 [hep-ph]`.

[314] J. M. Butterworth, J. R. Forshaw, and M. H. Seymour, "Multiparton interactions in photoproduction at HERA," *Z. Phys. C*, vol. 72, pp. 637–646, 1996. DOI: `10.1007/s002880050286`. arXiv: `hep-ph/9601371`.

[315] M. Bahr, S. Gieseke, and M. H. Seymour, “Simulation of multiple partonic interactions in Herwig++,” *JHEP*, vol. 07, p. 076, 2008. DOI: `10.1088/1126-6708/2008/07/076`. arXiv: `0803.3633 [hep-ph]`.

[316] A. Tumasyan *et al.* [incl. G. Pásztor], “Observation of same-sign WW production from double parton scattering in proton-proton collisions at $\sqrt{s} = 13$ TeV,” *Phys. Rev. Lett.*, vol. 131, p. 091 803, 9 Sep. 2023. DOI: `10.1103/PhysRevLett.131.091803`. arXiv: `2206.02681 [hep-ex]`.

[317] R. Fruhwirth, “Application of Kalman filtering to track and vertex fitting,” *Nucl. Instrum. Meth. A*, vol. 262, pp. 444–450, 1987. DOI: `10.1016/0168-9002(87)90887-4`.

[318] R. Frühwirth, “A gaussian-mixture approximation of the bethe–heitler model of electron energy loss by bremsstrahlung,” *Computer Physics Communications*, vol. 154, no. 2, pp. 131–142, 2003, ISSN: 0010-4655. DOI: `https://doi.org/10.1016/S0010-4655(03)00292-3`. `https://www.sciencedirect.com/science/article/pii/S0010465503002923`.

[319] W. Adam, R. Fruhwirth, A. Strandlie, and T. Todorov, “Reconstruction of electrons with the Gaussian sum filter in the CMS tracker at LHC,” *eConf*, vol. C0303241, TULT009, 2003. DOI: `10.1088/0954-3899/31/9/N01`. arXiv: `physics/0306087`.

[320] M. Aaboud *et al.*, “Electron and photon energy calibration with the ATLAS detector using 2015–2016 LHC proton-proton collision data,” *JINST*, vol. 14, no. 03, P03017, 2019. DOI: `10.1088/1748-0221/14/03/P03017`. arXiv: `1812.03848 [hep-ex]`.

[321] M. D. Schwartz, “TASI Lectures on Collider Physics,” in *Proceedings, Theoretical Advanced Study Institute in Elementary Particle Physics : Anticipating the Next Discoveries in Particle Physics (TASI 2016): Boulder, CO, USA, June 6-July 1, 2016*, R. Essig and I. Low, Eds. 2018, pp. 65–100. DOI: `10.1142/9789813233348_0002`. arXiv: `1709.04533 [hep-ph]`.

[322] K. Nikolics, “Measurement of the High Mass Drell-Yan Differential Cross Section in the electron-positron channel with the ATLAS Experiment at $\sqrt{s} = 7$ TeV,” PhD. dissertation, Geneva U., Feb. 2013. DOI: `10.13097/archive-ouverte/unige:28476`.

[323] G. Pásztor, “Measurements of vector-meson production with the ATLAS detector,” in *Proceedings of the 19th International Workshop on Deep-Inelastic Scattering and Related Subjects, Newport News, VA, USA, 11 - 15 April 2011.*, Sep. 2011. `https://cds.cern.ch/record/1379524`.

[324] E. Benhar Noccioli [co-supervisor: G. Pásztor], “Measurement of the properties of the Standard Model Higgs boson in the $H \to ZZ^* \to 4\ell$ decay channel with the ATLAS Experiment at CERN,” PhD. dissertation, Geneva U., 2015. DOI: `10.13097/archive-ouverte/unige:87493`.

[325] G. Aad *et al.*, “Performance of the ATLAS Trigger System in 2010,” *Eur. Phys. J. C*, vol. 72, p. 1849, 2012. DOI: `10.1140/epjc/s10052-011-1849-1`. arXiv: `1110.1530 [hep-ex]`.

[326] V. Khachatryan *et al.*, “The CMS trigger system,” *JINST*, vol. 12, P01020, 2017. DOI: `10.1088/1748-0221/12/01/P01020`. arXiv: `1609.02366 [physics.ins-det]`.

[327] CMS Collaboration, “CMS technical design report for the level-1 trigger upgrade,” CERN, CERN-LHCC-2013-011,CMS-TDR-012, 2013. `https://cds.cern.ch/record/1556311`.

[328] M. Abolins *et al.*, “The ATLAS Data Acquisition and High Level Trigger system,” *JINST*, vol. 11, no. 06, P06008, 2016. DOI: `10.1088/1748-0221/11/06/P06008`.

[329] E. Salvioni, G. Villadoro, and F. Zwirner, “Minimal Z’ models: Present bounds and early LHC reach,” *Journal of High Energy Physics*, vol. 2009, no. 11, p. 068, 2009.

[330] V. Barger, W.-Y. Keung, and E. Ma, “Gauge model with light W and Z bosons,” *Physical Review D*, vol. 22, no. 3, p. 727, 1980.

[331] C. Grojean, E. Salvioni, and R. Torre, “A weakly constrained W’ at the early LHC,” *Journal of High Energy Physics*, vol. 2011, no. 7, pp. 1–29, 2011.

[332] L. Randall and R. Sundrum, “Large mass hierarchy from a small extra dimension,” *Physical review letters*, vol. 83, no. 17, p. 3370, 1999.

[333] L. Randall and R. Sundrum, “An alternative to compactification,” *Physical Review Letters*, vol. 83, no. 23, p. 4690, 1999.

[334] K. Agashe, H. Davoudiasl, G. Perez, and A. Soni, “Warped gravitons at the cern lhc and beyond,” *Physical Review D*, vol. 76, no. 3, p. 036 006, 2007.

[335] L. Fitzpatrick, J. Kaplan, L. Randall, and L.-T. Wang, “Searching for the kaluza-klein graviton in bulk rs models,” *Journal of High Energy Physics*, vol. 2007, no. 09, p. 013, 2007.

[336] J. Rosiek, “Complete set of feynman rules for the minimal supersymmetric extension of the standard model,” *Physical Review D*, vol. 41, no. 11, pp. 3464–3501, Jun. 1990, ISSN: 0556-2821. DOI: `10.1103/physrevd.41.3464`.

[337] A. Canepa, “Searches for supersymmetry at the large hadron collider,” *Reviews in Physics*, vol. 4, p. 100 033, 2019, ISSN: 2405-4283. DOI: `https://doi.org/10.1016/j.revip.2019.100033`. `https://www.sciencedirect.com/science/article/pii/S2405428318300091`.

[338] ATLAS Collaboration, “Performance of the ATLAS Electron and Photon Trigger in p-p Collisions at sqrts = 7 TeV in 2011,” ATLAS-CONF-2012-048, May 2012. `https://cds.cern.ch/record/1450089`.

[339] A. M. Sirunyan *et al.*, “Measurement of the inelastic proton-proton cross section at $\sqrt{s} = 13$ TeV,” *JHEP*, vol. 07, p. 161, 2018. DOI: `10.1007/JHEP07(2018)161`. arXiv: `1802.02613 [hep-ex]`.

[340] A. Tumasyan *et al.* [incl. G. Pásztor], *The Phase-2 Upgrade of the CMS Beam Radiation Instrumentation and Luminosity Detectors*, G. Auzinger, A. Dabrowski, P. Lujan, G. Pásztor, and D. Stickland, Eds. Jul. 2021, approved by the LHCC, final version dated Dec. 2021. `http://cds.cern.ch/record/2759074`.

[341] A. M. Sirunyan *et al.*, “Measurements of the W boson rapidity, helicity, double-differential cross sections, and charge asymmetry in pp collisions at $\sqrt{s} = 13$ TeV,” *Phys. Rev. D*, vol. 102, p. 092 012, 2020. DOI: `10.1103/PhysRevD.102.092012`. arXiv: `2008.04174 [hep-ex]`.

[342] A. Tumasyan *et al.*, “Measurement of the mass dependence of the transverse momentum of lepton pairs in Drell-Yan production in proton-proton collisions at $\sqrt{s} = 13$ TeV,” *Eur. Phys. J. C*, vol. 83, no. 7, p. 628, 2023. DOI: `10.1140/epjc/s10052-023-11631-7`. arXiv: `2205.04897 [hep-ex]`.

[343] A. Tumasyan *et al.*, "Measurement of differential $t\bar{t}$ production cross sections in the full kinematic range using lepton+jets events from proton-proton collisions at $\sqrt{s} = 13$ TeV," *Phys. Rev. D*, vol. 104, no. 9, p. 092 013, 2021. DOI: `10.1103/PhysRevD.104.092013`. arXiv: `2108.02803 [hep-ex]`.

[344] A. Tumasyan *et al.*, "First measurement of the top quark pair production cross section in proton-proton collisions at $\sqrt{s} = 13.6$ TeV," *JHEP*, vol. 08, p. 204, 2023. DOI: `10.1007/JHEP08(2023)204`. arXiv: `2303.10680 [hep-ex]`.

[345] A. M. Sirunyan *et al.*, "Combined measurements of Higgs boson couplings in proton–proton collisions at $\sqrt{s} = 13\,\mathrm{TeV}$," *Eur. Phys. J. C*, vol. 79, no. 5, p. 421, 2019. DOI: `10.1140/epjc/s10052-019-6909-y`. arXiv: `1809.10733 [hep-ex]`.

[346] A. Dainese, M. Mangano, A. B. Meyer, A. Nisati, G. Salam, and M. A. Vesterinen, "Report on the physics at the HL-LHC, and perspectives for the HE-LHC," *CERN*, 2019. DOI: `10.23731/CYRM-2019-007`. `http://cds.cern.ch/record/2703572`.

[347] M. Cepeda *et al.*, "Report from Working Group 2: Higgs physics at the HL-LHC and HE-LHC," *CERN*, vol. 7, A. Dainese, M. Mangano, A. B. Meyer, A. Nisati, G. Salam, and M. A. Vesterinen, Eds., p. 221, 2019. DOI: `10.23731/CYRM-2019-007.221`. arXiv: `1902.00134 [hep-ph]`.

[348] ATLAS and CMS Collaborations, "Addendum to the report on the physics at the HL-LHC, and perspectives for the HE-LHC: Collection of notes from ATLAS and CMS," CERN-LPCC-2019-01,CMS-FTR-19-001,ATL-PHYS-PUB-2019-006,CERN-2019-007-ADD, 2019. DOI: `10.23731/CYRM-2019-007.Addendum`. arXiv: `1902.10229 [hep-ex]`.

[349] F. Antoniou, M. Hostettler, G. Iadarola, S. Papadopoulou, Y. Papaphilippou, D. Pellegrini, and G. Trad, "Can we predict luminosity?" In *Proceedings of the 7th Evian Workshop on LHC beam operation*, 2016, p. 125. `http://cds.cern.ch/record/2293678`.

[350] L. Evans and P. Bryant, "LHC machine," *JINST*, vol. 3, S08001, 2008. DOI: `10.1088/1748-0221/3/08/S08001`.

[351] I. Béjar Alonso, O. Brüning, P. Fessia, L. Rossi, L. Tavian, and M. Zerlauth, "High-Luminosity Large Hadron Collider (HL-LHC): Technical design report," *CERN*, 2020. DOI: `10.23731/CYRM-2020-0010`.

[352] P. Grafström and W. Kozanecki, "Luminosity determination at proton colliders," *Prog. Part. Nucl. Phys.*, vol. 81, pp. 97–148, 2015. DOI: `10.1016/j.ppnp.2014.11.002`.

[353] CMS Collaboration [incl. G. Pásztor], "Luminosity measurement in proton-proton collisions at 5.02 TeV in 2017 at CMS," CERN, CMS-PAS-LUM-19-001, 2021. `https://cds.cern.ch/record/2765655`.

[354] CMS Collaboration, "CMS luminosity measurement using 2016 proton-nucleus collisions at $\sqrt{s_{\mathrm{NN}}} = 8$ TeV [incl. G. Pásztor]," CERN, CMS-PAS-LUM-17-002, 2018. `https://cds.cern.ch/record/2628652`.

[355] A.M. Sirunyan *et al.* [incl. G. Pásztor], *The Phase-2 Upgrade of the CMS Beam Radiation, Instrumentation, and Luminosity Detectors: Conceptual Design*, G. Auzinger, A. Dabrowski, P. Lujan, and D. Stickland, Eds. Jan. 2020. `http://cds.cern.ch/record/2706512`.

[356] A. Hayrapetyan *et al.*, "Luminosity determination using Z boson production at the CMS experiment," CMS-LUM-21-001,CERN-EP-2023-163, Sep. 2023. arXiv: `2309.01008 [hep-ex]`.

[357] A. Babaev, T. Barklow, O. Karacheban, W. Kozanecki, I. Kralik, A. Mehta, G. Pásztor, T. Pieloni, D. Stickland, C. Tambasco, R. Tomas, and J. Wańczyk, "Impact of beam-beam effects on absolute luminosity calibrations at the cern large hadron collider," Jun. 2023, Accepted by *Eur. Phys. J. C* on 26 Oct 2023. arXiv: `2306.10394 [physics.acc-ph]`.

[358] S. van der Meer, "Calibration of the effective beam height in the ISR," CERN, CERN-ISR-PO-68-31, 1968. `https://cds.cern.ch/record/296752`.

[359] C. Rubbia, "Measurement of the luminosity of $p\bar{p}$ collider with a (generalized) van der Meer method," CERN, CERN $p\bar{p}$ Note 38, 1977. `https://cds.cern.ch/record/1025746`.

[360] R. Aaij *et al.*, "Precision luminosity measurements at LHCb," *JINST*, vol. 9, P12005, 2014. DOI: `10.1088/1748-0221/9/12/P12005`. arXiv: `1410.0149 [hep-ex]`.

[361] ATLAS Collaboration, "Luminosity determination in pp collisions at $\sqrt{s} = 13$ TeV using the ATLAS detector at the LHC," CERN-EP-2022-281, Dec. 2022. arXiv: `2212.09379 [hep-ex]`.

[362] D. Belohrad, L. Jensen, O. Jones, M. Ludwig, and J. Savioz, "The LHC fast BCT system: A comparison of design parameters with initial performance," CERN, CERN-BE-2010-010, 2010. `https://cds.cern.ch/record/1267400`.

[363] D. Belohrad, D. Esperante Pereira, J. Kral, and S. Pedersen, "Upgrade of the LHC bunch by bunch intensity measurement acquisition system," in *Proceedings, 5th International Beam Instrumentation Conference (IBIC 2016), Barcelona, Spain, September 11–15, 2016*, 2017, MOPG39. DOI: `10.18429/JACoW-IBIC2016-MOPG39`.

[364] M. Krupa and M. Gasior, "The Wall Current Transformer - a new sensor for precise bunch-by-bunch intensity measurements in the LHC," in *Proceedings, 5th International Beam Instrumentation Conference (IBIC 2016), Barcelona, Spain, September 11–15, 2016*, 2017, WEAL02. DOI: `10.18429/JACoW-IBIC2016-WEAL02`.

[365] C. Barschel, M. Ferro-Luzzi, J.-J. Gras, M. Ludwig, P. Odier, and S. Thoulet, "Results of the LHC DCCT calibration studies," CERN, CERN-ATS-Note-2012-026 PERF, 2012. `https://cds.cern.ch/record/1425904`.

[366] G. Papotti, T. Bohl, F. Follin, and U. Wehrle, "Longitudinal beam measurements at the LHC: The LHC Beam Quality Monitor," in *Proceedings, 2nd International Particle Accelerator Conference (IPAC 2011)*, 2011, 1852 (TUPZ022). `https://cds.cern.ch/record/1399087`.

[367] A. Jeff *et al.*, "Longitudinal density monitor for the LHC," *Phys. Rev. ST Accel. Beams*, vol. 15, p. 032 803, 2012. DOI: `10.1103/PhysRevSTAB.15.032803`.

[368] A. Jeff, "A longitudinal density monitor for the LHC," CERN-THESIS-2012-240, PhD. dissertation, University of Liverpool, 2012. `https://cds.cern.ch/record/1513180`.

[369] W. Kozanecki, T. Pieloni, and J. Wenninger, "Observation of beam-beam deflections with LHC orbit data," CERN, CERN-ACC-NOTE-2013-0006, 2013. `https://cds.cern.ch/record/1581723`.

[370] M. Bassetti and G. A. Erskine, "Closed expression for the electrical field of a two-dimensional Gaussian charge," CERN, CERN-ISR-TH-80-06, 1980. `https://cds.cern.ch/record/122227`.

[371] A. Babaev, "Coherent deflection of elliptic bunches colliding at crossing angle," Apr. 2021, Submitted to *Eur. Phys. J. C.* arXiv: `2104.02595 [physics.acc-ph]`.

[372] V. Balagura, "Van der Meer scan luminosity measurement and beam-beam correction," *Eur. Phys. J. C*, vol. 81, p. 26, 2021. DOI: `10.1140/epjc/s10052-021-08837-y`. eprint: `2012.07752` (hep-ex).

[373] W. Herr, "Beam-beam effects and dynamic β^*," in *Proceedings of the LHC Lumi Days*, 2012. `https://indico.cern.ch/event/162948/contributions/1417430`.

[374] CERN BE/ABP Accelerator Beam Physics Group, "Mad - methodical accelerator design," Jan. 2022. `https://madx.web.cern.ch/madx`.

[375] CERN Accelerators and Beam Physics Computing Working Group (ABP-CWG), "Combi (coherent multibunch beam-beam interactions)," Oct. 2019. `https://twiki.cern.ch/twiki/bin/view/ABPComputing/COMBI`.

[376] R. Alemany-Fernández *et al.*, "Cross-calibration of the LHC transverse beam-profile monitors," in *Proceedings of the 8th International Particle Accelerator Conference (IPAC2017)*, 2017, 437 (MOPAB130). DOI: `10.18429/JACoW-IPAC2017-MOPAB130`.

[377] T. Persson *et al.*, "LHC optics corrections in Run 2," in *Proceedings, 9th Evian Workshop on LHC beam operation*, 2019, p. 59. `https://cds.cern.ch/record/2750277`.

[378] S. M. White, "Determination of the absolute luminosity at the lhc," CERN-THESIS-2010-139, LAL-10-154, PhD. dissertation, Université Paris-Sud 11, 2010. `https://cdsweb.cern.ch/record/1308187`.

[379] M. Gasior, G. Baud, J. Olexa, and G. Valentino, "First operational experience with the LHC Diode ORbit and OScillation (DOROS) system," in *Proceedings of the 5th International Beam Instrumentation Conference (IBIC 2016)*, 2017, 43 (MOPG07). DOI: `10.18429/JACoW-IBIC2016-MOPG07`.

[380] M. Gasior, J. Olexa, and R. Steinhagen, "BPM electronics based on compensated diode detectors—results from development systems," in *Proceedings of the 2012 Beam Instrumentation Workshop (BIW'12)*, [Conf. Proc. **C1204151** (2012) MOPG010], 2012, 44 (MOPG010). `https://cds.cern.ch/record/1476070`.

[381] J. Olexa, "Design and optimization of the beam orbit and oscillation measurement system for the Large Hadron Collider," CERN-THESIS-2018-185, PhD. dissertation, Slovak University of Technology, 2018. `http://cds.cern.ch/record/2642370`.

[382] A. Chmielinska, L. Fiscarelli, E. Todesco, and W. Kozanecki, "Magnetic measurements of MCBC and MCBY orbit correctors under special cycling conditions," ERN-ACC-NOTE-2022-0013, 2022. `https://cds.cern.ch/record/2806949`.

[383] A. Chmielińska, L. Fiscarelli, M. Hostettler, W. Kozanecki, S. Russenschuck, and E. Todesco, "Magnetization in superconducting corrector magnets and impact on luminosity-calibration scans in the Large Hadron Collider," *Eur. Phys. J. Plus*, vol. 138, no. 9, p. 796, 2023. DOI: `10.1140/epjc/s10052-023-11713-6`. arXiv: `2304.06559 [physics.acc-ph]`.

[384] D. Gamba, “Conceptual specifications for the HL-LHC BPMs,” CERN, 2021. `https://edms.cern.ch/file/2387369`.

[385] H. Bartosik and G. Rumolo, “Production of the single bunch for van der Meer scans in the LHC injector chain,” CERN, CERN-ACC-NOTE-2013-0008, 2013. `https://cds.cern.ch/record/1590405`.

[386] M. Klute, C. Medlock, and J. Salfeld-Nebgen, “Beam imaging and luminosity calibration,” *JINST*, vol. 12, P03018, 2017. DOI: `10.1088/1748-0221/12/03/P03018`. arXiv: `1603.03566 [hep-ex]`.

[387] J. Knolle, “Measuring luminosity and the $\mathrm{t\bar{t}}Z$ production cross section with the CMS experiment,” CERN-THESIS-2020-185, DESY-THESIS-2020-020, PhD. dissertation, Universität Hamburg, 2020. DOI: `10.3204/PUBDB-2020-03187`.

[388] P. Major, “Studies of the factorisation of proton densities in van der Meer scans and its impact on precision luminosity measurements for CMS,” *PoS*, vol. EPS-HEP2019, p. 199, 2020. DOI: `10.22323/1.364.0199`.

[389] S. N. Webb, “Factorisation of beams in van der Meer scans and measurements of the ϕ^*_η distribution of $Z \to e^+e^-$ events in pp collisions at $\sqrt{s} = 8$ TeV with the ATLAS detector,” PhD. dissertation, University of Manchester, 2015. `https://cds.cern.ch/record/2020875`.

[390] CMS Collaboration, “CMS luminosity measurement using nucleus-nucleus collisions in run 2,” CERN, CMS-DP-2021-002,CERN-CMS-DP-2021-002, 2021. `https://cds.cern.ch/record/2751564`.

[391] V. Balagura, “Non factorization at lhcb: Two-dimensional vdm scans,” Jun. 2019, LHC Lumi Days 2019, CERN. `https://indico.cern.ch/event/813285/contributions/3406097`.

[392] A. Dabrowski, “Upgrade of the CMS instrumentation for luminosity and machine induced background measurements,” *Nucl. Part. Phys. Proc.*, vol. 273-275, p. 1147, 2016. DOI: `10.1016/j.nuclphysbps.2015.09.180`.

[393] M. Guthoff, “Instrumentation for beam radiation and luminosity measurement in the CMS experiment using novel detector technologies,” *Nucl. Instrum. Meth. A*, vol. 845, p. 565, 2017. DOI: `10.1016/j.nima.2016.06.028`.

[394] E. Ayala *et al.* [incl. G. Pásztor], “The Pixel Luminosity Telescope: a detector for luminosity measurement at CMS using silicon pixel sensors,” *Eur. Phys. J. C*, vol. 83, no. 7, p. 673, 2023. DOI: `10.1140/epjc/s10052-023-11713-6`. arXiv: `2206.08870 [physics.ins-det]`.

[395] CMS Collaboration [incl. G. Pásztor], “The Pixel Luminosity Telescope: A detector for luminosity measurements at CMS using silicon pixel sensors,” CMS-DP-2021-020, Jul. 2021. `https://cds.cern.ch/record/2781753`.

[396] J. MacQueen, “Some methods for classification and analysis of multivariate observations,” in *Proceedings of the fifth Berkeley symposium on mathematical statistics and probability*, Oakland, CA, USA, vol. 1, 1967, pp. 281–297.

[397] G. Battistoni *et al.*, “Overview of the FLUKA code,” *Ann. Nucl. Energy*, vol. 82, p. 10, 2015. DOI: `10.1016/j.anucene.2014.11.007`.

[398] T. T. Böhlen *et al.*, “The FLUKA code: Developments and challenges for high energy and medical applications,” *Nucl. Data Sheets*, vol. 120, p. 211, 2014. DOI: `10.1016/j.nds.2014.07.049`.

[399] M. Guthoff, "The new Fast Beam Condition Monitor using poly-crystalline diamond sensors for luminosity measurement at CMS," *Nucl. Instrum. Meth. A*, vol. 936, p. 717, 2019. DOI: `10.1016/j.nima.2018.11.071`.

[400] J. L. Leonard *et al.*, "Fast beam condition monitor for CMS: Performance and upgrade," *Nucl. Instrum. Meth. A*, vol. 765, p. 235, 2014. DOI: `10.1016/j.nima.2014.05.008`. arXiv: `1405.1926 [physics.ins-det]`.

[401] M. Hempel, "Development of a novel diamond based detector for machine induced background and luminosity measurements," PhD. dissertation, DESY, 2017. DOI: `10.3204/PUBDB-2017-06875`. `http://inspirehep.net/record/1611774/files/PhD_Thesis_v2.pdf`.

[402] M. Hostettler, K. Fuchsberger, G. Papotti, Y. Papaphilippou, and T. Pieloni, "Luminosity scans for beam diagnostics," *Phys. Rev. Accel. Beams*, vol. 21, p. 102 801, 2018. DOI: `10.1103/PhysRevAccelBeams.21.102801`. arXiv: `1804.10099 [physics.acc-ph]`.

[403] O. Karacheban and P. Tsrunchev, "Emittance scans for CMS luminosity calibration," *EPJ Web Conf.*, vol. 201, p. 04 001, 2019. DOI: `10.1051/epjconf/201920104001`.

[404] O. Karacheban, "Long-term monitoring of delivered luminosity & calibration stability in CMS," Jun. 2019, LHC Lumi Days 2019, CERN. `https://indico.cern.ch/event/813285/contributions/3406108`.

[405] CMS Collaboration, "Long-term monitoring of delivered luminosity & calibration stability in CMS," CERN, CMS-DP-2019-016,CERN-CMS-DP-2019-016, 2019. `https://cds.cern.ch/record/2681803`.

[406] A. Babaev, "Relative nonlinearity of BRIL luminometers derived from CMS μ scans," *PoS*, vol. LHCP2019, P. Roig Garcés, I. Bautista Guzman, A. Fernández Téllez, and M. I. Martínez Hernández, Eds., p. 042, 2019. DOI: `10.22323/1.350.0042`.

[407] J. Salfeld-Nebgen and D. Marlow, "Data-driven precision luminosity measurements with Z bosons at the LHC and HL-LHC," *JINST*, vol. 13, P12016, 2018. DOI: `10.1088/1748-0221/13/12/P12016`. arXiv: `1806.02184 [hep-ex]`.

[408] ATLAS Collaboration, "Luminosity Determination using $Z \to \ell\ell$ events at $\sqrt{s} =$ 13 TeV with the ATLAS detector," CERN, ATL-DAPR-PUB-2021-001, Feb. 2021. `http://cds.cern.ch/record/2752951`.

[409] A. M. Sirunyan *et al.*, "Performance of the CMS muon detector and muon reconstruction with proton-proton collisions at $\sqrt{s} = 13$ TeV," *JINST*, vol. 13, P06015, 2018. DOI: `10.1088/1748-0221/13/06/P06015`. arXiv: `1804.04528 [physics.ins-det]`.

[410] R. Hall-Wilton *et al.*, "Results from a beam test of a prototype PLT diamond pixel telescope," *Nucl. Instrum. Meth. A*, vol. 636, S130, 2011. DOI: `10.1016/j.nima.2010.04.097`.

[411] P. Lujan, "Performance of the Pixel Luminosity Telescope for luminosity measurement at CMS during Run 2," *PoS*, vol. 314, p. 504, 2017. DOI: `10.22323/1.314.0504`.

[412] CMS Collaboration, "The Phase-2 upgrade of the CMS tracker," CERN, CERN-LHCC-2017-009,CMS-TDR-014, 2017. `https://cds.cern.ch/record/2272264`.

[413] CMS Collaboration, “The Phase-2 upgrade of the CMS level-1 trigger,” CERN, CERN-LHCC-2020-004,CMS-TDR-021, 2020. `http://cds.cern.ch/record/2714892`.

[414] G. Pásztor, “The Phase-2 Upgrade of the CMS Detector,” *PoS*, vol. LHCP2022, p. 045, 2023. DOI: `10.22323/1.422.0045`.

[415] G. Pásztor, “Precision luminosity measurement with the CMS detector at HL-LHC,” *PoS*, vol. ICHEP2020, p. 864, 2021. DOI: `10.22323/1.390.0864`.

[416] A. Tumasyan *et al.*, “A portrait of the Higgs boson by the CMS experiment ten years after the discovery,” *Nature*, vol. 607, no. 7917, pp. 60–68, 2022. DOI: `10.1038/s41586-022-04892-x`. arXiv: `2207.00043 [hep-ex]`.

[417] G. Aad *et al.*, “A detailed map of Higgs boson interactions by the ATLAS experiment ten years after the discovery,” *Nature*, vol. 607, no. 7917, pp. 52–59, 2022, [Erratum: Nature 612, E24 (2022)]. DOI: `10.1038/s41586-022-04893-w`. arXiv: `2207.00092 [hep-ex]`.

[418] G. P. Salam, L.-T. Wang, and G. Zanderighi, “The Higgs boson turns ten,” *Nature*, vol. 607, no. 7917, pp. 41–47, 2022. DOI: `10.1038/s41586-022-04899-4`. arXiv: `2207.00478 [hep-ph]`.

[419] ATLAS Collaboration [incl. G. Pásztor], “Expected electron performance in the ATLAS experiment,” CERN, ATL-PHYS-PUB-2011-006, Apr. 2011. `http://cdsweb.cern.ch/record/1345327`.

[420] A. D. Martin, W. J. Stirling, R. S. Thorne, and G. Watt, “Parton distributions for the lhc,” *The European Physical Journal C*, vol. 63, no. 2, pp. 189–285, Jul. 2009, ISSN: 1434-6052. DOI: `10.1140/epjc/s10052-009-1072-5`.

[421] J. Beringer *et al.*, “Review of particle physics,” *Phys. Rev. D*, vol. 86, p. 010 001, 1 Jul. 2012. DOI: `10.1103/PhysRevD.86.010001`.

[422] J. Stirling, “Parton luminosity and cross section plots,” downloaded in Oct. 2020. `http://www.hep.ph.ic.ac.uk/~wstirlin/plots/plots.html`.

[423] C. Albajar *et al.*, “Beauty production at the CERN p anti-p collider,” *Phys. Lett. B*, vol. 256, pp. 121–128, 1991, [Erratum: Phys.Lett.B 262, 497 (1991)]. DOI: `10.1016/0370-2693(91)90228-I`.

[424] F. Abe *et al.*, “Measurement of the bottom quark production cross-section using semileptonic decay electrons in $p\bar{p}$ collisions at $\sqrt{s} = 1.8$ TeV,” *Phys. Rev. Lett.*, vol. 71, pp. 500–504, 1993. DOI: `10.1103/PhysRevLett.71.500`.

[425] F. Abe *et al.*, “Measurement of bottom quark production in 1.8 TeV $p\bar{p}$ collisions using semileptonic decay muons,” *Phys. Rev. Lett.*, vol. 71, pp. 2396–2400, 1993. DOI: `10.1103/PhysRevLett.71.2396`.

[426] B. Abbott *et al.*, “The $b\bar{b}$ production cross section and angular correlations in $p\bar{p}$ collisions at $\sqrt{s} = 1.8$ TeV,” *Phys. Lett. B*, vol. 487, pp. 264–272, 2000. DOI: `10.1016/S0370-2693(00)00844-3`. arXiv: `hep-ex/9905024`.

[427] M. Cacciari and P. Nason, “Is there a significant excess in bottom hadroproduction at the Tevatron?” *Phys. Rev. Lett.*, vol. 89, p. 122 003, 2002. DOI: `10.1103/PhysRevLett.89.122003`. arXiv: `hep-ph/0204025`.

[428] D. Acosta *et al.*, “Measurement of the J/ψ meson and $b-$hadron production cross sections in $p\bar{p}$ collisions at $\sqrt{s} = 1960$ GeV,” *Phys. Rev. D*, vol. 71, p. 032 001, 2005. DOI: `10.1103/PhysRevD.71.032001`. arXiv: `hep-ex/0412071`.

[429] M. Cacciari, S. Frixione, M. L. Mangano, P. Nason, and G. Ridolfi, "QCD analysis of first b cross-section data at 1.96-TeV," *JHEP*, vol. 07, p. 033, 2004. DOI: `10.1088/1126-6708/2004/07/033`. arXiv: `hep-ph/0312132`.

[430] M. L. Mangano, "The Saga of bottom production in $p\bar{p}$ collisions," *AIP Conf. Proc.*, vol. 753, no. 1, H. Weerts, Ed., pp. 247–260, 2005. DOI: `10.1063/1.1896706`. arXiv: `hep-ph/0411020`.

[431] M. Cacciari, S. Frixione, N. Houdeau, M. L. Mangano, P. Nason, and G. Ridolfi, "Theoretical predictions for charm and bottom production at the LHC," *JHEP*, vol. 10, p. 137, 2012. DOI: `10.1007/JHEP10(2012)137`. arXiv: `1205.6344 [hep-ph]`.

[432] ATLAS Collaboration, "ATLAS Monte Carlo tunes for MC09," CERN, ATL-PHYS-PUB-2010-002, Mar. 2010. `http://cds.cern.ch/record/1247375`.

[433] T. Sjostrand, S. Mrenna, and P. Z. Skands, "PYTHIA 6.4 Physics and Manual," *JHEP*, vol. 05, p. 026, 2006. DOI: `10.1088/1126-6708/2006/05/026`. arXiv: `hep-ph/0603175`.

[434] A. Sherstnev and R. S. Thorne, "Parton Distributions for LO Generators," *Eur. Phys. J. C*, vol. 55, pp. 553–575, 2008. DOI: `10.1140/epjc/s10052-008-0610-x`. arXiv: `0711.2473 [hep-ph]`.

[435] S. Frixione, P. Nason, and C. Oleari, "Matching NLO QCD computations with Parton Shower simulations: the POWHEG method," *JHEP*, vol. 11, p. 070, 2007. DOI: `10.1088/1126-6708/2007/11/070`. arXiv: `0709.2092 [hep-ph]`.

[436] J. Pumplin, D. R. Stump, J. Huston, H. L. Lai, P. M. Nadolsky, and W. K. Tung, "New generation of parton distributions with uncertainties from global QCD analysis," *JHEP*, vol. 07, p. 012, 2002. DOI: `10.1088/1126-6708/2002/07/012`. arXiv: `hep-ph/0201195`.

[437] G. Corcella, I. G. Knowles, G. Marchesini, S. Moretti, K. Odagiri, P. Richardson, M. H. Seymour, and B. R. Webber, "HERWIG 6: An Event generator for hadron emission reactions with interfering gluons (including supersymmetric processes)," *JHEP*, vol. 01, p. 010, 2001. DOI: `10.1088/1126-6708/2001/01/010`. arXiv: `hep-ph/0011363`.

[438] ATLAS Collaboration, "Updated Luminosity Determination in pp Collisions at root(s)=7 TeV using the ATLAS Detector," CERN, ATLAS-CONF-2011-011, Mar. 2011. `http://cds.cern.ch/record/1334563`.

[439] C. Anastasiou, L. J. Dixon, K. Melnikov, and F. Petriello, "High precision QCD at hadron colliders: Electroweak gauge boson rapidity distributions at NNLO," *Phys. Rev. D*, vol. 69, p. 094 008, 2004. DOI: `10.1103/PhysRevD.69.094008`. arXiv: `hep-ph/0312266`.

[440] ATLAS Collaboration, "Electron and photon reconstruction and identification in ATLAS: expected performance at high energy and results at 900 GeV," ATLAS-CONF-2010-005, Jun. 2010. `https://cds.cern.ch/record/1273197`.

[441] ATLAS Collaboration, "Measurements of the electron and muon inclusive cross-sections in proton-proton collisions at $\sqrt{s} = 7$ TeV with the ATLAS detector - supplemental material," downloaded in Jan. 2022. `https://atlas.web.cern.ch/Atlas/GROUPS/PHYSICS/PAPERS/STDM-2010-02`.

[442] ATLAS Collaboration, "Background Estimation for Inclusive SUSY Searches - The Tiles Method," ATL-PHYS-PUB-2009-077,ATL-COM-PHYS-2009-250, May 2009. `https://cds.cern.ch/record/1177160`.

[443] G. Aad *et al.* [incl. G. Pásztor], “Measurements of the electron and muon inclusive cross-sections in proton-proton collisions at $\sqrt{s} = 7$ TeV with the ATLAS detector,” *Phys. Lett. B*, vol. 707, pp. 438–458, 2012. DOI: `10.1016/j.physletb.2011.12.054`. arXiv: `1109.0525 [hep-ex]`.

[444] T. Adye, “Unfolding algorithms and tests using RooUnfold,” in *PHYSTAT 2011*, Code webpage: https://hepunx.rl.ac.uk/ adye/software/unfold/RooUnfold.html, CERN, 2011, pp. 313–318. DOI: `10.5170/CERN-2011-006.313`. arXiv: `1105.1160 [physics.data-an]`.

[445] A. Hocker and V. Kartvelishvili, “SVD approach to data unfolding,” *Nucl. Instrum. Meth. A*, vol. 372, pp. 469–481, 1996. DOI: `10.1016/0168-9002(95)01478-0`. arXiv: `hep-ph/9509307`.

[446] G. D’Agostini, “A Multidimensional unfolding method based on Bayes’ theorem,” *Nucl. Instrum. Meth. A*, vol. 362, pp. 487–498, 1995. DOI: `10.1016/0168-9002(95)00274-X`.

[447] P. M. Nadolsky, H.-L. Lai, Q.-H. Cao, J. Huston, J. Pumplin, D. Stump, W.-K. Tung, and C. .-P. Yuan, “Implications of CTEQ global analysis for collider observables,” *Phys. Rev. D*, vol. 78, p. 013 004, 2008. DOI: `10.1103/PhysRevD.78.013004`. arXiv: `0802.0007 [hep-ph]`.

[448] H.-L. Lai, J. Huston, Z. Li, P. Nadolsky, J. Pumplin, D. Stump, and C. .-P. Yuan, “Uncertainty induced by QCD coupling in the CTEQ global analysis of parton distributions,” *Phys. Rev. D*, vol. 82, p. 054 021, 2010. DOI: `10.1103/PhysRevD.82.054021`. arXiv: `1004.4624 [hep-ph]`.

[449] F. D. Aaron *et al.*, “Combined Measurement and QCD Analysis of the Inclusive $e^{\pm}p$ Scattering Cross Sections at HERA,” *JHEP*, vol. 01, p. 109, 2010. DOI: `10.1007/JHEP01(2010)109`. arXiv: `0911.0884 [hep-ex]`.

[450] R. D. Ball, V. Bertone, F. Cerutti, L. Del Debbio, S. Forte, A. Guffanti, J. I. Latorre, J. Rojo, and M. Ubiali, “Impact of Heavy Quark Masses on Parton Distributions and LHC Phenomenology,” *Nucl. Phys. B*, vol. 849, pp. 296–363, 2011. DOI: `10.1016/j.nuclphysb.2011.03.021`. arXiv: `1101.1300 [hep-ph]`.

[451] M. Cacciari, P. Nason, and C. Oleari, “A Study of heavy flavored meson fragmentation functions in e^+e^- annihilation,” *JHEP*, vol. 04, p. 006, 2006. DOI: `10.1088/1126-6708/2006/04/006`. arXiv: `hep-ph/0510032`.

[452] D. J. Lange, “The EvtGen particle decay simulation package,” *Nucl. Instrum. Meth. A*, vol. 462, S. Erhan, P. Schlein, and Y. Rozen, Eds., pp. 152–155, 2001. DOI: `10.1016/S0168-9002(01)00089-4`.

[453] D. de Florian *et al.*, “Handbook of LHC Higgs Cross Sections: 4. Deciphering the Nature of the Higgs Sector,” vol. 2/2017, Oct. 2016. DOI: `10.23731/CYRM-2017-002`. arXiv: `1610.07922 [hep-ph]`.

[454] T. Liu, K. Melnikov, and A. A. Penin, “Nonfactorizable QCD Effects in Higgs Boson Production via Vector Boson Fusion,” *Phys. Rev. Lett.*, vol. 123, no. 12, p. 122 002, 2019. DOI: `10.1103/PhysRevLett.123.122002`. arXiv: `1906.10899 [hep-ph]`.

[455] M. Czakon, R. V. Harlander, J. Klappert, and M. Niggetiedt, “Exact Top-Quark Mass Dependence in Hadronic Higgs Production,” *Phys. Rev. Lett.*, vol. 127, no. 16, p. 162 002, 2021. DOI: `10.1103/PhysRevLett.127.162002`. arXiv: `2105.04436 [hep-ph]`.

[456] M. Becchetti, R. Bonciani, V. Del Duca, V. Hirschi, F. Moriello, and A. Schweitzer, "Next-to-leading order corrections to light-quark mixed QCD-EW contributions to Higgs boson production," *Phys. Rev. D*, vol. 103, no. 5, p. 054 037, 2021. DOI: `10.1103/PhysRevD.103.054037`. arXiv: `2010.09451 [hep-ph]`.

[457] K. Asteriadis, F. Caola, K. Melnikov, and R. Röntsch, "NNLO QCD corrections to weak boson fusion Higgs boson production in the $H \to b\bar{b}$ and $H \to WW^* \to 4l$ decay channels," OUTP-21-23P,TTP21-032,P3H-21-066,CERN-TH-2021-146,TIF-UNIMI-2021-15, Oct. 2021. arXiv: `2110.02818 [hep-ph]`.

[458] A. Behring, W. Bizoń, F. Caola, K. Melnikov, and R. Röntsch, "Bottom quark mass effects in associated WH production with the $H \to b\bar{b}$ decay through NNLO QCD," *Phys. Rev. D*, vol. 101, no. 11, p. 114 012, 2020. DOI: `10.1103/PhysRevD.101.114012`. arXiv: `2003.08321 [hep-ph]`.

[459] X. Chen, T. Gehrmann, E. W. N. Glover, A. Huss, B. Mistlberger, and A. Pelloni, "Fully Differential Higgs Boson Production to Third Order in QCD," *Phys. Rev. Lett.*, vol. 127, no. 7, p. 072 002, 2021. DOI: `10.1103/PhysRevLett.127.072002`. arXiv: `2102.07607 [hep-ph]`.

[460] G. Aad *et al.*, "Measurement of the transverse momentum distribution of Drell–Yan lepton pairs in proton–proton collisions at $\sqrt{s} = 13$ TeV with the ATLAS detector," *Eur. Phys. J. C*, vol. 80, no. 7, p. 616, 2020. DOI: `10.1140/epjc/s10052-020-8001-z`. arXiv: `1912.02844 [hep-ex]`.

[461] The TEVNPH Working Group, "Combined CDF and D0 Upper Limits on Standard Model Higgs-Boson Production with up to 6.7 fb^{-1} of Data," FERMILAB-CONF-10-257-E,CDF-NOTE-10241,D0-NOTE-6096, Jul. 2010. arXiv: `1007.4587 [hep-ex]`.

[462] J. R. Andersen *et al.*, "Handbook of LHC Higgs Cross Sections: 3. Higgs Properties," S. Heinemeyer, C. Mariotti, G. Passarino, and R. Tanaka, Eds., Jul. 2013. DOI: `10.5170/CERN-2013-004`. arXiv: `1307.1347 [hep-ph]`.

[463] S. Dittmaier *et al.*, "Handbook of LHC Higgs Cross Sections: 2. Differential Distributions," Jan. 2012. DOI: `10.5170/CERN-2012-002`. arXiv: `1201.3084 [hep-ph]`.

[464] A. M. Sirunyan *et al.*, "Observation of Higgs boson decay to bottom quarks," *Phys. Rev. Lett.*, vol. 121, no. 12, p. 121 801, 2018. DOI: `10.1103/PhysRevLett.121.121801`. arXiv: `1808.08242 [hep-ex]`.

[465] M. Aaboud *et al.*, "Observation of $H \to b\bar{b}$ decays and VH production with the ATLAS detector," *Phys. Lett. B*, vol. 786, pp. 59–86, 2018. DOI: `10.1016/j.physletb.2018.09.013`. arXiv: `1808.08238 [hep-ex]`.

[466] G. Aad *et al.* [incl. G. Pásztor], "Search for the Higgs boson in the $\mathrm{H} \to \mathrm{WW}^{(*)} \to \ell\nu\ell\nu$ decay channel in pp collisions at $\sqrt{s} = 7$ TeV with the ATLAS detector," *Phys. Rev. Lett.*, vol. 108, p. 111 802, 2012. DOI: `10.1103/PhysRevLett.108.111802`. arXiv: `1112.2577 [hep-ex]`.

[467] A. M. Sirunyan *et al.*, "Observation of the Higgs boson decay to a pair of τ leptons with the CMS detector," *Phys. Lett. B*, vol. 779, pp. 283–316, 2018. DOI: `10.1016/j.physletb.2018.02.004`. arXiv: `1708.00373 [hep-ex]`.

[468] M. Aaboud *et al.*, "Cross-section measurements of the Higgs boson decaying into a pair of τ-leptons in proton-proton collisions at $\sqrt{s} = 13$ TeV with the ATLAS detector," *Phys. Rev. D*, vol. 99, p. 072 001, 2019. DOI: `10.1103/PhysRevD.99.072001`. arXiv: `1811.08856 [hep-ex]`.

[469] A. Tumasyan *et al.*, "Search for Higgs Boson Decay to a Charm Quark-Antiquark Pair in Proton-Proton Collisions at s=13 TeV," *Phys. Rev. Lett.*, vol. 131, no. 6, p. 061 801, 2023. DOI: `10.1103/PhysRevLett.131.061801`. arXiv: `2205.05550 [hep-ex]`.

[470] G. Aad *et al.*, "Direct constraint on the Higgs-charm coupling from a search for Higgs boson decays into charm quarks with the ATLAS detector," *Eur. Phys. J. C*, vol. 82, p. 717, 2022. DOI: `10.1140/epjc/s10052-022-10588-3`. arXiv: `2201.11428 [hep-ex]`.

[471] G. Aad *et al.* [incl. G. Pásztor], "Measurements of Higgs boson production and couplings in the four-lepton channel in pp collisions at center-of-mass energies of 7 and 8 TeV with the ATLAS detector," *Phys. Rev. D*, vol. 91, no. 1, p. 012 006, 2015. DOI: `10.1103/PhysRevD.91.012006`. arXiv: `1408.5191 [hep-ex]`.

[472] G. Aad *et al.*, "Measurement of Higgs boson production in the diphoton decay channel in pp collisions at center-of-mass energies of 7 and 8 TeV with the ATLAS detector," *Phys. Rev. D*, vol. 90, no. 11, p. 112 015, 2014. DOI: `10.1103/PhysRevD.90.112015`. arXiv: `1408.7084 [hep-ex]`.

[473] Y. Chen, A. Falkowski, I. Low, and R. Vega-Morales, "New Observables for CP Violation in Higgs Decays," *Phys. Rev. D*, vol. 90, no. 11, p. 113 006, 2014. DOI: `10.1103/PhysRevD.90.113006`. arXiv: `1405.6723 [hep-ph]`.

[474] G. Aad *et al.* [incl. G. Pásztor], "A particle consistent with the Higgs Boson observed with the ATLAS Detector at the Large Hadron Collider," *Science*, vol. 338, pp. 1576–1582, 2012. DOI: `10.1126/science.1232005`.

[475] G. Aad *et al.*, "Combined search for the Standard Model Higgs boson in *pp* collisions at $\sqrt{s} = 7$ TeV with the ATLAS detector," *Phys. Rev. D*, vol. 86, p. 032 003, 2012. DOI: `10.1103/PhysRevD.86.032003`. arXiv: `1207.0319 [hep-ex]`.

[476] A. L. Read, "Presentation of search results: The CL_s technique," *J. Phys. G*, vol. 28, M. R. Whalley and L. Lyons, Eds., pp. 2693–2704, 2002. DOI: `10.1088/0954-3899/28/10/313`.

[477] E. Gross and O. Vitells, "Trial factors for the look elsewhere effect in high energy physics," *Eur. Phys. J. C*, vol. 70, pp. 525–530, 2010. DOI: `10.1140/epjc/s10052-010-1470-8`. arXiv: `1005.1891 [physics.data-an]`.

[478] G. Aad *et al.* [incl. G. Pásztor], "Search for the Standard Model Higgs boson in the decay channel $\mathrm{H} \rightarrow \mathrm{ZZ}^{(*)} \rightarrow 4\ell$ with 4.8 fb^{-1} of pp collision data at $\sqrt{s} = 7$ TeV with ATLAS," *Phys. Lett. B*, vol. 710, pp. 383–402, 2012. DOI: `10.1016/j.physletb.2012.03.005`. arXiv: `1202.1415 [hep-ex]`.

[479] ATLAS Collaboration [incl. G. Pásztor], "Reconstruction of collinear final-state-radiation photons in Z decays to muons in $\sqrt{s} = 7$ TeV proton-proton collisions.," CERN, ATLAS-CONF-2012-143, 2012. `http://cds.cern.ch/record/1491697`.

[480] M. Cacciari, G. P. Salam, and G. Soyez, "The anti-k_t jet clustering algorithm," *JHEP*, vol. 04, p. 063, 2008. DOI: `10.1088/1126-6708/2008/04/063`. arXiv: `0802.1189 [hep-ph]`.

[481] T. Binoth, N. Kauer, and P. Mertsch, “Gluon-induced QCD corrections to pp $\rightarrow$ ZZ $\rightarrow \ell\bar{\ell}\ell'\bar{\ell}'$,” in *16th International Workshop on Deep Inelastic Scattering and Related Subjects*, Jul. 2008, p. 142. DOI: `10.3360/dis.2008.142`. arXiv: `0807.0024 [hep-ph]`.

[482] M. L. Mangano, M. Moretti, F. Piccinini, R. Pittau, and A. D. Polosa, “ALPGEN, a generator for hard multiparton processes in hadronic collisions,” *JHEP*, vol. 07, p. 001, 2003. DOI: `10.1088/1126-6708/2003/07/001`. arXiv: `hep-ph/0206293`.

[483] G. Aad *et al.*, “Performance of *b*-Jet Identification in the ATLAS Experiment,” *JINST*, vol. 11, no. 04, P04008, 2016. DOI: `10.1088/1748-0221/11/04/P04008`. arXiv: `1512.01094 [hep-ex]`.

[484] ATLAS Collaboration, “Calibration of the performance of *b*-tagging for *c* and light-flavour jets in the 2012 ATLAS data,” ATLAS-CONF-2014-046, Jul. 2014. `https://cds.cern.ch/record/1741020`.

[485] G. Cowan, K. Cranmer, E. Gross, and O. Vitells, “Asymptotic formulae for likelihood-based tests of new physics,” *Eur. Phys. J. C*, vol. 71, p. 1554, 2011, [Erratum: Eur.Phys.J.C 73, 2501 (2013)]. DOI: `10.1140/epjc/s10052-011-1554-0`. arXiv: `1007.1727 [physics.data-an]`.

[486] G. Aad *et al.* [incl. G. Pásztor], “Measurement of the Higgs boson mass from the H $\rightarrow \gamma\gamma$ and H $\rightarrow$ ZZ* $\rightarrow 4\ell$ channels with the ATLAS detector using 25 fb^{-1} of pp collision data,” *Phys. Rev. D*, vol. 90, no. 5, p. 052 004, 2014. DOI: `10.1103/PhysRevD.90.052004`. arXiv: `1406.3827 [hep-ex]`.

[487] I. W. Stewart and F. J. Tackmann, “Theory Uncertainties for Higgs and Other Searches Using Jet Bins,” *Phys. Rev. D*, vol. 85, p. 034 011, 2012. DOI: `10.1103/PhysRevD.85.034011`. arXiv: `1107.2117 [hep-ph]`.

[488] G. Aad *et al.* [incl. G. Pásztor], “Fiducial and differential cross sections of Higgs boson production measured in the four-lepton decay channel in pp collisions at $\sqrt{s} = 8$ TeV with the ATLAS detector,” *Phys. Lett. B*, vol. 738, pp. 234–253, 2014. DOI: `10.1016/j.physletb.2014.09.054`. arXiv: `1408.3226 [hep-ex]`.

[489] G. Aad *et al.*, “Search for Invisible Decays of a Higgs Boson Produced in Association with a Z Boson in ATLAS,” *Phys. Rev. Lett.*, vol. 112, p. 201 802, 2014. DOI: `10.1103/PhysRevLett.112.201802`. arXiv: `1402.3244 [hep-ex]`.

[490] G. Aad *et al.* [incl. G. Pásztor], “Measurements of Higgs boson production and couplings in diboson final states with the ATLAS detector at the LHC,” *Phys. Lett. B*, vol. 726, pp. 88–119, 2013, [Erratum: Phys.Lett.B 734, 406–406 (2014)]. DOI: `10.1016/j.physletb.2014.05.011`. arXiv: `1307.1427 [hep-ex]`.

[491] G. Passarino, “Higgs CAT,” *Eur. Phys. J. C*, vol. 74, p. 2866, 2014. DOI: `10.1140/epjc/s10052-014-2866-7`. arXiv: `1312.2397 [hep-ph]`.

[492] G. Aad *et al.* [incl. G. Pásztor], “Constraints on the off-shell Higgs boson signal strength in the high-mass ZZ and WW final states with the ATLAS detector,” *Eur. Phys. J. C*, vol. 75, no. 7, p. 335, 2015. DOI: `10.1140/epjc/s10052-015-3542-2`. arXiv: `1503.01060 [hep-ex]`.

[493] L. D. Landau, “On the angular momentum of a system of two photons,” *Dokl. Akad. Nauk SSSR*, vol. 60, no. 2, pp. 207–209, 1948. DOI: `10.1016/B978-0-08-010586-4.50070-5`.

[494] C.-N. Yang, “Selection Rules for the Dematerialization of a Particle Into Two Photons,” *Phys. Rev.*, vol. 77, pp. 242–245, 1950. DOI: `10.1103/PhysRev.77.242`.

[495] G. Aad *et al.* [incl. G. Pásztor], “Evidence for the spin-0 nature of the Higgs boson using ATLAS data,” *Phys. Lett. B*, vol. 726, pp. 120–144, 2013. DOI: `10.1016/j.physletb.2013.08.026`. arXiv: `1307.1432 [hep-ex]`.

[496] G. Aad *et al.*, “Study of the spin and parity of the Higgs boson in diboson decays with the ATLAS detector,” *Eur. Phys. J. C*, vol. 75, no. 10, p. 476, 2015, [Erratum: Eur.Phys.J.C 76, 152 (2016)]. DOI: `10.1140/epjc/s10052-015-3685-1`. arXiv: `1506.05669 [hep-ex]`.

[497] P. Artoisenet *et al.*, “A framework for Higgs characterisation,” *JHEP*, vol. 11, p. 043, 2013. DOI: `10.1007/JHEP11(2013)043`. arXiv: `1306.6464 [hep-ph]`.

[498] Y. Gao, A. V. Gritsan, Z. Guo, K. Melnikov, M. Schulze, and N. V. Tran, “Spin Determination of Single-Produced Resonances at Hadron Colliders,” *Phys. Rev. D*, vol. 81, p. 075 022, 2010, [Publishers note: 10.1103/PhysRevD.81.079905.] DOI: `10.1103/PhysRevD.81.075022`. arXiv: `1001.3396 [hep-ph]`.

[499] A. M. Sirunyan *et al.*, “A measurement of the Higgs boson mass in the diphoton decay channel,” *Phys. Lett. B*, vol. 805, p. 135 425, 2020. DOI: `10.1016/j.physletb.2020.135425`. arXiv: `2002.06398 [hep-ex]`.

[500] A. M. Sirunyan *et al.*, “Measurements of properties of the Higgs boson decaying into the four-lepton final state in pp collisions at $\sqrt{s} = 13$ TeV,” *JHEP*, vol. 11, p. 047, 2017. DOI: `10.1007/JHEP11(2017)047`. arXiv: `1706.09936 [hep-ex]`.

[501] ATLAS Collaboration, “Measurement of the Higgs boson mass in the $H \to ZZ^* \to 4\ell$ decay channel with $\sqrt{s} = 13$ TeV *pp* collisions using the ATLAS detector at the LHC,” ATLAS-CONF-2020-005, Apr. 2020. `https://cds.cern.ch/record/2714883`.

[502] M. Aaboud *et al.*, “Measurement of the Higgs boson mass in the H$\to$ ZZ$^* \to 4\ell$ and H $\to \gamma\gamma$ channels with $\sqrt{s} = 13$ TeV pp collisions using the ATLAS detector,” *Phys. Lett. B*, vol. 784, pp. 345–366, 2018. DOI: `10.1016/j.physletb.2018.07.050`. arXiv: `1806.00242 [hep-ex]`.

[503] G. Aad *et al.*, “Measurement of the Higgs boson mass in the $H \to ZZ^* \to 4\ell$ decay channel using 139 fb^{-1} of $\sqrt{s} = 13$ TeV *pp* collisions recorded by the ATLAS detector at the LHC,” *Phys. Lett. B*, vol. 843, p. 137 880, 2023. DOI: `10.1016/j.physletb.2023.137880`. arXiv: `2207.00320 [hep-ex]`.

[504] G. Aad *et al.*, “Measurement of the Higgs boson mass with $H \to \gamma\gamma$ decays in 140 fb^{-1} of $\sqrt{s} = 13$ TeV *pp* collisions with the ATLAS detector,” CERN-EP-2023-160, Aug. 2023. arXiv: `2308.07216 [hep-ex]`.

[505] A. Tumasyan *et al.*, “Measurement of the Higgs boson width and evidence of its off-shell contributions to ZZ production,” *Nature Phys.*, vol. 18, no. 11, pp. 1329–1334, 2022. DOI: `10.1038/s41567-022-01682-0`. arXiv: `2202.06923 [hep-ex]`.

[506] A. M. Sirunyan *et al.*, “Measurements of the Higgs boson width and anomalous HVV couplings from on-shell and off-shell production in the four-lepton final state,” *Phys. Rev. D*, vol. 99, no. 11, p. 112 003, 2019. DOI: `10.1103/PhysRevD.99.112003`. arXiv: `1901.00174 [hep-ex]`.

[507] M. Aaboud *et al.*, “Constraints on off-shell Higgs boson production and the Higgs boson total width in $ZZ \to 4\ell$ and $ZZ \to 2\ell 2\nu$ final states with the ATLAS detector,” *Phys. Lett. B*, vol. 786, pp. 223–244, 2018. DOI: `10.1016/j.physletb.2018.09.048`. arXiv: `1808.01191 [hep-ex]`.

[508] V. Khachatryan *et al.*, "Limits on the Higgs boson lifetime and width from its decay to four charged leptons," *Phys. Rev. D*, vol. 92, no. 7, p. 072 010, 2015. DOI: `10.1103/PhysRevD.92.072010`. arXiv: `1507.06656 [hep-ex]`.

[509] A. M. Sirunyan *et al.*, "Observation of t$\bar{t}$H production," *Phys. Rev. Lett.*, vol. 120, no. 23, p. 231 801, 2018. DOI: `10.1103/PhysRevLett.120.231801`. arXiv: `1804.02610 [hep-ex]`.

[510] M. Aaboud *et al.*, "Observation of Higgs boson production in association with a top quark pair at the LHC with the ATLAS detector," *Phys. Lett. B*, vol. 784, pp. 173–191, 2018. DOI: `10.1016/j.physletb.2018.07.035`. arXiv: `1806.00425 [hep-ex]`.

[511] G. Aad *et al.* [incl. G. Pásztor], "Observation of top-quark pair production in association with a photon and measurement of the $t\bar{t}\gamma$ production cross section in pp collisions at $\sqrt{s} = 7$ TeV using the ATLAS detector," *Phys. Rev. D*, vol. 91, no. 7, p. 072 007, 2015. DOI: `10.1103/PhysRevD.91.072007`. arXiv: `1502.00586 [hep-ex]`.

[512] ATLAS Collaboration [incl. G. Pásztor], "Search for $t\bar{t}Z$ production in the three lepton final state with 4.7 fb^{-1} of $\sqrt{s} = 7$ TeV *pp* collision data collected by the ATLAS detector," ATLAS-CONF-2012-126, Aug. 2012. `https://cds.cern.ch/record/1474643`.

[513] G. Aad *et al.*, "Measurement of the $t\bar{t}W$ and $t\bar{t}Z$ production cross sections in pp collisions at $\sqrt{s} = 8$ TeV with the ATLAS detector," *JHEP*, vol. 11, p. 172, 2015. DOI: `10.1007/JHEP11(2015)172`. arXiv: `1509.05276 [hep-ex]`.

[514] G. Aad *et al.*, "Evidence for the Higgs boson decay to a Z boson and a photon at the LHC," ATLAS-CONF-2023-025,CERN-EP-2023-114, Sep. 2023. arXiv: `2309.03501 [hep-ex]`.

[515] A. M. Sirunyan *et al.*, "Evidence for Higgs boson decay to a pair of muons," *JHEP*, vol. 01, p. 148, 2021. DOI: `10.1007/JHEP01(2021)148`. arXiv: `2009.04363 [hep-ex]`.

[516] G. Aad *et al.*, "A search for the dimuon decay of the Standard Model Higgs boson with the ATLAS detector," *Phys. Lett. B*, vol. 812, p. 135 980, 2021. DOI: `10.1016/j.physletb.2020.135980`. arXiv: `2007.07830 [hep-ex]`.

[517] ATLAS Collaboration, "Extrapolation of ATLAS sensitivity to $H \to b\bar{b}$ and $H \to c\bar{c}$ decays in VH production at the HL-LHC," CERN, ATL-PHYS-PUB-2021-039, Oct. 2021. `http://cds.cern.ch/record/2788490`.

[518] J. R. Andersen *et al.*, "Les Houches 2015: Physics at TeV Colliders Standard Model Working Group Report," in *9th Les Houches Workshop on Physics at TeV Colliders*, May 2016. arXiv: `1605.04692 [hep-ph]`.

[519] CMS Collaboration, "Combined Higgs boson production and decay measurements with up to 137 fb^{-1} of proton-proton collision data at $\sqrt{s} = 14$ TeV," CERN, CMS-PAS-HIG-19-005, 2020. `https://cds.cern.ch/record/2706103`.

[520] ATLAS Collaboration, "Interpretations of the ATLAS measurements of Higgs boson production and decay rates and differential cross-sections in pp collisions at $\sqrt{s} = 13$ TeV," ATLAS-CONF-2023-052, Sep. 2023. `https://cds.cern.ch/record/2870216`.

[521] CMS Collaboration, "Summary of Run-2 κ_λ and κ_{2V} measurements from HH production," Mar. 2023. `https://twiki.cern.ch/twiki/bin/view/CMSPublic/SummaryResultsHIG#Summary_of_Run_2_kappa_lambda_an`.

[522] G. Aad *et al.* [incl. G. Pásztor], “Search for WH production with a light Higgs boson decaying to prompt electron-jets in proton-proton collisions at $\sqrt{s}$=7 TeV with the ATLAS detector,” *New J. Phys.*, vol. 15, p. 043 009, 2013. DOI: `10.1088/1367-2630/15/4/043009`. arXiv: `1302.4403 [hep-ex]`.

[523] G. Pásztor, “Recent ATLAS results and preparations for Run 2,” in *22nd International Workshop on High Energy Physics and Quantum Field Theory (QFTHEP2015)*, Feb. 2016. arXiv: `1602.01536 [hep-ex]`.

[524] G. Pásztor, “Electroweak measurements with the CMS experiment,” in *52nd Rencontres de Moriond on QCD and High Energy Interactions, La Thuile, Italy, 25 Mar - 1 Apr 2017*, E. Auge, J. Dumarchez, and J. Tran Thanh Van, Eds., ARISF, Jun. 2017, pp. 43–46. `https://cds.cern.ch/record/2268199`.

[525] G. Pásztor, “Hard QCD Measurements at the LHC,” in *28th International Symposium on Lepton Photon Interactions at High Energies (LP17): Guangzhou (Guangdong), China, August 7-12, 2017*, Singapur: WSP, 2020, pp. 221–240. DOI: `10.1142/9789811207402_0015`. `https://cds.cern.ch/record/2313534`.

[526] G. Pásztor, “Precision tests of the Standard Model at the LHC with the ATLAS and CMS detectors,” *PoS*, vol. FFK2019, p. 005, 2020. DOI: `10.22323/1.353.0005`.

[527] G. Aad *et al.* [incl. G. Pásztor], “Measurement of the high-mass Drell–Yan differential cross-section in pp collisions at $\sqrt{s} = 7$ TeV with the ATLAS detector,” *Phys. Lett. B*, vol. 725, pp. 223–242, 2013. DOI: `10.1016/j.physletb.2013.07.049`. arXiv: `1305.4192 [hep-ex]`.

[528] G. Aad *et al.* [incl. G. Pásztor], “Search for high-mass resonances decaying to dilepton final states in pp collisions at $\sqrt{s} = 7$ TeV with the ATLAS detector,” *JHEP*, vol. 11, p. 138, 2012. DOI: `10.1007/JHEP11(2012)138`. arXiv: `1209.2535 [hep-ex]`.

[529] G. Aad *et al.* [incl. G. Pásztor], “Measurements of Wγ and Zγ production in pp collisions at $\sqrt{s}$=7 TeV with the ATLAS detector at the LHC,” *Phys. Rev. D*, vol. 87, no. 11, p. 112 003, 2013, [Erratum: Phys.Rev.D 91, 119901 (2015)]. DOI: `10.1103/PhysRevD.87.112003`. arXiv: `1302.1283 [hep-ex]`.

[530] A. M. Sirunyan *et al.* [incl. G. Pásztor], “Measurement of differential cross sections for Z boson pair production in association with jets at $\sqrt{s} = 8$ and 13 TeV,” *Phys. Lett. B*, vol. 789, pp. 19–44, 2019. DOI: `10.1016/j.physletb.2018.11.007`. arXiv: `1806.11073 [hep-ex]`.

[531] A. M. Sirunyan *et al.* [incl. G. Pásztor], “Measurement of vector boson scattering and constraints on anomalous quartic couplings from events with four leptons and two jets in proton–proton collisions at $\sqrt{s} = 13$ TeV,” *Phys. Lett. B*, vol. 774, pp. 682–705, 2017. DOI: `10.1016/j.physletb.2017.10.020`. arXiv: `1708.02812 [hep-ex]`.

[532] A. M. Sirunyan *et al.* [incl. G. Pásztor], “Evidence for electroweak production of four charged leptons and two jets in proton-proton collisions at $\sqrt{s} = 13$ TeV,” *Phys. Lett. B*, vol. 812, p. 135 992, 2021. DOI: `10.1016/j.physletb.2020.135992`. arXiv: `2008.07013 [hep-ex]`.

[533] A. Tumasyan *et al.* [incl. G. Pásztor], “Observation of electroweak W+W− pair production in association with two jets in proton-proton collisions at s=13TeV,” *Phys. Lett. B*, vol. 841, p. 137 495, 2023. DOI: `10.1016/j.physletb.2022.137495`. arXiv: `2205.05711 [hep-ex]`.

[534] A. M. Sirunyan *et al.* [incl. G. Pásztor], "Observation of electroweak production of Wγ with two jets in proton-proton collisions at $\sqrt{s} = 13$ TeV," *Phys. Lett. B*, vol. 811, p. 135 988, 2020. DOI: `10.1016/j.physletb.2020.135988`. arXiv: `2008.10521 [hep-ex]`.

[535] A. Tumasyan *et al.*, "Measurement of the electroweak production of Wγ in association with two jets in proton-proton collisions at $\sqrt{s} = 13$ TeV," *Phys. Rev. D*, vol. 108, no. 3, p. 032 017, 2023. DOI: `10.1103/PhysRevD.108.032017`. arXiv: `2212.12592 [hep-ex]`.

[536] A. Tumasyan *et al.* [incl. G. Pásztor], "Search for heavy resonances decaying to Z($\nu\bar{\nu}$)V(q$\bar{q}$') in proton-proton collisions at $\sqrt{s} = 13$ TeV," CMS-B2G-20-008,CERN-EP-2021-158, 2022, p. 012 004. DOI: `10.1103/PhysRevD.106.012004`. arXiv: `2109.08268 [hep-ex]`.

[537] A. M. Sirunyan *et al.* [incl. G. Pásztor], "Search for top squark production in fully-hadronic final states in proton-proton collisions at $\sqrt{s} = 13$ TeV," *Phys. Rev. D*, vol. 104, no. 5, p. 052 001, 2021. DOI: `10.1103/PhysRevD.104.052001`. arXiv: `2103.01290 [hep-ex]`.

[538] A. M. Sirunyan *et al.* [incl. G. Pásztor], "Search for supersymmetry with a compressed mass spectrum in the vector boson fusion topology with 1-lepton and 0-lepton final states in proton-proton collisions at $\sqrt{s} = 13$ TeV," *JHEP*, vol. 08, p. 150, 2019. DOI: `10.1007/JHEP08(2019)150`. arXiv: `1905.13059 [hep-ex]`.

[539] J. Baglio, C. Duhr, B. Mistlberger, and R. Szafron, "Inclusive production cross sections at N^{3}LO," *JHEP*, vol. 12, p. 066, 2022. DOI: `10.1007/JHEP12(2022)066`. arXiv: `2209.06138 [hep-ph]`.

[540] CMS Collaboration, "W and Z cross-section measurements as a function of center-of-mass energy," Aug. 2023, See also the references given on the figure. `https://twiki.cern.ch/twiki/bin/view/CMSPublic/PhysicsResultsCombined#W_and_Z_cross_section_measuremen`.

[541] G. Aad *et al.* [incl. G. Pásztor], "Measurement of the angular coefficients in Z-boson events using electron and muon pairs from data taken at $\sqrt{s} = 8$ TeV with the ATLAS detector," *JHEP*, vol. 08, p. 159, 2016. DOI: `10.1007/JHEP08(2016)159`. arXiv: `1606.00689 [hep-ex]`.

[542] M. Aaboud *et al.*, "Measurement of the W-boson mass in pp collisions at $\sqrt{s} = 7$ TeV with the ATLAS detector," *Eur. Phys. J. C*, vol. 78, no. 2, p. 110, 2018, [Erratum: Eur.Phys.J.C 78, 898 (2018)]. DOI: `10.1140/epjc/s10052-017-5475-4`. arXiv: `1701.07240 [hep-ex]`.

[543] ATLAS Collaboration, "Improved W boson Mass Measurement using 7 TeV Proton-Proton Collisions with the ATLAS Detector," CERN, ATLAS-CONF-2023-004, 2023. `https://cds.cern.ch/record/2853290`.

[544] K. Melnikov and F. Petriello, "Electroweak gauge boson production at hadron colliders through $O(\alpha_s^2)$," *Phys. Rev. D*, vol. 74, p. 114 017, 2006. DOI: `10.1103/PhysRevD.74.114017`. arXiv: `hep-ph/0609070`.

[545] Y. Li and F. Petriello, "Combining QCD and electroweak corrections to dilepton production in FEWZ," *Phys. Rev. D*, vol. 86, p. 094 034, 2012. DOI: `10.1103/PhysRevD.86.094034`. arXiv: `1208.5967 [hep-ph]`.

[546] A. Sherstnev and R. S. Thorne, "Different PDF approximations useful for LO Monte Carlo generators," in *16th International Workshop on Deep Inelastic Scattering and Related Subjects*, Jul. 2008, p. 149. DOI: `10.3360/dis.2008.149`. arXiv: `0807.2132 [hep-ph]`.

[547] S. Frixione and B. R. Webber, "Matching NLO QCD computations and parton shower simulations," *JHEP*, vol. 06, p. 029, 2002. DOI: `10.1088/1126-6708/2002/06/029`. arXiv: `hep-ph/0204244`.

[548] H.-L. Lai, M. Guzzi, J. Huston, Z. Li, P. M. Nadolsky, J. Pumplin, and C. .-P. Yuan, "New parton distributions for collider physics," *Phys. Rev. D*, vol. 82, p. 074 024, 2010. DOI: `10.1103/PhysRevD.82.074024`. arXiv: `1007.2241 [hep-ph]`.

[549] A. D. Martin, R. G. Roberts, W. J. Stirling, and R. S. Thorne, "Parton distributions incorporating QED contributions," *Eur. Phys. J. C*, vol. 39, pp. 155–161, 2005. DOI: `10.1140/epjc/s2004-02088-7`. arXiv: `hep-ph/0411040`.

[550] J. Alwall, M. Herquet, F. Maltoni, O. Mattelaer, and T. Stelzer, "MadGraph 5: Going Beyond," *JHEP*, vol. 06, p. 128, 2011. DOI: `10.1007/JHEP06(2011)128`. arXiv: `1106.0522 [hep-ph]`.

[551] S. Alekhin, J. Blumlein, and S. Moch, "Parton Distribution Functions and Benchmark Cross Sections at NNLO," *Phys. Rev. D*, vol. 86, p. 054 009, 2012. DOI: `10.1103/PhysRevD.86.054009`. arXiv: `1202.2281 [hep-ph]`.

[552] R. D. Ball *et al.*, "Parton distributions with LHC data," *Nucl. Phys. B*, vol. 867, pp. 244–289, 2013. DOI: `10.1016/j.nuclphysb.2012.10.003`. arXiv: `1207.1303 [hep-ph]`.

[553] A. D. Martin, W. J. Stirling, R. S. Thorne, and G. Watt, "Parton distributions for the LHC," *Eur. Phys. J. C*, vol. 63, pp. 189–285, 2009. DOI: `10.1140/epjc/s10052-009-1072-5`. arXiv: `0901.0002 [hep-ph]`.

[554] V. Khachatryan *et al.*, "Measurements of differential and double-differential Drell-Yan cross sections in proton-proton collisions at 8 TeV," *Eur. Phys. J. C*, vol. 75, no. 4, p. 147, 2015. DOI: `10.1140/epjc/s10052-015-3364-2`. arXiv: `1412.1115 [hep-ex]`.

[555] G. Aad *et al.*, "Measurement of the double-differential high-mass Drell-Yan cross section in pp collisions at $\sqrt{s} = 8$ TeV with the ATLAS detector," *JHEP*, vol. 08, p. 009, 2016. DOI: `10.1007/JHEP08(2016)009`. arXiv: `1606.01736 [hep-ex]`.

[556] P. Langacker, "The Physics of Heavy Z' Gauge Bosons," *Rev. Mod. Phys.*, vol. 81, pp. 1199–1228, 2009. DOI: `10.1103/RevModPhys.81.1199`. arXiv: `0801.1345 [hep-ph]`.

[557] D. London and J. L. Rosner, "Extra Gauge Bosons in E(6)," *Phys. Rev. D*, vol. 34, p. 1530, 1986. DOI: `10.1103/PhysRevD.34.1530`.

[558] G. Senjanovic and R. N. Mohapatra, "Exact Left-Right Symmetry and Spontaneous Violation of Parity," *Phys. Rev. D*, vol. 12, p. 1502, 1975. DOI: `10.1103/PhysRevD.12.1502`.

[559] R. N. Mohapatra and J. C. Pati, "Left-Right Gauge Symmetry and an Isoconjugate Model of CP Violation," *Phys. Rev. D*, vol. 11, pp. 566–571, 1975. DOI: `10.1103/PhysRevD.11.566`.

[560] E. Salvioni, G. Villadoro, and F. Zwirner, "Minimal Z-prime models: Present bounds and early LHC reach," *JHEP*, vol. 11, p. 068, 2009. DOI: `10.1088/1126-6708/2009/11/068`. arXiv: `0909.1320 [hep-ph]`.

[561] L. Basso, "Phenomenology of the minimal B-L extension of the Standard Model at the LHC," PhD. dissertation, Southampton U., 2011. arXiv: `1106.4462 [hep-ph]`.

[562] I. Antoniadis, "A Possible new dimension at a few TeV," *Phys. Lett. B*, vol. 246, pp. 377–384, 1990. DOI: `10.1016/0370-2693(90)90617-F`.

[563] I. Antoniadis, K. Benakli, and M. Quiros, "Direct collider signatures of large extra dimensions," *Phys. Lett. B*, vol. 460, pp. 176–183, 1999. DOI: `10.1016/S0370-2693(99)00764-9`. arXiv: `hep-ph/9905311`.

[564] G. Bella, E. Etzion, N. Hod, Y. Oz, Y. Silver, and M. Sutton, "A Search for heavy Kaluza-Klein electroweak gauge bosons at the LHC," *JHEP*, vol. 09, p. 025, 2010. DOI: `10.1007/JHEP09(2010)025`. arXiv: `1004.2432 [hep-ex]`.

[565] T. G. Rizzo, "Testing the nature of Kaluza-Klein excitations at future lepton colliders," *Phys. Rev. D*, vol. 61, p. 055 005, 2000. DOI: `10.1103/PhysRevD.61.055005`. arXiv: `hep-ph/9909232`.

[566] K. D. Lane, "Technihadron production and decay in low scale technicolor," *Phys. Rev. D*, vol. 60, p. 075 007, 1999. DOI: `10.1103/PhysRevD.60.075007`. arXiv: `hep-ph/9903369`.

[567] K. Lane and S. Mrenna, "The Collider Phenomenology of Technihadrons in the Technicolor Straw Man Model," *Phys. Rev. D*, vol. 67, p. 115 011, 2003. DOI: `10.1103/PhysRevD.67.115011`. arXiv: `hep-ph/0210299`.

[568] E. Eichten and K. Lane, "Low-scale technicolor at the Tevatron and LHC," *Phys. Lett. B*, vol. 669, pp. 235–238, 2008. DOI: `10.1016/j.physletb.2008.09.047`. arXiv: `0706.2339 [hep-ph]`.

[569] I. L. Shapiro, "Physical aspects of the space-time torsion," *Phys. Rept.*, vol. 357, p. 113, 2002. DOI: `10.1016/S0370-1573(01)00030-8`. arXiv: `hep-th/0103093`.

[570] A. S. Belyaev, I. L. Shapiro, and M. A. B. do Vale, "Torsion phenomenology at the LHC," *Phys. Rev. D*, vol. 75, p. 034 014, 2007. DOI: `10.1103/PhysRevD.75.034014`. arXiv: `hep-ph/0701002`.

[571] F. M. L. de Almeida Jr., A. A. Nepomuceno, and M. A. B. do Vale, "Torsion Discovery Potential and Its Discrimination at CERN LHC," *Phys. Rev. D*, vol. 79, p. 014 029, 2009. DOI: `10.1103/PhysRevD.79.014029`. arXiv: `0811.0291 [hep-ph]`.

[572] G. Aad *et al.*, "Search for high-mass dilepton resonances using 139 fb^{-1} of pp collision data collected at $\sqrt{s}$ =13 TeV with the ATLAS detector," *Phys. Lett. B*, vol. 796, pp. 68–87, 2019. DOI: `10.1016/j.physletb.2019.07.016`. arXiv: `1903.06248 [hep-ex]`.

[573] A. M. Sirunyan *et al.*, "Search for resonant and nonresonant new phenomena in high-mass dilepton final states at $\sqrt{s} = 13$ TeV," *JHEP*, vol. 07, p. 208, 2021. DOI: `10.1007/JHEP07(2021)208`. arXiv: `2103.02708 [hep-ex]`.

[574] R. S. Chivukula, M. J. Dugan, and M. Golden, "Analyticity, crossing symmetry and the limits of chiral perturbation theory," *Phys. Rev. D*, vol. 47, pp. 2930–2939, 1993. DOI: `10.1103/PhysRevD.47.2930`. arXiv: `hep-ph/9206222`.

[575] S. Chatrchyan *et al.*, "Measurement of the $W\gamma$ and $Z\gamma$ Inclusive Cross Sections in pp Collisions at $\sqrt{s} = 7$ TeV and Limits on Anomalous Triple Gauge Boson Couplings," *Phys. Rev. D*, vol. 89, no. 9, p. 092 005, 2014. DOI: `10.1103/PhysRevD.89.092005`. arXiv: `1308.6832 [hep-ex]`.

[576] A. Tumasyan *et al.*, “Measurement of $W^{\pm}\gamma$ differential cross sections in proton-proton collisions at $\sqrt{s} = 13$ TeV and effective field theory constraints,” *Phys. Rev. D*, vol. 105, no. 5, p. 052 003, 2022. DOI: `10.1103/PhysRevD.105.052003`. arXiv: `2111.13948 [hep-ex]`.

[577] G. Aad *et al.*, “Measurements of $Z\gamma$+jets differential cross sections in *pp* collisions at $\sqrt{s} = 13$ TeV with the ATLAS detector,” *JHEP*, vol. 07, p. 072, 2023. DOI: `10.1007/JHEP07(2023)072`. arXiv: `2212.07184 [hep-ex]`.

[578] J. M. Campbell and R. K. Ellis, “MCFM for the Tevatron and the LHC,” *Nucl. Phys. B Proc. Suppl.*, vol. 205-206, J. Blümlein, S.-O. Moch, and T. Riemann, Eds., pp. 10–15, 2010. DOI: `10.1016/j.nuclphysbps.2010.08.011`. arXiv: `1007.3492 [hep-ph]`.

[579] J. M. Campbell, R. K. Ellis, and C. Williams, “Vector boson pair production at the LHC,” *JHEP*, vol. 07, p. 018, 2011. DOI: `10.1007/JHEP07(2011)018`. arXiv: `1105.0020 [hep-ph]`.

[580] ATLAS Collaboration, “Standard Model Summary Plots February 2022,” ATL-PHYS-PUB-2022-009, Feb. 2022. `https://atlas.web.cern.ch/Atlas/GROUPS/PHYSICS/PUBNOTES/ATL-PHYS-PUB-2022-009`.

[581] A. M. Sirunyan *et al.*, “Measurement of the Wγ Production Cross Section in Proton-Proton Collisions at $\sqrt{s}$=13 TeV and Constraints on Effective Field Theory Coefficients,” *Phys. Rev. Lett.*, vol. 126, no. 25, p. 252 002, 2021. DOI: `10.1103/PhysRevLett.126.252002`. arXiv: `2102.02283 [hep-ex]`.

[582] CMS Collaboration, “Limits on anomalous triple and quartic gauge couplings,” Aug. 2023, See also references therein. `https://twiki.cern.ch/twiki/bin/view/CMSPublic/PhysicsResultsSMPaTGC`.

[583] D. D. Dietrich, F. Sannino, and K. Tuominen, “Light composite Higgs from higher representations versus electroweak precision measurements: Predictions for CERN LHC,” *Phys. Rev. D*, vol. 72, p. 055 001, 2005. DOI: `10.1103/PhysRevD.72.055001`. arXiv: `hep-ph/0505059`.

[584] E. Eichten, K. Lane, and A. Martin, “A Higgs Impostor in Low-Scale Technicolor,” FERMILAB-PUB-12-573-T,CERN-PH-TH-2012-273, Oct. 2012. arXiv: `1210.5462 [hep-ph]`.

[585] R. Foadi, M. T. Frandsen, and F. Sannino, “125 GeV Higgs boson from a not so light technicolor scalar,” *Phys. Rev. D*, vol. 87, no. 9, p. 095 001, 2013. DOI: `10.1103/PhysRevD.87.095001`. arXiv: `1211.1083 [hep-ph]`.

[586] M. Grazzini, S. Kallweit, and M. Wiesemann, “Fully differential NNLO computations with MATRIX,” *Eur. Phys. J. C*, vol. 78, no. 7, p. 537, 2018. DOI: `10.1140/epjc/s10052-018-5771-7`. arXiv: `1711.06631 [hep-ph]`.

[587] A. Tumasyan *et al.*, “Measurements of the electroweak diboson production cross sections in proton-proton collisions at $\sqrt{s} = 5.02$ TeV using leptonic decays,” *Phys. Rev. Lett.*, vol. 127, no. 19, p. 191 801, 2021. DOI: `10.1103/PhysRevLett.127.191801`. arXiv: `2107.01137 [hep-ex]`.

[588] M. Grazzini, S. Kallweit, J. M. Lindert, S. Pozzorini, and M. Wiesemann, “NNLO QCD + NLO EW with Matrix+OpenLoops: precise predictions for vector-boson pair production,” *JHEP*, vol. 02, p. 087, 2020. DOI: `10.1007/JHEP02(2020)087`. arXiv: `1912.00068 [hep-ph]`.

[589] J. Alwall *et al.*, “Comparative study of various algorithms for the merging of parton showers and matrix elements in hadronic collisions,” *Eur. Phys. J. C*, vol. 53, pp. 473–500, 2008. DOI: `10.1140/epjc/s10052-007-0490-5`. arXiv: `0706.2569 [hep-ph]`.

[590] R. Frederix and S. Frixione, “Merging meets matching in MC@NLO,” *JHEP*, vol. 12, p. 061, 2012. DOI: `10.1007/JHEP12(2012)061`. arXiv: `1209.6215 [hep-ph]`.

[591] P. Nason, “A New method for combining NLO QCD with shower Monte Carlo algorithms,” *JHEP*, vol. 11, p. 040, 2004. DOI: `10.1088/1126-6708/2004/11/040`. arXiv: `hep-ph/0409146`.

[592] T. Melia, P. Nason, R. Rontsch, and G. Zanderighi, “W+W-, WZ and ZZ production in the POWHEG BOX,” *JHEP*, vol. 11, p. 078, 2011. DOI: `10.1007/JHEP11(2011)078`. arXiv: `1107.5051 [hep-ph]`.

[593] F. Cascioli, T. Gehrmann, M. Grazzini, S. Kallweit, P. Maierhöfer, A. von Manteuffel, S. Pozzorini, D. Rathlev, L. Tancredi, and E. Weihs, “ZZ production at hadron colliders in NNLO QCD,” *Phys. Lett. B*, vol. 735, pp. 311–313, 2014. DOI: `10.1016/j.physletb.2014.06.056`. arXiv: `1405.2219 [hep-ph]`.

[594] F. Caola, K. Melnikov, R. Röntsch, and L. Tancredi, “QCD corrections to ZZ production in gluon fusion at the LHC,” *Phys. Rev. D*, vol. 92, no. 9, p. 094 028, 2015. DOI: `10.1103/PhysRevD.92.094028`. arXiv: `1509.06734 [hep-ph]`.

[595] A. Ballestrero, A. Belhouari, G. Bevilacqua, V. Kashkan, and E. Maina, “PHANTOM: A Monte Carlo event generator for six parton final states at high energy colliders,” *Comput. Phys. Commun.*, vol. 180, pp. 401–417, 2009. DOI: `10.1016/j.cpc.2008.10.005`. arXiv: `0801.3359 [hep-ph]`.

[596] V. Khachatryan *et al.*, “Measurement of the $pp \to ZZ$ Production Cross Section and Constraints on Anomalous Triple Gauge Couplings in Four-Lepton Final States at $\sqrt{s} = 8$ TeV,” *Phys. Lett. B*, vol. 740, pp. 250–272, 2015, [Erratum: Phys.Lett.B 757, 569–569 (2016)]. DOI: `10.1016/j.physletb.2016.04.010`. arXiv: `1406.0113 [hep-ex]`.

[597] A. M. Sirunyan *et al.*, “Measurements of the pp → ZZ production cross section and the Z → 4ℓ branching fraction, and constraints on anomalous triple gauge couplings at $\sqrt{s} = 13\,\mathrm{TeV}$,” *Eur. Phys. J. C*, vol. 78, p. 165, 2018, [Erratum: Eur.Phys.J.C 78, 515 (2018)]. DOI: `10.1140/epjc/s10052-018-5567-9`. arXiv: `1709.08601 [hep-ex]`.

[598] CMS Collaboration, “Measurement of the differential ZZ+jets production cross sections in pp collisions at $\sqrt{s} = 13$ TeV,” CERN, CMS-PAS-SMP-22-001, 2023. `https://cds.cern.ch/record/2859350`.

[599] L. Buonocore, G. Koole, D. Lombardi, L. Rottoli, M. Wiesemann, and G. Zanderighi, “ZZ production at nNNLO+PS with MiNNLO$_{PS}$,” *JHEP*, vol. 01, p. 072, 2022. DOI: `10.1007/JHEP01(2022)072`. arXiv: `2108.05337 [hep-ph]`.

[600] L. Breiman, J. Friedman, C. Stone, and R. Olshen, *Classification and Regression Trees.* Taylor & Francis, 1984, ISBN: 9780412048418. `https://books.google.hu/books?id=JwQx-WOmSyQC`.

[601] G. Aad *et al.*, “Observation of electroweak production of two jets and a Z-boson pair,” *Nature Phys.*, vol. 19, no. 2, pp. 237–253, 2023. DOI: `10.1038/s41567-022-01757-y`. arXiv: `2004.10612 [hep-ex]`.

[602] CMS Collaboration, "Summaries of CMS cross section measurements," 2023 August version. `https://twiki.cern.ch/twiki/bin/view/CMSPublic/PhysicsResultsCombined`.

[603] A. M. Sirunyan *et al.*, "Observation of electroweak production of same-sign W boson pairs in the two jet and two same-sign lepton final state in proton-proton collisions at $\sqrt{s} = 13$ TeV," *Phys. Rev. Lett.*, vol. 120, no. 8, p. 081801, 2018. DOI: `10.1103/PhysRevLett.120.081801`. arXiv: `1709.05822 [hep-ex]`.

[604] M. Aaboud *et al.*, "Observation of electroweak production of a same-sign W boson pair in association with two jets in pp collisions at $\sqrt{s} = 13$ TeV with the ATLAS detector," *Phys. Rev. Lett.*, vol. 123, no. 16, p. 161801, 2019. DOI: `10.1103/PhysRevLett.123.161801`. arXiv: `1906.03203 [hep-ex]`.

[605] A. M. Sirunyan *et al.*, "Measurements of production cross sections of polarized same-sign W boson pairs in association with two jets in proton-proton collisions at $\sqrt{s} = 13$ TeV," *Phys. Lett. B*, vol. 812, p. 136018, 2021. DOI: `10.1016/j.physletb.2020.136018`. arXiv: `2009.09429 [hep-ex]`.

[606] ATLAS Collaboration, "Differential cross-section measurements of the production of four charged leptons in association with two jets using the ATLAS detector," ATLAS-CONF-2023-024, May 2023. `https://cds.cern.ch/record/2859349`.

[607] A. Tumasyan *et al.*, "Evidence for WW/WZ vector boson scattering in the decay channel $\ell\nu$qq produced in association with two jets in proton-proton collisions at s=13 TeV," *Phys. Lett. B*, vol. 834, p. 137438, 2022. DOI: `10.1016/j.physletb.2022.137438`. arXiv: `2112.05259 [hep-ex]`.

[608] ATLAS Collaboration, "Measurement and interpretation of same-sign W boson pair production in association with two jets in pp collisions at $\sqrt{s} = 13$ TeV with the ATLAS detector," ATLAS-CONF-2023-023, May 2023. `https://cds.cern.ch/record/2859330`.

[609] A. M. Sirunyan *et al.*, "Measurements of production cross sections of WZ and same-sign WW boson pairs in association with two jets in proton-proton collisions at $\sqrt{s} = 13$ TeV," *Phys. Lett. B*, vol. 809, p. 135710, 2020. DOI: `10.1016/j.physletb.2020.135710`. arXiv: `2005.01173 [hep-ex]`.

[610] G. Aad *et al.*, "Differential cross-section measurements of the production of four charged leptons in association with two jets using the ATLAS detector," CERN-EP-2023-152, Aug. 2023. arXiv: `2308.12324 [hep-ex]`.

[611] J. Baglio *et al.* [incl. G. Pásztor], "VBSCan Mid-Term Scientific Meeting," in *VBSCan Mid-Term Scientific Meeting*, Apr. 2020. arXiv: `2004.00726 [hep-ph]`.

[612] A. Tumasyan *et al.*, "Measurement of the electroweak production of Zγ and two jets in proton-proton collisions at $\sqrt{s} = 13$ TeV and constraints on anomalous quartic gauge couplings," *Phys. Rev. D*, vol. 104, p. 072001, 2021. DOI: `10.1103/PhysRevD.104.072001`. arXiv: `2106.11082 [hep-ex]`.

[613] A. Tumasyan *et al.*, "Measurements of the pp $\rightarrow$ W$^{\pm}\gamma\gamma$ and pp $\rightarrow$ Z$\gamma\gamma$ cross sections at $\sqrt{s} = 13$ TeV and limits on anomalous quartic gauge couplings," *JHEP*, vol. 10, p. 174, 2021. DOI: `10.1007/JHEP10(2021)174`. arXiv: `2105.12780 [hep-ex]`.

[614] G. Perez, M. Sekulla, and D. Zeppenfeld, “Anomalous quartic gauge couplings and unitarization for the vector boson scattering process $pp \to W^+W^+jjX \to \ell^+\nu_\ell\ell^+\nu_\ell jjX$,” *Eur. Phys. J. C*, vol. 78, no. 9, p. 759, 2018. DOI: `10.1140/epjc/s10052-018-6230-1`. arXiv: `1807.02707 [hep-ph]`.

[615] D. Buttazzo, G. Degrassi, P. P. Giardino, G. F. Giudice, F. Sala, A. Salvio, and A. Strumia, “Investigating the near-criticality of the Higgs boson,” *JHEP*, vol. 12, p. 089, 2013. DOI: `10.1007/JHEP12(2013)089`. arXiv: `1307.3536 [hep-ph]`.

[616] ATLAS Collaboration, “SUSY Summary Plot Update June 2021,” ATL-PHYS-PUB-2021-019, Jun. 2021. `https://atlas.web.cern.ch/Atlas/GROUPS/PHYSICS/PUBNOTES/ATL-PHYS-PUB-2021-019`.

[617] CMS Collaboration, “CMS Supersymmetry Physics Results: Run 2 Summary plots – 13 TeV,” Apr. 2021. `https://twiki.cern.ch/twiki/bin/view/CMSPublic/PhysicsResultsSUS#Run_2_Summary_plots_13_TeV`.

[618] CMS Collaboration, “CMS summary on gluino pair production,” Mar. 2021. `https://twiki.cern.ch/twiki/pub/CMSPublic/PhysicsResultsSUS/T1tttt_limits_summary_cms.png`.

[619] CMS Collaboration, “CMS summary on top squark pair production,” Mar. 2021. `https://twiki.cern.ch/twiki/pub/CMSPublic/PhysicsResultsSUS/T2tt_limits_summary_cms.png`.

[620] A. Pierce, N. R. Shah, and S. Vogl, “Stop Co-Annihilation in the Minimal Supersymmetric Standard Model Revisited,” *Phys. Rev. D*, vol. 97, no. 2, p. 023 008, 2018. DOI: `10.1103/PhysRevD.97.023008`. arXiv: `1706.01911 [hep-ph]`.

[621] C. Wymant, “Optimising Stop Naturalness,” *Phys. Rev.*, vol. D86, p. 115 023, 2012. DOI: `10.1103/PhysRevD.86.115023`. arXiv: `1208.1737 [hep-ph]`.

[622] R. Gröber, M. M. Mühlleitner, E. Popenda, and A. Wlotzka, “Light Stop Decays: Implications for LHC Searches,” *Eur. Phys. J.*, vol. C75, p. 420, 2015. DOI: `10.1140/epjc/s10052-015-3626-z`. arXiv: `1408.4662 [hep-ph]`.

[623] J. Ellis, J. L. Evans, F. Luo, K. A. Olive, and J. Zheng, “Stop Coannihilation in the CMSSM and SubGUT Models,” *Eur. Phys. J.*, vol. C78, no. 5, p. 425, 2018. DOI: `10.1140/epjc/s10052-018-5831-z`. arXiv: `1801.09855 [hep-ph]`.

[624] G. Belanger, D. Ghosh, R. Godbole, and S. Kulkarni, “Light stop in the MSSM after LHC Run 1,” *JHEP*, vol. 09, p. 214, 2015. DOI: `10.1007/JHEP09(2015)214`. arXiv: `1506.00665 [hep-ph]`.

[625] P. Athron *et al.*, “A global fit of the MSSM with GAMBIT,” *Eur. Phys. J.*, vol. C77, no. 12, p. 879, 2017. DOI: `10.1140/epjc/s10052-017-5196-8`. arXiv: `1705.07917 [hep-ph]`.

[626] M. Benedikt and F. Zimmermann, “The physics and technology of the Future Circular Collider,” *Nature Rev. Phys.*, vol. 1, pp. 238–240, 2019. DOI: `10.1038/s42254-019-0048-0`.